NASA Conference Publication 10066
Part 1

Aerospace Applications of Magnetic Suspension Technology

(NASA-CP-10066-Pt-1) AEROSPACE APPLICATIONS N91-21188
OF MAGNETIC SUSPENSION TECHNOLOGY, PART 1 --THRU--
(NASA) 377 p CSCL 22B N91-21202
Unclas
G3/18 0007564

Edited by
Nelson J. Groom
Langley Research Center
Hampton, Virginia

Colin P. Britcher
Old Dominion University Research Foundation
Norfolk, Virginia

Proceedings of a workshop held at
NASA Langley Research Center
Hampton, Virginia
September 25–27, 1990

MARCH 1991

NASA
National Aeronautics and
Space Administration

Langley Research Center
Hampton, Virginia 23665-5225

CONTENTS

Part 1

INTRODUCTION vii

TECHNICAL PROGRAM (*presenters indicated in Italics*)

Session 2 - Pointing and Isolation Systems

Chairman - Claude R. Keckler, NASA Langley Research Center

1. MAGNETIC SUSPENSION SYSTEMS for SPACE APPLICATIONS 1
D.G. Havenhill, *P.J. Wolke*, Honeywell Inc.

2. ADVANCED MAGNETIC SUSPENSIONS for VIBRATION ISOLATION and FAST-ATTITUDE CONTROL of SPACE-BASED GENERIC POINTING MOUNTS 27
R.W. Bosley, A.N. Trivedi, AiResearch-Los Angeles Division, Allied-Signal Corp

3. A SUPERCONDUCTING LARGE-ANGLE MAGNETIC SUSPENSION 57
J. Downer, J. Goldie, R. Torti, SatCon Technology Corporation

Session 3 - Microgravity and Vibration Isolation I

Chairman - Duncan C. McCallum, Charles Stark Draper Laboratory

4. CONTROL ISSUES of MICROGRAVITY VIBRATION ISOLATION 77
C.R. Knospe, R.D. Hampton, University of Virginia

5. SLIDING MODE CONTROL of MAGNETIC SUSPENSIONS for PRECISION POINTING and TRACKING APPLICATIONS 143
K.M. Misovec, F.J. Flynn, *B.G. Johnson*, SatCon Technology Corporation
J.K. Hedrick, University of California at Berkeley

Session 4 - Bearing Applications

Chairman - Patrick J. Wolke, Honeywell, Inc.

6. MAGNETIC BEARINGS with ZERO BIAS 165
G.V. Brown, C.M. Grodsinsky, NASA Lewis Research Center

7. MAGNETIC BEARINGS for a SPACEFLIGHT OPTICAL DISK RECORDER 183
R. Hockney, V.Gondhalekar, T. Hawkey, SatCon Technology Corporation

8. FIVE-DEGREE-of-FREEDOM CONTROL of an ULTRA-PRECISION MAGNETICALLY-SUSPENDED LINEAR BEARING 199
D.L. Trumper, University of North Carolina at Charlotte
A.H. Slocum, Cranfield Institute of Technology

Session 5 - Wind Tunnel Model Suspension Systems
Chairman - Robert A. Kilgore, NASA Langley Research Center

9. MAGNETIC SUSPENSION and BALANCE SYSTEM ADVANCED STUDY - 1989 DESIGN 225
R.W. Boom, Y.M. Eyssa, *M.K. Abdelsalam*, G.E. McIntosh
Madison Magnetics Incorporated.

10. PROPULSION SIMULATOR for MAGNETICALLY-SUSPENDED WIND TUNNEL MODELS 249
P.B. Joshi, C.L. Goldey, G.P. Sacco, Physical Sciences Inc.
P. Lawing, NASA Langley Research Center

11. A SOLID-STATE CONTROLLABLE POWER SUPPLY for a MAGNETIC SUSPENSION WIND TUNNEL 281
T.S. Daniels, J.S. Tripp, NASA Langley Research Center

Session 6 - Large Gap Magnetic Suspension Systems
Chairman - Sharon S. Welch, NASA Langley Research Center

12. DESCRIPTION of the LARGE-GAP MAGNETIC SUSPENSION SYSTEM (LGMSS) GROUND BASED EXPERIMENT 303
N.J. Groom, NASA Langley Research Center.

13. LARGE GAP MAGNETIC SUSPENSION SYSTEM 325
M.K. Abdelsalam, Y.M. Eyssa, Madison Magnetics Incorporated

14. STABILITY CONSIDERATIONS for MAGNETIC SUSPENSION SYSTEMS USING ELECTROMAGNETS MOUNTED in a PLANAR ARRAY 355

N.J. Groom, NASA Langley Research Center, *C.P. Britcher*, Old Dominion University

Part 2*

Session 7 - Controls

Chairman - James A. Downer, SatCon Corporation

15. NONLINEAR COMPENSATION TECHNIQUES for MAGNETIC SUSPENSION SYSTEMS 377

D.L. Trumper, University of North Carolina at Charlotte.

16. A TIME DELAY CONTROLLER for MAGNETIC BEARINGS 389

K. Youcef-Toumi, S. Reddy, Massachusetts Institute of Technology.

17. MICROGRAVITY VIBRATION ISOLATION: An OPTIMAL CONTROL LAW for the ONE-DIMENSIONAL CASE 413

R.D. Hampton, University of Virginia

C.M. Grodsinsky, NASA Lewis Research Center

P.E. Allaire, D.W. Lewis, C.R. Knospe, University of Virginia

18. MEASUREMENT and CALCULATION of FORCES in a MAGNETIC JOURNAL BEARING ACTUATOR 477

J. Knight, E. McCaul, Z. Xia, Duke University

Session 8 - Rotating Machinery

Chairman - Paul E. Allaire, University of Virginia

19. DYNAMIC MODELLING and ANALYSIS of a MAGNETICALLY SUSPENDED FLEXIBLE ROTOR 499

D.C. McCallum, Charles Stark Draper Laboratory

20. CRITICAL SPEEDS and FORCED RESPONSE SOLUTIONS for ACTIVE MAGNETIC BEARING TURBOMACHINERY, Part I 539

J. Keesee, D. Rawal, *R.G. Kirk*, Virginia Polytechnic Institute and State University

*Published under separate cover.

21. CRITICAL SPEEDS and FORCED RESPONSE SOLUTIONS for ACTIVE MAGNETIC BEARING TURBOMACHINERY, Part II 559

D. Rawal, J. Keesee, *R.G. Kirk*, Virginia Polytechnic Institute and State University

Session 9 - Science and Applications of Superconductivity

Chairman - Pierce L. Lawing, NASA Langley Research Center

22. REDUCTION in BEARING SIZE due to SUPERCONDUCTORS in MAGNETIC BEARINGS 583

D.K. Rao, P. Lewis, J.F. Dill, Mechanical Technology Incorporated

23. CHEMICAL SPRAY PYROLYSIS of Tl-Ba-Ca-Cu-O HIGH-T_c SUPERCONDUCTORS for HIGH-FIELD BITTER MAGNETS 607

L.P. de Rochemont, J.G. Zhang, M.R. Squillante, Radiation Monitoring Devices

A.M. Hermann, H.M. Duan, University of Colorado

R.J. Andrews, Rome Air Development Center

W.C. Kelliher, NASA Langley Research Center

Session 10 - PANEL DISCUSSION-Applications of Superconductivity

Chairman - Dantam K. Rao, Mechanical Technology Incorporated

Panel Members - G.V. Brown, NASA Lewis Research Center 629

M.K. Abdelsalam, Madison Magnetics Incorporated

D. Eisenhaure, SatCon Technology Incorporated

W. Kelliher, NASA Langley Research Center

Session 11 - Microgravity and Vibration Isolation II

Chairman - Colin P. Britcher, Old Dominion University

24. DEVELOPMENT and DESIGN of a MAGNETIC INERTIALLY REFERENCED ISOLATION SYSTEM for MICROGRAVITY EXPERIMENTATION 643

K. Logsdon, C.M. Grodsinsky, NASA Lewis Research Center

25. ACTIVE VIBRATION ISOLATION MOUNTS 655

H.M. Chen, R. Dorman, D. Wilson, Mechanical Technology Incorporated

presented by J. Hurley, MTI

26. VIBRATION ISOLATION of SCIENCE EXPERIMENTS in SPACE - DESIGN of a LABORATORY TEST SETUP 679

B.B. Banerjee, P.E. Allaire, C.R. Knospe, University of Virginia

Session 12 - Sensors

Chairman - Nelson J. Groom, NASA Langley Research Center

27. DEVELOPMENT of a SUITABLE INDUCTIVE SENSOR for MAGNETIC BEARINGS 705

D.P. Plant, FARE Incorporated

R.B. Zmood, Royal Melbourne Institute of Technology

J. A. Kirk, University of Maryland

28. The NEW ELECTRO-OPTICAL DISPLACEMENT MEASURING SYSTEM for the 13 inch MSBS 721

T.D. Schott, P. Tcheng, NASA Langley Research Center

29. The OPTICAL POSITION MEASUREMENT SYSTEM for a LARGE-GAP SUSPENSION SYSTEM (LGMSS) 731

S.S. Welch, NASA Langley Research Center

J.I. Clemmons Jr., Vigyan Research Associates

APPENDIX - LIST OF ATTENDEES 767

INTRODUCTION

Development of magnetic suspension technology for aerospace applications has significantly increased in recent years. These applications range from magnetic suspension of wind tunnel models to magnetic bearings for high speed rotating machinery such as momentum storage devices and combined control and energy storage devices for spacecraft. Traditionally there has been little or no interaction between researchers working in the area of large gap magnetic suspension and small gap magnetic suspension because of the sharp division between areas of application. However, recent requirements for spacecraft related applications have resulted in large gap technology being considered for applications which have normally been associated with small gap systems.

In order to examine the state of technology of all areas of magnetic suspension with potential aerospace applications, and to review related recent developments in sensors and controls approaches, superconducting magnet technology, and design/implementation practices, a three-day Workshop on Aerospace Applications of Magnetic Suspension Technology was held at the Langley Research Center in Hampton, Virginia, on September 25-27, 1990. The workshop was sponsored by the Langley Research Center in coordination with the Office of Aeronautics, Exploration, and Technology (OAET) in NASA Headquarters and was chaired by the following people:

Nelson J. Groom, Chairman
NASA Langley Research Center
Hampton, VA 23665-5225

Sharon S. Welch, Co-Chairman
NASA Langley Research Center
Hampton, VA 23665-5225

Dr. Colin P. Britcher, Technical Program Chairman
Dept. of Mechanical Engineering and Mechanics
Old Dominion University
Norfolk, VA 23508

Emily E. Kornegay, Administrative Chairman
NASA Langley Research Center
Hampton, VA 23665-5225

A total of 28 papers were presented covering the areas of pointing and isolation systems, microgravity and vibration isolation, bearing applications, wind tunnel model suspension systems, large gap magnetic suspension systems, controls, rotating machinery, science and applications of superconductivity, and sensors. In addition to the presentations, there was a panel discussion on applications of superconductivity. A list of attendees is presented in the Appendix.

PRECEDING PAGE BLANK NOT FILMED

N91-21189

MAGNETIC SUSPENSION SYSTEMS for SPACE APPLICATIONS

Douglas G. Havenhill, Patrick J. Wolke

Honeywell Incorporated

Satellite Systems Operations

19019 North 59th Avenue

Glendale

AZ 85308-9650

INTRODUCTION

History

For over 20 years Honeywell Inc., Satellite Systems Operations in Glendale, Arizona, has designed, built, and tested magnetic suspensions for bearing systems and for vibration isolation and precision pointing of spaceborne equipment. Starting in the 1970s, with the development of momentum wheel bearings and the Advanced Vernier System (AVS), Honeywell has designed, built, and tested systems ranging from magnetic bearings for a small optical scanner to a six-degree-of-freedom magnetic suspension that requires six 3200-Newton actuators to rapidly retarget a large optical telescope while maintaining precision isolation.

The magnetic actuator has evolved to a high-bandwidth, low-power, precision linear force device that can be optimally arranged in a system to provide better than 80 dB of isolation in all six degrees of freedom. The active control structure permits flexibility in configuring systems to support a wide variety of payloads and to tailor the responses of the system. As an example, systems have been built that isolate a payload in the translational degrees of freedom while precisely pointing and isolating it in the rotational degrees of freedom. Our broad range of experience makes Honeywell a leader in the spaceborne magnetic suspension field. This paper provides an overview of the techniques used in our magnetic suspension systems and a review of the systems already developed, which demonstrate the usefulness, applicability, and flight readiness of magnetic suspension to a broad range of payloads and environments.

Programs

Table 1 provides a brief synopsis of selected magnetic isolation and pointing system programs that have been worked at Honeywell. The AVS, developed for the National Aeronautics and Space Administration (NASA) Langley Research Center (LaRC), demonstrated 0.03-arc-second pointing stability in the presence of simulated Shuttle reaction jet disturbances.

The Annular Suspension and Pointing System (ASPS), shown in Figure 1, was the first major magnetic isolation and pointing system developed for spaceborne payloads by Honeywell Inc., Satellite Systems Operations. The ASPS is composed of a two-axis course gimbal system, known as the Advanced Gimbal System (AGS), and the magnetic pointing and isolation system, known as the Advanced Vernier System (AVS).

The AVS is a six-degree-of-freedom magnetic suspension system that is situated atop the two-gimbal course-pointing system. It is designed to provide isolation of payloads from space shuttle disturbances, as well as to provide pointing stability and vernier control much better than the gimbal system alone [1, 2, 3, 4, 5, 6, 7, 8, 9]. The ASPS control system was designed to operate the gimbals in a follow-up mode to the AVS for large rotations. A more detailed view of the AVS engineering model, which was developed and tested, is shown in Figure 2. A unique feature of this device is its ability to provide full 360 degrees of rotation in roll. The armature is a continuous ring with an L-shaped cross-section; three magnetic actuators apply force axially and three apply force radially. Actuator stabilization was achieved with gap feedback control. Roll control was achieved with an AC induction motor and a roll resolver.

Table 1. Honeywell Magnetic Suspension Systems Background

Dates	Customer	Description
1976 - 1984	NASA LaRC	Contract to design, build, and lab test a magnetically suspended experiment pointing system for the shuttle AVS.
1977 - 1980	NASA LaRC	Contract to complete development and lab test of a magnetically suspended Annular Momentum Control Device (AMCD).
1984 - 1986	NASA LaRC	Contract to study an advanced AMCD for Space Station power and control.
1985 - 1986	Internal Research and Development (IR&D)	Develop, build, and lab test ISODRIVE, a magnetically suspended vibration isolating gimbal.
1985 - 1986	IR&D	Develop, build, and lab test Fluid Experiment Apparatus Magnetic Isolation System (FEAMIS), a magnetic isolation system for the Fluid Experiment Apparatus, planned to fly on the Shuttle.
1986 - 1987	NASA Ames Research Center (ARC)	Contract to study passive and active magnetic isolation and pointing systems for the Astrometric Telescope Facility (ATF) on the Space Station.

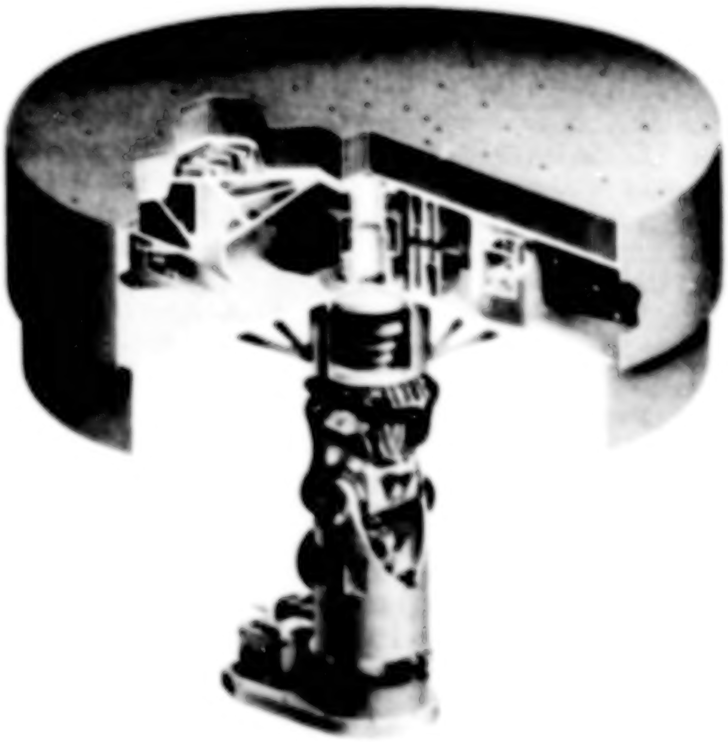

Figure 1. Annular Suspension and Pointing System

ORIGINAL PAGE
BLACK AND WHITE PHOTOGRAPH

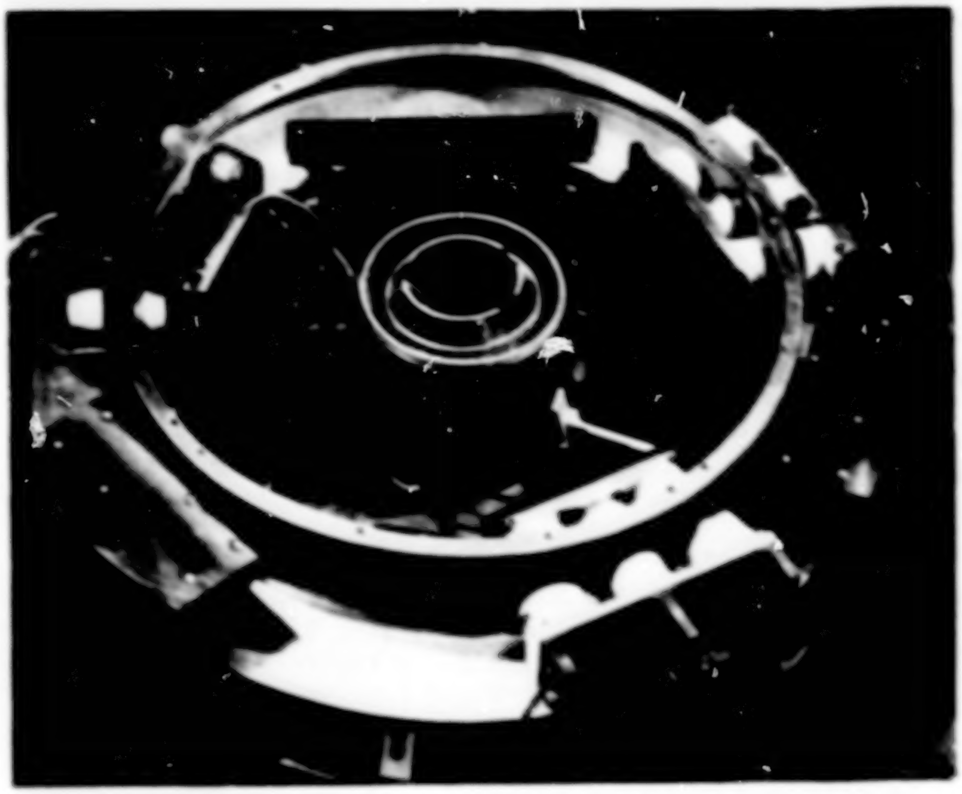

Figure 2. Laboratory Magnetic Isolation and Pointing System ASPS Vernier

A key feature of any isolation system for active payloads is its ability to provide power and signal services across the isolation gap to the payload, without compromising the isolator. For the AVS, power transfer to the payload was achieved with a large-gap, noncontacting power transformer located on the AVS center. This device was developed and tested and provided up to 2.5 kilowatts of power with extremely low disturbance forces. Concepts for large-range-of-motion optical data couplers were also considered.

With the advent of the Shuttle, interest in materials processing in space began to rise. Continuous disturbance levels greater than 0.1 μg are thought to cause significant degradation of crystalline structures grown in space. Honeywell responded by developing a magnetic isolation system, shown in Figure 3, for materials-processing applications. This device, originally developed for Rockwell's Fluid Experiment Apparatus Magnetic Isolation System (FEAMIS), was built and tested at Honeywell [10]. FEAMIS provides six-degree-of-freedom isolation with a bandwidth of 3 Hz and ultimate isolation of greater than 60 dB. Based on more recent technology developments, it is feasible to retrofit FEAMIS to achieve isolation bandwidths less than 0.1 Hz.

The envelope of the FEAMIS was constrained to fit within confines of the Shuttle mid-deck locker as shown in Figure 4. The structure was designed to minimize weight requirements by launching and landing with the payload detached. On orbit, an astronaut lowers and attaches the payload to the isolator. Mechanical clamps are included in the system to prevent uncontrolled motions of the payload and payload mounting plate while the FEAMIS is unpowered. The clamps are released by manual cranks readily accessible to the astronaut. The isolator is then powered by a single switch. Power and signal services to the payload are provided by low-stiffness cable harnesses.

ORIGINAL PAGE
BLACK AND WHITE PHOTOGRAPH

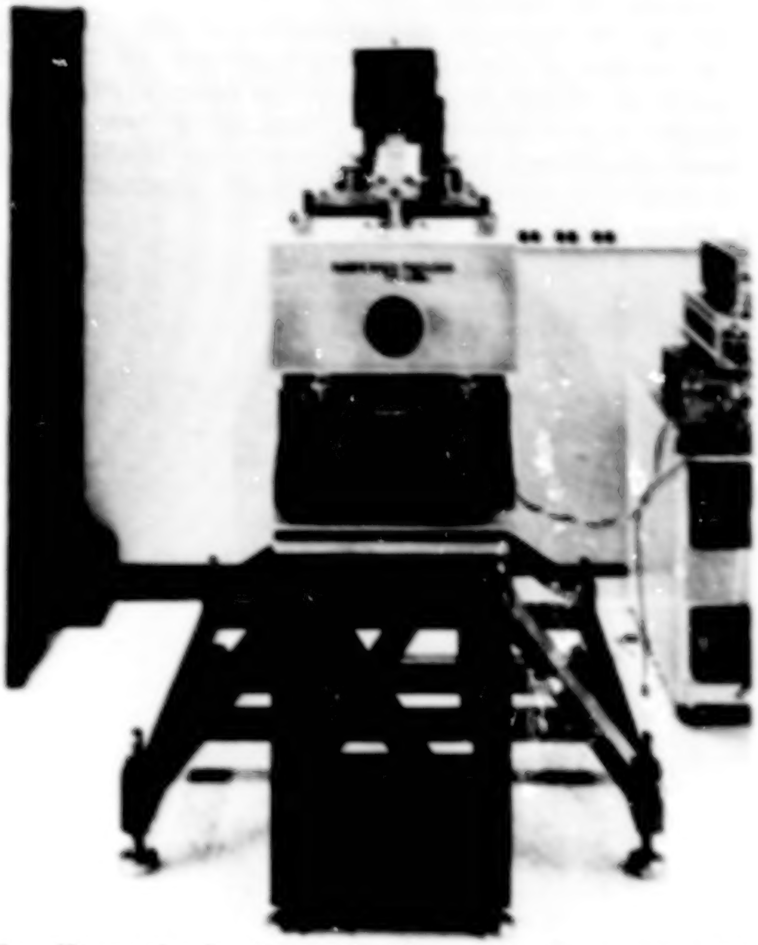

Figure 3. Magnetic Isolator for Materials Processing FEAMIS

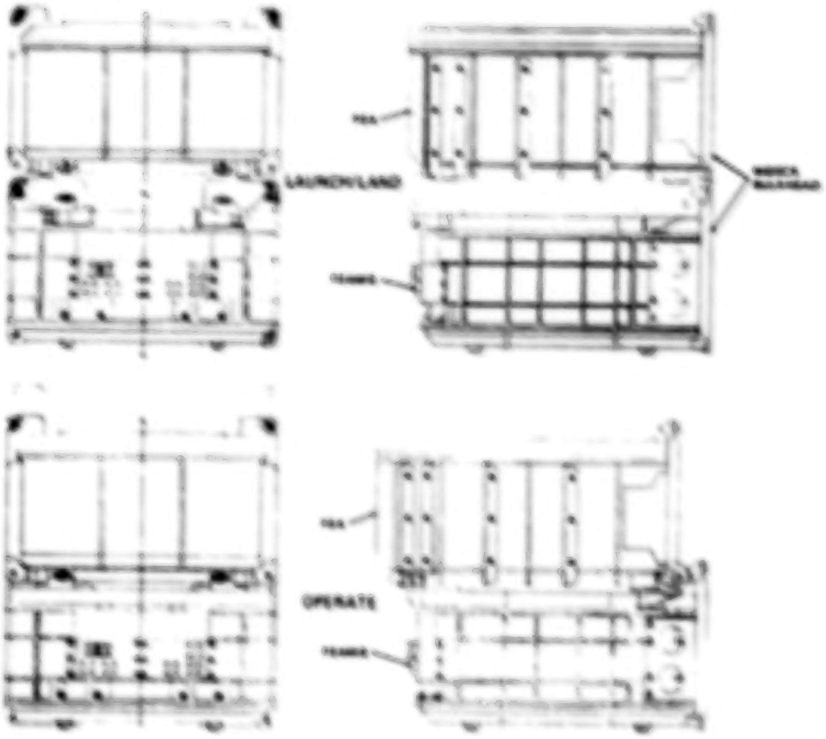
LAUNCH/LAND
FEAMIS
OPERATE
FEAMIS

Figure 4. FEAMIS/Payload Attachment

The layout of component hardware within the FEAMIS is shown in Figure 5. The actuators are configured in an axial/tangential array. The armature plates for the tangential actuators are readily seen attached to the payload mounting plate in the lower portion of the photograph. The base structure at the top of the photograph contains the electromagnets, proximity sensors, cages, and all electronics (not shown) necessary for operation of the FEAMIS. This system was the first to use Honeywell's patented flux-feedback approach for control of the magnetic actuators.

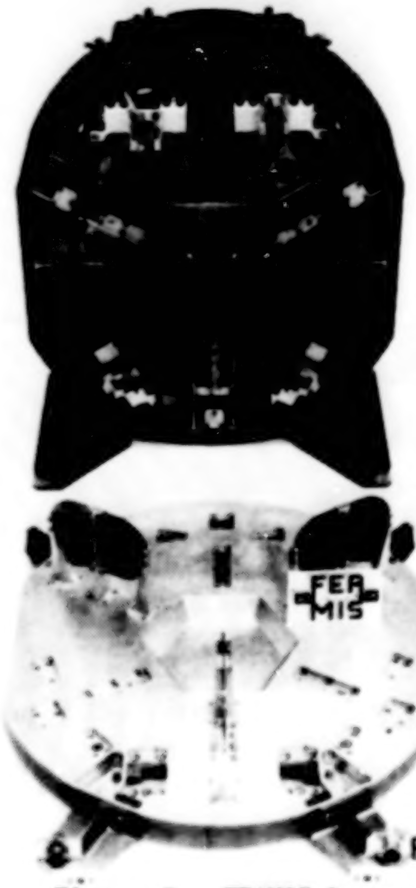

ORIGINAL PAGE
BLACK AND WHITE PHOTOGRAPH

Figure 5. **FEAMIS Layout**

Accomplishments

Significant accomplishments to date include:

- Demonstration of 0.03-arcsecond pointing stability
- Demonstration of >80-dB isolation
- Demonstration of decoupled pointing and isolation capability
- Demonstration of an all-active six-degree-of-freedom magnetic isolation system
- Demonstration of <0.1-Hz isolation bandwidths

Key Concepts

It is important at this point to define what is meant by the terms pointing and isolation. Pointing refers to the angular positioning of a suspended payload to a commanded angle. This angle could be in some local coordinate system, but more likely a target coordinate system will be used, such as inertial or earth coordinates.

Isolation refers to the reduction in amplitude of base forces transmitted to the suspended payload. Configured as an isolator, magnetic suspension can be likened to a sophisticated six-degree-of-freedom spring, whose spring rate and damping can be independently established for each degree of freedom.

SYSTEM CONSIDERATIONS

To achieve six degrees of freedom of control via one-degree-of-freedom actuators, it can be shown that a minimum set of six actuators is required. There is flexibility in how the actuators are arranged, as long as they do not act through a single point in space. (A singular condition would then exist.) Redundancy may be implemented either by dual coils on each of the six actuators or by an overdetermined set of actuators (e.g., six of eight). Figure 6 illustrates these options.

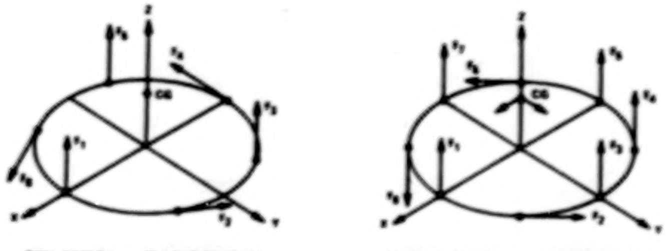

SIX AXIAL – TANGENTIAL

EIGHT AXIAL – TANGENTIAL

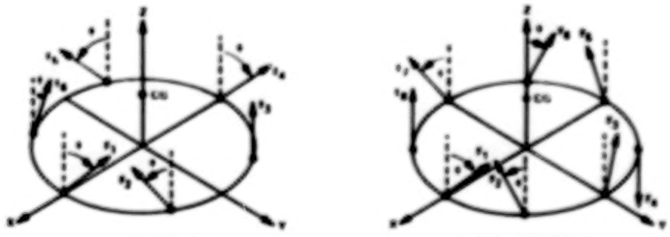

SIX SKEWED
(ϕ = 30, 45°)

EIGHT SKEWED
(ϕ = 30, 45°)

Figure 6. Actuator Configuration Trade-off

The cylindrical (axial-tangential) arrangement of actuators often offers the most compact arrangement of hardware; however, in instances where there is a large asymmetry in the force-torque requirement envelope and/or a large offset of the payload center of gravity (cg) from the centroid of the actuator array, a substantial disparity in the force requirement of the three axial actuators versus the three tangential actuators can exist. This is not an optimal design from a weight and cost standpoint. A skewed arrangement of actuators often resolves the situation, permitting a single, minimum-size actuator to be used. Honeywell has implemented computer optimization routines to quickly and accurately determine optimal arrangements. In some cases, actuator force requirements have been reduced over 50 percent.

Adding dual coils to actuators or adding additional actuators to the array for redundancy will increase weight and power and add redundancy management complexity to the system. Usually a trade study must be performed for the particular system to assess the benefits and drawbacks of each approach; based on the system requirements, a best-design approach can then be selected.

One of the major advantages of the magnetic actuator is its ability to apply force in one direction without constraining motion in any other direction. This unique feature allows a system designer considerable freedom to select a control policy specifically tailored to the payload. To demonstrate this design flexibility, consider a payload suspended by an array of six magnetic actuators. The total force applied to the payload is given by:

$$F = \sum_{i=1}^{6} (d_i \; F_i) \tag{1}$$

where:
F = total force applied to payload
F_i = force delivered by i^{th} actuator
d_i = a unit vector in the direction of the force

Similarly, the total torque about the payload's center of mass would be:

$$T = \sum_{i=1}^{6} r_i \times (d_i \; F_i) \tag{2}$$

where:
T = total torque about center of mass
r_i = position vector of actuator with respect to center of mass

Writing equations (1) and (2) in matrix form yields:

$$\begin{bmatrix} F \\ T \end{bmatrix} = \begin{bmatrix} d_1 & d_2 & \bullet\bullet\bullet & d_6 \\ r_1 \times d_1 & r_2 \times d_2 & \bullet\bullet\bullet & r_6 \times d_6 \end{bmatrix} \begin{bmatrix} F_1 \\ F_2 \\ \bullet \\ \bullet \\ \bullet \\ F_6 \end{bmatrix} \tag{3}$$

Taking the inverse of the matrix on the right side of equation (3) yields:

$$\begin{bmatrix} F_1 \\ F_2 \\ \bullet \\ \bullet \\ \bullet \\ F_6 \end{bmatrix} = \begin{bmatrix} d_1 & d_2 & \bullet\bullet\bullet & d_6 \\ r_1 \times d_1 & r_2 \times d_2 & \bullet\bullet\bullet & r_6 \times d_6 \end{bmatrix}^{-1} \begin{bmatrix} F_c \\ T_c \end{bmatrix} \tag{4}$$

Now, if the center of mass of the payload is known and the actuators are error free, the above matrix can be implemented in the control law (as shown in Figure 7) to produce forces through and torques about the center of mass. Since the resulting system is completely decoupled, it is possible to tailor the response of each degree of freedom independently. Error-free actuators and certain knowledge of the center-of-mass location are impossible, and these constitute two error sources in magnetic suspension systems. The sensitivity to these errors depends on the relative bandwidths of the control loops used to command the actuators. Minimization of these errors is essential to achieve precision levels of isolation at low frequencies.

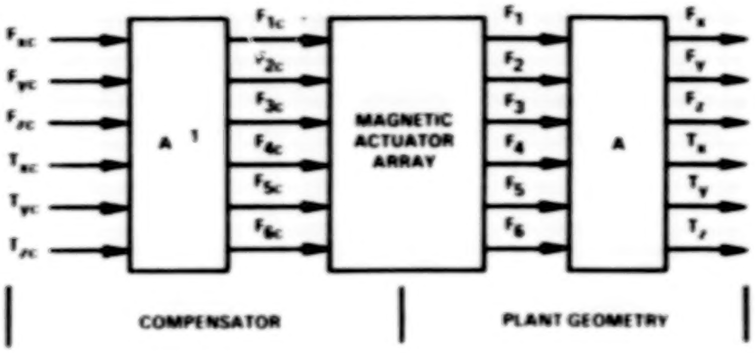

F_{xc}
F_{yc}
F_{zc}
T_{xc}
T_{yc}
T_{zc}
A^{-1}
F_{1c}
F_{2c}
F_{3c}
F_{4c}
F_{5c}
F_{6c}
MAGNETIC ACTUATOR ARRAY
F_1
F_2
F_3
F_4
F_5
F_6
A
F_x
F_y
F_z
T_x
T_y
T_z
COMPENSATOR
PLANT GEOMETRY

Figure 7. Magnetic Suspension Decoupling Technique

Magnetic Suspension as an Isolator

To use magnetic suspension as an isolator, the relative motion of the payload with respect to the base must be controlled. Rigid-body and low-frequency motion of the base must be followed by the payload, while high-frequency vibrations must not be transmitted to the payload. Usually, in magnetic suspension, the gap between payload and base is measured by proximity sensors mounted at or near the actuator locations; these may be the same proximity sensors used for inner-loop linearization. By combining the six measurements, relative translations and rotations can be determined. Controlling relative motions with low-bandwidth control laws that roll off quickly results in an excellent isolation response. The block diagram of a six-degree-of-freedom isolator is shown in Figure 8. If the payload is nearly rigid, the control compensators can be designed independently and the response of each axis tailored to the disturbance environment expected.

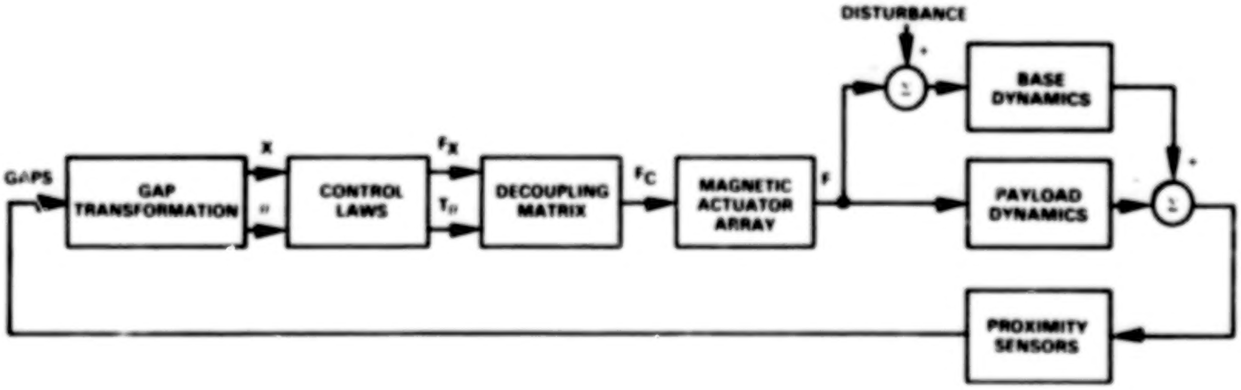

DISTURBANCE
+
Σ
BASE DYNAMICS
GAPS
GAP TRANSFORMATION
X
θ
CONTROL LAWS
F_X
T_θ
DECOUPLING MATRIX
F_C
MAGNETIC ACTUATOR ARRAY
F
PAYLOAD DYNAMICS
+
Σ
PROXIMITY SENSORS

Figure 8. Block Diagram of a Magnetic Suspension Isolator

Magnetic Suspension as a Pointer

If pointing is desired, the translation loops are configured as isolators, and the rotational loops are closed on an inertial sensor. Inertial control also preserves isolation capability but with a different transfer function. Large angles of rotation relative to the base are achieved most effectively by mounting the suspension on top of a gimbal stack and closing the gimbal loops to minimize the relative motion between the payload and the base. This permits the design of magnetic actuators with reasonably small gaps. Configuring the translational loops as isolators decouples the payload from base vibrations that may corrupt pointing performance [11]. Also, as has recently been proven [15], the soft interface provided by the magnetic suspension ameliorates structural flexibility problems encountered in end-mounted pointers. Figure 9 illustrates the control system structure required for pointing applications.

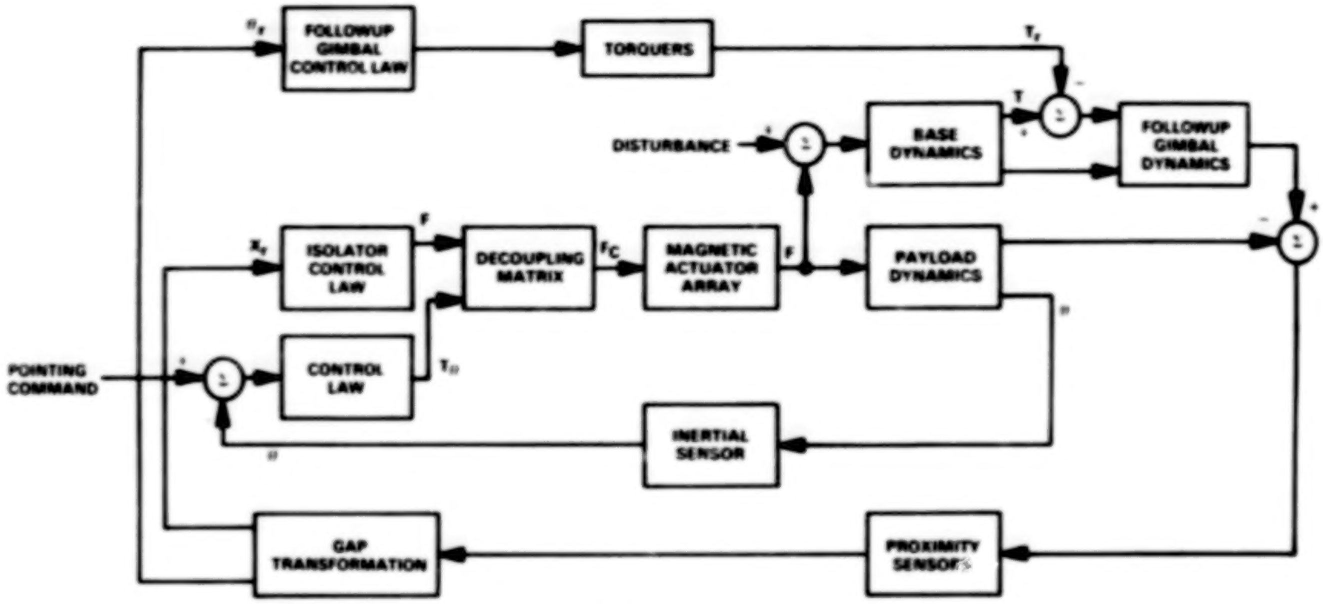
θ_r
FOLLOWUP GIMBAL CONTROL LAW
TORQUERS
T_r
T
DISTURBANCE
BASE DYNAMICS
FOLLOWUP GIMBAL DYNAMICS
X_r
ISOLATOR CONTROL LAW
F
DECOUPLING MATRIX
F_C
MAGNETIC ACTUATOR ARRAY
F
PAYLOAD DYNAMICS
θ
POINTING COMMAND
CONTROL LAW
T_θ
INERTIAL SENSOR
θ
GAP TRANSFORMATION
PROXIMITY SENSORS

Figure 9. Block Diagram of a Pointing System using Magnetic Suspension

ACTUATOR REQUIREMENTS

To derive the actuator requirements it is necessary to understand the relationship between actuator performance and system performance; in particular, how actuator error sources couple into pointing system and isolation system performance. Generally, magnetic actuator force error sources can be grouped into three categories:

- Errors due to gap motion
- Scale factor errors
- Nonlinearities

This section will describe how these error sources affect pointing and isolation performance.

Pointing Systems

Consider the planar configuration shown in Figure 10. A payload with mass, M, and moment of inertia, J, is suspended in two degrees of freedom with respect of the carrier. Carrier and payload translate only in X, and the payload may rotate through a small angle θ. Figure 11 is a block diagram depicting the structure of the pointing control system for this case. References [11] and [12] contain an excellent derivation of the relationship between carrier motion and pointing error. For our purposes, examining the block diagram yields the following conclusions:

- Scale factor errors in translation become anomalous torque disturbances in the pointing axis.
- Force errors due to gap motion couple into the pointing error.
- Force errors due to nonlinearities also affect the pointing stability.

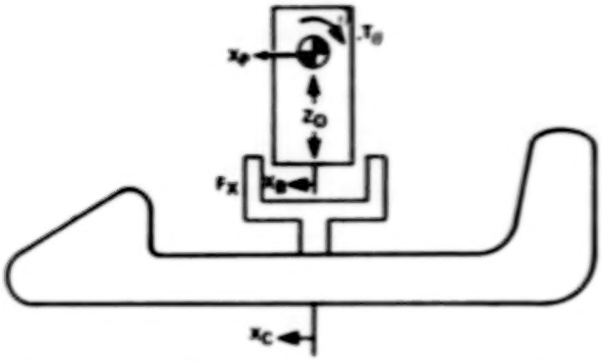
x_P
T_θ
Z_G
F_X
x_B
x_C

Figure 10. Two-Degree-of-Freedom Example

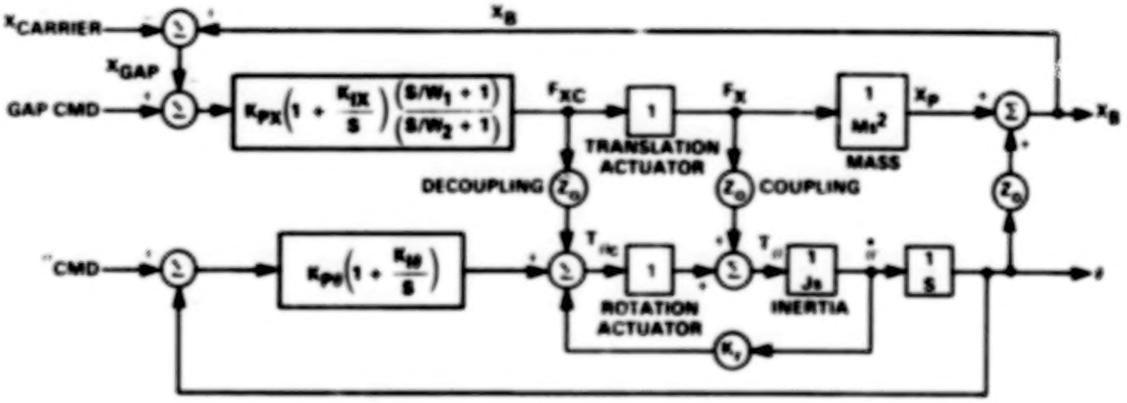
x_CARRIER
x_B
x_GAP
GAP CMD
K_PX(1 + K_IX/S)((S/W_1 + 1)/(S/W_2 + 1))
F_XC
1
TRANSLATION ACTUATOR
F_X
1/Ms^2
MASS
x_P
x_B
DECOUPLING
Z_G
COUPLING
Z_G
Z_G
θCMD
K_Pθ(1 + K_Iθ/S)
T_θC
1
ROTATION ACTUATOR
T_θ
1/Js
INERTIA
θ̇
1/S
θ
K_r

Figure 11. Two-Degree-of-Freedom Block Diagram

The quantitative results of these errors depend on the relative bandwidths of the pointing and isolation sensors; however, pointing systems usually require high-performance, magnetic-force actuators.

Isolation Systems

The goal of an isolation system is to limit the motion of the payload due to carrier motion while allowing the payload to fly with the carrier. In order to accomplish this, a very low-bandwidth (0.01 to 1 Hz) control loop is closed on the gap measurement. Because the system tends to be uncoupled, it can be modeled as six single-degree-of-freedom isolators. Figure 12 illustrates a single-degree-of-freedom system.

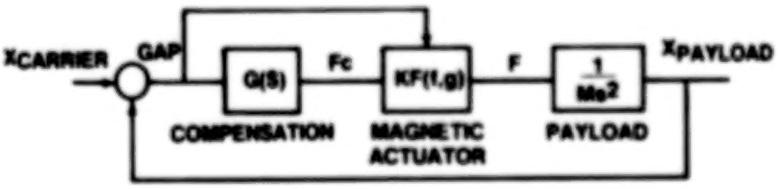
X_CARRIER
GAP
G(S)
COMPENSATION
Fc
KF(I,g)
MAGNETIC ACTUATOR
F
1/Ms^2
PAYLOAD
X_PAYLOAD

Figure 12. Single-Degree-of-Freedom Isolation System

For this application, scale-factor errors cause slight changes in bandwidth but have negligible impact on pointing performance. Force errors due to gap motion result in dF/dg term, which acts like a mechanical spring shunting the armature to the stator. The effect of this residual spring is to limit low-frequency isolation performance.

Minimizing the appropriate error sources becomes the primary objective of the actuator designer. Techniques for minimizing the error sources include:

- Flux leakage and fringing minimization
- Actuator bandwidth selection
- Actuator control sensor selection

Magnetic Actuator Description

A typical magnetic actuator used in Honeywell suspension devices is shown in Figure 13. This particular actuator was used in the FEAMIS. The actuator consists of two opposing horseshoe electromagnets acting on an armature plate. The electromagnets are mounted to the base, the passive armature is attached to the payload, and they are separated by a large air gap.

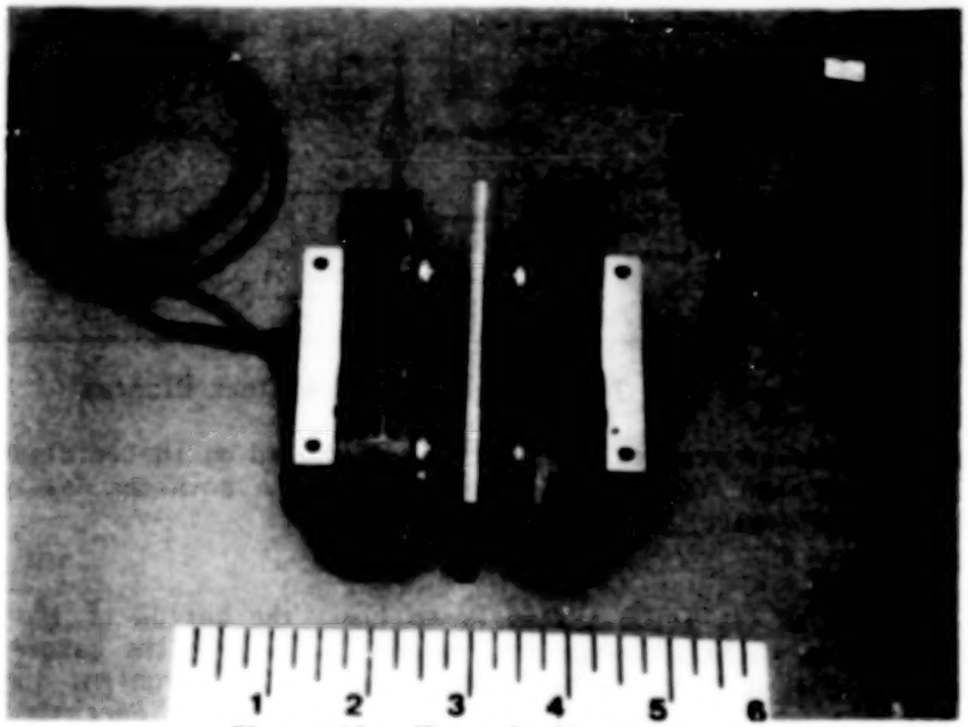

Figure 13. Magnetic Actuator

This type of actuator has been traded against others, such as Lorentz force (voice coil) actuators used for several isolation suspensions at Honeywell. It has repeatedly proved to have better weight and power characteristics, which are key parameters in any space application. Its inductance is much larger than the Lorentz force actuator, and, therefore, it is a poor performer in the high-frequency force regime; however, isolators are rarely required to apply large high-frequency forces, and the Honeywell electromagnet pair design has proved suitable for all applications to date. The large inductance acts to filter voltage driver noise, making this actuator an extremely low-force noise device, which has been substantiated by test data.

ORIGINAL PAGE
BLACK AND WHITE PHOTOGRAPH

Another advantage of the electromagnet pair actuator is its even mass distribution and the fact that the payload attachment can be made entirely passive. The Lorentz force actuator has a large percentage of its mass associated with its permanent magnet (passive) side, and a small mass percentage associated with the coil (active) side. Thus, one is confronted with attaching a large mass to the payload or carrying power to, and dissipating it on, the payload side; both are often undesirable situations. With the electromagnet pair actuator, a reasonably sized passive armature is attached to the payload, and the active electromagnetics are attached to a relatively large base.

The Lorentz force actuator has the advantage of a linear force response to current, whereas the Honeywell actuator is nonlinear. This makes the electronics for the Lorentz force actuator simpler to implement; however, several solutions to the nonlinear force law of the electromagnet pair actuator exist and have been implemented with only some additional complexity.

MAGNETIC ACTUATOR CONTROL TECHNIQUES

Because the force output of an electromagnet is unidirectional and dependent upon the square of the flux linkage or current, controlling the actuator requires some circuitry to control output. One way to do this is to examine the sign of the command, take the square root of the magnitude of the command, and apply current the appropriate coil. This technique requires square-root electronics, which are sensitive and poorly behaved, and inherently have a dead band around zero force. A number of different techniques for controlling the magnetic actuator have been developed and used by Honeywell. This section will describe these techniques and emphasize the relative advantages and disadvantages of each technique.

- Gap/Current Feedback
  - Technique

    One way to control the actuator force is to modulate the currents in both coils as a function of the gap and the force command. To illustrate this technique, consider the equation that describes the force exerted by the actuator:

$$F = K\left[\frac{I_1^{\,2}}{(g_o - \delta_g)^2} - \frac{I_2^{\,2}}{(g_o + \delta_g)^2}\right]$$

where:

g_o = nominal gap

δg = gap motion

I_1 = current in one actuator coil

I_2 = current in the second coil

K = force constant of actuator

Now consider introducing a current into each actuator winding, which consists of a bias current and a current proportional to a commanded force, and multiplying the total current in winding 1 by $(g_o - \delta_g)$ and the total current in winding 2 by $(g_o + \delta_g)$. The force equation becomes:

$$F = K\left[\frac{(I_o + K_f F_c)^2\left(\frac{g_o - \delta_g}{g_o}\right)^2}{(g_o - \delta_g)^2} - \frac{(I_o - K_f F_c)^2\left(\frac{g_o + \delta_g}{g_o}\right)^2}{(g_o + \delta_g)^2}\right]$$

By selecting $K_f = g_0{}^2/4KI_o$, the force output becomes equal to the commanded force. Therefore, the actuator appears to be a linear device to the outer-loop control system. A block diagram of a circuit implementation is shown in Figure 14. This technique was used successfully on the AVS built for NASA's Langley Research Center.

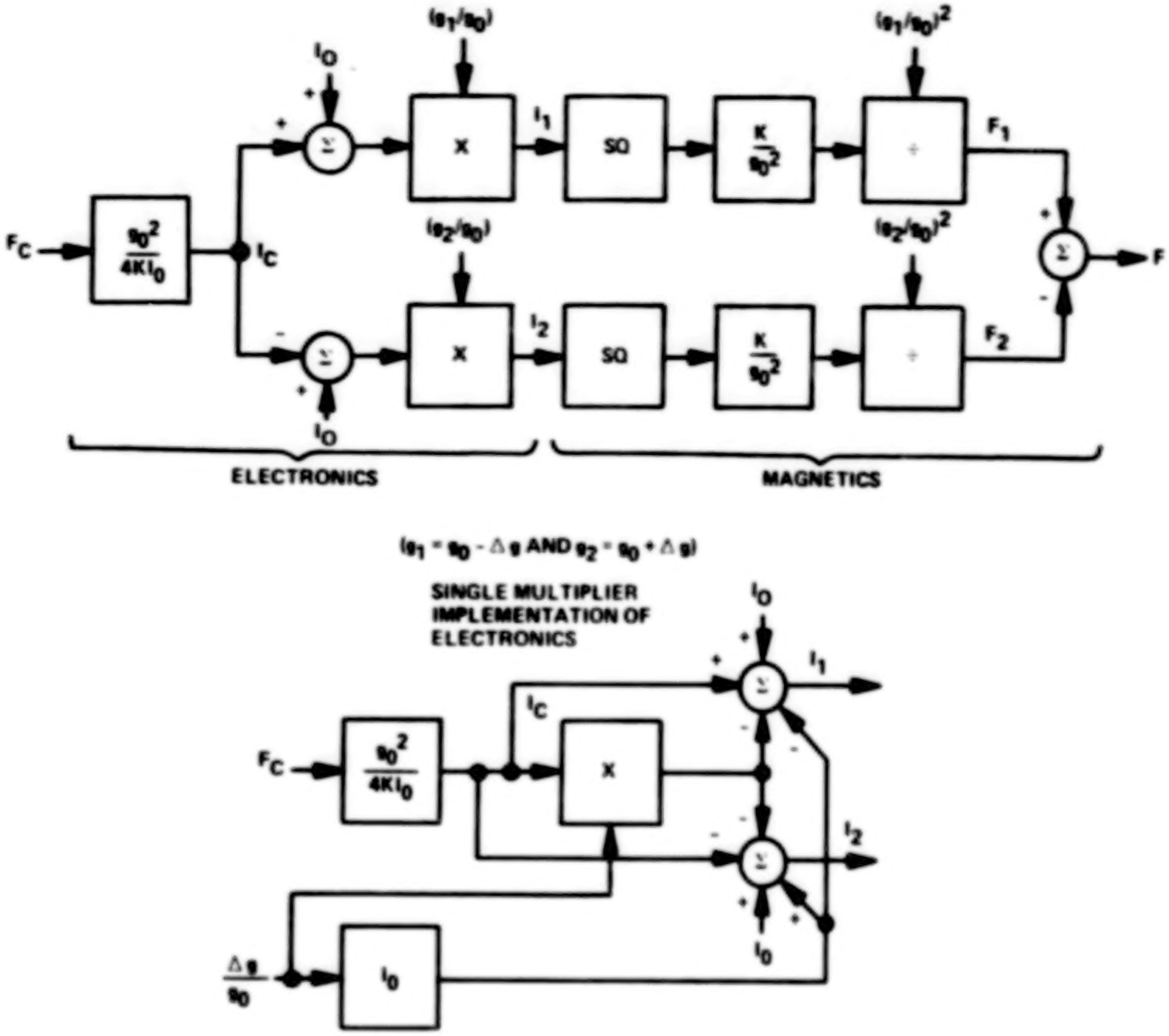

(g_1/g_0)
$(g_1/g_0)^2$
I_0
+
+
Σ
X
I_1
SQ
$\frac{K}{g_0^2}$
÷
F_1
F_C
$\frac{g_0^2}{4KI_0}$
I_C
(g_2/g_0)
$(g_2/g_0)^2$
+
Σ
−
F
−
Σ
+
X
I_2
SQ
$\frac{K}{g_0^2}$
÷
F_2
I_0
ELECTRONICS
MAGNETICS
$(g_1 = g_0 - \Delta g \text{ AND } g_2 = g_0 + \Delta g)$
SINGLE MULTIPLIER IMPLEMENTATION OF ELECTRONICS
I_0
I_1
I_C
F_C
$\frac{g_0^2}{4KI_0}$
X
I_2
$\frac{\Delta g}{g_0}$
I_0
I_0

Figure 14. Current/Gap Force Linearization Technique

- Advantages/Disadvantages

  The primary advantages of the gap/current technique are:
  - The force produced is directly proportional to the commanded force.
  - The electronics implementation is simple.

  The disadvantages of the technique are:
  - A gap sensor is required.
  - A linear relationship between flux and current is required. Therefore, low-hysteresis iron must be used, which usually results in a heavy actuator because linear materials saturate at relatively low flux densities.
  - The introduction of a bias current results in continuous power dissipation.

- Flux Feedback
  - Technique

The gap/current force equation has a dual in terms of flux. The force produced by the actuator is given by:

$$F = K(\lambda_1^2 - \lambda_2^2)$$

where:

λ_1 = flux linkage produced by magnet 1
λ_2 = flux linkage produced by magnet 2
K = force constant

Again, the actuator can be linearized by introducing a bias flux. Let $\lambda_1 = \lambda_o + K_f F_c$ and $\lambda_2 = \lambda_o - K_f F_c$. The force equation becomes:

$$F = K[(\lambda_o + K_f F_c)^2 - (\lambda_o - K_f F_c)^2] = 4\lambda_o K K_f F_c$$

If we let $\lambda_o = 1/4K$, we get $F = F_c$.

To implement flux feedback (Figure 15), flux is measured by a Hall-effect sensor. A high-bandwidth control loop is closed on the flux signal, creating a force actuator. The flux feedback technique has been used on the FEAMIS and the ISODRIVE and is currently the preferred control approach.

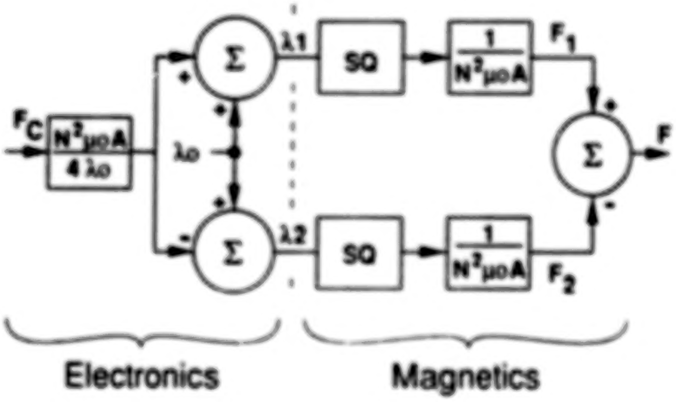

Figure 15. Flux Linearization Technique

- Advantages/Disadvantages

Advantages of the flux feedback implementation are:

- Simple circuit implementation.
- Force produced is proportional to the commanded force.
- Because force produced by a magnet is directly proportional to the square of flux, the magnet can be made using high-hysteresis materials without affecting the linearity of the actuator. This feature results in a lighter, lower-power actuator.

The major drawback for this technique is that it requires a flux sensor that is linear and stable over temperature variations. It must also be placed within the air gap, making packaging a challenging task. Honeywell has developed circuit techniques that will compensate temperature for Hall-effect devices.

- Force Feedback
  - Technique
  - Force Feedback

In applications that require a high-precision forcer, such as an isolation and pointing system, it becomes necessary to close an outer loop around the current loops (gap feedback) or the flux loops. The outer loop is closed by feeding back a measured value of the force applied to the payload. Figure 16 is a block diagram of the force loop and the required compensation.

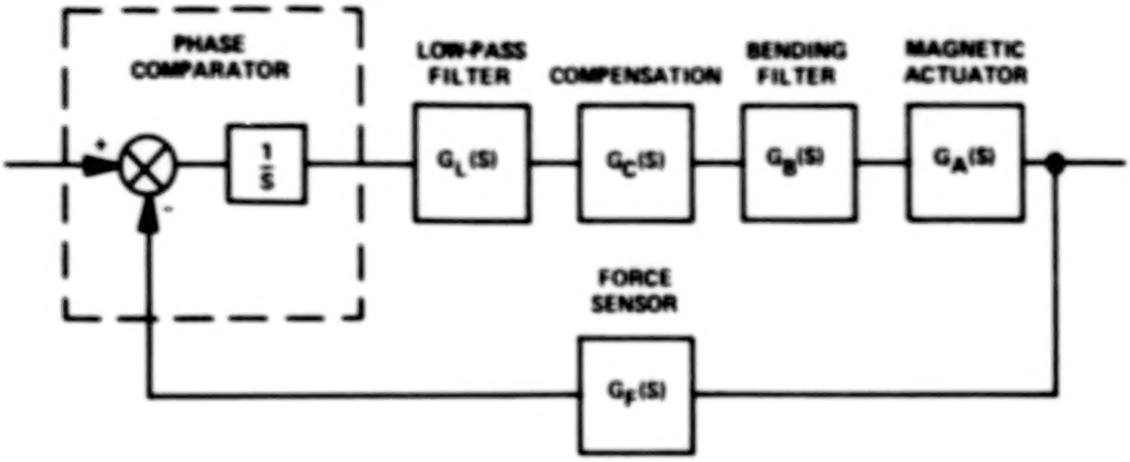

Figure 16. Force Feedback Control Loop

The force loop is an analog control loop. The precision force sensor employs a quartz crystal, which outputs a frequency-modulated signal representing the applied force. The additional circuitry required can be divided into three major functions: (1) the phase comparator and filter, (2) force-loop control compensation, and (3) a bending filter.

The phase comparator is used to differentiate the command- and frequency-modulated sensor frequencies. The particular logic circuit used is called a sequential frequency-phase detector. The output is a square wave that varies from a tristate level to high or low, depending on which frequency is higher; the duty cycle of the square wave is determined by the phase difference between the signals. This output is passed through a low-pass filter to extract the DC component containing the phase information and a level shifter to obtain a signal with polarity to drive the remainder of the control circuitry.

It is interesting to note the smooth transition that is made from digital to analog. The duty cycle (and hence the measured phase error) is a continuous function in the operating region; no sampling or quantization is introduced in the feedback path. The phase comparator also contributes a free integration that is used as part of the force-loop forward path.

The compensation for the force loop consists of an integrator and a lead/ lag filter. The integrator is added for two reasons. The first is to increase the system type to a Type 2. This forces the velocity error coefficient to infinity, which means that the loop will be able to follow ramp frequency commands. Secondly, the presence of the second integrator downstream from the phase comparator forces it to seek zero phase error in the steady state, thereby placing the nominal operating point in the center of the linear region. The double integrator in the forward path, along with higher frequency lags associated with those of comparator filter and the actuator, appears similar to a simple mass sytem. The lead/lag filter is added to stabilize the loop, using a standard form with displacement control loops.

The final element required is a bending mode (or notch) filter to decrease the effects of resonance associated with the force sensor. The sensor acts as a spring between the rotor and payload. Because the payload is much larger than the rotor, the natural frequency of this mass/spring system is determined by the rotor mass and sensor stiffness. This mode is lightly damped and occurs in the region from 100 to 130 Hz in the prototype sensors.

- Advantages/Disadvantages

The major advantage of force feedback is that extremely linear and accurate forces can be produced by the actuator. Force sensors utilizing quartz resonator techniques provide the necessary precise force measurement and stiffness. Drawbacks to the force sensor technique are:

- The relatively low stiffness of the force sensor limits achievable bandwidth of the actuator.
- The force sensor is rather fragile, necessitating complex and expensive mechanical mounting to provide protection.

When system considerations dictate extremely precise and linear forcers, the force feedback technique is the best choice.

TEST DATA

To verify the magnetic suspension isolation concept, tests have been run on a variety of hardware including single-degree-of-freedom and six-degree-of-freedom systems. This section briefly describes the tests conducted and provides samples of the results obtained.

To verify the magnetic suspension isolation concept, isolation tests were conducted using a linearized single-axis magnetic actuator [13]. The actuator was constructed from high-hysteresis, cold-rolled steel, and force was linearized using the flux-sensing technique.

To measure isolation performance, a low-frequency isolation loop was closed around the linearized actuator, using a capacitive position sensor. This sensor monitored the relative gap between the spacecraft-mounted assembly (stator) and the payload-mounted assembly (armature). This isolation loop was designed for a 10-Hz bandwidth with fifth-order rolloff.
A simplified block diagram of the system configuration is shown in Figure 17.

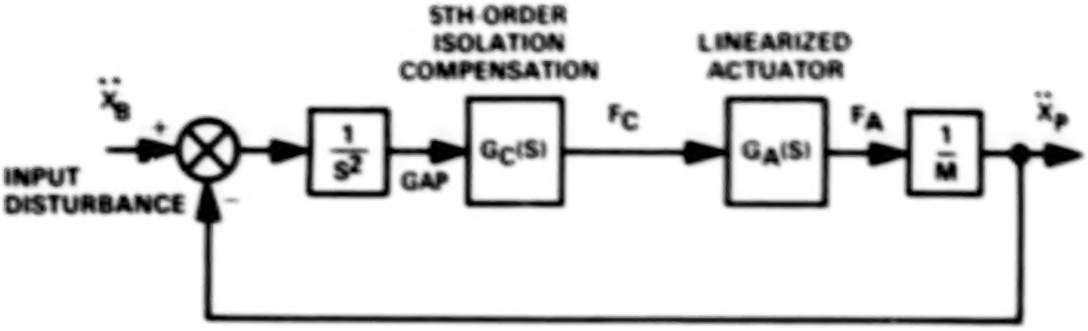

Figure 17. Simplified Magnetic Isolator Block Diagram

Prior to testing, dynamic modeling of the linearized actuator revealed that back emf and square-law linearization techniques inhibited ideal high-frequency rolloff of the isolation loop. These studies also indicated that the effects were related to the linearized actuator bandwidth and decreased as the actuator bandwidth increased. To demonstrate this phenomenon, the initial bandwidth of the linearized actuator was designed for 300 Hz and later increased to 600 Hz.

To measure the isolation properties of the magnetic isolator, the stator assembly was mounted to a sine-swept shaker to simulate spacecraft disturbance over frequency. The armature assembly consisted of a solid block and was suspended from the ceiling. The actuator test setup is shown in Figure 18. Because the actuator exerts force in only one axis, the remaining degrees of freedom were constrained by side ropes as shown.

Isolation data was measured using accelerometers (mounted on both the stator and armature assemblies) and recorded using a Hewlett Packard 5423A dynamic analyzer. Due to shaker and accelerometer limitations, the lowest recorded frequency of the measured data was 5 Hz.

The initial isolation results from the measured accelerometer signals are shown in Figure 19. Also shown is the anticipated response based on dynamic models of the linearized actuator, including the effects of back emf and bias linearization for a 300-Hz actuator. At frequencies below 60 Hz the measured data agrees with the anticipated results, demonstrating the 10-Hz isolation bandwidth, fifth-order rolloff, and as much as 80 dB of isolation; however, at frequencies above 60 Hz the deviation in the measured data was found to be caused by acoustic coupling. Sound waves from the shaker and stator during vibration impinged on the armature and were measured by the sensitive accelerometer.

To verify this phenomenon, the measurements were repeated with the isolation electronics disconnected. The measured transmissibility between the stator and armature accelerometers in this configuration is shown in Figure 20. Also shown are the anticipated results, the original measurement, and the difference of the two measurements as calculated by the dynamic analyzer. While somewhat noisy, the corrected data agrees with the anticipated results, thereby demonstrating that acoustic coupling is the source of degradation in the original measurement. To further improve measured isolation data, a technique was developed utilizing the flux feedback signals from the actuator. The difference between these signals is proportional to the applied

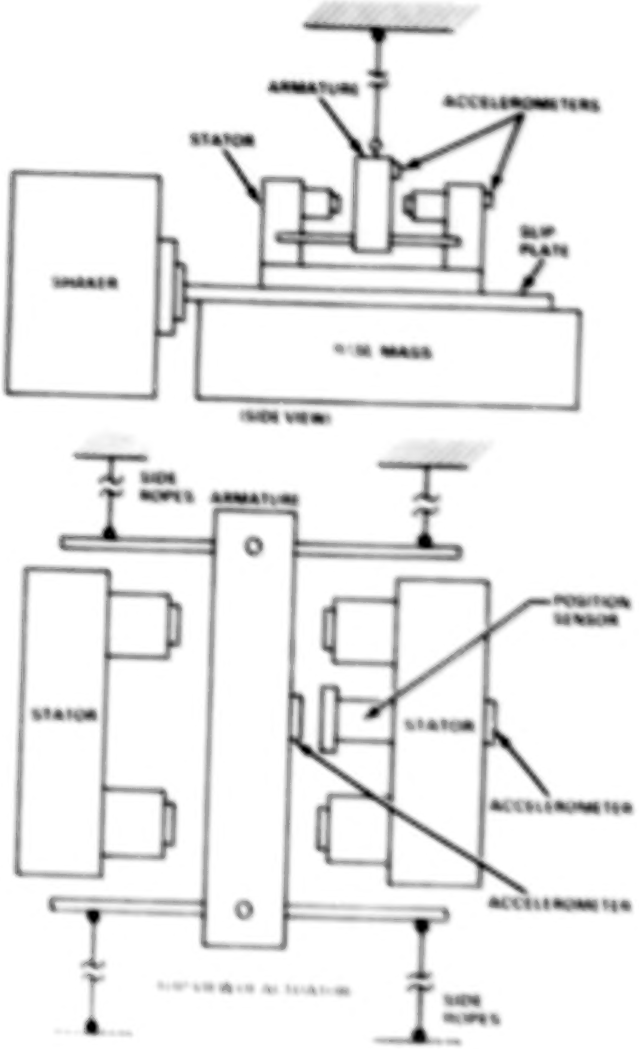
ARMATURE
ACCELEROMETERS
STATOR
SHAKER
SLIP PLATE
MASS
(SIDE VIEW)
SIDE ROPES
ARMATURE
POSITION SENSOR
STATOR
STATOR
ACCELEROMETER
ACCELEROMETER
SIDE ROPES

Figure 15. Magnetic Actuator Test Configuration

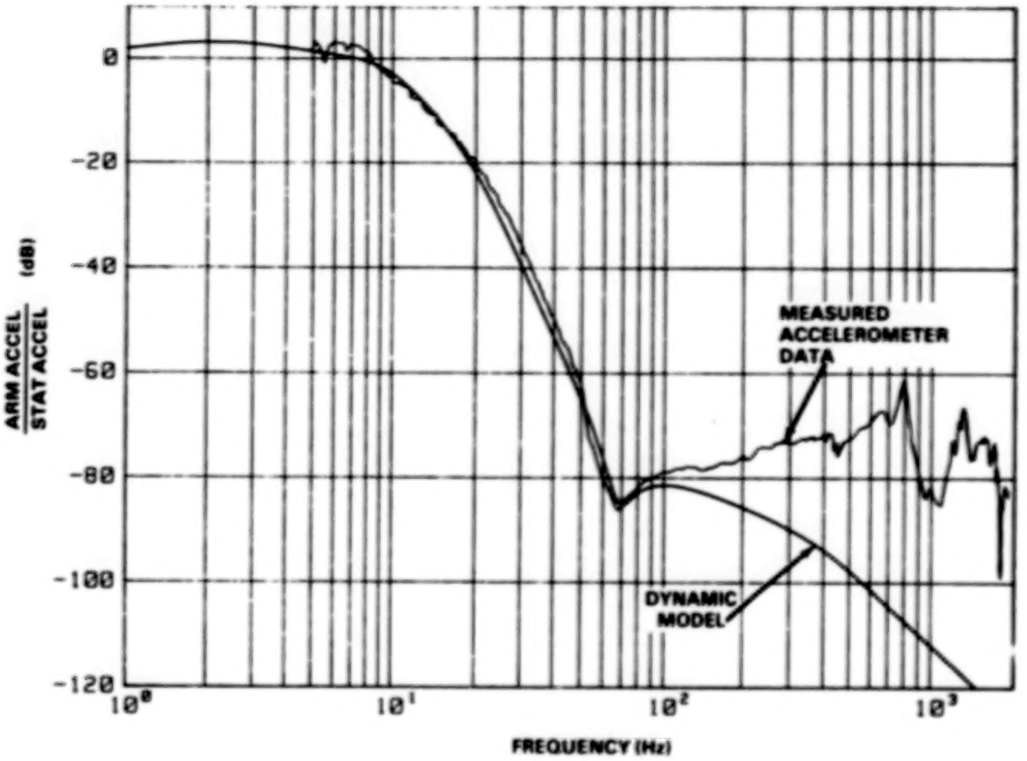

Figure 19. Comparison of Isolation Characteristics Between Measured Accelerometer Response and Dynamic Model Prediction

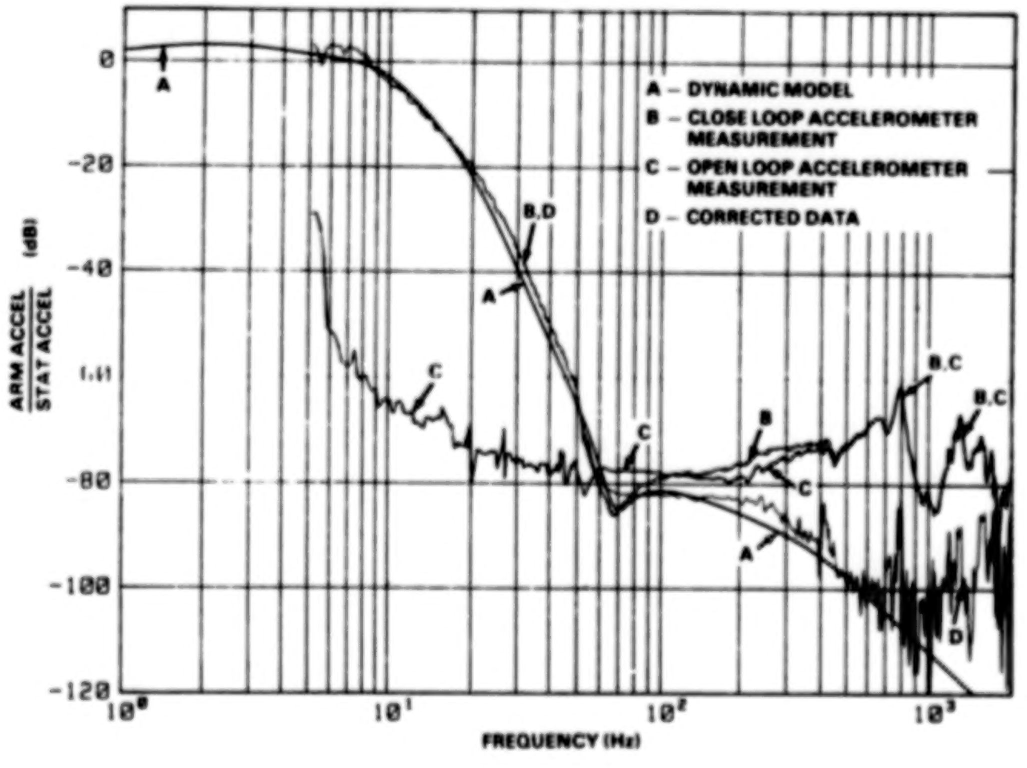

Figure 20. Isolation Characteristics Showing Results Corrected for Acoustics

force (i.e., acceleration) and is not affected by ambient acoustics. Using this flux feedback difference signal to measure armature acceleration, the isolation tests were repeated. The measured isolation response using this technique is shown in Figure 21, along with the anticipated results and corrected data from Figure 20. Note the improved signal and high correlation between this measurement and the corrected data results. The dip in the measured data (Figure 19) near 700 Hz is caused by a structural resonance in the stator assembly where one accelerometer was mounted. The leveling off near -90 dB above 1000 Hz is due to the electronic noise floor of the measurement equipment.

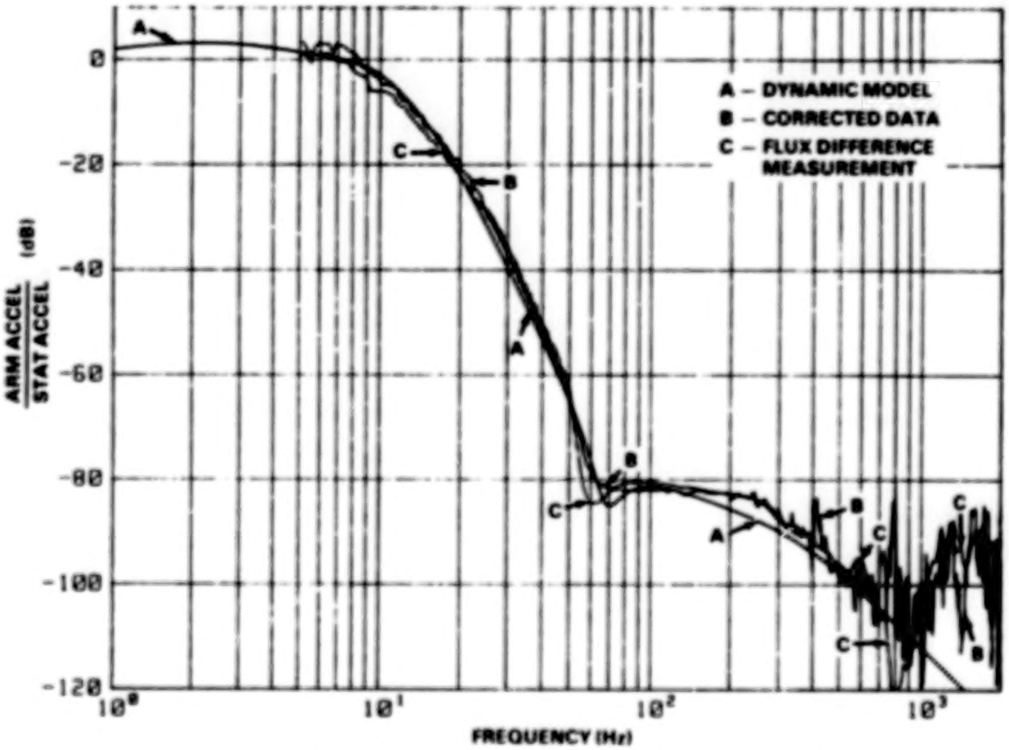

Figure 21. Isolation Characteristics Comparing Flux Difference Measurements to Corrected Data

To further verify the dynamic model and demonstrate how increasing the actuator bandwidth can improve the isolation characteristics, the actuator bandwidth was increased from 300 to 600 Hz, and the tests were repeated.

The measured and anticipated isolation characteristics for the 600-Hz configuration are shown in Figure 22. Also shown are the measured and anticipated characteristics for the 300-Hz actuator. Note the improved attenuation below 400 Hz. Here again, the leveling off near -90 dB is due to the electronic noise floor, and the dip near 700 Hz is due to stator structural resonance.

Test Summary

The single-axis magnetic isolator proved to exhibit excellent isolation characteristics, with as much as 90 dB of attenuation demonstrated to 2000 Hz. These tests also verified the accuracy of the dynamic model, which includes the anomalies due to back emf and bias linearization.

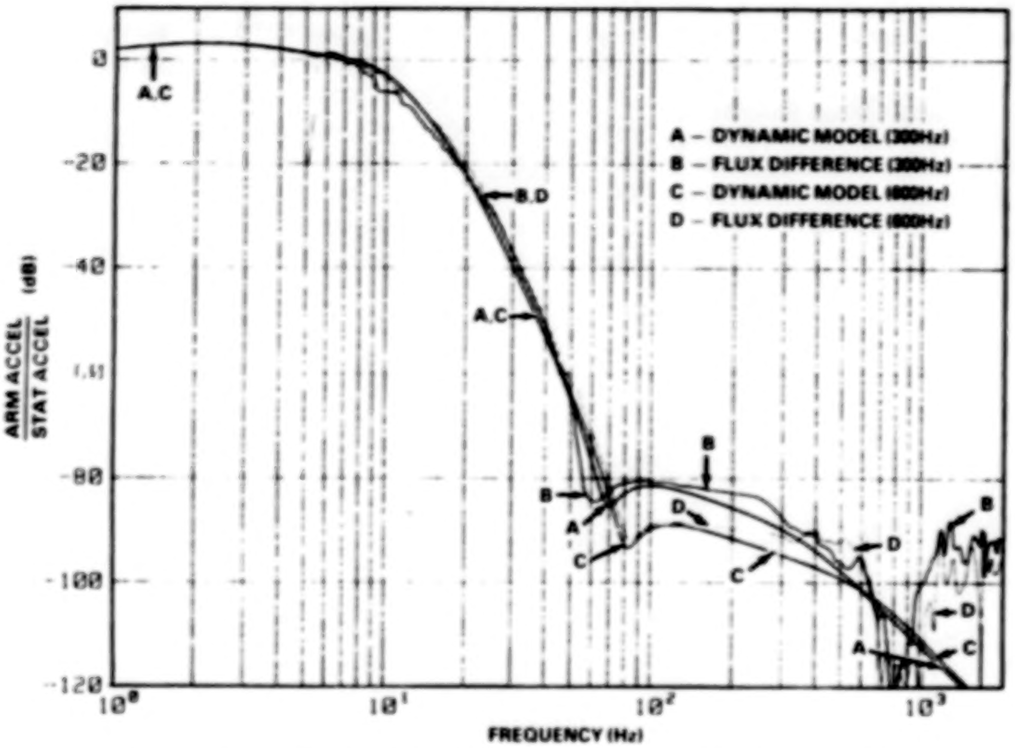

Figure 22. Isolation Characteristics Showing Effects of Increased Actuator Bandwidth

Since these tests were conducted, further improvements in the actuator bandwidths have been demonstrated in the laboratory, with bandwidths as high as 2000 Hz realized. In an isolation configuration, these high-bandwidth actuators would provide even higher attenuations than those presented here.

Advanced Vernier System (AVS)

The AVS has been extensively tested to prove its pointing capabilities [14]. Figure 23 is a photograph of the AVS test setup, and Figure 24 illustrates the equipment used to perform the testing. Because the gravity balance device corrupts the test data, a complete nonlinear simulation of the test setup was made. The results of the tests were compared with simulation runs to show analytical and test agreement. Of primary concern was the pointing error due to Shuttle Vernier Reaction Control System thruster disturbances. Simulated disturbances were applied to the AVS, and the response was measured. Figure 25 shows the result of one of these runs. Overall, the mean pointing error was 1.36 arc seconds versus an analytically predicted error of 1.22 arc seconds. This excellent agreement of data provides confidence that the techniques utilized to predict magnetic suspension pointing performance are sound.

FEAMIS

The test arrangement for FEAMIS is shown in Figure 26. The FEAMIS was mounted on a single-axis slip plate that was coupled to a linear shaker motor. A counterbalance arrangement offloaded the FEAMIS to allow it to levitate in a 1-g field. Accelerometers were mounted on the base and the simulated payload. The outputs of the two accelerometers were run into an HP5423 dynamics analyzer, and the transmissibility function was computed; Figure 27 shows the obtained transmissibility. The data compares with the predicted response and demonstrates 100-dB/decade rolloff and greater than 60-dB attenuation of high-frequency disturbances.

ORIGINAL PAGE
BLACK AND WHITE PHOTOGRAPH

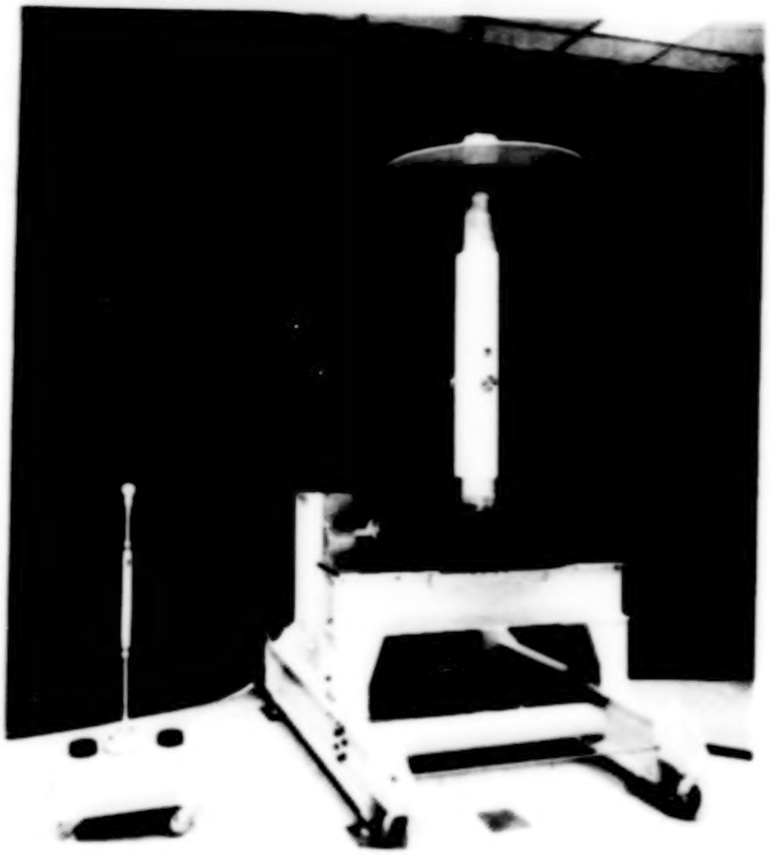

Figure 23. AVS with Suspended Payload Simulator

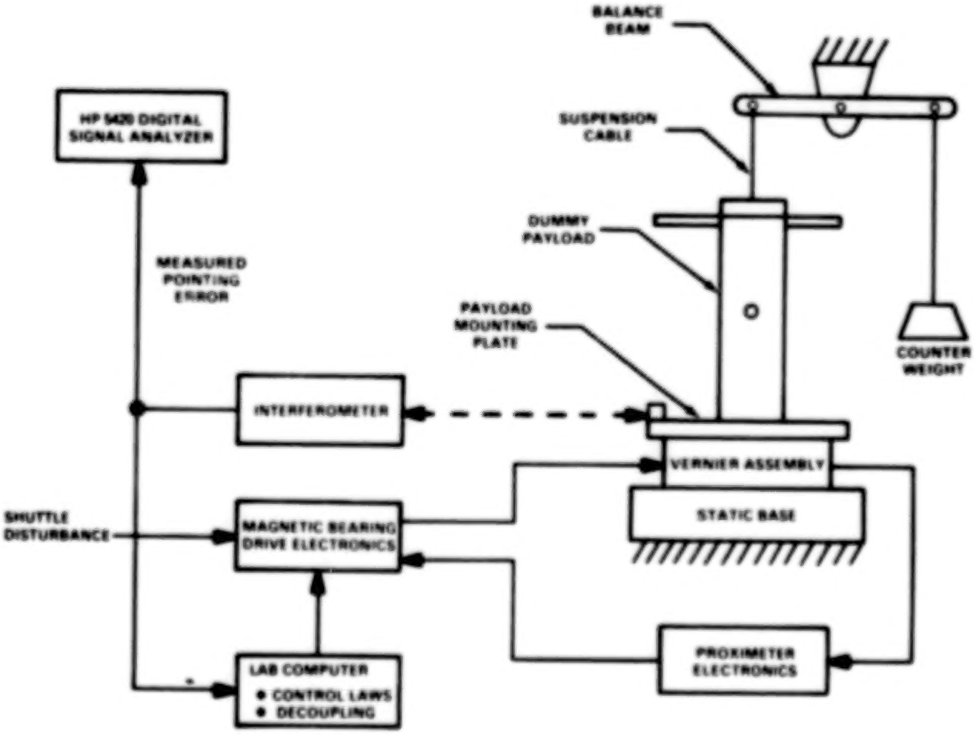
BALANCE BEAM
HP 5420 DIGITAL SIGNAL ANALYZER
SUSPENSION CABLE
DUMMY PAYLOAD
MEASURED POINTING ERROR
PAYLOAD MOUNTING PLATE
COUNTER WEIGHT
INTERFEROMETER
VERNIER ASSEMBLY
SHUTTLE DISTURBANCE
MAGNETIC BEARING DRIVE ELECTRONICS
STATIC BASE
PROXIMETER ELECTRONICS
LAB COMPUTER
● CONTROL LAWS
● DECOUPLING

Figure 24. Laboratory Test Setup

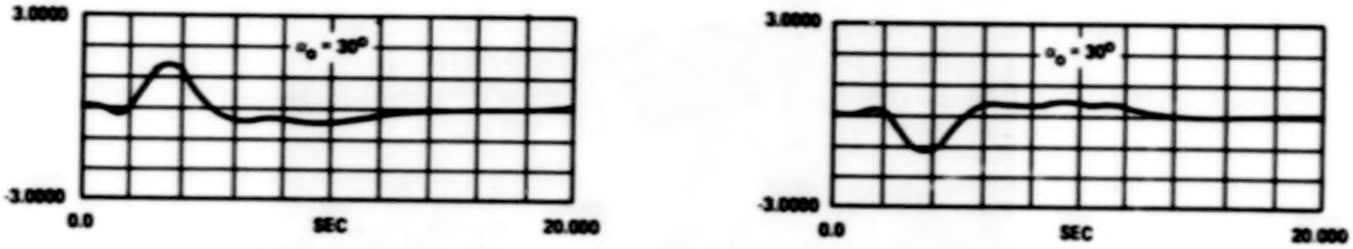

Figure 25. Pointing Error due to Simulated Shuttle VRCS Firing

ORIGINAL PAGE
BLACK AND WHITE PHOTOGRAPH

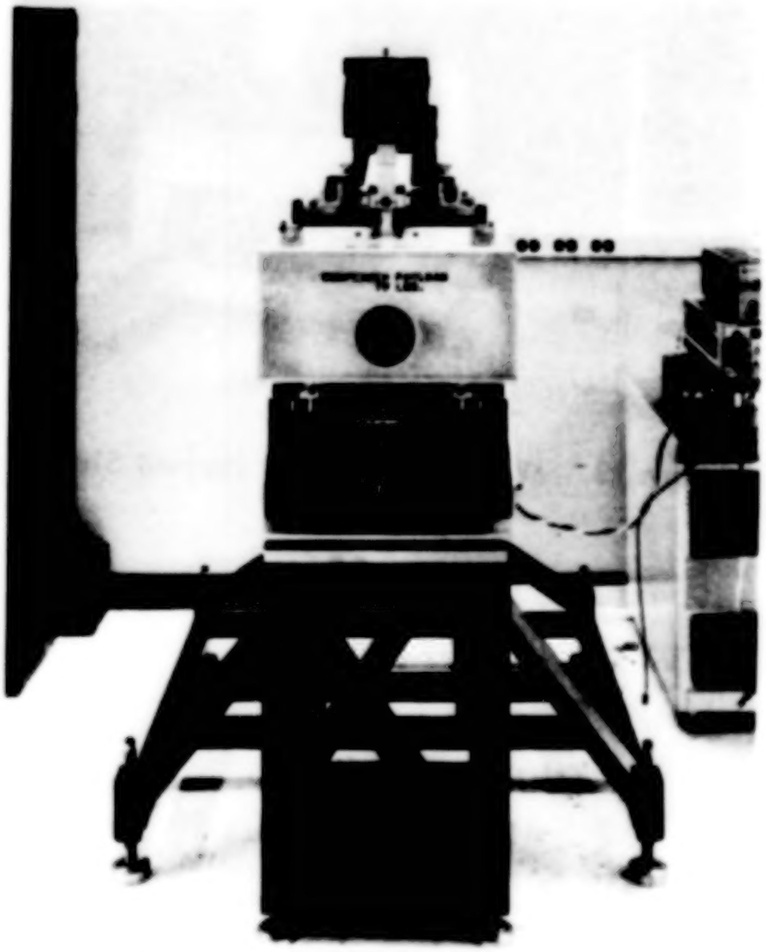

Figure 26. FEAMIS Test Setup

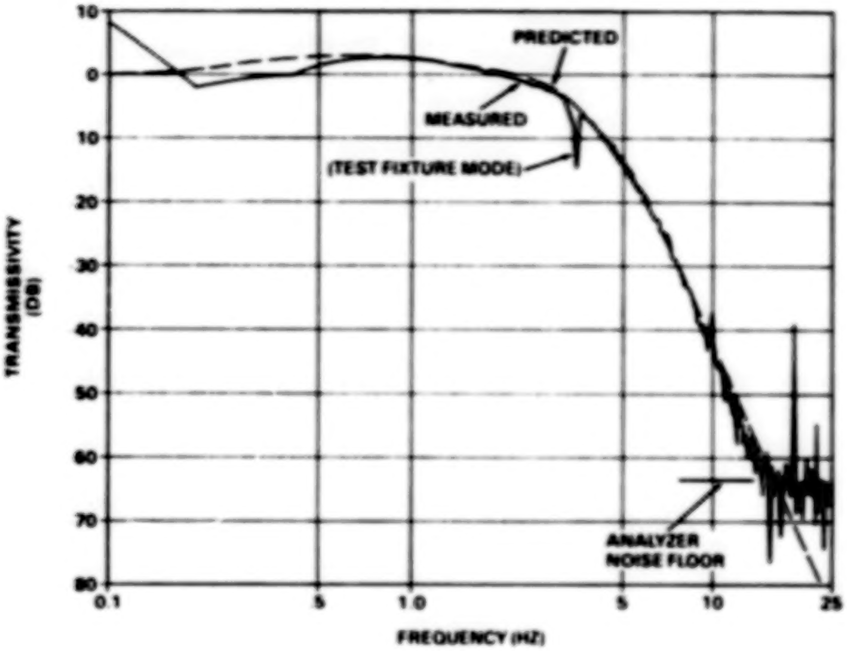

Figure 27. FEAMIS Isolation Characteristic

Conclusion

Honeywell's background in magnetic suspension technology has grown from a large diversity of programs. Extensive testing proves that magnetic suspension's noncontacting nature makes it uniquely suited for precision-pointing and isolation systems.

This wealth of experience and knowledge base has demonstrated that magnetic suspension systems for precision isolation and pointing of payloads in space is no longer a concept requiring significant development, but is a well-proven reality. What remains to be shown is the ultimate performance achievable in space with a flight demonstration.

REFERENCES

1. W.W. Anderson and S.M. Joshi. "The Annular Suspension and Pointing (ASP) System for Space Experiments and Predicted Pointing Accuracies." NASA TR R-488, December 1975.

2. W.W. Anderson and N.J. Groom. "Magnetic Suspension and Pointing System." U.S. Letters Patent No. 4,088,018, May 9, 1978.

3. W.W. Anderson and N.J. Groom. "Magnetic Suspension and Pointing System." U.S. Letters Patent No. 4,156,548, May 29, 1979.

4. D.C. Cunningham, T.P. Gismondi, and G.W. Wilson. "System Design of the Annular Suspension and Pointing System (ASPS)." AIAA Paper 78-1311, Palo Alto, CA, August 1978.

5. C.R. Keckler, K.S. Kibler, and L.F. Rowell. Determination of ASPS Performance for Large Payloads in the Shuttle Orbiter Disturbance Environment. NASA TM-80136, October 1979.

6. W.W. Anderson, N.J. Groom, and C.T. Woolley. "Annular Suspension and Pointing System." Article No. 78-1319R, Journal of Guidance and Control, Vol. 2, No. 5, September 1979.

7. D.C. Cunningham, et al. Design of the Annular Suspension and Pointing System. NASA CR-3343, January 1980.

8. R.V. VanRiper. "A Precision Pointing System for Shuttle Experiment Payloads." 17th Space Congress, May 1980.

9. R.V. Van Riper. "High Stability Shuttle Pointing System." SPIE Paper 265-12, Los Angeles Technical Symposium, February 1981.

10. T. Allen, D.D. Havenhill, and K.D. Kral. "FEAMIS: A Magnetically Suspended Isolation System for Space-Based Materials Processing." Annual AAS Guidance and Control Conference, February 1986.

11. B.J. Hamilton. "Stability of Magnetically Suspended Optics in a Vibration Environment." SPIE Paper 295-21, San Diego Technical Symposium, August 1981.

12. B.J. Hamilton. "Magnetic Suspension: The Next Generation in Precision Pointing." AAS Paper 82-034, Rocky Mountain Guidance and Control Conference, February 1982.

13. D.D. Havenhill and K.D. Kral. "Payload Isolation using Magnetic Isolation." AAS Paper 85-014, Rocky Mountain Guidance and Control Conference, February 1985.

14. B.J. Hamilton. Laboratory Evaluation of the Pointing Stability of the ASPS Vernier System. NASA CR-159307, June 1980.

15. J. Sellers. Impact of Magnetic Isolation on Pointing Performance in the Presence of Structural Flexibility. NASA CR-172481, February 1985.

N91-21190

ADVANCED MAGNETIC SUSPENSIONS for VIBRATION ISOLATION and FAST-ATTITUDE CONTROL of SPACE-BASED GENERIC POINTING MOUNTS

Robert W. Bosley, Anil N. Trivedi
AiResearch-Los Angeles Division
Allied-Signal Corp
2525 West 190th Street
P.O. Box 2960
Torrance
CA 90509-2960

ALLIED SIGNAL, INC

1988 SALES $11.9 BIL

EMPLOYEES 110,000

LISTED IN FORTUNE'S TOP 50 U.S. INDUSTRIAL COMPANIES

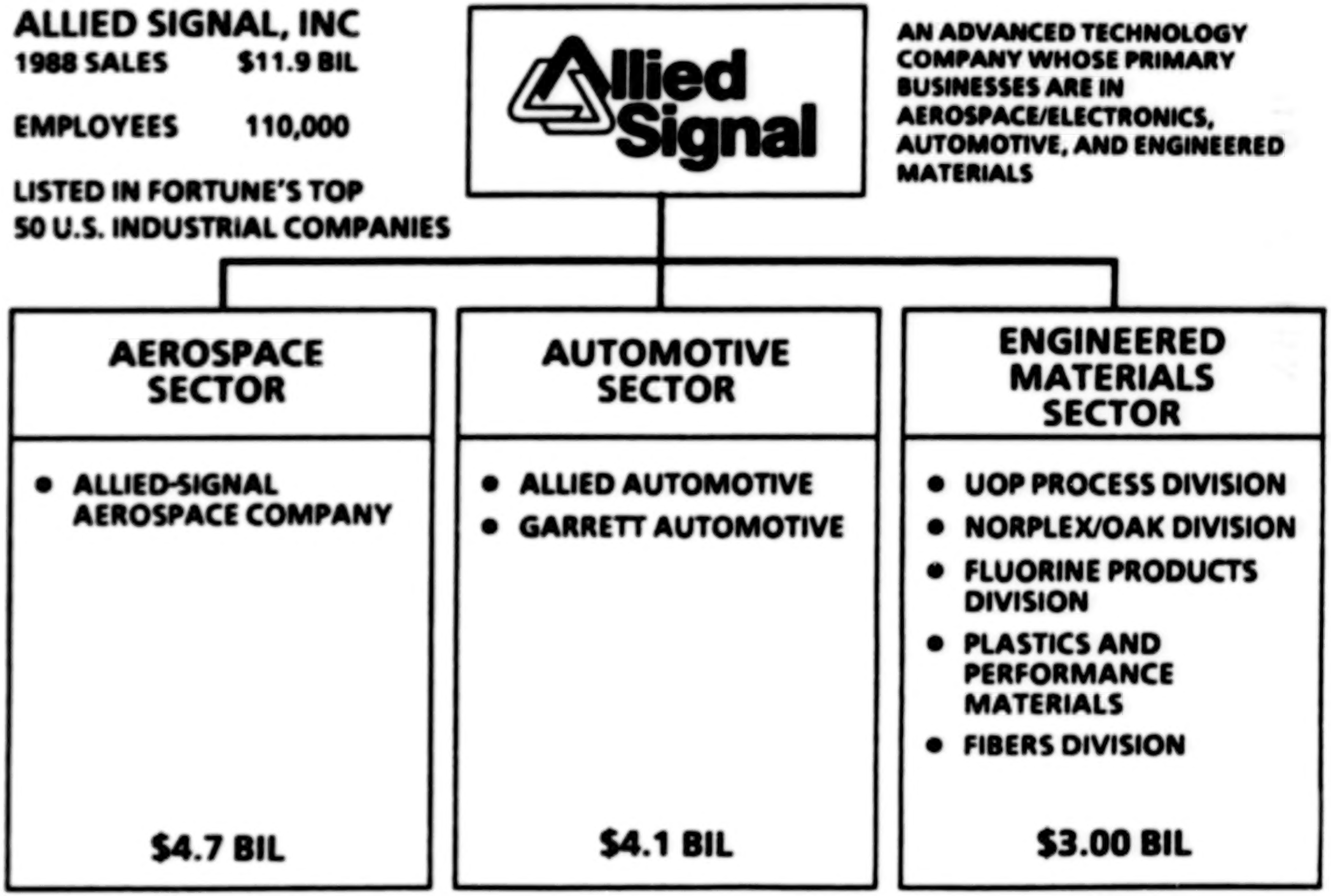

AlliedSignal

AN ADVANCED TECHNOLOGY COMPANY WHOSE PRIMARY BUSINESSES ARE IN AEROSPACE/ELECTRONICS, AUTOMOTIVE, AND ENGINEERED MATERIALS

AEROSPACE SECTOR

- ALLIED-SIGNAL AEROSPACE COMPANY

$4.7 BIL

AUTOMOTIVE SECTOR

- ALLIED AUTOMOTIVE
- GARRETT AUTOMOTIVE

$4.1 BIL

ENGINEERED MATERIALS SECTOR

- UOP PROCESS DIVISION
- NORPLEX/OAK DIVISION
- FLUORINE PRODUCTS DIVISION
- PLASTICS AND PERFORMANCE MATERIALS
- FIBERS DIVISION

$3.00 BIL

B-12112
[illegible]

DESIGN CRITERIA FOR GENERIC POINTING MOUNTS

- POINTING PAYLOAD:
  - SMALL (ounces)
  - LARGE (tons)
- AUTOMATICALLY ADAPT SERVO SYSTEM CONTROL LAWS TO INTERCHANGEABLE PAYLOADS
- CONTINUOUSLY ADAPT CONTROL LAWS TO POINTING ERRORS (POSITION, VELOCITY & ACCELERATION)
- ARTICULATION ANGLES UP TO 240 DEGREES
- TRANSMIT POWER/COMMANDS/DATA TO PAYLOAD WITHOUT CABLES
- MINIMIZE DATA RATE REQUIREMENT FOR INTERFACING WITH SPACE CRAFT

PRECEDING PAGE BLANK NOT FILMED

DESIGN CRITERIA FOR GENERIC POINTING MOUNTS

THE GENERIC POINTING MOUNT IS DESIGNED TO AIM A VARIETY OF INTERCHANGEABLE POINTING PAYLOADS USING MAGNETIC SUSPENSION AND ADAPTIVE CONTROL TECHNOLOGIES. TO CHANGE PAYLOADS REQUIRES ONLY THE MECHANICAL DETACHMENT OF THE OLD PAYLOAD AND THE ATTACHMENT OF THE NEW PAYLOAD. THE MOUNT'S SERVO SYSTEM AUTOMATICALLY SENSES THE CHANGE IN THE PAYLOAD AND MEASURES THE MULTIAXIS INERTIAS AND RESONANT CHARACTERISTICS OF THE NEW PAYLOAD. THE SERVO SYSTEM AUTOMATICALLY AND CONTINUOUSLY ADAPTS THE SERVO CONTROL LAWS TO OPTIMIZE THE ISOLATION OF THE PAYLOAD FROM SPACECRAFT VIBRATIONS, TO OPTIMIZE THE DAMPING OF PAYLOAD RESONANCES, AND TO MINIMIZE THE POINTING ERROR SETTLING TIMES FOR EACH INTERCHANGEABLE PAYLOAD AND AS THE VARIOUS MULTIAXIS POINTING ERRORS CHANGE WITH TIME. THE TRANSMISSION OF POWER AND COMMANDS TO THE PAYLOAD AND THE TRANSMISSION OF DATA FROM THE PAYLOAD ACROSS THE MAGNETIC SUSPENSION GAP IS ACCOMPLISHED WITHOUT THE USE OF CABLES. ARTICULATION IN TIP, TILT AND ROLL AXES ALLOWS 75% OF THE SPHERICAL SKY TO BE WITHIN THE MOUNTS AIMING CONE. DATA COMMUNICATION RATES BETWEEN THE POINTING MOUNT AND THE SPACECRAFT ARE MINIMIZED BY USE OF ARTICULATED AND NON ARTICULATED INERTIAL MEASUREMENT UNITS (IMU'S) COUPLED TO SPACECRAFT ORBIT AND ATTITUDE COMPUTATIONAL UNITS.

WHY IS THE PROPOSED DESIGN GENERIC?

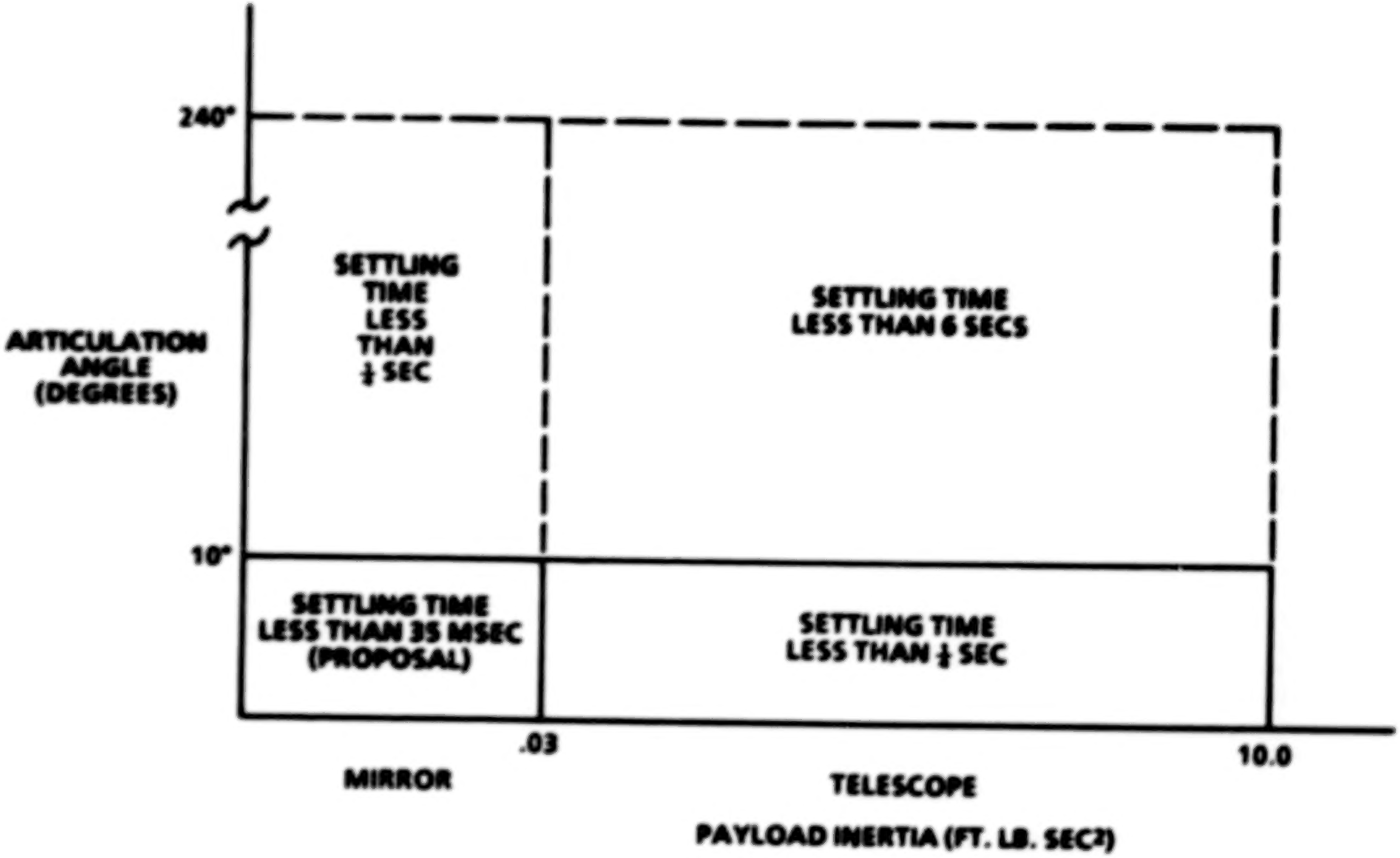

*SETTLING TIME IS FOR SIX ORDERS OF MAGNITUDE ERROR REDUCTION

WHY IS THE PROPOSED DESIGN GENERIC?

THE PROPOSED MOUNT IS GENERIC IN THAT IT CAN AIM EITHER LOW OR HIGH INERTIA PAYLOADS OVER REQUIRED ARTICULATION ANGLES THAT CAN RANGE FROM A FEW DEGREES TO 240 DEGREES. VARYING PAYLOAD INERTIA OR ARTICULATION ANGLE DOES AFFECT POINTING ERROR SETTLING TIME BUT DOES NOT AFFECT POINTING ACCURACY OR STABILITY. POINTING ERRORS CAN BE REDUCED BY SIX ORDERS OF MAGNITUDE FOR A MIRROR PAYLOAD HAVING AN INITIAL POINTING ERROR OF 10 DEGREES IN ONLY 35 MILLISECONDS. AS SHOWN, THE SETTLING TIME FOR THE MOST DEMANDING CONDITION (HIGH INERTIA, LARGE ARTICULATION ANGLE) DOES NOT EXCEED 6 SECONDS.

GENERIC POINTING MOUNT SYSTEM FEATURES

MEASURING PAYLOAD MECHANICAL IMPEDANCES	AUTOMATIC
CHANGING CONTROL LAWS TO MATCH PAYLOAD	STANDARD (IN SPACE)
VIBRATION ISOLATION	MASS DAMPING
VIBRATION DAMPING APPROACH	INERTIA VELOCITY ANTI-NODAL DAMPING FOR ALL PAYLOAD RESONANT MODES
MAXIMUM ARTICULATION ANGLE (TIP & TILT)	240°
POWER TRANSMISSION TO PAYLOAD	MICROWAVE
COMMANDS TO AND DATA FROM PAYLOAD	OPTICAL
GIMBALS	MAGNETIC
NUMBER OF PIVOT POINTS	ONE

IW-00202

GENERIC POINTING MOUNT SYSTEM FEATURES

MOST OF THE FEATURES DESCRIPTIONS ARE SELF-EXPLANATORY, EXCEPT FOR VIBRATION ISOLATION AND VIBRATION DAMPING. CONVENTIONAL MAGNETIC SUSPENSIONS USE A PSEUDO VELOCITY SIGNAL (DERIVED BY LIMITED GAIN DIFFERENTIATION OF THE MEASURED GAP ACROSS THE SUSPENSION) IN THEIR CONTROL LOOPS TO ACHIEVE DAMPING OF STRUCTURAL RESONANT MODES. THEY ALSO USE SINGLE POINT IMPEDANCE CONTROL. THE GENERIC POINTING MOUNT USES THE INERTIALLY REFERENCED VELOCITY OF THE PAYLOAD TO ACHIEVE DAMPING AND USES AN APPROACH THAT EFFECTIVELY DAMPS ALL MODES AT THEIR ANTINODES REGARDLESS OF MODE SHAPE.

GENERIC POINTING MOUNT PERFORMANCE CHARACTERISTICS

PARAMETER	
SETTLING TIME: (10 TO $3X10^{-6}$ DEG)	0.0463 SEC
NUMBER OF CYCLES TO STEADY STATE	0.50 CYCLE
SLEW RATE	26.2 RAD/SEC
BANDWIDTH	
TRANSLATION RELATIVE TO INERTIAL FRAME	100 HZ
TRANSLATION RELATIVE TO PLATFORM	0.02 HZ
TIP	47.7 TO 450 HZ
TILT	47.7 TO 450 HZ

IW-08201

PRECEDING PAGE BLANK NOT FILMED

GENERIC POINTING MOUNT FUNCTIONAL BLOCK DIAGRAM

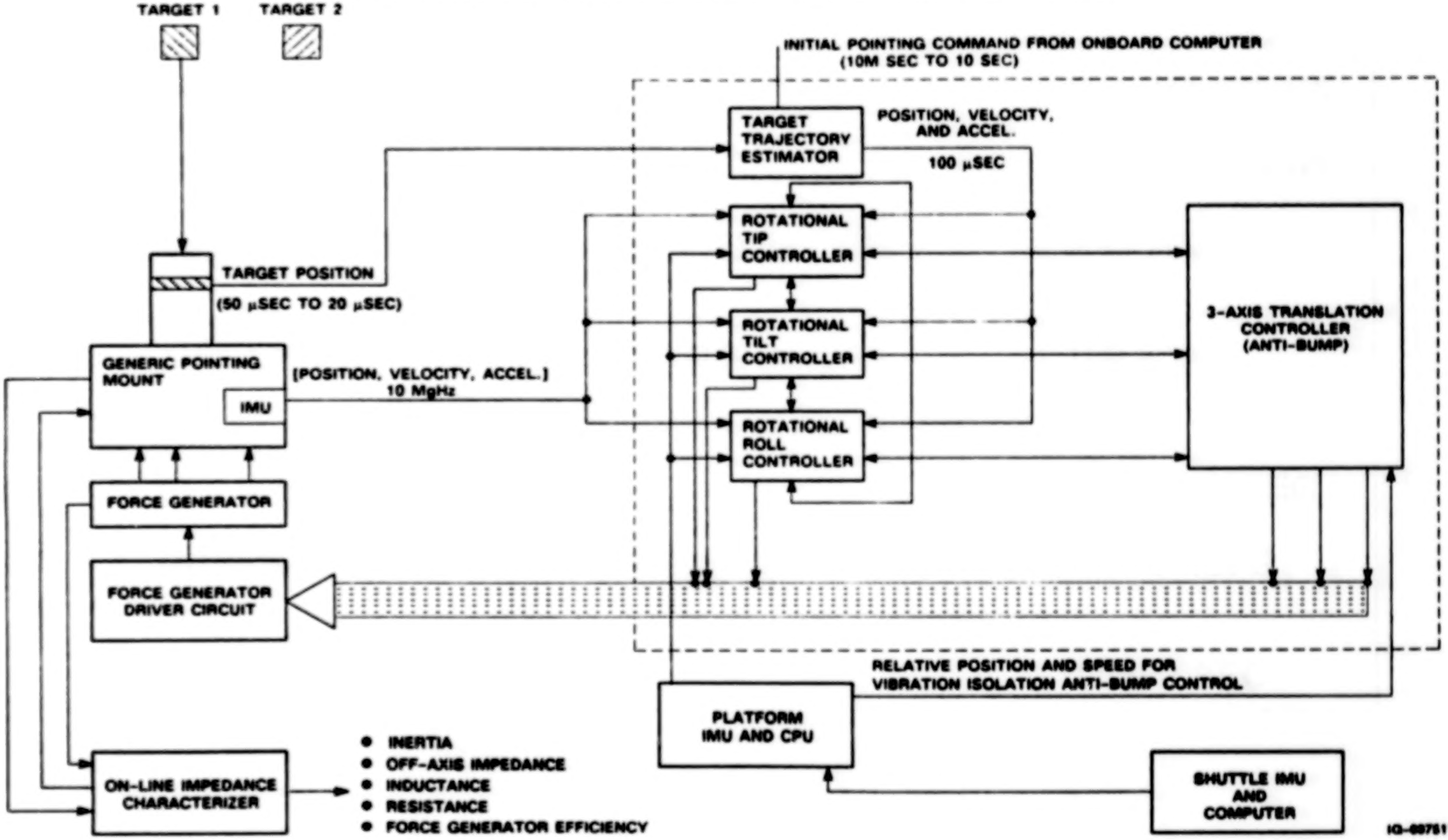
TARGET 1
TARGET 2
INITIAL POINTING COMMAND FROM ONBOARD COMPUTER (10M SEC TO 10 SEC)
TARGET TRAJECTORY ESTIMATOR
POSITION, VELOCITY, AND ACCEL.
100 μSEC
TARGET POSITION
(50 μSEC TO 20 μSEC)
ROTATIONAL TIP CONTROLLER
ROTATIONAL TILT CONTROLLER
ROTATIONAL ROLL CONTROLLER
3-AXIS TRANSLATION CONTROLLER (ANTI-BUMP)
GENERIC POINTING MOUNT
IMU
(POSITION, VELOCITY, ACCEL.) 10 MgHz
FORCE GENERATOR
FORCE GENERATOR DRIVER CIRCUIT
RELATIVE POSITION AND SPEED FOR VIBRATION ISOLATION ANTI-BUMP CONTROL
PLATFORM IMU AND CPU
SHUTTLE IMU AND COMPUTER
ON-LINE IMPEDANCE CHARACTERIZER
● INERTIA
● OFF-AXIS IMPEDANCE
● INDUCTANCE
● RESISTANCE
● FORCE GENERATOR EFFICIENCY

IG-00751*

IG-00751

GENERIC POINTING MOUNT FUNCTIONAL BLOCK DIAGRAM

THE GENERIC POINTING MOUNT USES A SIX AXIS SERVO CONTROL TO ACHIEVE THE PROPER POINTING ANGLES AND TO PREVENT TRANSMISSION OF VIBRATION TO THE PAYLOAD. IT REQUIRES AN ARTICULATED IMU THAT MOVES WITH THE PAYLOAD. TO MINIMIZE THE NEED FOR SPACECRAFT ORBITAL AND ATTITUDE DATA, AN NON-ARTICULATED IMU IS USED. A MULTIDIMENSIONAL TARGET TRAJECTORY ESTIMATOR IS USED TO SPEED UP THE POINTING CONTROL LOOPS. SYSTEM PARAMETERS MAY CHANGE WITH TIME AND THE SERVOSYSTEM CAN BECOME NONLINEAR DUE TO MANY FACTORS (E.G., FORCE COIL VOLTAGE APPROACHING SUPPLY BUSS VOLTAGE). THEREFORE THE SERVOCONTROL MEASURES SYSTEM PARAMETERS ON-LINE WITH AN IMPEDANCE CHARACTERIZER TO PREDICT NONLINEARITIES BEFORE THEY ARE ENCOUNTERED.

GENERIC POINTING MOUNT

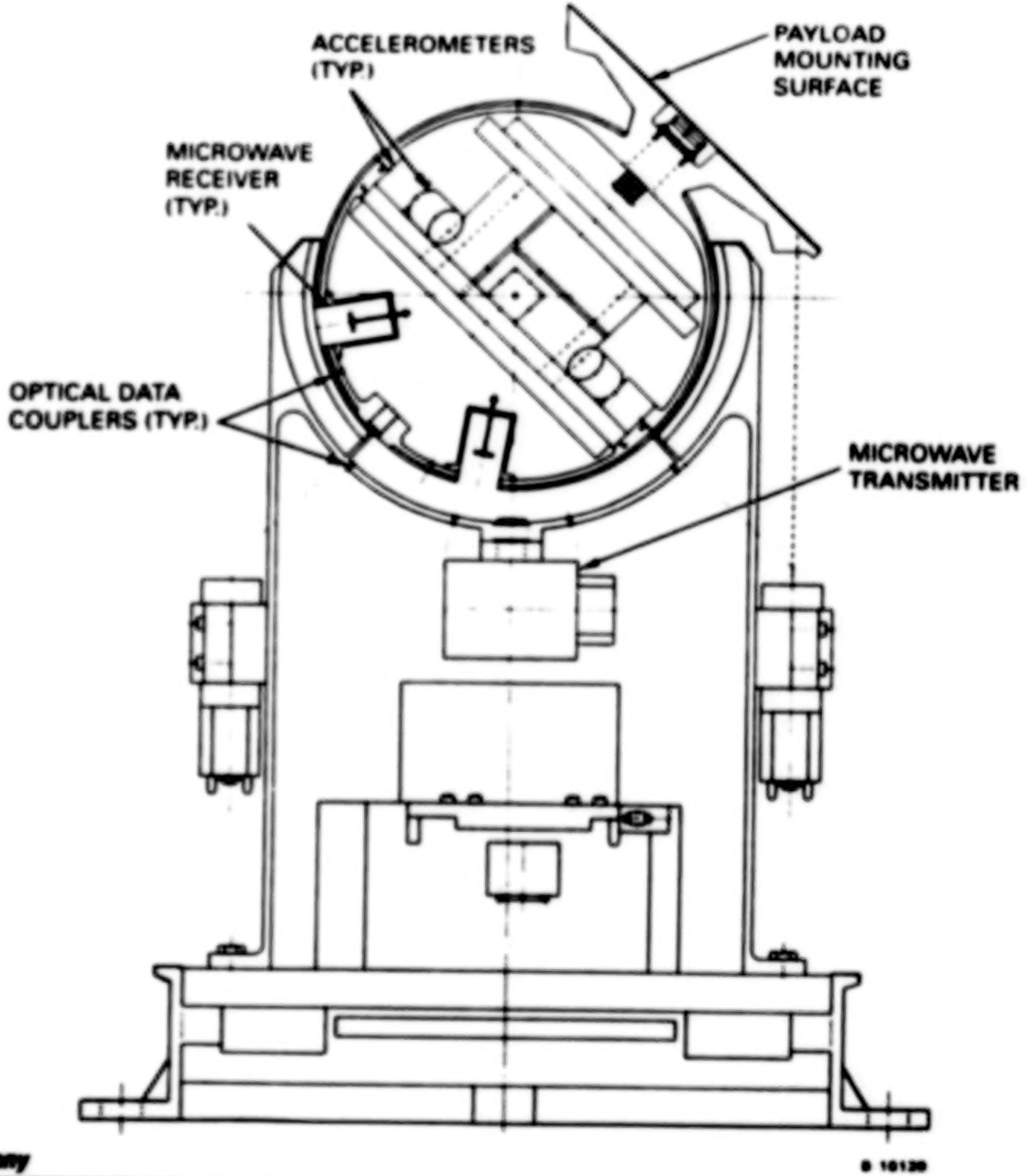
ACCELEROMETERS (TYP.)
PAYLOAD MOUNTING SURFACE
MICROWAVE RECEIVER (TYP.)
OPTICAL DATA COUPLERS (TYP.)
MICROWAVE TRANSMITTER
B 10130

IG-00751

GENERIC POINTING MOUNT

THE GENERIC POINTING MOUNT USES A SPHERICAL MAGNETIC FORCE/TORQUE GENERATOR TO APPLY TORQUES IN THREE AXES AND TRANSLATIONAL FORCES IN THREE AXES TO A 10" SPHERE ATTACHED TO A PAYLOAD MOUNTING SURFACE. THE SPHERE CAN ARTICULATE 120 DEGREES IN THE TIP AND TILT AXES AND CAN ROTATE WITHOUT LIMIT IN THE ROLL AXIS. BY MOUNTING THE PAYLOAD AT A 60 DEGREE ANGLE RELATIVE TO THE MOUNT AXIS, ROLLING THE PAYLOAD CAN ALLOW IT TO "LOOK OVER THE HORIZON" AND THUS OBTAIN AN EFFECTIVE 240 DEGREE OF TIP AND TILT ARTICULATION. RING LASER GYROSCOPES AND ACCELEROMETERS ARE USED BY BOTH IMU'S. POWER IS TRANSMITTED ACROSS THE MAGNETIC SUSPENSION GAP BY MICROWAVES. COMMANDS AND DATA ARE TRANSMITTED ACROSS THE GAP BY OPTICAL LINK ARRAYS. AUTO COLLIMATORS ARE USED TO CALIBRATE THE IMU'S. THE DESIGN IS SCALABLE FOR LARGER SIZE PAYLOADS.

TIP AXIS ROTATIONAL CONTROL AND PLANT BLOCK DIAGRAM

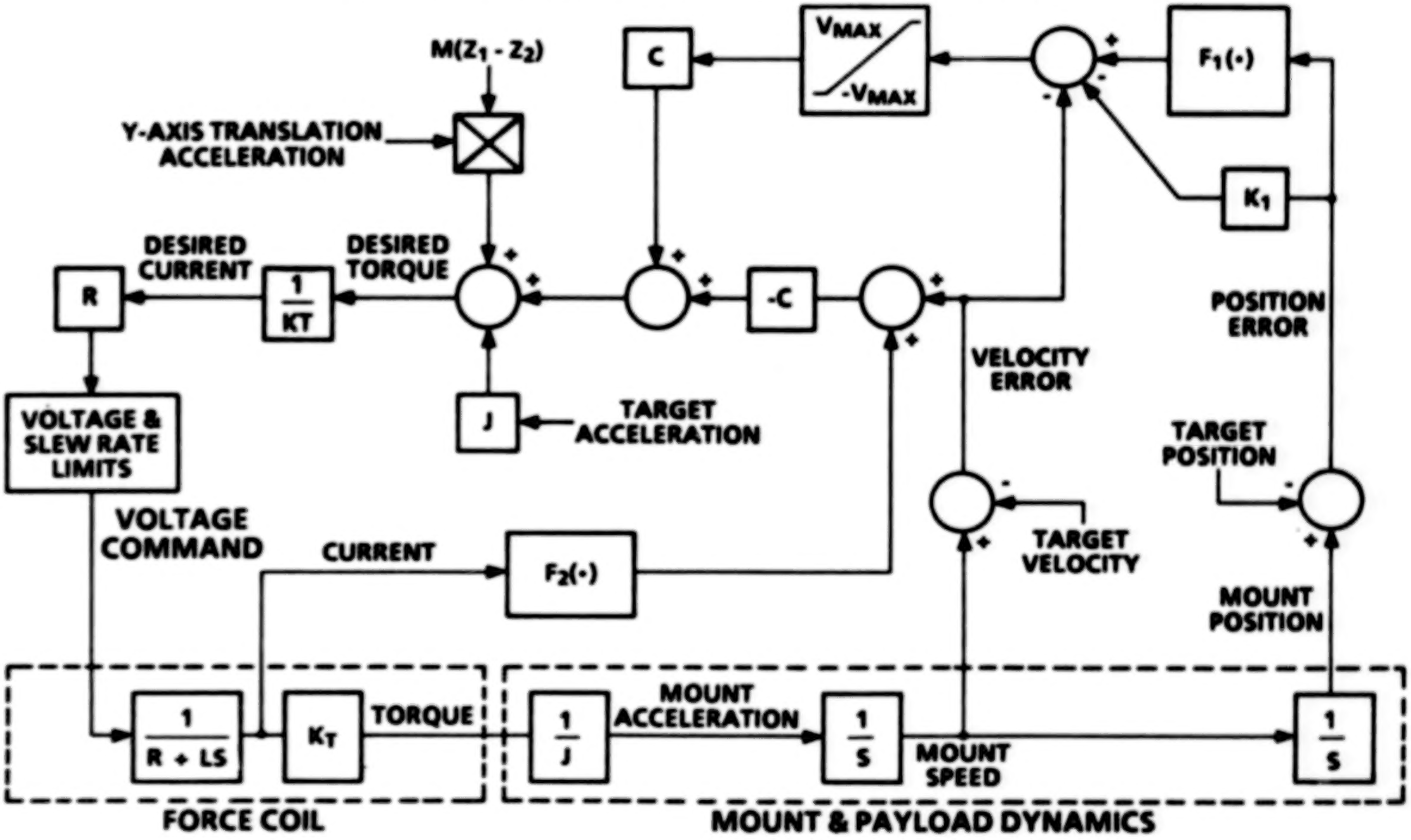
M(Z1 - Z2)
Y-AXIS TRANSLATION ACCELERATION
C
VMAX
-VMAX
F1(•)
K1
DESIRED CURRENT
R
1/KT
DESIRED TORQUE
-C
POSITION ERROR
VELOCITY ERROR
J
TARGET ACCELERATION
VOLTAGE & SLEW RATE LIMITS
TARGET POSITION
TARGET VELOCITY
VOLTAGE COMMAND
CURRENT
F2(•)
MOUNT POSITION
1/(R + LS)
KT
TORQUE
1/J
MOUNT ACCELERATION
1/S
MOUNT SPEED
1/S
FORCE COIL
MOUNT & PAYLOAD DYNAMICS

Allied-Signal Aerospace Company

AiResearch Los Angeles Division

B-15232

TIP AXIS ROTATIONAL CONTROL
AND PLANT BLOCK DIAGRAM

CONVENTIONAL MAGNETIC SUSPENSIONS CAN BE CHARACTERIZED AS MASS-SPRING-DAMPING RESONANT SERVOSYSTEMS WHERE THE MASS IS PRIMARILY DUE TO THE PHYSICAL INERTIA OF THE SUSPEND OBJECT, AND THE SPRING AND DAMPING ARE ESTABLISHED BY THE SERVOSYSTEMS SENSORS, CIRCUITRY AND MAGNETIC FORCE GENERATORS. THE SERVOSYSTEM DAMPING CAN USUALLY BE EFFECTIVELY ACHIEVED ONLY OVER A LIMITED FREQUENCY RANGE IF VELOCITY IS DERIVED BY DIFFERENTIATION. IN CONTRAST, THE GENERIC POINTING MOUNT CAN BE CHARACTERIZED AS A MASS-DAMPING SYSTEM WITH NO "CLASSICAL" SPRING. AN IDEAL VELOCITY ERROR IS CONTINUOUSLY DETERMINED AND SET AS A SERVOSYSTEM OBJECTIVE FUNCTION TO ASSURE THAT ZERO ERROR FOR POSITION VELOCITY, ACCELERATION, AND JERK CAN BE ACHIEVED SIMULTANEOUSLY. THIS ASSURES MINIMUM SETTLING TIME. THE CALCULATION OF THE IDEAL VELOCITY HAS TO ACCOUNT FOR CLAMPS AND NONLINEARITIES (E.G., LIMITED BUSS VOLTAGE, VELOCITY LIMITS ON GYROSCOPES, ETC.) THAT WILL BE ENCOUNTERED DURING THE ENTIRE (FUTURE) PERIOD. THE SERVOSYSTEM APPLIES TORQUES AND FORCES TO PREVENT POINTING ERRORS DUE TO FUTURE OFF-AXIS DISTURBANCES. THIS IS PRIMARILY DUE TO NON-SYMMETRIES BETWEEN THE INERTIAS IN THE VARIOUS PAYLOAD AXES.

VELOCITY TRAJECTORY PLANNER

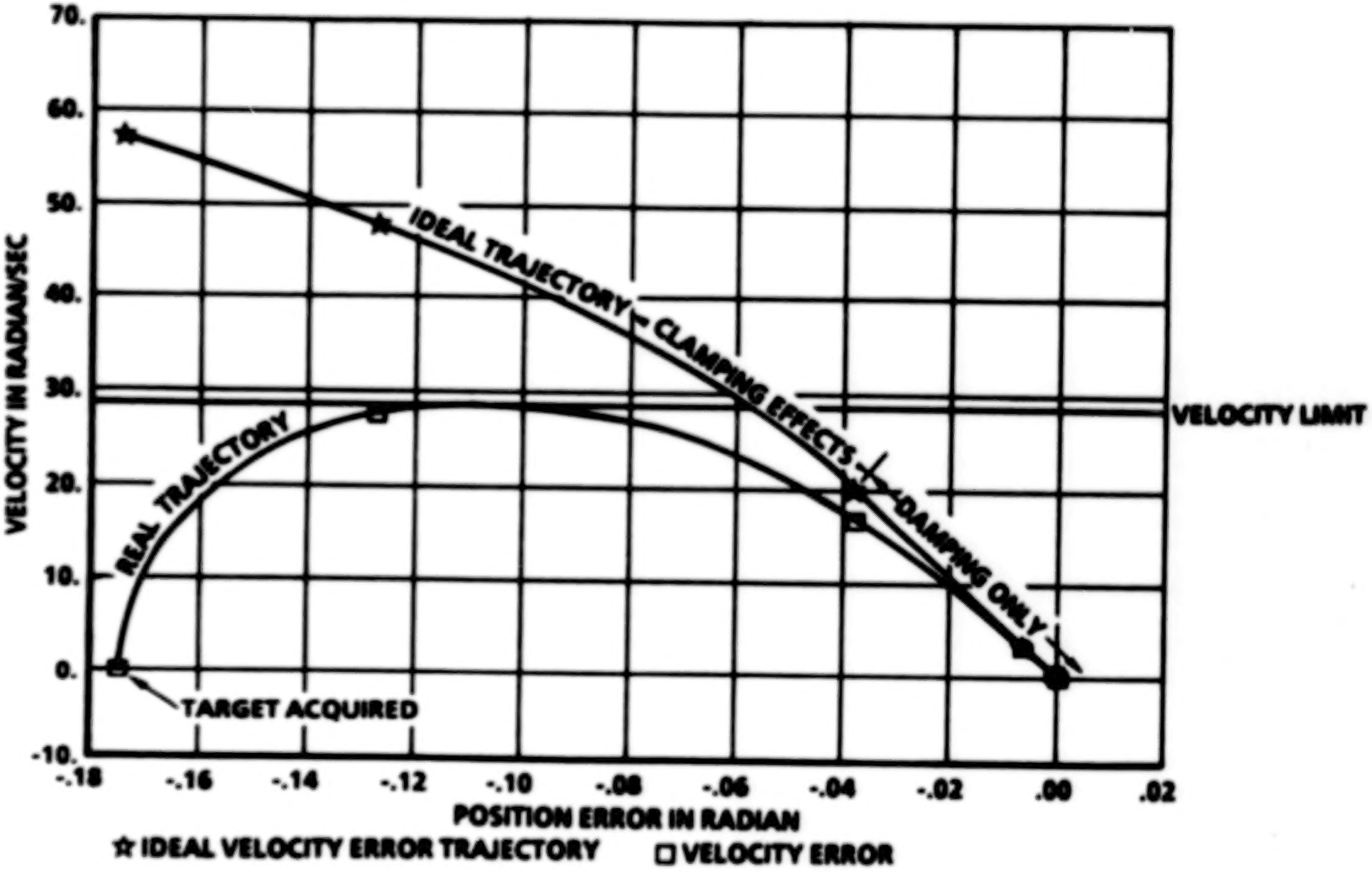

VELOCITY TRAJECTORY PLANNER

AT ANY GIVEN TIME, THE POINTING MOUNT AND PAYLOAD WILL HAVE MULTIPLE POINTING ERRORS (POSITION, VELOCITY, ACCELERATION, JERK, VOLTAGE/CURRENT/FREQUENCY) IN BOTH THE TIP AND TILT AXIS. SIMILAR ERRORS WILL ALSO EXIST IN THE ROLL AND THREE TRANSLATIONAL AXES. IT IS DESIRABLE TO REDUCE ALL OF THESE ERRORS TO ZERO AT THE SAME TIME AND AS QUICKLY AS POSSIBLE WITHOUT OSCILLATIONS. FOR A MASS-DAMPING SYSTEM THERE IS AN IDEAL RATIO OF VELOCITY ERROR TO POSITION ERROR THAT WILL ZERO OUT ALL ERRORS AT THE SAME TIME. THIS RATIO IS A FUNCTION OF THE INERTIA AND THE DAMPING CONSTANT. IF POSITION ERRORS ARE SMALL, THE SERVOSYSTEM CAN OPERATE LINEARLY AND THE IDEAL VELOCITY ERROR WILL BE PROPORTIONAL TO THE POSITION ERROR BUT WITH OPPOSITE SIGN. IF POSITION ERRORS ARE LARGE, MANY NONLINEARITIES (E.G., VELOCITY OR VOLTAGE CLAMPS) CAN CAUSE THE IDEAL VELOCITY ERROR TO BE A NONLINEAR FUNCTION OF POSITION ERROR. IF THE IDEAL VELOCITY IS EXCEEDED, OVERSHOOT WILL OCCUR IN POSITION ERROR. IF THE VELOCITY PROFILE IS WELL BELOW THE IDEAL TRAJECTORY, IT WILL CAUSE EXCESSIVE SETTLING TIMES.

IMPROVED VIBRATION ISOLATION AND DAMPING

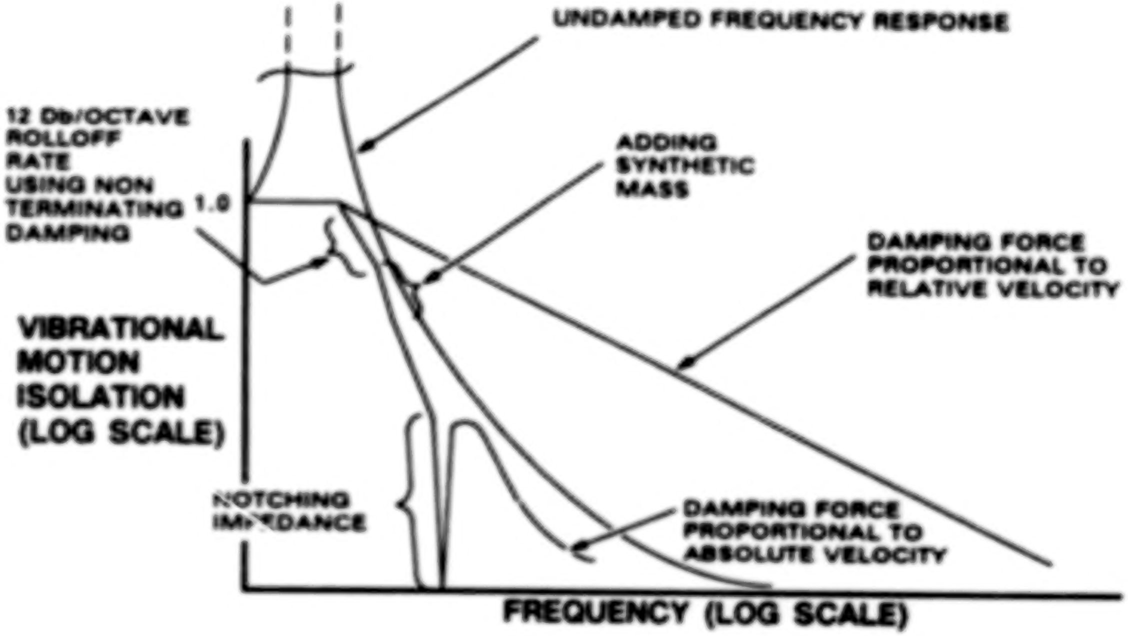

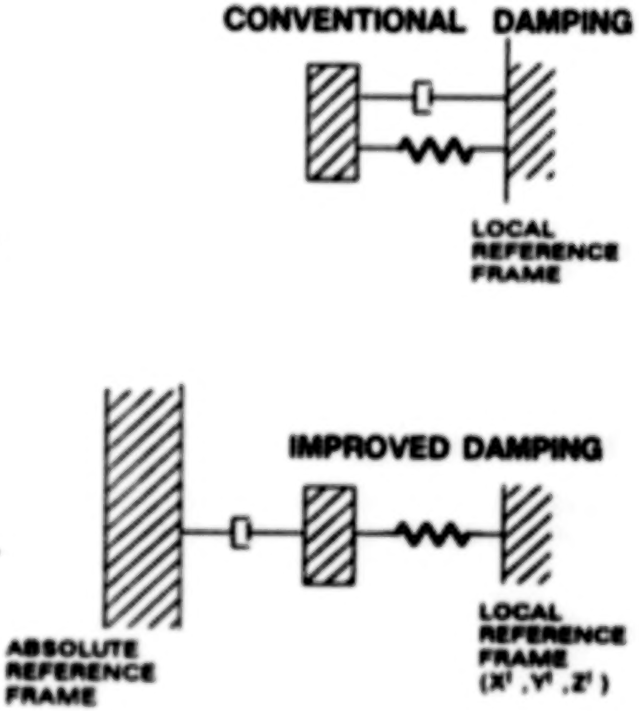
CONVENTIONAL DAMPING
LOCAL REFERENCE FRAME
IMPROVED DAMPING
ABSOLUTE REFERENCE FRAME
LOCAL REFERENCE FRAME (X', Y', Z')

IMPROVEMENTS AVALABLE:

- NOTCHED IMPEDANCE
- ANTI-NODAL DAMPING FOR ILL MODES
- ORTHOGONAL MODAL DAMPING
- INERTIAL MASS ENHANCEMENT
- FORCE REFLECTION

IMPROVED VIBRATION ISOLATION AND DAMPING

MANY ADVANCED TECHNOLOGIES ARE AVAILABLE TO ISOLATE VIBRATION AND DAMP RESONANCES WITH MAGNETIC SUSPENSIONS. THESE INCLUDE:

- NOTCHING THE SUSPENSION IMPEDANCE TO ZERO AT THE FREQUENCIES OF KNOWN RESONANCES.
- DAMPING FLEXURAL CRITICALS SO AS TO SIMULATE ANTINODAL DAMPING REGARDLESS OF MODE SHAPE.
- CONTROLLING THE SUSPENSION IMPEDANCES TOTALLY INDEPENDENTLY FOR EACH RESONANCE. THIS CANNOT BE ACHIEVED WITH SINGLE POINT IMPEDANCE SUSPENSIONS.
- ENHANCE THE "APPARENT" INERTIAL MASS FOR SUSPENDED OBJECTS BY APPLYING MAGNETIC FORCES PROPORTIONAL TO ACCELERATION.
- REFLECT VIBRATIONAL FORCES THAT PASS THROUGH A SUSPENSION BACK TO THE SOURCE.
- INCREASE ROLL OFF RATE OF SUSPENSION ISOLATION VERSUS FREQUENCY BY USING INERTIALLY REFERENCED VELOCITY RATHER THAN RELATIVE VELOCITY FOR DAMPING.

POSITION RESPONSE NOMINAL CONDITIONS WITH TRAJECTORY PLANNER & LIMITERS

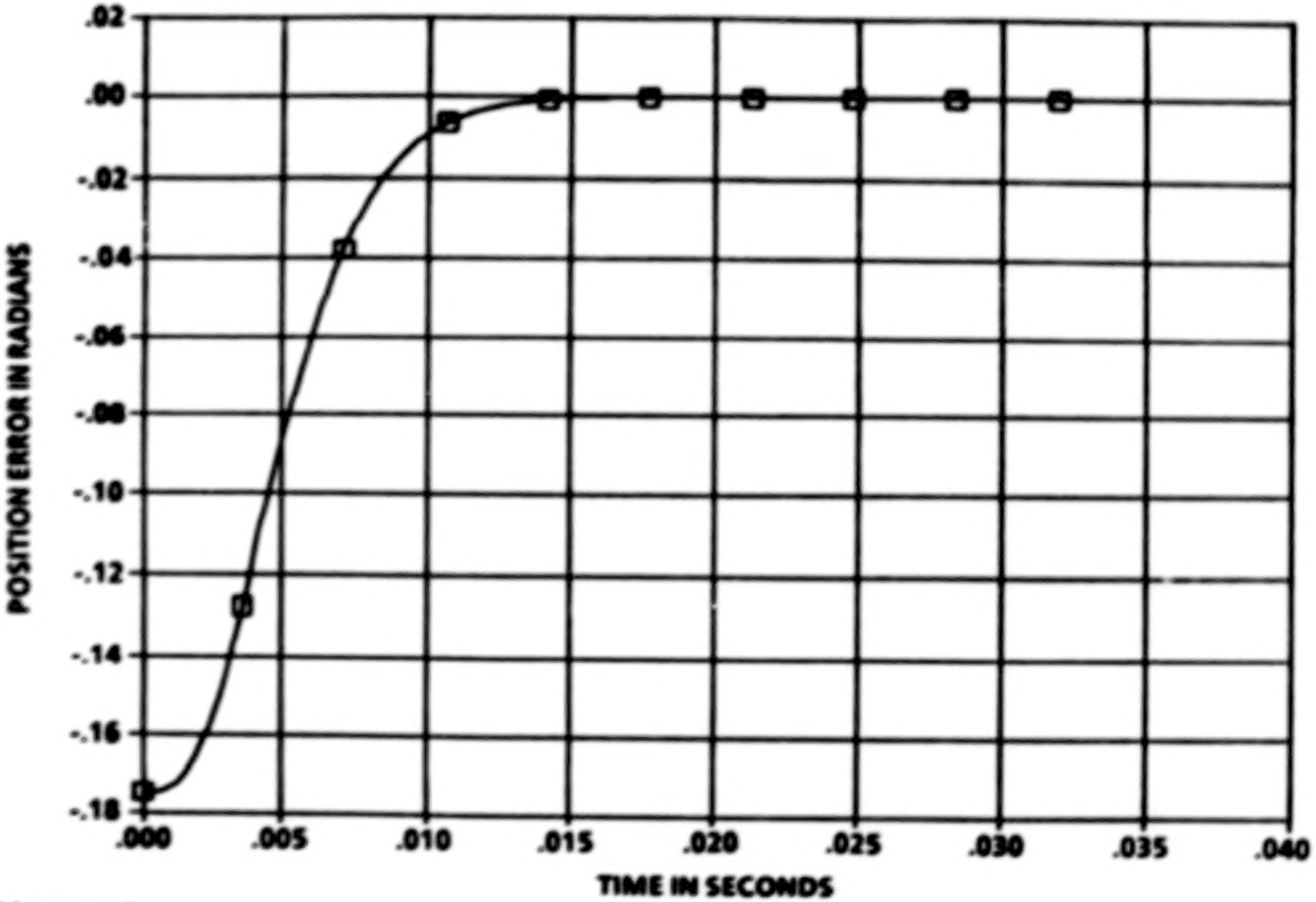

POSITION RESPONSE NOMINAL CONDITIONS WITH TRAJECTORY PLANNER & LIMITERS

THE GENERIC POINTING MOUNT CAN REDUCE POINTING ERRORS BY SIX ORDERS OF MAGNITUDE IN LESS THAN 35 MILLISECONDS IF PRECISE AND ACCURATE SENSORS ARE UTILIZED.

SETTLING TIME VERSUS INERTIA

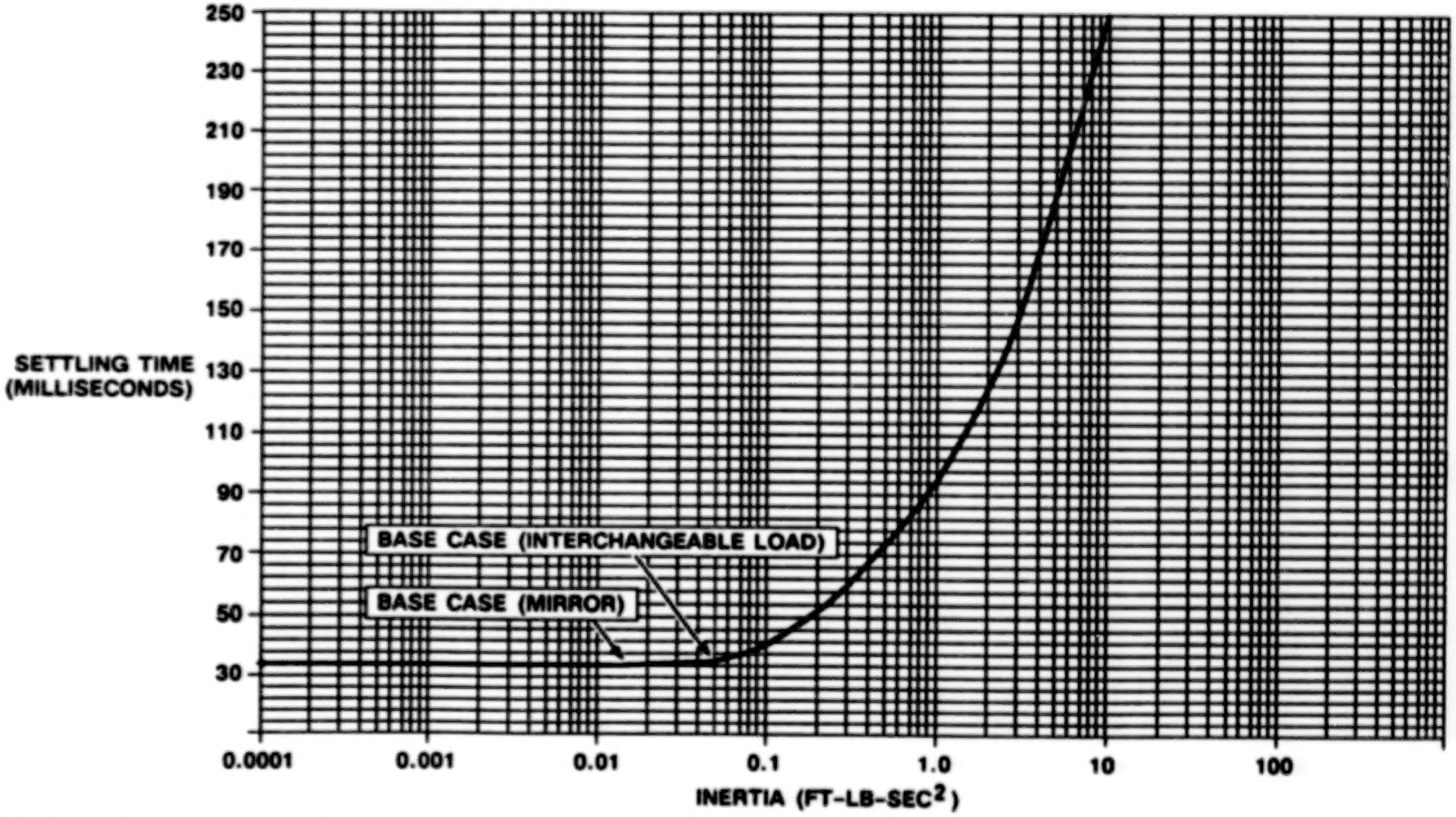

SETTLING TIME VERSUS INERTIA

(FOR AN INITIAL 10 DEGREE POINTING ERROR)

INCREASING PAYLOAD INERTIA DOES NOT INCREASE SETTING TIME (FOR 6 ORDERS OF MAGNITUDE ERROR REDUCTION) UNTIL THE MAGNETIC TORQUE GENERATOR BECOMES SATURATED. THE SETTLING INCREASES NON-LINEARITY BEYOND THIS POINT

SETTLING TIME VERSUS INITIAL POSITION ERROR BASELINE CASE (MIRROR)

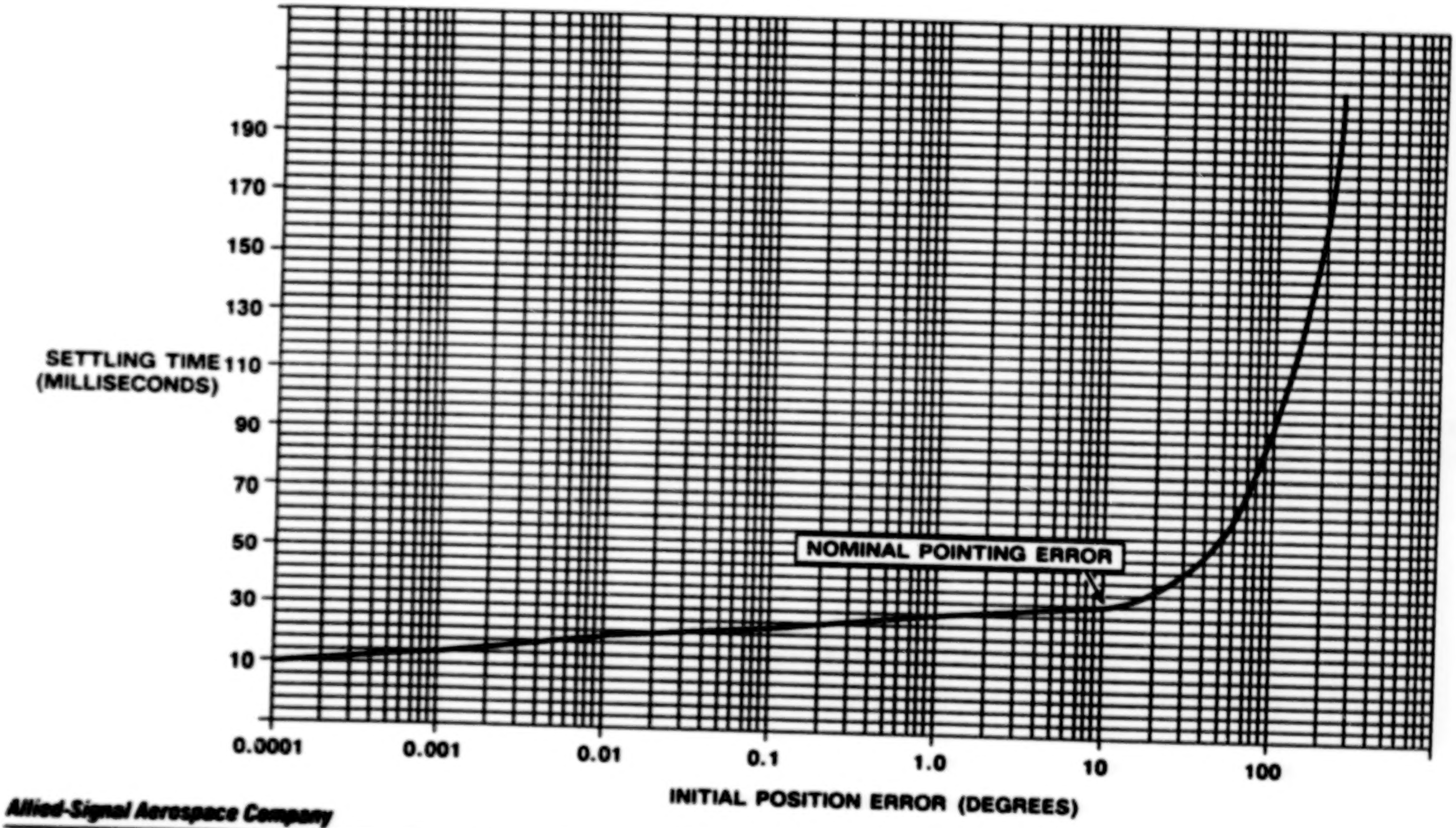

SETTLING TIME VERSUS INITIAL POSITION ERROR
BASELINE CASE (MIRROR)

SETTLING TIME INCREASES ONLY AS A FUNCTION OF THE SQUARE ROOT OF INITIAL POSITION ERROR UNTIL THE MAGNETIC TORQUE GENERATOR IS SATURATED. IT IS NON-LINEAR BEYOND THIS POINT.

SUMMARY OF SYSTEM FEATURES

- GENERIC POINTING MOUNT FOR INTERCHANGEABLE PAYLOADS
- SYSTEM AUTOMATICALLY ADAPTS CONTROL LAWS TO EACH PAYLOAD
- POINTING CONTROL IN THREE AXES AROUND A SINGLE PIVOT POINT
- 240-DEG ARTICULATION ANGLES

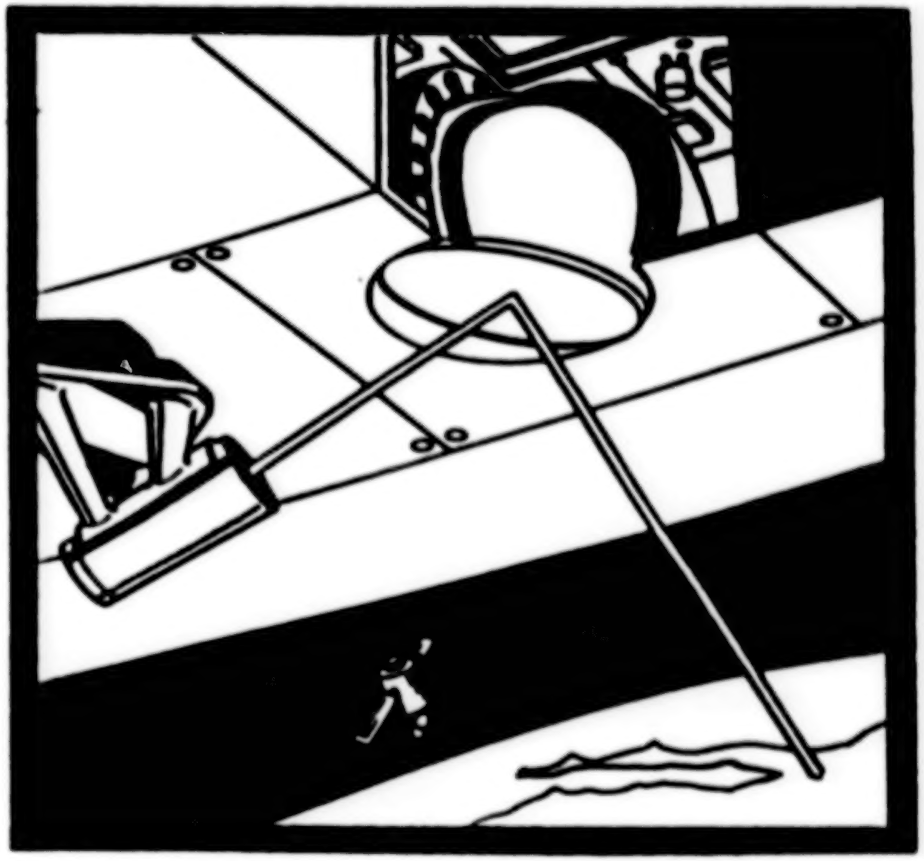

OTHER APPLICATIONS FOR GENERIC MAGNETIC SUSPENSION TECHNOLOGIES

MAGNETIC SUSPENSIONS PROVIDE IMPROVED:

- ISOLATION AND POINTING
- VIBRATION CANCELLATION
- BEARINGS

SPACE TELESCOPES

SUBMARINES

SHORT ROTORS

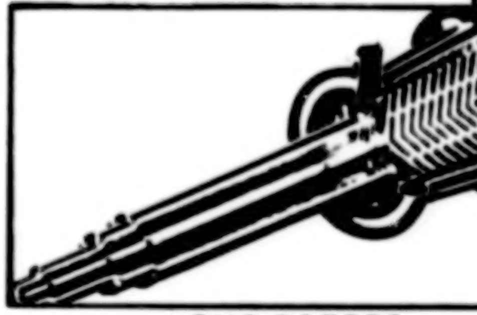

LONG ROTORS

F-55706-E

N91-21191

A SUPERCONDUCTING LARGE-ANGLE MAGNETIC SUSPENSION

James Downer, James Goldie, Richard Torti
SatCon Technology Corporation
12 Emily Street
Cambridge
MA 02139-4507

PRECEDING PAGE BLANK NOT FILMED

A Superconducting Large-angle Magnetic Suspension

James Downer, James Goldie, and Richard Torti

SatCon Technology Corporation
12 Emily Street
Cambridge, MA 02139

Presented at: Workshop on Aerospace Applications of Magnetic Suspension Technology
NASA Langley Research Center, Hampton, VA; September 25, 1990

Low-noise torque sources will be used to control and point large future missions such as Space Station, co-orbiting platforms, and the Hubble Space Telescope. Conventional torquing actuators will have problems in terms of life and vibration. On Earth, magnetic suspensions using superconductors are desirable in applications in which large clearance spaces or extreme precision is needed.

SatCon Technology Corporation has been developing the component technologies required for an advanced control moment gyro (CMG) type of slewing actuator for large payloads. The key component of the CMG is a large-angle magnetic suspension (LAMS). The LAMS combines the functions of the gimbal structure, torque motors, and rotor bearings of a CMG. The LAMS uses a single superconducting "source coil" and an array of cryoresistive "control coils" to produce a specific output torque more than an order of magnitude greater than conventional devices.

SatCon is currently designing, developing, and testing a laboratory-scale superconducting LAMS. The LAMS system is based around an available superconducting solenoid, an array of twelve room-temperature normal control coils, and a multi-input, multi-output control system. The purpose of the experiment is to demonstrate the control laws for stabilizing and controlling the LAMS system. The controller is, of course, the key component of most magnetic suspension systems.

1. INTRODUCTION

This paper discusses the ongoing development of a novel magnetic suspension system technology demonstration experiment at SatCon Technology Corporation. The goal of this program is to demonstrate an innovative approach to the design of magnetic suspension systems in which a superconducting coil is employed in order to eliminate conventional magnetic cores and permanent magnets. The design was motivated by recent progress in superconducting materials and by the requirements for an advanced control moment gyro (CMG) type of slew actuator which is currently under development. The slew actuator is intended for use with large spacecraft.

SatCon is currently working toward the demonstration of superconducting large-angle magnetic suspension (LAMS) technology in the laboratory by designing, developing, and testing a reduced-scale superconducting LAMS system. The laboratory system is based around a commercially-available superconducting solenoid and an array of twelve room-temperature normal control coils. The purpose of the experiment is to demonstrate the required control system technology. The controller is, of course, the key component of most magnetic suspension systems.

2. BACKGROUND

Slewing of large payloads will require control torque and angular momentum storage capacities that are large in comparison to the capabilities of available actuators.

Control Moment Gyros

The most common type of momentum exchange effector, the control moment gyro (CMG), exchanges angular momentum by varying the angular orientation of a constant-speed flywheel through the use of gimbals. Figure 1 describes the acceleration phase of a slew maneuver in terms of applying a torque to a spacecraft over a fixed period of time. The torque is applied through the azimuth-axis torquer. The flywheel precesses about the elevation axis to conserve angular momentum.

The Large-angle Magnetic Suspension (LAMS) [3]

The use of a mechanical gimbal structure such as the one shown in Figure 1 is the conventional approach for CMG design. An alternative approach which consolidates the functions of mechanical bearing and gimbal systems has been demonstrated. A large-angle magnetic suspension (LAMS) is a five-axes, actively-controlled magnetic bearing designed to accommodate a certain amount of angular motion about the lateral axes of the flywheel [1,2]. Research [2] indicates that the mass of a LAMS can be made to be less than that of a gimbal system by a factor five (depending on the amount of angular freedom).

The Superconducting LAMS

A superconducting LAMS is an advanced design which may be used in a CMG to deliver large torques to a spacecraft without the need for an excessively massive magnetic core or the consumption of a large amount of power. The superconducting LAMS, as its name suggests, employs a superconducting coil and thus eliminates all conventional magnetic structures in order to produce an energy-efficient, light-weight design.

Figure 2 is a partially cut-away view which shows the rotating components (superconducting coil and flywheel) and cryogenic housing of a two-degree-of-freedom CMG which employs a superconducting LAMS. The superconducting "source" coil is a solenoid which operates without an electrical input. The current in the solenoid persists because of the lack of resistance in the superconducting material. The spherical case which surrounds the rotating components also serves as the cryostat for the superconducting solenoid. The superconducting LAMS employs a total of twelve (12) normal (non-superconducting) "control" coils which interact with the fields produced by the source coil solenoid in order to apply forces and torques.

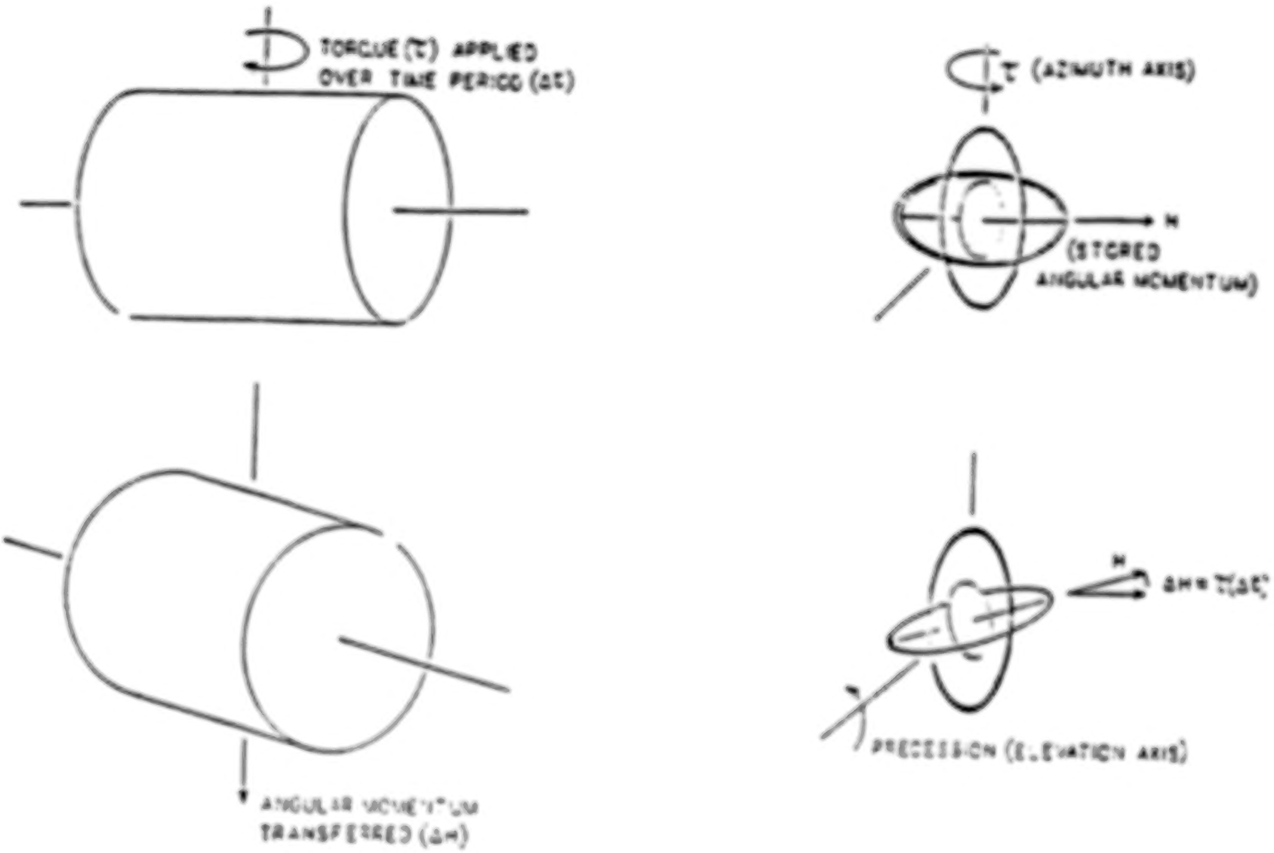

TORQUE (τ) APPLIED
OVER TIME PERIOD (Δt)
ANGULAR MOMENTUM
TRANSFERRED (ΔH)
τ (AZIMUTH AXIS)
H
(STORED
ANGULAR MOMENTUM)
H
ΔH = τ(Δt)
PRECESSION (ELEVATION AXIS)

Figure 1. CMG Operating Principle

ORIGINAL PAGE IS
OF POOR QUALITY

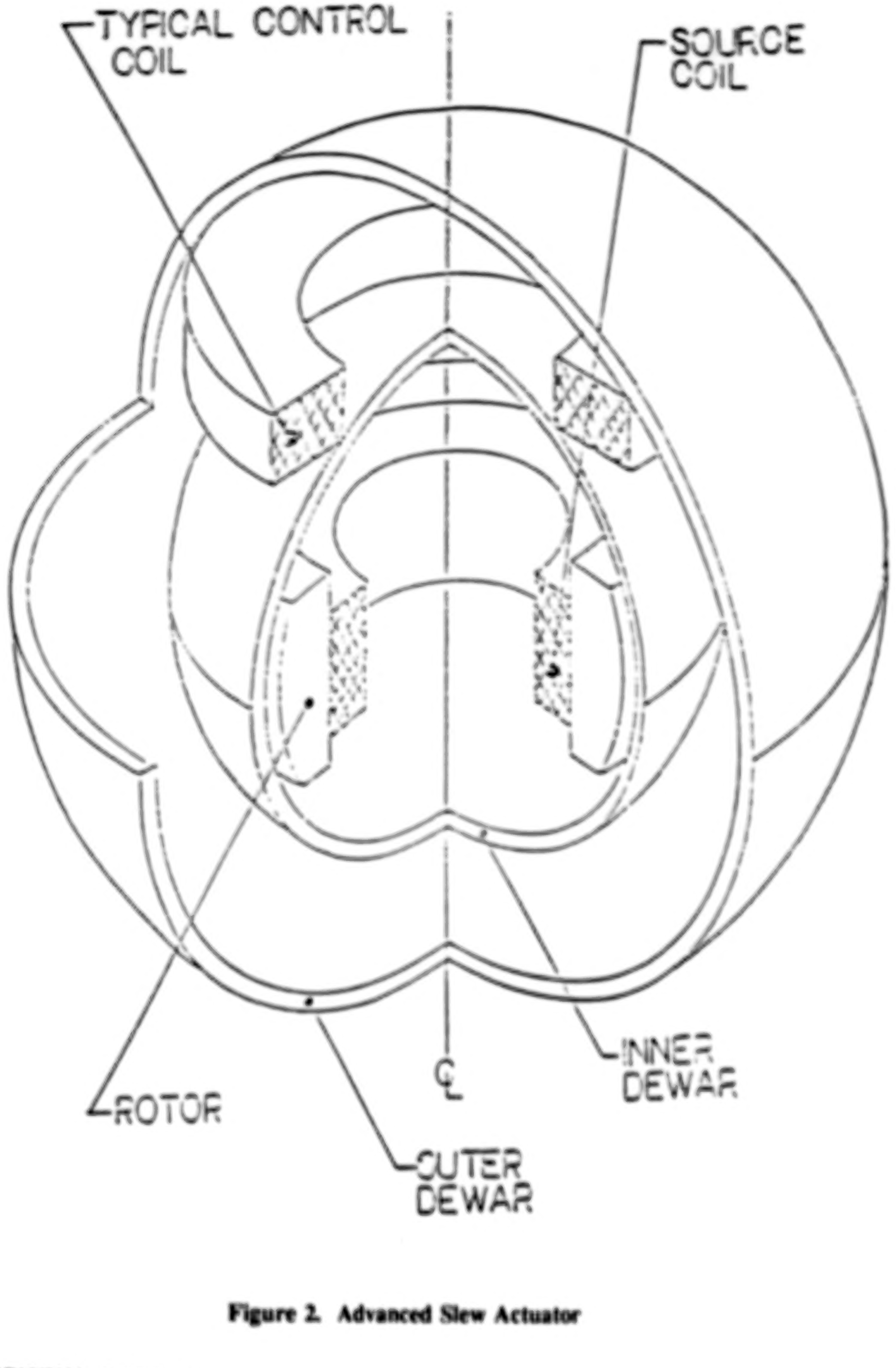
TYPICAL CONTROL COIL
SOURCE COIL
ROTOR
CL
INNER DEWAR
OUTER DEWAR

Figure 2. Advanced Slew Actuator

ORIGINAL PAGE IS
OF POOR QUALITY

An emerging technology, high purity aluminum conductors cooled to the boiling point temperature of liquid hydrogen, was found to be the best choice for the control coils. These "hyperconductors" allowed substantial improvements in mass and power consumption over what is obtainable through the use of copper conductors.

Table 1 contains the performance parameters (mass tabulation and power consumption) for the key components of the superconducting LAMS. These represent a vast improvement over what could be achieved with more conventional technology.

Table 1. Superconducting LAMS Performance

Control Torque	13,500 Nm
Mass Tabulation	
Control Coils	65 kg
Dewar	57 kg
Stator Total	122 kg
Source Coil	57 kg
LAMS total	179 kg
Power	57 W

3. TESTBED OVERVIEW

This section presents an overview of the prototype LAMS system. The description is arbitrarily divided into separate descriptions of the mechanical design, the magnetics design, the controller design, the sensor system design, and the electronics design.

Mechanical Design

The configuration of the testbed allows the LAMS to be operated as it would be in an actual CMG application (an array of twelve control coils) while maintaining the capability of a better demonstration with an array of six control coils. Each of the coils will be sized such that six of them can support the weight of the superconductor and dewar.

The system configuration drawing (Figure 3) shows three views of the hardware. The superconducting magnet and its dewar are shown in a horizontal attitude suspended by the control coils. The top view shows the upper six coils when twelve control coils are used for suspension. The front and side views show the base structure which supports the control coil. These front and side views show the superconductor and dewar suspended by six and twelve coils respectively.

The coils are supported by a pair of 300-series (non-magnetic) stainless steel weldments which form a dodecahedron. Six pentagon-shaped 0.090" sheets, each with a central hole, are welded at their edges to form the two separable halves of the dodecahedron. The two halves are joined by captive threaded fasteners and can be readily separated for either maintenance or reconfiguration purposes. The coil support sets on a separate base which is also 300-series stainless. It is formed from two rings connected by welded gussets to provide good stiffness.

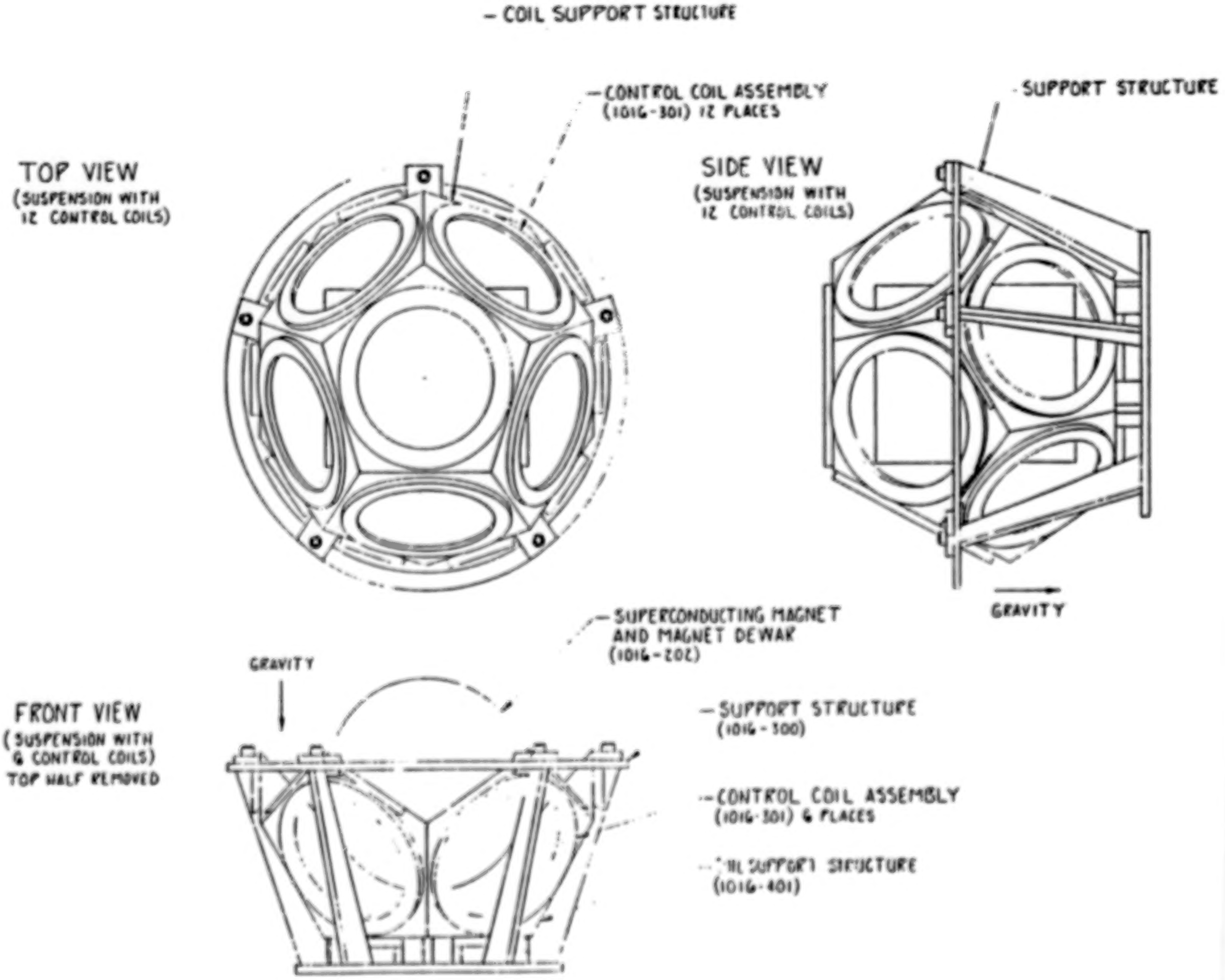
-COIL SUPPORT STRUCTURE
-CONTROL COIL ASSEMBLY (1016-301) 12 PLACES
-SUPPORT STRUCTURE
TOP VIEW
(SUSPENSION WITH 12 CONTROL COILS)
SIDE VIEW
(SUSPENSION WITH 12 CONTROL COILS)
GRAVITY
-SUPERCONDUCTING MAGNET AND MAGNET DEWAR (1016-202)
GRAVITY
FRONT VIEW
(SUSPENSION WITH 6 CONTROL COILS) TOP HALF REMOVED
-SUPPORT STRUCTURE (1016-300)
-CONTROL COIL ASSEMBLY (1016-301) 6 PLACES
-COIL SUPPORT STRUCTURE (1016-401)

Figure 3. System Configuration

ORIGINAL PAGE IS
OF POOR QUALITY

Superconducting Magnet and Cryostat Design

The superconducting solenoid is surrounded by a helium bath enclosed in a dual chamber vacuum dewar. The magnet is charged by means of removable current leads penetrating the dewar from the bottom through a thermally baffled stack. In a similar manner, liquid helium is filled through an inverted port. This port is normally sealed at its top. It utilizes a thin layer of helium gas for minimizing heat loss down the neck. The addition of an aluminum shield surrounding the aids in thermally tying the coil to liquid helium temperature thereby allowing operation at liquid levels well below the coil height and at full coil pitch.

The cryogenic system is illustrated in Figure 4. The coil is centered within the spherical cover and is supported by brackets attached to the base of the inner shell. The cryostat consists of three shells of domed metal welded to cylindrical side supports which are welded to their respective bases. The three penetrations into the helium bath provide access for power leads, helium filling, and diagnostics and persistent switch.

Several features of the design are directed toward allowing ±60° pitch of the magnetic axis without excessive loss of helium due to either pouring or increased heat loss to the vessel or feedthrus. In order to increase thermal tying of the coil to the 4° K thermal sink, the high thermal conductivity of aluminum is employed both in the fabrication of the inside shell of the dewar and by the addition of an additional shell bolted to the base which surrounds the coil. This arrangement helps to "pin" the temperature of the coil at 4° K even when the coil is not bathed in liquid. In this way, we will be able to operate the coil in the persistent mode with only enough liquid to wet the base of the inner dewar. To minimize thermal conduction through the coil input leads from the power lead stack, the leads will be guided away from the dewar wall and thermally connected to the base of the inner dewar before connection to the coil.

The three walled dewar assembly consists of two inner sections of 0.06" aluminum cylinders welded to the respective domes and bases and another section of stainless steel. The vacuum of both sections is common with the vacuum in both the power lead and helium fill ports. Each compartment is rigidly connected to the other by fiberglass cylinders attached to the grooved rings which join each dome to its respective cylinder. The space between the chambers is also filled with superinsulation to minimize radiation loss. The middle partition is thermally connected to the outer wall of the power lead port and should float near 100° K.

The power lead port is surrounded by single section vacuum dewar to minimize heat load into the helium bath from lead chamber which itself is cooled by venting helium gas. The inside wall is of stainless to minimize thermal conduction to the outside cap and is fitted with bellows to accommodate linear thermal expansion. The bayonet shaped conductors at the top of the assembly connect to the superconducting coil input leads.

In order to minimize liquid sloshing into the port, venting is from the top center of the helium vessel via tubes to the lead ports. The quench disc provides high throughput release in case of a magnet quench. The low pressure relief valve (~1 psi) prevents slow buildup of boiloff gas.

Controller Design

The controller design is aimed towards designing a controller which is robust to small plant changes (micro variations) and accommodating to gross plant variations (macro variations). The controller must take into account sensor characteristics as well as plant and model uncertainties.

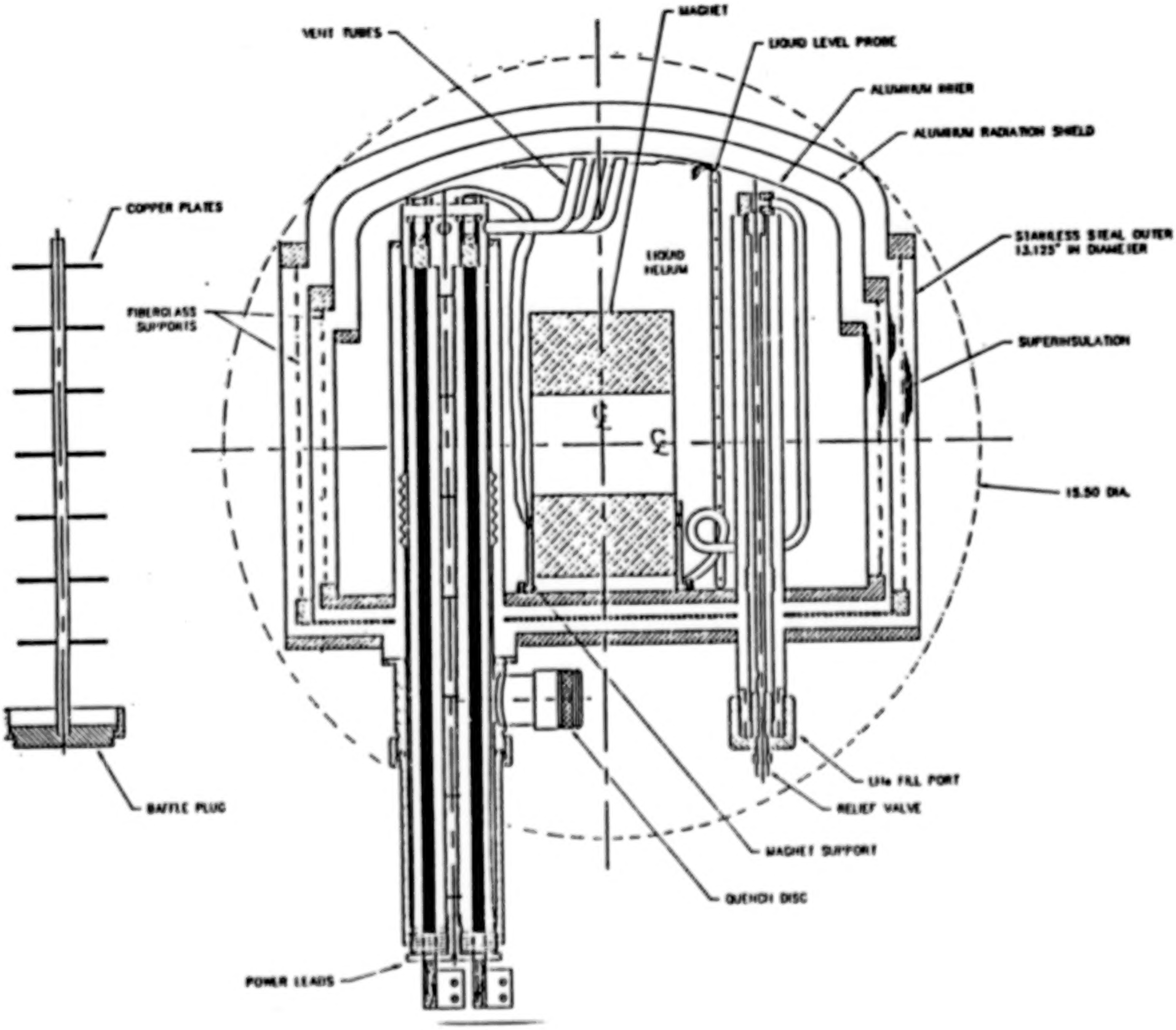
MAGNET
VENT TUBES
LIQUID LEVEL PROBE
ALUMINUM INNER
ALUMINUM RADIATION SHIELD
COPPER PLATES
STAINLESS STEAL OUTER
13.125" IN DIAMETER
LIQUID
HELIUM
FIBERGLASS
SUPPORTS
SUPERINSULATION
℄
℄
15.50 DIA.
BAFFLE PLUG
LHe FILL PORT
RELIEF VALVE
MAGNET SUPPORT
QUENCH DISC
POWER LEADS

Figure 4. Magnet and Cryostat Design, Elevation View

ORIGINAL PAGE IS
OF POOR QUALITY

The LAMS shows large variations in the stiffness and control coefficients as a function of the superconducting coil orientation. Two reference frames referred to here as the fixed and the local coordinate frames are shown in Figure 5. The plant variations are periodic, sinusoidal in nature, and predictable if the orientation (Θ and ϕ) are known. Normally controllers for plants with large parameter variations are difficult to design. The controller concept as shown in Figures 6, 7, and 8 takes advantage of the predictable nature of the variations to arrive at an elegant control scheme.

The control of the superconducting coil is considered in stages:

(i) a servo/command-following control of the orientation of the superconducting coil in the fixed reference frame as described by the Euler angles Θ and ϕ.

(ii) the regulation of the position of the superconducting coil in the local reference frame X'Y'Z' such that the coil axis orientation remains invariant.

The servo control rotates the superconducting coil to some desired orientation (Θ_{des} and ϕ_{des}). The displacements ($\Delta x'$, $\Delta y'$, $\Delta z'$) are the displacements of the superconducting source coil center of mass from the origin of the X'Y'Z' reference frame and ($\Delta\alpha'$, $\Delta\gamma'$) are the rotations of the superconducting coil around the X' and Y' axis. $\Delta x'$, $\Delta y'$, $\Delta z'$ $\Delta\alpha'$ and $\Delta\gamma'$ are regarded to be small variations around nominally zero values.

The controller is built around a fixed gain linear quadratic regulator (LQR) and a state estimator based on a fixed gain Kalman filter. The regulator (Figure 7) and the Kalman filter (Figure 8) are designed with reference to the local frame of reference X'Y'Z'. The Kalman filter takes into account the sensor characteristics to arrive at an optimal estimate of the states, essentially ($\Delta x'$, $\Delta y'$, $\Delta z'$, $\Delta\alpha'$, $\Delta\gamma'$) and respective velocities, of the superconducting coil. The states are regulated to zero by the LQ regulator using the state estimates generated by the Kalman filter. The transformation (Γ) relating the X'Y'Z' frame to the XYZ frame (and the inverse) form the "interface" between the orientation measurements made in the fixed reference frame, the LQ regulator and the control coils providing the regulation forces.

In this scheme only the transformations are dependent on the orientation angles (Θ and ϕ). The plant uncertainties are accommodated in the LQ regulator design. The deviations of the controller performance are bounded by the maximum bounds on the plant modelling errors and plant variations.

The controller implementation will be using a floating point DSP. The fixed gain LQ regulator, the Kalman filter and the transformations will be executed in real time by the DSP. The transformations are the most computationally intensive part of the controller implementation.

Sensor System Design

The sensor system consists of a three-degree-of-freedom translation sensing system and a two-degree-of-freedom rotation sensing system. The design of the system is illustrated in Figure 9.

Translational Sensors

The three degrees of translation will be sensed by capacitive devices operating at about 1 kHz. These devices are inherently simple, impose minimal constraints on the spherical surface, are insensitive to ambient magnetic fields, and require only a target smoothness less than the desired resolution.

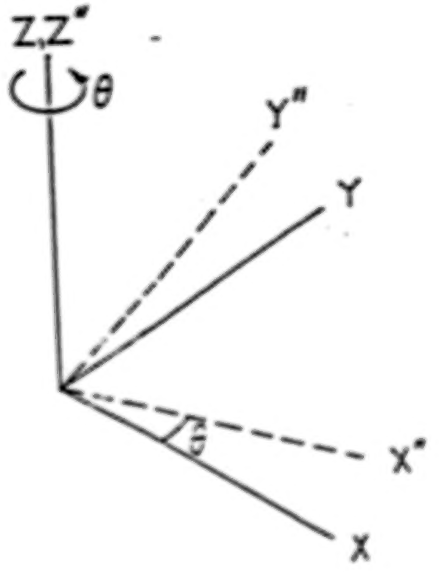

θ rotation around the Z axis to give the intermediate axis X",Y",Z". Z and Z" remain coincident.

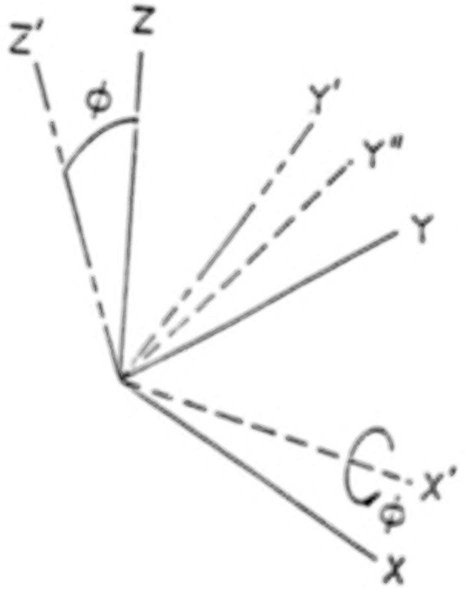

φ rotation around the X" axis to give the axis X',Y',Z'. X" and X' remain coincident.

Figure 5. Euler Angles

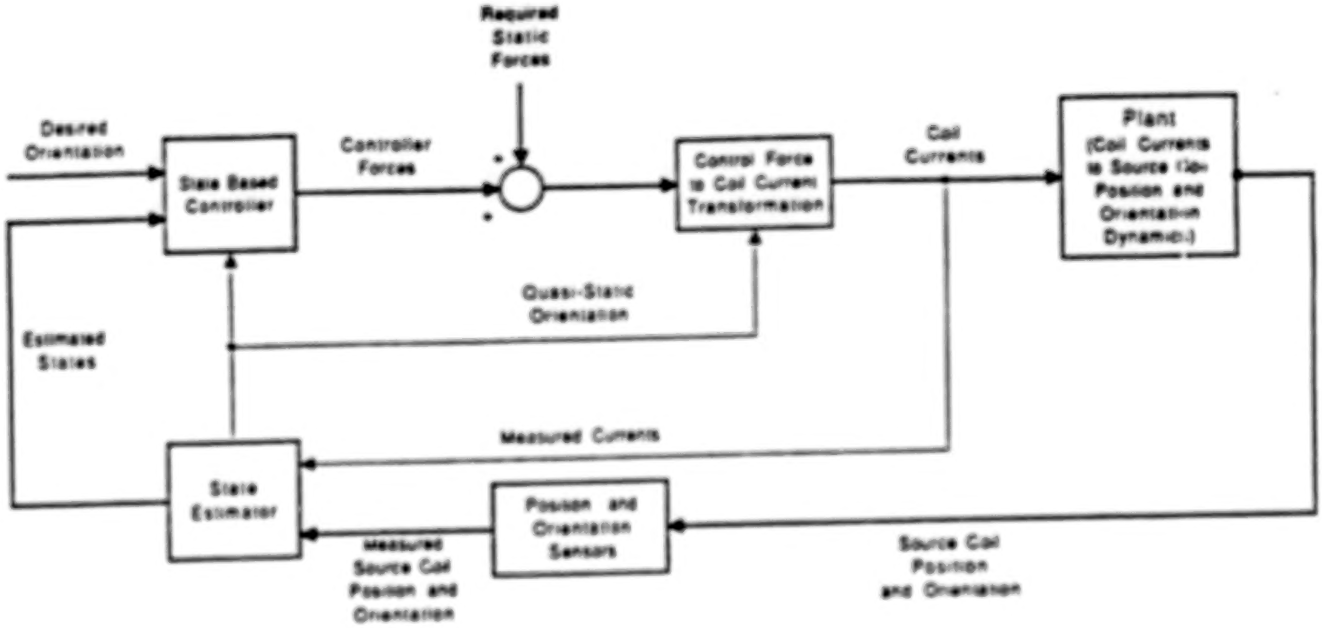
Required
Static
Forces
Desired
Orientation
State Based
Controller
Controller
Forces
+
+
Control Force
to Coil Current
Transformation
Coil
Currents
Plant
(Coil Currents
to Source Coil
Position and
Orientation
Dynamics)
Quasi-Static
Orientation
Estimated
States
Measured Currents
State
Estimator
Position and
Orientation
Sensors
Measured
Source Coil
Position and
Orientation
Source Coil
Position
and Orientation

Figure 6. Controller Architecture

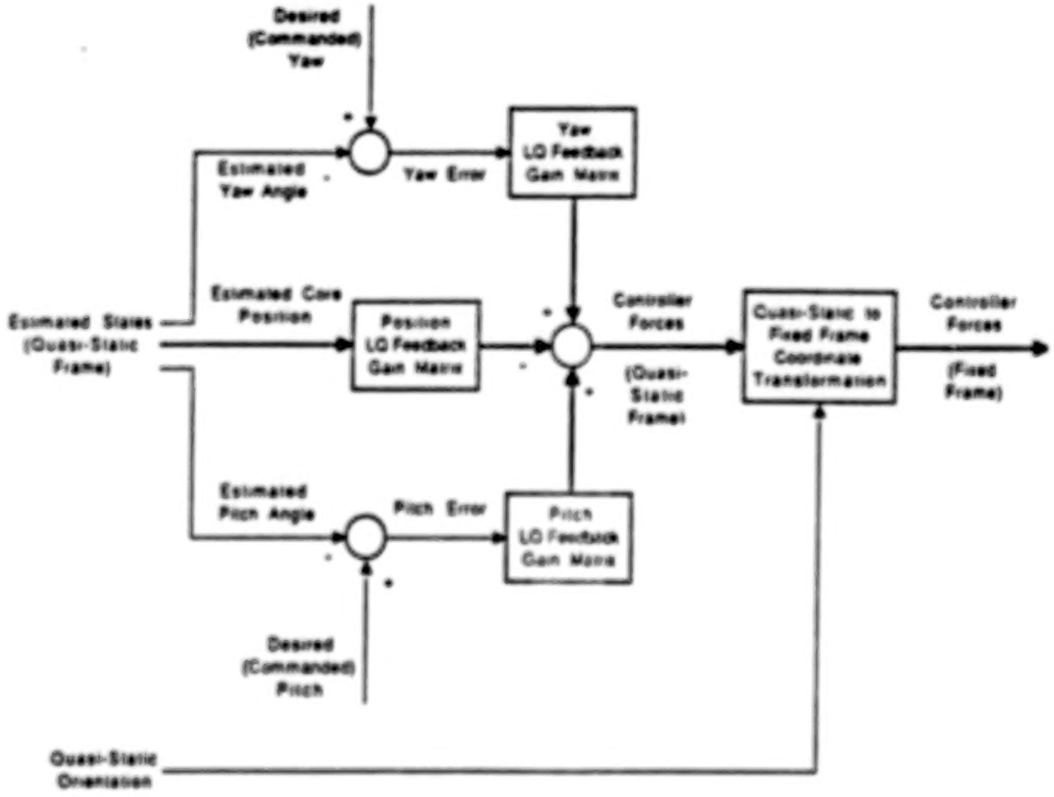
Desired (Commanded) Yaw
+
Estimated Yaw Angle
-
Yaw Error
Yaw LQ Feedback Gain Matrix
Estimated States (Quasi-Static Frame)
Estimated Core Position
Position LQ Feedback Gain Matrix
+
-
+
Controller Forces
(Quasi-Static Frame)
Quasi-Static to Fixed Frame Coordinate Transformation
Controller Forces
(Fixed Frame)
Estimated Pitch Angle
Pitch Error
Pitch LQ Feedback Gain Matrix
-
+
Desired (Commanded) Pitch
Quasi-Static Orientation

Figure 7. Regulator Architecture

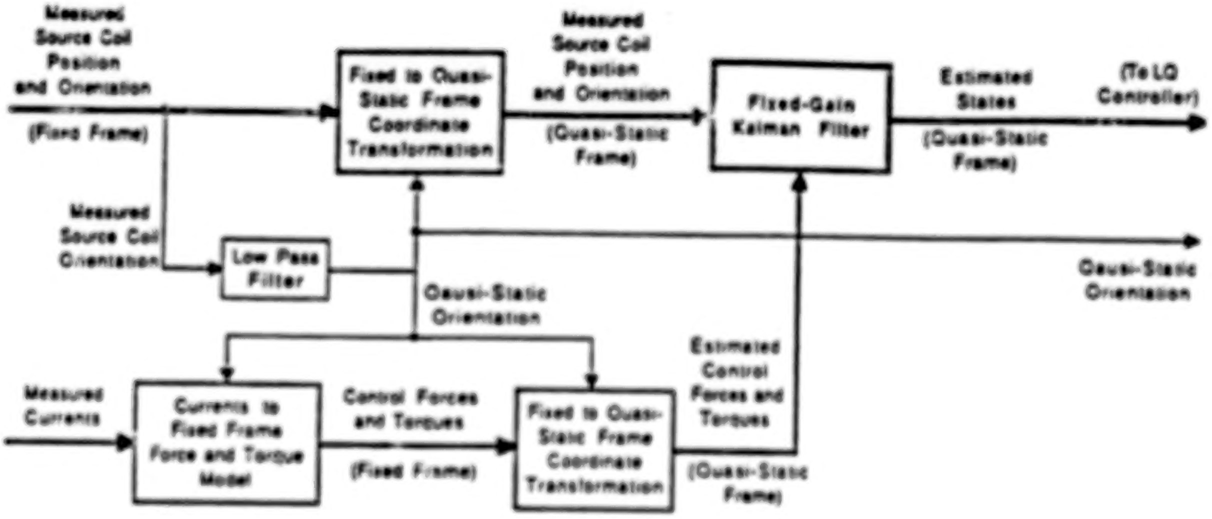
Measured Source Coil Position and Orientation
(Fixed Frame)
Fixed to Quasi-Static Frame Coordinate Transformation
Measured Source Coil Position and Orientation
(Quasi-Static Frame)
Fixed-Gain Kalman Filter
Estimated States
(Quasi-Static Frame)
(To LQ Controller)
Measured Source Coil Orientation
Low Pass Filter
Quasi-Static Orientation
Quasi-Static Orientation
Measured Currents
Currents to Fixed Frame Force and Torque Model
Control Forces and Torques
(Fixed Frame)
Fixed to Quasi-Static Frame Coordinate Transformation
Estimated Control Forces and Torques
(Quasi-Static Frame)

Figure 8. Kalman Filter

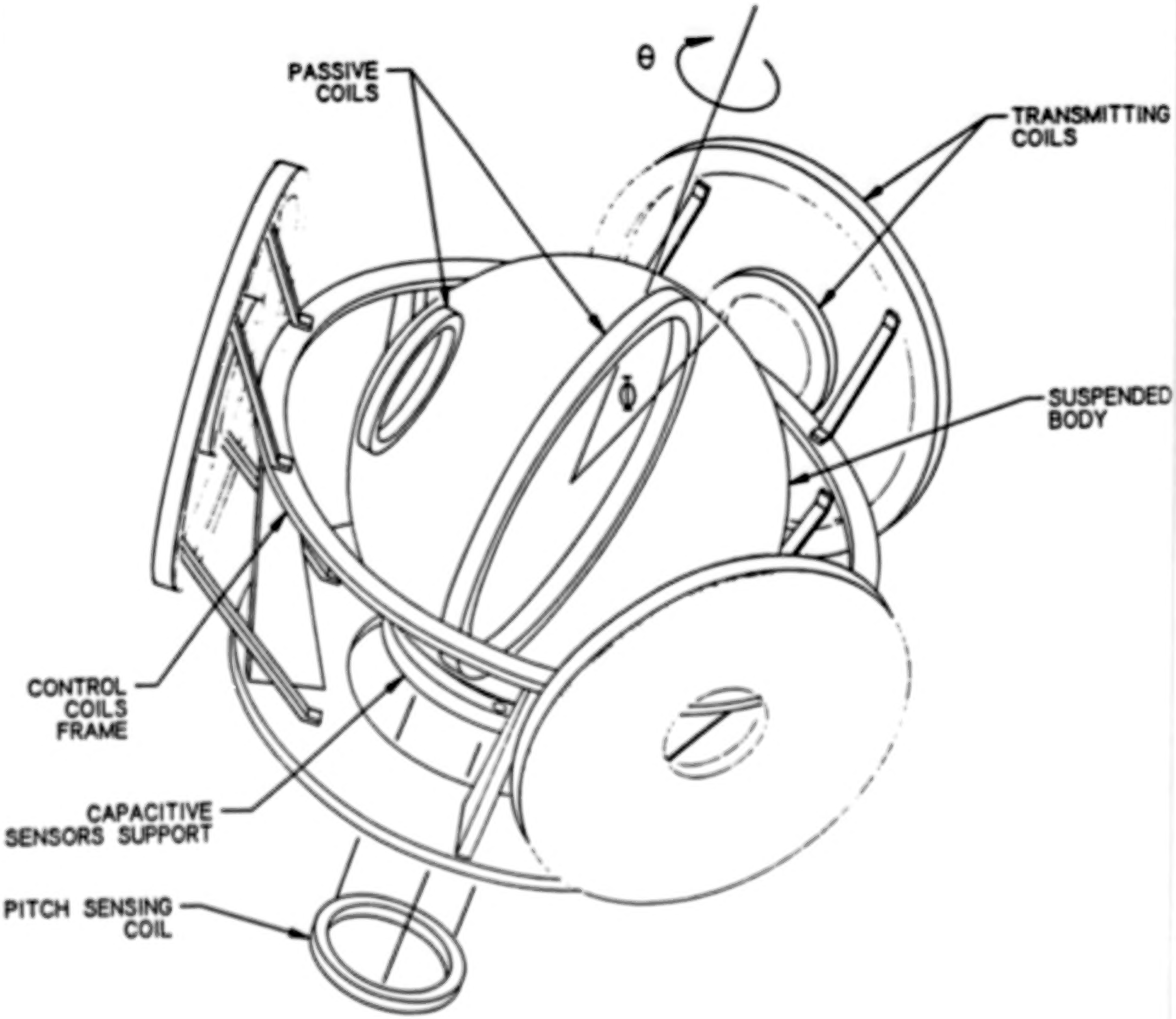
PASSIVE COILS
θ
TRANSMITTING COILS
Φ
SUSPENDED BODY
CONTROL COILS FRAME
CAPACITIVE SENSORS SUPPORT
PITCH SENSING COIL

Figure 9. Position Sensing System

Rotation Sensing

The two rotational angles will be determined from the mutual inductance between a set of stationary transmitting coils placed outside the control coil set and two passive coils moving with the cryostat/magnet. Both the transmitters and moving coils will employ series capacitors which will cancel inductance terms thereby enhancing sensitivity. The control coil set which are well coupled to the transmitters will be fitted with band trapping filters designed to present a high impedance to induced voltages.

Three transmitters arranged at 120° intervals will determine both the angle of rotation in the horizontal plane, Φ, and Θ, the pitch angle around the horizontal plane, by measuring the coupling to a coaxially-mounted polar coil in the sphere. The inherent rotational degeneracy will be resolved by a second sensing coil placed at the spherical "surface" in conjunction with four additional external transmitting coils operating at a different frequency.

The mechanical arrangement of the coils is illustrated in Figure 9. As implemented here, mutual inductance sensing involves exciting outside static coils with a fixed current then coupling this energy into passive coils on the rotating body at a frequency well above the minimum response rates required for the control system. The power coupled into the cryostat of the superconducting magnet must not cause excessive helium loss while induction in the control coil set must not interfere with proper operation.

Both the transmitting primary and passive secondary coil self-inductances are made resonant with series-placed capacitors. The change in mutual inductance (calculated from the coil voltage driven with a constant current) is then used to track rotation. The effective circuit is shown in Figure 10.

The baseline design will utilize two passive coils of 10 to 30 turns with capacitive shunts on the sphere. The large coil will be resonant at 50 kHz, the smaller at 38 kHz. The fixed set will consist of seven coils of two sizes. Each large coil will be resonant at 50 kHz and be driven with a constant current oscillator. The voltage across each coil will be filtered, demodulated, and routed to the DSP for use by the control coil amplifiers. The small coils will be resonant at 38 kHz and be connected in the same way.

Electronics Design

The LAMS system electronics interfaces between the position sensors and the control coils to implement the algorithm required for proper five degrees-of-freedom control. This section specifies the baseline design of these electronics.

Current technology allows several alternative component choices for implementing digital controllers. The digital signal processor (DSP) is the most recent and most advanced of the digital technologies featuring high-speed processing due both to its higher clock frequency and to the use of an internal hardware multiplier. In addition, the data and address interfaces are structured for rapid data handling.

Figure 11 shows the block diagram of the baseline control electronics with a DSP at its core. Five sample-and-holds (S/H) are used on the five analog position signals to ensure data simultaneity. The analog multiplexer (MPX) sequentially feeds the values to the analog-to-digital-converter (A/D) for processing and subsequent inputting to the DSP. The DSP requires both read-only memory (ROM) for program storage, and random-access memory (RAM) for data storage. Six digital-to-analog converters (D/A) are used to output the command voltages, each with its own data latch to hold the latest output value. The D/A's directly drive the switching power amplifiers which produce the command currents in the control coils, thereby completing the feedback path.

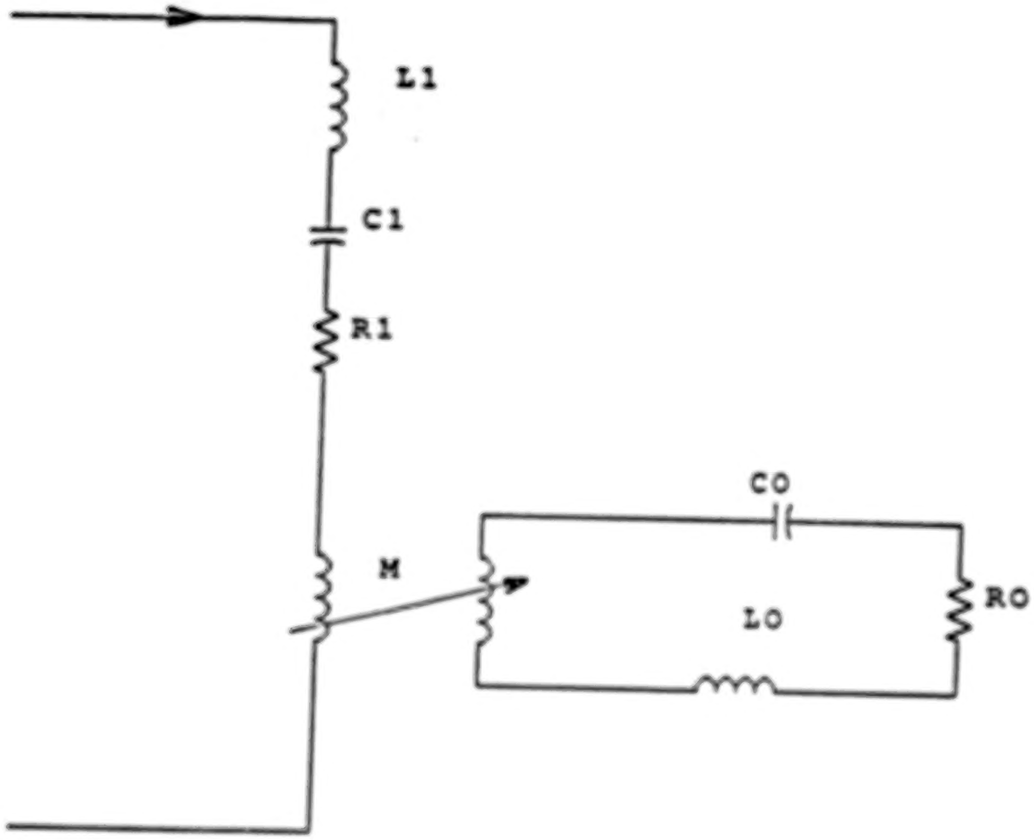
L1
C1
R1
M
CO
LO
RO

M is mutual inductance between coils; rotating coil components denoted by '0;' excited coil by '1.'

Figure 10. Single Coil Sensing Circuit

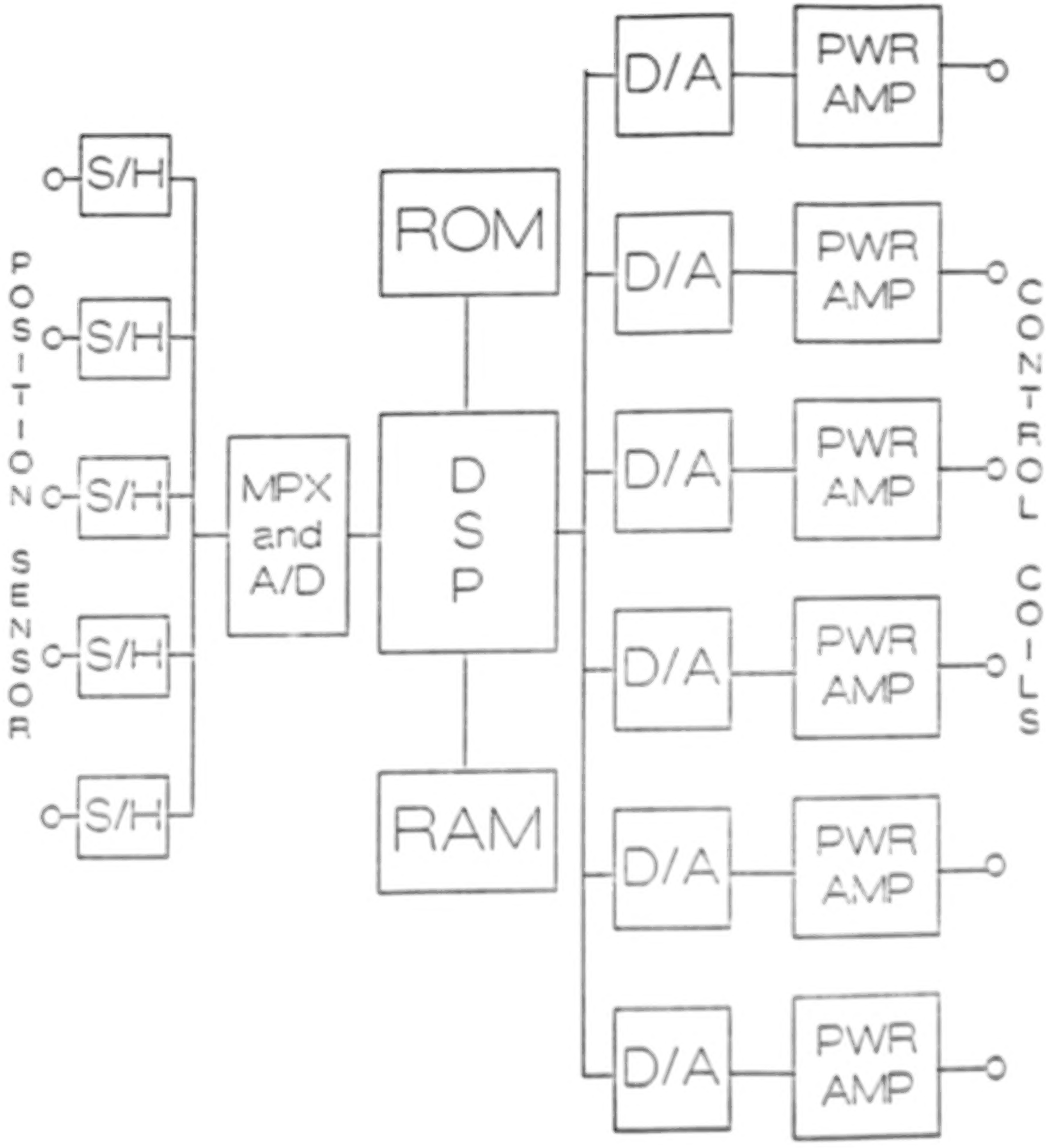
S/H
S/H
S/H
S/H
S/H
POSITION SENSOR
MPX and A/D
ROM
DSP
RAM
D/A
D/A
D/A
D/A
D/A
D/A
PWR AMP
PWR AMP
PWR AMP
PWR AMP
PWR AMP
PWR AMP
CONTROL COILS

Figure 11. Electronics Block Diagram

4. CONCLUSION

This paper has described the design of a prototype for an innovative type of superconducting magnetic suspension system. This control system demonstration experiment which is currently being constructed will provide a significant milestone in the overall development program.

REFERENCES

1. J. Downer, D. Eisenhaure, R. Hockney, B. Johnson, and S. O'Dea, "Magnetic Suspension Design Options for Satellite Attitude Control and Energy Storage," Proceedings of the 20th Intersociety Energy Conversion Engineering Conference, pp. 2.424-430.

2. J. Downer, Design of Large-angle Magnetic Suspensions, ScD Thesis, Massachusetts Institute of Technology, May 1986.

3. J. Downer, D. Eisenhaure, R. Hockney, and B. Johnson, "Application of Magnetic Bearings to High-Torque, Satellite Attitude Control Wheels," 22nd Intersociety Energy Conversion Engineering Conference, Philadelphia, PA, August 1987.

N91-21192

CONTROL ISSUES of MICROGRAVITY VIBRATION ISOLATION

Carl R. Knospe, Richard D. Hampton
Department of Mechanical and Aerospace Engineering
University of Virginia
Thornton Hall, McCormick Road
Charlottesville
VA 22901

PRECEDING PAGE BLANK NOT FILMED

ABSTRACT

Active vibration isolation systems contemplated for microgravity space experiments may be designed to reach given performance requirements in a variety of ways. An analogy to passive isolation systems proves to be illustrative but lacks the flexibility as a design tool of a control systems approach and may lead to poor designs. For example, it is shown that a focus on equivalent stiffness in isolation system design leads to a controller that sacrifices robustness for performance. Control theory as applied to vibration isolation is reviewed and passive analogies discussed. The loop shaping trade–off is introduced and used to design a single degree of freedom feedback controller. An algebraic control design methodology is contrasted to loop shaping and critiqued. Multi–axis vibration isolation and the problems of decoupled single loop control are introduced through a two degree of freedom example problem. It is shown that center of mass uncertainty may result in instability when decoupled single loop control is used. This results from the ill conditioned nature of the feedback control design. The use of the Linear Quadratic Regulator synthesis procedure for vibration isolation controller design is discussed.

NOMENCLATURE

A	System dynamic matrix
a	Acceleration feedback coefficient
B	System input matrix
b	Rotational stiffness feedback cofficient
$C(s)$	Complimentary sensitivity function
c	Damping
$d, D(s)$	Direct disturbance force
$\bar{D}(s)$	Equivalent disturbance
$f, F, F(s)$	Actuator force
$G(s)$	Plant transfer function
$H(s)$	Feedback transfer function
I	Moment of inertia
k	Stiffness
$M, M(s)$	Control moment
n	Rotational damping feedback
$P(s)$	Umbilical precompensation transfer function
Q	State weighting matrix
q	Actuator placement
R	Control weighting matrix
$S(s)$	Sensitivity function
$T(s)$	Feedforward transfer function
u	Control vector
$v(s)$	Measurement noise
$x, X(s)$	Experiment position
$\bar{x}$	State vector

NOMENCLATURE (Continued)

$y, Y(s)$	Wall position
$\mathscr{y}$	accelerometer measurements
$z, Z(s)$	Decoupled measurements
Δ	Center of Mass error
$\theta, \Theta(s)$	Angular position
ω_n	Natural frequency
ζ	Percent critical damping

Subscripts

a	Acceleration
cl	closed loop
p	position

I. INTRODUCTION

Active vibration isolation for microgravity space experiments has generated much interest lately. A variety of disturbances aboard manned space orbiters contaminate the desired microgravity environment. These accelerations cover a frequency band from DC to 100 Hz. Low frequency ($< 10^{-3}$ Hz) sources include drag, solar pressure oscillations, tidal effects, and gravity gradient forces. At the higher frequencies, manned activity, thruster firing, and orbiter systems contribute most significantly. A comprehensive treatment of the orbiter acceleration environment is presented in [1] from which Figure 1, a characterization of the environment is taken.

The need for the active isolation of materials processing and fluid science experiments in the frequency range .01 to 10 Hz has been demonstrated by Jones, Owen, and Owens [1,2,3]. Above this ragne passive isolation systems could be used. Below .01 Hz the rattlespace available for the experiment is not large enough to accommodate the relative motion. Therefore, these accelerations must be passed by the isolation system to the experiment.

Active isolation systems for microgravity and pointing applications have been designed and constructed by many investigators [3,4,5]. These systems generally use conventional P.I.D. control of a non–contacting actuator, either Lorentz or electromagnetic, to achieve low frequency disturbance attenuation. While an actual microgravity experiment may require umbilicals for cooling and power (at this point, it is not clear whether these functions can be performed otherwise as described in [4]) the isolation systems designed and tested so far preclude an umbilical from consideration. These systems achieve their performance by the very low stiffness made possible by low gain feedback of the relative position of the experiment to the mounting surface. Without an umbilical this stiffness may be set by the designer at will. However, when an umbilical is present, the umbilical stiffness presents a lower bound on achievable stiffness unless the feedback loop is used to introduce a negative stiffness. In this paper, the issues of control system design for the *generic* (i.e., with umbilical) microgravity experiment will be considered.

Previous research in the area of active microgravity vibration isolation has established the importance of the umbilical in control system design. Jones et. al [6] present a good preliminary examination of the single–degree–of–freedom control issues for intrusive and non–intrusive isolation systems. Grodsinsky [7] examined the use of acceleration and velocity feedback. Many of the issues these researchers have discussed are revisited here from a control theory perspective. Analysis of the six–degree–of–freedom problem in the literature has been restricted to one–loop–at–a–time design. Generally the effects of cross coupling between the various degrees of freedom have been ignored. Owens and Jones [2] have investigated the effect of cross coupling due to center of mass displacement for a single loop based controller. This work examines this important problem for the non–intrusive experiment platform case where relative position feedback is sufficient. The authors concluded that satisfactory performance can be achieved if the control loops are designed for the decoupled degrees of freedom and not autonomously for each local position. It should be noted that high gains are not required to achieve isolation for the umbilical–free case. An example is presented in this paper which shows that decoupled single loop design may not be sufficient for the generic isolation problem.

Any microgravity isolation system design should meet the following specifications for translational axes:

(1) Unity transmissibility from D.C. to 0.001 Hz so as to prevent the experiment from impacting its enclosure's walls.

(2) At least 40 Db attenuation above 0.1 Hz [3].

(3) Both stability and performance robustness under errors due to changes in umbilical/experiment properties, non–collocation or misalignment of sensors and actuators, center of mass uncertainties, and unmodeled cross coupling between the degrees of freedom.

Robustness refers to the ability of the control system to perform satisfactorily when the true plant varies from the nominal plant. Performance requirements of the type (2) for rotational degrees of freedom have not yet been specified to the knowledge of the authors.

In this paper we shall examine the control system issues associated with active microgravity vibration isolation. The purpose here is not to develop new control theory but to apply existing concepts to the problem. We hope that this paper will serve a tutorial function for vibration engineers involved with the microgravity problem. The thesis of this paper is that control system design, not passive isolator design familiar to vibration engineers, is the proper tool for anlaysis and synthesis. First, the control theory required for the examination is reviewed in Section II. Section III reviews passive isolation and applies it as an analogy to control system design. In Section IV classical loop shaping is applied to the isolation problem and a controller is designed. A discussion of the result and a passive system analogy follow. An example multi–degree–of–freedom system is explored in Section V and system robustness is examined. Section VI concludes with an examination of the Linear Quadratic Regulator for the isolation problem.

II. Control Theory Preliminaries

We examine here the prerequisite control theory for the examination to follow. While the actual isolation problem is multi–dimensional, a single–degree–of–freedom example will be examined first.

The one-degree-of-freedom microgravity vibration isolation problem, depicted in Figure 2, consists of an experiment of mass m connected by an umbilical and an actuator to a wall of the experiment enclosure. The umbilical is modeled here as a linear element with stiffness k and damping c. The wall's motion (displacement y) is transferred through the umbilical to the experiment resulting in its motion (displacement x). Direct disturbances may also act on the experiment due to the experiment's processes (e.g. motors, valves, shutters). While it may seem that there is no need to distinguish between umbilical and direct disturbances, they are indeed different. The distinction lies in the fact that the actuator influences through the experiments motion the force transmitted through the umbilical; direct disturbance forces, however, are independent of actuator force. This distinction carries through to both passive isolator performance and control system design.

The equation of motion for the experiment is

$$m\ddot{x} + c\dot{x} + kx = c\dot{y} + ky + d + f \tag{1}$$

where d is the direct disturbance force and f is the actuator force. We assume here that the spacecraft wall is of sufficient impedance so as to not be affected by the actuator force. Under Laplace transformation Eqn. (1) yields

$$X(s) = \left[\frac{cs + k}{ms^2 + cs + k}\right] Y(s) + \left[\frac{1}{ms^2 + cs + k}\right][D(s) + F(s)] \tag{2a}$$

or

$$\ddot{X}(s) = \left[\frac{cs + k}{ms^2 + cs + k}\right] \ddot{Y}(s) + \left[\frac{s^2}{ms^2 + cs + k}\right][D(s) + F(s)] \tag{2b}$$

and this is illustrated in Figures 3a and 3b, a block diagram for the isolation system. Here, H(s) is the feedback transfer function, T(s) is the feedforward transfer function, and $v_1(s)$, $v_2(s)$ are measurement noises. The actuator force is therefore a linear function of the wall and the experiment motion. The subscripts p and a throughout this paper refer to whether the model used is in position or acceleration form.

If the umbilical properties were known explicitly and measurement noise is sufficiently small, then transmitted disturbances can be rejected with only feedforward control. Note however that direct disturbances can only be attenuated through feedback. As always, the primary purpose of feedback here is to account for uncertainties, either in the disturbance or in the plant model.

The price paid for this property of feedback is the requirement that the feedback be stabilizing over the range of uncertainties in the *nominal plant*, the plant model assumed for design. The nominal stability of the closed loop system may be checked by a variety of methods, the most popular for single–input–single–output (SISO) systems being the Nyquist and Bode plots. Implicit in these methods are measures of system robustness. The Nyquist stability criterion can be generalized straightforwardly to multi–input–multi–output (MIMO) systems, however the robustness measures do not carry over as straightforwardly.

Both Figure 3a and 3b can be generically expressed in the form of Figure 4 where G(s) is the plant, P(s) is umbilical's pre–compensation of the wall disturbance and $\overline{D}(s)$ is the equivalent disturbance to the system. Figure 4 has been presented in unity feedback form so as to introduce the concept of loop shaping and the trade–offs inherent in control system design. Denote the transfer functions between $\overline{D}(s)$ and X(s), the *sensitivity function*, as

$$S(s) \equiv \frac{X(s)}{D(s)} = \frac{1}{1 + GH} \qquad (3)$$

and between $v_2(s)$ and $x(s)$, the ***complementary sensitivity function***, as

$$C(s) \equiv \frac{X(s)}{v_2(s)} = \frac{GH}{1 + GH} \qquad (4)$$

Note that $S(s) + C(s) = 1$. Therefore, a feedback controller designed to attenuate external disturbances at a particular frequency

$$|S(j\omega_0)| << 1.0 \qquad |GH(j\omega_0)| >> 1.0$$

cannot attenuate the measurement noise signal at that frequency

$$|C(j\omega_0)| \approx 1.0$$

Likewise, a controller designed to reject a certain frequency measurement noise, $|C(j\omega_0)| << 1.0$, must pass the external disturbance at this frequency, $|S(j\omega_0)| \approx 1.0$. Classical design of control systems usually involves separating (if possible) the frequency spectrum into regions where input disturbances (measurement noise here) and output disturbances (external disturbance here) predominate. The methodology, known as loop shaping, consists of choosing H(s) so that GH is large and therefore S(s) is small at frequencies where output disturbances are dominant, and choosing H(s) so that GH is small and therefore C(s) is small at frequencies where input disturbances are dominant. This would be a relatively simple task if the designer only needed to be concerned with the magnitude of GH. However, stability of the feedback system requires that the argument of GH at crossover, where $|GH(j\omega_0)| \equiv 1.0$, be greater than $-180°$. That is, the system must have some phase margin. Since the phase of a transfer function is tied to its magnitude's (in dB) derivative with respect to frequency, as was shown by Bode [8], the loop shaping's results are fundamentally limited by the difference in frequency between the input and output disturbances. The designer may only change through shaping H(s) the magnitude in dB of GH at so fast a rate. Thus, the frequency bands where the magnitude of the sensitivity function and complimentary sensitivity function may be small must be separated in frequency by a crossover region of a certain width (which is dependent on G(s) as well as how small $|C(s)|$ and $|S(s)|$ must be).

The trade–off between rejection of input and output disturbances through feedback is also inherent in passive isolation systems. Suppose we are capable of choosing the umbilical stiffness and damping of Figure 2 so as to design a passive isolator. Note that the transfer function relations

$$\frac{\tilde{X}(s)}{\tilde{Y}(s)} = \frac{G(s)}{1 + G(s)} \qquad \frac{\tilde{X}(s)}{D(s)/m} = \frac{1}{1 + G(s)} \tag{5}$$

apply where

$$G(s) = \left(\frac{cs + k}{ms^2}\right)$$

From this, it is easy to see that direct disturbances act as output disturbances while wall accelerations act as input disturbances. The difference between designing an isolation mount for base disturbances and for direct disturbances is well known and understood by vibration engineers. A soft mount is appropriate for isolating against base disturbances while a stiff mount is appropriate for direct disturbances excitation. The loop shaping capability of springs and dampers is however very restricted. Indeed, one cannot shape the loop to yield an unstable system. An active control system may have its loop shaped to an arbitrary specification provided it is possible to meet the specification with a stable system. Here lies the chief advantage of designing an isolation system from a control paradigm: the interaction of the conflicting specifications, stability, and robustness is clear throughout the loop shaping procedure. Sensitivity and complimentary sensitivity functions are extendable to MIMO systems through the use of singular values.

Robustness in single-input-single-output controller design is measured by *gain* and *phase margins*. The gain margin is the range of gain that can be introduced into the loop while maintaining stability. Similarly, the phase margin is the amount of phase that can be introduced into the loop while maintaining stability. The practical importance of the margins is that the gain and phase of the nominal plant is not the same as that of actual plant. These margins may be easily determined from Nyquist or Bode plots. Loop shaping also implies that a compensator H(s) should not be so large as to extend the crossover frequency of the compensated system into the higher frequency range where nominal models are very inaccurate.

Robustness for MIMO systems can also be specified in terms of the simultaneous gain and phase variations that may be introduced into the loops while preserving stability. However, this description does not account for unmodeled coupling in the dynamics. Uncertainty may be represented in terms of an additive (in parallel) or multiplicative (in series) transfer function matrix appended to the plant. (While these are the most common there are other representations.) Using either uncertainty representation it can be easily shown by the small gain theorem that stability can be guaranteed if uncertainties in the plant are required to be bounded by a norm of the compensated plant. This is best represented in terms of the frequency dependent singular values of the plant and uncertainty transfer function matrices. This measure, however, is conservative since it allows cross coupling dynamics between channels that in actuality could never occur. The structured singular value methodology attempts to alleviate this conservatism through structuring the uncertainty model. Readers interested in a general treatment of MIMO stability and robustness should consult Ref. 9.

III. Passive Isolation: An Analogy

We now examine the design of an active vibration isolation system for microgravity space experiments from an analogy to passive isolators. Indeed, the primary reason for pursuing an active rather than passive system is not the increased flexibility in loop shaping but the limitations of active systems in attaining a stiffness low enough to meet the isolation requirements. This is true even when no umbilical is present.

For the generic system model of Eqn. (1) with the nominal values

$m = 220$ kg

$k = 20$ N/m

$c = 6.63$ N·s/m (5% of critical damping)

The transmissibility curve between base and experiment acceleration, shown in Figure 5 is given by

$$\frac{\ddot{X}(s)}{\ddot{Y}(s)} = \frac{2\zeta\omega_n s + \omega_n^2}{s^2 + 2\zeta\omega_n s + \omega_n^2} \tag{6}$$

with

$$\omega_n \equiv \sqrt{k/m} = 0.3 \text{ rad/sec} = 0.048 \text{ Hz}$$

$$\zeta = \sqrt{c^2/4mk} \approx 0.05$$

Also depicted in Figure 5 are the transmissibility specifications (1) and (2) discussed in Section 1. While the system satisfies the unity transmissibility criterion, note that the natural frequency is not low enough to meet the 40 dB attenuation requirement. The system is also deficient in the magnification of disturbances at and near the resonance. Clearly any modification to the umbilical's dynamics through feedback should include increased damping through a positive gain on experiment velocity. Feedback of inertial experiment velocity permits the damping coefficient ζ to be increased in the denominator of Eqn. (6) without changing it in the numerator. Thus, the resonance can be removed without affecting the roll-off rate (since the zero of Eqn. (6) is not changed).

If the umbilical were softer, say with k = 0.20 N/m, both specifications (1) and (2) could be met by the passive system. Unfortunately, an active system cannot lower the stiffness with positive gains on position feedback. An active system may be used to insert a negative stiffness spring in parallel with the umbilical. For example, for the nominal plant with the controller transfer functions of Figure 3a equal to

$$H_p(s) = -(6.0s + 19.8) \qquad T_p(s) = -(6.0s + 19.8) \tag{7}$$

The natural frequency of the system is moved an order of magnitude lower. (Here, a negative damper has also been introduced so as to maintain the system's 5% critical damping for the purpose of comparison. If less negative damping is introduced in order to remove the resonance, even more negative stiffness must be introduced to meet the 40 dB specification.) Note that this vibration engineering approach, that is, lowering the stiffness, requires the near cancellation of the umbilical's stiffness with that introduced via feedback. If the negative stiffness exceeds that of the umbilical, the equivalent stiffness of the system will be negative and the system will be unstable. It is not surprising then that the introduction of negative stiffness via the controller has no robustness whatsoever. The design using Eqn. (7) has less than 0.1° phase margin. The root locus for the system, shown in Figure 6, clearly indicates this potential for instability. A focus on equivalent stiffness in isolation system design thus leads to control systems which sacrifice robustness for performance. In addition, a design which achieves isolation through lowering the system stiffness cannot attenuate direct disturbances over the same frequency band, as discussed in Section II.

From a vibration engineering viewpoint, an alternative means of achieving rejection of disturbances is to rigidly fasten it to an inertial structure. While there is no such structure in space, it is possible to achieve this result by a high positive gain feedback on experiment position. (The inertial position must be obtained by integrating an accelerometer reading twice. This does pose a problem since this procedure is marginally stable. However, this problem may be ameliorated through replacing the integrators with a second order low pass filter. The authors are aware of this method being employed successfully on a six–degree–of–freedom magnetic suspension isolation rig at NASA Lewis Research Center.) This acts as a very stiff spring tying the experiment to inertial space. The controller and resulting transfer functions in this case are

$$H_p(s) = 2000 \qquad\qquad T_p(s) = 0 \tag{8}$$

$$\frac{\tilde{X}(s)}{\tilde{Y}(s)} = \frac{6.63s + 20}{220s^2 + 6.63s + 2020}$$

$$\frac{\tilde{X}(s)}{D(s)/m} = \frac{220s^2}{220s^2 + 6.63s + 2020}$$

While this controller meets the 40 dB specification, it does not have unity transmissibility below 0.001 Hz. An experiment controlled in this fashion will collide into the wall. The feedforward transfer function may be adjusted to provide unit gain via

$$T_p(s) = \frac{-2000}{159s + 1}$$

This feedforward with the feedback term of Eqn. (8) effectively acts to base disturbances as a high relative stiffness up to 0.001 Hz changing to a large inertial stiffness. The resulting transmissibility $\tilde{X}(S)/\tilde{Y}(s)$ is presented in Figure 7. Note that since the feedback loop introduced no damping, the original resonance is still present although less damped and at a higher frequency. This may be corrected by adding an inertial damping into the feedback loop. While this design method may be used to meet the specifications with robustness it has three faults: (1) it requires inertial experiment position, inertial wall position, and inertial experiment velocity measurements which are problematic to obtain, (2) it requires very high gains in both feedforward and feedback loops to obtain attenuation, and (3) an extension of the method to multi–degree–of–freedom systems would be difficult. It is also possible that when a flexible wall is considered, rather than the infinite impedance structure assumed, that the system will be unstable.

As another method of fastening the experiment to inertial space, one may employ inertial damping via feedback. By feeding back the inertial experiment velocity with a high gain, it is almost possible to achieve both the 40 dB and unity transmissibility specification without resorting to feedforward. For example, with

$$H_p(s) = 1000\ s \qquad T_p(s) = 0$$

the resultant transmissibility are shown in Figure 8. Unfortunately, the roll–off rate here is approximately 20 dB/decade and therefore it is impossible to achieve both specifications simultaneously. This method has the advantage over the inertial spring of being a great deal simpler and requiring only one inertial measurement (experiment velocity which requires only one integration of accelerometer measurements).

Another passive analogy is the lowering of the natural frequency of the umbilical by increasing the experiment mass. An increased experiment mass would attenuate direct disturbances as well as those transmitted through the umbilical. In addition, at frequencies below the natural frequency of the umbilical, the isolation system would have unity transmissibility. Of course, for space applications any additional mass is very costly. To lower the natural frequency by an order of magnitude would require increasing the experiment mass by a factor of one hundred. Clearly, it is not practical to accomplish increased isolation through the addition of real mass. However, it is possible to increase the effective mass of the system through feedback. This will be examined in the next section, as this idea most properly evolves out of loop shaping.

To summarize, the passive isolation analogy to control system design yields some insight but falls short as a design tool on three counts: (1) it does not have the flexibility to shape the response with its simple analogical elements, stiffness, damping, and mass, so as to achieve the performance requirements, (2) it cannot be easily or effectively generalized to multi–degree–of–freedom problems, (3) it completely ignores the robustness problem inherent to active control systems. We advocate, therefore, that vibration engineers consider active isolation a controls problem and use an automatic controls framework for tackling it.

IV. The Control System Approach

A simple controller is now designed for the system described by Eqn. (1) and the nominal values. The authors refer the reader back to Figure 5 where transmissibility curve between experiment and wall accelerations (or positions) is presented again along with the design specifications (1) and (2). The goal is to design a feedback control $H_p(s)$ that results in the closed loop transfer function

$$G_{cl}(s) \equiv \frac{X(s)}{Y(s)} = \frac{G_p(s)P(s)}{1 + G_p(s)H_p(s)} \tag{9}$$

satisfying both constraints; that is

$$|G_{cl}(j\omega_o)| \approx 1.0 \qquad \frac{\omega_o}{2\pi} < 0.001 \text{ Hz}$$

$$|G_{cl}(j\omega_o)| < 0.01 \qquad \frac{\omega_o}{2\pi} > 0.1 \text{ Hz}$$

Here, $G_p(s)$ and $P(s)$ are as indicated in the block diagram of the system, Figure 3a. Note that the uncontrolled system $G_p(s)P(s)$ satisfies the first of these constraints.

therefore, $H_p(S)$ should be very small in the low frequency band so that the closed loop system will continue to satisfy the unit transmissibility specification. Therefore, this specification yields a condition like

$$| G H_p(j\omega_o) | < 0.01$$

$$| H_p(j\omega_o) | < 0.2 \qquad \frac{\omega_o}{2\pi} < 0.001 \text{ Hz}$$

At and above 0.1 Hz, the attenuation of the uncontrolled system is not sufficient. It is desirable to increase the attenuation by approximately two orders of magnitude. This may be accomplished by requiring $H_p(s)$ to be very large in this frequency range, approximately

$$| G H_p(j\omega_o) | > 100.$$

$$| H_p(j\omega_o) | > 2000. \qquad \frac{\omega_o}{2\pi} > 0.1 \text{ Hz}$$

These two design specifications on $H_p(s)$ are shown in Figure 9 along with a simple function satisfying these conditions,

$$H_p(s) = 5000 s^2 \tag{10}$$

This controller design results in the closed loop transmissibility between experiment and wall accelerations which is plotted in Figure 10. Note that both specifications (1) and (2) are met. Inertial damping should be added to this design to eliminate the resonance. It is easily seen from a root locus plot that this design is robust with respect to changes in umbilical/experiment properties, Figure 11, and actuator finite bandwidth, Figure 12. In practice, this design would be improved by rolling off the controller gain. This limits the controller bandwidth so as to not affect possible unmodeled lightly–damped high frequency modes of the system (e.g. wall flexure). A controller design would probably also include a weak position integral feedback to provide a slow centering force so that accelerometer bias and noise does not result in wall collision.

The reader might object to the controller of Eqn. (10) since it is improper (i.e., has more zeros than poles). However, this controller is realizable. Note that $H_p(s)$ multiplies the position measurement to yield the control force. Since the factor s^2 in the time domain is equivalent to two differentiations with respect to time, Eqn. (10) prescribes constant gain acceleration feedback. This, as discussed earlier, increases the effective mass of the system. (Of course, if we modify Eqn. (10) to limit the controller bandwidth, then the mass analogy only holds within the band.)

While both transmitted and direct disturbances are attenuated, the experiment acceleration level will be approximately the same as the accelerometer measurement noise level. This results from the transmissibility between experiment acceleration and measurement noise being nearly one due to the high gain feedback. This is a fundamental issue as discussed in Section II; one must trade–off the rejection of disturbances to the system and the rejection of measurement noise. Since the disturbances may be up to one thousand times larger than the measurement noise (accelerometer resolution typically 1 μg) the controller is designed to reject disturbances. The performance of the control system is thus directly a function of the quality of the accelerometer.

Recently, an alternative approach to design of active vibration isolation control systems for microgravity experiments was presented in Reference [10]. A desired transmissibility ratio $G_{cl}(s)$ is specified along with the plant model $G_p(s)$

and P(s). Eqn. (9) is then solved via algebraic manipulation for the feedback controller $H_p(s)$ that yields the desired transmissibility (feedback of relative position is also allowed and may be used; if used, a second condition must then be specified for solution). While this approach resembles loop shaping in that it attempts to achieve a certain transmissibility, it is fundamentally different in that it does not properly consider the plant. The algebraic procedure in essence first eliminates the plant and then replaces it with one which will yield the desired transmissibility. As a control design procedure, this methodology has serious flaws: (1) the stability of the resulting system may be entirely dependent on perfect knowledge of the plant, (2) the procedure incorporates none of the known relationships and fundamental trade–offs between stability and attenuation; it implies that any specified transmissibility is achievable, and (3) for systems with right half plane poles/zeros, the methodology may attempt cancellation with right half plane zeros/poles. For a simple controls problem, the algebraic manipulation method may result in a good controller. However, for more difficult problems, the method is questionable. An extension of this methodology to multi–input–multi–output control would be plagued by many problems.

To summarize, controller design for single–degree–of–freedom vibration isolation problems is best performed through the classical control framework of loop shaping where the natural interplay between performance, stability and robustness are evident. For multiple degree of freedom isolation problems, recent advances in controller design, such as the extension of loop shaping principles via frequency weighting and singular values [11] seems to be most promising. In order to emphasize the question of coordination in control of MIMO systems, we next examine a multiple–degree–of–freedom isolation problem.

V. A Multiple–Degree–of–Freedom System

A common misunderstanding among many engineers unfamiliar with control system design is the nature of the differences between SISO and MIMO control problems. The relative ease with which the uninitiated comprehend the elimination of one error signal through negative error feedback yields the false impression that the MIMO control problem is little more than the feeding back of multiple error signals. This impression, however, is not totally groundless. Indeed, many MIMO controllers in use today were designed by a single–loop–at–a–time procedure. Design with this method can be quite difficult, time consuming, and non–intuitive. Robustness is difficult to check except by analyzing all the possible permutations to the nominal plant. The fundamental problem in MIMO design is the coordination of the control in coupled channels when the plant is not well known (poorly modeled or time varying).

Easily decoupled active vibration isolation control problems may be deceptively simple. Unmodeled cross–coupling due to inaccuracies in center of mass, sensor, and/or umbilical locations can result in poor performance and even instability. An example isolation problem illustrates. Figure 13 shows a two–degree–of–freedom isolation system composed of an isolated platform (width 0.5 meters and height 0.2 meters, depth unspecified), two accelerometers, two actuators, an umbilical, and a translating base. The platform may translate vertically or rotate about its center of mass. The actuators and accelerometers are positioned a distance of $q = 0.2$ m symmetrically about the assumed center of mass location. An umbilical of stiffness k (no damping) runs between this location and the base. The platform has mass m and inertia I. The equations of motion for the platforms translation $x(t)$ and rotation $\theta(t)$ are

$$m\ddot{x} + k\Delta\theta + kx = f_1 + f_2 + d_1$$
$$I\ddot{\theta} + k\Delta^2\theta + k\Delta x = (q + \Delta)f_2 - (q - \Delta)f_1 + d_2 \tag{11}$$

where d_1 and d_2 are the disturbances, and Δ is the error in the assumed center of mass. The accelerometer readings are

$$y_1 = \ddot{x} - (q - \Delta)\ddot{\theta}$$
$$y_2 = \ddot{x} + (q + \Delta)\ddot{\theta} \tag{12}$$

The nominal system ($\Delta = 0$) can be decoupled to one in terms of the degrees of freedom by the change in variables

$$F = f_1 + f_2$$
$$M = q(f_2 - f_1)$$
$$z_1 = (y_1 + y_2)/2 \tag{13}$$
$$z_2 = q\,(y_2 - y_1)/2$$

which are nominally the translational force, the moment, the translational acceleration, and the angular acceleration for the platform respectively. The nominal transfer function for the system are then

$$Z_1(s) = \left[\frac{s^2}{ms^2 + k}\right](F(s) + D_1(s))$$

$$Z_2(s) = \left[\frac{1}{I}\right](M(s) + D_2(s))$$

For translational motion, the natural frequency of the platform is $\sqrt{k/m}$. The rotational motion of the platform is free since the umbilical is attached to the center of mass. To compensate the nominal system, feedback can be designed for each mode of the system separately since the system is decoupled. Translational acceleration and velocity feedback is first used to add effective mass and damping

$$F(s) = -(a + \frac{c}{s})\, Z_1(s) \tag{14}$$

This lowers the natural frequency of translational motion yielding the closed loop transfer function

$$Z_1(s) = \left[\frac{s^2}{(m+a)s^2 + cs + k} \right] D_1(s)$$

Next, angular deflection feedback is used to constrain low frequency rotational motion and some damping is provided

$$M(s) = -(\frac{n}{s} + \frac{b}{s^2})\, Z_2(s) \tag{15}$$

yielding

$$Z_2(s) = \left[\frac{s^2}{Is^2 + ns + b} \right] D_2(s)$$

The following values are used to illustrate this example.

PLATFORM	CONTROL SYSTEM
$m = 400$ kg	$a = 31600$ kg
$k = 50$ N/m	$c = 1000$ N·s/m
$I = 10$ kg·m^2	$b = 0.015$ N·m
	$n = 0.2$ N·m·s

where the control system values are in effective units. This control design lowers the natural frequency of translational motion from 0.056 Hz to 0.006 Hz with 40% of critical damping. The controlled rotational motion has a natural frequency of 0.006 Hz with 26% of critical damping. This controller design would yield very effective isolation on the nominal system.

The actual closed loop transfer functions will be different from the nominal due to the error in the center of mass, Δ. The transmissibility can be derived from Eqns. (11–15) as follows

$$[ms^2 + k]X(s) + [k\Delta]\Theta(s) = F(s) + D_1(s)$$

$$[Is^2 + k\Delta^2]\Theta(s) + [k\Delta]X(s) = M(s) + \Delta F(s) + D_2(s)$$

$$Z_1(s) = [s^2]X(s) + [\Delta s^2]\Theta(s)$$

$$Z_2(s) = [s^2]\Theta(s)$$

$$F(s) = -[a + c/s]\,Z_1(s)$$

$$M(s) = -[n/s + b/s^2]\,Z_2(s)$$

yielding

$$\left[\frac{(m+a)s^2 + cs + k}{s^2}\right] Z_1(s) + [m\Delta]\, Z_2(s) = D_1(s)$$

$$\left[\frac{(as^2 + s + k)\Delta}{s^2}\right] Z_1(s) + \left[\frac{Is^2 + ns + b}{s^2}\right] Z_2(s) = D_2(s)$$

The poles of this system are given by the roots of the characteristic equation

$$[(m + a)s^2 + cs + k][Is^2 + ns + b] - [m\Delta][\Delta(as^2 + cs + k)] = 0 \qquad (16)$$

For the nominal plant, $\Delta = 0$, the roots of the Eqn. (16) result in the prescribed natural frequencies and critical dampings. However, as the center of mass error increases, the poles migrate and the system becomes unstable. For an error as small as 6 millimeters, instability occurs. A plot of the pole movement versus error in center of mass is shown in Figure 14. This sensitivity results from the ill conditioned character of the required controller. Ill conditioned here means that the controller's gain to an output signal varies strongly with the signal's direction. This results in a control system which is not robust to this model's uncertainty (cent[illegible]f mass) [12]. A proper MIMO controller design might remedy this problem. In any case, an analysis of the problem from a MIMO control perspective would indicate the potential instability and the nature of the trade–off between performance and robustness. (The authors note that increasing the damping and stiffness for the rotational mode improves the system robustness significantly, while changing the damping or effective mass for the translational mode has little effect.)

VI. Linear Quadratic Regulator for Isolation

MIMO control design, since it requires a high degree of coordination, must proceed by a synthesis procedure. One such method is Linear Quadratic Regulator (LQR) synthesis [13]. This produces a state feedback controller which is optimal with respect to the quadratic (two norm) performance function

$$J = \int_{-\infty}^{\infty} \bar{x}^T(j\omega)\, Q\, \bar{x}(j\omega) + u^T(j\omega)\, R\, u(j\omega)\, d\omega \tag{17}$$

where Q and R are respectively the symmetric (usually diagonal) state and control weighting matrices, and $\bar{x}(j\omega)$ and $u(j\omega)$ are the Fourier transforms of the state and control vectors. The state (positions and velocities for vibration isolation) satisfies the differential equation

$$\dot{\bar{x}} = A\bar{x} + Bu$$

The quadratic performance function of LQR, Eqn. (17), is well suited to this problem since vibration isolation quality is usually measured in terms of root–mean–square. However, some modification of the performance function is necessary to apply this synthesis procedure to microgravity isolation controller design. The reader will note that state feedback for the isolation problem is feedback of experiment positions, velocities, angles, and angular velocities. Thus, LQR can only result in inertial stiffness and inertial damping feedback. As was shown in Section III, these isolation techniques cannot yield acceptable isolation performance. Thus, an LQR performance function of the form of Eqn. (17) will not yield a satisfactory controller. Note that the differential equation does not include a disturbance term. Consequently, the controller is optimal with respect to white noise. Since the power spectrum of the microgravity environment is not of this shape, the LQR controller will not be optimal with respect to rejection of the disturbance. Through the incorporation of a disturbance model (essentially a shaping filter) the LQR problem may be modified to yield an optimal disturbance accommodating (i.e. rejection) controller. This incorporates the addition of pseudo–states to the state variable model [14].

Closely related to disturbance accommodation is the concept of frequency weighted LQR performance functions [15]. Here, the Q and R matrices are chosen to be even rational functions of frequency. This results in the addition of pseudo–states to the state variable model. Through choice of the weighting functions, the designer can in essence shape the control loops [11]. This also permits the weighting of experiment acceleration. It should be noted that for successful application of LQR theory to the microgravity isolation problem frequency shaped cost functions must be used. Without this, the control resulting from the synthesis procedure would attenuate the vibration at frequencies below 0.001 Hz (non–unity transmissibility). The reader should note that the well known robustness characteristics of LQR controllers do not apply to most frequency shaped designs or to plants with unmodeled cross coupling.

VII. Conclusions

Successful active isolation for microgravity experiments can be achieved but only if the problem is analyzed from a controls perspective. A passive isolation analogy, while useful for an understanding of the control problem, is not an effective design tool. Design of active vibration control systems can best be carried out through loop shaping. For intrusive isolation platforms, this results in a high gain acceleration feedback design. A two–degree–of–freedom example was used to illustrate the instability that can result under unmodeled cross coupling when the control system is designed via decoupling/single loop design procedures. The source of this sensitivity was ill conditioning of the controller. The Linear Quadratic Regulator was examined for the isolation problem. For synthesis of an effective controller, the procedure must be modified to include loop shaping.

Acknowledgements

This work was supported in part by NASA Lewis Research Center and the Commonwealth of Virginia. Some of this research was performed at NASA LRC as part of the Summer Faculty Fellowship Program.

References

1. Owen, R. G. and Jones, D. I. Microgravity Isolation Mount: Columbus Application Study (WP.1.1), European Space Agency, Technical Note BTN–001, Sept. 1988.
2. Owens, A. R. and Jones, D. I. "Toward a Practical Microgravity Environment", Proceedings of the Third European Space Mechanisms and Tribology Symposium, Madrid, Spain, Oct. 1987, pp. 245–250.
3. Jones, D. I., Owens, A. R., Owen, R. G. and Roberts, G. Microgravity Isolation Mount: Design Report, European Space Agency, Technical Note BTN–009, Sept. 1989.
4. Grodsinsky, C. M. and Brown, G. V. "Non–intrusive Inertial Vibration Isolation Technology for Microgravity Space Experiments," NASA TM–201386, January 1990.
5. Hamilton, B. J., Andrus, J. H. and Carter, D. R. "Pointing Mounts with Active Vibration Isolation for Large Payloads," 10th Annual Guidance and Control Conference, American Astronautical Society, Keystone, Colorado, Jan. 1987.
6. Jones, D. I., Owens, A. R. and Owen, R. G. "A Microgravity Isolation Mount," Acta Astronautica, Vol. 15, No. 6/7, pp. 441–448, 1987.
7. Grodsinsky, C. M., "Development and Approach to Low–Frequency Microgravity Isolation Systems," NASA Technical Paper 2987, Aug. 1990.
8. Bode, H. W., Network Analysis and Feedback Amplifier Design, Van Nostrand, New York, 1945.
9. Maciejowski, J. M., Multivariable Feedback Design, Addison Wesley, New York, 1989.

10. Sinha, A., Kao, C. K., and Grodsinsky, C. M. "A New Approach to Active Vibration Isolation for Microgravity Space Experiments," NASA TM 102470, Feb. 1990.

11. Safanov, M. G., Laub, A. J., and Hartmann, G. L., "Feedback Properties of Multivariable Systems: The Role and Use of the Return Difference Matrix," IEEE Transactions on Automatic Control, Vol. 26, No. 1, Feb. 1981.

12. Skogestad, S., Morari, M., and Doyle, J. C. "Robust Control of Ill–Conditioned Plants: High Purity Distillation," IEEE Transactions on Automatic Control, Vol. 33, No. 12, Dec. 1988.

13. Anderson, B. P. O. and Moore, J. B., Linear Optimal Control, Prentice Hall, Englewood Cliffs, New Jersey, 1972.

14. Johnson, C. D., "Accommodation of External Disturbances in Linear Regulator and Servomechanism Problems," IEEE Transactions on Automatic Control, Vol. 16, No. 6, Dec. 1971.

15. Gupta, N. K., "Frequency–Shaped Cost Functionals: Extension of Linear–Quadratic–Gaussian Design Methods," Journal of Guidance and Control, Vol. 3, No. 6, Nov. 1980.

Figure 1: The Microgravity Environment (from [1])

Figure 2: The One–Degree–of–Freedom Microgravity Vibration Isolation Problem

Figure 3: Displacement (a) and Acceleration (b) Isolation System Block Diagrams

Figure 4: Unity Feedback Form of Control System

Figure 5: Specifications (1) and (2) and Uncompensated Transmissibility $\ddot{X}(s)/\ddot{Y}(s)$

Figure 6: Root Locus for Equivalent Stiffness Design with respect to Umbilical Stiffness Error

Figure 7: Transmissibility $\ddot{X}(s)/\ddot{Y}(s)$ for Inertial Stiffness with Feedforward Design

Figure 8: Transmissibility $\ddot{X}(s)/\ddot{Y}(s)$ for Inertial Damping Design

Figure 9: Designs Specifications and $H_p(s)$

Figure 10: Resultant Transmissibility for Loop Shaped Design

Figure 11: Root Locus of Loop Shaped Design with respect to Umbilical Stiffness Error

Figure 12: Root Locus of Loop Shaped Design with respect to Actuator Finite Bandwidth, ω_b = actuator pole break frequency

Figure 13: Two–Degree–of–Freedom Active Isolation System

Figure 14: Root Locus of Two–Degree–of–Freedom with respect to Center of Mass Error Δ

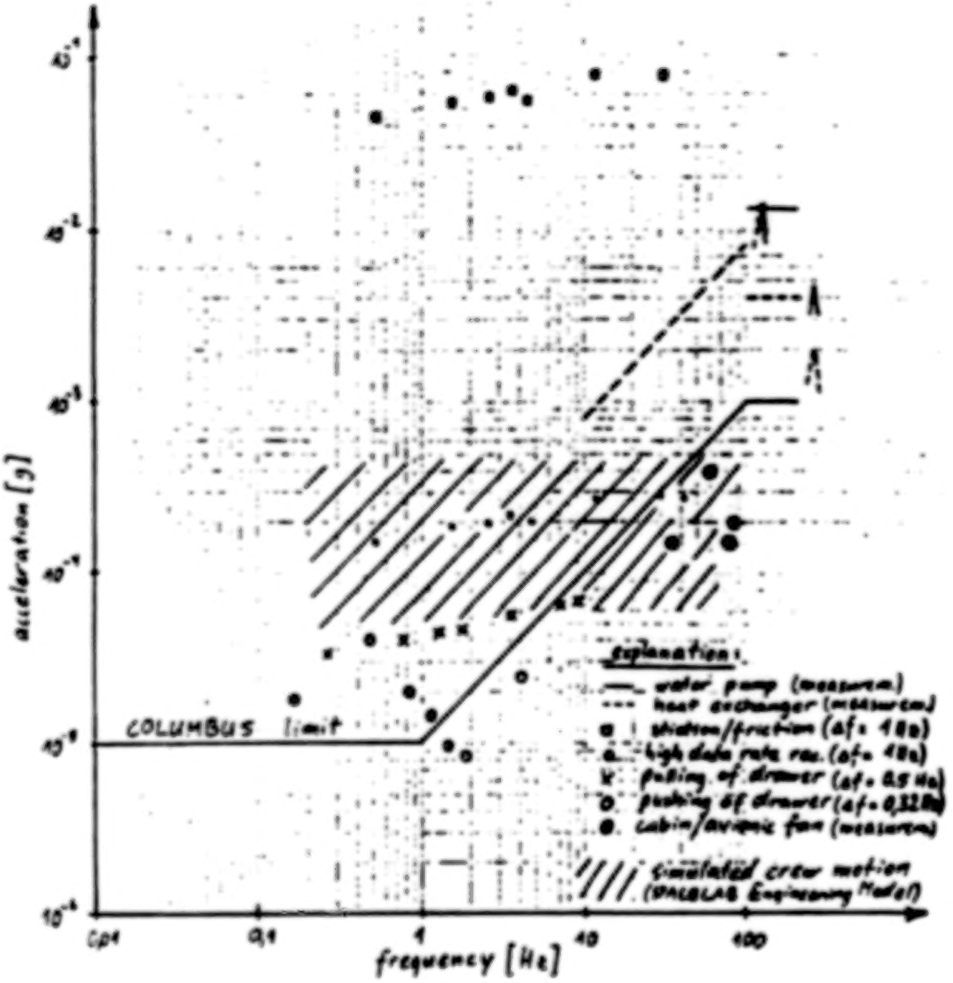

Figure 1: The Microgravity Environment (from [1])

ORIGINAL PAGE IS
OF POOR QUALITY

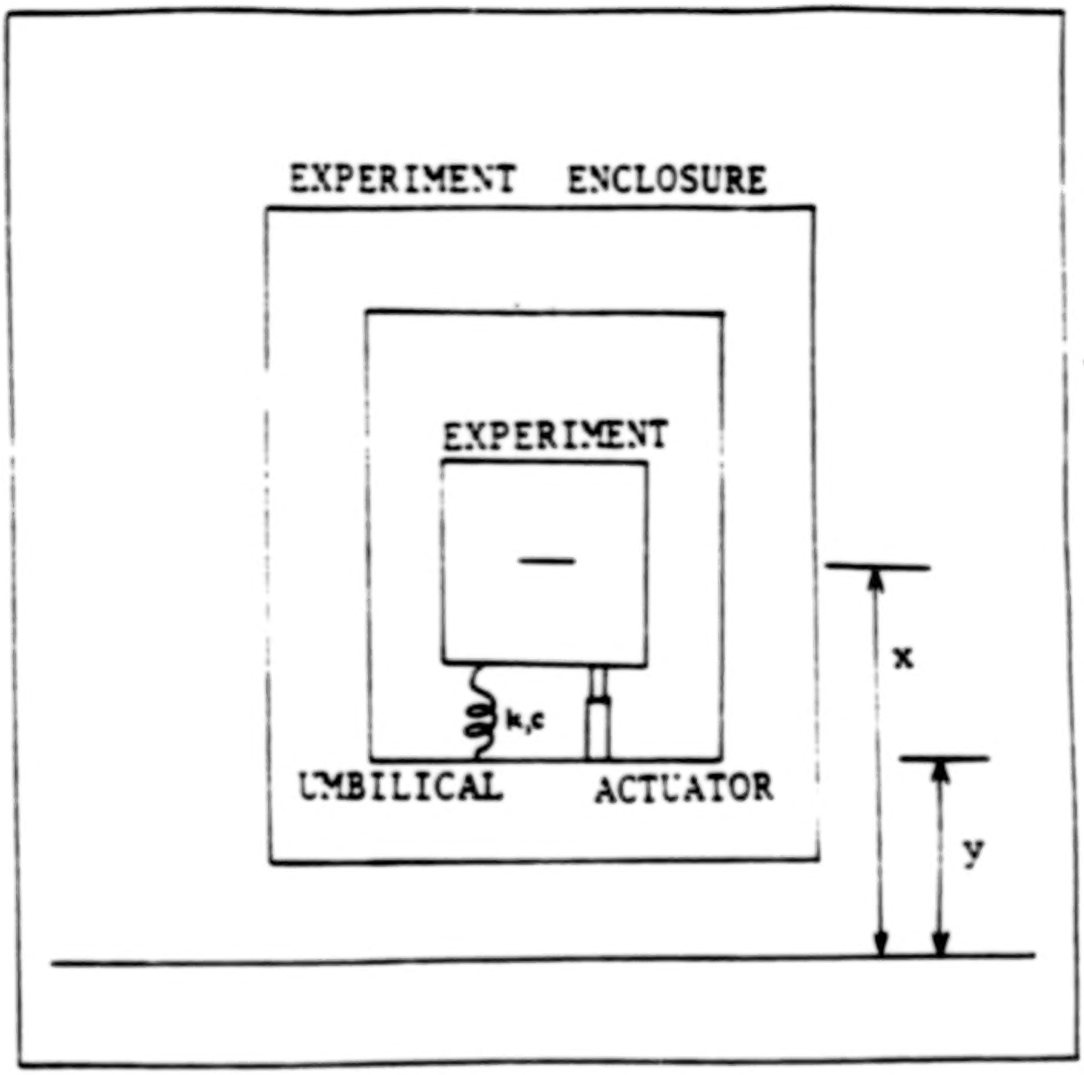
EXPERIMENT ENCLOSURE
EXPERIMENT
k,c
UMBILICAL
ACTUATOR
x
y

Figure 2: The One–Degree–of–Freedom Microgravity Vibration Isolation Problem

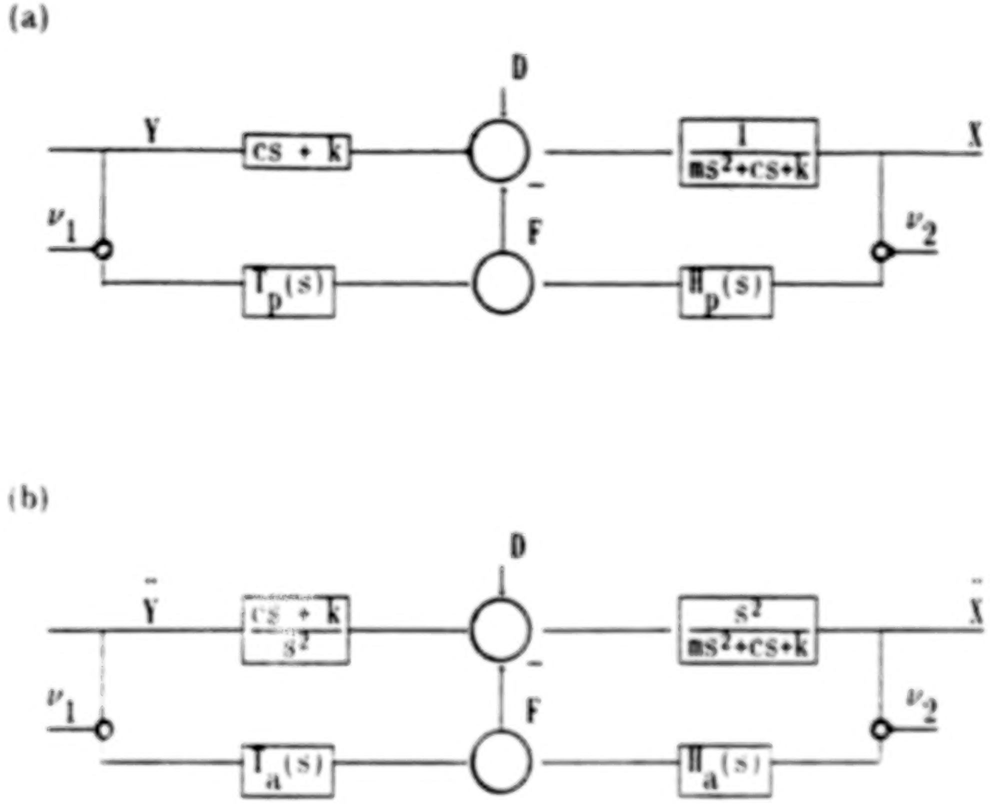
(a)
D
Y
cs + k
1
ms²+cs+k
X
ν1
F
ν2
Tp(s)
Hp(s)
(b)
D
Ÿ
cs + k
s²
s²
ms²+cs+k
Ẍ
ν1
F
ν2
Ta(s)
Ha(s)

Figure 3: Displacement (a) and Acceleration (b) Isolation System Block Diagrams

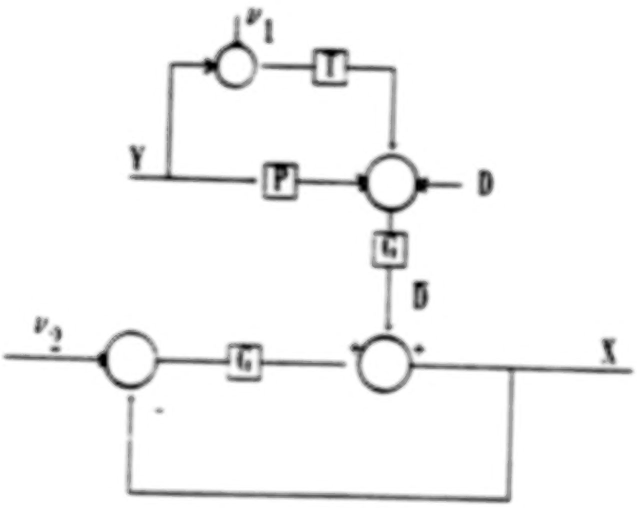

ν_1
T
Y
P
D
G
$\bar{D}$
ν_2
G
+
+
X
-

Figure 4: Unity Feedback Form of Control System

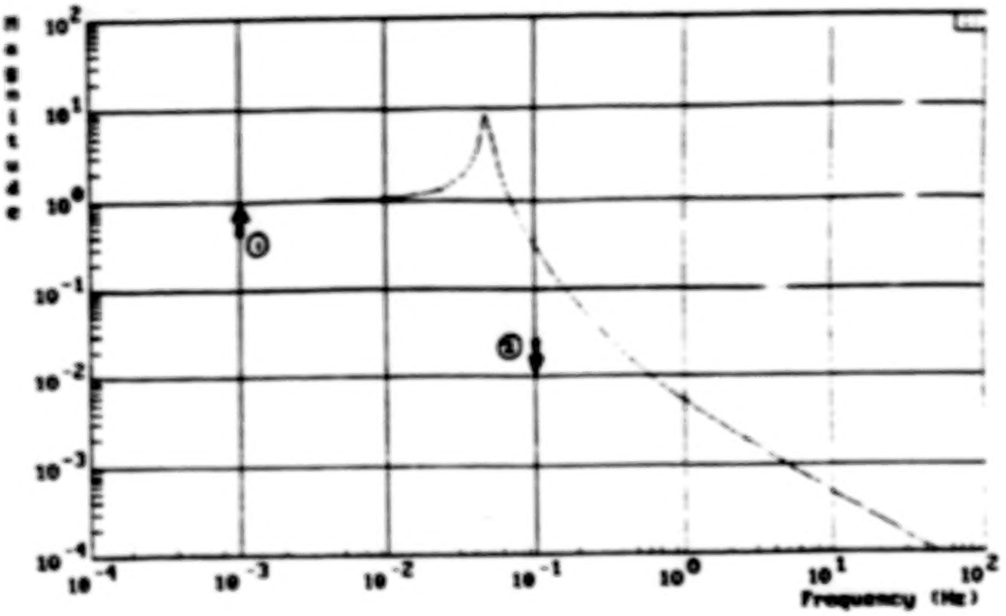

Figure 5: Specifications (1) and (2) and Uncompensated Transmissibility $\bar{X}(s)/\bar{Y}(s)$

ORIGINAL PAGE IS
OF POOR QUALITY

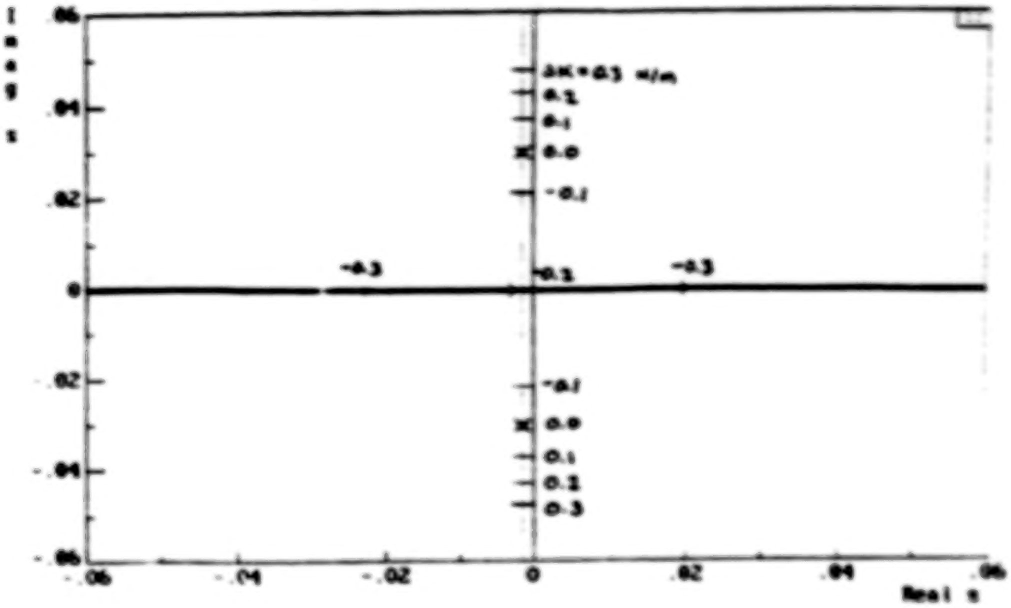

Figure 6: Root Locus for Equivalent Stiffness Design with respect to Umbilical Stiffness Error

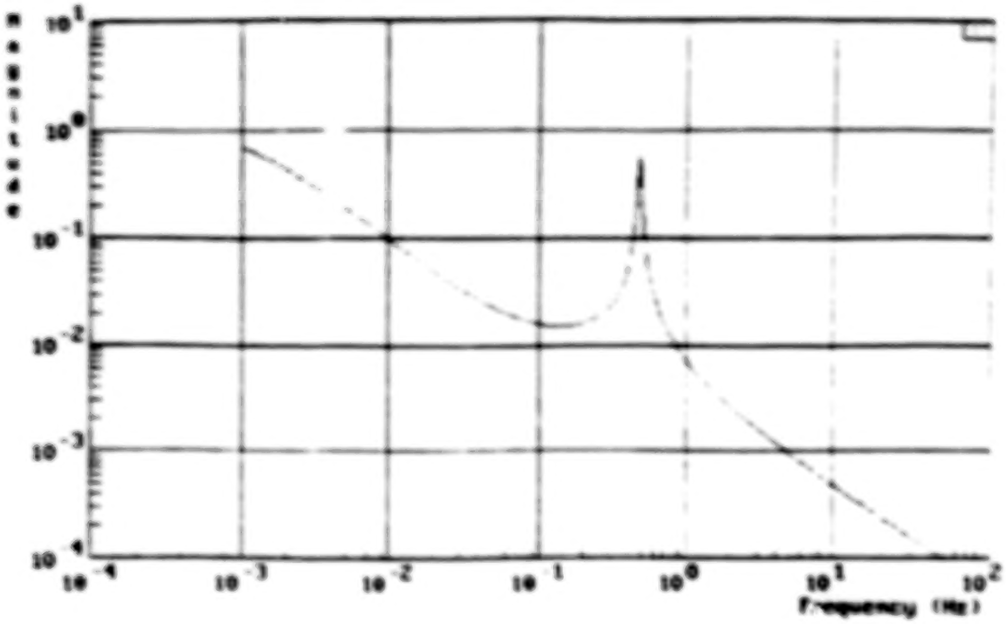

Figure 7: Transmissibility $\bar{X}(s)/\bar{Y}(s)$ for Inertial Stiffness with Feedforward Design

ORIGINAL PAGE IS
OF POOR QUALITY

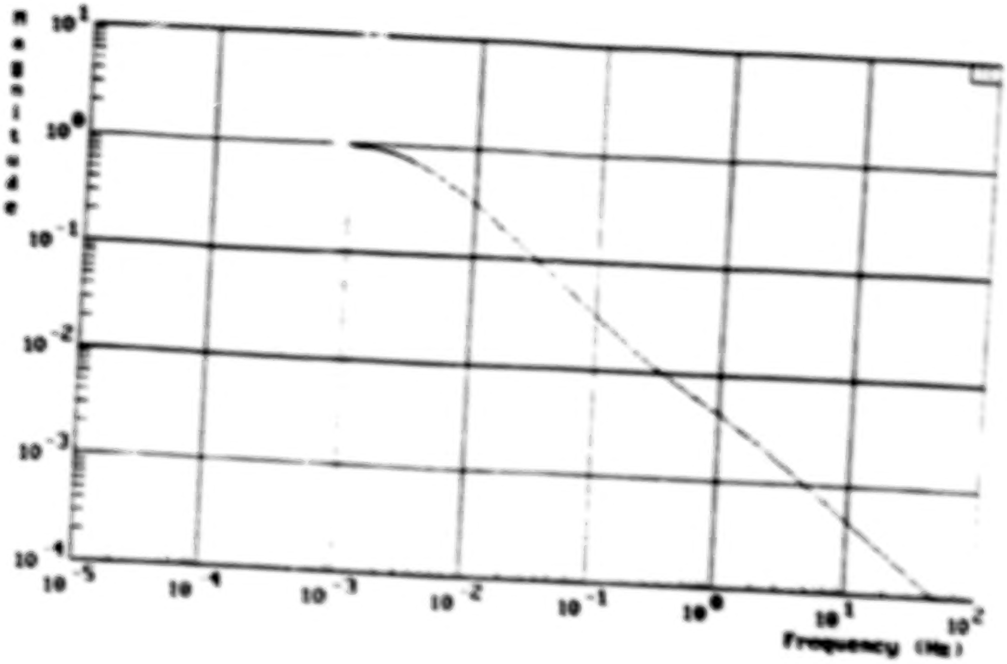

Figure 8: Transmissibility $\bar{X}(s)/\bar{Y}(s)$ for Inertial Damping Design

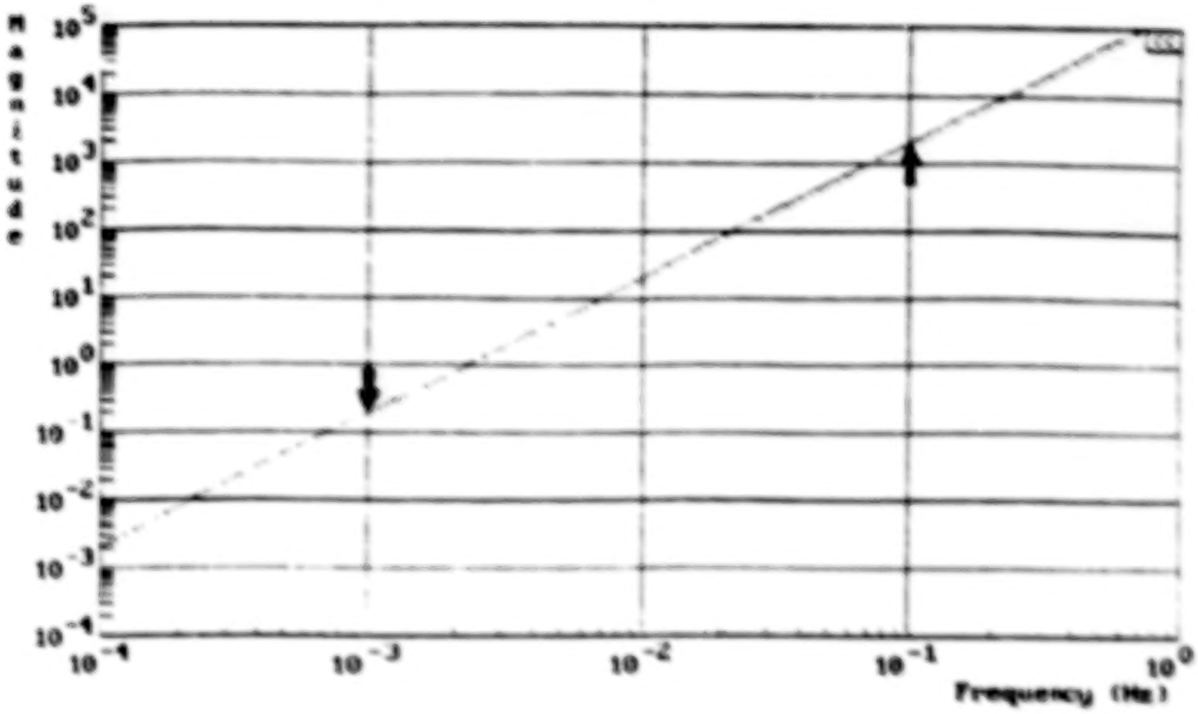

Figure 9: Designs Specifications and $H_p(s)$

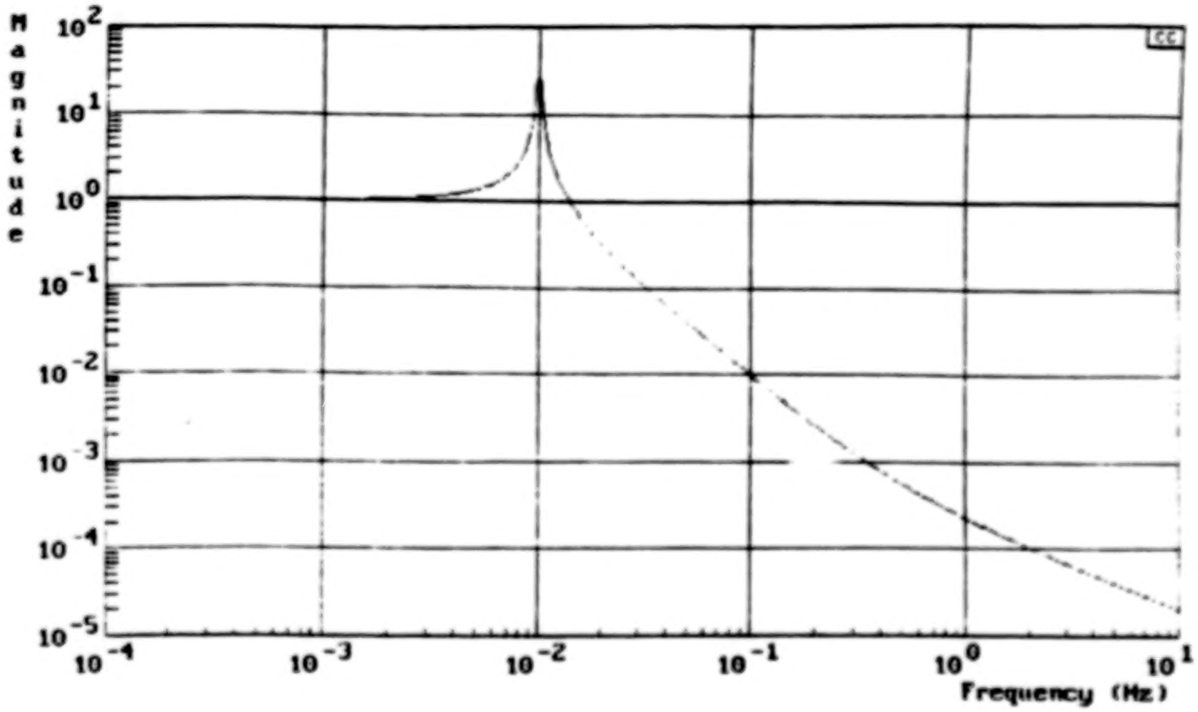

Figure 10: Resultant Transmissibility for Loop Shaped Design

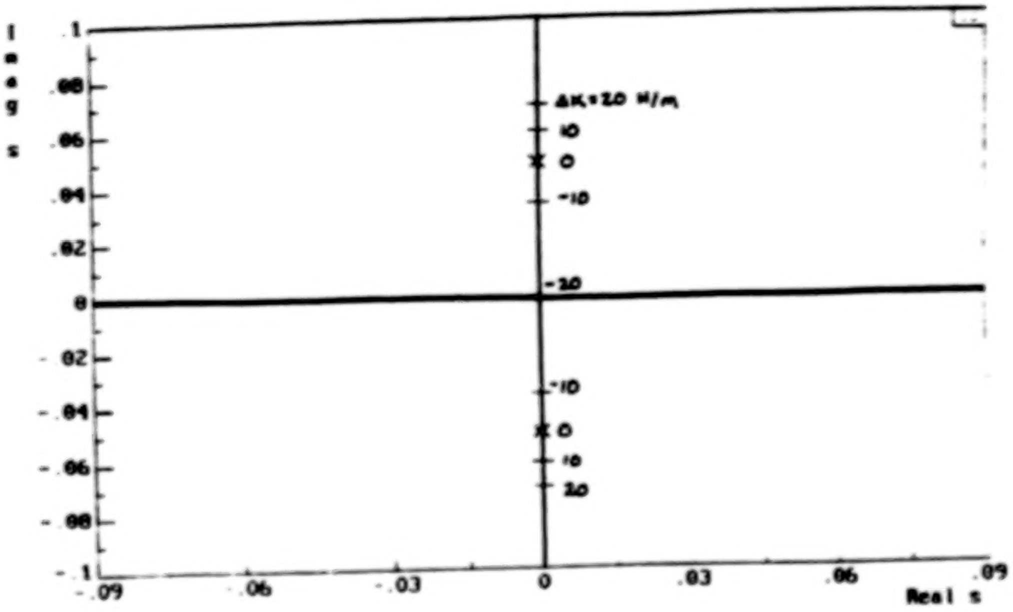

Figure 11: Root Locus of Loop Shaped Design with respect to Umbilical Stiffness Error

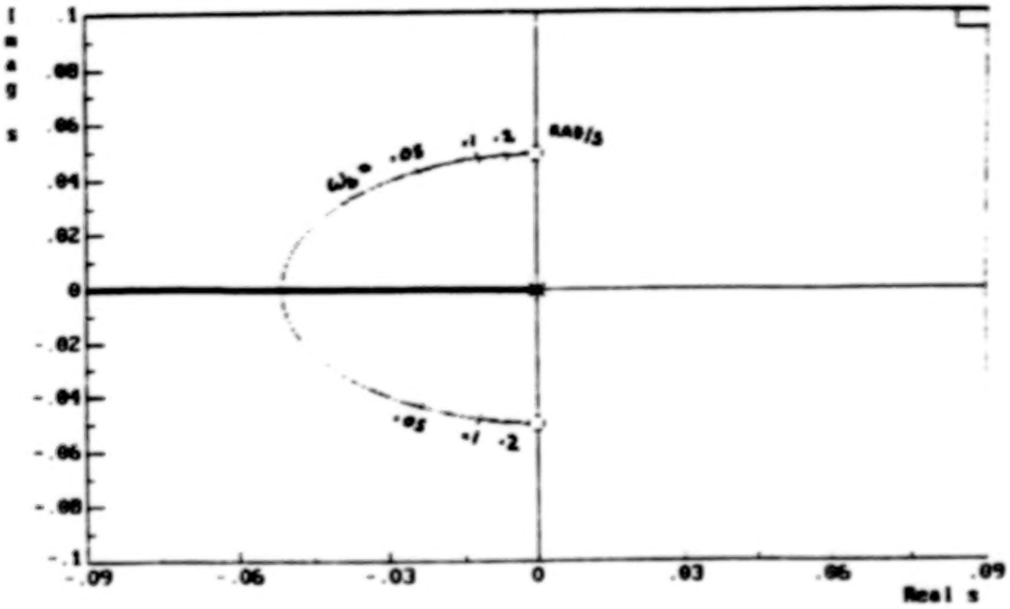

Figure 12: Root Locus of Loop Shaped Design with respect to Actuator Finite Bandwidth. ω_b = actuator pole break frequency

ORIGINAL PAGE IS
OF POOR QUALITY

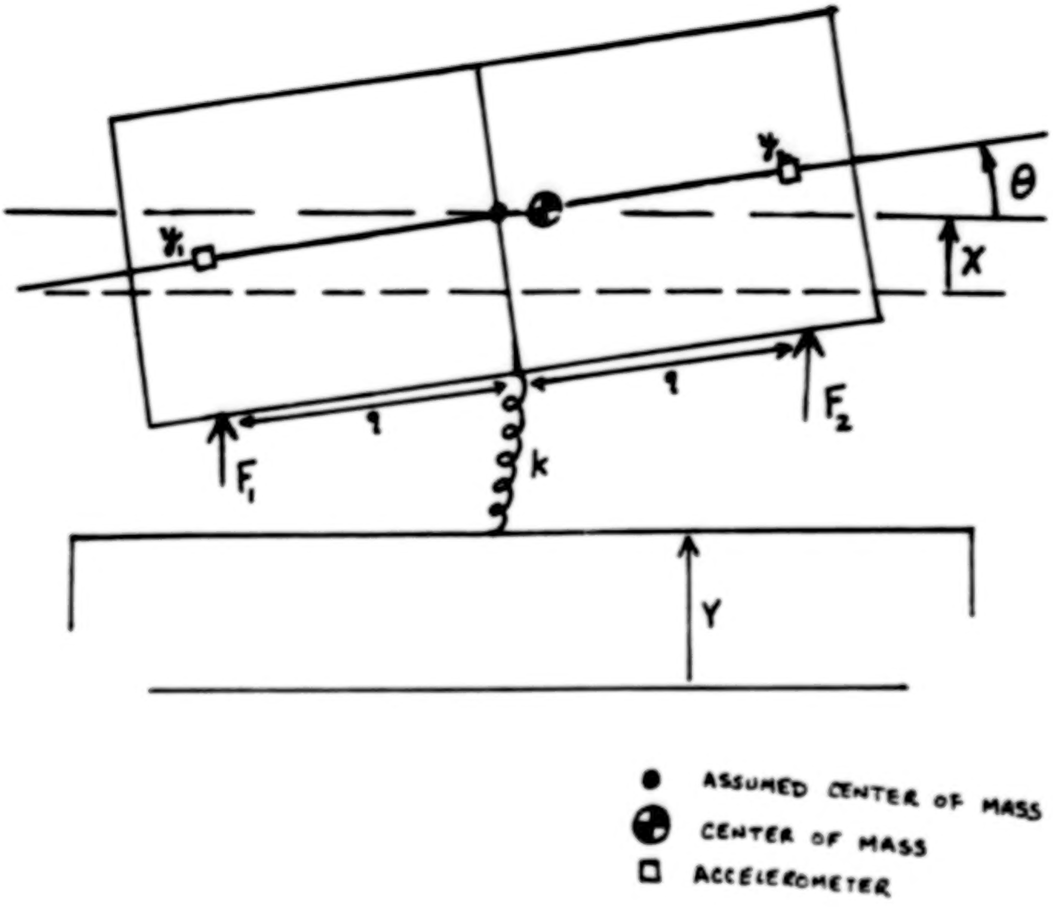
y1
y2
θ
X
l
l
F1
F2
k
Y
● ASSUMED CENTER OF MASS
● CENTER OF MASS
□ ACCELEROMETER

Figure 13: Two–Degree–of–Freedom Active Isolation System

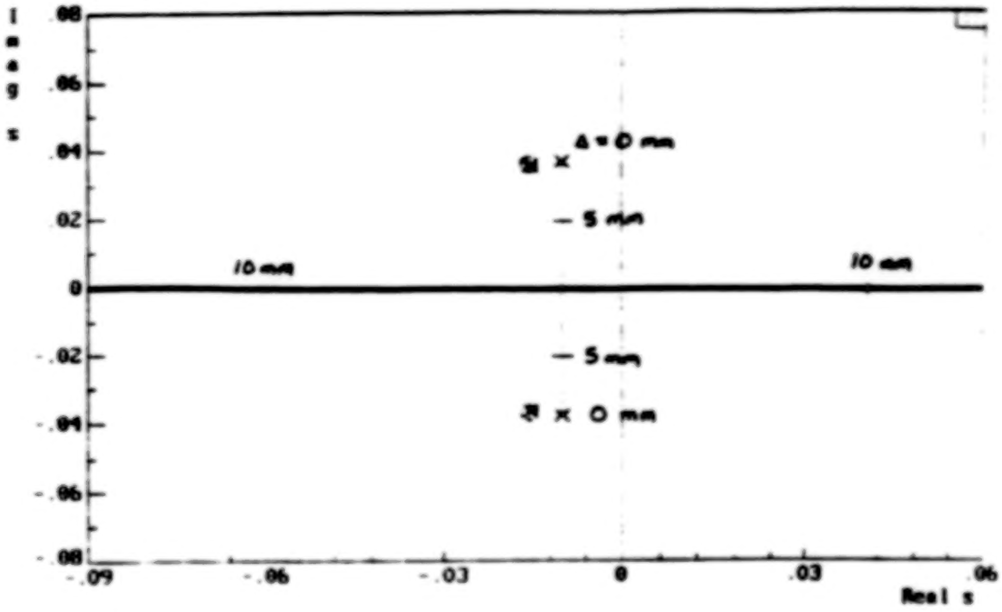

Figure 14: Root Locus of Two–Degree–of–Freedom with respect to Center of Mass Error Δ

ORIGINAL PAGE IS
OF POOR QUALITY

CONTROL ISSUES OF MICROGRAVITY VIBRATION ISSOLATION

C.R. Knospe, Research Assistant Professor
R.D. Hampton, Graduate Student

Workshop on Aerospace Applications
of Magnetic Suspension
September 25, 1990

PROBLEM:

ORBITAL ENVIRONMENT CONTAMINATED BY BROADBAND DISTURBANCES

UNACCEPTABLE FOR FLUIDS AND MATERIALS EXPERIMENTS

UMBILICAL NEEDED

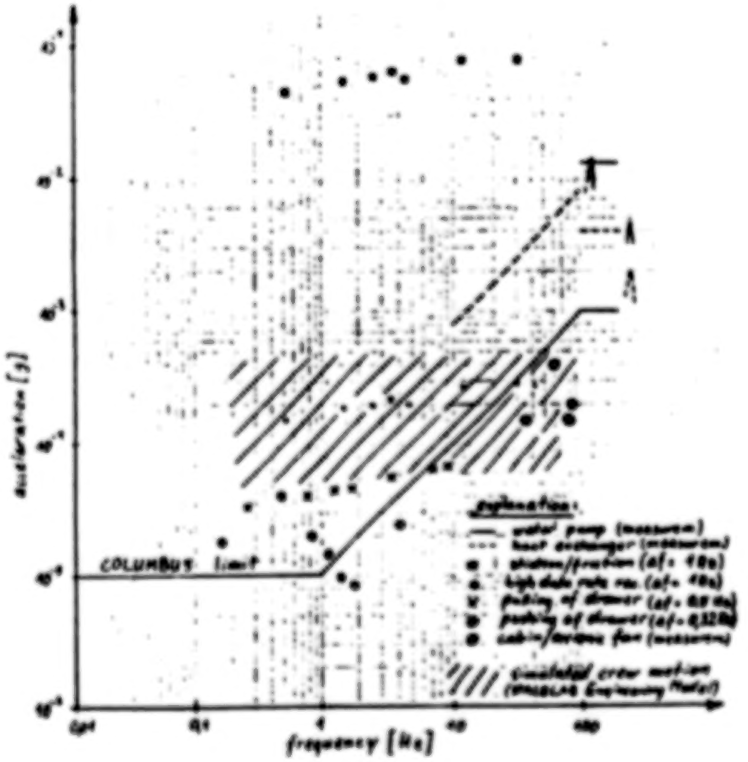

ORIGINAL PAGE IS
OF POOR QUALITY

PERFORMANCE SPECIFICATIONS

- UNITY TRANSMISSIBILITY FROM DC TO 0.001 Hz
- 40 dB ATTENUATION ABOVE 0.1 Hz
- BOTH STABILITY AND PERFORMANCE ROBUSTNESS

Robustness: The ability to withstand ummodelled effects

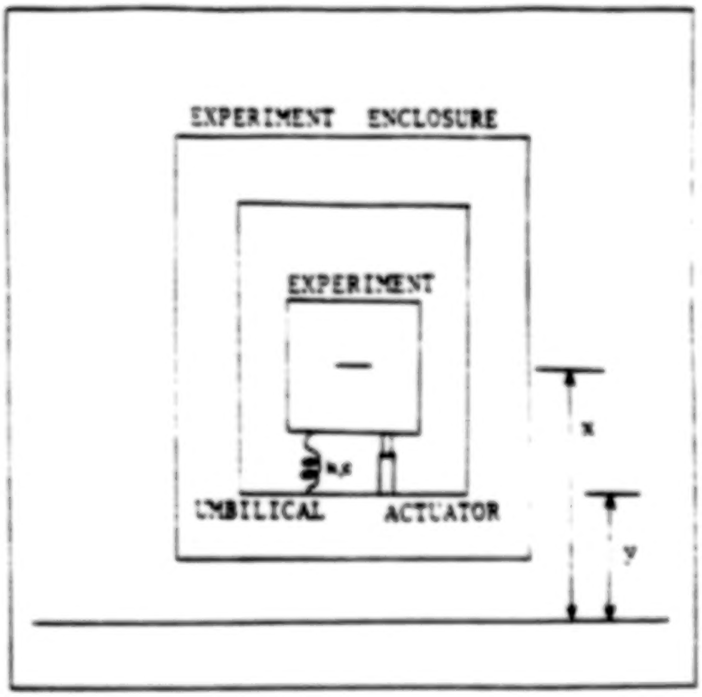
EXPERIMENT ENCLOSURE
EXPERIMENT
k,c
UMBILICAL
ACTUATOR
x
y

ORIGINAL PAGE IS
OF POOR QUALITY

OUTLINE

(1) CONTROL THEORY REVIEW

(2) PASSIVE ISOLATION ANALOGIES

(3) CONTROLLER DESIGN

(4) MDOF EXAMPLE

(5) LINEAR QUADRATIC REGULATOR

(6) CONCLUSIONS

SYSTEM BLOCK DIAGRAMS

POSITION FORM

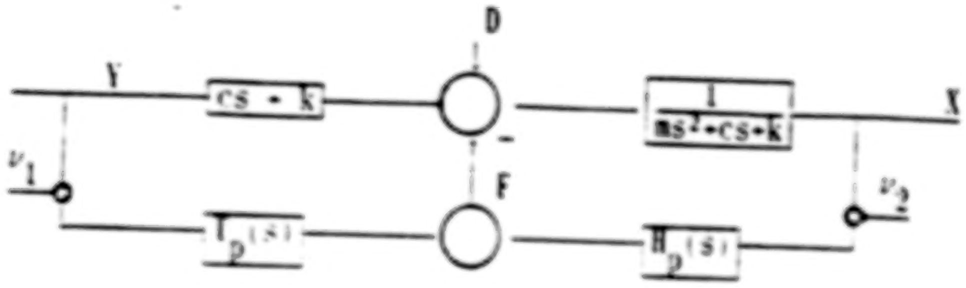
D
Y
cs + k
1/(ms²+cs+k)
X
-
ν1
F
ν2
I_p(s)
H_p(s)

ACCELERATION FORM

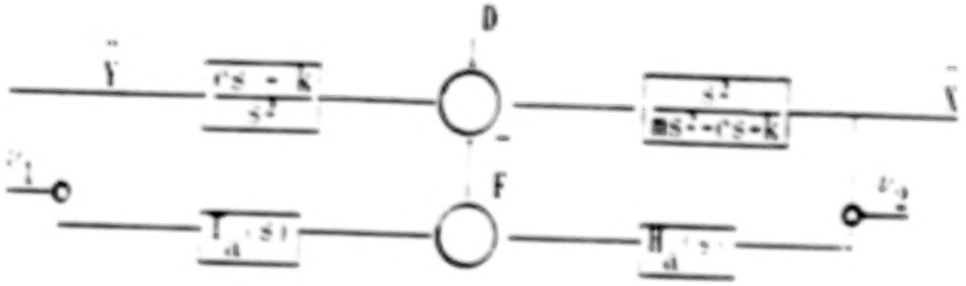
D
Ÿ
(cs + k)/s²
s²/(ms²+cs+k)
Ẍ
-
ν1
F
ν2
I_a(s)
H_a(s)

UNITY FEEDBACK FORM

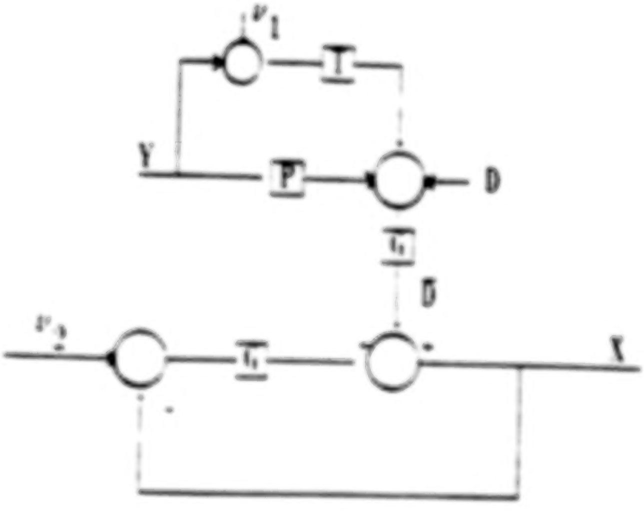
ν1
I
Y
P
D
G
D̄
ν2
G
X
-

THE LOOP SHAPING TRADE-OFF

SENSITIVITY FUNCTION

$$S(s) \equiv \frac{X(s)}{\bar{D}(s)} = \frac{1}{1 + GH}$$

COMPLIMENTARY SENSITIVITY FUNCTION

$$C(s) \equiv \frac{X(s)}{V_2(s)} = \frac{GH}{1 + GH}$$

THE TRADE-OFF

$$S(s) + C(s) \equiv 1$$

ORIGINAL PAGE IS
OF POOR QUALITY

LOOP SHAPING: PASSIVE ISOLATION

SPRING-MASS SYSTEM:

$$\frac{\ddot{X}(s)}{\ddot{Y}(s)} = \frac{G}{1 + G}$$

$$\frac{\ddot{X}(s)}{D(s)/m} = \frac{1}{1 + G}$$

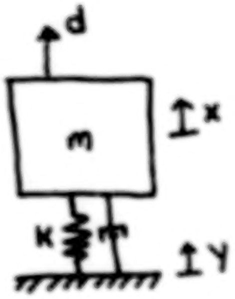

$$G(s) = \frac{cs + k}{ms^2}$$

Direct disturbances act as output disturbances while wall accelerations act as input disturbances.

Passive isolation design:
  soft mount for base disturbance
  stiff mount for direct disturbance

LOOP SHAPING DESIGN

BODE PLOTS:

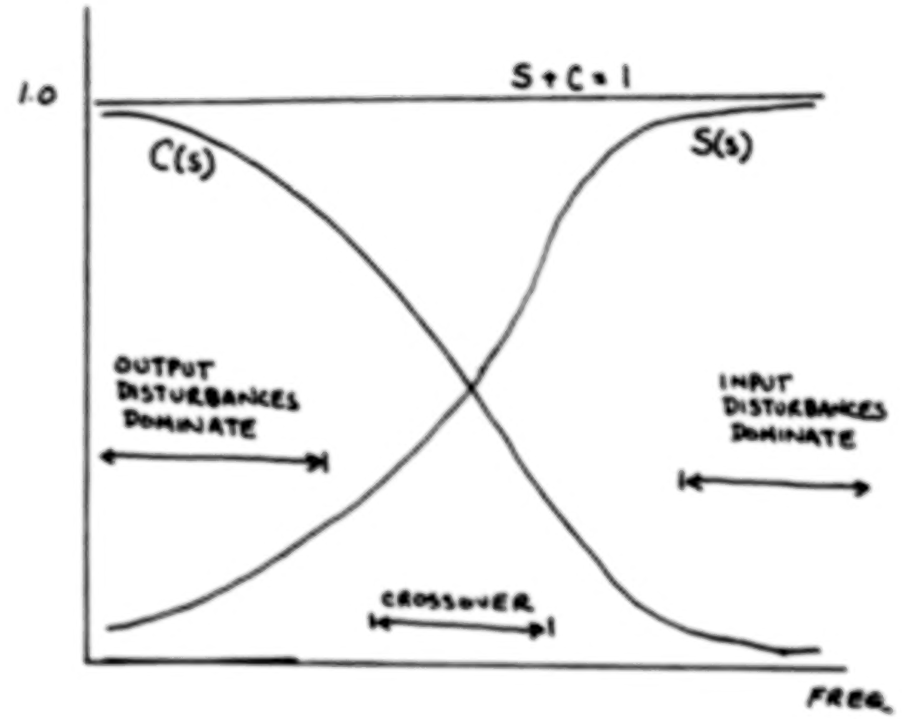

The classical conrol framework displays the trade-offs between input and output disturbance rejection and stability and robustness.

PASSIVE ISOLATION ANALOGIES

THREE ANALOGIES:

- RELATIVE STIFFNESS
- INERTIAL STIFFNESS
- INERTIAL DAMPING

SYSTEM MODEL:

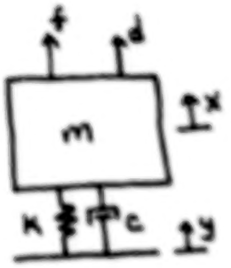

m=220 kg
k=20 N/m
c=6.63 N s/m

TRANSMISSIBILITY:

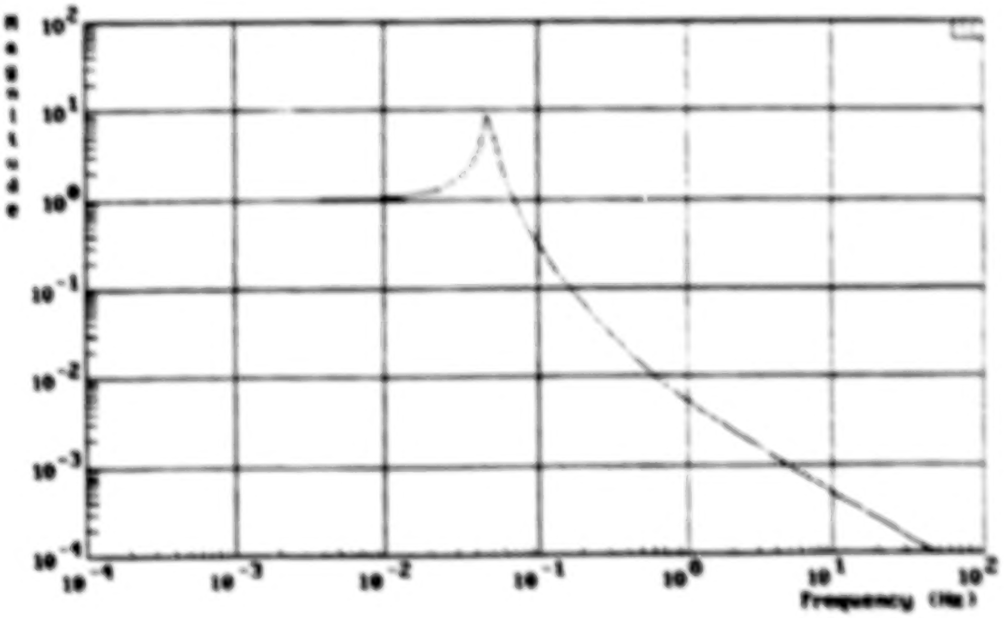

EQUIVALENT STIFFNESS

Lower the natural frequency of the umbilical by adding negative stiffness to the system through the controller

ROBUSTNESS PROBLEM: If the negative stiffness added exceeds that of the umbilical, the system is unstable. But, to lower the natural frequency significantly, the negative stiffness introduced must be nearly that of the umbilical.

Root locus plot:

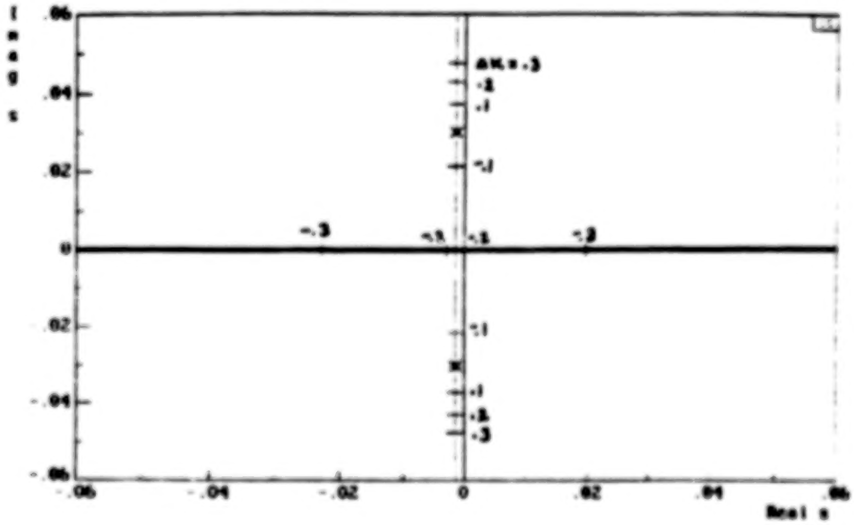

Design has less than 0.1 degree phase margin.

INERTIAL STIFFNESS

Fasten the experiment platform rigigly to an inertial structure through inertial position feedback

PROBLEM: The natural frequency of the system is actually increased; isolation is obtained by lowering the DC gain of the system.Therefore,the resultant system does not have unity transmissibility up to 0.001 Hz. This can be fixed with feedforward.

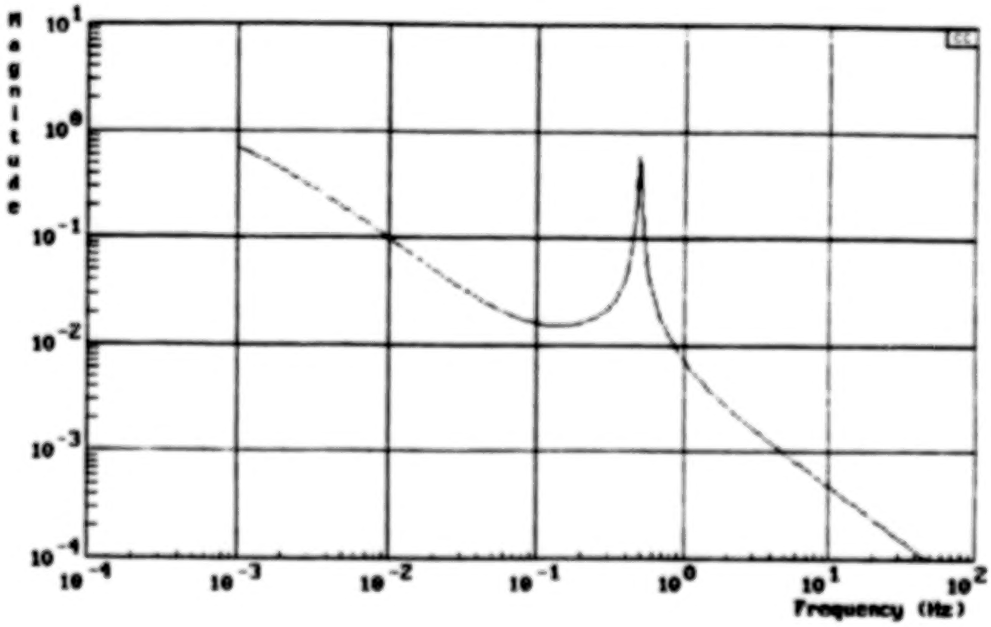

Requires inertial position and velocity measurements.

INERTIAL DAMPING

Prevent experiment movement through fastening the system to inertial space via a damper. This may be accomplished through inertial velocity feedback.

- **This method does not compromise the system's DC gain.**

PROBLEM: The resulting transmissibility only rolls off at 20 dB/decade. Therefore, the 40 dB at 0.1 Hz and unity transmissibility up to 0.001 Hz design specifications cannot be both achieved.

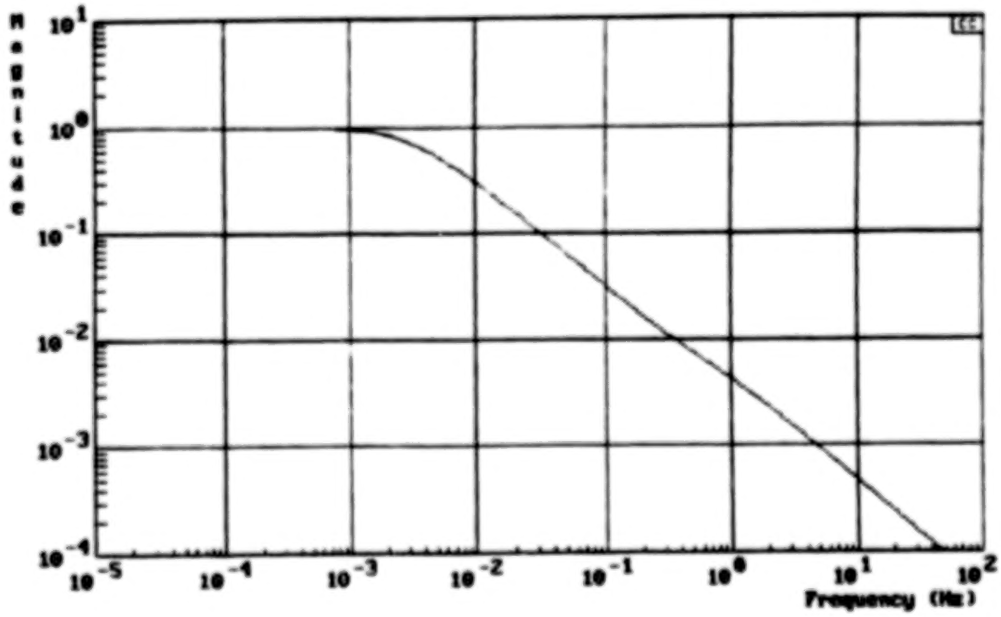

PASSIVE ISOLATION ANALOGIES:

The passive isolation analogies yield some insight into control system design.

THREE LIMITATIONS AS A DESIGN TOOL:

- Inflexibility to shape the response with simple analogical elements, stiffness and damping.

  This inflexibility can be seen in the inability of the analogical elements to yield an unstable controller.

- Inability to easily and effectively extend to multiple-degree-of-freedom problems.

- Completely ignores the robustness problem inherent to active control system design.

LOOP SHAPING DESIGN

CLOSED LOOP TRANSFER FUNCTION:

$$G_{cl}(s) \equiv \frac{X(s)}{Y(s)} = \frac{G_p P}{1 + G_p H_p}$$

SPECIFICATIONS:

$$|G_{cl}| \approx 1.0 \qquad |G_p H_p| < 0.01 \qquad |H_p| < 0.2, \; \frac{\omega}{2\pi} < 0.001\,\text{Hz}$$

$$|G_{cl}| < 0.01 \qquad |G_p H_p| > 100 \qquad |H_p| > 2000, \; \frac{\omega}{2\pi} > 0.1\,\text{Hz}$$

Low frequency: Unity transmissibility
High frequency: 40 dB attenuation

DESIGN SPECIFICATIONS AND FEEDBACK CONTROLLER

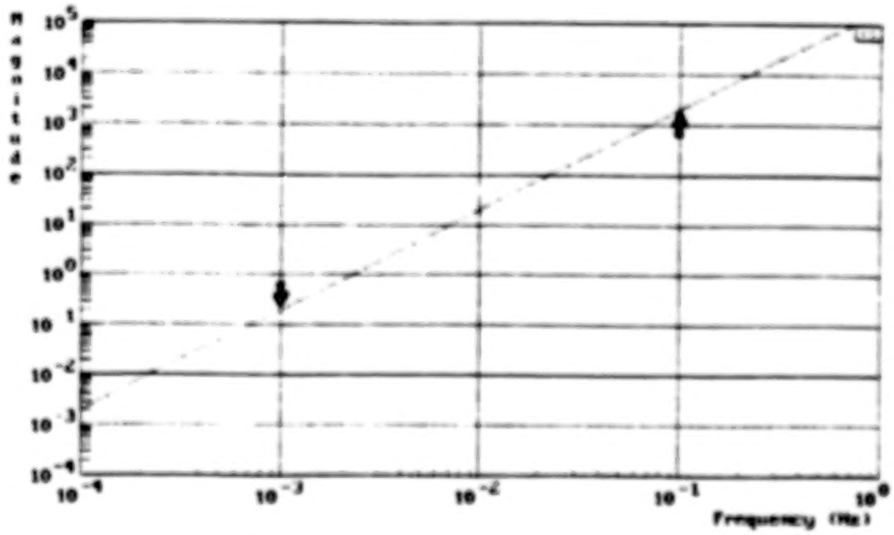

ACCELERATION FEEDBACK

LOOP SHAPING DESIGN

RESULTING TRANSMISSIBILITY:

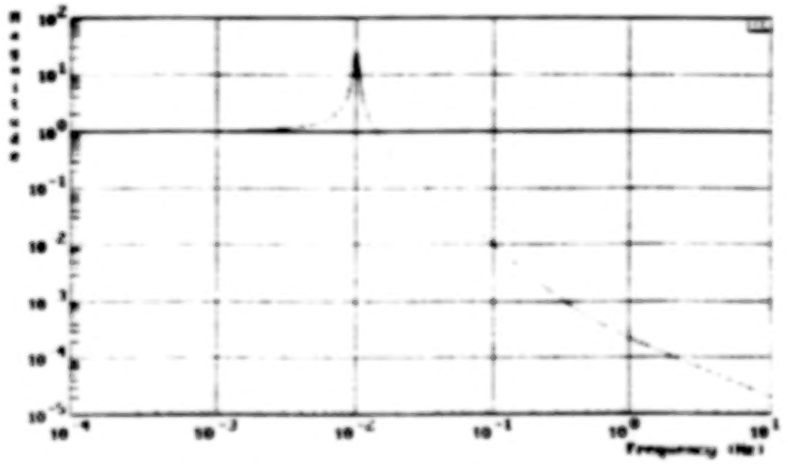

ROBUSTNESS ANALYSIS THROUGH ROOT LOCUS:

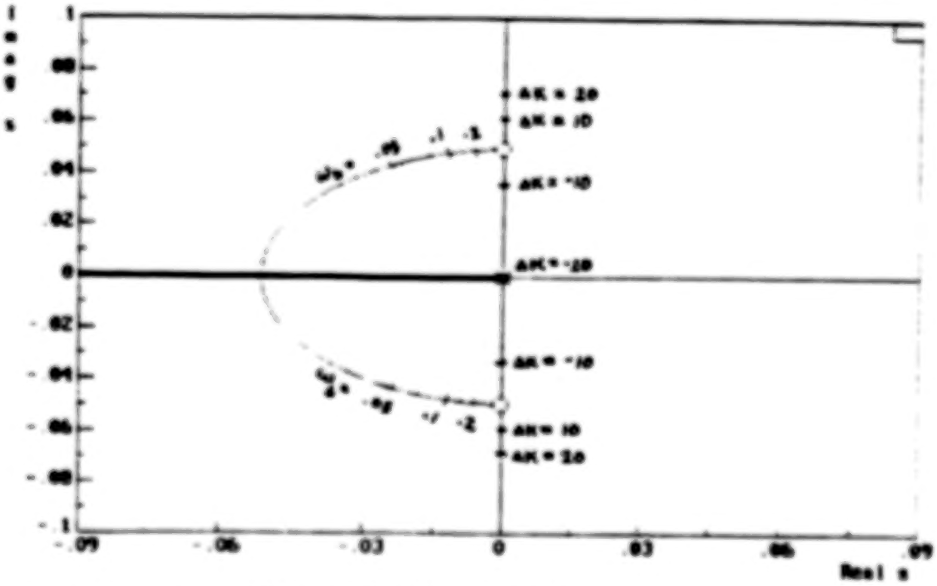

Need to modify this design to

- add damping to remove resonance
- limit control system bandwidth
- add integral term to provide centering

MDOF DESIGN EXAMPLE

EXAMPLE PROBLEM:

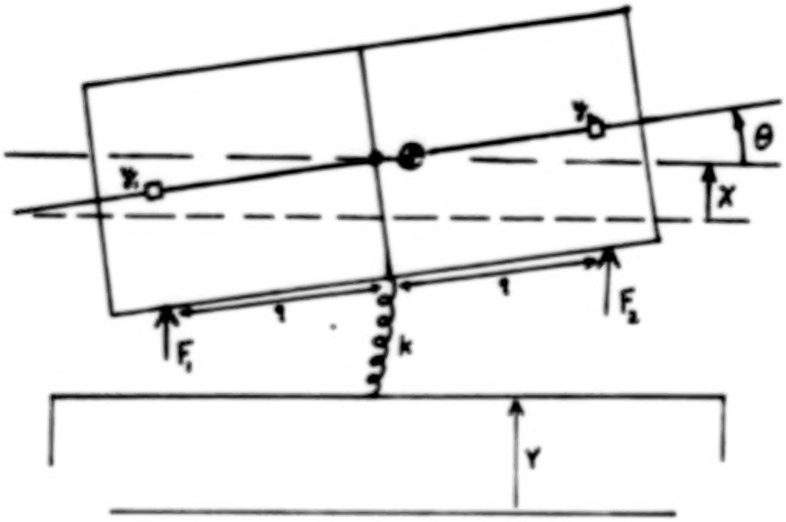

METHODOLOGY:

Decoupling system to rotational and translational modes, designing SISO controllers for each mode.

- Rotational mode requires angular position and velocity feedback.
- Translational mode requires translational acceleration and velocity feedback.

ROBUSTNESS TO CENTER OF MASS UNCERTAINTY

Decoupling is dependent on accurate knowledge of the center of mass location.

Characteristic Equation:

$$\left[(m+a)s^2+cs+k\right]\left[Is^2+ns+b\right]-\Delta^2\left[m(as^2+cs+k)\right]=0$$

Root Locus with respect to Center of Mass Uncertainty

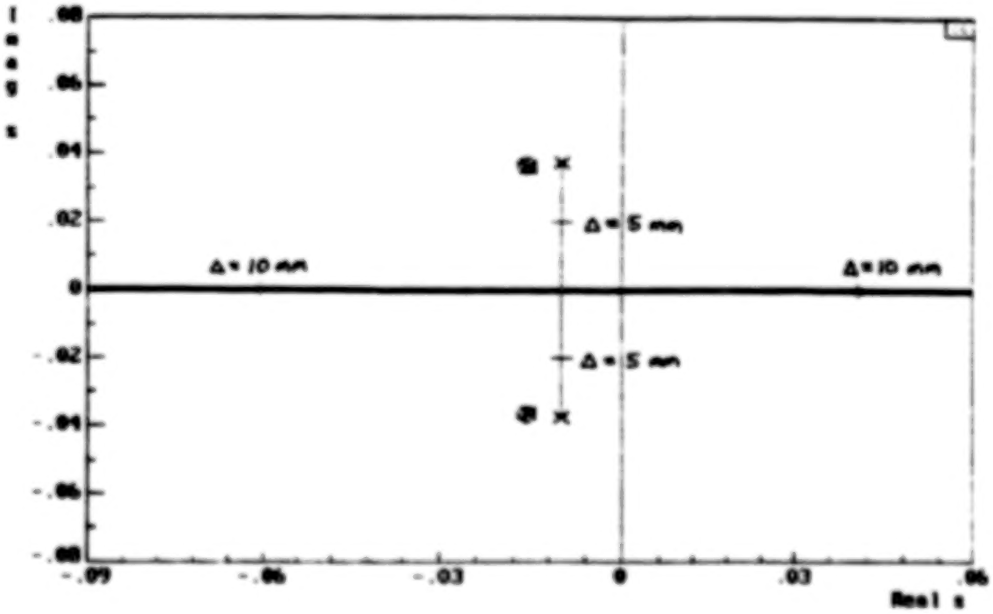

As little as 6 mm uncertainty can produce instability.

LINEAR QUADRATIC REGULATOR

MIMO control design, since it requires a high degree of coordination, must proceed by a synthesis procedure.

LQR SYNTHESIS:

- Quadratic Norm Performance Function
- State Feedback Controller

PROBLEMS:

- State feedback is feedback of inertial positions and velocities. The resulting system does not have unity transmissibility at DC.
- Ignores the disturbances. Actually treats them as white noise.
- Weak at loop shaping

FIXES:

- Frequency weighted performance functions
- Disturbance accomodation

Both these require the addition of psuedo-states and permit loop shaping via singular value analysis.

CONCLUSIONS

- The active isolation problem should be examined from a control perspective.
- Design proceeds best from the classical control framework of loop shaping.
- Loop shaping results in an acceleration feedback design which increases the effective mass of the isolation platform.
- Decoupling/SISO design procedures for MIMO control problems may result in controllers with poor robustness.
- Linear Quadratic Regulator synthesis for the microgravity problem requires frequency weighted cost functions and disturbance accomodation.

The authors wish to acknowledge G. Brown and C. Grodsinsky for many helpful discussions of this problem. This work was supported in part by NASA Lewis Research Center and the Commonwealth of Virginia. Some of this research was performed at NASA LRC as part of the Summer Faculty Fellowship Program.

N91-21193

SLIDING MODE CONTROL of MAGNETIC SUSPENSIONS for PRECISION POINTING and TRACKING APPLICATIONS

Kathleen M. Misovec, Frederick J. Flynn, Bruce G. Johnson
SatCon Technology Corporation
12 Emily Street
Cambridge
MA 02139-4507

J. Karl Hedrick
University of California at Berkeley
Berkeley
CA 94720

SLIDING MODE CONTROL OF MAGNETIC SUSPENSIONS FOR PRECISION POINTING AND TRACKING APPLICATIONS

Kathleen M. Misovec, SatCon Technology Corporation, Cambridge, MA

Frederick J. Flynn, SatCon Technology Corporation, Cambridge, MA

Bruce G. Johnson, SatCon Technology Corporation, Cambridge, MA

J. Karl Hedrick, Prof. of Mechanical Engineering, University of California at Berkeley, Berkeley, CA

Presented at: Workshop on Aerospace Applications of Magnetic Suspension Technology
NASA Langley Research Center, Hampton, VA; Sept. 25, 1990

ABSTRACT

This paper examines a recently developed nonlinear control method, sliding mode control, as a means of advancing the achievable performance of space-based precision pointing and tracking systems that use nonlinear magnetic actuators. The appeal of sliding mode control is its direct treatment of system nonlinearities. Analytic results indicate that sliding mode control improves performance compared to linear control approaches. In order to realize these performance improvements, precise knowledge of the plant is required. Additionally, the interaction of an estimation scheme and the sliding mode controller has not been fully examined in the literature. Estimation schemes were designed for use with this sliding mode controller that do not seriously degrade system performance. We designed and built a laboratory testbed to determine the feasibility of utilizing sliding mode control in these types of applications. Using this testbed, experimental verification of our analyses is ongoing.

INTRODUCTION

Space-based precision pointing and tracking systems typically operate in environments that require high levels of vibration isolation to achieve desired tracking performance. Consider the system illustrated in Fig. 1. The "tracking body" could be a telescope or a laser. The tracking body must rapidly point from target to target, a maneuver commonly referred to as slewing. A one meter diameter target located 10,000 km from the tracking body mandates slewing accuracies on the order of 100 nanoradians. The tracking body, however, is attached to a vibrating space structure. Disturbance vibrations are typically caused by machinery on the space structure. Any disturbance vibration that is transmitted to the tracking body can cause imprecision in the slewing

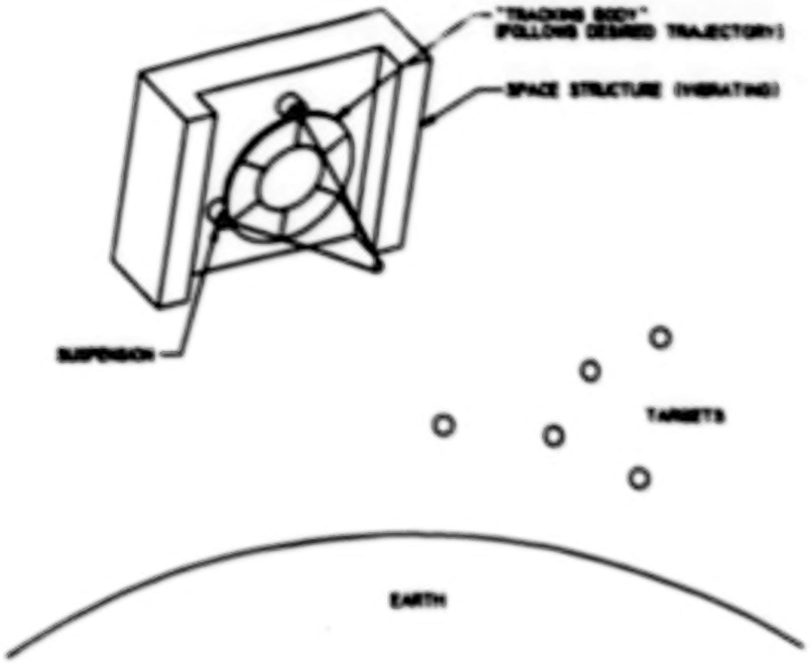

Figure 1. Space-Based Precision Pointing and Tracking

maneuver. Even a small amount of disturbance vibration can be catastrophic to the mission because the slewing requirements are extremely stringent. For example, the SAVI (Space Active Vibration Isolation) program is an earth-based full-scale test-bed of a magnetic suspension for pointing and slewing a 6000 kg mirror. Specifications are 80 db of isolation from 1 Hz to 2 kHz (6).

Nonlinear magnetic actuators, because of their high force per mass capability, are a promising means of achieving the required isolation while providing forces or torques for slewing. An inherent feature of the actuators, however, is coupling between the magnetic gap and the force. This coupling produces an undesirable path between disturbance vibrations and precision tracking forces. To date, vibration isolation systems utilizing these actuators face limitations on achievable isolation, especially under load, if slewing.

The actuators consist of a ferromagnetic material wrapped with a current-carrying coil (Fig. 2). Ferromagnetic material is also attached to the tracking body. An attractive force is exerted by the actuator on the tracking body. An equal and opposite force is exerted by the tracking body on the space structure, but this effect is negligible because the space structure is typically much more massive than the tracking body. Because the force on the tracking body is attractive force only, two actuators per degree of freedom are required. Force couples produce control torques. To first order, the force is proportional to the square of the ratio of current to gap. Thus, it is nonlinear in both current and gap. Another interesting feature is that the actuator is open-loop unstable. Indeed if the tracking body is initially in equilibrium at the centered position with equal currents in the actuators, and it is perturbed towards one of the actuators, at fixed current, the attractive force toward this actuator will increase, which is a destabilizing effect. We can also see this effect if we linearize the force-gap-current relation as is shown in the figure. For destabilizing force proportional to the displacement. For the suspension system, there is an associated unstable frequency determined by the unstable spring stiffness and the tracking body mass.

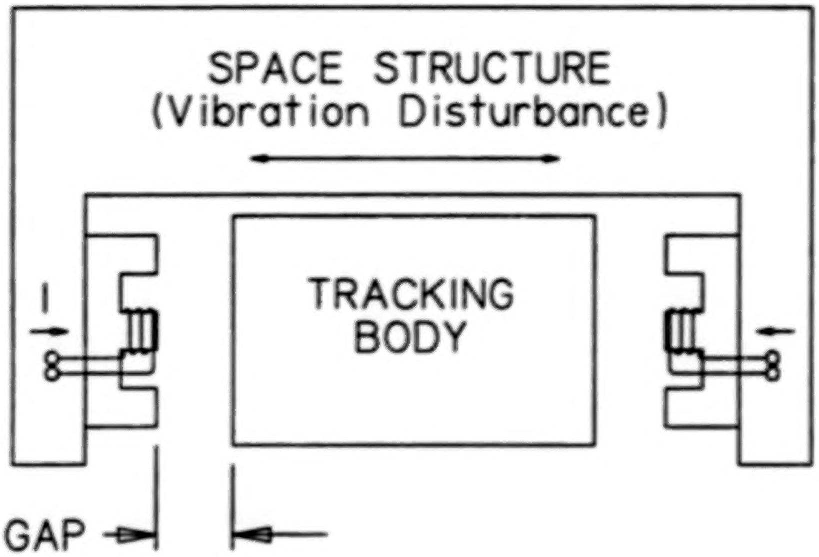

$$F = \frac{I^2}{gap^2} = B^2$$

$$F = -K_G \, \Delta gap + K_I \, \Delta I$$

Figure 2. Electromagnetic Actuator

A variety of options are available for use in the control of this type of magnetic suspension. These include gap feedback, flux feedback, and force feedback. Flux feedback is being used in the SAVI program. The motivation in this type of control scheme is the fact that when the force is linearized about a bias flux, the relationship between incremental force and flux is linear. The primary drawback of this approach arises because the flux sensor measures flux at the point where the sensor is located. In reality, the flux varies along the face of the actuators, and this variation looks like a modelling error in the flux-force relationship. This in turn may increase the tracking (slewing) error of the system. Gap sensors, on the other hand can give very precise information about the force because the precise gap sensors are available and the geometry of the actuator is fixed and known. However, as shown, the relationship between force, current and gap is nonlinear. The linearized relationship can be used in a linear control system such as the one shown in Fig. 3. A linear control system with inertial position feedback, however, can not meet the strict specifications of this type of problem. An examination of a linear control approach will illustrate the engineering difficulties of precision pointing and tracking systems. Space structure vibration is an output disturbance to this control system. Space structure motion (disturbance vibration) changes the gap between the structure and the tracking body causing an undesirable path, via the actuator, between the vibration disturbance and inertial position. In these applications, broad frequency range disturbances are present up to typical closed loop system bandwidths.

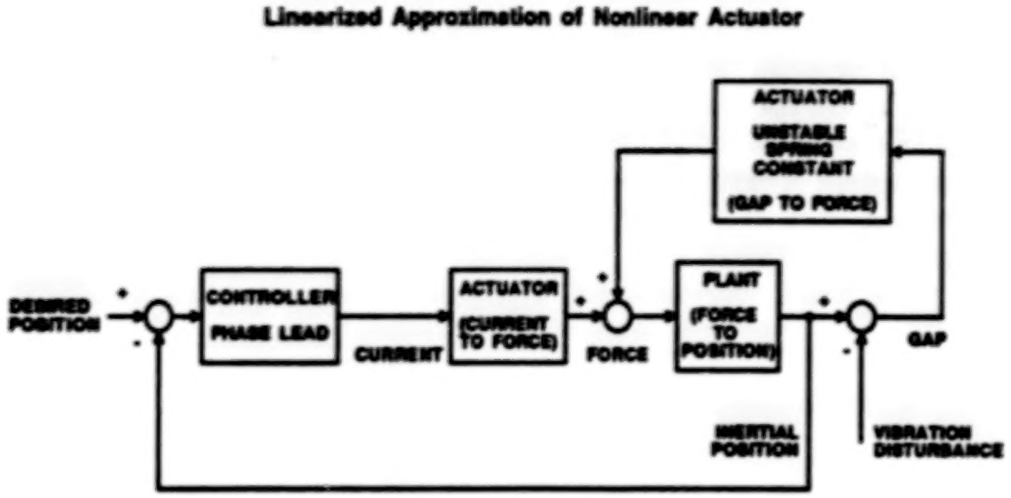
Linearized Approximation of Nonlinear Actuator
ACTUATOR
UNSTABLE SPRING CONSTANT
(GAP TO FORCE)
DESIRED POSITION
+
-
CONTROLLER
PHASE LEAD
CURRENT
ACTUATOR
(CURRENT TO FORCE)
+
+
FORCE
PLANT
(FORCE TO POSITION)
+
-
GAP
INERTIAL POSITION
VIBRATION DISTURBANCE

Figure 3. Block Diagram of Phase Lead Controller

At the open loop crossover frequency, the magnitude of the transfer function between inertial position and disturbance is dependent only on the unstable spring frequency and the crossover frequency, independent of the type of linear controller. The magnitude of this transfer function should be small for good tracking performance. As Eq. (1) shows, we have two options, increase the crossover frequency of the system or decrease the spring frequency.

$$\text{At crossover } (\omega_C)\ \frac{\text{Position}}{\text{Disturbance}} = \frac{\omega_U^2}{2(\omega_U^2 + \omega_C^2)} \qquad (1)$$

ω_U = Actuator unstable frequency
ω_C = Crossover frequency

The problem is that we are limited in both of these options. More precisely, the unstable spring frequency, which is a result of the coupling between force and gap can not be decreased indefinitely because of limitations on actuator power and size. The crossover frequency is limited as well by system bandwidth constraints. For example in the SAVI program, flexible structure modes of the mirror support structure start at 10-15 Hz. A control system with a higher bandwidth would excite these modes and is therefore undesirable. The key point is that for the vibration isolation levels required for many types of precision pointing and tracking systems, it is impossible to meet the specifications with linear controllers.

We examined sliding mode control, a recently developed nonlinear control method (5,2), as an alternative approach that has the potential to achieve higher levels of performance than are currently attainable. Fig. 4 is a rather complicated block diagram illustrating the sliding mode approach. The control goal is to have the tracking body (plant) follow a desired (reference) inertial trajectory. Nonlinear magnetic actuators produce forces on the plant changing it's inertial position. Vibration disturbances of the space structure change the gap between the tracking body and the space structure producing the undesirable vibration path between vibration disturbance and inertial position. The sliding mode controller has the potential to achieve better performance than linear controllers because it's structure directly compensates for this vibration path. A set of control forces is calculated based on the difference between the estimated inertial state and the desired inertial state. A feedfoward term is also included. Gap sensor measurements are used in a nonlinear plant inversion of the gap-force-current relation to obtain control currents.

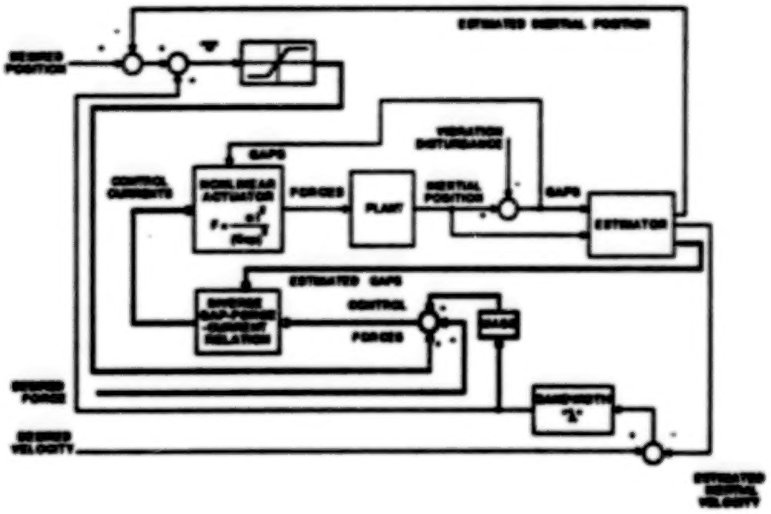
ESTIMATED INERTIAL POSITION
DESIRED POSITION
VIBRATION DISTURBANCE
GAPS
CONTROL CURRENTS
NONLINEAR ACTUATOR
FORCES
PLANT
INERTIAL POSITION
GAPS
ESTIMATOR
ESTIMATED GAPS
INVERSE GAP-FORCE-CURRENT RELATION
CONTROL
FORCES
MASS
DESIRED FORCE
BANDWIDTH "λ"
DESIRED VELOCITY
ESTIMATED INERTIAL VELOCITY

Figure 4. Sliding Mode Control Block Diagram

Lyaponov analysis guarantees that the controller with perfect state feedback will be stable in the presence of bounded modelling uncertainty and disturbances. The sliding mode control "balance condition" approximates the tracking error along a certain trajectory and is dependent on the modelling uncertainty bounds. The aim of the controller is to cancel out the effects of the unwanted vibration disturbance path. While the sliding mode control structure eliminates the weaknesses in the linear control approach, for high levels of performance, this approach depends strongly on having highly accurate plant models as well as precise measurement devices and a well-designed estimation scheme.

TEST-BED DESCRIPTION AND SYSTEM MODELLING

Testbed Description

The goal of the testbed is to capture the important features of the space-based precision pointing and tracking application in earth-based, laboratory-sized hardware. As shown in Fig. 5, the tracking body consists of a 7 kg mass supported on an air table, which eliminates the gravity-biasing effects. This mass, which will be called the isolated mass, has three degrees of freedom; two translational labelled x and y and one angular, labelled Θ. Magnetic actuators that produce forces on the isolated mass are mounted on moving rails. Four E-core actuators are used for both translational x (tracking/slew) direction and for the angular θ direction. Two pot core actuators are used to provide forces in the ± y direction. Sensors include gap sensors, an angular velocity sensor, an accelerometer, and LVDT rail position sensors ⑦.

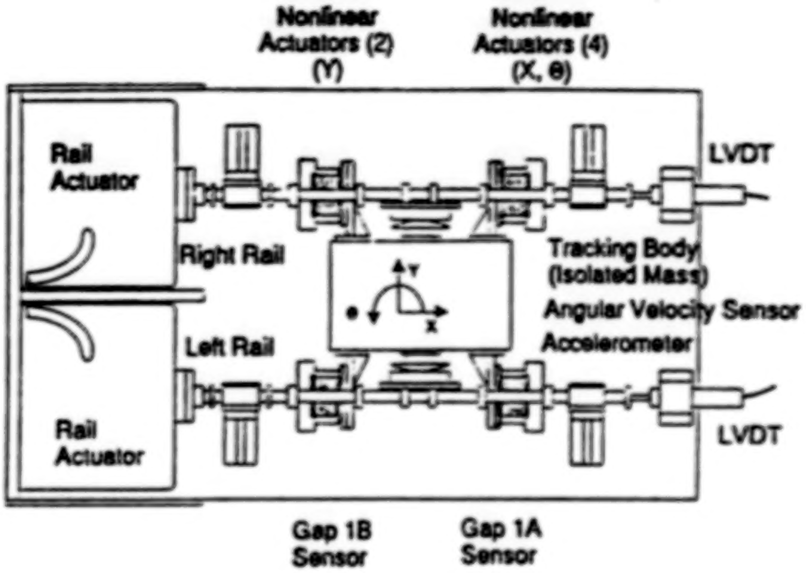
Nonlinear Actuators (2) (Y)
Nonlinear Actuators (4) (X, θ)
Rail Actuator
LVDT
Right Rail
Tracking Body (Isolated Mass)
Y
θ
X
Angular Velocity Sensor
Accelerometer
Left Rail
Rail Actuator
LVDT
Gap 1B Sensor
Gap 1A Sensor

Figure 5. Top View of Testbed

The baseline test scenario consists of large amplitude (many times the nominal magnetic gap), low frequency motion in the x-direction. The moving rails, under separate linear position control loops, simulate the vibrating space structure in addition to allowing the slew motion. Disturbance vibrations can be introduced in the x and θ directions. Angular disturbances are input by differentially exciting the rails. Simulation results in this paper consist of single frequency tracking under the presence of a single frequency angular vibration disturbance. Broadband disturbances should be considered at a later time with the acquisition of a better angular sensor. Performance measures of rms tracking error and vibration isolation are considered.

System Modelling: Dynamics

By applying Newton's laws, we can obtain the dynamic equations of motion of the isolated mass (Eq. (2), (3), and (4)).

$$\begin{aligned} m\ddot{x} &= (F_{1A} - F_{1B}) + (F_{2A} - F_{2B}) \\ &= \left(\frac{\alpha_x I_{1A}^2}{2(g_{1A}+C_x)^2} - \frac{\alpha_x I_{1B}^2}{2(g_{1B}+C_x)^2}\right) \\ &+ \left(\frac{\alpha_x I_{2A}^2}{2(g_{2A}+C_x)^2} - \frac{\alpha_x I_{2B}^2}{2(g_{2B}+C_x)^2}\right) \end{aligned} \qquad (2)$$

$$\begin{aligned} I\ddot{\theta} &= L\,(F_{1A}-F_{1B}) - L\,(F_{2A} - F_{2B}) \\ &= L\left(\frac{\alpha_x I_{1A}^2}{2(g_{1A}+C_x)^2} - \frac{\alpha_x I_{1B}^2}{2(g_{1B}+C_x)^2}\right) \\ &- L\left(\frac{\alpha_x I_{2A}^2}{2(g_{2A}+C_x)^2} - \frac{\alpha_x I_{2B}^2}{2(g_{2B}+C_x)^2}\right) \end{aligned} \qquad (3)$$

$$\begin{aligned} m\ddot{y} &= F_{3A} - F_{3B} \\ &= \frac{\alpha_y I_{3A}^2}{2(g_{3A}+C_y)^2} - \frac{\alpha_y}{2}\frac{I_{3B}^2}{(g_{3B}+C_y)^2} \end{aligned} \qquad (4)$$

where

m = mass
I = Moment of inertia
F_{1A} = Force actuator 1A
I_{1A} = Current actuator 1A
g_{1A} = Gap actuator 1A
C_x = Modelling constant
L = Moment arm (m)

The controller for the slew (x) direction and the angular (θ) direction is designed as if they were decoupled. This is due to the fact that there are more inputs than degrees of freedom. Referring to Eq. (2) and (3), we see the slew direction is controlled by an addition of $(F_{1A} - F_{1B})$ and $(F_{2A} - F_{2B})$ while angle θ as controlled by the difference. The y axis is decoupled from both the x and the θ axes.

Based on more detailed magnetic actuator modelling as well as experimental actuator testing, the x, θ axis actuator models are accurate to within 1% for the range of gaps we run in our experiments. This bound is used in the sliding mode controller design (7).

System Modelling: Kinematics

Kinematic relationships are used in the estimation scheme. At low frequencies, the accelerometer and angular velocity sensor do not provide good information. Low frequency state estimates can be obtained based on gap sensor and LVDT rail measurements by manipulating the kinematic relationships presented below.

A schematic representation of the test-bed geometry at two different positions of the isolated mass and rails is shown in Fig. 6. Small angle approximations are used to obtain the following relations. An expression for each gap can be obtained in terms of inertial position of the isolated mass, x, the inertial angular position of the isolated mass, θ, the nominal (centered) gap, g_o and a position of the associated linear actuator rail, x_{LAL} or x_{LAR} (Eq. (5-8)).

$$g_{1A} = (x_{LAL}+g_o) - (x + L\theta) \tag{5}$$

$$g_{1B} = -(x_{LAL} - g_o) + (x + L\theta) \tag{6}$$

$$g_{2A} = (x_{LAR} + g_o) - (x - L\theta) \tag{7}$$

$$g_{2B} = (x - L\theta) - (x_{LAR} - g_o) \tag{8}$$

SLIDING MODE CONTROLLER DESIGN

The controller must choose six currents based on gap measurements, position errors, velocity errors and desired accelerations. Following the standard sliding mode control approach (2,5), a sliding surface, s is defined for each degree of freedom (Eq. (9-11)).

$$s_x = (\dot{x} - \dot{x}_d) + \lambda(x - x_d) \tag{9}$$

$$s_\theta = (\dot{\theta} - \dot{\theta}_d) + \lambda(\theta - \theta_d) \tag{10}$$

$$s_y = (\dot{y} - \dot{y}_d) + \lambda(y - y_d) \tag{11}$$

where

x, x_d, $\dot{x}$ = x position, desired x position, x velocity
y, y_d, $\dot{y}$ = y position, desired y position, y velocity
θ, θ_d, $\dot{\theta}$ = θ position, desired θ position, θ velocity

The control law for each degree of freedom is chosen so that the appropriate s^2 remains a Lyaponov function of the system subject to bounded disturbances and modelling errors. By using a time-varying boundary layer concept, the control laws avoid high frequency control actions that could excite unmodelled dynamics. The boundary layer concept is an interpolation of the control laws about the $s=0$ surface. The interpolation is made time-varying to achieve the optimum tradeoff between tracking error and parametric uncertainty along a desired trajectory. The basic philosophy behind sliding mode control is that when the system is outside an invariant region, the $s=0$ ± boundary layer surface,

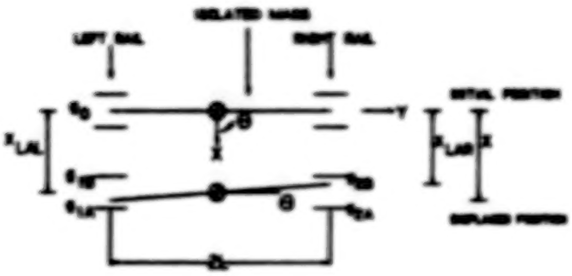

Figure 6. Testbed Kinematics

the control action is designed to be such that Eq. (12)

$$\frac{d}{dt} s^2 < 0 \tag{12}$$

or equivalently Eq. (13) ($\eta > 0$)

$$\dot{s} < -\eta\,|s| \tag{13}$$

Fig. 7 shows that this control action will always move the system towards the boundary layer of the s=0 region. When s is positive, the time derivative of s is negative, when s is negative, the time derivative of s is positive. The system will reach the region within time constraints of the order of $1/\lambda$ where λ is the controller bandwidth. Once inside the boundary layer region, the tracking error in position and velocity remains bounded. The bounds on tracking error can be quantified in terms of modelling uncertainty, maximum disturbance bounds, desired trajectory parameters and system bandwidth. This relationship is called the "balance condition" and is discussed more in (5).

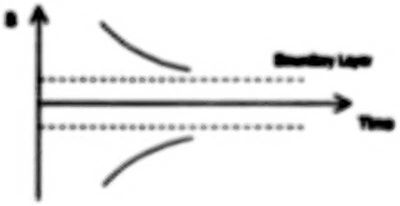

Figure 7. Sliding Mode Condition

The controller computes a set of two net control forces $F_{control\,x}$ and $F_{control\,y}$, and a net control torque $\tau_{control\,\theta}$. Then the currents are chosen to achieve this set of control actions. Notice that the choice of a set of 6 control currents to achieve three control actions is not unique. We chose the straightforward approach of using only one actuator of a given pair at a time. (For example if actuator 1A is on actuator 1B is off). This choice is acceptable as long as the current controllers are designed to switch fast enough for the types of experimental tests to be run.

The net control force or torque for a particular degree of freedom has two components. One component is chosen as if the system were on the s=0 surface and the control action is to stay on the surface. This part of the control action is derived by making $\dot{s}=0$ and using the system model equations of motion. There is a feedfoward term and a term proportional to the velocity error. On the s=0, surface, this control action brings the tracking error to zero exponentially. The second component of control force or torque, the saturation function term, insures that ds^2/dt will remain decreasing outside the $s=0\pm\phi$ region in spite of disturbances and uncertainties.

$$F_{control\ y} = m_e\left(\ddot{y}_d + \lambda(\dot{y}_d - \dot{y}) + \overline{K}_y\ \mathrm{sat}\left(\frac{s_y}{\phi_y}\right)\right)$$

$$F_{control\ x} = m_e\left(\ddot{x}_d + \lambda(\dot{x}_d - \dot{x}) + \overline{K}_x\ \mathrm{sat}\left(\frac{s_x}{\phi_x}\right)\right) \qquad (14)$$

$$\tau_{control\ \theta} = I_e\left(\ddot{\theta}_d + \lambda(\dot{\theta}_d - \dot{\theta}) + \overline{K}_\theta\ \mathrm{sat}\left(\frac{s_\theta}{\phi_\theta}\right)\right)$$

In Eq. (14), the K terms are dependent on the modelling uncertainty and the disturbance bounds. Also m_e and I_e are the assumed mass and moment of inertia respectively.

After the controller calculates the control forces and torque, it chooses a set of currents to achieve those forces Eq. (15-17).

$$F_{control\ x} - \frac{\tau_{control\ \theta}}{L_e} \geq 0:$$

$$I_{2A} = \sqrt{\frac{(g_{2A} + C_x)^2}{\alpha_{xe}}\left(F_{controlx} - \frac{\tau_{control\theta}}{L_e}\right)}$$

$$I_{2B} = 0$$

$$F_{control\ x} - \frac{\tau_{control\theta}}{L_e} < 0:$$

$$I_{2A} = 0$$

$$I_{2B} = \sqrt{\frac{-(g_{2B} + C_x)^2}{\alpha_{xe}}\left(F_{controlx} - \frac{\tau_{control\theta}}{L_e}\right)}$$

(15)

$$F_{control\,x} + \frac{\tau_{control\,\theta}}{L_\theta} \geq 0:$$

$$I_{1A} = \sqrt{\frac{(g_{1A} + C_x)^2}{\alpha_{xo}}\left(F_{control\,x} + \frac{\tau_{control\,\theta}}{L_\theta}\right)}$$

$$I_{1B} = 0$$

$$F_{control\,x} + \frac{\tau_{control\,\theta}}{L_\theta} < 0:$$

$$I_{1A} = 0$$

$$I_{1B} = \sqrt{\frac{-(g_{1B} + C_x)^2}{\alpha_{xo}}\left(F_{control\,x} + \frac{\tau_{control\,\theta}}{L_\theta}\right)}$$

(16)

$$F_{control\,y} \geq 0:$$

$$I_{2A} = \sqrt{\frac{2}{\alpha_{yo}}(g_{2A} + C_y)^2 F_{control\,y}}$$

$$I_{2B} = 0$$

$$F_{control\,y} < 0:$$

$$I_{2A} = 0$$

$$I_{2B} = \sqrt{\frac{-2}{\alpha_{yo}}(g_{2B} + C_y)^2 F_{control\,y}}$$

(17)

CONTROLLER ANALYSIS

Comparison of sliding mode and conventional controllers For comparison, a phase lead controller, typically used in magnetic suspension systems, was designed for the test-bed. Additionally, since the sliding mode controller has the advantage of having information about the desired trajectory which is used in a feedfoward path, a third controller was designed consisting of a linear phase lead controller and a nonlinear feedfoward term which utilized gap measurements and desired force. A block diagram of this controller is shown in Fig. 8.

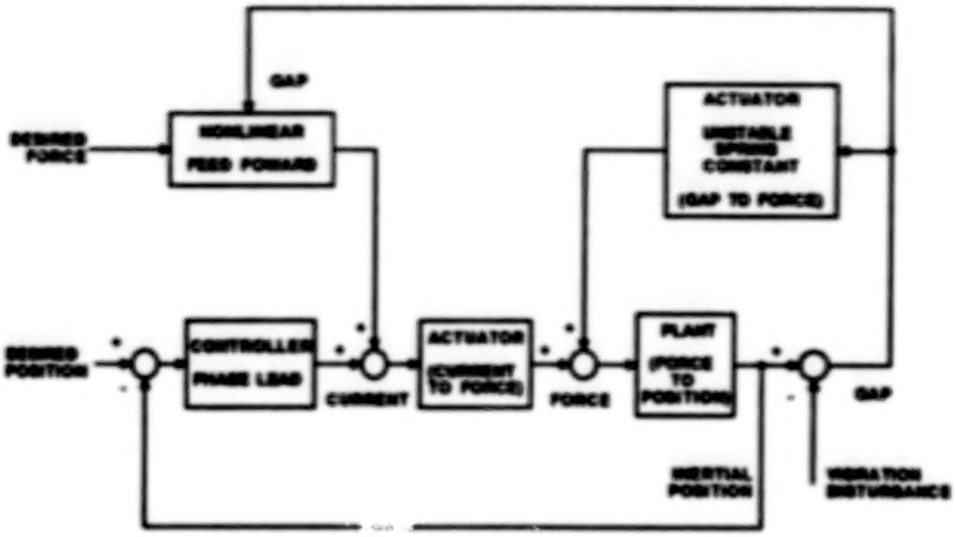

Figure 8. Block Diagram of Phase Lead with Feedforward Controller

The sliding mode bandwidth parameter (λ) and the closed loop bandwidth of the phase lead and phase lead with feedfoward were chosen to be 40 Hz. Simulations were run for the test scenarios which include a large amplitude, low frequency slewing maneuver and a small amplitude higher frequency angular disturbance. Performance measures of rms tracking error, stability margins and vibration disturbance attenuation were examined. Additionally, robustness of the three types of controllers to a particular type of modelling uncertainty was investigated.

Fig. 9 is a performance comparison plot of rms tracking error to a desired slew maneuver vs vibration disturbance amplitude. Both tracking error and vibration disturbance amplitude are normalized by the nominal gap. Perfect measurement and estimation systems are assumed. The slew maneuver is a 1 cm 5 Hz sinusoid and the vibration disturbance is an angular disturbance at 23 Hz. The magnitude of the angular vibration disturbance can be found using small angle approximations. This plot shows that the sliding mode controller has better tracking performance by two orders of magnitude than the phase lead controller. At very small disturbance amplitudes, the phase lead with feedfoward is comparable in tracking performance to the sliding mode controller, but this performance deteriorates significantly with larger disturbance amplitudes. Another interesting feature of this plot is that the sliding mode controller has higher stability margins than the other control approaches. The stability margin is reached when one or more of the magnetic gaps to go the zero. The plot shows that the phase lead and phase lead with feedfoward can handle disturbances up to about 20% and 30% of the nominal gap. This sliding mode controller can handle disturbances that are 90% of the nominal gap. Furthermore, this particular sliding mode controller was only designed to handle angular disturbances that were 50% of the nominal gap, the controller could easily be designed for higher disturbances in order to achieve even higher stability margins by trading off against tracking performance.

The ability of the sliding mode controller to operate near over the full range of it's magnetic gap is another advantage over linear controllers. Linear controllers, which are

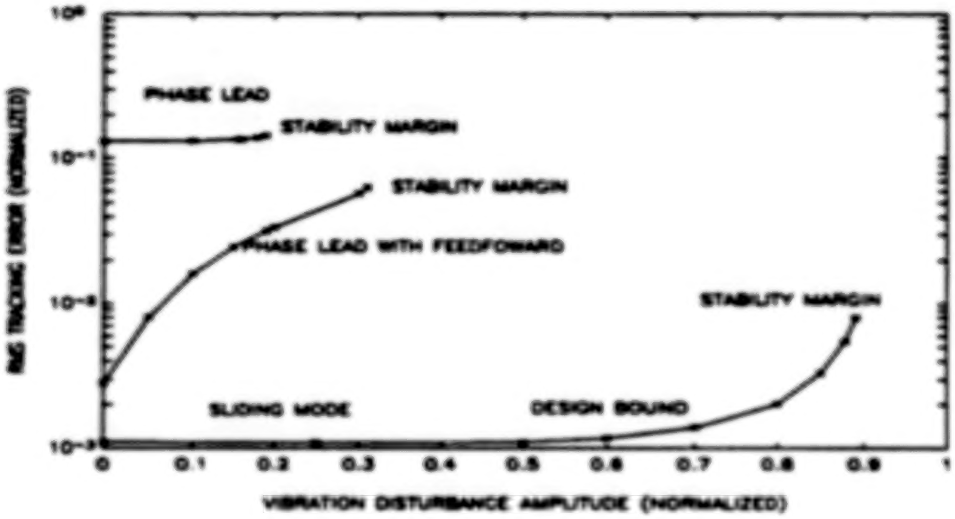

Figure 9. Controller Performance Comparison

biased about an operating current, can only operate in a reduced gap range to avoid attraction to one or the other biased actuator. The sliding mode controller has superior stability range and start-up capabilities.

Another performance measure to assess the potential of the sliding mode controller is vibration disturbance attenuation. This is a measure of how much disturbance energy is transmitted to the tracking body. Figure 10 shows vibration disturbance attenuation vs vibration disturbance frequency. The plot is again based on simulations a 1 cm 5 hz slew and a angular vibration disturbance. The magnitude of the angular disturbance is about .004 rad, which corresponds to approximately half the nominal gap when using small angle approximations. Vibration disturbance attenuation is defined to be the ratio in db of output angular disturbance energy to input angular disturbance energy. An alternative measure is disturbance attenuation at the disturbance frequency. This would be calculated by comparing the power spectral densities of the angular output response and the angular input disturbance. However, unlike linear systems, a nonlinear system can spread its response over the frequency domain. Due to this fact, the energy measure of vibration disturbance attenuation is preferred because it is a broadband measurement.

The sliding mode controller achieves better disturbance attenuation than the phase lead or the phase lead with feedfoward approaches. Performance at disturbance frequencies near the closed loop bandwidth is of particular interest because in this disturbance frequency range linear controllers have limited capability, as discussed earlier. For these simulations, analysis (Eq. 1) indicated the limiting value of isolation to be approximately -9 db for a phase lead controller. The plot shows that this limitation is accurate. The sliding mode controller, because of its different structure, is not limited to this performance value. It achieves about -40 db at disturbance frequencies near the closed loop bandwidth, a 30 db improvement over linear controllers. Using the balance condition, this isolation performance can be directly related to modelling accuracy, bandwidth and sampling time of the sliding mode controller.

Although this plot shows the sliding mode control has better performance than the

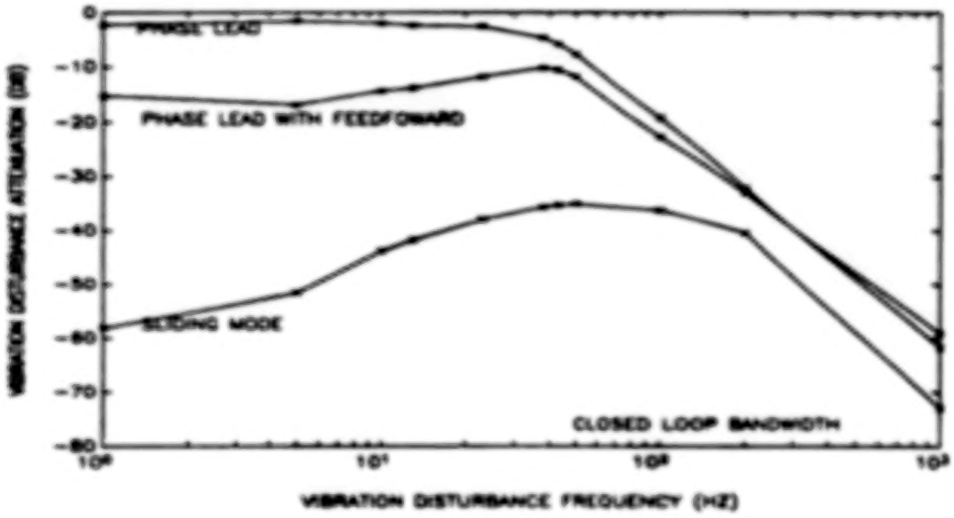

Figure 10. Controller Performance Comparison

other approaches at low disturbance frequencies, improved linearized control approaches can be designed by increasing the loop gain at low frequencies. This would result in a controller which had better disturbance attenuation at low frequencies than the phase lead and phase lead with feedfoward; however, it would still be limited at disturbance frequencies near the closed loop bandwidth.

Robustness to modelling uncertainty is an important capability for any control design. In the presence of parameter uncertainty, dynamic parameter variation, or model structure uncertainty, a robust controller maintains a specified level of performance and remains stable. For this type of actuator, the force proportionality to the current squared is a very good approximation; however, the force dependence on the gap is more uncertain. One reason for this modelling uncertainty is due to the curvature of the actuator target surfaces. Curvature is useful because it reduces cross-coupling between axes, however, it introduces a variation in gap. As discussed earlier, the force-gap-current models used in Eq. 4-6, are accurate to within 1% for gaps which ranged from plus or minus 50% of the nominal gap (7).

In order to investigate the effect of modelling uncertainty on controller performance and stability, we varied the force-gap-current proportionality term used in the controller models by plus or minus 10% of the value use in the plant simulation model. Fig. 11 is a plot of rms tracking error (normalized by the nominal gap value) as a function of modelling uncertainty in the force-gap-current proportionality term. The x axis is the ratio of the proportionality term used in the controller to the proportionality term used in the plant simulation model. A value of one indicates the controller is using a perfect model. These simulations were based on a 1 cm 5 hz sinusoidal slew in the presence of a 23 Hz .004 radian sinusoidal angular disturbance. The sliding mode controller has better tracking performance than the phase lead and the phase lead with feedfoward controllers when the uncertainty in the proportionality term ranges to plus or minus ten percent. However, these performance advantages are very sensitive to modelling uncertainty. Good modelling is essential for performance improvements to be realized.

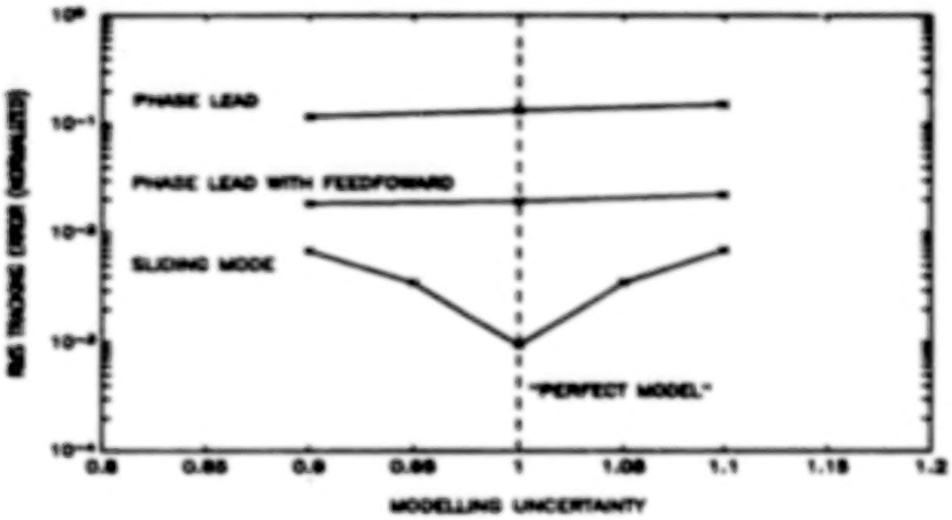

Figure 11. Controller Robustness Comparison

The Effects of Discrete Time, Estimation Errors, and Measurement Errors.

Realistic factors which will decrease the attainable performance of the system include effects due to the discrete time nature of the controller, finite word-length, measurement system imperfections, and estimation errors. The stability of the sliding mode controller with an estimation scheme has not been fully examined in the literature; however, simulations indicated that estimators can be designed for this system that do not seriously degrade performance or cause instability.

Controller currents are held constant over the sampling period. Additionally, due to control law computation time, there is a time delay between measurement of sensor data and control action. For this test-bed, the computation time is approximately 250 milliseconds. The sampling rate is 1000 Hz.

The measurement system errors include gap sensor nonlinearities and angular velocity sensor dynamics. The LVDT dynamics are high frequency effects and thus are neglected. The moving rails are under closed loop control and these effects are also negligible. The effects of sensor noise is not presented in this paper; they are expected to be negligible.

Fig. 12 shows a plot of the gap vs gap sensor voltage. The gap sensors were Mechanical Technology Incorporated ASP-50-ILA units with greater than 1 mm 1% linear range. The simulations used a third order fits to simulate the sensor. The estimation schemes considered also used third order fits to obtain gap from gap voltage.

Fig. 13 is the angular velocity sensor magnitude response vs frequency. The angular velocity sensor was an Applied Technology Associates magneto-hydrodynamic angular rate sensor (4). At low frequencies (less than .5 Hz), the angular velocity sensor magnitude response falls off. In this frequency range, any estimation scheme must utilize gap and LVDT rail measurements and the kinematic relations (Eq. 5-8).

The first estimation scheme presented here makes use of information from all of the sensors. At low frequencies, the inertial sensors do not provide good information, so

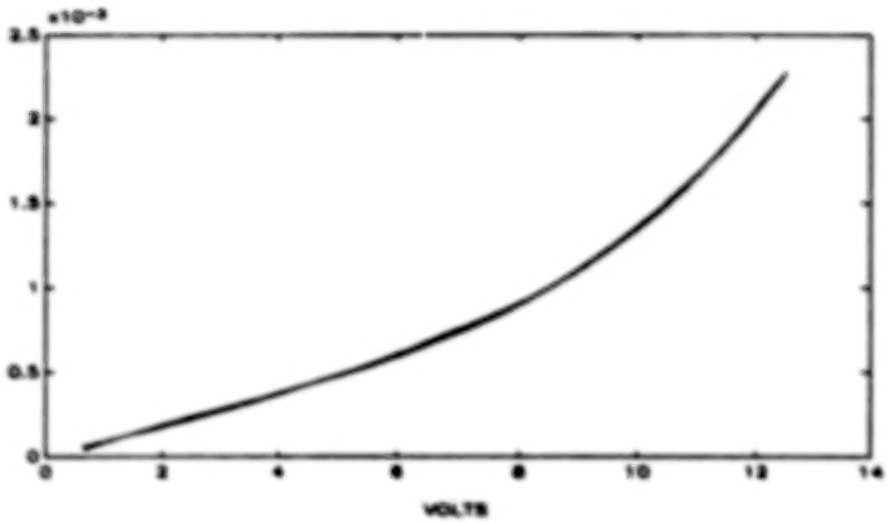

Figure 12. Gap Sensor Nonlinearity

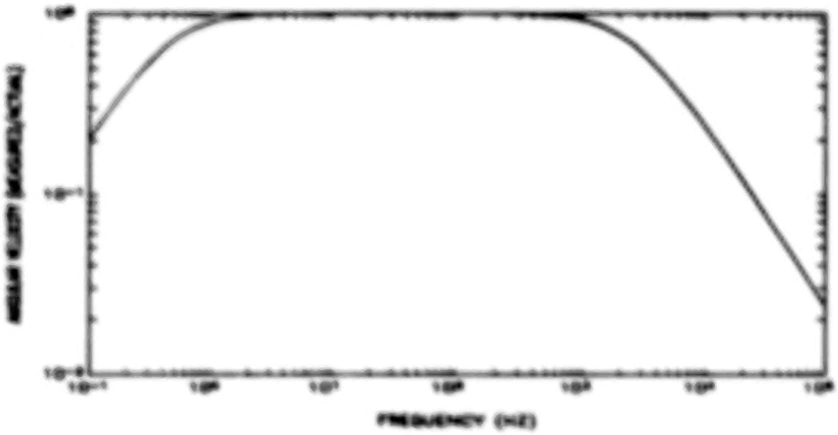

Figure 13. Angular Velocity Sensor Frequency Response

the gap sensors and LVDT measurements are used. The angular estimation filters have been designed to utilize angular velocity sensor information all the way down to its capacity at .5 Hz (Fig. 13). The angular position estimate uses mostly the low frequency estimate based on gaps and LVDT's for frequencies under 2 Hz. For simpler implementation, the x-axis filters in this particular estimator are using mostly low frequency information for x estimates. Future work should make better use of the accelerometer for inertial measurements; this requires low frequencies (compared to the sampling rate) in the estimation filter to remove the dc bias and was not considered in this phase of the work because of problems with implementation. Subsampling is one option to alleviate these numerical problems.

The first estimation scheme will not work in the testbed. The angular velocity sensor has too much broadband noise to get good angular position and velocity estimates. A second estimation scheme was designed which used only the gap and LVDT rail position measurements. The kinematic relationships are used (Eq. 5-8) to get estimates of angular and translational (x) position. The positions are then filtered to get velocity estimates.

Table 1 is based on a simulations of a 1 cm, 5 Hz slew with .0045 radian, 25 Hz angular vibration disturbance. The sliding mode controller bandwidth parameter is 40 Hz. The table shows three measures of performance: normalized rms tracking error, vibration disturbance attenuation at the vibration disturbance frequency, and broadband vibration disturbance attenuation. The performance measures are best with a perfect model, measurement system and estimation scheme. The rms tracking error is .16% of nominal gap and the vibration disturbance attenuation measures -35 and -33.8 db respectively. The effects due to modelling error are small. The effects of time delay between measurement and control action degrade tracking performance by an order of magnitude. Isolation performance is also reduced to about -30 db. The effect of estimation errors degrade tracking performance by an order of magnitude and do not significantly affect isolation performance. The second estimation scheme is tracking better than the first for this particular controller design. The effects of imperfect measurements, namely gap sensor nonlinearity and angular velocity sensor dynamics, also degrades tracking and does not significantly degrade isolation performance.

The effect of the estimator becomes more important with higher bandwidth controllers. For example, simulations of a 1 cm 5 Hz slew with a .0045 radian, 23 Hz angular disturbance with 160 Hz. bandwidth controller were performed. The perfect model, measurement and estimation case achieved -60 db of vibration isolation. The first estimation scheme, which utilized the inertial sensors measurements, had a performance reduction to -30 db of isolation when using perfect measurements. The second estimation scheme, which utilized only gap and rail measurements, was not adequate and the stability margin of the controller was reached.

HARDWARE RESULTS

To date, the testbed subcomponents have been tested and the testbed assembled and functionally tested. The sliding mode control algorithms have been implemented with a Texas Instruments TMS320-C25 digital signal processor coded directly in assembly language. Preliminary closed-loop tests were performed with a high bandwidth (160 Hz) controller in which the sliding mode control currents were reduced by a constant scaling factor. This factor was introduced because the current drives need to be modified to accept larger currents than originally specified.

Tests were performed in which the isolated mass was displaced by a full gap displacement and the desired position was the nominal centered position. Figure 14 shows the results of these experimental tests and two simulations. The modified simulation reflects the scaling of control currents and the gap sensor nonlinearity. The "perfect" simulation assumes perfect model, perfect measurement, perfect estimation and no current scaling factor. The rise time for the "perfect" simulation and for the experimental test are both about .075 seconds. The modified simulation takes about twice as long but reflects the oscillatory behavior about the final value. The modified simulation is very sensitive to scaling factor and the gap sensor nonlinearity fit.

TABLE 1.
The Effects of Discrete Time and Estimation Errors.

40 Hz Bandwidth Controller
1 cm 5 Hz slew
.0045 rad 25 Hz Disturbance

Effects	Comments	RMS Error / Nominal Gap	Vibration Disturbance Attenuation at Vibration Disturbance Frequency (db)	Vibration Disturbance Attenuation (db)
	Perfect Model Perfect Measurements Perfect Estimation No Time Delay	.0016	-35.0	-33.8
Modelling Error	1% Modelling Error Perfect Measurements Perfect Estimation No Time Delay	.002	-34.9	-33.7
Discrete Time	Perfect Model Perfect Measurements Perfect Estimation 1/4 sampling period delay (.0025 sec)	.05	-29.9	-28.6
Estimation Errors	Perfect Model Perfect Measurement No Time Delay			
	Estimator 1	.06	-34.9	-33.7
	Estimator 2	.03	-34.1	-32.9
Measurement and Estimation Errors	Perfect Model Imperfect Measurement No Time Delay			
	Estimator 1	.06	-33.5	-32.5
	Estimator 2	.03	-32.	-29.7

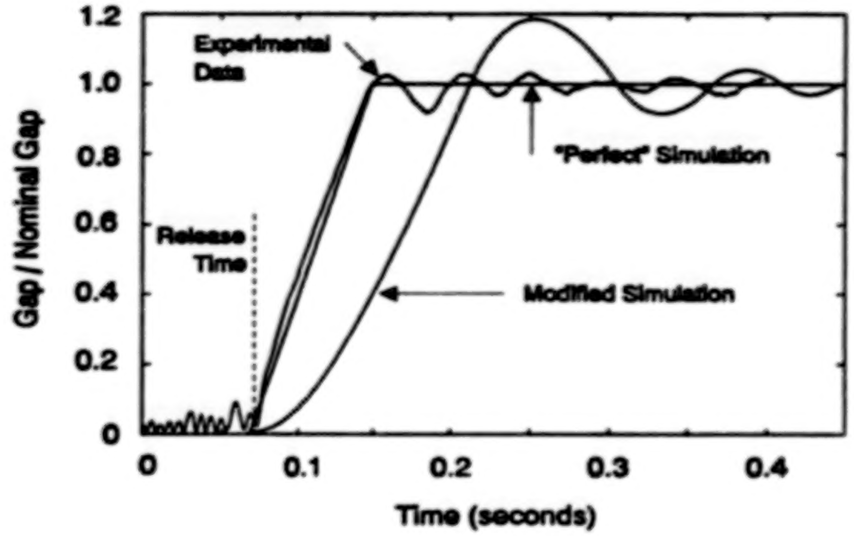

Figure 14. Initial Offset Test

Additionally, slew and angular vibration isolation tests with the hardware were performed for a 2.5 mm 1 Hz slew and single frequency angular disturbances ranging form .0009 to .003 radians up to 30 Hz. Vibration isolation measures of ranging from -23 to -36 db were observed for this range of disturbances. Simulation results were in the same range; however, they are very sensitive to the gap sensor nonlinearity which is not precisely known for the experimental tests that were run. After testbed modifications, we have since measured the gap sensor nonlinearity. Simulations presented earlier incorporate this nonlinearity. The next step in hardware verification is to increase the current drive capabilities. This will allow experimental comparisons to the simulations presented in this paper.

CONCLUSIONS AND RECOMMENDATIONS

Control algorithm development and system simulations have shown that sliding mode control is an attractive approach to providing precision tracking in the presence of disturbance vibrations. The sliding mode controller has a number of advantages over conventional designs. Most important is improved performance. For this testbed, the sliding mode controller can increase the vibration isolation while slewing by 30 db compared to a conventional control algorithm. Although controller performance improvements are very sensitive to actuator modelling accuracy, high levels of modelling accuracy can be achieved for aerospace applications by experimental testing.

Issues associated with the "real world" application of sliding mode control were investigated. Perhaps the most important was the incorporation of a state estimator with the sliding mode controller. System performance was depends on the quality of the measurements and the estimation scheme. A number of other estimator designs are now being investigated, including a linearized Kalman filter, extended (nonlinear) Kalman filter, and sliding mode observers (1,3,8). Estimation errors become more important as the controller bandwidth is increased.

A laboratory testbed was designed and built and preliminary testing has been performed. Further testing is ongoing.

Recommendations for future research are to apply sliding mode control to an existing precision pointing and tracking application. This entails determining the modelling accuracy and computational requirements to meet the vibration isolation requirements of the particular application.

ACKNOWLEDGEMENTS

The research was conducted by SatCon Technology Corporation under Phase II Small Business Innovation Research (SBIR) Contract DASG60-88-C-0040 sponsored by the Strategic Defense Initiative Organization (SDIO) Innovative Science and Technology Office and managed by the U.S. Army Strategic Defense Command (ASDC) in Huntsville, AL. The authors would like to thank Dr. David Lukins and Dr. John Phillips of ASDC for their guidance.

REFERENCES

1 Misawa, E.A., Hedrick, J.K., "Nonlinear Observers-A State-of-the-Art Survey," ASME Journal of Dynamic Systems, Measurement and Control, III(3), Sept. 1989, pp. 344-352.

2 Slotine, J-J.E., "Sliding Controller Design for Non-Linear Systems," International Journal of Control, 40(2), 1984, pp. 421-434.

3 Yao, W.H. and Hedrick, J.K. "Nonlinear Adaptive Control of a Three Degree of Freedom Magnetic Suspension System,", Internal Report, Feb. 28, 1990, Department of Mechanical Engineering, Univ. of California, Berkeley, Calif.

4 "MHD Angular Motion Sensor Model IETL-001", Preliminary, Mar. 16, 1989, Applied Technology Associates, Inc., Albuquerque, NM.

5 Asada, H., Slotine, J.-J.E., "Trajectory Control," Robot Analysis and Control, 1st Ed., Wiley, New York, 1986, pp. 133-179.

6 AFAL/ARBH, Statement of Work, Space Active Vibration Isolation (SAVI), Kirtland AFB, NM, 1985.

7 Johnson,B.G., Misovec,K.M., Flynn,F., Anastas,G. Avakian,K.,Downer,J.,Gondahaleker,V.,Hockney, R.,"Active Magnetic Vibration Isolation Using Sliding Mode Control", R06-90, Sept. 1990, SatCon Technology Corporation, Cambridge, MA.

8 Misovec, K.M. "A Comparison of Estimation Approaches for Use in a Sliding Mode Control Magnetic Vibration Isolation Testbed", to be published, Sept. 1990, SatCon Technology Corporation, Cambridge, MA.

N91-21194

MAGNETIC BEARINGS with ZERO BIAS

Gerald V. Brown, Carlos M. Grodsinsky
NASA Lewis Research Center
Mail Stop 23-3
Cleveland
OH 44135

Proposed for Presentation at the
Workshop on Aerospace Applications
of Magnetic Suspension Technology,
NASA Langley Research Center,
Sept. 25-27, 1990

MAGNETIC BEARINGS WITH ZERO BIAS

By

G. V. Brown and C. M. Grodsinsky
NASA Lewis Research Center

ABSTRACT

A magnetic bearing operating without a bias field has supported a shaft rotating at speeds up to 12,000 rpm with the usual four power supplies and with only two. A magnetic bearing is commonly operated with a bias current equal to half of the maximum current allowable in its coils. This linearizes the relation between net force and control current and improves the force slewing rate and hence the band width. The steady bias current dissipates power, however, even when no force is required from the bearing. The power wasted is equal to two-thirds of the power consumed at maximum force output. This paper examines the zero bias idea and finds both advantages and drawbacks.

Various workers have recognized that with digital controls the linearization ordinarily provided by the bias field could be accomplished within the control code simply by directing the power supplies to provide currents proportional to the square root of the desired force. Only those coils toward which force is needed would be energized. In situations where only a steady force is required, this technique saves substantial power. For zero force, no power is required at all.

In dynamic situations, current and force slew rate problems arise which require compromise of the zero-bias ideal but can be solved in a variety of ways with substantially less power consumption than the usual bias method.

Without bias, it is possible to reduce the number of controllable power supplies from the two usually required per bearing axis to only one per axis by using diodes in series with the coils on opposite sides of the bearing and connecting the two sides in parallel to a single supply. Then current of positive sense from the power supply flows through one coil and of negative sense through the other. In dynamic situations inductive effects cause currents to flow in both sides at once, again compromising the zero-bias ideal, giving errors in the desired force and thus generating higher harmonics in the force, but actually improving the force slewing rate. This method has been demonstrated successfully on the test rig at speeds up to 12,000 rpm.

Computer simulations of time histories of coil currents, power supply voltages, individual coil forces and net axis forces are shown for a few possible control strategies. The slew rate problems are not prohibitive at frequencies normally encountered in rotors. Performance data is presented for those strategies which have been actually implemented.

Any control law (such as the PD law in the first equation can be used to calculate a net force desired from the magnets acting on one axis of a bearing as shown in the figure. The force actually exerted by the magnets is given by the second equation. In the usual bias current approach, linearization and other advantages are obtained by setting $I_1 = I_b + I_c$ and $I_2 = I_b - I_c$, where I_b is the constant bias current and I_c is the control current. The net force obtained is proportional to I_c.

$$F = - kx - c\dot{x} - \ldots$$

$$F = \alpha \left(I_1^2/g_1^2 - I_2^2/g_2^2 \right)$$

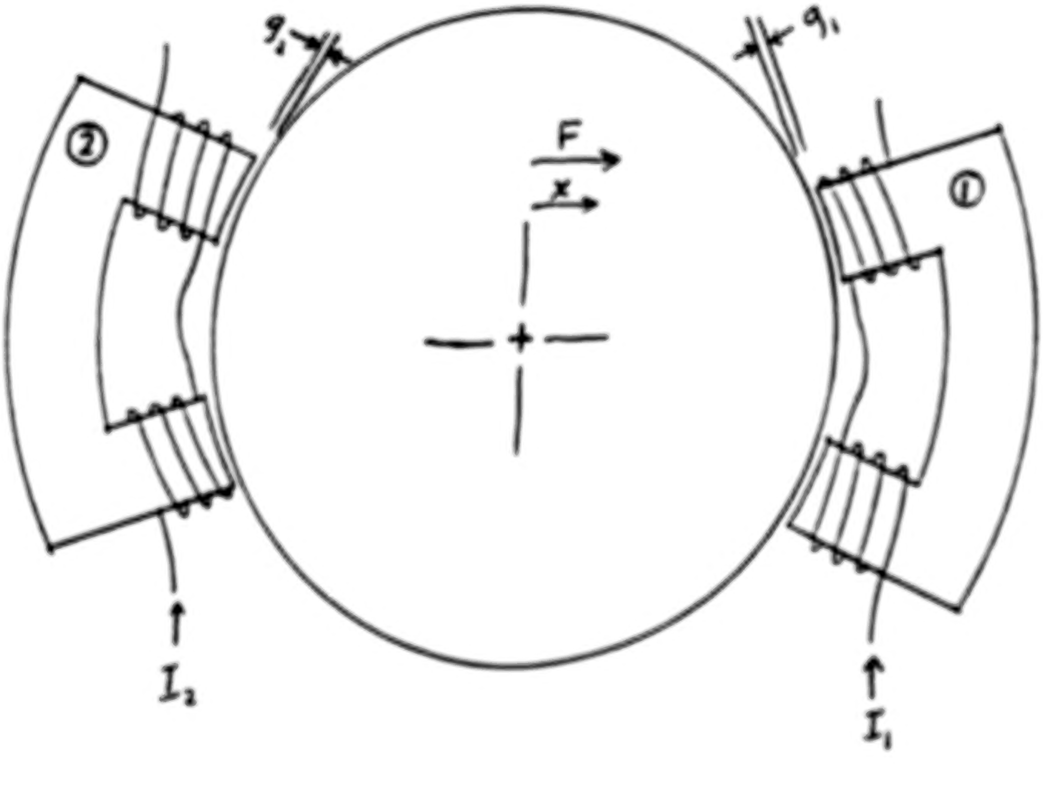

There are a number of favorable and unfavorable consequences of this commonly used linearization scheme, which include the following:

BIAS CURRENT LINEARIZATION

ADVANTAGES

LINEAR FORCE vs CONTROL CURRENT

REDUCED POSITION DEPENDENCE OF FORCE

MAXIMUM FORCE SLEWING RATE

DISADVANTAGES

WASTED ELECTRICAL POWER

HIGHER COIL TEMPERATURE, HENCE LOWER LOAD CAPACITY

INCREASED ROTOR EDDY CURRENTS (typical configurations)

TWO POWER SUPPLIES REQUIRED PER AXIS

To see how much power is wasted by the ever-present bias current, consider the top figures below which show the currents and power consumed in an example bearing under zero load (left figure) and at maximum load toward the top magnet (right figure). (Each electromagnet has 1 ohm resistance.) The power at no load is 2/3 of the power at maximum load. By comparison the lower figures show the power consumed by a bearing operating under zero and maximum load without bias. The power saving from eliminating bias is 100% at zero load and 33% at maximum load.

BIASED

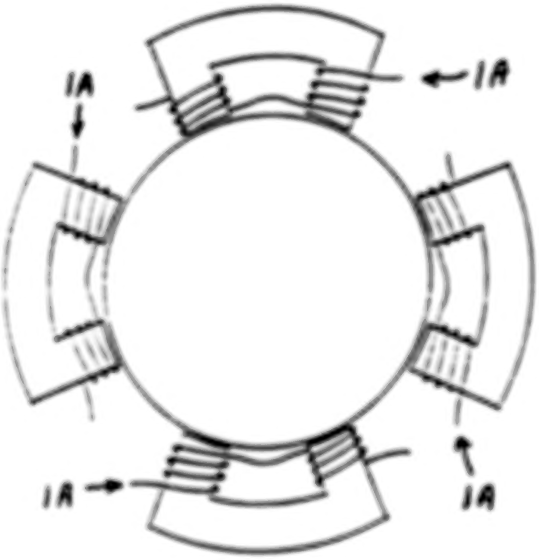

4 WATTS

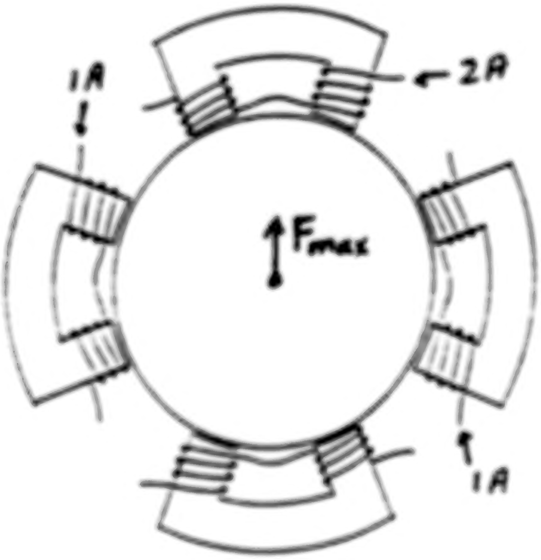

6 WATTS

UNBIASED

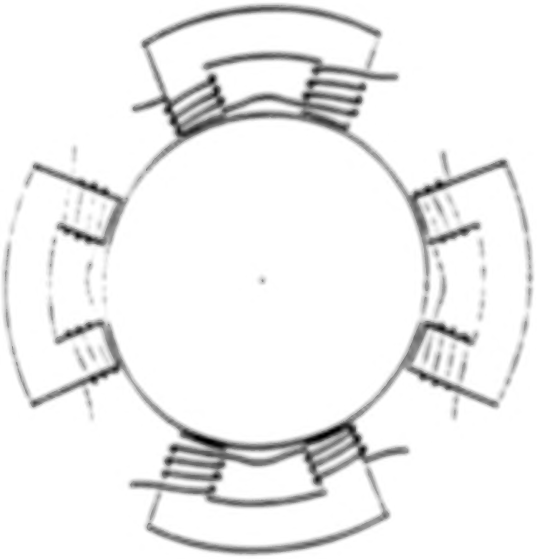

0 WATTS

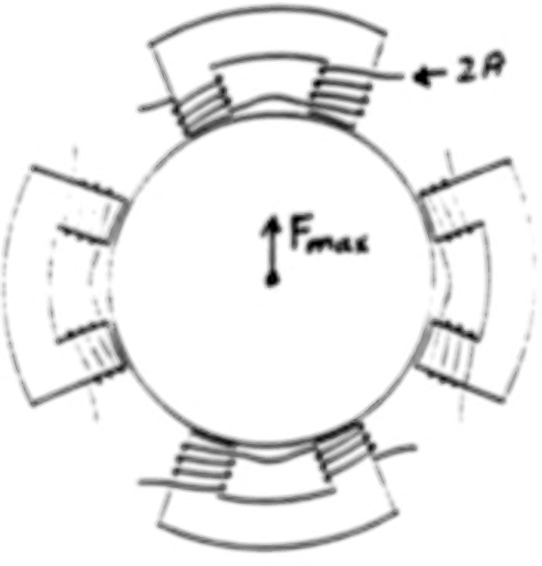

4 WATTS

The "root" method of linearization has been considered by several researchers [1-4] and has been actually implemented [4]. The simplest philosophy is to use the control law, equation 1, to calculate a desired force and then to choose currents I_1 and I_2 to give that desired force consistent with equation 2. The minimum power consumption is obtained if one activates only that magnet toward which force is required. The required currents are then given by equation 3.

$$F = -kx - c\dot{x} - \ldots \qquad (1)$$

$$F = \alpha \left(I_1^2/g_1^2 - I_2^2/g_2^2 \right) \qquad (2)$$

$$\begin{aligned} &\text{for } F > 0: \quad I_2 = 0, \; I_1 = g_1 \sqrt{F/\alpha} \\ &\text{for } F < 0: \quad I_1 = 0, \; I_2 = g_2 \sqrt{-F/\alpha} \end{aligned} \qquad (3)$$

---

[1] Bleuler, H., "Decentralized Control of Magnetic Rotor Bearing Systems," Ph.D. Dissertation, Swiss Federal Institute of Technology, ETH report number 7573, Zurich, Switzerland, 1984.

[2] Maslen, E., Hermann, P., Scott, M., and Humphris, R. R., "Practical Limits to the Performance of Magnetic Bearings: Peak Force, Slew Rate, and Displacement Sensitivity," Transactions of the ASME, Journal of Tribology, Vol. 111, pp 331-336, April, 1989.

[3] Higuchi, T. et al, "Digital Control system for Magnetic Bearings with Automatic Balancing", Proceedings of the Second International Symposium on Magnetic Bearings, Tokyo, Japan, 1990.

[4] Ishida, S., "Linear Compensation for Magnetic Bearings", Proceedings of the Second International Symposium on Magnetic Bearings, Tokyo, Japan, 1990.

Root method linearization has been accomplished with analog controls but is perhaps more appropriate for digital controls, which can be used to ameliorate the slew rate problems. The major problems and advantages of the root method are as follows:

ROOT METHOD LINEARIZATION

DISADVANTAGES

ROOT AND MULTIPIER CIRCUITS FOR ANALOG CONTROL

FORCE SLEW RATE PROBLEMS, HENCE PHASE SHIFTS AND HARMONIC GENERATION

STRONGER POSITION DEPENDENCE OF FORCE (if neglected)

REQUIRES SWITCHING POWER SUPPLY FOR FULL POWER SAVING

ADVANTAGES

REDUCED ELECTRICAL POWER

LOWER COIL TEMPERATURE, HENCE HIGHER LOAD CAPACITY

REDUCED ROTOR EDDY CURRENTS

ONE OR TWO POWER SUPPLIES PER AXIS

A simple magnetic actuator and power supply circuit (one for each electromagnet) for use with the root method is represented below. The bipolar power operational amplifier can supply an output voltage between V_{max} and $-V_{max}$ with respect to ground. These voltage limits imply current slew rate limits in the inductive load, which are similar whether linearization is attained by bias current or by the root method. However the force slewing rate is generally lower in the root method, reaching zero when the current is zero.

Circuit parameters used in subsequent simulation calculations are V_{max} = 25 volts, L = 10 mh, R_{coil} = 0.8 ohms, R_s = 0.1 ohms.

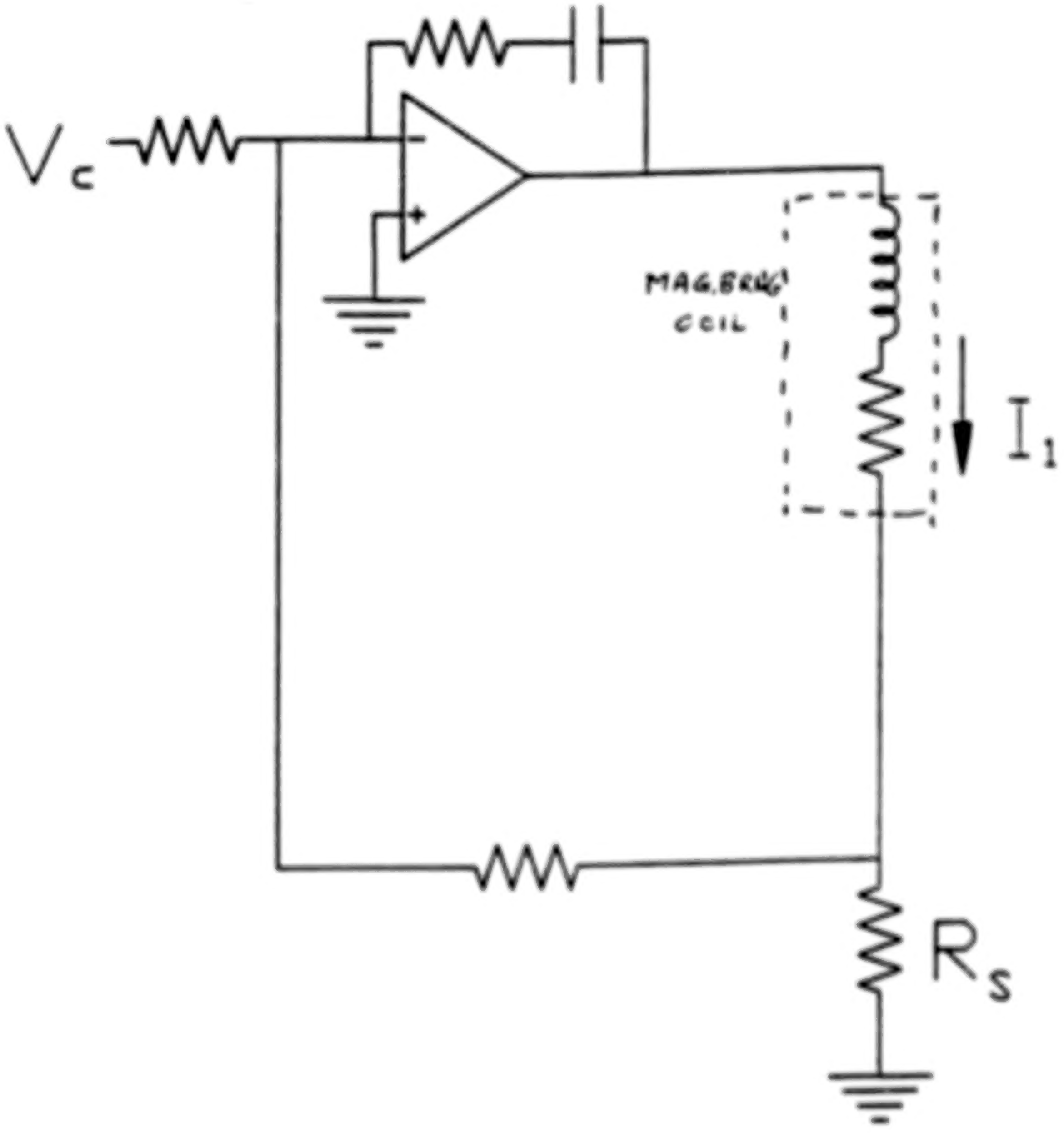

To show clearly the force slewing problem details, some computer simulations were performed for the two opposing magnets on an axis, each driven as shown in the previous figure. Shaft displacement is presumed negligible. Consider a purely dynamic load for which the control law asks for a force proportional to cos Ωt. We consider just one half period. The root method requests $I_1 \propto \sqrt{(\cos \Omega t)}$ and $I_2 = 0$ in the first quarter period and $I_1 = 0$ and $I_2 \propto -\sqrt{(-\cos \Omega t)}$ in the second quarter period. The negative sign is added before the root in I_2 only for plotting clarity. These currents requested from the power supplies are plotted as functions of time in the figure as I_s. The actual value of I_1 follows I_s until the power supply reaches its negative rail at time A and thereafter I_1 decreases to zero at an approximately linear rate, producing too much force in the positive direction. Worse, I_2 cannot start at the infinite requested rate, producing less force than requested until time B. The resulting force error (which generates a phase lag and harmonics) is shown, plotted on a scale where the requested cosine force has an amplitude of 1. The frequency and the current amplitude (half the bearing maximum current) were chosen to yield a sizable error and are higher than required in many applications.

The total force exerted could be Fourier analyzed to see whether its harmonics would excite higher shaft frequencies.

A small rotor has been run to 12000 rpm, through two critical speeds, using this method.

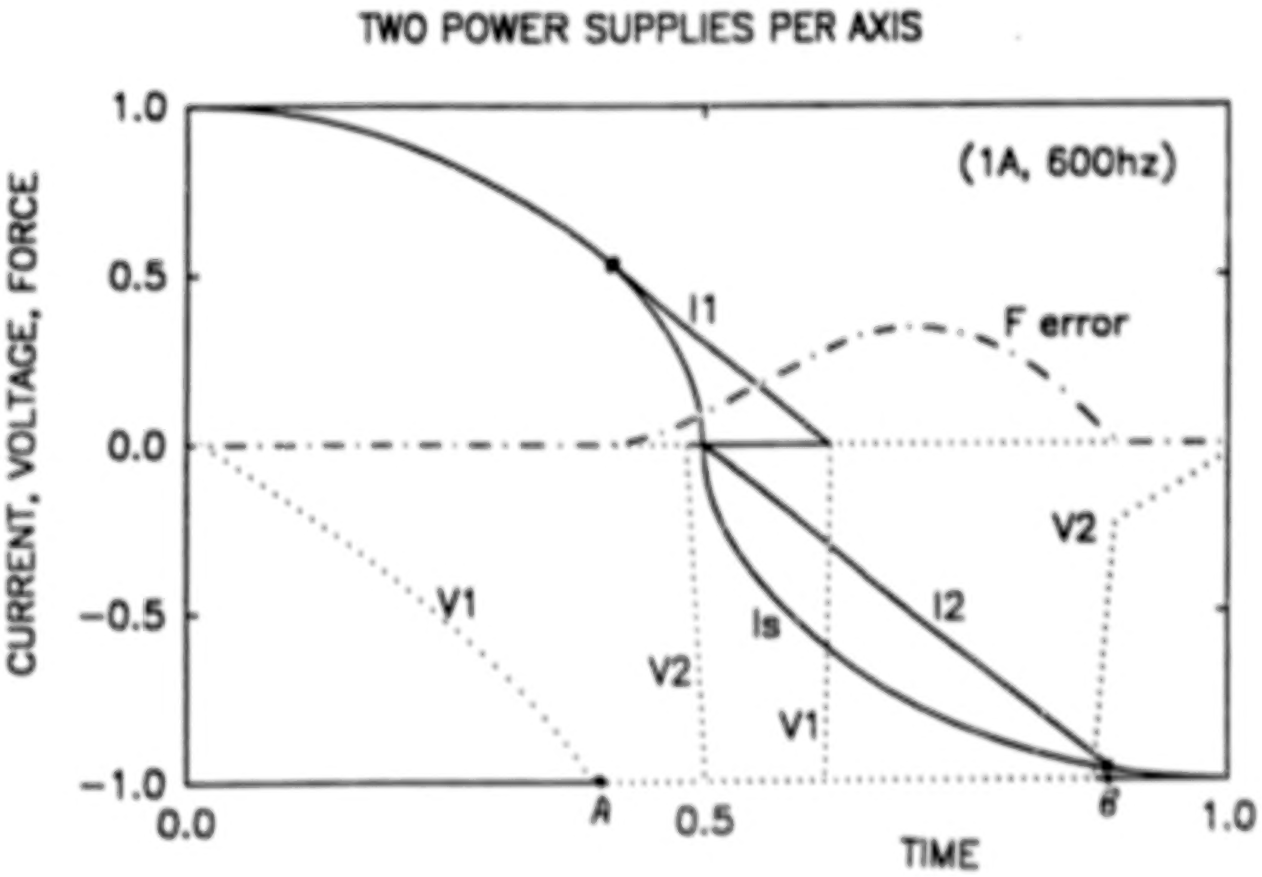

Experimental measurements of I_1 and I_2 were made with a rotor supported by conventional bearings with a magnetic bearing near one of the conventional ones. A pure cosine signal was fed to a digital controller which consequently requested $I_1 \propto \sqrt{(\cos \Omega t)}$ and $I_2 \propto \sqrt{(-\cos \Omega t)}$ in alternate half cycles. The results are plotted below for $-\pi \le \Omega t \le \pi$. The solid curves are the requested currents and the dash - dot and dash curves are the actual I_1 and I_2 respectively.

At low frequencies the deviations due to the current slew rate limits can hardly be seen, but at higher frequencies become serious.

85 hz, 0.4 A

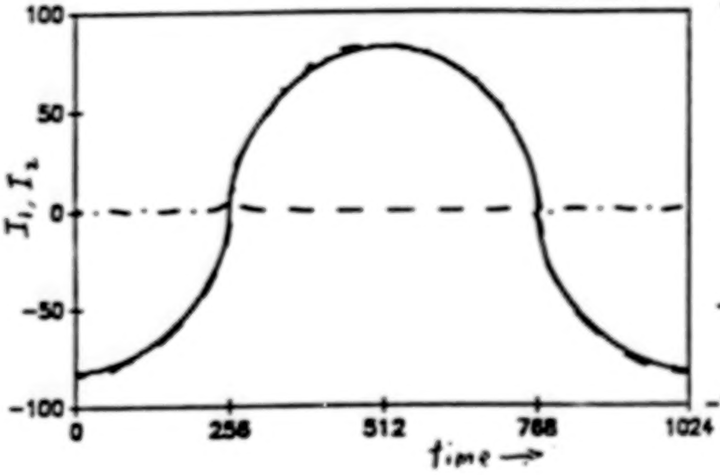

520 hz, 0.4A

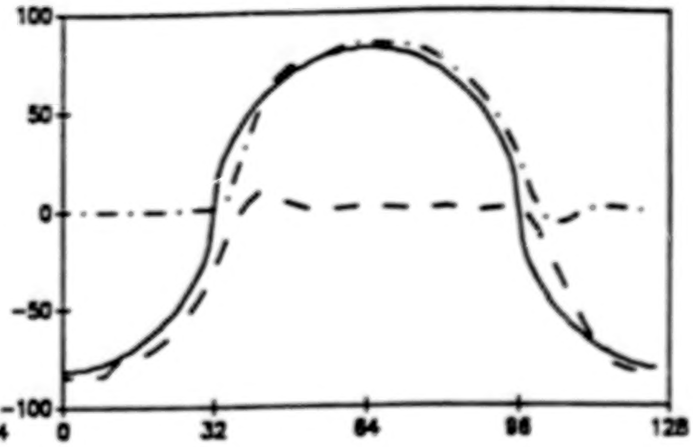

130 hz, 0.4 A

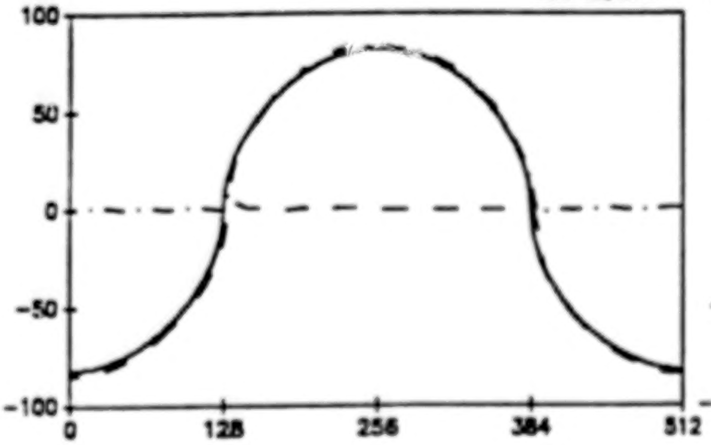

1040 hz,0.4A

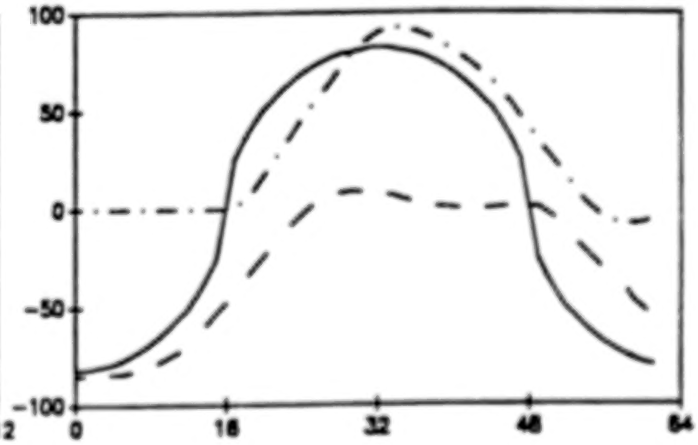

260 hz, 0.4 A

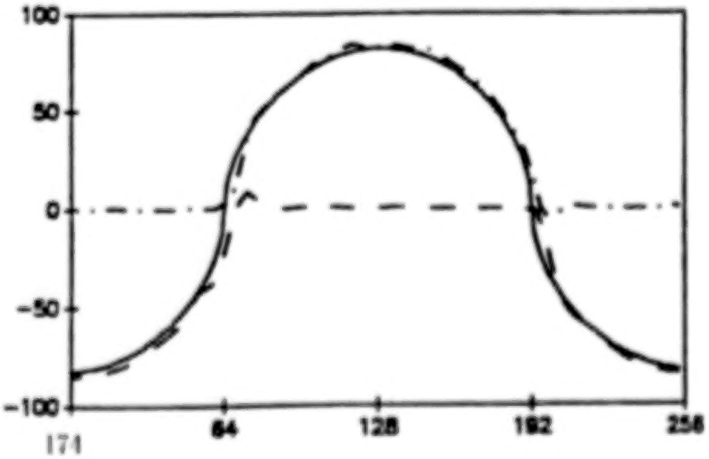

One obvious method of reducing the force error is to start the current I_2 earlier, for example when I_1 reaches its slew limit. (One could either measure or calculate when V_1 reaches its rail.) One result, shown below from a numerical simulation, is to substantially reduce the force error. Even earlier initiation of I_2 might virtually eliminate the contribution of the force error to the fundamental frequency, removing most of the phase lag.

The goal of using only one at a time of the opposing magnets has been compromised, of course, slightly increasing power consumption in order to improve frequency response.

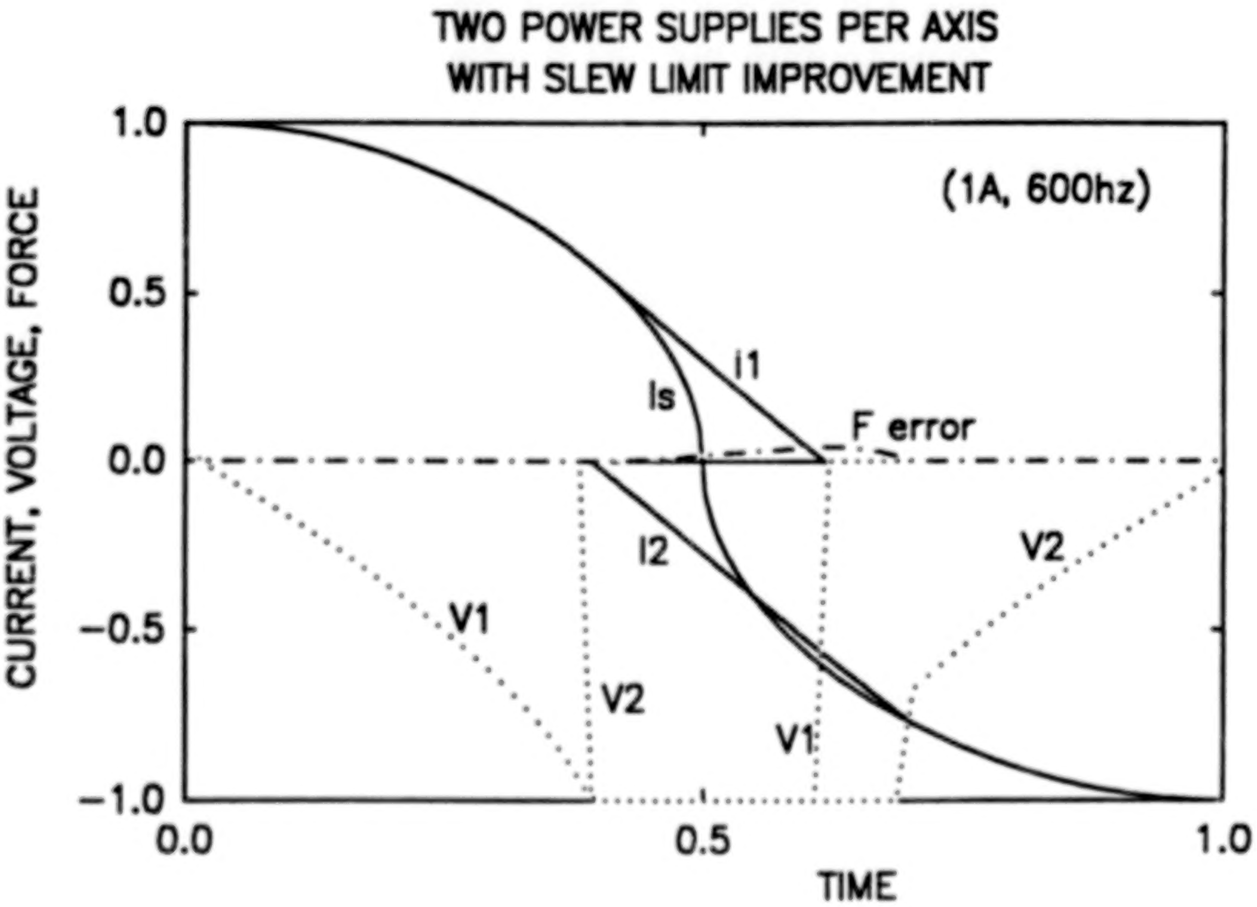

In the previous simulations one notes that the two power supply voltages have the same sign (negative) during most of the half cycle. One is tempted to use a single supply to power both coils in parallel, providing diodes to insure that under steady conditions only one coil carries current. Under dynamic conditions both coils carry current because of inductive behavior. But positive power supply vltage increases I_1 and decreases I_2 (subject to $I_1 \geq 0$ and $I_2 \leq 0$). The power supply sense resistor R_s carries $I_1 + I_2$.

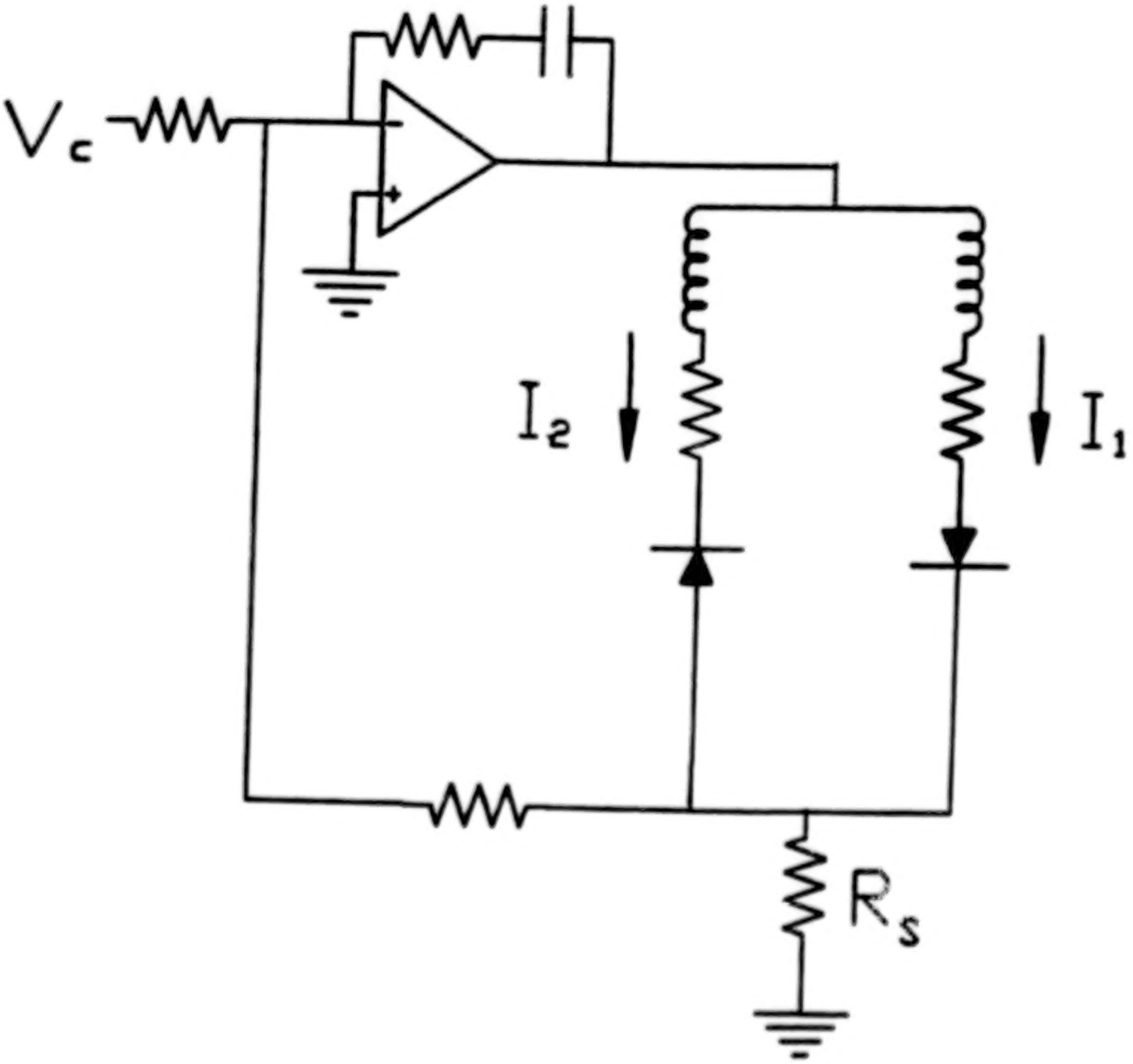

The numerical simulation bears out that both coils usually are active, but in such a way that force slewing is improved. (Actually the force lags even worse early in the half cycle but leads later, contributing less to the fundamental frequency of the force error.) The controller asks the single power supply for the current I_s, which is equal to $I_1 + I_2$.

A small rotor was supported under this scheme to 12000 rpm through two critical speeds.

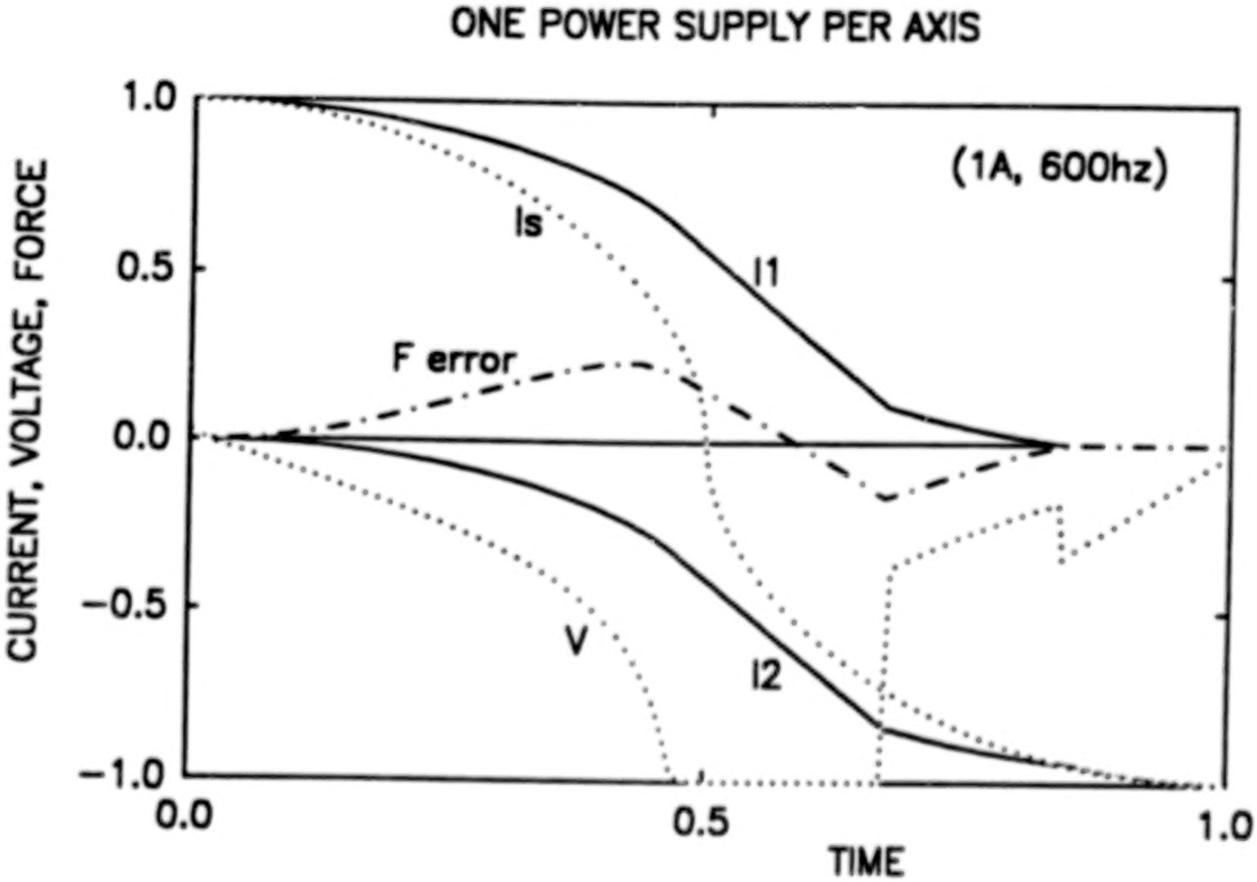

Experimental currents, measured under the same conditions as before, again show reasonable fidelity to the requested values at low frequency and large deviations at high frequency. Additional kinks in the curves may be related to diode switching (forward drop was neglected in the simulation) or to rotor motion.

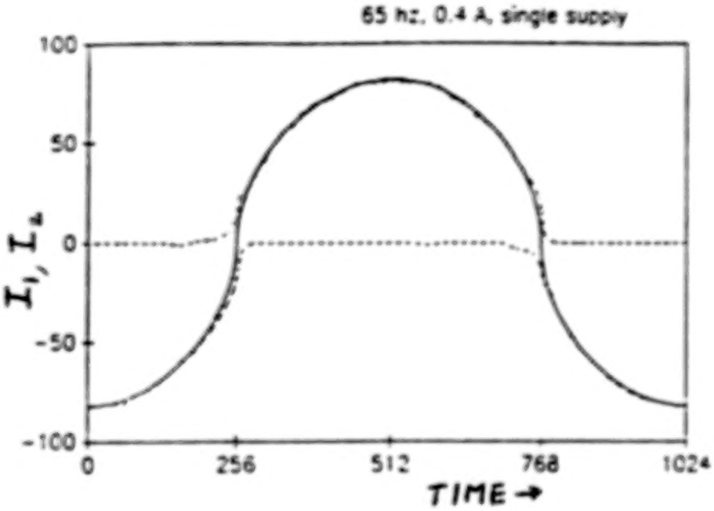

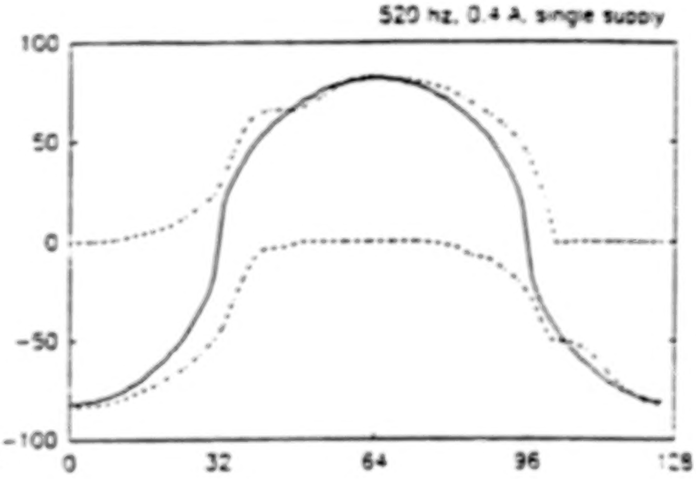

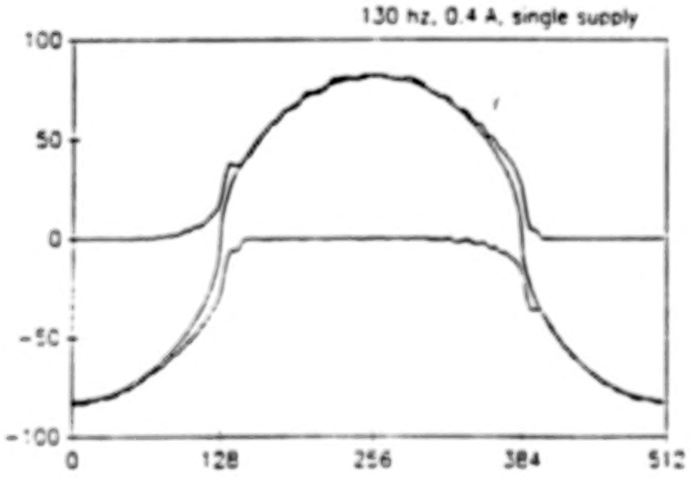

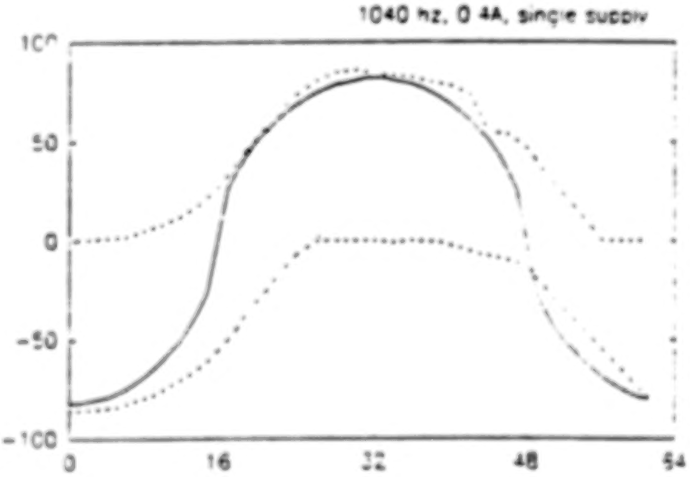

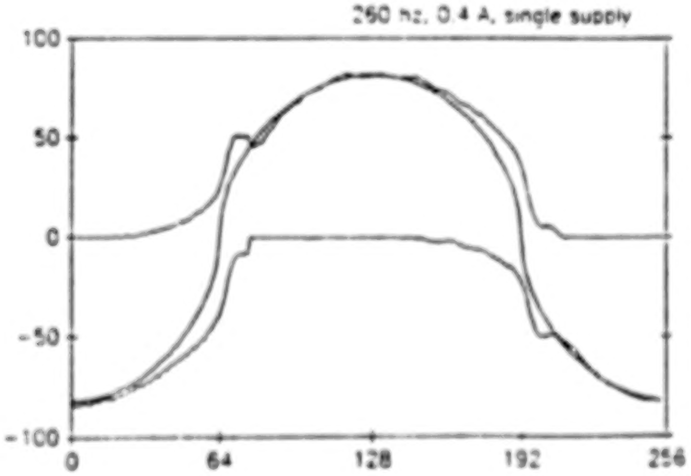

The force error produced by a single power supply per axis could no doubt be reduced by taking account in the controller that currents flow in both magnets at once but that the sense resistor can sense only their difference.

Another type of approach is to put sense resistors (or other current sensors) in both legs as shown below and use the resulting values of I_1 and I_2 in the controller. One such approach that has been simulated numerically avoids taking square roots altogether and instead compares the desired force and an "observed" force $I_1^2/g_1^2 - I_2^2/g_2^2$ to form an error function and an output to the power supply, as in the equation below. The power supply can be used as a simple voltage amplifier.

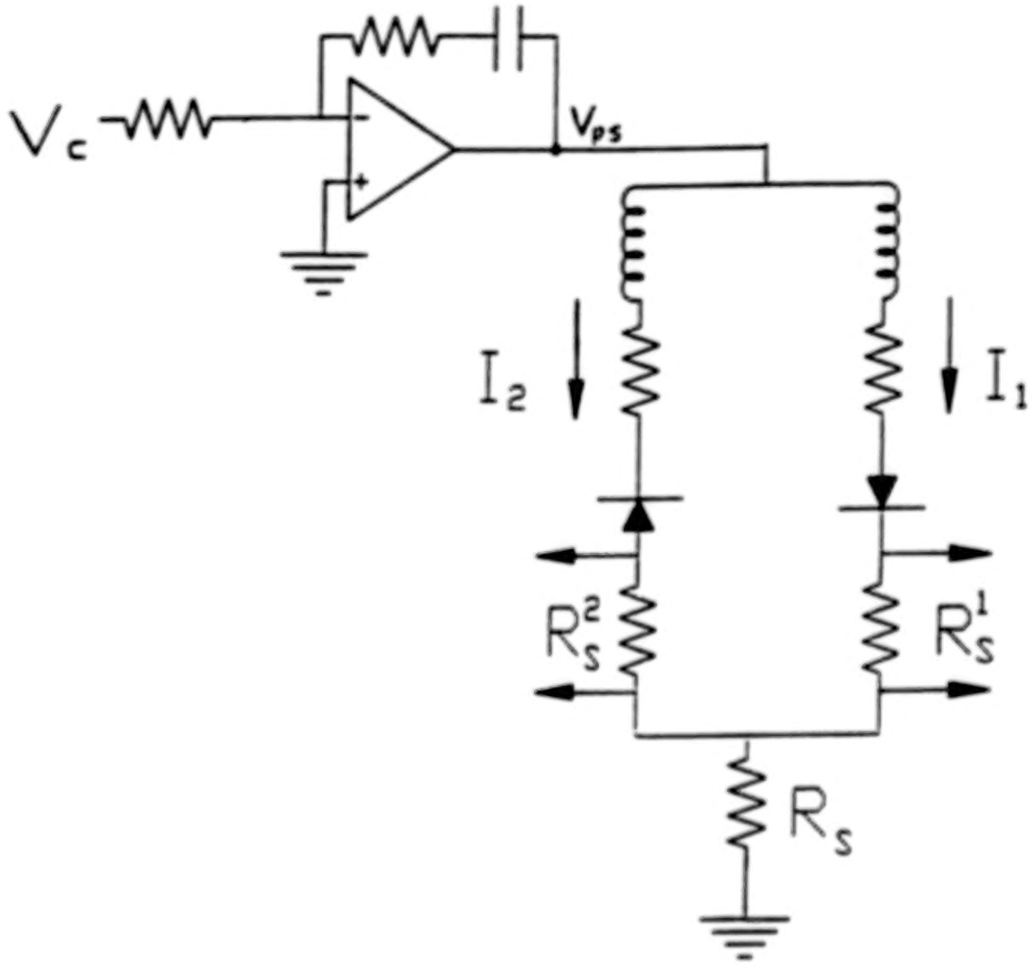

The result (simulation shown below) is remarkably similar to the behavior of the biased system, shown in the following figure at maximum dynamic load. Differences are mainly due to the different effects of resistive voltage drops in the two cases. The present method is superior to the bias case with respect to power consumption because at smaller dynamic load both currents reach zero in every cycle rather than having a fixed DC offset. On the other hand increasing dynamic loads will not be followed as quickly in the present case.

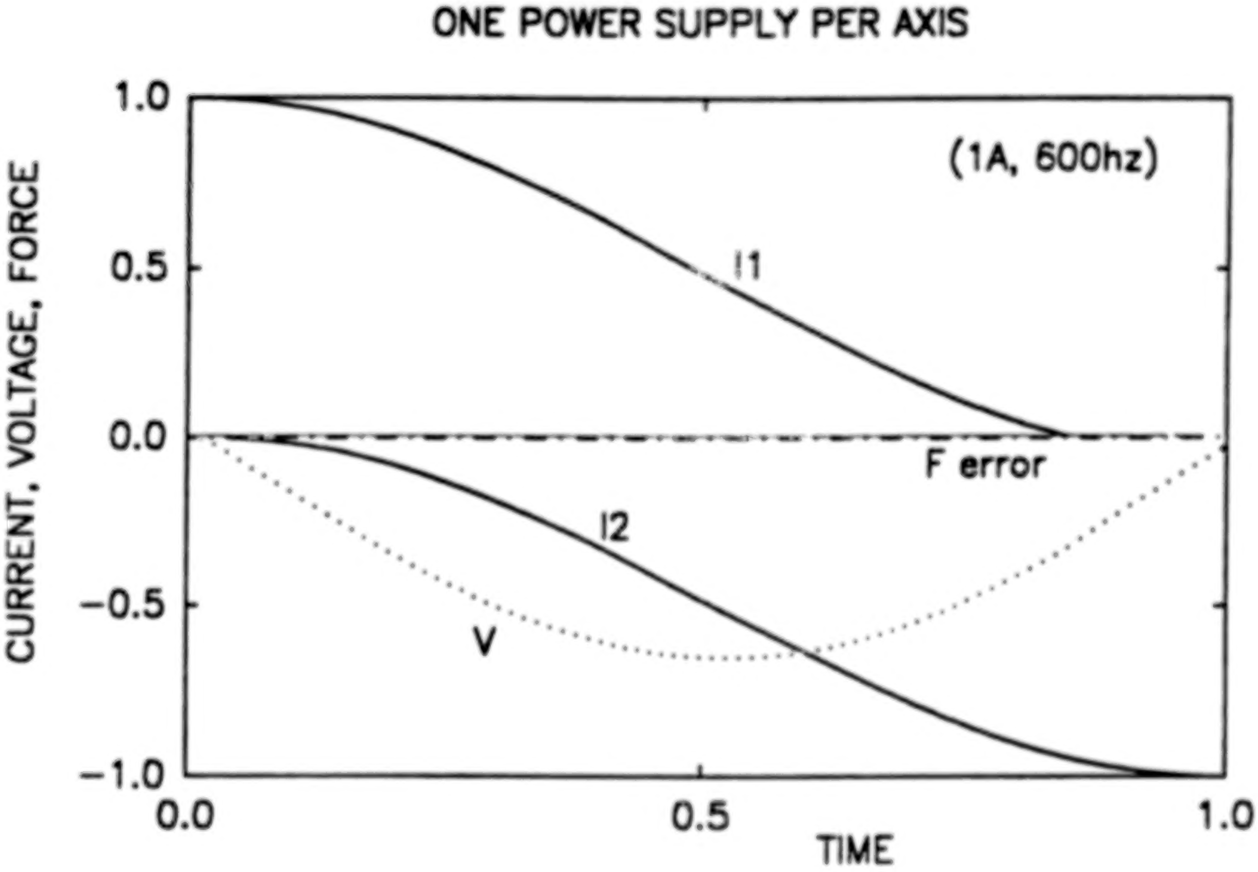

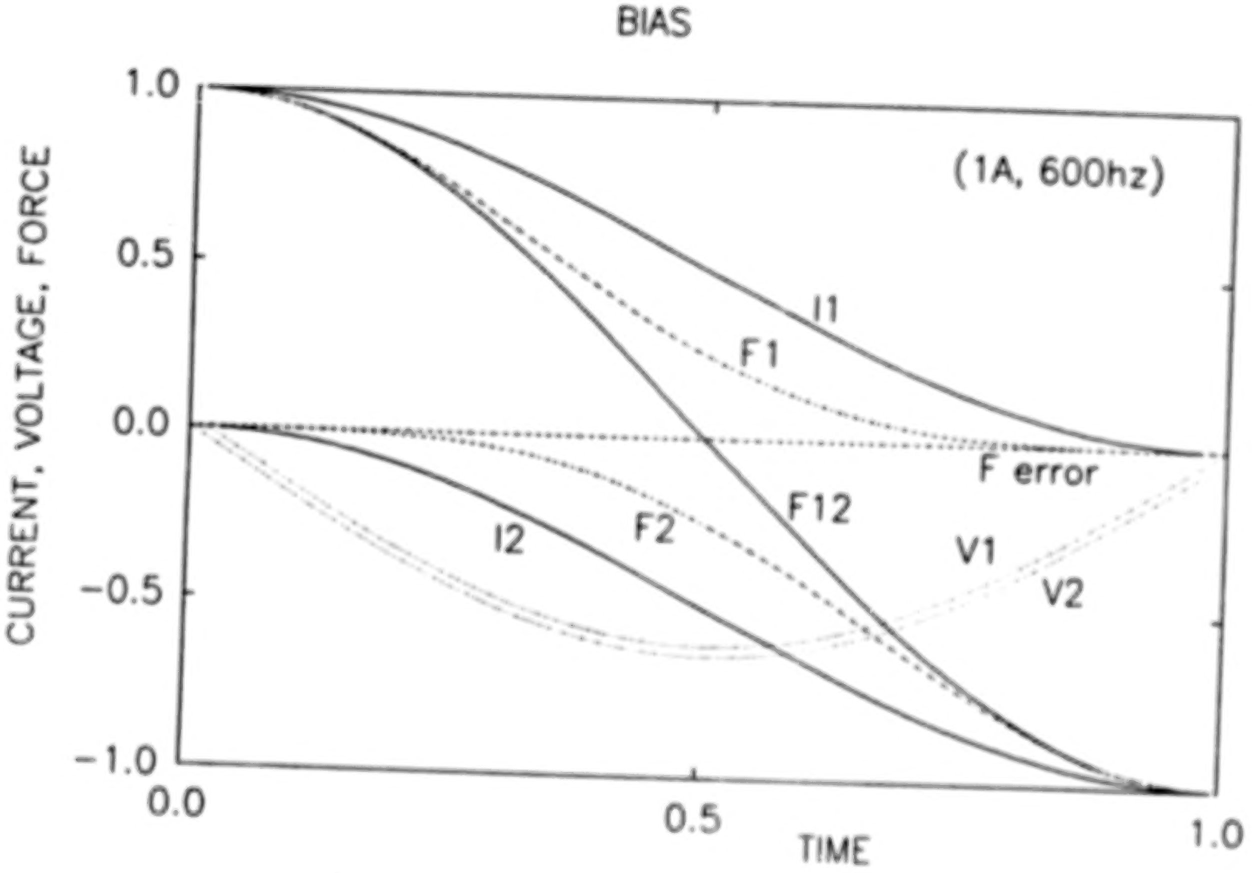
BIAS
(1A, 600hz)
CURRENT, VOLTAGE, FORCE
1.0
0.5
0.0
−0.5
−1.0
0.0
0.5
1.0
TIME
I1
F1
F error
F12
F2
I2
V1
V2

CONCLUSIONS

ELECTRICAL POWER CAN BE SAVED

COIL HEATING CAN BE REDUCED

ROTOR EDDY CURRENTS CAN BE REDUCED

HARMONICS ARE GENERATED IN THE SIMPLEST METHOD

MANY IMPROVEMENT STRATEGIES ARE POSSIBLE

REDUCED NUMBER OF POWER SUPPLIES IS POSSIBLE

METHOD IS MORE SUITED TO DIGITAL THAN ANALOG CONTROL

SIMPLEST METHOD DEMONSTRATED ON A ROTOR TO 12000 RPM
WITH ONE AND TWO POWER SUPPLIES PER AXIS

FURTHER INVESTIGATION WARRANTED

N91-21195

MAGNETIC BEARINGS for a SPACEFLIGHT OPTICAL DISK RECORDER

Richard Hockney, Vijay Goodhalekar, Timothy Hawkey
SatCon Technology Corporation
12 Emily Street
Cambridge
MA 02139-4507

Magnetic Bearings for a Spaceflight Optical Disk Recorder

Richard Hockney, Vijay Gondhalekar, Timothy Hawkey

SatCon Technology Corporation
12 Emily Street
Cambridge, MA 02139

Presented at: Workshop on Aerospace Applications of Magnetic Suspension Technology
NASA Langley Research Center, Hampton, VA - September 1990

ABSTRACT

Optical-disk data recording technology is being developed by NASA for space applications. This technology has made possible devices which provide capacities of tens of gigabits, and data-rates of hundreds of megabits-per-second through the use of arrays of solid-state lasers applied to a magneto-optic disk. Bearings are an area where improvements are needed to allow these systems to be utilized in space applications. The porous-graphite air bearings used for the linear translator of the read/write head in the prototype unit, as well as the bearings used in the rotary spindle would be replaced by either magnetic bearings or mechanical (ball or roller) bearings. Based upon past experience, roller or ball bearings are not feasible for the translation stage. Unsatisfactory, although limited, experience exists with ball bearing spindles also. Magnetic bearings are an excellent alternative for both the translational and rotational stages of the devices.

This paper reports on the development and testing of a magnetic bearing system for the translator of the read/write head in a magneto-optic disk drive. The asymmetrical three-pole actuators with permanent-magnet bias support the optical head, and its tracking and focusing servos, through their radial excursion above the disk. The specifications for the magnetic bearing are presented, along with the configuration of the magnetic hardware. Development of a five degree-of-freedom collision model is examined which allowed assessment of the system response during large-scale transients. This model also aided in the establishing the philosophy and strategy for system start-up which are discussed. Finally, experimental findings and the results of performance testing are presented including the roll-off of current-to-force due to eddy-current loss in the magnetic materials.

1. SPECIFICATIONS

Definition of the specifications for the magnetic bearings for the optical disk buffer was facilitated by the decision to make the baseline design capable of retrofit into the existing NASA prototype. This then determined both the maximum dimensions and allowed volume for the electromagnetic hardware, and the amount of mass to be suspended. The stiffness required was determined from a calculation of the static stiffness of the existing air-bearings.

The structural modes of the supported structures were established using finite-element model analysis of the existing device. Since the linear motor on the translator head would be replicated, its velocity and acceleration profiles were specified. Finally, the maximum level of stray magnetic field both in the area of the recording head and near the disk were established from knowledge of the sensitivity of the magnetic domains in the recording material. The detailed specifications for the magnetic bearings are listed in Table 1.

Table 1. Specifications

Stiffness	
Parallel to disk	14×10^6 N/m
Normal to disk	9×10^6 N/m
Suspended mass	0.9 kilogram
Maximum force	18 newtons
Position Accuracy	2.5 microns
bandwidth	100 hertz
Maximum dimensions	
Length	2.9 centimeter
Width	3.8 centimeter
Height	3.2 centimeter
Maximum acceleration	21 meters/sec^2
Maximum velocity	1.2 meters/sec
Maximum stray magnetic-field	
At read/write head	3 millitesla
At disk surface	0.2 tesla

2. MAGNETIC ACTUATORS

The prime objective of the translator bearing design was the definition of a magnetic-bearing alternative requiring minimal modifications of the existing system. The current system is shown in Figure 1. The read/write head is mounted in the aluminum carriage between the linear motors which are central to the whole assembly. Producing high forces, the linear motors use large samarium-cobalt magnets that create large magnetic fields in the air-gap (1.2 tesla). The shafts that carry the return flux are therefore large and double as air bearing surfaces. Actually, the air bearings are made by milling slots in the iron shaft and covering them with porous graphite. Air is then pumped into the slots and through the graphite, forming a cushion of air between the shaft and the aluminum carriage which it supports.

For an easy retrofit, the entire bearing and shaft structure cannot occupy more space than the current air bearing shaft. As such, the geometric constraints were the most restrictive. The tight spacing drove many of the design parameters and eliminated many configuration options. A second major restriction was imposed by magnetic flux of the linear motors. The twin voice-coil motors must move the read/write heads at high acceleration and, as such, require large magnetic flux density. This means that there must be a large pole-area facing the linear motor magnet (for uniform flux), and that the shaft must have sufficient cross sectional area to carry the return flux back to the motor magnet.

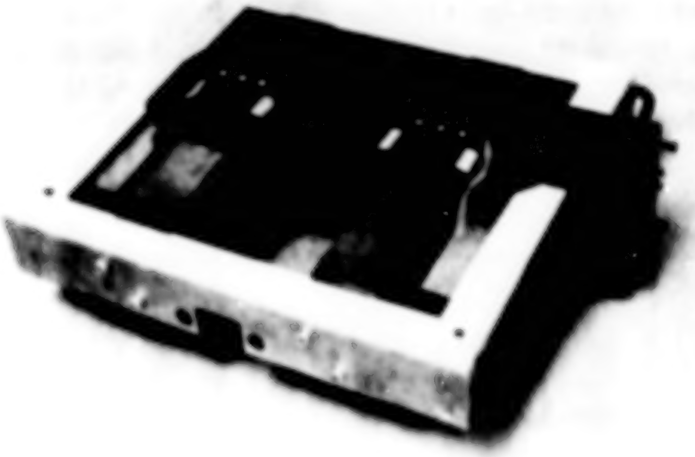

Figure 1. Present Air-Bearing System

uniform flux), and that the shaft must have sufficient cross sectional area to carry the return flux back to the motor magnet.

Together these restrictions quickly narrowed the actuator design options to that shown in Figure 2. Normally, a radially symmetrical four- or eight-pole design is used for magnetic bearings, but the linear-motor magnet flux prevented pole placement on one side. Fortunately, all five required degrees-of-freedom can be controlled with a three-pole design because the two bearing sets are mirror images of each other as shown in Figure 3, and can be coupled to provide the proper support. This configuration was chosen as the baseline because its layout is both simple mechanically and it has low internal flux-density. A permanent magnet is employed to provide bias flux. The bias flux is used because it provides a linear force-per-amp scale factor, and because it reduces power consumption for a given force capability. The complete magnetic design parameters are listed in Table 2.

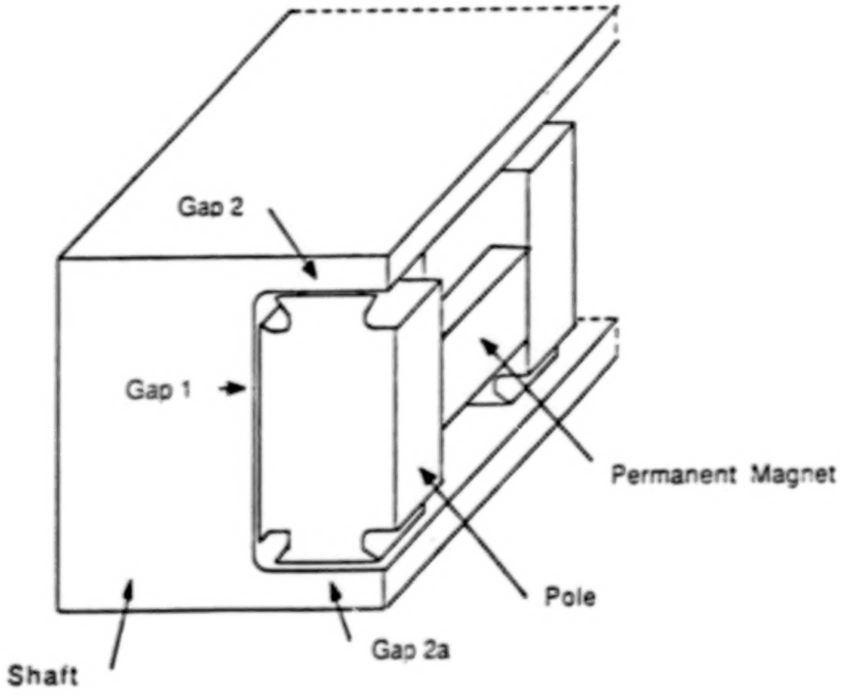

Figure 2. Actuator Design

Table 2. Design Parameters

X-Axis	
Unstable Frequency	45 Hz
Bias Field	0.149 T
Pole Area	$3.78 \times 10^{-4}\,m^2$
Nominal Gap	$2.54 \times 10^{-4}\,m$
Turns	130
Inductance	27 mHy
Wire Size	AWG32
Max Current (2g)	720 mA
Z-Axis	
Unstable Frequency	48 Hz
Bias Field	0.126 T
Pole Area	$1.67 \times 10^{-4}\,m^2$
Nominal Gap	$3.05 \times 10^{-4}\,m$
Turns	120
Inductance	21 mHy
Wire Size	AWG33
Max Current (2g)	580 mA
Magnet Parameters	
Material	SmCo
Energy Product	19 MGOe
Size	0.27cm x 0.45cm x 0.48 cm

C-3

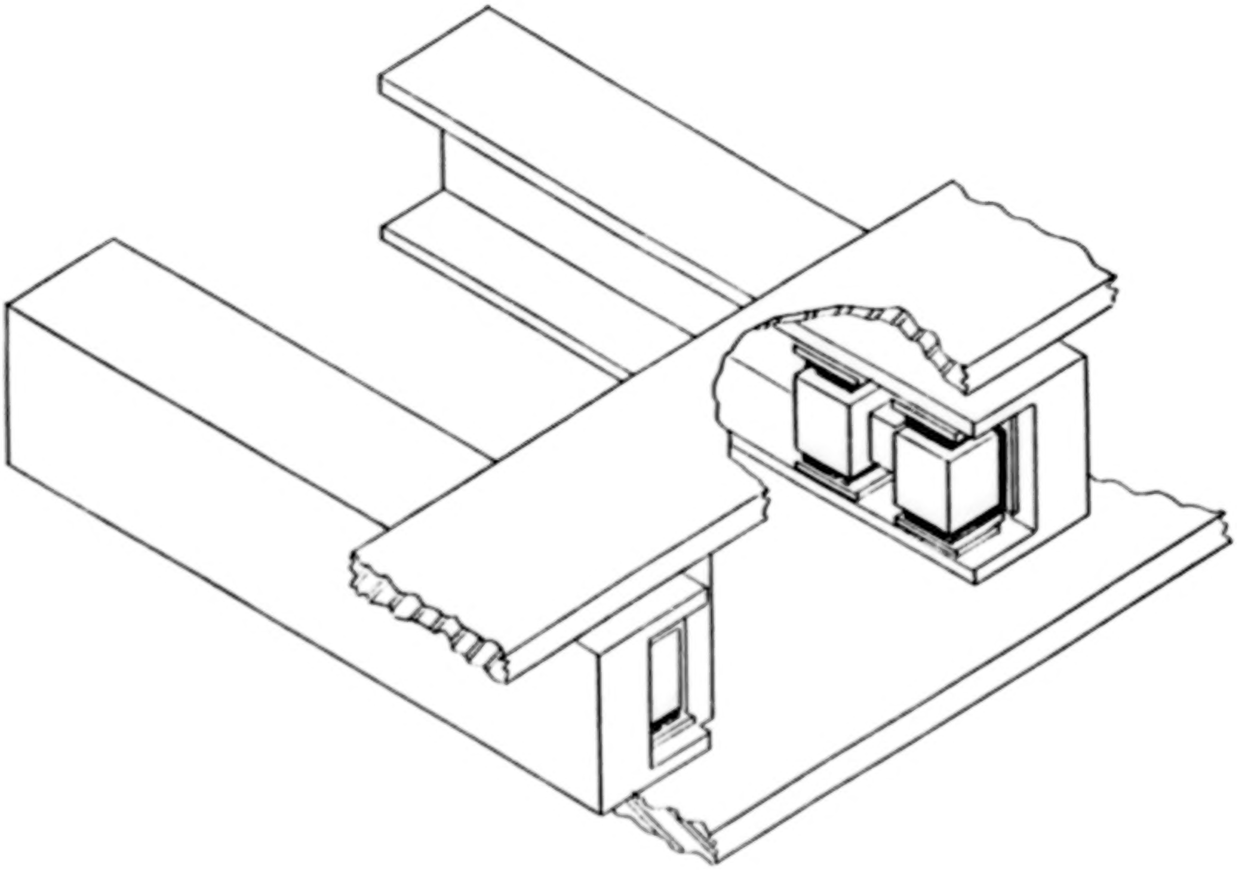

Figure 3. Magnetic Bearing System

3. START-UP/SHUT-DOWN PROCEDURE

A model was developed to simulate the collisions between bearing slide and frame in order to verify the stability characteristics of the bearing under very large disturbance conditions, and determine the transients occurring during startup and shutdown. Figure 4 shows the terminology and coordinate frame used in system modelling. The model is based in the following assumptions:

(1) All collisions are elastic, conserving both the total energy and linear/angular momentum,

(2) The frame mass M_f is much greater than slide mass M_s,

(3) The slide is assumed to be a thin, i.e its Z dimension or thickness is very small compared to the X dimension,

Sensor Orientation

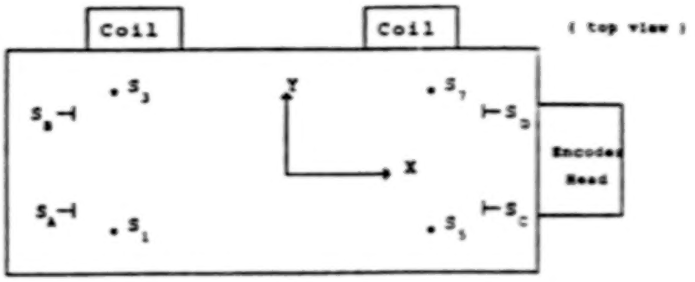

Coil Orientation

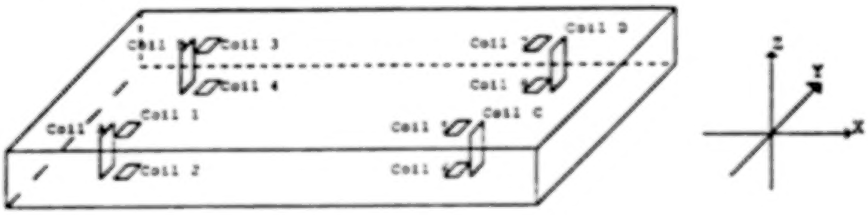

Figure 4. Terminology and Coordinate Frame

(4) Collisions are only along the X and Z axes, and are such that the collisions along the X axis occur only on the faces A, B, C or D, and collisions along the Z axis only at the corners 1 to 8 of Figure 3.

These assumptions imply that:

(a) a collision along the X axis will result in an instantaneous change in the X and Θ_z velocity components of the slide, and

(b) that a collision along the Z axis will result in an instantaneous change in the Z, Θ_x and Θ_y velocity components of the slide.

These equations are used in the nonlinear simulation to model collisions both during start-up and during large-scale transients. A start-up/shut-down strategy is considered necessary for the magnetic bearing to ensure smooth transition between the two extreme conditions of bearing parameter variation when the bearing slide is located in one corner of the frame as against the nominally centered operating condition. This procedure is complicated by the necessity to design the controller so that the bearing is insensitive to the direction of gravity when being tested under 1g conditions. The following assumptions were made to establish a start-up/shut-down strategy:

(1) No "gravity-direction" sensing allowed

(2) May start from the same corner each time

(3) The shut-down procedure brings the bearing to rest in the same corner every time

(4) The compensation may be changed when the bearing has passed from start-up to a nominally centered operating condition.

(5) Signal cross-coupling may be added to cancel the bearing cross-coupling terms when starting-up.

(6) The bearing may be started-up with suitable bias currents.

The start-up strategy adopted under the above assumptions is:

(a) Inject currents into the control coils such that start-up is from the corner $-\Delta x$, $-\Delta z$ which are the extreme possible displacements along the negative X and Z axes. Referring to Figure 3 this position is corner 2.

(b) Inject bias currents I_{Bac}, I_{Bbd}, I_{B12}, I_{B34}, I_{B56}, I_{B78} such that the actuators exert zero force on the bearing slide. The forces on the bearing are solely due to gravity.

(c) Command the control loops for regulating the X and Z displacements of the bearing slide with reference signals x_{ref} and z_{ref} which place it just slightly away from the start-up corner.

(d) Ramp the reference signals x_{ref} and z_{ref} down to zero at a rate slow enough assure dynamic stability of the regulation loops.

The resulting start-up waveforms are shown in Figure 5, where the bottom trace is the waveform used to command both the currents and the positions. The upper trace shows the start-up response of both the X and Z position signals.

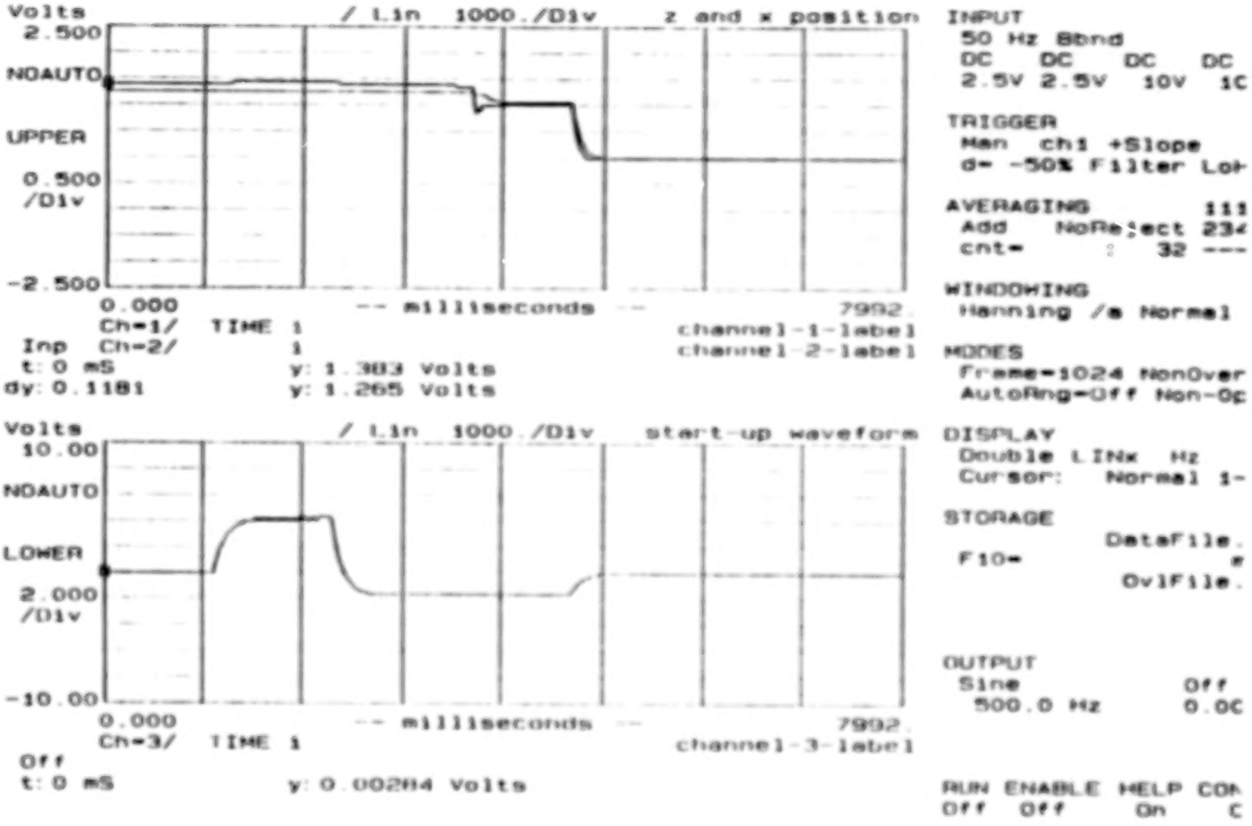

```
Ch-1/   TIME 1                          channel-1-label
Inp  Ch-2/        1                     channel-2-label
t: 0 mS
dy: 0.1181          y: 1.383 Volts
                    y: 1.265 Volts

Ch-3/   TIME 1                          channel-3-label
Off
t: 0 mS             y: 0.00284 Volts

INPUT
 50 Hz Bbnd
 DC   DC    DC   DC
 2.5V 2.5V  10V  1C

TRIGGER
 Man  ch1 +Slope
 d= -50% Filter Lo

AVERAGING          111
 Add    NoReject  234
 cnt=      :   32 ---

WINDOWING
 Hanning /a Normal

MODES
 Frame=1024 NonOver
 AutoRng=Off Non-Op

DISPLAY
 Double LINx  Hz
 Cursor:   Normal 1-

STORAGE
           DataFile.
 F10-              #
            OvlFile.

OUTPUT
 Sine           Off
  500.0 Hz      0.0C

RUN ENABLE HELP CON
Off  Off    On    C
```

Figure 5. Start-Up Waveform

ORIGINAL PAGE IS
OF POOR QUALITY

4. TEST RESULTS

The results of the static testing were good. The primary concerns were force gains, and eddy-current effects. A typical force versus current transfer function is shown in Figure 6. Though the force-per-amp gains are lower than expected, the system overdesign still allows production of the force levels required for 2g acceleration. The cross-coupling at the centered position is less than 2% X-current to Z-force, and less than 1% Z-current to X-force. At the worst case, one-half gap displacement in both X and Z, the cross coupling is only 12% X-current to Z-force, and 6% Z-current to X-force.

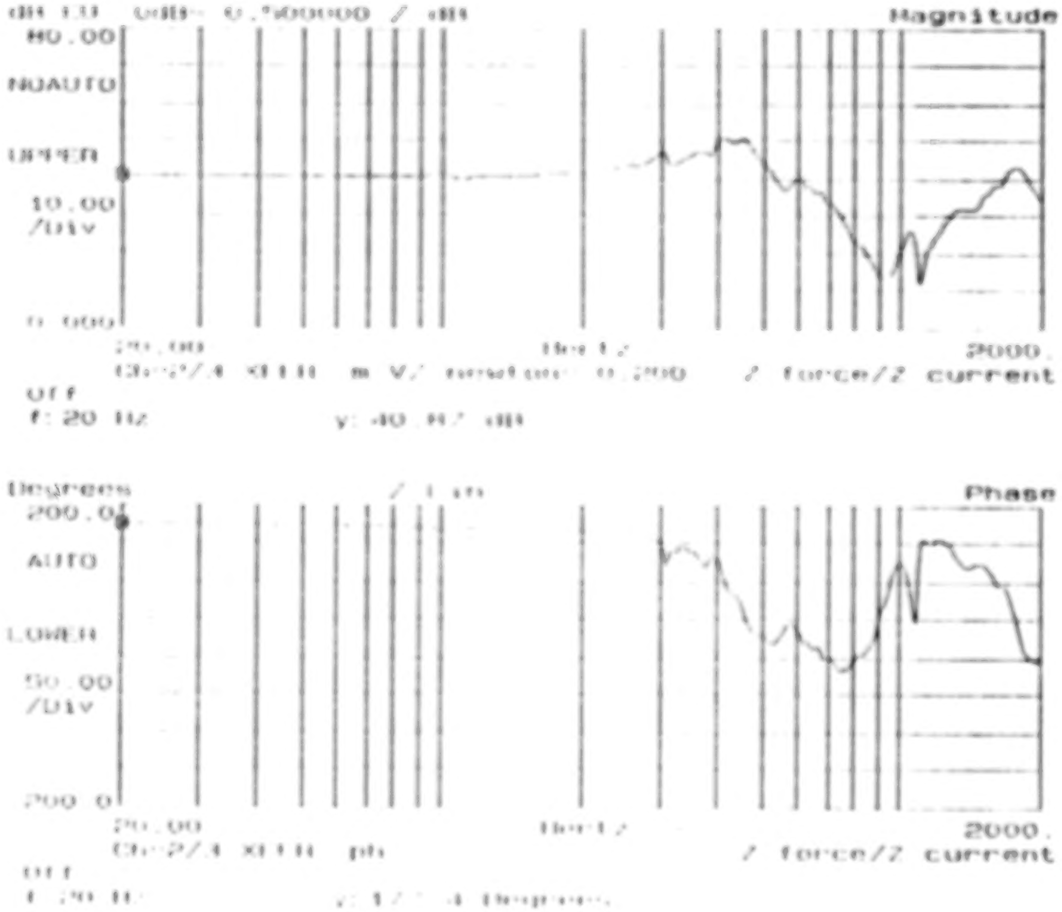

Figure 6. Force vs. Current Frequency Response

The eddy-current test results were also good. There were concerns that the force roll-off due to magnetic losses would limit the achievable bandwidth of the control loop. Fortunately, current to magnetic-field measurements, one of which is shown in Figure 7, indicate that the roll off is beyond 500 Hz with a phase loss of only 10° at 100 Hz.

ORIGINAL PAGE IS
OF POOR QUALITY

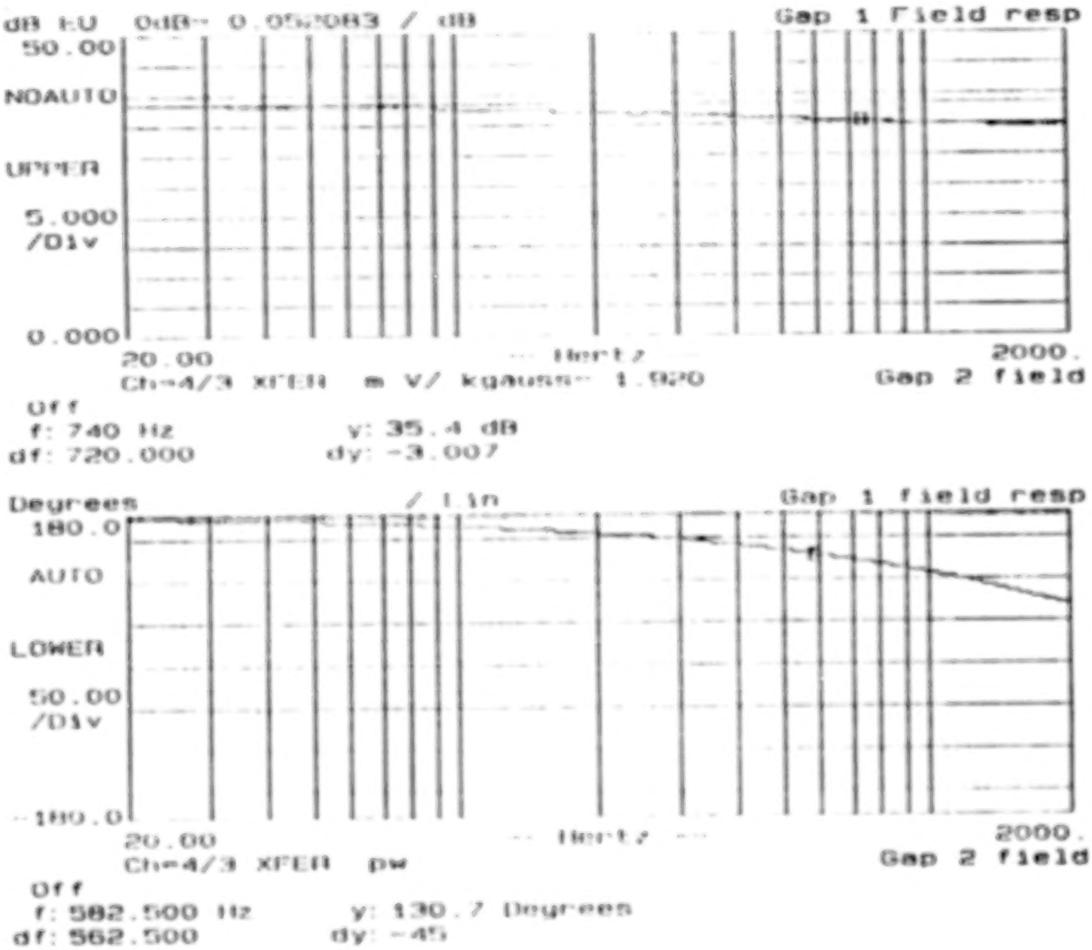

Figure 7. Flux vs. Current Frequency Response

Interaction between the linear-motor coils and the magnetic bearings was another area of concern. Preliminary analysis indicated that the disturbances should be small, but the geometry of the problem is too complicated for accurate analysis. The static test show the coupling gains to be less than 1 newton/amp below 100 Hz in the x-axis, and less than 0.5 newton/amp in the z-axis for excitation of one motor coil. Closed-loop testing consisted of frequency and step response measurements and disturbance sensitivity evaluation. A typical open-loop frequency response is shown in Figure 8. The loops were adjusted for gain crossover at 100 Hz, giving phase margins from 35 to 63 degrees. A typical step response is shown in Figure 9. The loops show little overshoot and good settling time.

The sensitivity of the magnetic bearing system to external disturbances was quantified in two ways: interaction with the linear motor, and bench-top "bang." Linear motor interaction was measured by the transfer function from linear motor current to both effort and motion in all five degrees-of-freedom. The θ_z loop had a significantly larger effort response than any other loop. This is due to the fact that both the sensors which measure θ_z, and the actuators which produce the torque about the Z axis had to be mounted along one of the short axes of the translator while the inertia about the θ_z axis is along the long axis. This mismatch results in a significantly reduced torque capability in the θ_z loop, and presents an interesting lesson for the design of future magnetic bearing systems.

ORIGINAL PAGE IS
OF POOR QUALITY

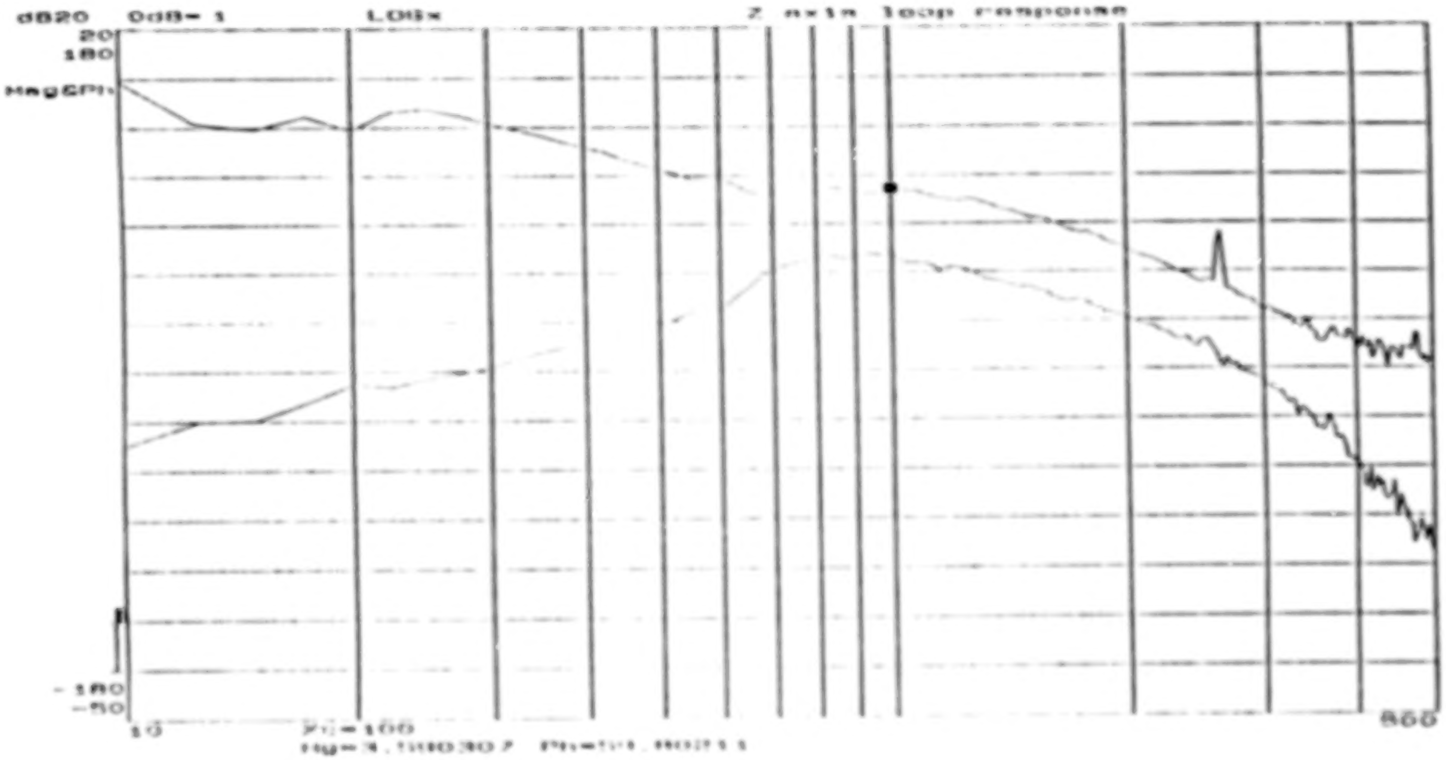

Figure 8. Open-Loop Frequency Response

The peak in the θ_y effort response occurs at about 95 Hz and is 18 volts/amp where saturation occurs at approximately 12 volts. The effort response does fall off rather quickly at both lower and higher frequencies, reaching 7 volts/amp at both 10 Hz and 200 Hz. The worst-case motion responses were 10 μ/amp in the Z loop and 0.2 mRad/amp in the θ_y loop.

ORIGINAL PAGE IS
OF POOR QUALITY

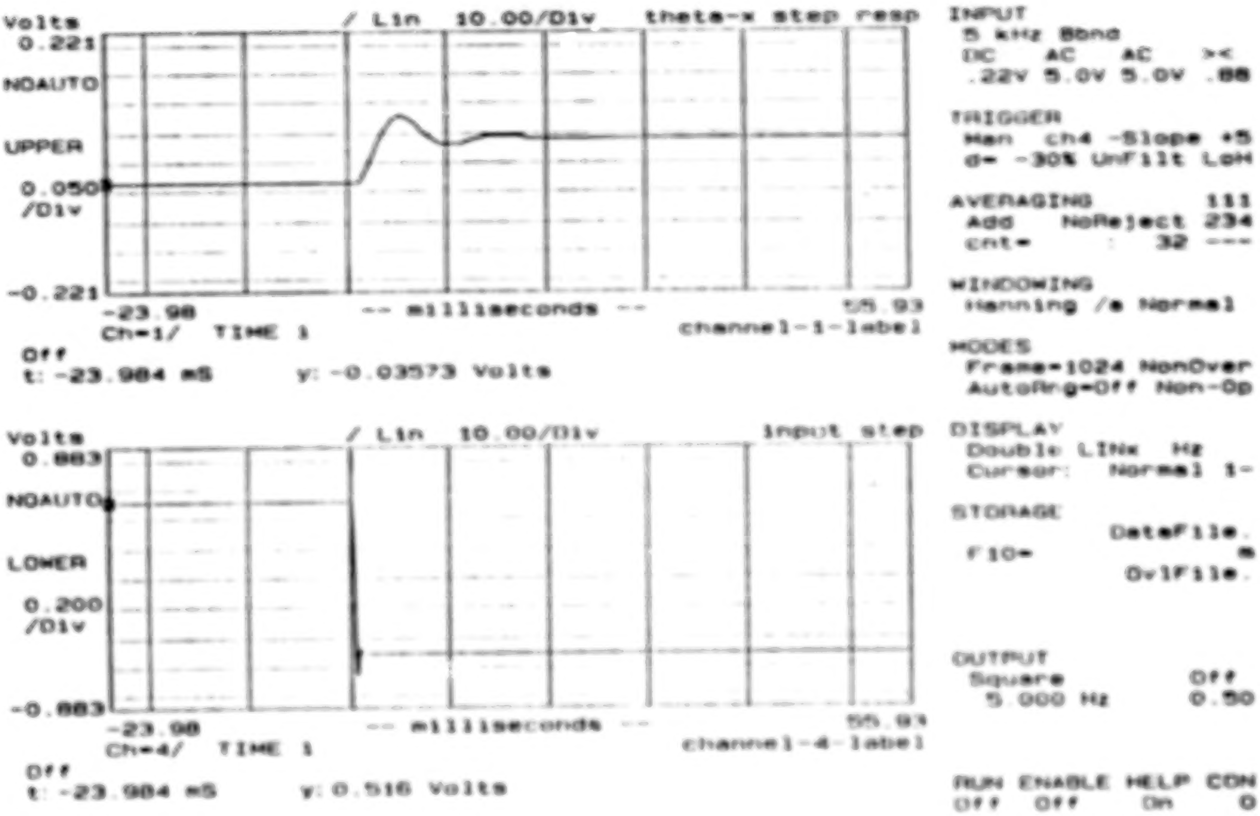

```
Off
t: -23.984 mS        y: -0.03573 Volts

Off
t: -23.984 mS        y: 0.516 Volts
```

```
INPUT
 5 kHz Bbnd
 DC    AC    AC    ><
 .22V 5.0V 5.0V  .88

TRIGGER
 Man  ch4 -Slope +5
 d= -30% UnFilt LoH

AVERAGING        111
 Add    NoReject 234
 cnt=     :   32 ---

WINDOWING
 Hanning /e Normal

MODES
 Frame=1024 NonOver
 AutoRng=Off Non-Op

DISPLAY
 Double LINx   Hz
 Cursor:   Normal 1-

STORAGE
             DataFile.
 F10=                =
              OvlFile.



OUTPUT
 Square          Off
  5.000 Hz       0.50


RUN ENABLE HELP CON
Off   Off    On    0
```

Figure 9. Step Response

A typical bench-top "bang" result is displayed by the displacement signals in the X and Z position loops in Figure 10. The range of the vertical axes on this plot represents the complete mechanical gap available for motion of the translator; thus, these plots show numerous collisions with the frame in the X axis. In all cases the loops recovered gracefully without significant overshoot.

ORIGINAL PAGE IS
OF POOR QUALITY

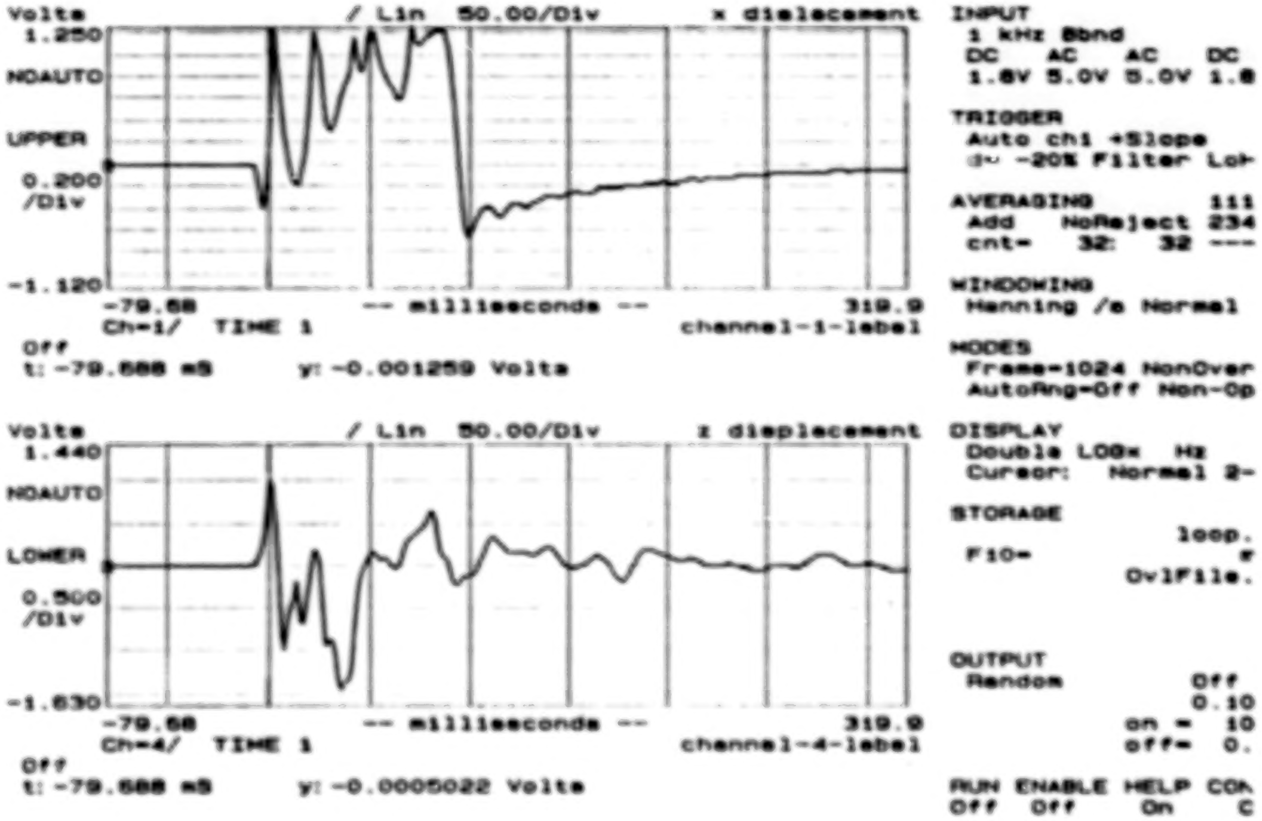

```
INPUT
 1 kHz Bbnd
 DC    AC    AC    DC
 1.6V 5.0V 5.0V 1.6
TRIGGER
 Auto ch1 +Slope
 d~ -20% Filter Lo-
AVERAGING          111
 Add   NoReject 234
 cnt-   32:   32 ---
WINDOWING
 Hanning /s Normal
MODES
 Frame-1024 NonOver
 AutoRng-Off Non-Op
DISPLAY
 Double LOGx  Hz
 Cursor:   Normal 2-
STORAGE
                 loop.
 F10-                r
              OvlFile.

OUTPUT
 Random          Off
                 0.10
              on =  10
              off=  0.
RUN ENABLE HELP COM
Off  Off    On    C
```

Figure 10. Bench-Top "Bang" Transient

5. CONCLUSIONS

The magnetic bearing control loops perform well, achieving 100 Hz nominal bandwidth with phase margins between 37 and 63 degrees. The lag in the actuator response from current to force produced by eddy-current losses introduces only 10 degrees of phase lag in the loop response at 100 Hz. The worst-case position resolution is 0.02 μ in the displacement loops and 1 μrad in the rotation loops. The system is very robust to shock disturbances, recovering smoothly even when collisions occur between the translator and frame. The start-up/shut-down circuit has proven very effective both in achieving initial levitation and in minimizing the "clunk" during turn-off.

The predominant shortcoming of the present system design is the gross mismatch between the center-of-mass of the translator and the center-of-effort of the magnetic actuators. This mismatch means that, in order to decouple the rotation loops from the displacement loops, some of the actuators must produce virtually no force. This restriction severely limits both the gain and the total force capability of the displacement loops. In addition, the large differences in actuator gains makes the process of adjusting the loop-decoupling very difficult. A system in which the center-of-mass was located close to the center-of-effort would be nearly inherently decoupled making any slight adjustment a trivial process. These effects should be considered in future system designs.

6. ACKNOWLEDGEMENTS

This work was performed for NASA, Goddard Space Flight Center under SBIR contract number NAS5-30309. The authors would like to acknowledge the guidance provided by John Sudey and Michael Hagopian of NASA.

7. REFERENCES

Downer, J.R., "Design of Large Angle Magnetic Suspensions," ScD Thesis, Massachusetts Institute of Technology, May 1986.

Hockney, R., and T. Hawkey, Magnetic Bearings for an Optical-Disk Buffer, SBIR Phase I Final Report. SatCon Technology Corp., R08-87, September 1987.

Roters, H., Electromagnetic Devices, New York: John Wiley & Sons, Inc., 1941.

Studer, P.A., Magnetic Bearings for Instruments in the Space Environment, NASA Technical Memorandum 78048, Goddard Space Flight Center, Greenbelt, Maryland, 1978.

N91-21196

FIVE DEGREE-of-FREEDOM CONTROL of an ULTRA-PRECISION MAGNETICALLY-SUSPENDED LINEAR BEARING

David L. Trumper
University of North Carolina at Charlotte
Department of Electrical Engineering
Charlotte
NC 28223

A.H. Slocum
Cranfield Institute of Technology
Cranfield Institute for Precision Engineering
Cranfield
Bedford MK43 0AL
England

Five-Degree-of-Freedom Control
# of an
Ultra-Precision Magnetically-Suspended Linear Bearing.

David L. Trumper
Dept. of Electrical Engineering
Univ. of N. Carolina at Charlotte
Charlotte, NC 28223

Alexander H. Slocum
Cranfield Unit for Prec. Eng.
Cranfield Inst. of Tech.
Cranfield, Bedford MK43 OAL
England

1 Introduction

Highly-precise positioning is important in many aerospace applications. Magnetic bearings represent an attractive approach for achieving this positioning. The authors have constructed a high precision linear bearing which represents the experimental implementation of an idea presented in [1]. This system has been investigated as part of the the first author's Ph.D. thesis [2].

A 10.7 kg platen measuring 125 mm by 125 mm by 350 mm is suspended and controlled in five degrees of freedom by seven electromagnets. Position of the platen is measured by five capacitive probes which have nanometer resolution. The suspension acts as a linear bearing, allowing linear travel of 50 mm in the sixth degree of freedom. In the laboratory this bearing system has demonstrated position stability of 5 nm peak-to-peak. This is believed to be the highest position stability yet demonstrated in a magnetic suspension system. Performance at this level confirms that magnetic suspensions can address motion control requirements at the nanometer level.

The experimental effort associated with this linear bearing system is described. Major topics are the development of models for the suspension, implementation of control algorithms, and measurement of the actual bearing performance. Suggestions for future improvement of the bearing system are given.

2 System Overview

The linear bearing system grew out of the Ångstrom Resolution Measuring Machine (ÅRMM) proposed in [1]. The operating principle of the ÅRMM is to suspend a platen using seven electromagnets such that the platen is capable of 50 mm travel in the direction of the long axis of the platen. Two such suspended platens are then arranged so that their long axes of travel are perpendicular and lie in a horizontal plane. In this manner a sample attached to one platen can be scanned by a probe attached to the second platen. Thus the sample can be scanned over a square area of length and width equal to the travel of the two platens.

In the current work, a single platen-suspension was built in order to demonstrate proof-of-concept for this system. The basic operating principles of the linear bearing suspension are described in the remainder of this section.

Three electromagnets act on the top surface of the platen and four electromagnets act on the sides of the platen. The three top electromagnets serve to control the platen's roll, pitch and vertical translation. Gravity is used to bias the suspension so as to supply force in the downward direction. The four side electromagnets are arranged in pairwise opposition, two on each side of the platen, so as to act in a push-pull fashion. These electromagnets control the platen's yaw and lateral translation. The sixth degree of freedom which is translation in the direction of the long axis of the platen is currently not controlled.

Since five platen degrees of freedom are controlled, five independent position measurements are required. This is achieved by locating capacitance probes in the center of each of the three top electromagnets and in the center of two side magnets. This arrangement allows the measurement of the five controlled platen degrees of freedom. Travel in the long axis of the platen is not measured in our implementation.

The platen consists of a hollow, rectangular-section steel tube, with dimensions of 125 mm by 125 mm by 350 mm. This tubular form was chosen to be compatible with the taut-wire inchworm driver proposed in [1] to effect travel in the long axis of the platen. This inchworm drive was not implemented in the current effort.

The manner in which the electromagnet forces act on the platen is shown in Figure 1. Here, each arrow represents the force applied by the corresponding electromagnet. This force is normal to the platen, and acts through the center of the electromagnet. The black dots in the figure indicate the locations at which the capacitance probes measure position.

A mechanical drawing of the platen is shown in Figure 2. It consists of a 5 inch square steel tube which was surface ground on all four faces for mechanical accuracy, nickel plated to prevent corrosion, and then annealed for better magnetic properties and dimensional stability. The platen weighs 10.7 kilograms.

The design uses one large electromagnet and six small electromagnets. Both types contain a permanent magnet as well as the electromagnet coil. The electromagnets are glued into aluminum blocks, which are then bolted to cast-iron support brackets on both sides of the platen. When not in suspension, the platen rests on a three-legged table referred to as the landing pad. The assembled system is shown in the mechanical drawings of Figures 3, 4, and 5. The 0.005" air gap between the platen and the bearing faces is too small to be seen in these views.

3 Linear Model

A linear model for the suspension dynamics is developed by first achieving active suspension through empirical tuning of the suspension controller as described in [2]. Once suspension is achieved, the magnet force linear parameters are measured through the experiment described in the next section. These linear parameters are then inserted into a linear dynamical model to yield the suspension linear model. This model is valid for small motions about the nominal operating point where the platen is centered between the electromagnets and centered in the axial degree of freedom.

3.1 Magnet Force Experiments

The force/position/current characteristics of the three top electromagnets are measured as follows. The platen is suspended at the nominal operating point (zero volts on each position probe), and the seven current drive bias potentiometers are adjusted so that the five modal control signals are approximately zero. That is, in this state, the DC component of current in each drive is supplied by the bias potentiometer setting. An additional mass is placed inside the platen, resting on the center of the bottom face of the interior of the platen. In this manner, the additional mass is directly below the platen center of mass. Thus, an additional force of Mg is applied to the platen, with no resulting torques about the platen center of mass. Four masses are used: 50, 100, 200, and 500 grams, respectively. For each mass value, the platen is cycled through a range of approximately $\pm 17\mu$m in vertical translation. At 20 points in this range, the three top magnet coil currents and the three top probe voltages are measured. The resulting data for the large top magnet shown in Figure 6. The data for the two small top electromagnets are similar and are not shown here.

The electromagnet force data is fitted in the least squares sense to the linearized force model

$$i = mx + cF + d, \tag{1}$$

or

$$F = \frac{1}{c}i - \frac{m}{c}x - \frac{d}{c}, \tag{2}$$

where F is the additional force applied to the magnet, i is the coil current, x is the probe voltage, and m, c, and d are constants to be determined by the least squares fit. Note that d represents the operating point bias current.

A small hysteresis effect is present in the magnet force curves. This results from hysteresis in the electromagnet and platen materials. Also, the curves do not form closed loops; this is due to the fact that the set of measurements for each loop required approximately 30 minutes to complete. For the development of the linearized model, the hysteresis is absorbed by the averaging process, as all data

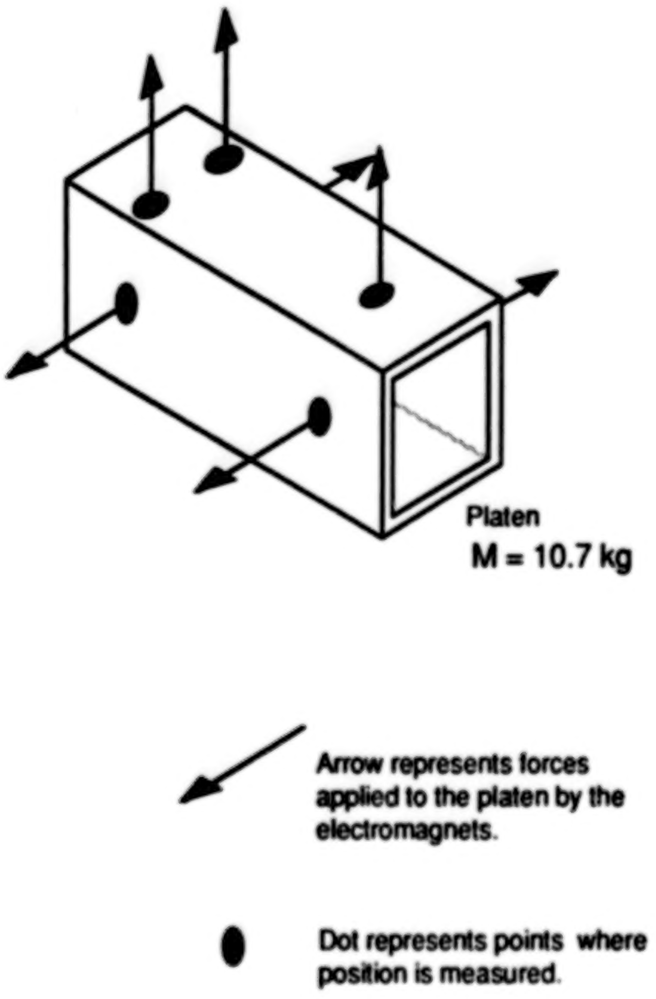
Platen
M = 10.7 kg
Arrow represents forces applied to the platen by the electromagnets.
Dot represents points where position is measured.

Figure 1: Schematic view of platen showing application of electromagnet forces and location of capacitance-probe position measurements.

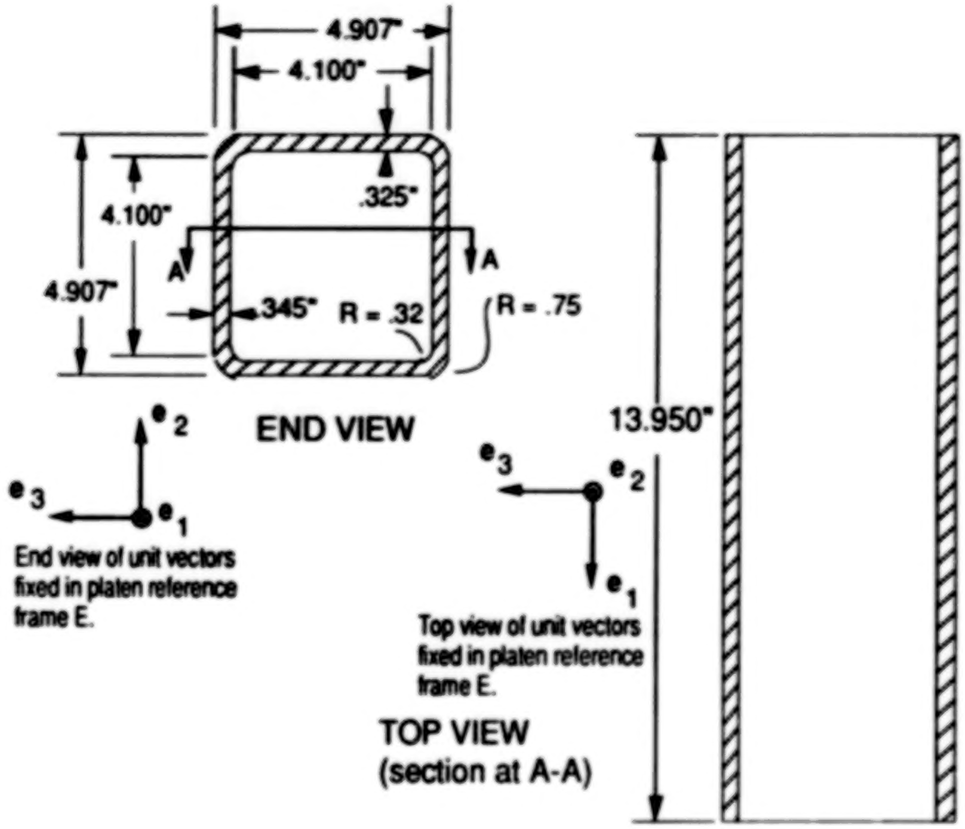
4.907"
4.100"
.325"
4.100"
4.907"
A
A
.345"
R = .32
R = .75
END VIEW
13.950"
e_2
e_3
e_1
End view of unit vectors fixed in platen reference frame E.
e_3
e_2
e_1
Top view of unit vectors fixed in platen reference frame E.
TOP VIEW (section at A-A)

Figure 2: Platen mechanical drawings. Body frame *E* coordinates are shown.

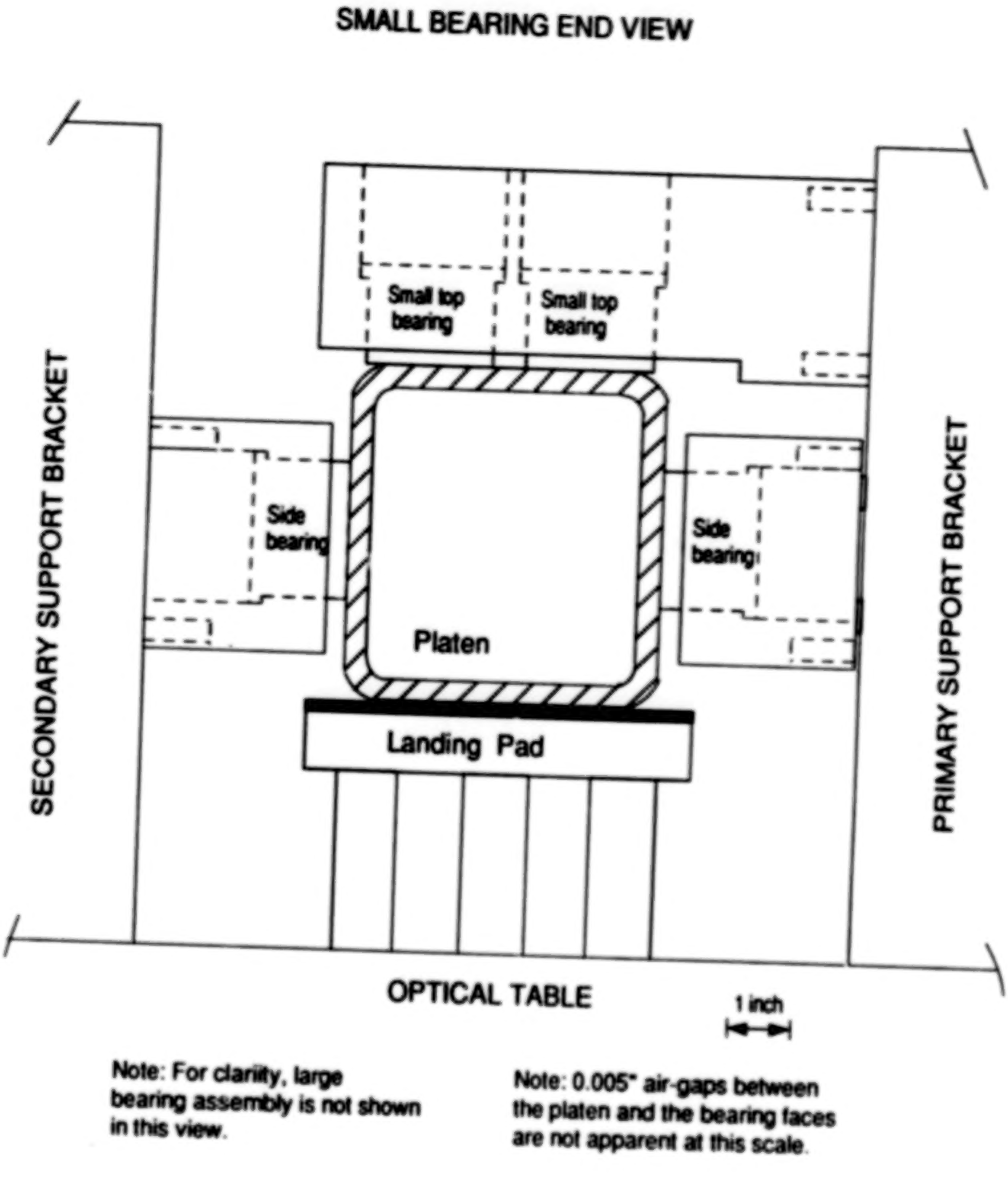
SMALL BEARING END VIEW
Small top bearing
Small top bearing
SECONDARY SUPPORT BRACKET
PRIMARY SUPPORT BRACKET
Side bearing
Side bearing
Platen
Landing Pad
OPTICAL TABLE
1 inch
Note: For clariity, large bearing assembly is not shown in this view.
Note: 0.005" air-gaps between the platen and the bearing faces are not apparent at this scale.

Figure 3: Suspension system small bearing end view.

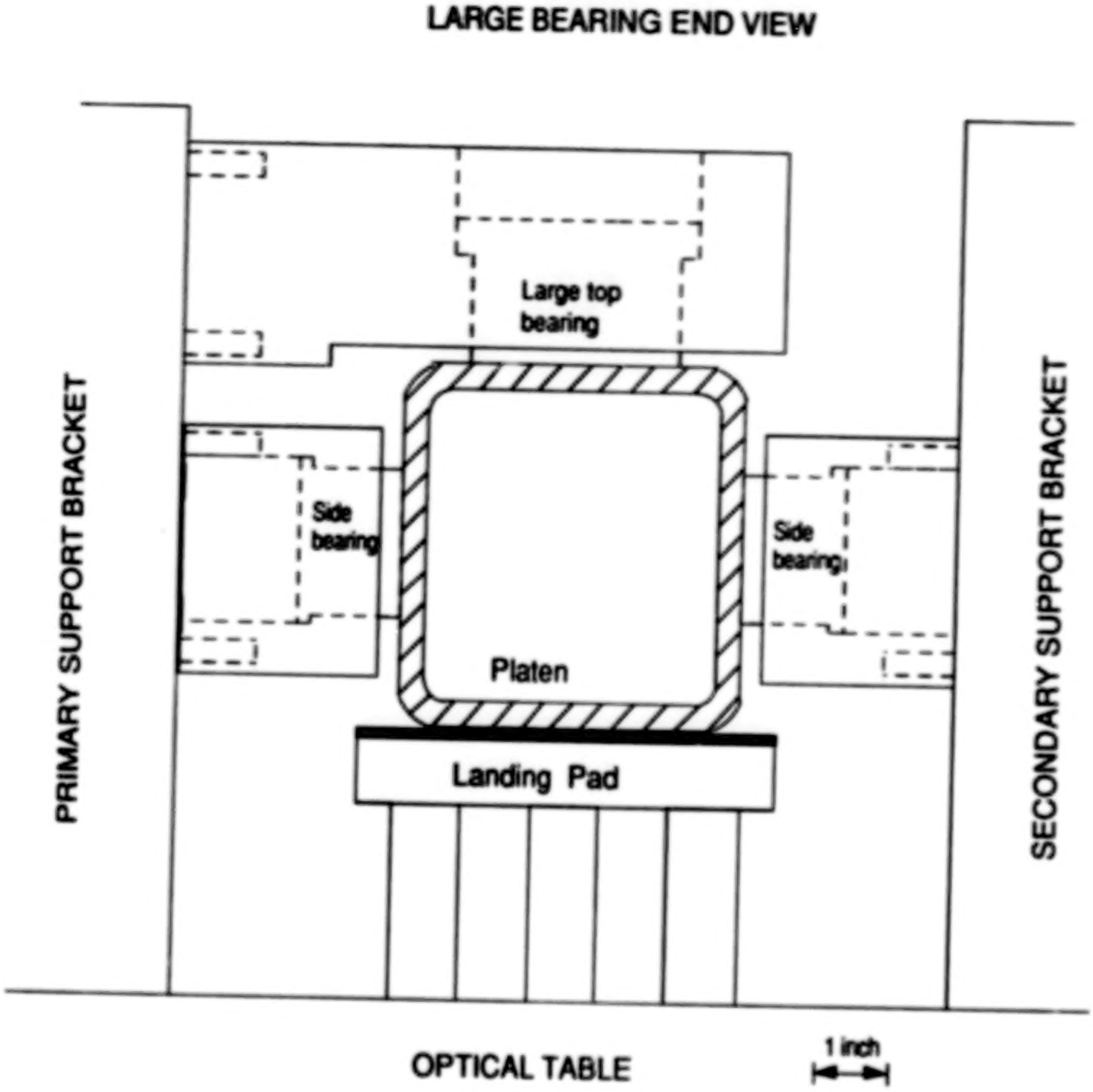
LARGE BEARING END VIEW
Large top bearing
Side bearing
Side bearing
Platen
Landing Pad
PRIMARY SUPPORT BRACKET
SECONDARY SUPPORT BRACKET
OPTICAL TABLE
1 inch

Note: For clarity,small bearing assembly is not shown in this view.

Note: 0.005" air-gaps between the platen and the bearing faces are not apparent at this scale.

Figure 4: Suspension system large bearing end view.

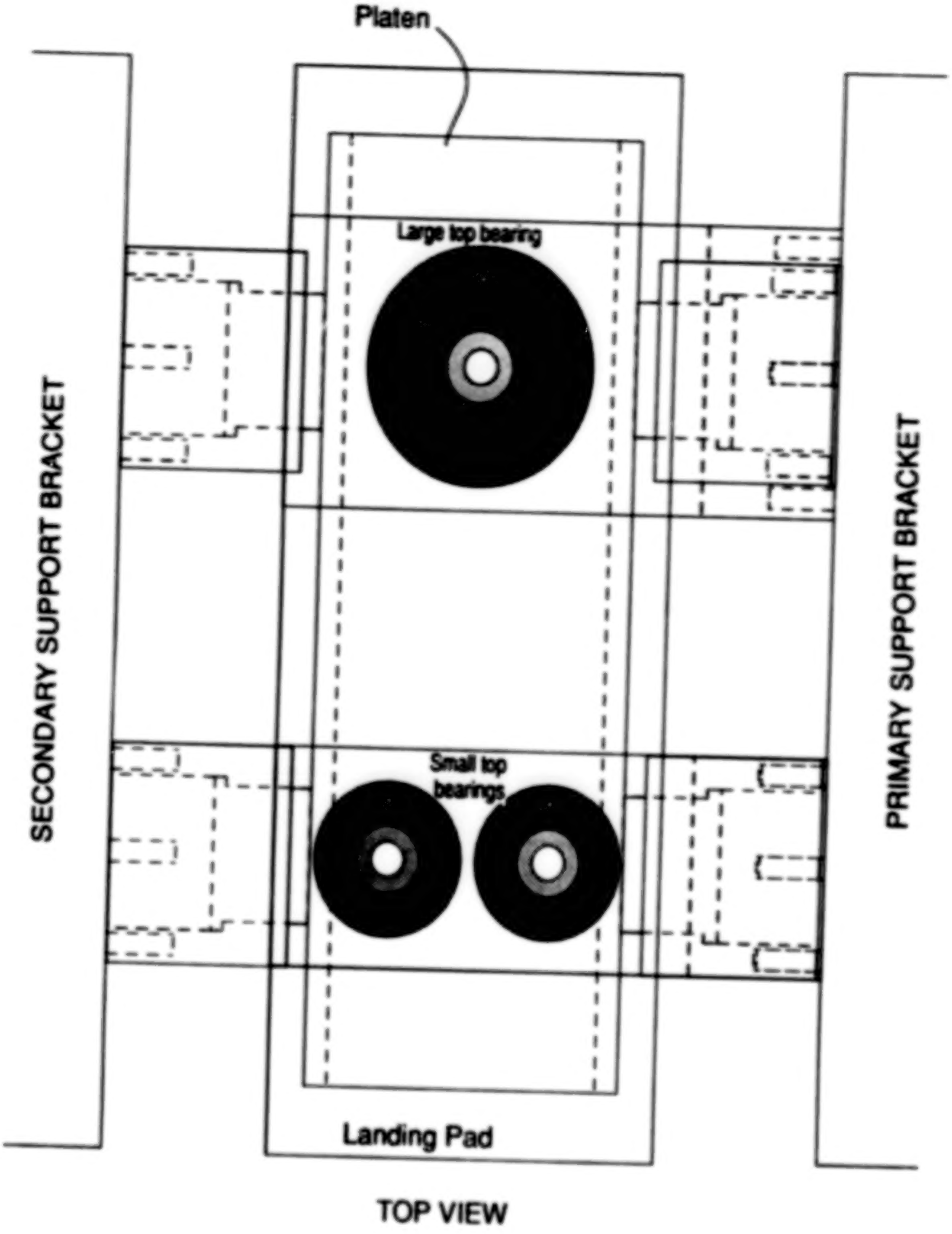
Platen
Large top bearing
Small top bearings
SECONDARY SUPPORT BRACKET
PRIMARY SUPPORT BRACKET
Landing Pad
TOP VIEW

Figure 5: Suspension system top view.

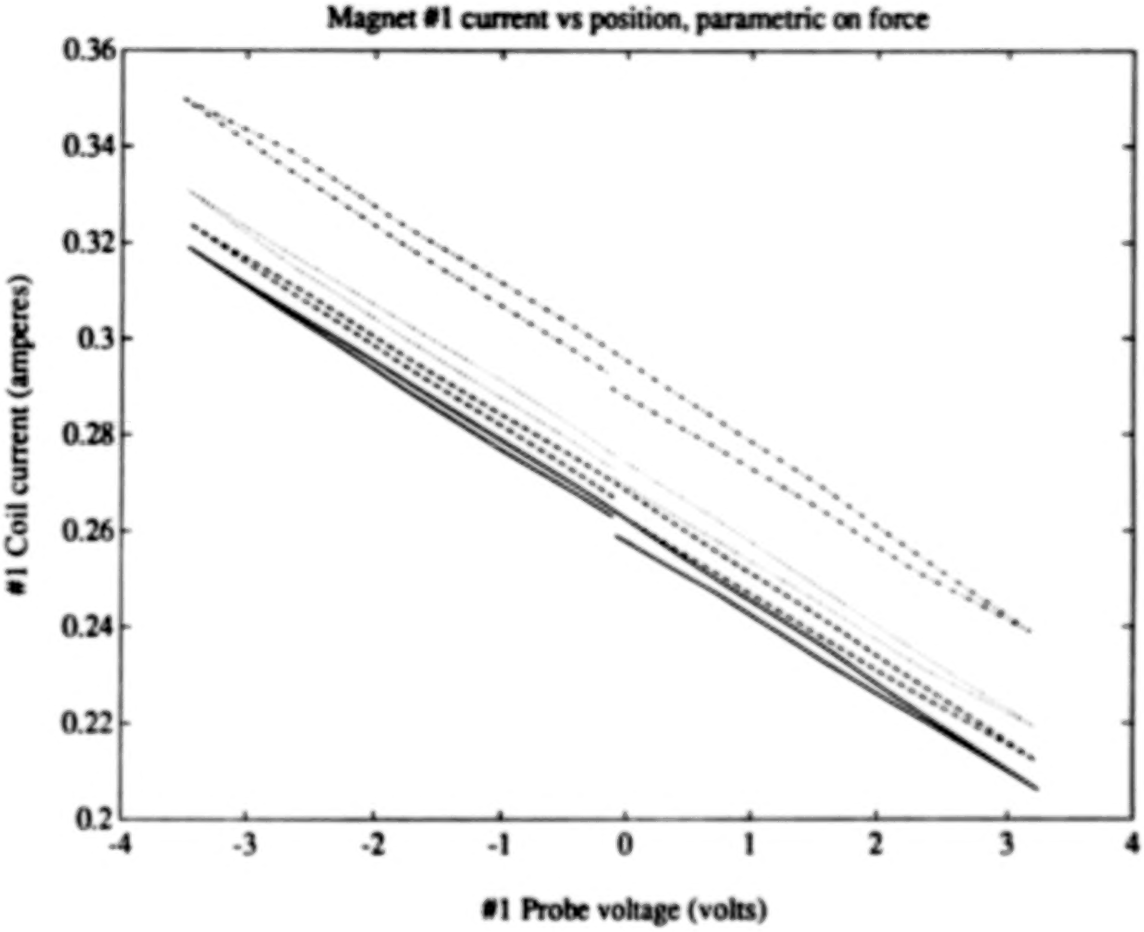

Figure 6: Magnet #1 (large) coil current vs. position probe voltage, for four additional mass values: 50, 100, 200, and 500 grams respectively from bottom to top.

points are given equal weight in the least squares fit. This is equivalent to taking the centerline of the hysteresis curve.

Two models are developed, one for the large magnet and one for the small magnets. The two top magnets are assumed to be identical, and their characteristics are averaged before fitting parameters. Note that the large magnet carries half the additional load, and each of the small magnets carry one fourth of the additional load. For the large magnet, the least squares fit is given by the parameters $m = -1.68 \times 10^{-2}$ amps/volt, $c = 1.36 \times 10^{-4}$ amps/gram, and $d = 2.58 \times 10^{-1}$ amps. For the small magnet, the least squares fit is given by the parameters $m = -1.94 \times 10^{-2}$ amps/volt, $c = 2.81 \times 10^{-4}$ amps/gram, and $d = 5.04 \times 10^{-1}$ amps.

For the purposes of control, the magnet linear force models are represented by $\hat{F}_j = k_i \hat{i}_j + k_x \hat{x}_j$ where $\hat{F}_j$, $\hat{i}_j$, and $\hat{x}_j$ are the j^{th} electromagnet incremental force, current, and air-gap, respectively. The constants k_i and k_x are determined from the force measurements. For the large magnet this yields $k_{il} = 7.21 \times 10^1$ Newtons/amp, and $k_{xl} = 2.38 \times 10^5$ Newtons/meter. For the small electromagnet, $k_{is} = 3.49 \times 10^1$ Newtons/amp, and $k_{xs} = 1.33 \times 10^5$ Newtons/meter. Here, the subscripts l and s are appended to indicate the large and small electromagnets respectively.

Experiments similar to those described above were also conducted to measure the magnet torques exerted on the platen [2]. These torque terms were then included in the dynamic model.

Since the four lateral magnets are operated at approximately the same bias currents and air gaps as the two small top magnets, the parameters developed here apply to the lateral magnets as well.

A dynamic analyzer was used to measure the suspension transfer functions. The measured transfer functions had a higher roll-off rate at high frequencies than would be predicted by just Newton's law, i.e., greater than $1/\omega^2$. It was found to be necessary to add a pair of poles to the model to match this roll-off. These poles have time constants of 0.6 and 0.2 msec respectively and are included in series with each coil current.

The platen mass is 10.7 kg. Its moments of inertia are calculated as $I_1 = 4.76 \times 10^{-2}$ kg m^2, $I_2 = 1.37 \times 10^{-1}$ kg m^2, and $I_3 = 1.35 \times 10^{-1}$ kg m^2 about the $\mathbf{e}_1$, $\mathbf{e}_2$, and $\mathbf{e}_3$ axes respectively. All suspension magnets are axially displaced from the platen center of mass by a distance $L_m = 92.1$mm. The two top electromagnets are also laterally displaced by a distance $W_m = 31.8$mm.

Using this information and the magnet force models developed above yields the suspension state equations. The vertical and lateral dynamics are essentially uncoupled. That is, vertical translation, roll and pitch motions which are controlled by the three top electromagnets, are essentially decoupled from lateral translation and yaw motions which are controlled by the four side magnets. The control design issues for the two decoupled systems are thus considered independently. In the remainder of this report we focus on the vertical system. For similar issues addressed in the control of the lateral system see [2].

The suspension state equations for the vertical dynamics are

$$\dot{\mathbf{w}}_v = A_v \mathbf{w}_v + B_v \mathbf{i}_v \tag{3}$$

$$\mathbf{y}_v = C_v \mathbf{w}_v \tag{4}$$

where $\mathbf{w}_v = [\, w_{v1}\ w_{v2}\ w_{v3}\ w_{v4}\ w_{v5}\ w_{v6}\ \hat{q}_1\ \hat{q}_3\ \hat{x}_2\ \hat{u}_1\ \hat{u}_3\ \hat{u}_5 \,]^T$, $\mathbf{i}_v = [\, \hat{i}_1\ \hat{i}_2\ \hat{i}_3 \,]^T$, and $\mathbf{y}_v = [\, \hat{q}_1\ \hat{q}_3\ \hat{x}_2 \,]^T$. Here, $w_{v1} \cdots w_{v6}$ are states associated with the high-frequency poles, $\hat{q}_1$ is incremental rotation in radians about the $\mathbf{e}_1$ axis, $\hat{q}_3$ is incremental rotation in radians about the $\mathbf{e}_3$ axis, and $\hat{x}_2$ is incremental translation in meters in the $\mathbf{e}_2$ axis. State variables $\hat{u}_1$, $\hat{u}_3$, and $\hat{u}_5$ are rotational and linear velocities given by the time derivatives of $\hat{q}_1$, $\hat{q}_3$, and $\hat{x}_2$, respectively. Currents i_1, i_2, and i_3 are the coil currents in the single large and two small top electromagnets, respectively. The numerical values of the system matrices A_v, B_v, C_v, and D_v are given in the Appendix.

4 Controller Design

The controller design is based upon the linear suspension state equations given in the previous section. The controller is designed to decouple modal motions about the principal axes of the platen and is implemented in analog electronics. Only the vertical system controller is presented here.

The modal controller design includes a network at the input of the plant which serves to convert from modal control signals to individual current setpoints and a network at the output of the plant which converts from the individual probe voltages to signals which represent the modal motions. A block diagram showing this control architecture is given in Figure 7. All the data paths carry three-vectors, although they are shown as single lines in the figure.

The open-loop suspension dynamics, current-drive dynamics and controller dynamics are given by their associated system matrices. The matrix T_{py} transforms the platen position y into the probe voltages v_p. The matrix T_{mp} transforms the the probe voltages v_p into voltages v_m which represent motions in the roll, pitch and vertical translation modes. The voltages v_m are subtracted from the modal setpoints v_s to give the modal errors v_e. These three errors are processed by three independent modal controllers to give the control voltages v_u which represent drives to the three modes. The matrix T_{iu} transforms the control voltages v_u into voltages v_i which control the current setpoints for the three current drives. The current drives establish currents i which act as inputs to the plant, thereby driving the platen position y.

The position probes have a sensitivity of 5 volts per 0.001" or 1.97×10^5 volts per meter, increasing as the air gap decreases. Thus the matrix T_{py} is given by

$$T_{py} = 1.97 \times 10^5 T_{gy} = \begin{bmatrix} 0 & -1.81 \times 10^4 & 1.97 \times 10^5 \\ 6.25 \times 10^3 & 1.81 \times 10^4 & 1.97 \times 10^5 \\ -6.25 \times 10^3 & 1.81 \times 10^4 & 1.97 \times 10^5 \end{bmatrix} \tag{5}$$

where T_{gy} transforms from the suspension position to the three probe air-gaps, and is given by

$$T_{gy} = \begin{bmatrix} 0 & -L_m & 1 \\ W_m & L_m & 1 \\ -W_m & L_m & 1 \end{bmatrix} = \begin{bmatrix} 0 & -0.0921 & 1 \\ 0.0318 & 0.0921 & 1 \\ -0.0318 & 0.0921 & 1 \end{bmatrix} \tag{6}$$

The matrix T_{mp} is defined as

$$T_{mp} = \begin{bmatrix} 0 & 0.5 & -0.5 \\ -0.5 & 0.25 & 0.25 \\ 0.5 & 0.25 & 0.25 \end{bmatrix} \tag{7}$$

The relative scaling of the elements in the array is dictated by the suspension geometry. The absolute levels are chosen so that the voltages v_m saturate[1] only when all three probe outputs are saturated. The transformation T_{mp} is implemented in op-amp circuitry as shown in Figure 8.

The matrix T_{iu} is defined as

$$T_{iu} = \begin{bmatrix} 0 & -1 & 1 \\ 1 & 1 & 1 \\ -1 & 1 & 1 \end{bmatrix} \tag{8}$$

The relative scaling of the elements in the array is dictated the ratio of the large and small magnet current constants. That is, the magnitude ratio of the 1-2 and 1-3 entries to the 2-2, 3-2, 2-3, and 3-3 entries is equal to $2 * k_{is}/k_{il}$ which is approximately equal to unity. The absolute levels are chosen so that the entries are of unity magnitude. This allows an easier circuit implementation and is such that a single modal control signal can saturate the current drives. The transformation T_{iu} is implemented in op-amp circuitry as shown in Figure 9.

4.1 Current drive implementation

The current drive circuit implementation is shown in Figure 10. Current is sensed with a 1 Ω power resistor, and controlled via the IRF510 power FET. The coil is protected with a 2 amp fuse, and the series combination of the MUR1560 diode and 5 Ω resistor form a flyback network to allow coil current to continue to flow even when the FET is turned off suddenly. The 0.01 μF capacitor connected between the FET drain and ground is empirically selected to damp a closed-loop oscillation at about 500 kHz. A shown in the schematic, the +12 return, analog ground, and chassis ground are connected at only one point, in order to ensure that no coil currents flow in the analog ground; the common point is at the ground end of the current sense resistor. In parallel with the [illegible] current sense resistor, a 50 μA meter in series with a 37.5 kΩ resistor provides a front-panel indication of coil current.

---

[1] The probe outputs and the op amps used to implement these coordinate transformations saturate at about ±13 volts.

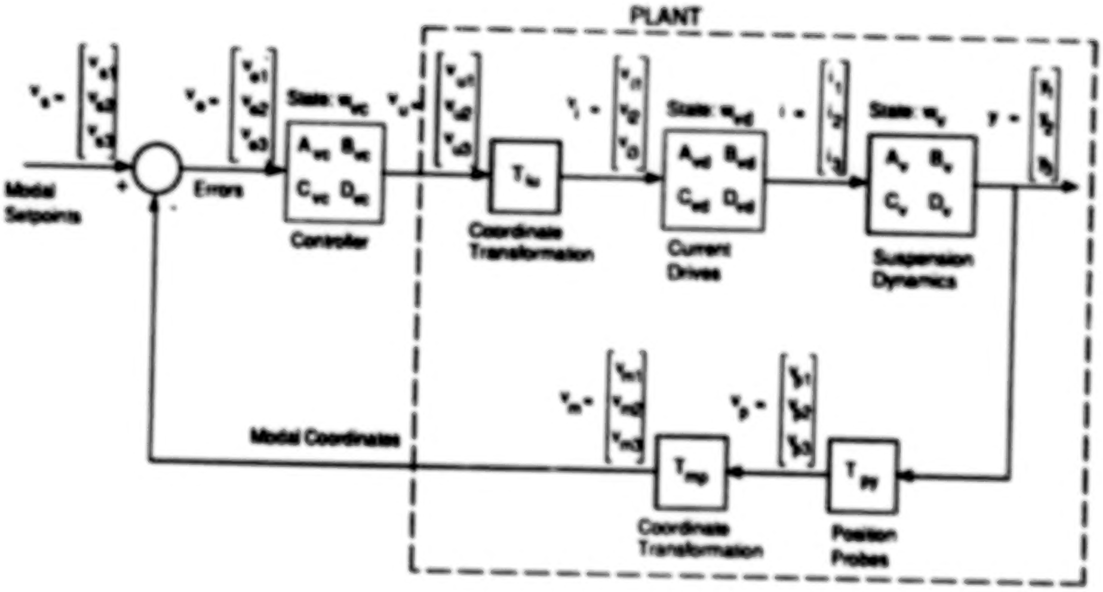
PLANT
Modal Setpoints
+
-
Errors
State: w
Controller
Coordinate Transformation
Current Drives
Suspension Dynamics
Modal Coordinates
Coordinate Transformation
Position Probes

Figure 7: Block diagram for the vertical control loop.

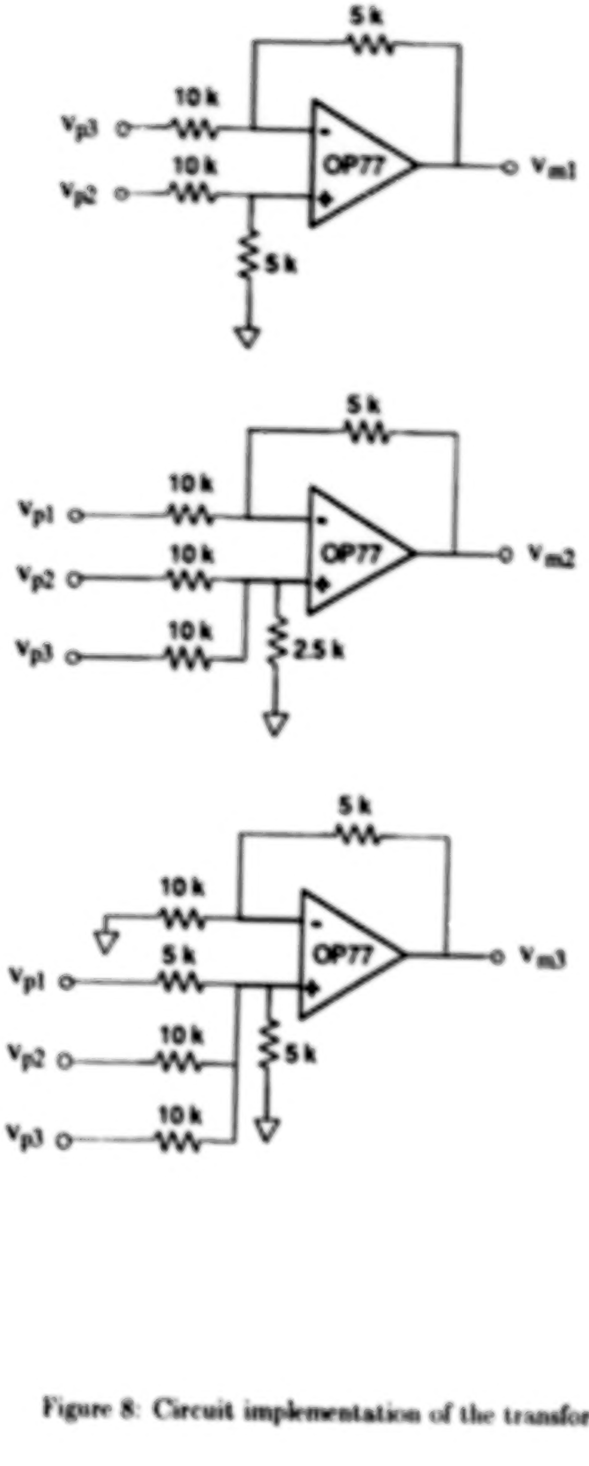
5 k
10 k
Vp3
10 k
Vp2
OP77
Vm1
5 k
5 k
10 k
Vp1
10 k
Vp2
OP77
Vm2
10 k
Vp3
2.5 k
5 k
10 k
5 k
Vp1
OP77
Vm3
10 k
Vp2
5 k
10 k
Vp3

Figure 8: Circuit implementation of the transformation T_{mp}.

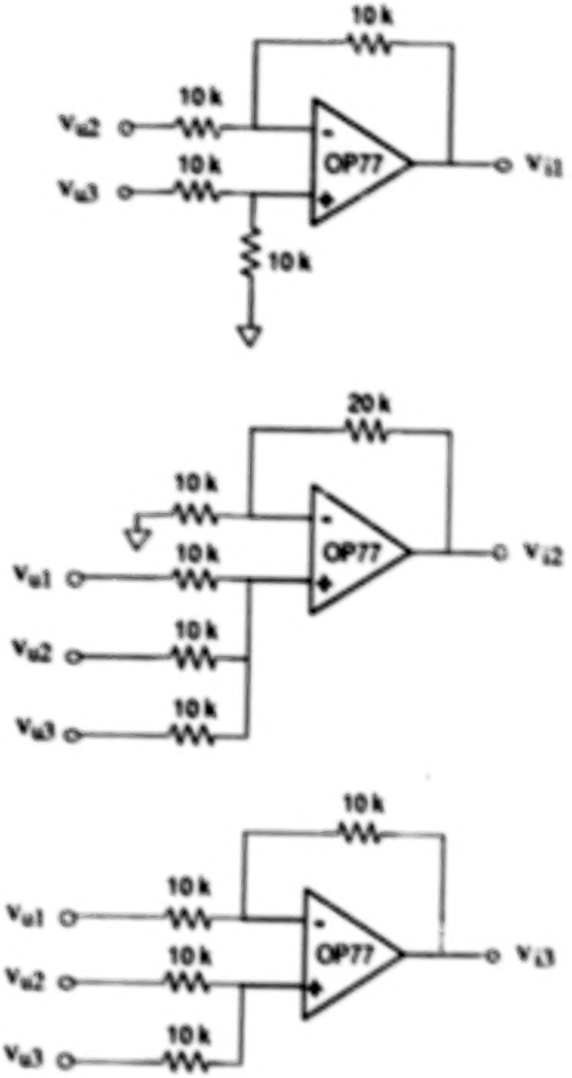
10k
Vu2
10k
Vu3
OP77
Vi1
10k
20k
10k
10k
Vu1
OP77
Vi2
10k
Vu2
10k
Vu3
10k
10k
Vu1
OP77
Vi3
10k
Vu2
10k
Vu3

Figure 9: Circuit implementation of the transformation T_{iu}.

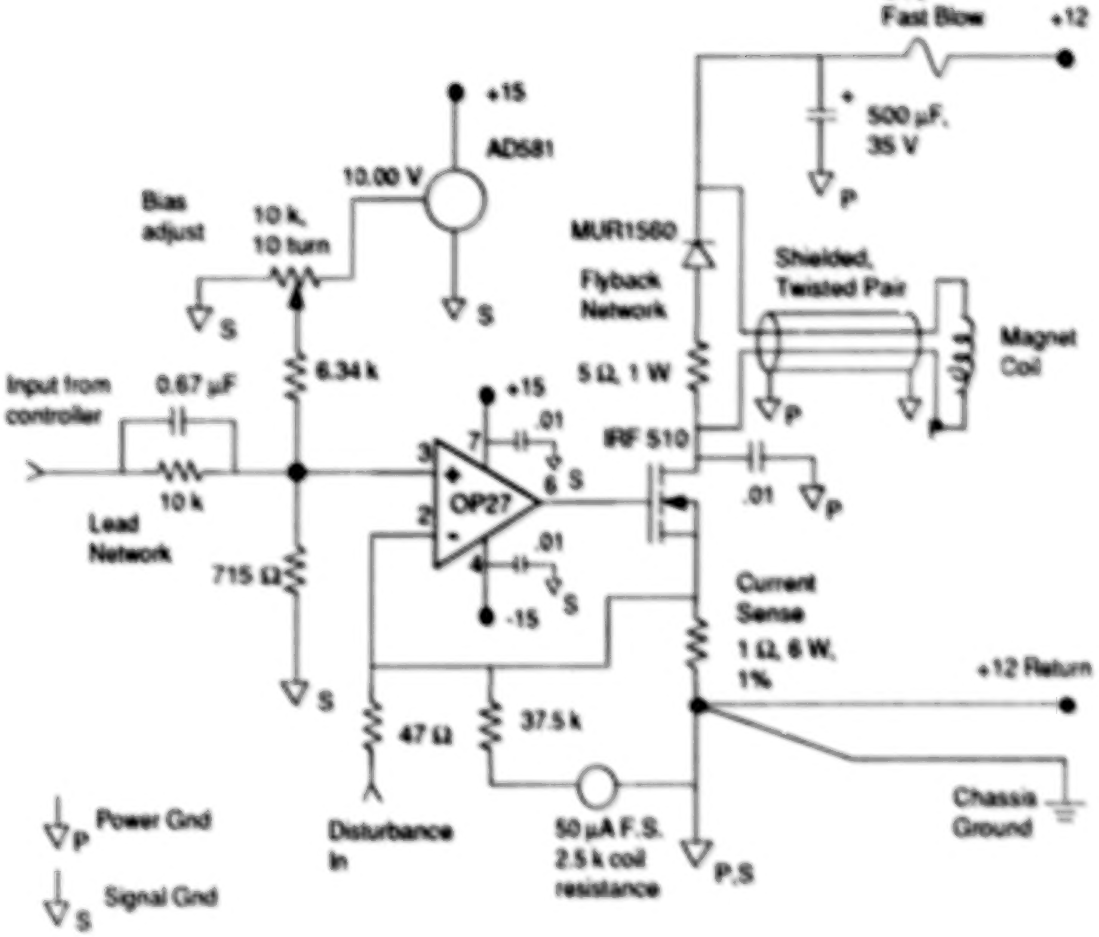
2 A,
Fast Blow
+12
+15
AD581
+
500 µF,
35 V
P
10.00 V
Bias
adjust
10 k,
10 turn
MUR1560
Shielded,
Twisted Pair
Flyback
Network
S
S
Magnet
Coil
5 Ω, 1 W
P
Input from
controller
0.67 µF
6.34 k
+15
.01
IRF 510
7
3
+
S
6
OP27
10 k
Lead
Network
2
-
.01
.01
P
4
715 Ω
S
Current
Sense
-15
1 Ω, 6 W,
1%
+12 Return
S
47 Ω
37.5 k
Chassis
Ground
P
Power Gnd
Disturbance
In
50 µA F.S.
2.5 k coil
resistance
P,S
S
Signal Gnd

Figure 10: Current source for driving electromagnets.

The OP-27 op amp is used as the current controller for its low noise (especially in the 0.1–10 Hz band), high slew rate, and wide frequency response. The network at the noninverting input allows setting the DC current level through a 10 kΩ, 10 turn potentiometer, and couples current input signals through a lead network with a DC attenuation of 15, and unity gain at high frequencies. This lead network is included here because all anticipated position controller designs require lead compensation in the vicinity of crossover, and this allowed saving an additional stage in the position controller circuitry. Such savings are important, as five position control channels need to be constructed.

With the input attenuation of 15 and the 1 Ω current sense resistor, the amplifier has a closed-loop response of 15 Volts input per ampere of coil current output. The 47 Ω resistor at the inverting input of the OP-27 allows the injection of disturbances into the current loop and is of the correct resistance to be driven by a standard signal generator. An AD581 voltage reference supplies 10 Volts to bias the upper end of the potentiometer.

The large magnet has a coil resistance $R_{cl} = 4.4\ \Omega$, and inductance $L_{cl} = 48$ mH at the nominal operating point. The small magnet has a coil resistance $R_{cs} = 2.9\ \Omega$, and inductance $L_{cs} = 19$ mH at the nominal operating point.

Including the lead compensation term, each of the current drives has a transfer function from input v_{ij} to output i_j given by

$$\frac{i_j(s)}{v_{ij}(s)} = \frac{1}{\alpha}\frac{\alpha\tau s + 1}{\tau s + 1} \tag{9}$$

where $\alpha = 15$ and $\tau = 4.47 \times 10^{-4}$. Combining the three vertical system current drives in parallel yields the current source system equations as

$$\begin{aligned} \dot{w}_{vd} &= A_{vd}w_{vd} + B_{vd}v_i & (10) \\ i &= C_{vd}w_{vd} + D_{vd}v_i & (11) \end{aligned}$$

where

$$\begin{aligned} A_{vd} &= \mathrm{diag}(-2.24 \times 10^3,\ -2.24 \times 10^3,\ -2.24 \times 10^3) & (12) \\ B_{vd} &= \mathrm{diag}(1,\ 1,\ 1) & (13) \\ C_{vd} &= \mathrm{diag}(-2.09 \times 10^3,\ -2.09 \times 10^3,\ -2.09 \times 10^3) & (14) \\ D_{vd} &= \mathrm{diag}(1,\ 1,\ 1) & (15) \end{aligned}$$

For the purposes of design, the region contained within the dashed line in Figure 7 is considered to be the plant which is controlled by the controller. Combining all the information developed above yields the plant system matrices as

$$\begin{aligned} \dot{w}_{vp} &= A_{vp}w_{vp} + B_{vp}v_u & (16) \\ v_m &= C_{vp}w_{vp} + D_{vp}v_u & (17) \end{aligned}$$

where $w_{vp} = [\ w_v'\ w_{vd}'\ ]'$ and

$$A_{vp} = \begin{bmatrix} A_v & B_vC_{vd} \\ 0 & A_{vd} \end{bmatrix} \tag{18}$$

$$B_{vp} = \begin{bmatrix} B_vD_{vd}T_{iu} \\ B_{vd}T_{iu} \end{bmatrix} \tag{19}$$

$$C_{vp} = [\ T_{mp}T_{py}C_v \quad 0\ ] \tag{20}$$

$$D_{vp} = [0] \tag{21}$$

where the indicated zero blocks are of the appropriate dimensions.

The three vertical system controllers take the form of lag-compensators. Lag compensation is used to develop higher disturbance rejection. Recall that the current drives already implement lead compensation; the lead term is necessary in order to stabilize the loops. The controllers use lag networks with a lag factor of only ten. This does not allow as good disturbance rejection as controllers which place the lag pole at the origin by using an integrator. However it is very difficult to initialize the suspension if integrators are used in the compensator. This difficulty is due to integrator windup. In the future, the best solution is to use a dual-mode controller which gates-out an integral term until the suspension is initialized.

The controllers are designed under the assumption that the plant is decoupled. That is, the roll controller is designed to control the transfer function $v_{m1}(s)/v_{u1}(s)$, the pitch controller is designed to control the transfer function $v_{m2}(s)/v_{u2}(s)$, and the heave controller is designed to control the transfer function $v_{m3}(s)/v_{u3}(s)$. All three controllers take the form of lag compensators designed for a 100 Hz crossover.

The controller designs are

$$\frac{v_{ui}(s)}{v_{ei}(s)} = k_i \frac{\tau_a s + 1}{\tau_b s + 1} \qquad i = 1, 2, 3 \tag{22}$$

where τ_a = 9.1 milliseconds, τ_b = 100 milliseconds, $k_1 = 111$, $k_2 = 17$, and $k_3 = 12$. The circuit implementation of the transfer functions (22) is shown in Figure 11.

The only difference among the three controllers is in the value of the DC gain which is set by the resistor R_i'. The roll controller has $R_1' = 1$ k, the pitch controller has $R_2' = 6.5$ k, and the heave controller has $R_3' = 9.6$ k, as shown in the figure.

The compensation of the three loops is similar and thus only the roll loop will be presented. The loop-transmission in roll is shown in Figure 12 and the predicted step-response in roll is shown in Figure 13. The measured roll step response shown in Figure 14 matches the predicted response very closely. Specifically, the time from the beginning of the step to the first peak is about 5 msec in both the predicted and measured responses, and the peak-overshoot value is about 1.75 times the final value. The step response was averaged on a digital oscilloscope to reduce the noise background.

The large overshoot in the step response is due primarily to the inclusion of the lead compensation in the loop forward path. This overshoot could be reduced by preceding the loop with a command pre-filter, or more simply, by including the lead compensation in the feedback path. Since the lead network has a DC gain of unity, this option would not compromise low-frequency position accuracy.

The second trace in Figure 14 shows the cross-coupling into the platen pitch motion. The pitch response is not symmetric with respect to the two step edges; this indicates that even at these small signal-levels, nonlinear terms are significant.

Note that when the step in roll occurs, the initial cross-coupling transient is toward positive pitch in both cases. This observation can be explained by the nonlinearity in electromagnet force as a function of current. At the edge of the step-command in roll, the currents in the two small top electromagnets are driven differentially away from their operating point values. For steps where the air-gaps change by as little as 50 nm, the initial current transients have magnitudes of several tenths of an Ampere.

This is a large variation relative to the operating point current of 0.5 Ampere. Since the electromagnet force varies as i^2, symmetrically increasing and decreasing the small top electromagnet currents will result in a net *increase* in the sum of the two electromagnet forces. This increase is independent of the direction of the roll step. Increased force from the small electromagnets drives the platen in the positive pitch direction. Thus the initial transient will be in the direction of increasing pitch independent of the direction of the step in roll.

As before, including a command prefilter, or placing the lead compensation in the feedback path will greatly reduce the magnitude of the transient currents and thereby the magnitude of the nonlinear cross-coupling. This effect can also be overcome even for large steps by including nonlinear compensation laws in the controller which invert the electromagnet nonlinearity [3].

5 Position Stability

The closed-loop system has demonstrated 5 nm position stability. However, due to a flaw in the electronics of the position probes, this stability can be demonstrated only in three degrees of freedom. If more than three of the capacitance probes are used simultaneously, a very significant cross-talk between the channels results.

The five position probes operate by sensing a capacitance which varies with the spacing between the probe and platen. The five probes are inserted and glued into the central hole in the three top electromagnets and in the two primary side electromagnets. By this arrangement, motion can be measured in

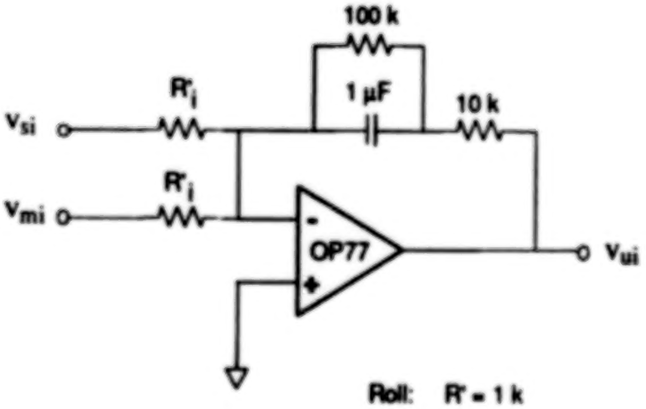
100 k
R'i
1 µF
10 k
vsi
R'i
vmi
-
OP77
+
vui

Roll: R' = 1 k

Pitch: R' = 6.5 k

Heave: R' = 9.6 k

Figure 11: Vertical controller circuit implementation.

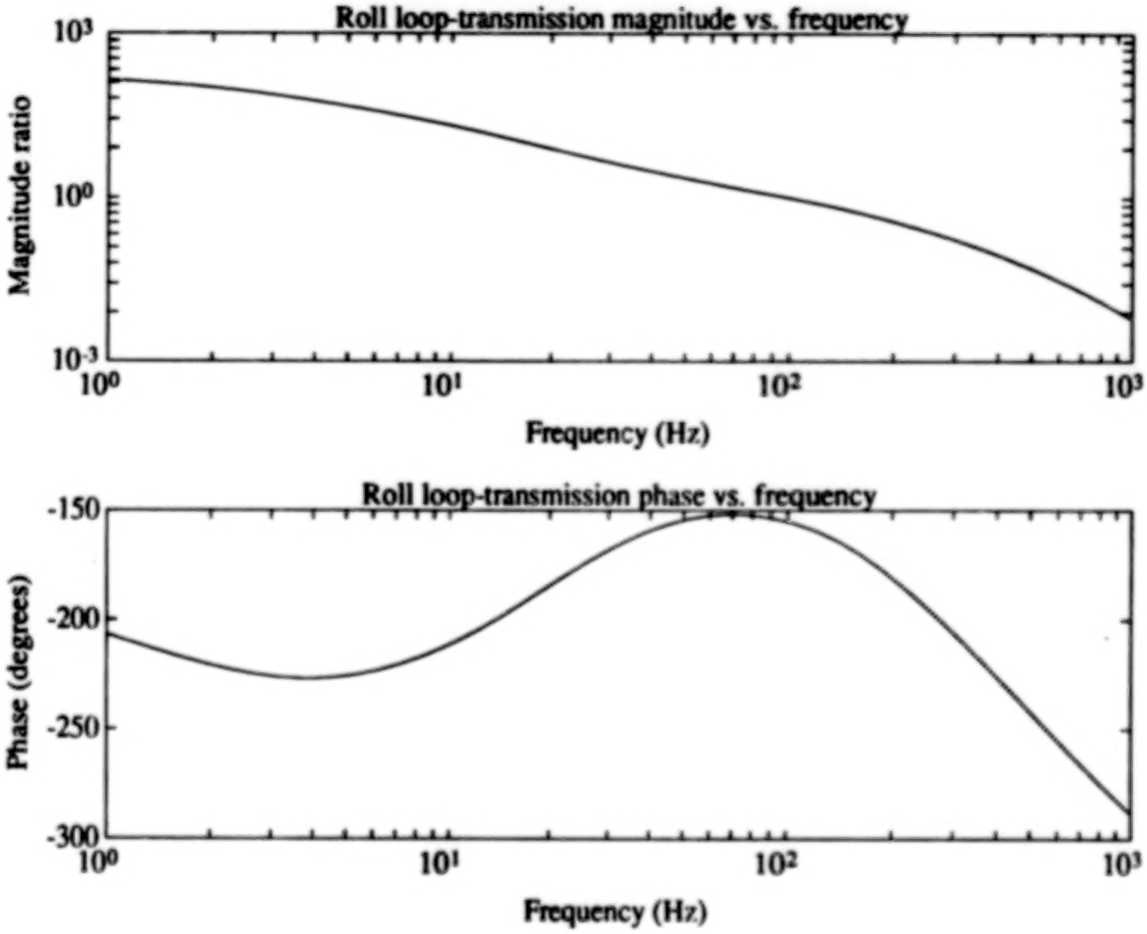

Figure 12: Roll loop-transmission $v_{m1}(s)/v_{e1}(s)$ magnitude and phase versus frequency. Crossover is at 100 Hz.

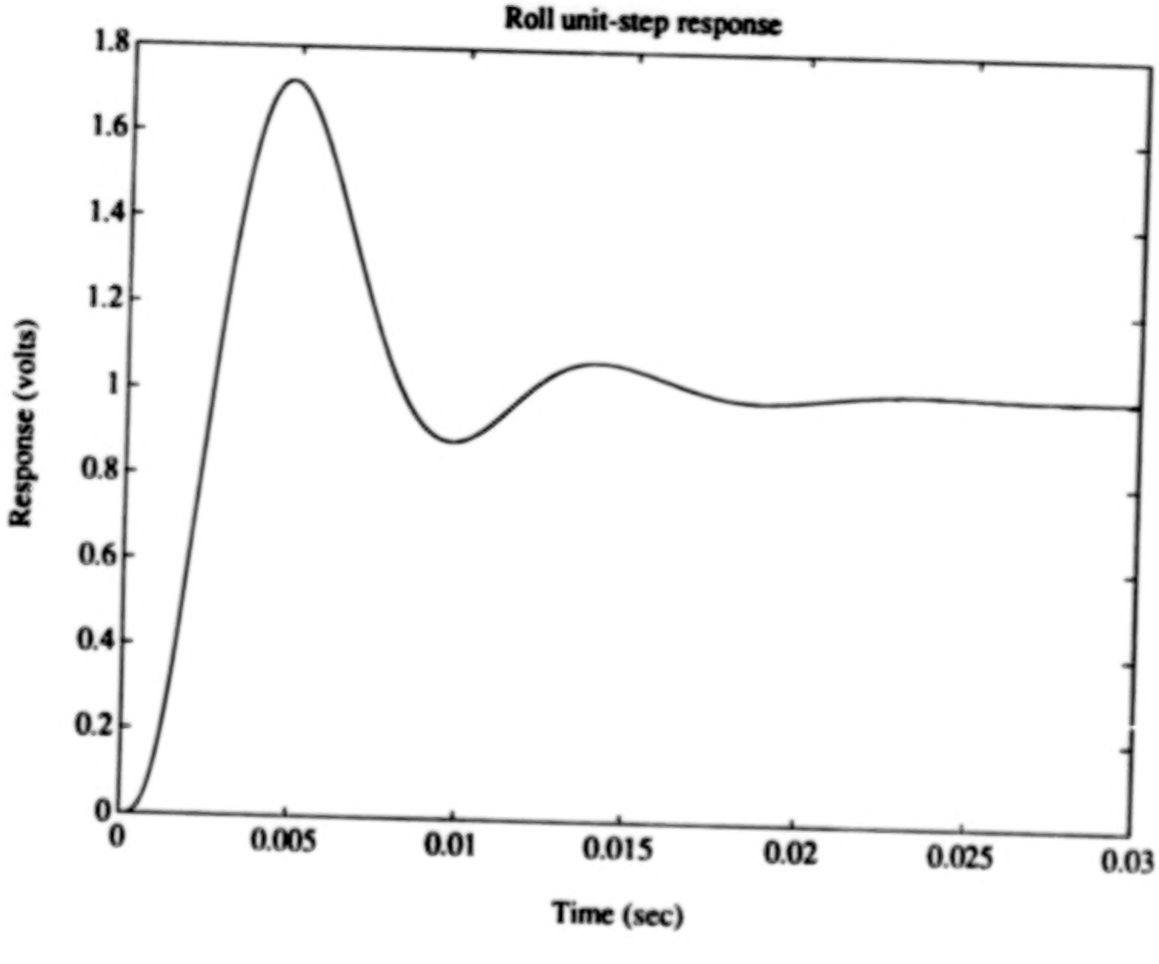

Figure 13: Roll unit-step response predicted by models.

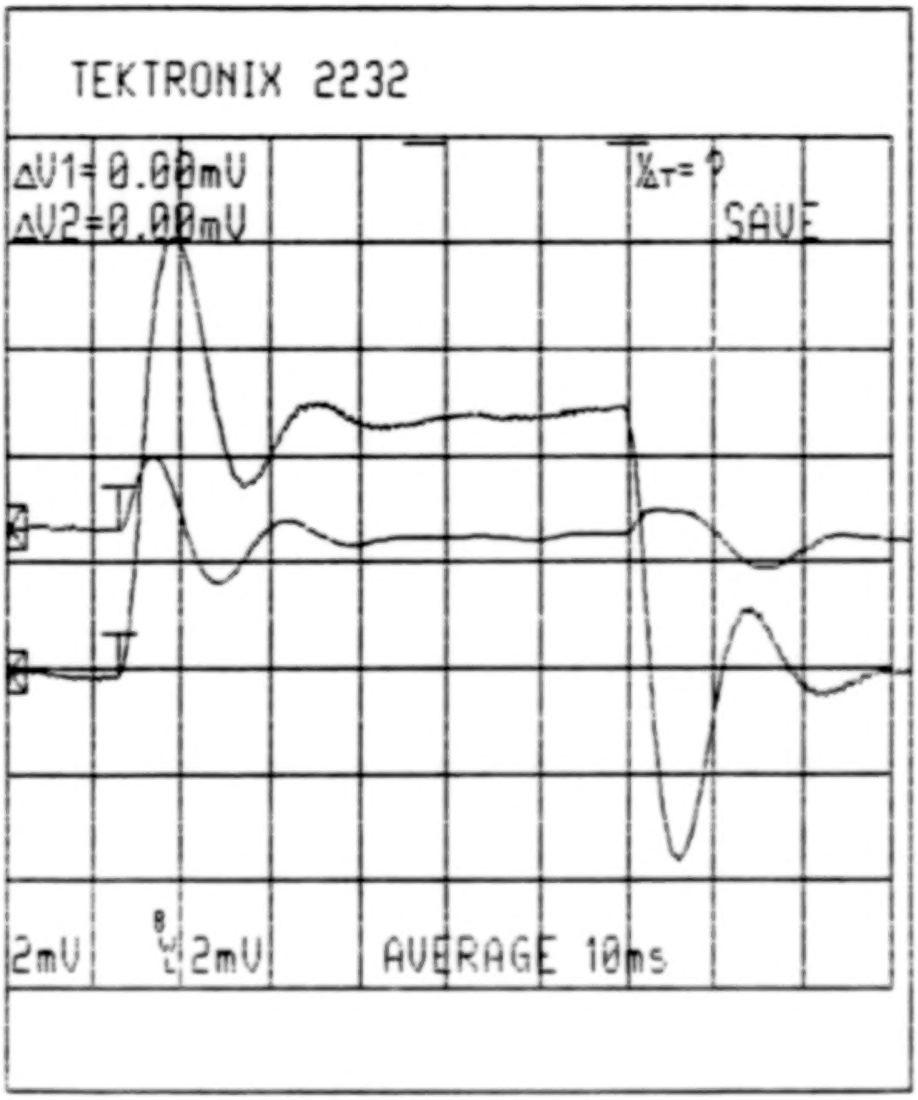

Figure 14: Actual roll step-response $v_{m1}(t)$. Second trace shows undesired cross-coupling response in pitch $v_{m2}(t)$.

Probe #	Crystal Freq. (MHz)	Excitation Freq. (MHz)
1	4.00	1.00
2	5.00	1.25
3	6.00	1.50
4	4.00	1.00
5	5.00	1.25

Table 1: Probe oscillator and excitation frequencies.

the five degrees of freedom which are controlled by the electromagnets. The probes are manufactured by Pioneer Technology, Inc., of Sunnyvale, CA. They operate with an air gap of 0.005". The probes are driven by electronics which produce an output voltage of 5 volts per 0.001" of motion over a travel of ±0.0025". Their specified accuracy is ±0.2% of full scale with a linearity of 0.1% of full scale, and a bandwidth of 10 kHz.

The electronics for all five probes is contained in a single chassis, and consists of a card cage containing individual circuit boards connected to each probe. Each circuit board uses a local quartz crystal oscillator to set the frequency of probe excitation. Unfortunately, only three separate frequencies are used for the five probe boards. This leads to significant beat frequency noise between the probes which are operated at the same nominal frequency. This problem is described in more detail below.

The crystal oscillator is divided down by a factor of 4 to give the probe excitation frequency. The crystal frequencies and excitation frequencies for the five probes are summarized in Table 1. When all five probes are connected, probe pairs #1–#4 and #2–#5 interact with a low frequency beat signal because they are operating on independent but nearly identical frequencies. The beat signal is at about 10 Hz with an amplitude on the order of tenths of a volt. The existence of this beat signal means that the true position stability capabilities of the suspension can not be demonstrated when all five of the probes are in use. They can be demonstrated if some of the probes are disabled; for instance if #4 and #5 are turned off, then the three top electromagnets can be used to stabilize the system in the vertical degrees of freedom, and with low noise contribution from the probes.

This is the approach which has been taken in the current work. The system positioning noise baseline is demonstrated using only the vertical system operating on the first three probes alone. When all five degrees of freedom are controlled, there is significant noise; however, the system step responses can be characterized through averaging on a digital oscilloscope, and the system frequency responses can be measured using a dynamic analyzer since this instrument is inherently narrow-band.

An alternate approach which is clearly more desirable in the long-term is to change the probe operating frequencies so that they run on five independent frequencies. For instance, using crystals at 4.5 and 5.5 MHz to drive probes #4 and #5 will eliminate any low-frequency beat tones. This option will implemented at UNC-Charlotte on the next version of the experimental system, allowing high stability in all five controlled degrees of freedom.

The probe noise-baseline when only the three top probes are connected and are facing fixed targets is shown in Figure 15. The voltages have been low-pass filtered to a 1 kHz bandwidth by a passive network preceding the oscilloscope input. The traces are taken with the oscilloscope in peak detect mode, so that short duration noise pulses are captured. All three probes have output noise voltages on the order of 1 mV p-p. This establishes a noise baseline for the three top electromagnets used alone. An approximately 10 Hz signal can be seen in the trace for probe #2. This is due to cross-coupling with probe #4 even when probe #4 is disconnected from the instrumentation card-cage.

When in suspension, the position stability is currently limited by the probe noise, even when only three degrees of freedom are active. This is demonstrated by the trace shown in Figure 16. The peak-to-peak noise is on the order of that shown with the probes facing a fixed target, i.e., 5 nm. Thus we expect that even higher stability can be demonstrated with probes having lower noise. This is believed to be the highest stability yet demonstrated by a magnetic suspension.

This performance is achieved with the experiment isolated from vibration by an optical table on gas-spring legs. Lightly tapping the optical table or the support brackets with a screwdriver results

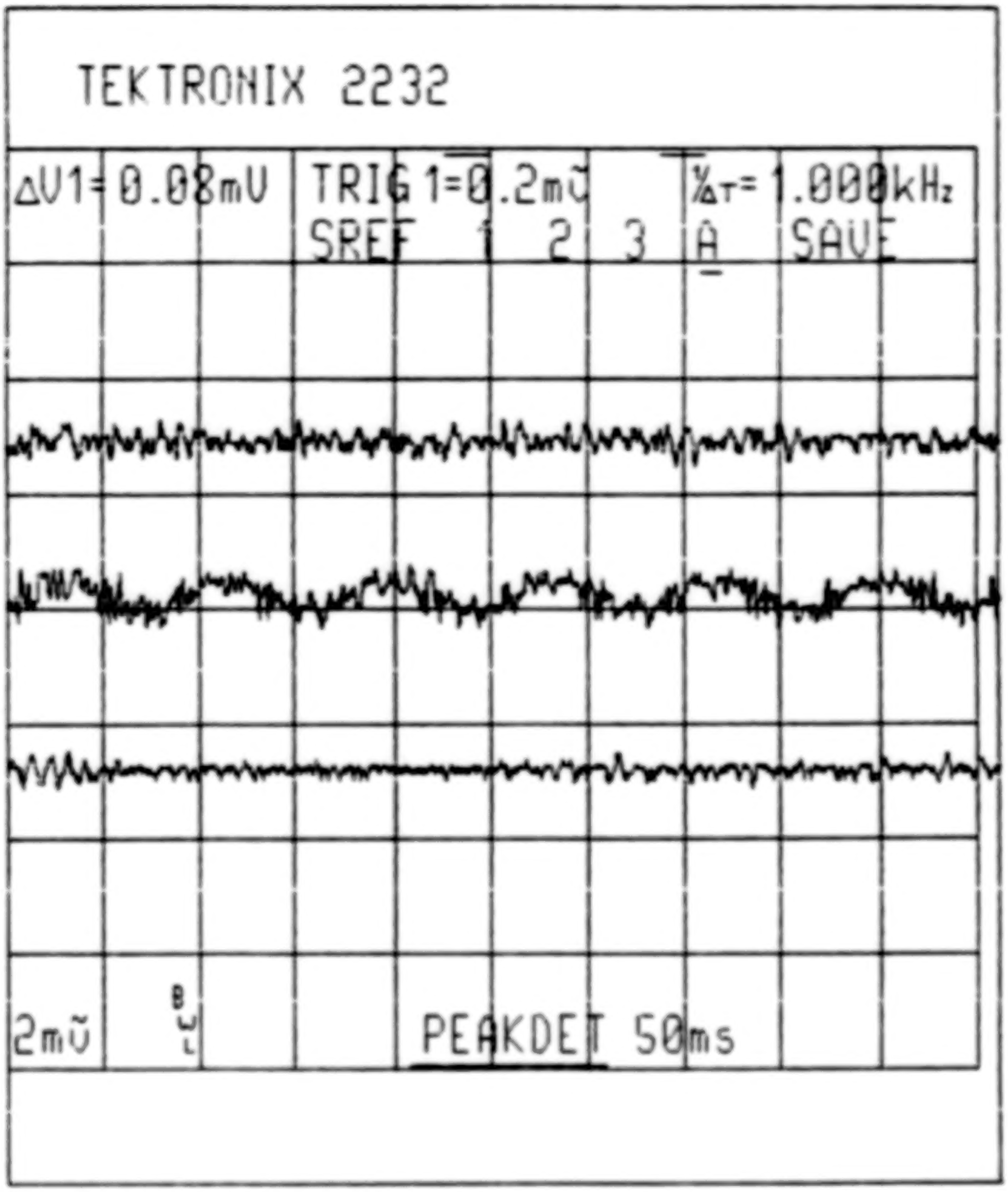

Figure 15: Baseline noise of probes #1, #2, and #3 with probes #4 and #5 disconnected.

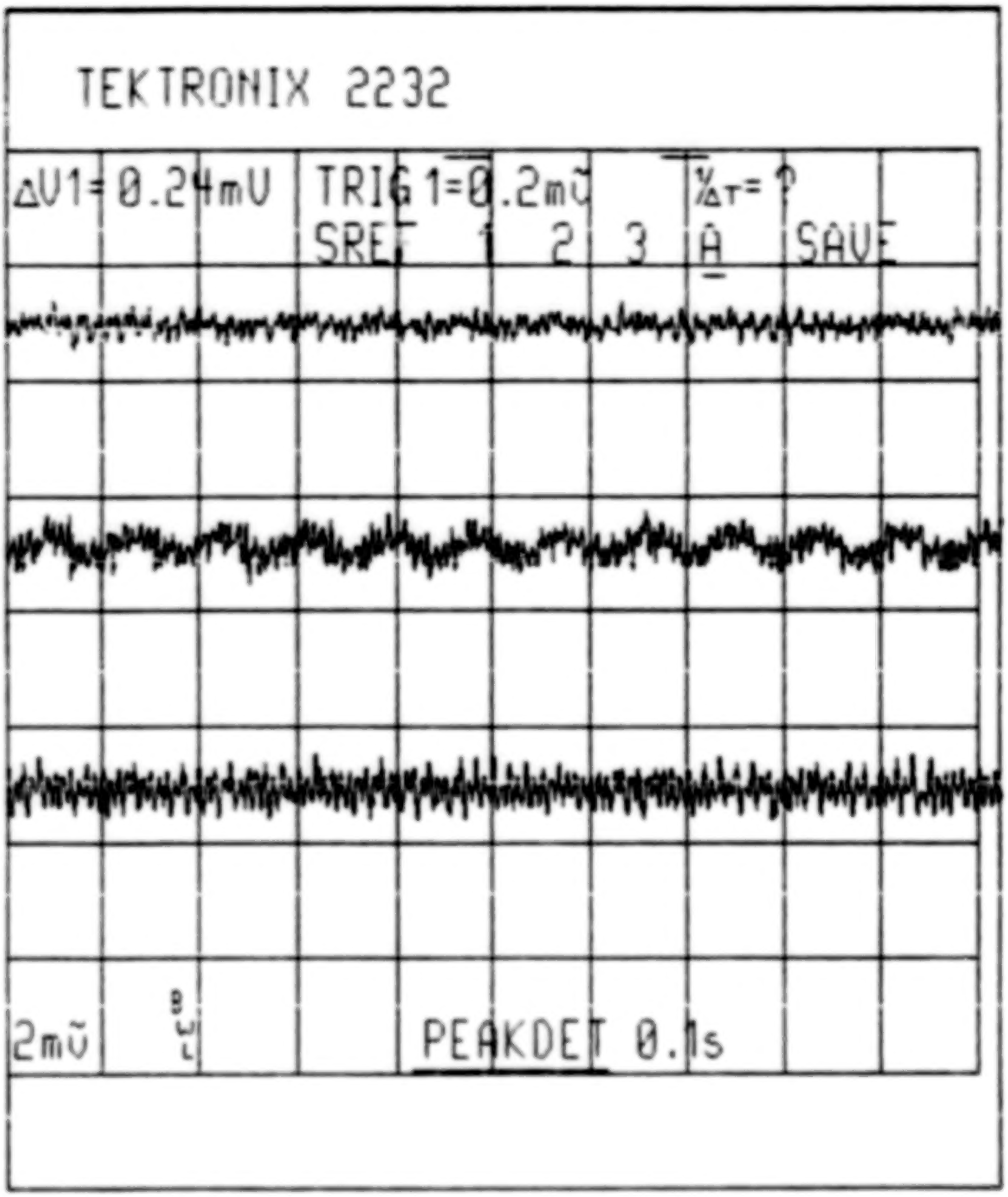

Figure 16: Vertical system suspension stability. Three traces show output voltages of probes #1, #2, and #3 from top to bottom respectively. One millivolt corresponds to approximately 5 nm.

in hundreds of nanometers of motion. Even the relatively stiff support brackets can be deflected by measurable amounts with the application of light finger pressure. These observations help to give a physical feel for the minute motions being measured.

Note that in Figure 16 the low-frequency (10 Hz) signal in the output from probe #2 is attenuated relative to the case where the probe is facing a fixed target. This happens because that component and all low-frequency (relative to loop crossover) noise components in the probe signal are attenuated by the closed position-loop. Thus, under closed-loop conditions the platen is actually moving such that the low-frequency components of the probe noise are nulled. The noise base-line shown in Figure 16 however gives a bound on the magnitude of this effect as less than 5 nm p-p. It is preferable to verify the position stability with an independent measurement such as can be provided by a laser interferometer. This approach will be taken in the current development effort at UNC-Charlotte.

6 Conclusions

A novel linear bearing system has been described which has demonstrated position stability of 5 nm in a low-disturbance environment. This level of stability serves as proof-of-concept for the construction of magnetic bearing systems which address nanometer-resolution motion control. With improved sensors, it is expected that Ångstrom-scale motion control can be achieved, allowing magnetic bearings to be used in stages for scanned probe microscopy with atomic resolution.

7 Acknowledgements

This work forms part of a thesis submitted by the first author to the Department of Electrical Engineering and Computer Science at M.I.T. in partial fulfillment of the requirements for the degree of Doctor of Philosophy [2]. The authors gratefully acknowledge the assistance of Van Pham, Tim Hawkey, Eric Heatzig, Dave Gessel, and Art Rudolf at M.I.T., and Carl Much, Mike Johnson, Pete Rossini, Paul Mitiguy, and Hardy Prince at M.I.T. Lincoln Laboratory. This work was sponsored by the Department of the Air Force, and performed at the M.I.T. Lincoln Laboratory.

8 References

[1] Slocum, A.H., and Eisenhaure, D.B., "Design Considerations for Ultra-Precision Magnetic Bearing Supported Slides," NASA Magnetic Suspension Technology Conference, Hampton, Va. Feb. 2-4, 1988.

[2] Trumper, D.L., "Magnetic Suspension Techniques for Precision Motion Control," Ph.D. Thesis, Dept. of Elec. Eng. and Comp. Sci., M.I.T., Camb., Mass., Sept., 1990.

[3] Trumper, D.L., "Nonlinear Compensation Techniques for Magnetic Suspension Systems," NASA Workshop on Aerospace Applications of Magnetic Suspension Technology, Hampton, VA, Sept. 25-27, 1990.

9 Appendix

The numerical values of the vertical suspension matrices are shown below.

```
Av =

  Columns 1 through 6

 -6.6667e+03  -8.3333e+06            0            0            0            0
  1.0000e+00            0            0            0            0            0
           0            0  -6.6667e+03  -8.3333e+06            0            0
           0            0   1.0000e+00            0            0            0
           0            0            0            0  -6.6667e+03  -8.3333e+06
```

```
            0              0              0              0     1.0000e+00              0
            0              0              0              0              0              0
            0              0              0              0              0              0
            0              0              0              0              0              0
            0              0              0     1.9399e+08              0    -1.9399e+08
            0    -4.0981e+08              0     1.9837e+08              0     1.9837e+08
            0     5.6048e+07              0     2.7130e+07              0     2.7130e+07

  Columns 7 through 12

            0              0              0              0              0              0
            0              0              0              0              0              0
            0              0              0              0              0              0
            0              0              0              0              0              0
            0              0              0              0              0              0
            0              0              0              0              0              0
            0              0              0     1.0000e+00              0              0
            0              0              0              0     1.0000e+00              0
            0              0              0              0              0     1.0000e+00
   1.1936e+04              0              0              0              0              0
            0     3.1654e+04     1.9098e+04              0              0              0
            0     2.4051e+02     4.7015e+04              0              0              0

Bv =

     1     0     0
     0     0     0
     0     1     0
     0     0     0
     0     0     1
     0     0     0
     0     0     0
     0     0     0
     0     0     0
     0     0     0
     0     0     0
     0     0     0

Cv =

     0     0     0     0     0     0     1     0     0     0     0     0
     0     0     0     0     0     0     0     1     0     0     0     0
     0     0     0     0     0     0     0     0     1     0     0     0

Dv =

     0     0     0
     0     0     0
     0     0     0
```

N91-21197

MAGNETIC SUSPENSION and BALANCE SYSTEM ADVANCED STUDY - 1989 DESIGN

Roger W. Boom, Y.M. Eyssa, Moustafa K. Abdelsalam, Glen E. McIntosh
Madison Magnetics Incorporated
216 Walnut Street
Madison
WI 53705

Magnetic Suspension and Balance System Advanced Study - 1989 Design

R. W. Boom, Y. M. Eyssa,
M. K. Abdelsalam, and G. E. McIntosh
Madison Magnetics, Inc.
Madison, Wisconsin

ABSTRACT

The objectives of this study are to experimentally confirm several advanced design concepts on Magnetic Suspension and Balance Systems (MSBS). The advanced design concepts were identified as potential improvements by Madison Magnetics, Inc. (MMI) during 1984 and 1985 studies of an MSBS utilizing 14 external superconductive coils and a superconductive solenoid in the airplane test model suspended in a wind tunnel. The design concepts, now based on confirmed experiments, are substituted in the 1985 MSBS design to provide the new 1989 MSBS design.

Specifically, the objectives are: 1) full-scale solenoid construction and test for the F16 airplane model, 2) small-scale solenoid development toward high current density, 3) mechanical tests of new permanent magnet wings materials, and 4) a new MSBS design using these accomplishments.

The 1989 improvements over previous MMI designs are: the weight and power savings result in a 1989 inflation-adjusted cost estimate of $19.1 M compared to $21.5 M in 1985 and to $88 M in 1981. The improvements are due to: the holmium insert in the model coil; 100% of wing volume is new permanent magnet material; fiberglass-epoxy structure instead of stainless steel; and shorter saddle roll coils.

INTRODUCTION

Magnetic suspension and balance systems (MSBS) for wind tunnels have been increasingly developed and utilized during the past 25 years. The primary aerodynamic advantage of MSBS is the elimination of air flow disturbances caused by the test model mechanical support system and by the required alterations in the test model. The primary technological advantages of MSBS are that static and dynamic forces and torques on the test model can be applied and recorded (from magnet currents) without the severe sting restraints.

The potential availability of MSBS for large transonic tunnels improves steadily in line with the development of the new high temperature superconductor materials and the expanded use of low temperature superconductive magnet systems in many fields, such as: high energy physics and energy storage. Compact superconductive systems provide high magnetic fields on the test model.

The design studies by General Electric [1] in 1981 and by Madison Magnetics in 1984 [2] and 1985 [3], and a pilot model at Southampton in 1983 [4] show that practical full-size superconductive MSBS systems can be built well within the present state of the art for superconductive systems. Design improvements and cost reductions continue in this Phase II-1989 design study for a MSBS suitable for an 8' x 8' test section at Mach 0.9 with ± 0.1% control forces at 10 Hz for an F16 model airplane.

The new conceptual MSBS designs for 8' x 8' wind tunnels in this study by Madison Magnetics Inc. (MMI) continue the trend of improvements that was started with the MMI-1984 and MMI-1985 MSBS designs. This MMI-1989 design has more flexibility in magnet choices and more control capabilities with simpler coil configurations than previously.

The objectives of this study cover experimental projects to demonstrate improved components and extensions of the MMI design studies labeled here as MMI-1989 MSBS design.

A full-scale model core solenoid is built, tested, and qualified for use in an F16 airplane model. The critical aspects of a solenoid in a tight-fitting portable cryostat container are dealt with by experimental staged improvements until a workable final system is completed. The recommendations for best design based on this experiment provide a conservative, high magnetic moment model core solenoid at 30 kA/cm^2 which will be a good candidate for the first 8' x 8' tunnel.

The use of the permanent magnet material Nd-Fe-B (Neomax trade name) for wings of an F16 model is solidified by bending strength measurements which show that Neomax is strong enough to use without stainless steel skin support. The general replacement of magnetized soft iron wings by high performance rare earth permanent magnet material is an enormous advance for MSBS model roll characteristics. External superconductive roll coils can thereby be significantly smaller, less powerful, and less expensive.

An extended MSBS design is undertaken to essentially solidify the 1985 design with the actual experimental achievements replacing previous conceptual designs. The solenoid parameters are about as predicted, except now the magnetic moment is known and proven. Not all design and construction choices were best; in particular the design was too tight as a result of trying for too high a magnetic moment. But at least now it is known what is critical and what should be achieved. A clear example of one item illustrates the more general conclusions to this work: in a prescribed 75 cm long envelope MMI built and tested a solenoid with active windings 70 cm long, which leaves only 2.5 cm on each end for support and thermal transition from 4.2 K to 300 K. Based on this construction experiment we recommend 5 cm on each end to get better helium hold time.

The MMI-1989 redesign has an improvement of 30% reduction in ampere-meters and 50% reduction in energy stored in the 14 suspension coils over the 1985 design. These improvements are mainly due to the removal of skin support in model wings and optimizing the locations of the 14 suspension coils.

MODEL SOLENOID AND CRYOSTAT

Model Solenoid

The goal of constructing and testing high current density model solenoid with holmium core is to demonstrate that a high pole strength and high magnetic moment practical solenoid can be built to commercial specifications, and become certified as available for use.

Table 1 lists the model solenoid (shown in Figure 1) parameters. The parameters along with the holmium mandrel achieves the 4.45 X 10^4 Am magnetic pole strength as listed in Table 2.

Table 1
Magnet Parameters

Magnet A	
(1) Winding inner diameter	3.263 in. (8.288 cm)
(2) Winding outer diameter	4.459 in. (11.326 cm)
(3) Winding length	12.904 in. (32.776 cm)
(4) Number of turns	24,849
Magnet B	
(1) Winding inner diameter	3.263 in. (8.288 cm)
(2) Winding outer diameter	4.459 in. (11.326 cm)
(3) Winding length	12.997 in. (33.012 cm)
(4) Number of turns	24,854
The parameters for the assembled system are:	
Total turns	49,703
Total ampere-turns needed	3,326,606
Current required	66.93 A
Field at the windings (no holmium)	6.16 T
Inductance (no holmium)	29 H
Persistent switch heater current	0.039 A
Magnet charge rate	4 A/min.

Table 2

Initial Model Coil Specifications

	ID (cm)	OD (cm)	LENGTH (cm)	WEIGHT (kg)	MAGNETIC POLE STRENGTH (Am)
Winding	8.26	11.5	70	26.8	3.75×10^4
Mandrel	6.14	8.26	70	14.5	0.70×10^4
Total				41.3	4.45×10^4

The solenoid manufacture is conducted according to ordinary commercial standards to demonstrate that such solenoids could be routinely available. The manufacturer, American Magnetics (AMI) was free to select the conductor, lead system, protection system and winding design details. The conductor is a standard 1.35:1 Cu:NbTi ratio. AMI wound the coil in two half-coils with the current contacts being made in the center. Breaking the coil in the center also facilitates the assembly of the persistent switch and diodes which are located inside the magnet bore for lack of space to put them elsewhere.

In constructing the magnet, the holmium cylinders are machined down to a smaller OD than the stainless steel mandrel ID to prevent cooldown over-stressing the windings.

During magnet tests, the two magnet half core tested individually at 4.2 K both achieving 72 and 73.3 A. The magnet system is then assembled and tested several times as a unit.

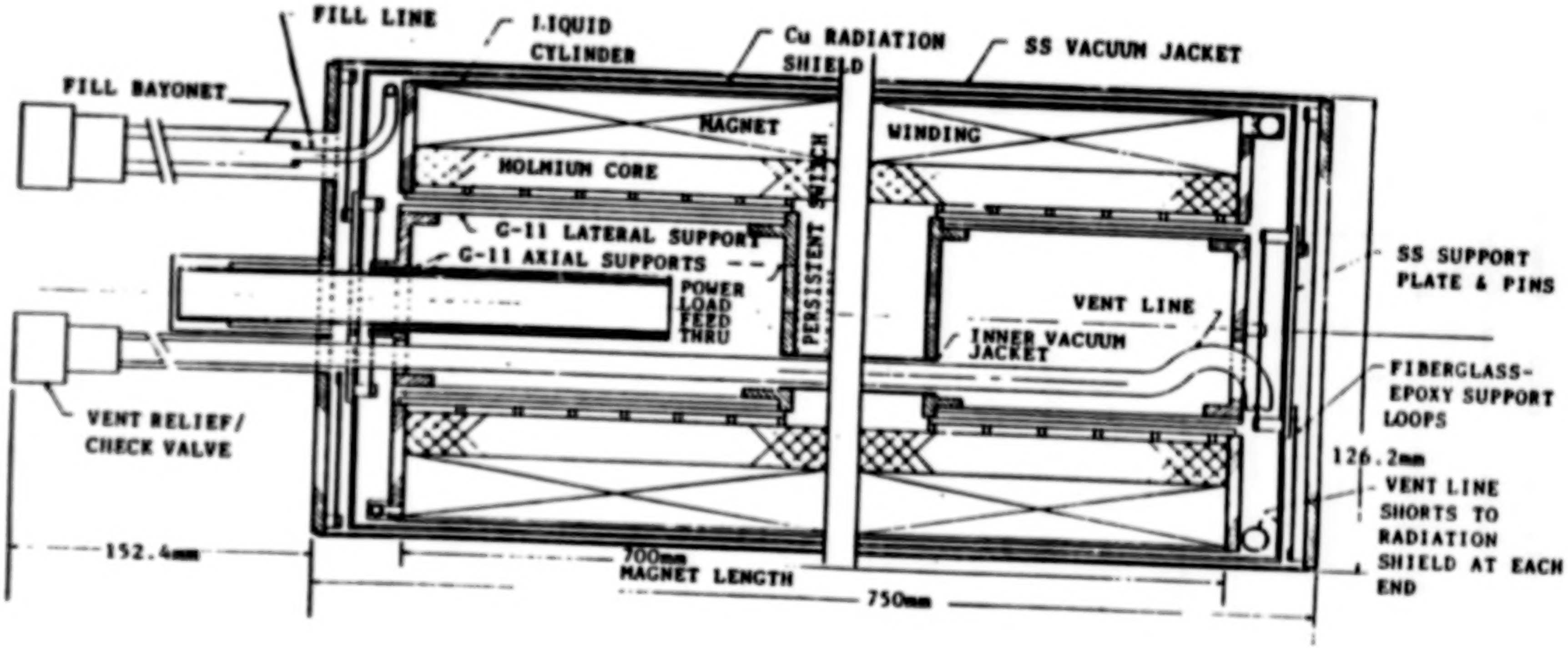
FILL LINE
LIQUID CYLINDER
Cu RADIATION SHIELD
SS VACUUM JACKET
FILL BAYONET
MAGNET
WINDING
HOLMIUM CORE
PERSISTENT SWITCH
G-11 LATERAL SUPPORT
G-11 AXIAL SUPPORTS
POWER LOAD FEED THRU
SS SUPPORT PLATE & PINS
VENT LINE
INNER VACUUM JACKET
FIBERGLASS-EPOXY SUPPORT LOOPS
VENT RELIEF/ CHECK VALVE
126.2mm
VENT LINE SHORTS TO RADIATION SHIELD AT EACH END
152.4mm
700mm MAGNET LENGTH
750mm

Figure 1. Core Magnet Cryostat.

The first two tests became shakedown tests to fix leaks that initially prevented achieving 5 psi (gauge), and to change the persistent switch for locking at 5 psi.

July 28, 1988 The third test went to 70 A without transition, and was pressurized to 5 psi*. The switch was locked in and the magnet was left in the persistent mode for 20 minutes. While maintaining the pressure of 5 psi, the magnet was discharged and charged again to 70 A. The switch was locked in again, and the magnet remained in the charged condition for 1 hour without problem. After discharge, the pressure was released, and the system warmed up.

July 29, 1988 In the final test holmium cylinders were installed in both halves of the magnet. The magnet then was charged to the desired current of 66.9 A. The switch was locked in and the system pressurized to 5 psi, and discharged and charged 5 psi pressure. The switch operated without trouble. Several cycles to 66.9 A followed without quenches.

Such performance is satisfactory and meets all requirements for commercial acceptance. In operation a build-up of pressure to 5 psi is planned.

---

* 5 psi is the pressure for off-gassing after final assembly and is at 4.55 K.

Model Cryostat

The designed and constructed cryostat is shown in Figure 1. Considerations for thin materials, close alignment, and tight spacing dominate the manufacturing process. A careful design and a high level of welding craftsmanship is required to deal with the thin materials and tight mechanical specifications. The close alignment requirements are intentionally severe in order to achieve a maximum magnetic moment.

The most difficult assembly operations are due to the tight spacing. However, these fabrication challenges are acceptable and do not require any redesign. The redesign of the next cryostat, based on the results of all experiments, would include the following key items.

1. The space between each end of the winding mandrel and the outer container would be 5 cm (increased from 2.5 cm).
2. The G-11 CR cantilevered re-entry support cylinders on each end would be much stiffer to limit deflection.
3. The coil would be wound with 20 to 30 A wire to reduce lead losses.
4. The helium annular region around the solenoid would be 0.34 cm.
5. Such redesign would simplify construction and repair and achieve the helium hold time of 5 hours.

System Test of Solenoid and Cryostat

Successful electrical and cryogenic tests used 200 liters of liquid helium. Several preliminary current ramps had premature quenches in the 15-25 A range. After increasing the helium flow-through, the quenches take place in the 60-67 A range. Each run is a slow current ramp-up at .05 to 0.1 A/sec and requires about 30 minutes for the sequence of warm-up (quench) plus cooldown plus current ramp. The training sequence was 63 A, 64 A, 66.9 A, 67 A, and 67 A. During all runs, the helium flow rate and current charging rates are varied. The solenoid meets specifications of 66.9 A.

The persistent current switching is easy to operate. The AMI power supply has a second built-in small power supply to heat the persistent switch across the solenoid. By turning off the heater power, the switch becomes superconducting and traps the existing current in the solenoid and, at the same time, is a short circuit on the leads from the solenoid power supply. A series of switching on-off steps and a long persistent hold at 60 A demonstrates that the system operates disconnected from the power supply. Thus, the system meets all specifications.

The cryostat and solenoid manufacture and tests are successfully completed and qualified per specifications.

WING MAGNETIC MATERIAL

An MSBS magnet system must be capable of rolling the airplane model around its longitudinal axis. Roll is achieved

by exerting a magnetic torque on the magnetic model wing. In this design the wings are fabricated from permanent magnet material, $Nd_2Fe_{14}B$. The mechanical bending strength of the wing at ambient and liquid nitrogen temperatures determines if the wing is self-supporting or must be supported by an extra stainless steel skin as shown in Fig. 2. A steel skin is undesirable because it occupies space that could have been magnetic material. The purpose of this test is to measure the ultimate bending strength of the wing magnet material.

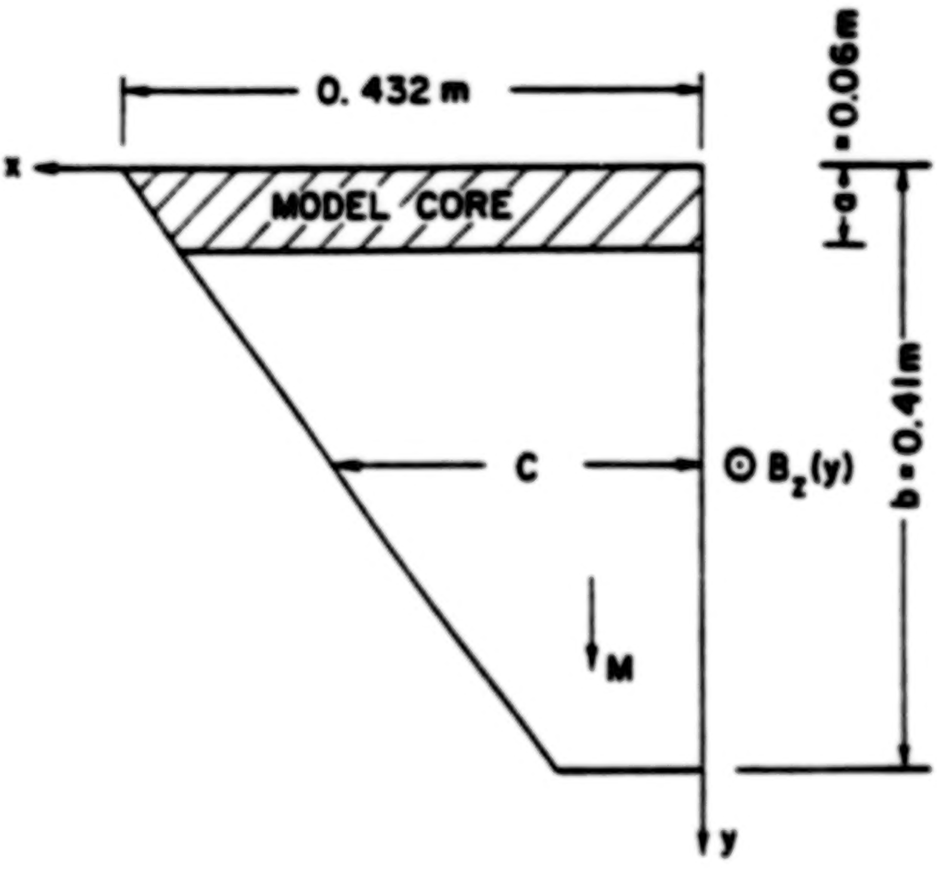

Figure 2. F16 Fighter Wing.

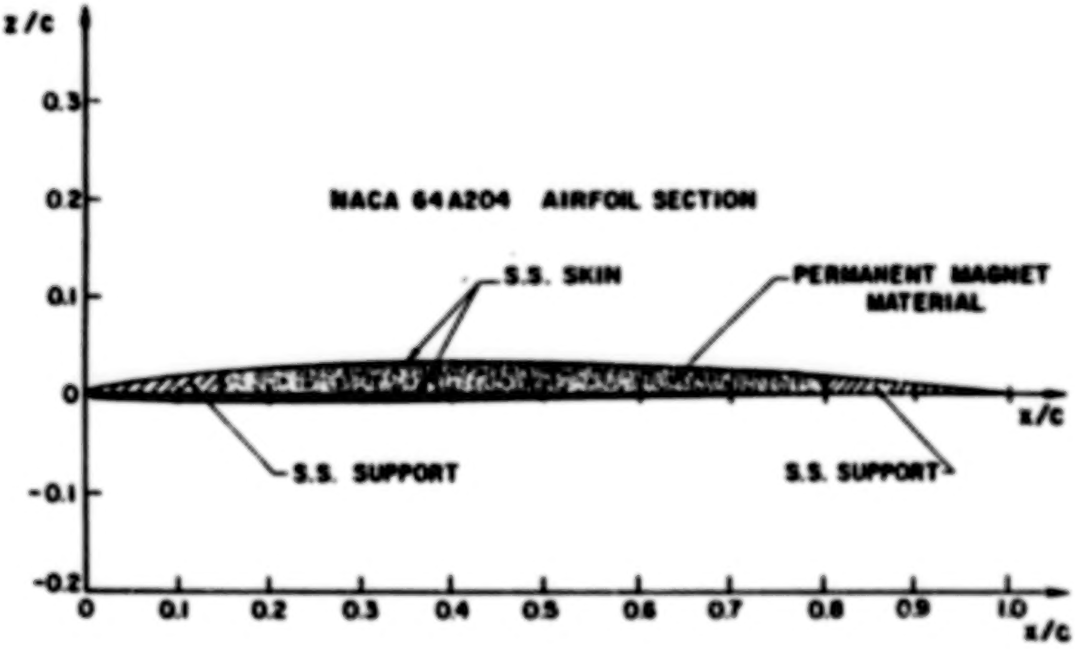

z/c
0.3
0.2
0.1
0
-0.1
-0.2
NACA 64A204 AIRFOIL SECTION
S.S. SKIN
PERMANENT MAGNET MATERIAL
S.S. SUPPORT
S.S. SUPPORT
x/c
0
0.1
0.2
0.3
0.4
0.5
0.6
0.7
0.8
0.9
1.0
x/c

Figure 2a. Wing Cross-Sectional Area at any Chord C Showing Stainless Steel Support, Skin, and Permanent Magnet Material

Experiment Design

A three-point load test fixture is used with a hydraulic testing machine. The load is measured with a calibrated load cell. A continuous flow of liquid nitrogen keeps the sample immersed in LN_2 during the low temperature test.

For the low temperature test, the sample in the test fixture is held in place with adhesive tape inside the empty nitrogen container. The crosshead is lowered gradually until the loading cylinder touches the specimen and loads the specimen to about 15-20 lb. At this point LN_2 is transferred to the dewar. Once the liquid covers the specimen completely, load is gradually increased until failure. The same procedure is followed at ambient temperature without the nitrogen.

Neomax-35 Samples

$Nd_2Fe_{14}B$ material is available in various shapes and dimensions from Sumitomo Special Metals Co. under the commercial name Neomax. It is available in both magnetized and non-magnetized states. The samples are 0.375" diam x 1.375" long rods with aspect ratio (L/D) = 3.93. Although this is less than the recommended aspect ratio for flexure testing, it was the closest commercial size available. At this aspect ratio the shear deformation is important. However, because there is no need to measure the material modulus, the shear effect is neglected. Physical and mechanical properties of Neomax are listed in Table 3. Magnetic properties of Neomax as tested by the vendor are shown in Fig. 3.

Table 3

Physical and Mechanical Properties of the Neomax Wing Material

Density (g/cm^3)	7.4
Electrical resistivity (μΩcm)	144
Vickers hardness (H_v)	600
Flexural strength (MPa)	250
Coefficient of thermal expansion Parallel (10^{-6}/K) Normal (10^{-6}/K)	 5.8 -1.3
Specific heat (cal/kgK)	120
Thermal conductivity (cal/mK)	7700
Young's modulus (GPa)	160
Rigidity (GPa)	64
Poisson's ratio (ν)	0.24

Test

Three specimens are tested to failure in liquid nitrogen and one is tested to failure at ambient temperature and compiled in Table 4. The ambient temperature bending strength is in good agreement with the typical material strength quoted by the manufacturer. The average ultimate strength at LN_2 is 50% higher than the room temperature strength. However, there is no difference in the typical brittle failure mode at the two temperatures. Tension cracks are initiated in the most stressed fibers and then propagate perpendicular to the sample axis.

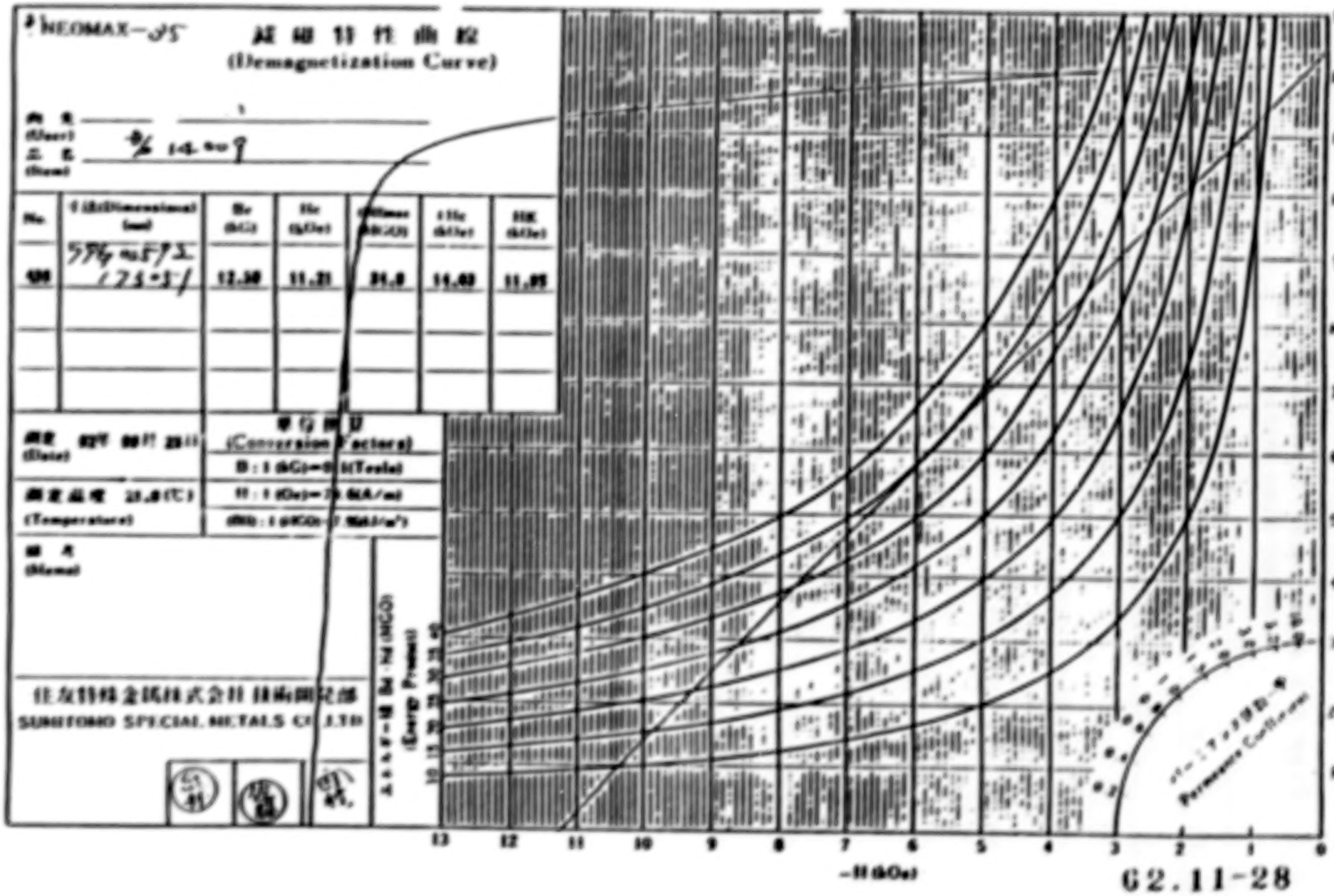

Figure 3. Magnetic Properties of the Tested NEOMAX-35 (Nd Fe B Material)

Table 4

Ultimate Bending Strength of NEOMAX-35 at 300 and 77K

Sample #1 at 77K	412 MPa
Sample #2 at 77K	417 MPa
Sample #3 at 77K	368 MPa
Average strength at 77K	397 MPa
Sample #4 at 300K	264 MPa

The wing material is strong enough to be self-supporting. The Neomax can fully occupy the wing volume. Therefore, the wing can provide 15% higher volume magnetization than used in the MMI-1985 design of the wind tunnel MSBS.

MSBS DESIGN

Background

The 1984 [2] and 1985 [3] MSBS designs by MMI include design improvements which reduce the costs to less than 25% of the earliest estimates [1]. The major improvements for the 1984 system, sketched in Fig. 4 are:

- A 70 cm long potted persistent superconducting solenoidal coil, 11.5 cm O.D., and 6.1 tesla is the model core. A superconducting coil produces higher magnetic moments and pole strengths than a magnetized iron core or a permanent magnet core.
- The model wings contain permanent magnets that occupy 85% of the wing volume; 15% of the wing

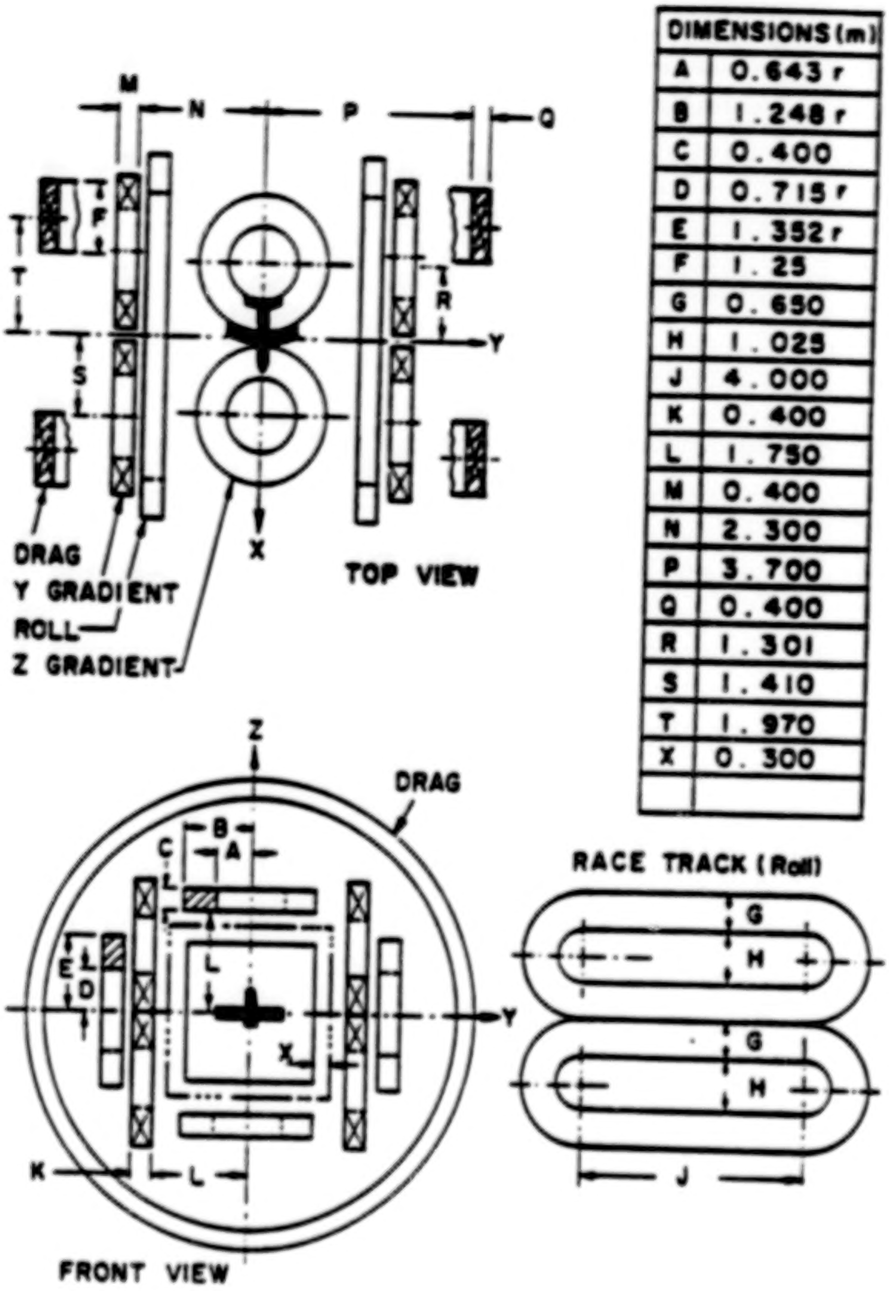
M
N
P
Q
F
T
R
S
Y
X
DRAG
Y GRADIENT
ROLL
Z GRADIENT
TOP VIEW
Z
DRAG
B
A
C
L
E
L
D
L
X
K
L
FRONT VIEW
RACE TRACK (Roll)
G
H
G
H
J

DIMENSIONS (m)	
A	0.643 r
B	1.248 r
C	0.400
D	0.715 r
E	1.352 r
F	1.25
G	0.650
H	1.025
J	4.000
K	0.400
L	1.750
M	0.400
N	2.300
P	3.700
Q	0.400
R	1.301
S	1.410
T	1.970
X	0.300

Figure 4. 1984 MSBS Magnet System.

volume is high strength stainless steel.

- Z and Y gradient coils in Fig. 4 are symmetric arrays of four bipolar solenoid to control and manipulate the model. The superconductor composite-conductor for all coils is an 11-kA low-loss cryostable conductor.
- The drag coils to counterbalance wind drag forces are large diameter solenoids.
- The roll R coils are four race-track coils optimized for minimum ampere-meters.

The 1985 MSBS design (Fig. 5) added four major improvements:

1. A holmium coil mandrel in the suspended model to increase the core pole tip magnetic moment by 18.7% from 3.75×10^4 Am to 4.45×10^4 Am.
2. A new permanent magnet material $Nd_{15}Fe_{77}B_8$ in the suspended model wings which reduces the external roll magnet size by about 25%.
3. New roll and drag coils shown in Fig. 5 for a more economical and compact design.
4. Fiberglass-epoxy slabs as the principal structure to reduce ac losses.

These four improvements reduced the ampere-meters and energy stored in all 14 external magnets as shown in Table 5.

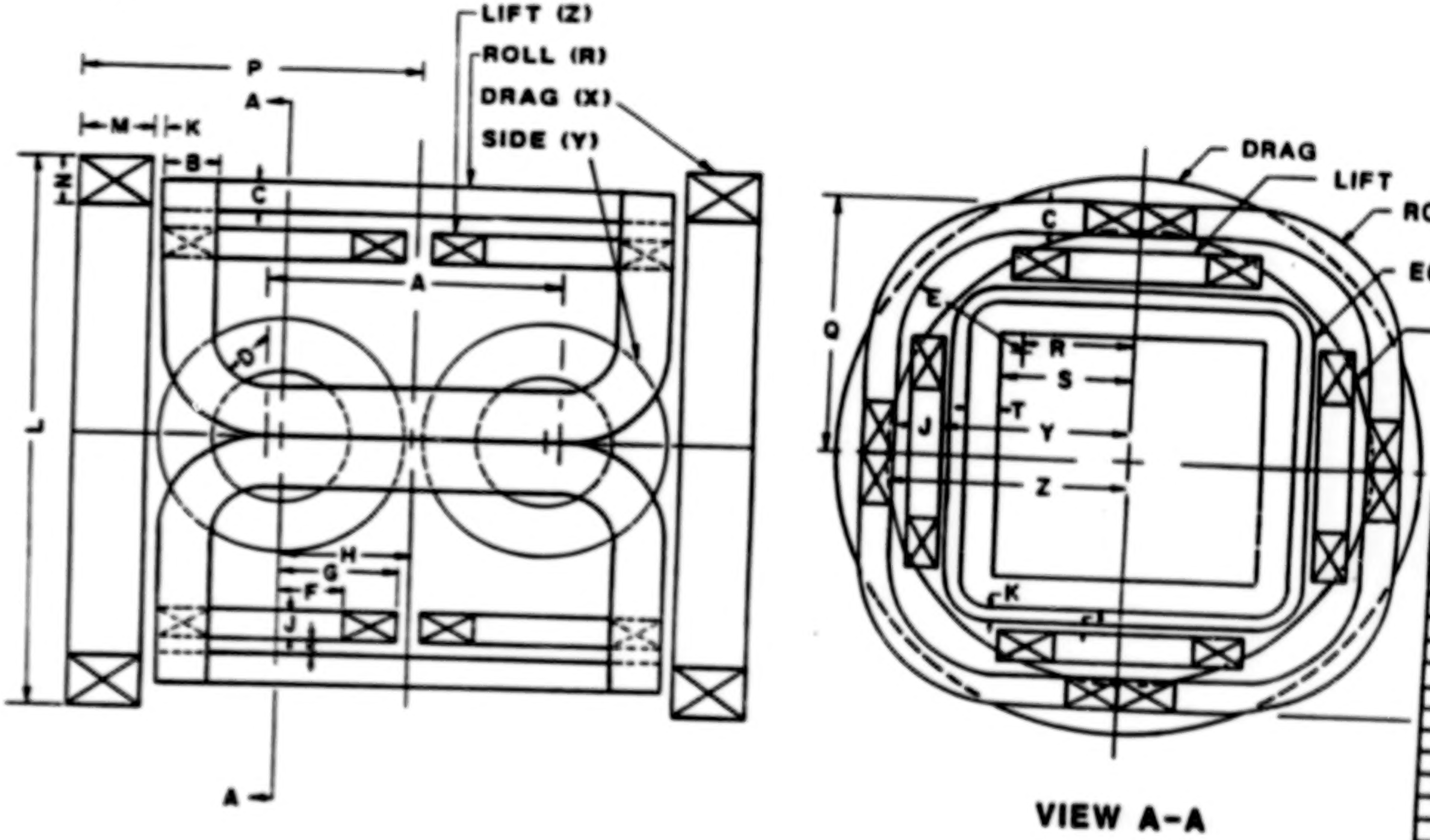
LIFT (Z)
ROLL (R)
DRAG (X)
SIDE (Y)
P
A
M
K
B
N
C
L
A
D
H
G
F
J
A
DRAG
LIFT
ROLL
EGG CRATE
SIDE
C
E
Q
R
S
T
J
Y
Z
K
VIEW A-A

DIMENSIONS (m)	
A	2.800
B	0.500
C	0.300
D	0.500
E	1.200
F	0.644
G	1.153
H	1.250
J	0.300
K	0.152
L	5.514
M	0.700
N	0.500
P	3.252
Q	2.505
R	1.005
S	1.219
T	0.305
X	0.076
Y	1.753
Z	2.205

Figure 5. 1985 MSBS Magnet System

1989 MSBS DESIGN

In 1989 further improvements are based on tests of a full-size superconductive solenoid model coil; tests of wing materials; and with design improvements. These improvements yield 30% ampere-meter savings over the 1985 MSBS design. The 1989 MSBS design changes are:

1. Elimination of stainless steel support in the wings, which occupied 15% of the wing volume. Mechanical tests of wing materials show that the Neomax is strong enough to be self supporting to withstand maximum magnetic and lift forces.
2. The tested model core solenoid achieves 92% of the projected magnetic moment assumed in 1985.
3. Smaller roll R coils result from the 100% volume of magnetic material in the wing and allow a more optimum rearrangement (see Fig. 6).

The 1989 improvements in ampere-meters and energy stored are seen in Table 5.

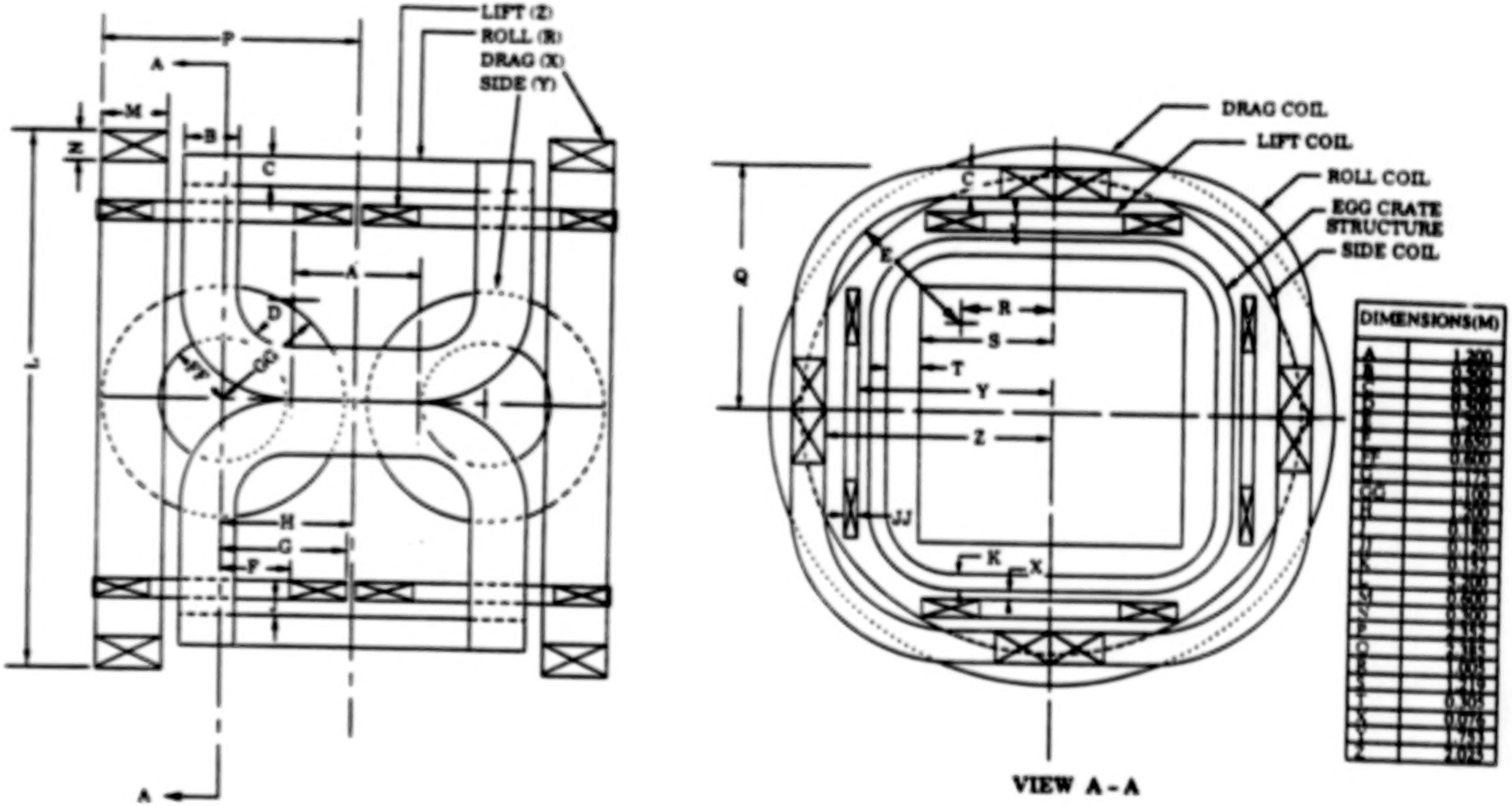
LIFT (Z)
ROLL (R)
DRAG (X)
SIDE (Y)
P
A
M
B
N
C
J
L
A
D
GG
FF
H
G
F
A
DRAG COIL
LIFT COIL
ROLL COIL
EGG CRATE STRUCTURE
SIDE COIL
Q
C
E
R
S
T
Y
Z
JJ
K
X
VIEW A - A

DIMENSIONS(M)	
A	1.200
B	[illegible]
C	[illegible]
D	[illegible]
E	[illegible]
F	[illegible]
FF	[illegible]
G	[illegible]
GG	[illegible]
H	[illegible]
J	[illegible]
JJ	[illegible]
K	[illegible]
L	[illegible]
M	[illegible]
N	[illegible]
P	[illegible]
Q	[illegible]
R	[illegible]
S	[illegible]
T	0.305
X	[illegible]
Y	[illegible]
Z	[illegible]

Figure 6. 1989 MSBS Magnet System

Table 5

Madison Magnetics MSBS 1984, 1985 and 1989 Designs

COILS	X	Y	Z	R	TOTAL	%
1984 Design						
Ampere-meters (MAm)	362	100*	86	207	755	100
Energy Stored (MJ)	656	60	50	140	906	100
1985 Design						
Ampere-meters (MAm)	172	71**	71	154	468	62
Energy Stored (MJ)	216	38	38	116	408	45
1989 Design						
Ampere-meters (MAm)	106	53	74	108	341	45
Energy Stored (MJ)	93	25	44	58	220	25

* The Y coils in the 1984 design are recalculated for this table to correct an earlier error.

** Actual ampere-meters needed for Y coils are 63 MAm. For simplicity of design and to have a complete symmetry, the Y coils are sized the same as the Z coils.

The ampere-meters of conductor in the 1989 design decrease to 45% and the stored energy decreases to 25%, with comparable system savings as shown in Table 5.

CONCLUSION

The study has experimentally confirmed several advanced design concepts on magnetic suspension and balance systems. The 1989 MSBS redesign is based on the results of these experiments. Savings up to 30% in supporting magnet ampere meters and 50% in energy stored over the 1985 design are achieved.

REFERENCES

[1] H.L. Bloom, et al., "Design Concepts and Cost Studies for Magnetic Suspension and Balance Systems," NASA CR-165917, July 1982.

[2] R.W. Boom, Y.M. Eyssa, G.E. McIntosh, and M.K. Abdelsalam, "Magnetic Suspension and Balance System Study," NASA CR-3802, July 1984.

[3] R.W. Boom, Y.M. Eyssa, G.E. McIntosh, and M.K. Abdelsalam, "Magnetic Suspension and Balance System Advanced Study," NASA CR-3937, October 1985.

[4] C.P. Britcher, M.J. Goodyer, R.G. Scurlock, and Y.Y. Wu, "A Flying Superconducting Magnet and Cryostat for Magnetic Suspension of Wind-Tunnel Models," Cryogenics, April 1984.

[5] W. Schauer and F. Arendt, "Field Enhancement in Superconducting Solenoids by Holmium Flux Concentrators," Cryogenics, October 1983.

[6] R.W. Hoard, et al., "Field Enhancement of a 12.5 T Magnet Using Holmium Poles," IEEE Trans. on Magnetics, Vol. MAG-21, No. 2, March 1985.

N91-21198

PROPULSION SIMULATOR for MAGNETICALLY-SUSPENDED WIND TUNNEL MODELS

Prakash B. Joshi, C.L. Goldey, G.P. Sacco
Physical Sciences Inc.
20 New England Business Center
Andover
MA 01810

Pierce L. Lawing
NASA Langley Research Center
Mail Stop 238
NASA Langley Research Center
Hampton
VA 23665-5225

PROPULSION SIMULATOR FOR MAGNETICALLY-SUSPENDED WIND TUNNEL MODELS

P.B. Joshi, C.L. Goldey, and G.P. Sacco
Physical Sciences Inc.
Andover, Massachusetts

and

P. Lawing
NASA Langley Research Center
Hampton, Virginia

I. Introduction

The wind tunnel has been an indispensable tool for aeronautical research and aircraft configuration development for the past 80 years. During that period, tunnels have evolved in speed, increased in size, improved in flow quality, advanced in flow measurement techniques, and become sophisticated in the use of digital computers for data acquisition, reduction, and analysis. Throughout this advancement, the ability of the wind tunnel to faithfully simulate the aerodynamic forces and moments on a model, which can be related to the forces and moments on the full scale aircraft, has always been limited by uncertainties in measurements due to support and wall interference effects. Support interference can lead to significant errors in measured aerodynamic force and moment coefficients and static stability derivatives. These errors become very large at transonic speeds and/or high angles-of-attack. Magnetic suspension and balance systems (MSBS) were developed originally to eliminate the support interference problems. They also have the additional advantages of providing dynamic stability derivatives, two-body force measurements, and improved tunnel productivity. About 25 years ago wind tunnel development shifted emphasis from MSBSs to cryogenic tunnels which can duplicate the full-sale flight Mach and Reynolds numbers simultaneously. This capability has recently become available with the completion of the National Transonic Facility at NASA Langley Research Center (LaRC). Now, the community of experimentalists is advocating the development of MSBSs for large wind tunnels including the cryogenic tunnels. Further impetus for this development has been provided by advancements in the technologies of superconductivity, control systems, and computers.

One of the capabilities desired in magnetic suspension wind tunnels is the simulation of propulsison-induced aerodynamic forces and moments, which arise as a result of interactions beetween propulsive jets and the free stream. Such a simulation has always been a difficult task, even in conventional wind tunnels. The main reasons have been the problems of introducing high pressure air into the model, questions regarding proper scaling parameters, construction of models out of metric and non-metric sections, and accurately determining the force/moment contribution to the non-metric section. The model support is sometimes an advantage in that it provides a means of bringing air on-board either through ducts which can be secured to the support or through a passage drilled in the support. At times, however, the support can be a disadvantage in that it can prevent the discharge of air at the desired location, as would be the case for a sting support.

Propulsion simulation for magnetically suspended model presents special practical problems because there can be no physical connection between a compressed air reservoir and the model. Thus, propulsive gases must be generated on-board the model and then exhausted at desired locations on the model, Figure 1. The problem involves defining proper thrust (mass flow rate and velocity) requirements for the propulsive jet(s) and accomplishing gas generation within the volume of the model. Propulsion simulation in its entirety, whether for conventional or magnetically-suspended models, involves both engine intake and exhaust jet flows. Only the latter is addressed in the work presented here. Our rationale is that the first step in simulation of propulsion should be to introduce the effects of the exhaust jet and that the complexities of allowing properly matched inlet flows should be deferred to later stages of development.

Under Phase I of an investigation sponsored by NASA LaRC, the feasibility of generating exhaust jets of appropriate characteristics on-board magnetically-suspended models was examined. Four concepts of remotely-operated propulsion simulators were considered. Three conceptual designs involving conventional technologies such as compressed gas cylinders, liquid monopropellants, and solid propellants were developed. The fourth concept, a laser-assisted thruster, which can potentially simulate both inlet and exhaust flows, was found to require very high power levels (tens of kilowatts). This concept needs further research. The results of Phase I investigation, including a comparative evaluation of the four concepts, are discussed in Ref. 1.

The objective of current Phase II investigation sponsored by NASA LaRC is to demonstrate the measurement of aerodynamic forces/moments, including the effects of exhaust jets, in MSBS wind tunnels. Two propulsion simulator models are being developed, a small-scale and a large-scale unit, both employing compressed, liquified carbon dioxide as propellant. The small-scale unit has been designed, fabricated, and statically-tested at Physical Sciences Inc. (PSI). It will be tested, either as a part of a wind tunnel model or by itself, in the 7-in. University of Southampton MSBS tunnel to measure forces/moments with jet on/off. The MSBS hardware and software is presently being modified for this purpose to be compatible with the impulsive thrust forces associated with propulsive jets. The large-scale simulator is in the preliminary design stage as of this writing. It will be fabricated and statically-tested at PSI.

This paper presents the small-scale simulator design/development and discusses the data from its static testing on a thrust stand. The analysis of this data provides important information for the design of the large-scale unit. The paper concludes with a description of the preliminary design of that device.

II. Propulsion Simulator Design Considerations

Before describing the small-scale simulator, it is appropriate to discuss the design requirements. Since the existing MSBS wind tunnels [2] allow the installation of relatively small models, a very limited volume is available for a propulsion device. Further, the magnetic core used for levitation also needs some space within the model, and the restrictions on the size of the propulsion simulator can indeed be significant. The largest operational MSBS wind tunnel in the U.S. at NASA LaRC has a 13-in. diameter test section. Another MSBS facility at University of Southampton, England, which is more versatile in that it has angle-of-attack variation capability, has only a 7-in. wide test section. In this wind tunnel, the model envelope would typically be 6 to 8-in. in length with 1 to 1.5-in. diameter centerbody. In the NASA tunnel, models 18-in. long by 3-in. diameter can be installed.

Since no external connections can be made to bring jet fluid to a model in an MSBS, the propellant must be carried on-board. The model volume limitations directly translate into the mass of the propellant which can be stored on-board. In turn, this limits the duration over which the exhaust jet can be maintained. For practical applications, this means frequent model refurbishing and thus potentially reduced tunnel productivity with propulsion simulation.

Because no physical connections exist with a magnetically-levitated model, it is necessary to control the propulsive model remotely. Therefore, the source of electrical energy required to open/close valves or initiate ignition must either be carried on-board and triggered externally by such means as radio control or laser.

The characteristics of a particular MSBS also impose some restrictions on the propulsion simulator. These are the weight of the simulator module which can be suspended and the level of the thrust force. The restrictions arise due to the limitations on the amount of current which can be driven through the coils of the external electromagnets (Figure 1). Another consideration is that the model position changes due to the thrust rise (or fall) with time, when propulsion is turned on (or off). This movement must be controllable by the control system of the MSBS.

Finally, any propulsive gas generation technique must be compatible with the particular wind tunnel hardware involved and its operational requirements. Even small quantities of particulate matter or water vapor in the exhaust may not be acceptable in some facilities.s Furthermore, there may be considerations of safety of personnel, requiring special precautions in some cases.

The design considerations are summarized in Table 1. The implementation of these requirements into the simulator design is discussed in Ref. 1.

Perhaps the simplest propulsion simulator is a compressed gas cylinder attached to a nozzle and turned on/off by means of a remotely-controlled valve. However, the mass of gas which can be carried under reasonable pressures in volumes typical of a MSBS wind tunnel models, is so small that the resulting thrust time (or run time) will be of the order of tens of milliseconds. Furthermore, the gas container will have to be refilled under high pressure innumerable times, which makes this approach impractical. A way around this problem is to use gases that liquify easily under pressure at room temperature, so that a significantly larger mass can be stored in a given volume. Among common substances, the candidates are carbon dioxide (CO_2) and ammonia (NH_3). Table 2 lists the physical properties of these gases along with another substance, sulfur dioxide (SO_2) which has some desirable properties.

The ideal propellant gas should have a high density in liquid phase to pack as large a mass as possible in a given volume and a low molecular weight (see Appendix A). Low heat of vaporization is desired so that, as the liquid changes into vapor, it does not draw such a large amount of heat from itself and surrounding walls that it freezes. Low vapor pressure is also desirable, because it means that liquification occurs at lower pressure at a given temperature. Thus, the pressure regulation necessary to drop the pressure to say 45 to 60 psia ($P_{tj}/p_\infty = 3\text{-}4$) is relatively straightforward. That is, compact regulators, necessary in the present application, are easy to find.

Table 1. General Design Considerations for Propulsion Simulators

• Compactness	Smallest size possible for demonstration in current available MSBS tunnels
• High Density Propellant	Ability to carry the largest propellant mass in a given volume inside the model to maximize run time for a specified mass flow rate
• Relatively Lightweight	To minimize the size of magnetic core within the model and currents in external electromagnets
• Remote or Minimum Interference Activation	If remote activation is not feasible, the disturbance to flow field and magnetic field must be negligibly small
• Thrust Level	Compatible with particular MSBS capability
• Thrust versus Time Characteristics	Compatible with MSBS control system capability. Stable thrust duration must be sufficiently long so that data can be obtained after model becomes steady
• Safe Operation	Propellant material should be non-toxic, non-corrosive, with minimum of particulates

Table 2. Physical Properties of Propellant Gases

Gas	Molecular Weight	Vapor Pressure at 70°F (psi)	Density of Liquid (gm/cm^3)	Heat of Vaporization (cal/gm)
CO_2	44	840	0.75	36
NH_3	17	129	0.61	283
SO_2	64	50	1.38	83

An examination of Table 2 shows that each gas has certain advantages and disadvantages. Ammonia has the lowest molecular weight and reasonably low vapor pressure, but it has extremely high heat of vaporization and the lowest density. Sulfur dioxide, on the other hand, has the lowest vapor pressure and highest density (38 percent above water), but the latter is offset by its high molecular weight. The heat of vaporization of SO_2 is considerably lower than that of NH_3. Carbon dioxide has a molecular weight between that of NH_3 and SO_2, the lowest heat of vaporization, and density slightly higher than that of ammonia. A disadvantage of CO_2 is its high vapor pressure (56 atm).

There are some practical advantages of CO_2 that make its choice as a propellant almost inevitable. It is commercially available in cartridges (or cylinders) which vary in weight from a few grams to hundreds of grams. The cylinders are very compact, a cylinder containing 16g of CO_2 measures 3.5 in. long × 1.6 in. diameter, a 60g cylinder measures 5.1 in. long × 0.865 in. diameter.

As these cylinders have wide commercial applications (air guns, life vests, inflatable boats, beverage industry), they are available in any desired quantity at a very low cost. For example, the price of a 16g CO_2 cylinder is less than $2. Another advantage of these cylinders is that they are available in stainless steel (which is non-magnetic) or as magnetizable steel. This is potentially useful because the mass of the cylinder itself can serve as a part o the magnetic core. CO_2 cylinders can be obtained as customized components from Sparklet Devices, Inc.

CO_2 also has some operational advantages over NH_3 and SO_2. In practice, the mass flow rate of the gases will be small (<100 g/s) compared to that in the wind tunnel (~2 kg/s in University of Southampton 7-in. tunnel and 7 kg/s in NASA LaRC 13-in. tunnel) and the duration will be typically less than 5s for one thrusted run. Thus the propellant gases will get quickly mixed, diluted, and dispersed int he wind tunnel-free stream. In open circuit tunnels, of course, the products will leave the test section and not be circulated. CO_2 is a clean, non-contaminating, non-corrosive, and safe gas. NH_3 and SO_2 on the other hand are somewhat corrosive, and can be irritants to eyes and lungs, if released accidentally. The use of these gases then entails special precautions not necessary to CO_2.

Some disadvantages of the compressed gas concept are that miniaturized, remotely operated valves are required to turn the jet on/off, and further, a battery power supply and switch must be incorporated in the model. An inherent limitation of the concept is that the total temperature of the jet is close to room temperature. Therefore, a hot jet is not possible unless heat is added before exhausting the gas, which represents an additional complication. The problem of cooling of the cylinder as the liquid vaporizes can be minimized by surrounding the cylinder with an annular magnetic core which can provide the necessary thermal mass.

It is shown in Appendix A that the thrust and mass flow ranges for a propulsive jet on a typical 1/40-scale model of a fighter aircraft are 2.5 to 3.2 kgf and 0.08 to 0.01 kg/s of CO_2 gas, respectively.

The primary objective of the present work is to demonstrate the operation of a thrusting, propulsive model in an MSBS, and to measure the resulting forces/moments. The University of Southampton wind tunnel to be used for testing has a 7-in. octagonal test section. The small test section size and the desire to achieve high angles of attack (~45 deg), limits the model size. This limitation, in turn, restricts the number and the size of flow control components (a pressure regulator, an on/off solenoid valve, for example) that can be incorporated into the model. It was decided, therefore, to design and build two models: a small-scale simulator for demonstration in an MSBS and a large-scale simulator for static testing only. The small-scale model was developed principally to (1) demonstrate generation of an exhaust jet using CO_2 propellant, (2) guide in the design of the large-scale unit, and (3) verify the control and force/moment measurement of a thrusted model in the Southampton MSBS. The larger model, currently in preliminary design stage, is being developed to (1) generate exhaust jets of desired characteristics, and (2) demonstrate the feasibility of propulsion simulation on larger wind tunnel models representative of practical applications.

The large-scale simulator will be a versatile design for generating a jet with pressure ratio, mass flow, and thrust requirements outlined in Appendix A. Furthermore, this design will permit intermittent, on/off operation of the jet. By contrast, the small-scale simulator is designed to be such that the propellant and some components must be replaced after every jet "run". Moreover, no attempt is made to tailor the jet characteristics to the requirements of Appendix A for the small-scale device.

III. Small-Scale Propulsion Simulator Design

Figure 2 shows the small-scale simulator design which is a 1-1/8-in. diameter cylinder, 8-in. long, with hemispherical ends. The principal components are a 16g, liquified CO_2 cylinder (manufactured by Sparklet Devices), a cap-piercing hardened pin and squib mechanism (adapted from a design by Special Devices, Inc. (SDI)), battery and electronics assembly housed in the nose, three removable sets of copper spheres, and a nozzle. These components are housed inside a tube, 1/8-in. thick, made from an electromagnetic alloy formulated by Connecticut Metals, Inc. (CMI). The total weight of the simulator is about 600g with approximately 500g of magnetizable materials. The latter includes the material of the CO_2 cylinder and other miscellaneous components such as retainer rings, fasteners, spacers, etc. Figure 3 shows the distribution of the magnetizable mass in the simulator.

The simulator consists of three major subassemblies: nose section, center section, and nozzle section. The nose section, which screws onto the center section, contains the battery (Kodak K28A) used as a power source for firing the squib (made by Cartridge Actuated Devices, Inc.) and the electronics assembly. The latter consists of a light-activated switch (EG&G, VTIC1110), a small mirror, and a silicon controlled rectifier, all mounted on a 0.06-in. thick circuit board. The battery is held inside a retaining clamp onto which the circuit board is mounted. An optical filter is embedded in the wall of the nos section. The filter allows HeNe laser wavelength (632.8 nm) to pass to the light activated switch. A pair of 22 AWG wires runs from the circuit board to the squib in the center section.

The center section of the simulator contains the CO_2 cartridge with its threaded neck screwed into a cylinder retainer which is held in place by a squib retainer. The pin-squib mechanism (made by SDI) is screwed into the threaded hole at the center of the squib retainer. The SDI design was modified such that inexpensive squibs made by Cartridge Actuated Devices could be incorporated into it. Had this modification not been done, the complete SDI pin/squib mechanism would have required replacement after each firing, costing about $150. Our design modification makes it possible to replace the squib only, for approximately $5 to $10. Earlier in the program, the "standard" piercing pin in the SDI component was used. This pin (also called "large" pin) as shown in Figure 4(a), had an internal hollow passage 0.050-in. diameter to draw CO_2 from the cylinder. Two holes, 0.050-in. diameter, in the 0.045-in. thick walls of the standard pin, expel the CO_2 into a stagnation chamber. The gas then flows from the chamber into a cavity surrounding the squib assembly through four oval passages drilled into the squib retainer (Figure 5). Another pin, with smaller outside and inside diameters, and with smaller ports for expelling CO_2, was also used during development, Figure 4b. Both pins were case-hardened to ensure reliable penetration of the diaphragm of the CO_2 cylinder. Moreover, hardening also improved the usable life of the firing pin. Two holes (not shown in Figure 2) are drilled into the wall of the center section for measuring pressure in the stagnation chamber and in the cavity upstream of the nozzle section. The two 22 AWG wires connecting the squib to the electronics in the nose section pass through a lengthwise groove machined in the wall of the center section.

The nozzle section screws onto the backend of the center section of the simulator. It contains three baffle assemblies which can be loaded with copper spheres of 1 or 2 mm diameter.

Each assembly consists of a copper housing (a ring as shown in Figure 2) with a copper wire mesh at each end for retaining the spheres. Each assembly can be individually removed and replaced by a ring made of the CMI electromagnetic alloy. The purpose of the three copper plugs was to introduce a drop in total pressure as the CO_2 negotiated a tortuous path, and secondly, to vaporize any fine solid particles of CO_2 which may be present in the flow. As will be discussed later, the copper plugs were not always effective. A convergent passage was drilled into the nozzle with a baseline diameter of 0.098 in. A separate nozzle section with exit diameters of 0.298 in. was also used. Both nozzle sections were tested. The larger nozzle, used on a 1/40-scale model, corresponds to 12-in. full-scale throat diameter. A pressure tap was drilled into the nozzle wall downstream of the copper plugs and upstream of the exit orifice.

The operation of the small-scale simulator consists of shining a HeNe laser beam onto the optical filter in the nose section. The light switch is activated and the SCR then draws approximately 1 amp current from the battery to fire the squib. Explosion of the squib drives the pin (which moves against O-ring friction) into the diaphragm which caps the CO_2 cylinder. Only about 45 psi pressure is needed to rupture the diaphragm and the squib supplies 70 to 150 psi from the gaseous products of explosion. After penetration the pin stays in place due to the friction of the O-ring inside the housing of the SDI squib assembly. CO_2 liquid-gas mixture flows through the center passage in the pin and escapes through the two holes drilled in the walls (Figure 4). Upon passage through the squib retainer (Figure 5), the CO_2 flows through the copper plug(s) into the nozzle chamber and out through the orifice producing a jet.

IV. Results of Static Testing of Small-Scale Simulator

As mentioned under Design Considerations, the small scale model was developed primarily to verify the control of and force/moment measurement on an impulsively-thrusted model in an MSBS and to guide in the design of the large-scale unit. Toward these objectives, a series of static tests was conducted. The tests were designed to yield thrust versus time history and pressure versus time history, the latter at three locations within the simulator. The thrust versus time data are necessary for design of the MSBS control system so that the model stays in place as it reacts to the propulsive jet turning on/off. The pressure data, which are diagnostic in nature, provide important insight into the effectiveness of the copper plug(s) in creating a pressure drop and into the gas dynamic processes within the simulator.

The schematic of the static-test set-up is shown in Figure 6. A load cell manufactured by Sensotec was used to obtain force (i.e., thrust) data. The pressure transducers were supplied by D.J. Industries and located as shown in Figure 6b. The pressure P_2 and P_1 give a measure of the effectiveness of the copper spheres in creating a pressure drop. The pressures P_2 and P_3 give a measure of the gas dynamic processes and losses due to jet impingement on the cylindrical walls of the simulator. The load cell and transducer signals were sampled at 1 kHz. Visual observations of the jet just outside the nozzle exit plane indicated whether or not mist was present. The presence of mist shows that the copper spheres were not very effective in vaporizing the tiny solid particles formed during the expansion of CO_2 from compressed liquid to vapor.

The test variables were:

- Simulator orientation:

  In the vertically-up orientation shown in Figure 6a, vapor rather than liquid is being drawn through the pin upon its penetration into the CO_2 cylinder. In a vertically-down configuration, one expects the liquid to be drawn through the pin, and the vaporization to take place in the stagnation chamber (pressure P_3 in Figure 6a). Of course, in practice, the simulator will be used mostly in a horizontal position or with the jet pointing downward, except in few instances of negative angle-of-attack. The effects of simulator orientation, therefore, are expected to be important. Static tests were conducted in all three orientations.

- Copper plug structure:

  The copper plug(s) were introduced in the small-scale simulator to act as a pressure-drop device and also to aid in vaporizing small solid particles in the CO_2 stream. The data on effectiveness of the plug in performing these functions are necessary to guide the design of the large-scale simulator. For example, a pressure regulator and a heater (i.e., vaporizer) may have to be incorporated, if the copper plugs are found to be not very effective.

- Pin design:

  The internal passage diameter of the piercing pin (Figure 4) determines the maximum possible mass flow rate through the propulsive device and thus its internal pressure and thrust versus time characteristics. Tests were conducted using a so-called "standard" or "large" pin, Figure 4a, and a "small" pin, Figure 4b.

- Nozzle diameter:

  The nozzle diameter determines the actual mass flow rate through the simulator and thus thrust level duration. Further, the nozzle area is an important design parameter of the aircraft configuration being tested. Two values of diameter, 0.098 and 0.295, were used in the static tests.

Selected data from the simulator tests are presented in Figures 7 through 16. Each figure contains thrust and pressure versus time history. The three pressures, P_1, P_2, and P_3 are given on the same plot. Appendix B contains the small-scale simulator test matrix.

Figure 7 shows thrust and pressure curves for the baseline simulator configuration without any copper plugs. After an initial spike which reaches 4 lbf, the thrust rises to a maximum of about 1.9 lbf in about 0.1s and decreases gradually over the next 1.2s. An average thrust of about 1 lbf over a duration of 0.5s is achieved. The rise in thrust is due to the increase of pressure as the CO_2 fills up the simulator volume. The fall in thrust thereafter is directly due to the dropping stagnation pressure inside the simulator as the CO_2 escapes through the nozzle. The thrust behavior correlates well with the pressure history in Figure 7b. The pressures P_2 and P_3 are coincident in this figure. Unfortunately, the P_1 transducer was overpressurized and saturated during this run. The initial spike in Figure 7a is a ubiquitous feature of most thrust data. It represents the impact of the piercing pin on the diaphragm of the CO_2 cylinder. The duration of this spike is a few milliseconds. It should also be pointed out the time elapsed from the instant that the laser triggers the light-activated switch to the instant the pin impacts the cylinder is of the order of 20 to 50 ms. This interval includes the electronics reaction time and the firing of the squib.

Figure 8 shows thrust and pressure histories when three sets of copper plugs, each packed with 2 mm diameter copper spheres, are placed upstream of the nozzle. A comparison of Figures 7 and 8 shows that the thrust curves are nearly the same and the pressures are also substantially similar. Thus, for the simulator with a large (or standard) piercing pin, the copper plug has little effect on the flow and pressures inside the simulator.

Figures 9 and 10 show the effect of simulator orientation on thrust and pressure characteristics. In Figure 9, the simulator was horizontal and incorporated the same copper plugs as the configuration in Figure 8. The peak thrust in the horizontal orientation is slightly higher and falls off somewhat faster than the vertically-up orientation of Figure 8. The data in Figure 9 is also more noisy and is believed to be an artifact of the simulator cantilevered from the load cell. The pressures in Figure 9b are seen to be greater than those in Figure 8b, which explains the thrust behavior. Figure 10 shows data for the simulator firing the jet vertically down. The copper plugs are the same as for Figures 8 and 9. A comparison between Figure 8 and Figure 10 reveals that the thrust is substantially higher when liquid CO_2 is drawn because greater mass of CO_2 enters the stagnation chamber in a given time. Further, the thrust maintains its higher level for about 0.5s before beginning to drop-off rapidly. This behavior suggests that the liquid CO_2 escaping into the stagnation chamber of the simulator (Figure 2) vaporizes. During this process, liquid-vapor equilibrium is maintained, and the pressure tends to remain constant. However, the pressure drops as the CO_2 vapor leaves through the nozzle. The net effect of these two opposing processes is to reduce the rate at which pressure and thrust drop. A comparison of Figures 10b and 8b shows higher pressure for the vertically-down orientation. Also, the behavior of pressure with respect to time in Figure 10b explains the thrust history in Figure 10a.

Figure 11 shows an interesting observation when the CO_2 mass flow rate into the stagnation chamber is extremely high. This condition occurred when the piercing pin was pushed back (due to the wear of an O-ring in the squib assembly) by the high pressure CO_2, resulting in efflux through a larger area (0.095-in. diameter) than the normal two-hole configuration (0.05-in. diameter each), Figure 4. The consequence is very high peak thrust, ~5 lbf which drops off rapidly, Figure 11a. The pressure has now reached a very high value, almost 600 psi, Figure 11b.

Figure 12 illustrates the effect of changing the copper plug arrangement to one set of 1 mm diameter copper spheres and tightly packed bronze wool replacing the other two sets. Comparison with Figure 8 shows the thrust and pressure histories to be very similar in both cases. Thus, the structure of the plug has very little effect on the flow processes within the simulator. Note in Figure 12b that the three pressures, P_1, P_2, and P_3 at different locations (Figure 6) are very close. This indicates that with the 0.098-in. diameter exit nozzle, the simulator behaves essentially like a closed vessel which is pressurized by the CO_2, maintaining pressure equilibrium throughout its volume. This would explain the ineffectiveness of the copper plug observed thus far.

Figure 13 shows the effect of reducing the mass flow rate from the CO_2 cylinder by using the "small" pin design of Figure 4b. Comparison with Figure 12, which presents data for the large pin in Figure 4a, reveals lower thrust level and longer duration with the small pin, as one would expect. The peak thrust is approximately 1.4 lbf and the average thrust is about 0.75 lbf over 0.75s. The pressures with the small pin (Figure 13b) are correspondingly lower in comparison with the large pin (Figure 12b).

Figure 14 through 16 contain data of the case of a larger nozzle diameter (0.295 in.) with both the large and small piercing pins. With the standard, large pin, the thrust in Figure 14a may be compared with Figure 12a. As one would expect, with a larger nozzle, the pressures are lower (Figures 14b versus 12b) and the thrust is lower, but it drops off at a slower rate. The slower rate is due to reduced mass flow rate through the nozzle, resulting from lower (i.e., subsonic) pressure ratio relative to the ambient. The effect of removing the copper plug with the 0.295-in. diameter nozzle on the simulator is to decrease significantly the thrust as seen from Figure 15a, indicating that the plug, rather than the nozzle, was the controlling area for the mass flow rate. The pressures throughout the simulator volume, especially upstream of the nozzle, are low (and noisy), Figure 15b. Finally, Figure 16 illustrates the thrust and pressure histories for the simulator configuration with a 0.295-in. diameter nozzle, "small" pin, and a plug made of one set of 1 mm diameter copper spheres plus bronze wool. When compared with "large" pin data of Figure 14, the thrust (and pressures) are lower with the small pin.

During the series of static tests, visual observations of the CO_2 jet from the nozzle indicated presence of white mist frequently, even with the copper plugs and bronze wool in place. Thus the effectiveness of the copper spheres in vaporizing solid particles upon contact is questionable. It is possible that the particles are so fine that they follow the gas streamlines without actually making contact with the spheres.

It can be summarized from results of the static tests of the small-scale simulator that a working device for wind tunnel testing in the University of Southampton's MSBS has been developed. Toward the design of the large-scale simulator, it appears that the copper plugs have little effect on pressure regulation (especially at the higher mass flow rates and higher thrust level with the small diameter nozzle) and on solid particle vaporization. The internal passage diameter of the piercing pin which controls the mass flow rate from the CO_2 cylinder has a significant effect on the simulator's thrust and fluid dynamics. Finally, as expected, the spatial orientation of the simulator has a significant effect on its thrust characteristics.

V. Large Scale Propulsion Simulator Preliminary Design

As mentioned earlier, the large-scale simulator design is based upon the lessons learned from the small-scale simulator experience. The large-scale device is intended only for static testing on a thrust stand. It is apparent from the review of the small-scale test data that an active pressure control component and a means of vaporizing small solid CO_2 particles must be incorporated into the large-scale design. Furthermore, one must be able to turn the simulator on/off during wind tunnel testing. The thrust and mass flow requirements are as defined in Appendix A.

Taking the above requirements into account, a preliminary design of the large-scale simulator, shown in Figure 17, has been developed. The overall envelope is 2.5-in. diameter and

16-in. long. It incorporates an aluminum cylinder made by Clift Impact Division of Parker Corporation for CO_2 storage. The cylinder incorporates a siphon to ensure that liquid CO_2, rather than vapor, is drawn to meet the large mass flows required (~80 g/s). The flow of liquid CO_2 is turned on/off by a miniature solenoid valve made by General Valve Corporation. It is operated by an on-board battery via a light activated switch. The liquid CO_2 flows through numerous conduits drilled inside a heated copper block and vaporizes in the process. More heat is added to the CO_2 as it flows through a vaporizer which incorporates a number of thin, twisted plates to provide large surface area. The entire copper block/vaporizer assembly is wrapped in a 150W Kapton film heater and surrounded by insulation. The heater will be run on external AC power prior to a propulsion test run. In MSBS applications, the power connection can be in the tunnel walls or at the model itself. In the former case, it may be permissible to let two small wires float in the wind tunnel stream. The flow from the vaporizer enters a pressure regulator (Tescom Corporation) which can be set to yield the required pressure ratio across the nozzle. The regulator must maintain a constant outlet pressure as its inlet pressure varies from approximately 900 to 100 psia. For nozzle pressure ratios of 2 through 5, the nozzle pressure must in the range 30 to 75 psia. The flow from the regulator enters a nozzle chamber through a series of holes drilled into an impingement plate. The function of this plate is to distribute the flow uniformly. The entire simulator assembly will be contained in a cylinder machined out of the electromagnetic alloy developed by CMI Company. The estimated weight of the large scale simulator is 3.9 kg including 1.9 kg of magnetizable materials.

As of this writing, all the components for the large scale design have been selected and detail design is in progress.

VI. Summary of Results

A small-scale propulsion simulator has been developed and statically-tested to determine its thrust versus time characteristics. The device will be tested in the University of Southampton MSBS wind tunnel in the near future.

The mechanical and electronics systems of the small-scale simulator were thoroughly tested and improved as necessary during the static tests. Hardened piercing pins have been developed and O-ring (inside the squib assembly) replacement frequency has been established to substantially increase reliability of the device.

The copper plugs incorporated in the small-scale design appeared to have little effect on pressure regulation or on vaporization of small, solid CO_2 particles. Although not entirely conclusive, this points to the need of a pressure regulator and a vaporizer device in the large-scale simulator design.

Static tests of the small scale simulator have shown that its spatial orientation has a significant effect on the thrust versus time characteristics. Furthermore, the internal passage diameter of the piercing pin, which controls the mass flow rate from the CO_2 cylinder, has a significant effect on the simulator's thrust and fluid dynamics.

Based on the experience from the small scale simulator development and testing, a preliminary design of the large-scale simulator has been completed. Detail design of this device is in progress. This simulator will be subjected to static tests later in this program.

VII. Recommendations for Future Work

The large-sale simulator currently being developed needs further design trade-off studies. The pressure regulator and vaporizer components are compact, but still they take up substantial volume and weight which would otherwise be available for additional propellant. Although the use of porous media (copper spheres, bronze wool) has not proved effective in the small-scale simulator, it must be recognized that the volumes employed were modest (1-in. diameter × 1-in. long cylinder). Also, the influence of the flow area of the porous plug relative to nozzle area has not been fully investigated thus far. It is possible that a substantially longer porous plug (yet smaller in length than the regulator plus vaporizer) may be effective. To determine this, it will be useful to develop an analytical model of the flow within the simulator and of the vaporization/efflux from the CO_2 cylinder. Such a model can be used for parametric design studies characteristics and for predicting thrust versus time behavior.

VIII. References

1. Joshi, P.B., et al., "Propulsion Simulation for Magnetically-Suspended Wind Tunnel Models," Physical Sciences Inc., PSI-2055/TR-859, NASA Contract No. NAS1-18616, September 1988.

2. Tuttle, M.H., Kilgore, R.A., and Boyden, R.P., "Magnetic Suspension and Balance Systems, A Selected, Annotated, Bibliography," NASA TM 84661, July 1983.

Acknowledgements

This work was supported by NASA Langley Research Center under Contract No. NAS1-18845. The authors wish to acknowledge the comments and contributions of Dr. Evan Pugh at Physical Sciences Inc. and Dr. Michael Goodyear at University of Southampton during this investigation.

APPENDIX A

Reference 1 shows that the characteristics of current jet engines require

$$\frac{\dot{m}}{A}\sqrt{RT_{oj}} = 1000 - 1200 \text{ lbm/in}^2\text{-s} \cdot \text{ft/s} \quad \text{(A-1)}$$

$$\frac{T}{A} = 40 - 50 \text{ lbf/in}^2 \quad \text{(A-2)}$$

$$\frac{P_{oj}}{p_\infty} = 2.5 - 4.5 \quad \text{(A-3)}$$

where:

$\dot{m}$ = mass flow rate lbm/s
A = nozzle throat area
R = R_{univ}/mol wt
= gas constant of propellant, ft-lbf/lbm °R
T_{oj} = stagnation temperature of exhaust, °R
T = thrust, lbf
P_{oj} = stagnation pressure of exhaust, lbf/in^2
p_∞ = ambient pressure, lbf/in^2.

To keep $\dot{m}$ small (for maximum "run" time out of a given storage volume), T_{oj} must be high and molecular weight low - i.e., higher jet velocity. The area A is determined by geometrical scaling of the model. The pressure ratio is determined by similarity of jet expansion characteristics.

It is of interest to determine the mass flow rates of typical propellant gases from the requirements stated above. For this purpose an exit area for the jet, A, must be chosen. The 1/40-scale throat area for an F-404 engine at maximum power is approximately 0.14 in.^{2} or 0.43-in. diameter. Table A-1 shows the required mass rates for typical gases, carbon dioxide and helium, at room temperature (300°K) and at 1200°K. It is clear that helium at high temperature has the smallest mass flow rate. However, in a typical 5s run, approximately 60g or 15 moles of helium will be needed. For this amount of helium to be carried in a cylinder approximately 1-in. diameter and 5-in. long, the required pressure will be in excess of 5000 atm or density greater than 1 gm/cm^3! As discussed in the main text, carbon dioxide is a more attractive propellant in spite of its greater molecular weight because it can be carried in liquified form under pressure.

Table A-1. Typical Mass Flow Rate and Thrust Requirements

Gas	Molecular Weight	Mass Flow Rate*, g/s		Thrust (kgf)
		@ T° = 300°K	@ T° = 1200°K	
CO_2	44	80-100	40-50	2.5-3.2
He	4	25-30	12-15	2.5-3.2

*A = 0.14 in.^{2} (0.43-in. diameter) with parameters as specified by Eqs. (A-1) to (A-3).

The mass flow requirements in Table A-1 must be adjusted if a smaller jet area must be chosen due to model size constraints dictated by common MSBS wind tunnels. A 1/40-scale F-16 (which has the F-404 engine) has a wing span of 9.3 in. and can be accommodated in the 13-in. NASA LaRC MSBS tunnel, but not in the University of Southampton tunnel.

APPENDIX B

Small Scale Simulator Test Matrix

Test No.	Configuration			Pin Size	Comment
	Orientation	Cu Plug	Nozzle Diameter (in.)		
1	Vertical (up)	2 mm-1 set	0.098	Large	No pressure data
2	Vertical (up)	2 mm-1 set	0.098	Large	Cylinder didn't open - pin OD was larger than center section of bottle diaphragm
3	Vertical (up)	None	0.098	Large	Good
4	Vertical (up)	2 mm-1 set	0.098	Large	Dull pin
5	Vertical (up)	2 mm-1 set	0.098	Large	Repeat of 4
6	Vertical (up)	2 mm-1 set	0.098	Large	Hardened pin - OD too large
7	Vertical (up)	2 mm-1 set	0.098	Large	Pin OD turned down by 0.005 in. - worked
8	Vertical (up)	2 mm-3 sets	0.098	Large	Good shot
9	Vertical (up)	2 mm-3 sets	0.098	Large	Blocked pin orifice
10	Vertical (up)	2 mm-3 sets	0.098	Large	Pin pushed out of CO_2 cylinder, overpressurization, P_1 transducer failed
11	Vertical (up)	2 mm-3 sets	0.098	Large	Good shot, no P_1 data
12	Horizontal	2 mm-3 sets	0.098	Large	Good shot, not much CO_2 cloud
13	Horizontal	2 mm-3 sets	0.098	Large	Good shot, repeat of 12
14	Vertical (down)	2 mm-3 sets	0.098	Large	Good shot, repeat of 13
15	Vertical (down)	2 mm-3 sets	0.098	Large	Good shot, repeat of 14

Small Scale Simulator Test Matrix (Continued)

Test No.	Configuration			Pin Size	Comment
	Orientation	Cu Plug	Nozzle Diameter (in.)		
16	Horizontal	2 mm-1 set 1 mm-2 sets	0.098	Large	Pin pushed out of bottle, P_1 working
17	Horizontal	2 mm-1 set 1 mm-2 sets	0.098	Large	Good shot, redo 16
18	Horizontal	2 mm-1 set 1 mm-2 sets	0.098	Large	Good shot, repeat of 17
19	Horizontal	2 mm-1 set 1 mm-2 sets	0.098	Large	Good shot, repeat of 18. P3 adjusted to measure total pressure
20	Horizontal	1 mm-1 set bronze wool	0.098	Large	Good
21	Horizontal	1 mm-1 set bronze wool	0.098	Large	Good
22	Horizontal	1 mm-1 set bronze wool	0.098	Small	Pin pushed out of bottle - OD of pin same as large pin
23	Horizontal	1 mm-1 set bronze wool	0.098	Small	Redo 23 - good run. OD reduced. Note $P_2 v P_3$ pressure drop, longer run at flatter thrust
24	Horizontal	1 mm-1 set bronze wool	0.098	Small	Repeat of 24
25	Horizontal	2 mm-1 set bronze wool	0.295	Large	Very high thrust, short run 0.2s, P_2 - P_3, P_1 low - substantial drop through plug
26	Horizontal	2 mm-1 set bronze wool	0.295	Large	Redo 25, good
27	Horizontal	2 mm-1 set bronze wool	0.295	Large	Repeat 26

Small Scale Simulator Test Matrix (Concluded)

Test No.	Configuration			Pin Size	Comment
	Orientation	Cu Plug	Nozzle Diameter (in.)		
28	Horizontal	None	0.295	Large	Initial "ringing" in thrust profile. Pressures too low, in transducer noise, 60 cycle noise on force
29	Horizontal	None	0.295	Large	Redo 28, same result
30	Horizontal	1 mm-1 set bronze wool	0.295	Small	Low thrust level, longer run
31	Horizontal	1 mm-1 set bronze wool	0.295	Small	Repeat of 30

Notes:

1. The P_1 pressure transducer saturated during Test 8 and failed during Test 10. It was replaced in Test 16.

2. Following Test 19, the orientation of the CO_2 jet from the pin was adjusted such that it impinged directly on the P_3 pressure port, providing a more reliable measure of stagnation pressure.

3. Pressure transducer ranges were:

   P_3: 1000 psi
   P_2: 500 psi for runs < Test 16
   : 5000 psi for runs ≥ Test 16
   P_1: 100 psi for runs < Test 16
   : 500 psi for runs ≥ Test 16

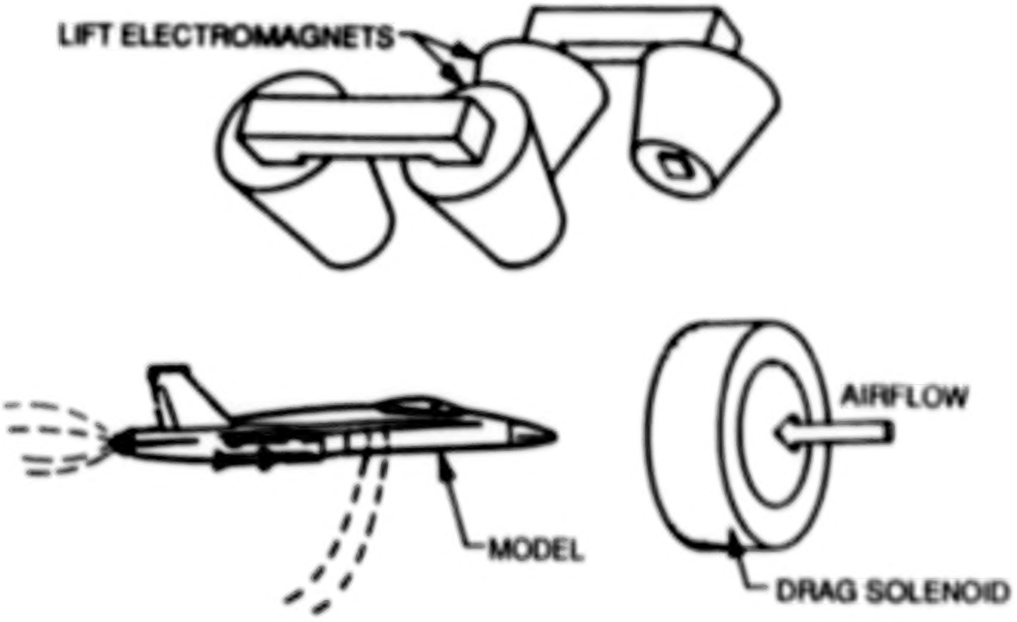
LIFT ELECTROMAGNETS
AIRFLOW
MODEL
DRAG SOLENOID
A-5752

Figure 1. Schematic of Propulsion Simulation on a Magnetically Suspended Model

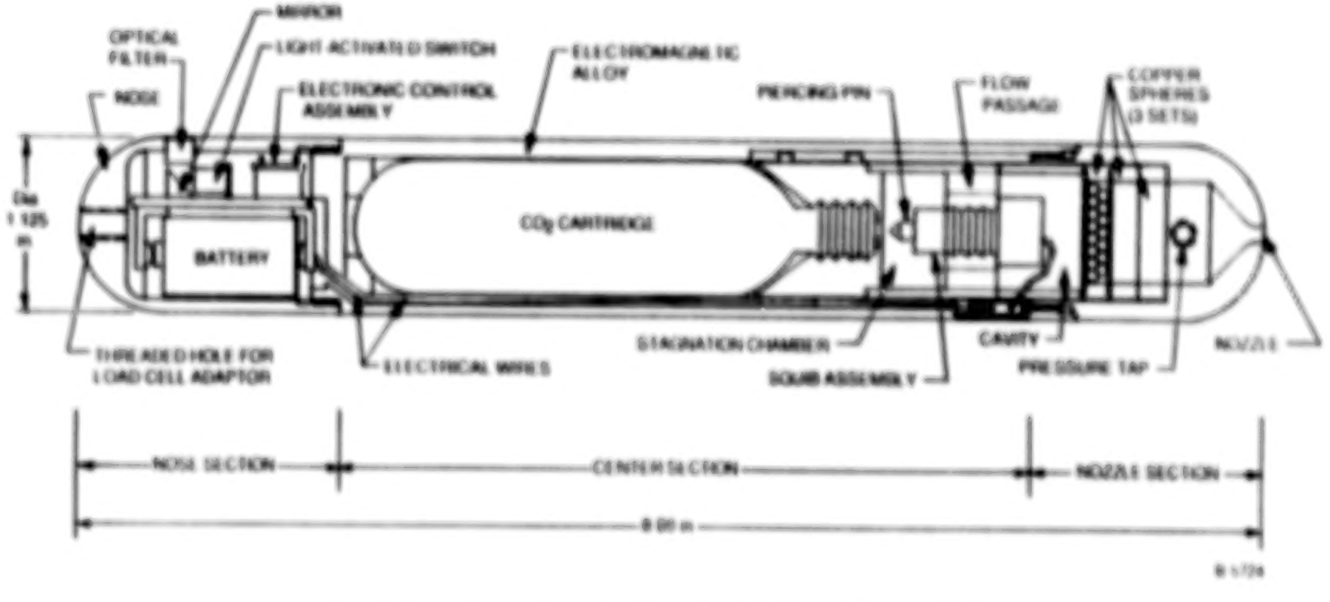
MIRROR
OPTICAL FILTER
LIGHT ACTIVATED SWITCH
ELECTROMAGNETIC ALLOY
NOSE
ELECTRONIC CONTROL ASSEMBLY
PIERCING PIN
FLOW PASSAGE
COPPER SPHERES (3 SETS)
Dia 1.125 in
BATTERY
CO_2 CARTRIDGE
THREADED HOLE FOR LOAD CELL ADAPTOR
ELECTRICAL WIRES
STAGNATION CHAMBER
SQUIB ASSEMBLY
CAVITY
PRESSURE TAP
NOZZLE
NOSE SECTION
CENTER SECTION
NOZZLE SECTION
8.00 in

Figure 2. Small-Scale Propulsion Simulator Design

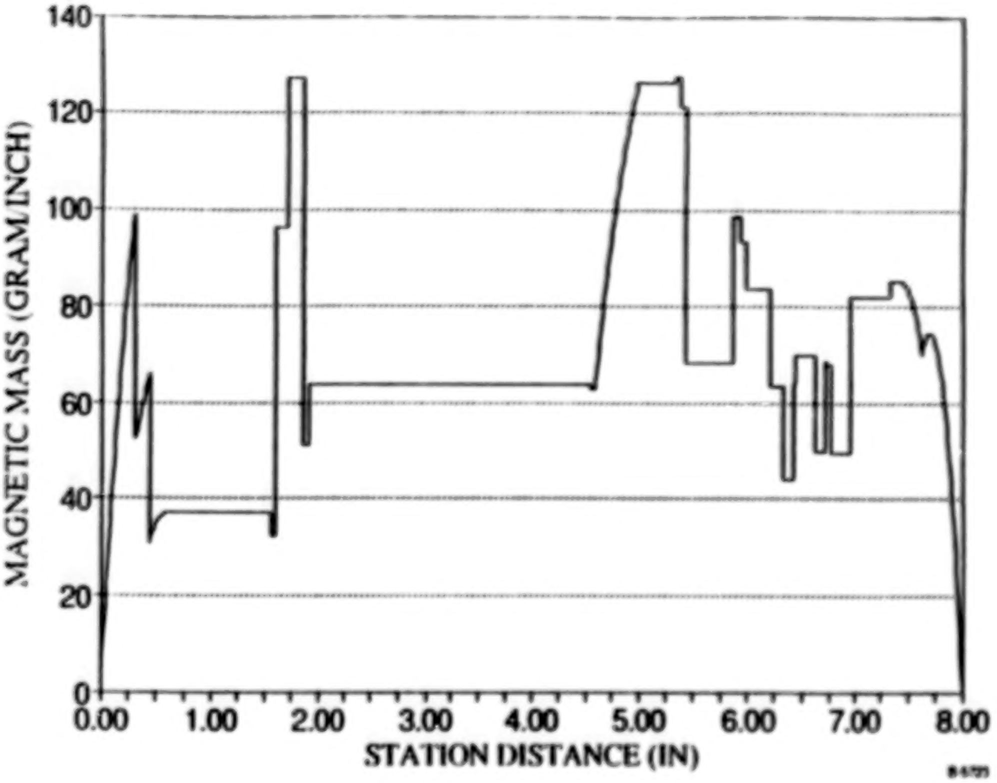

Figure 3. Magnetic Mass Distribution in the Small Scale Simulator

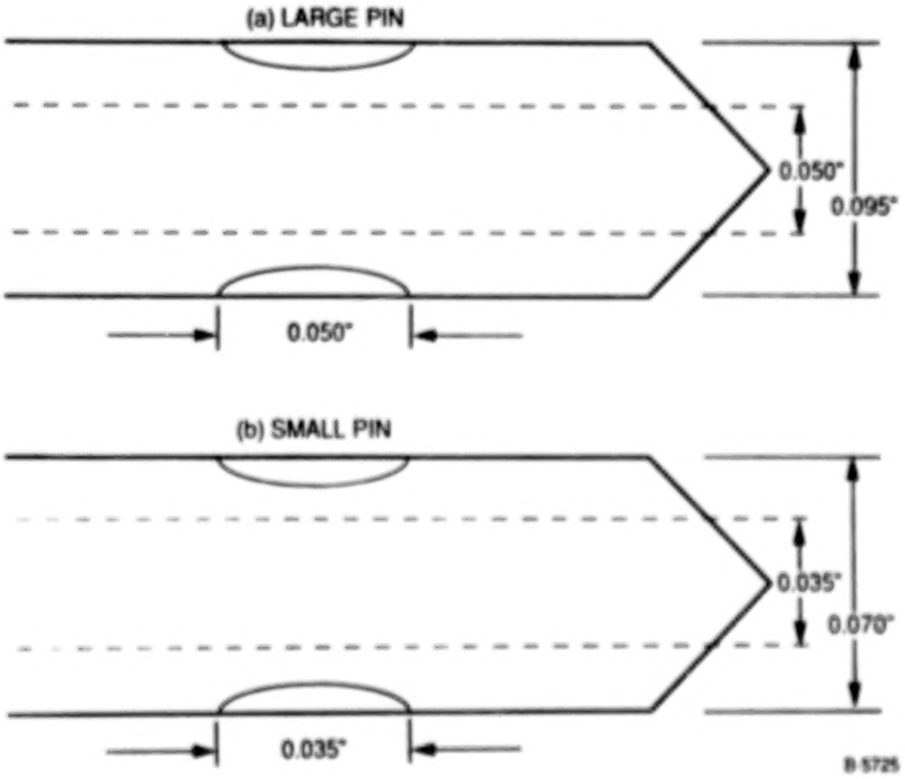
(a) LARGE PIN
0.050"
0.095"
0.050"
(b) SMALL PIN
0.035"
0.070"
0.035"
B-5725

Figure 4. Large and Small Piercing Pin Design for Small Scale Simulator

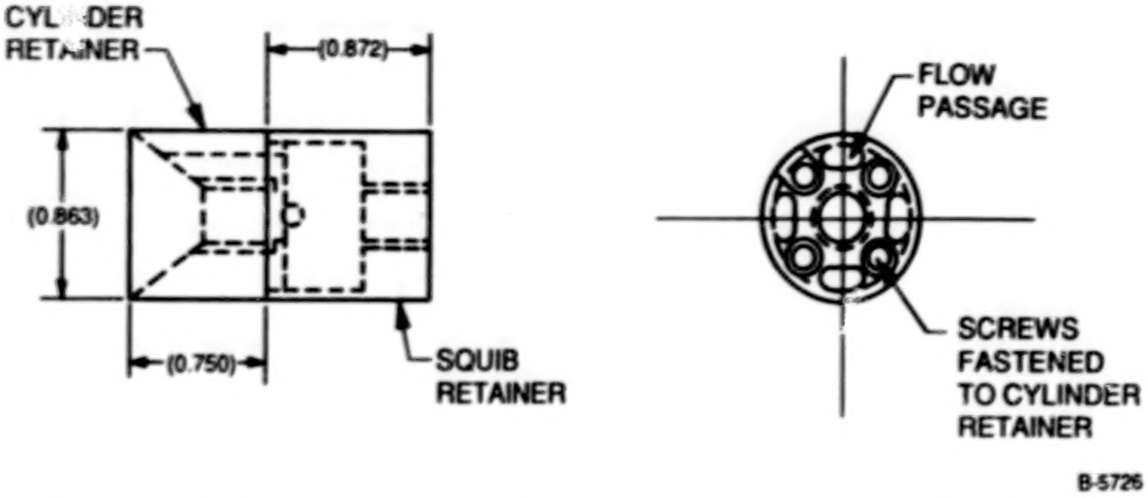
CYLINDER RETAINER
(0.872)
(0.863)
(0.750)
SQUIB RETAINER
FLOW PASSAGE
SCREWS FASTENED TO CYLINDER RETAINER
B-5726

Figure 5. Cylinder and Squib Retainer Arrangement in Small Scale Simulator

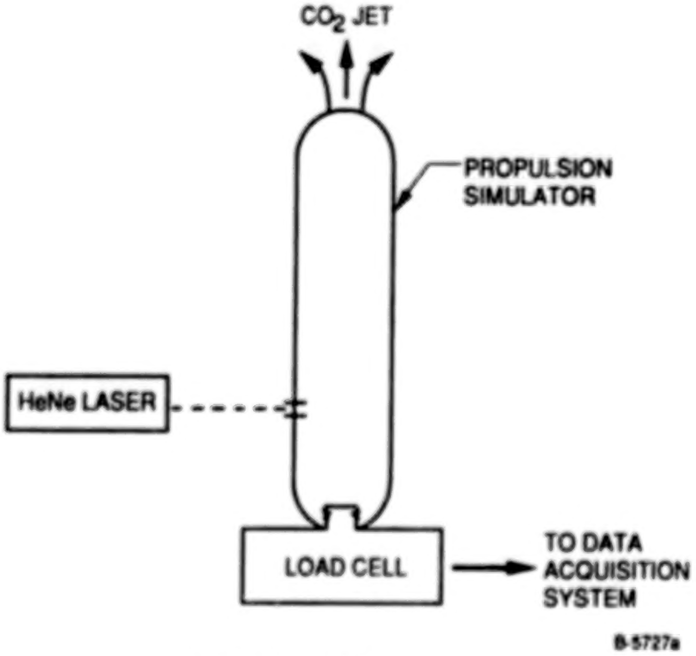
CO_2 JET
PROPULSION SIMULATOR
HeNe LASER
LOAD CELL
TO DATA ACQUISITION SYSTEM
B-5727a

(a) Thrust Measurements

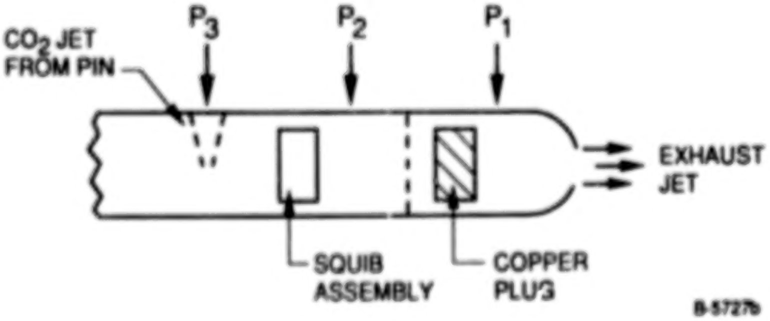
CO_2 JET FROM PIN
P_3
P_2
P_1
EXHAUST JET
SQUIB ASSEMBLY
COPPER PLUG
B-5727b

(b) Pressure Measurement

Figure 6. Schematic of Small-Scale Simulator Static Testing

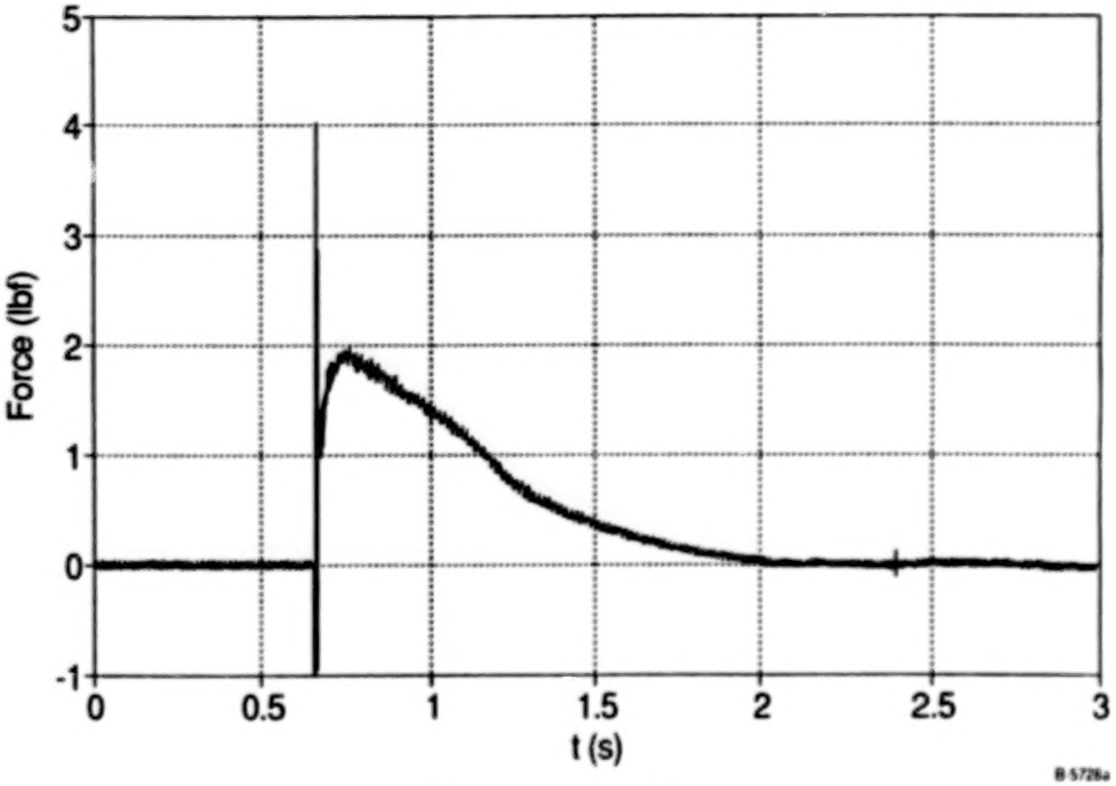

(a) Thrust versus Time

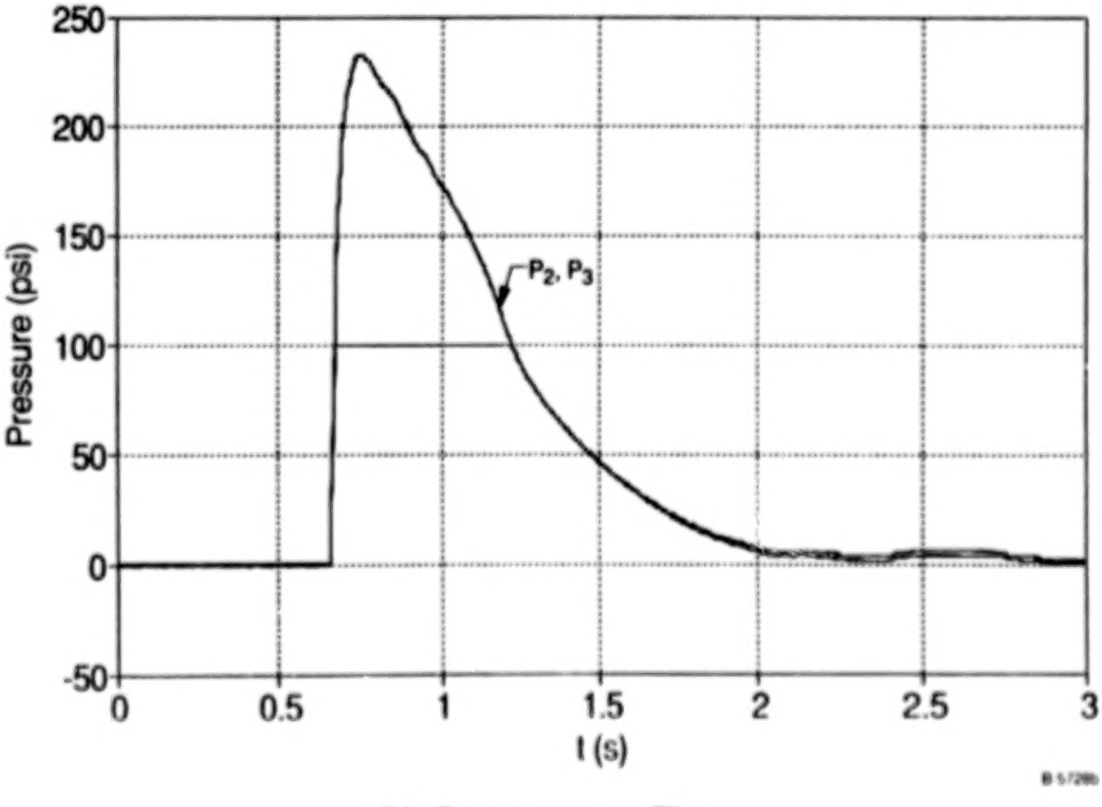

(b) Pressure versus Time

Figure 7. Thrust and Pressure Time History for Baseline Configuration Without Copper Plug (large pin, 0.098-in. diameter nozzle, vertical up orientation)

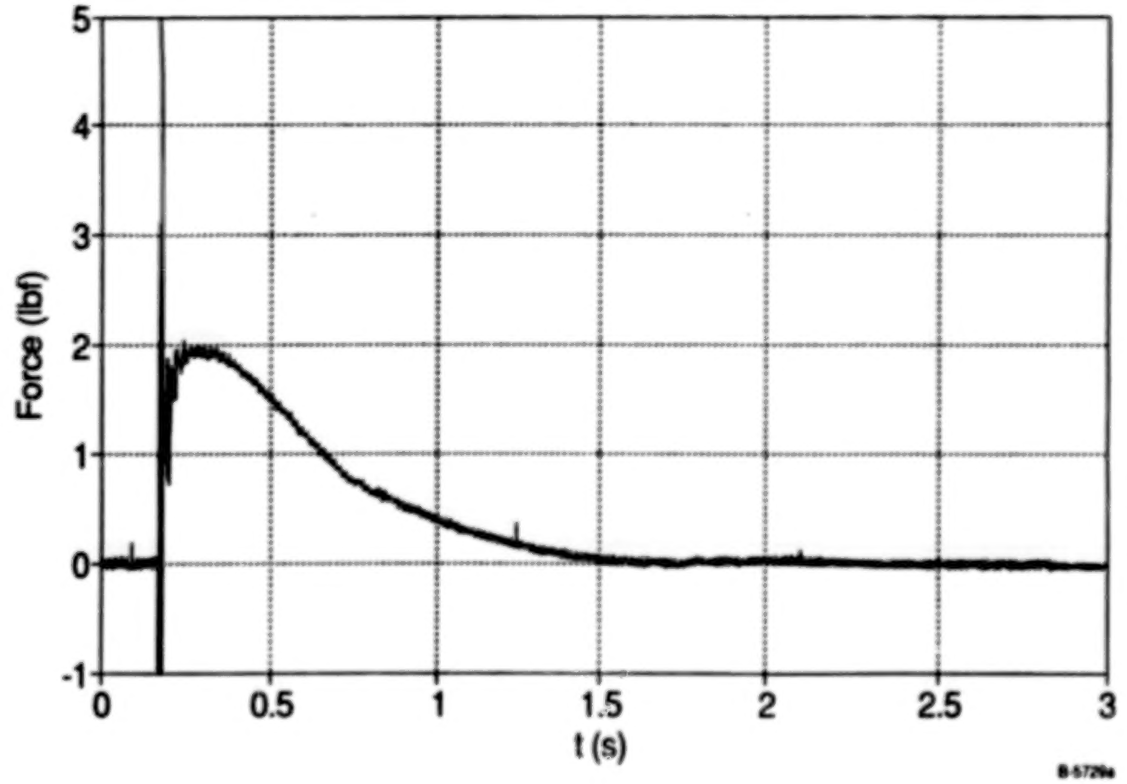

(a) Thrust versus Time

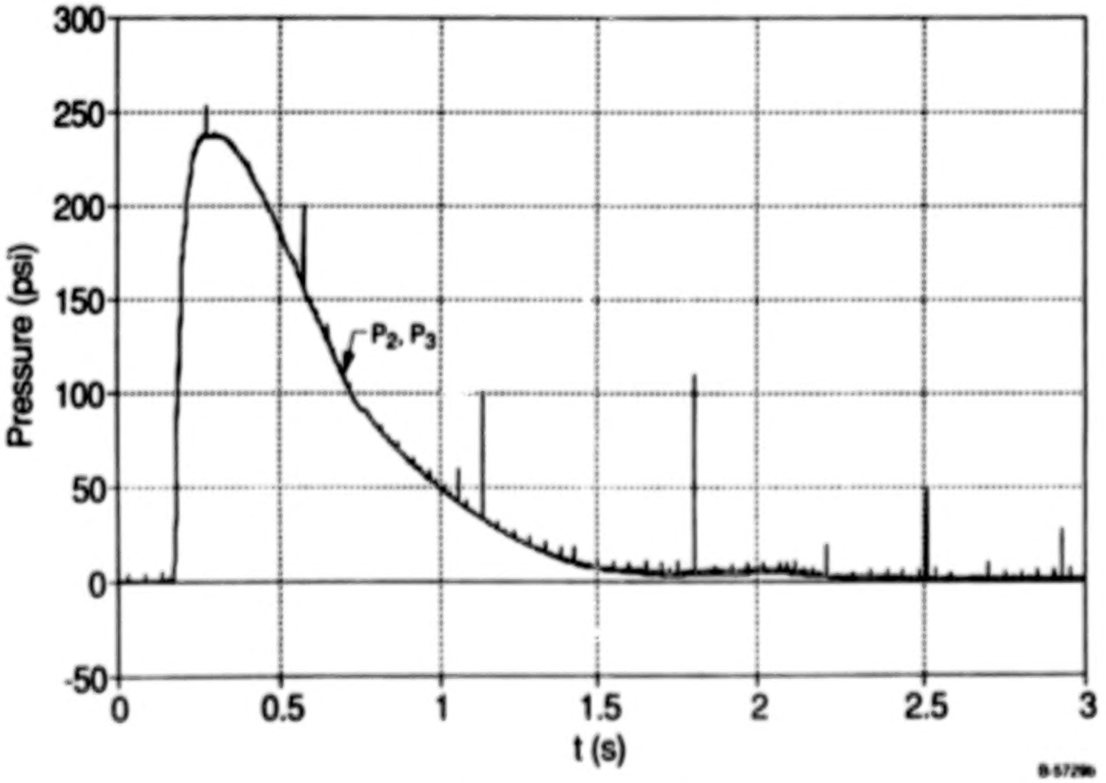

(b) Pressure versus Time

Figure 8. Effect of Three Sets of 2 mm Diameter Copper Spheres son Thrust and Pressure Time History (large pin, 0.098-in.diameter nozzle, vertical up simulator orientation)

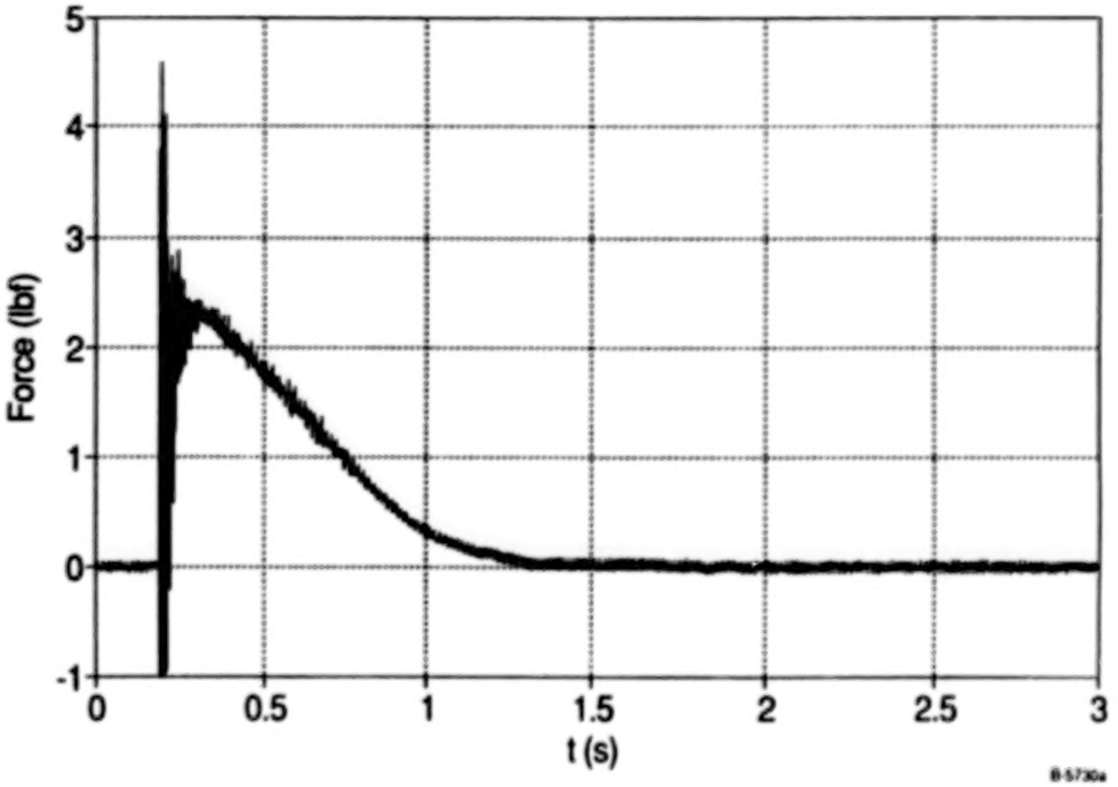

(a) Thrust versus Time

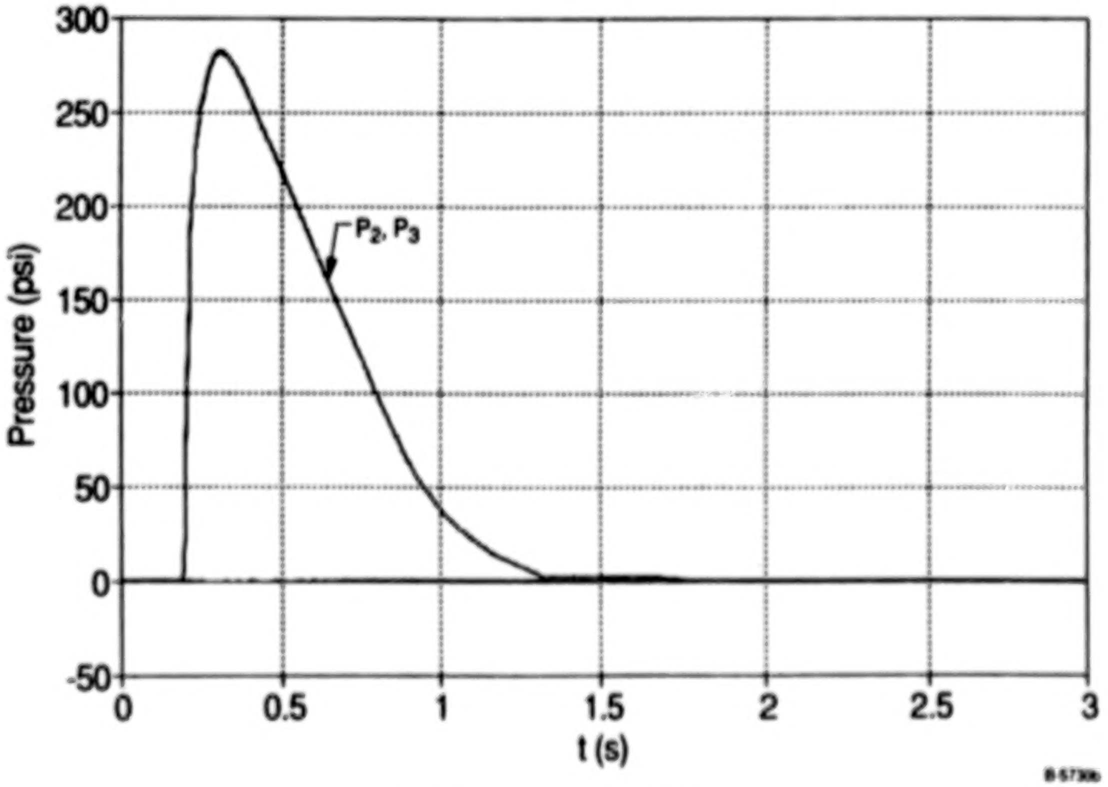

(b) Pressure versus Time

Figure 9. Effect of Horizontal Simulator Orientation on Thrust and Pressure Time History (large pin, 0.098-in.diameter nozzle, three sets of 2 mm copper spheres)

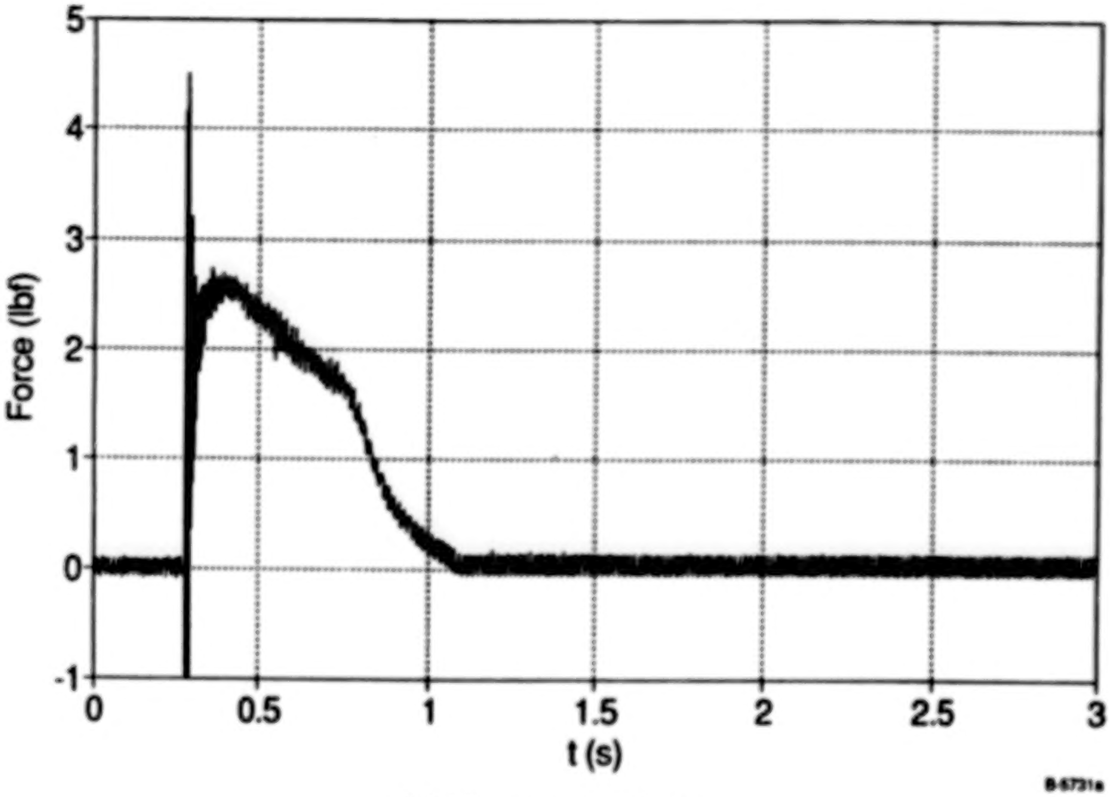

(a) Thrust versus Time

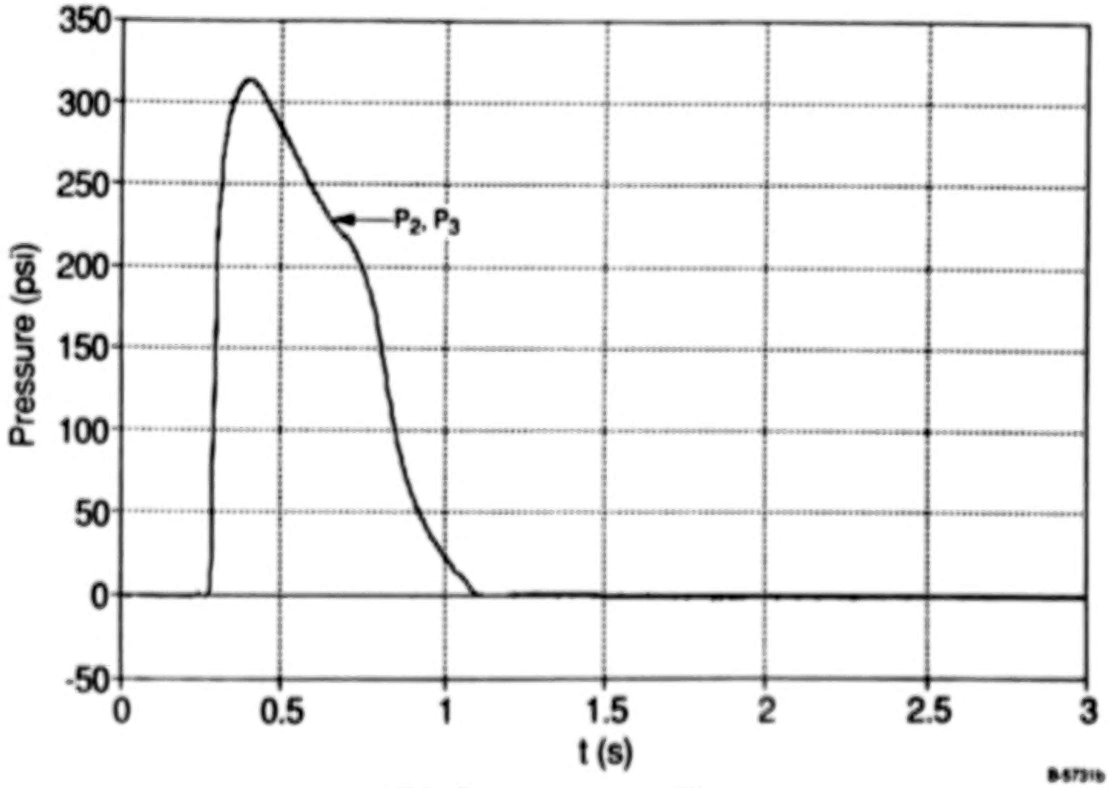

(b) Pressure versus Time

Figure 10. Effect of Vertical Down Simulator Orientation on Thrust and Pressure Time History (large pin, 0.098-in.diameter nozzle, three sets of 2 mm copper spheres)

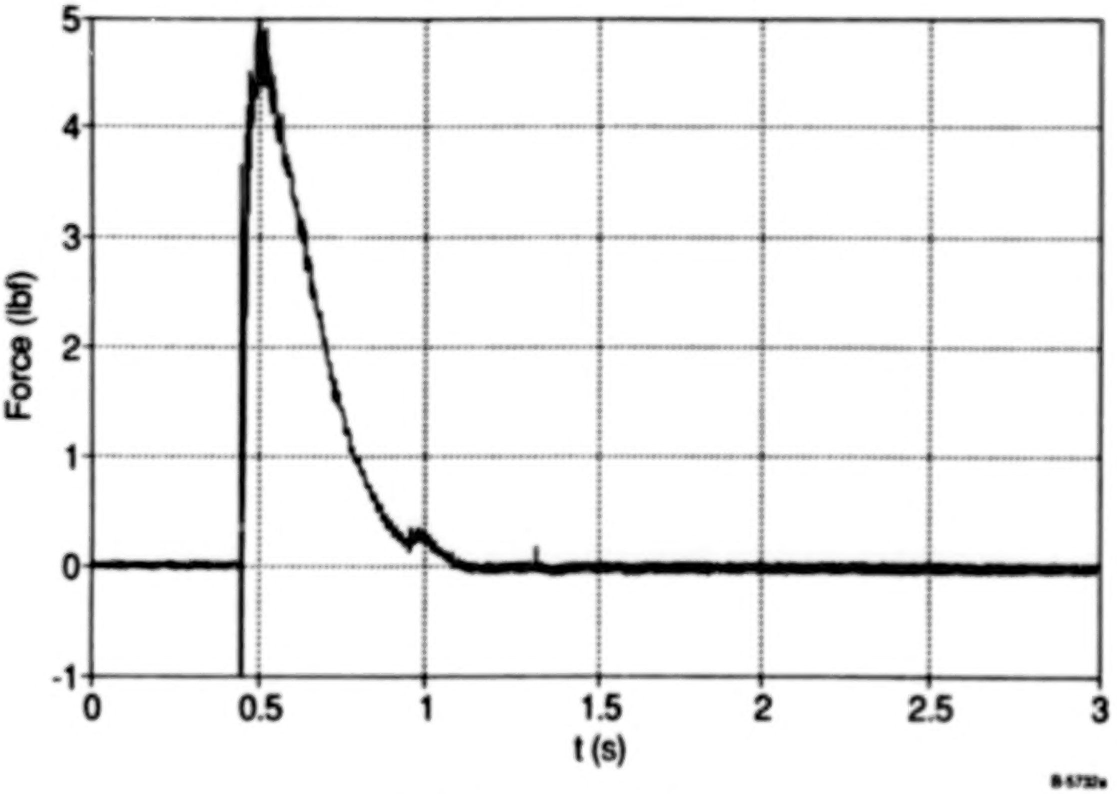

(a) Thrust versus Time

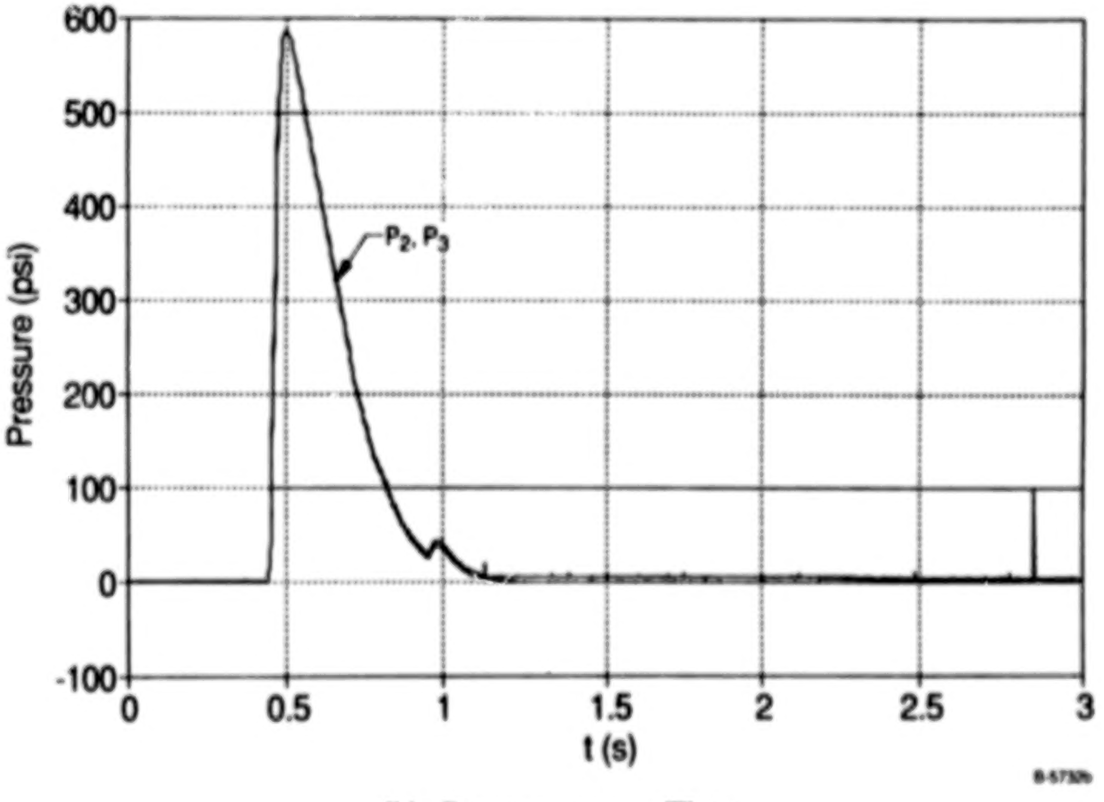

(b) Pressure versus Time

Figure 11. Effect of Increased CO_2 Mass Flow Rate on Thrust and Pressure Time History (large pin, 0.098-in.diameter nozzle, three sets of 2 mm copper spheres, vertical up simulator orientation)

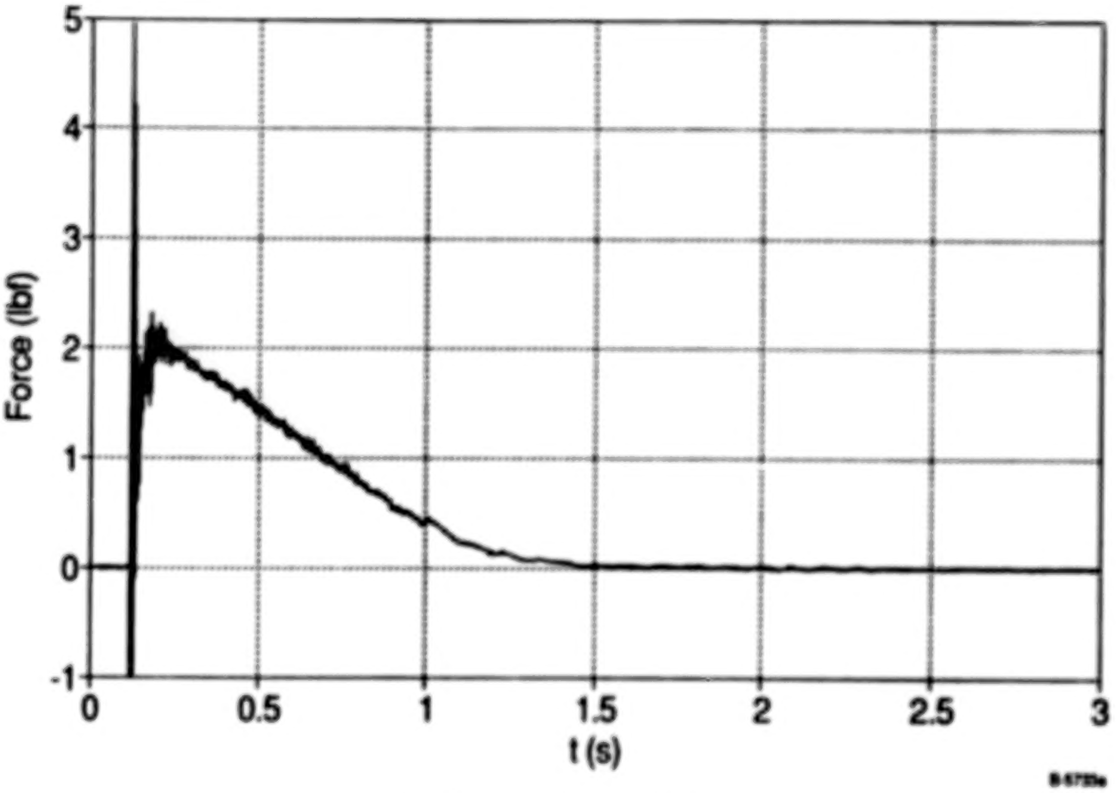

(a) Thrust versus Time

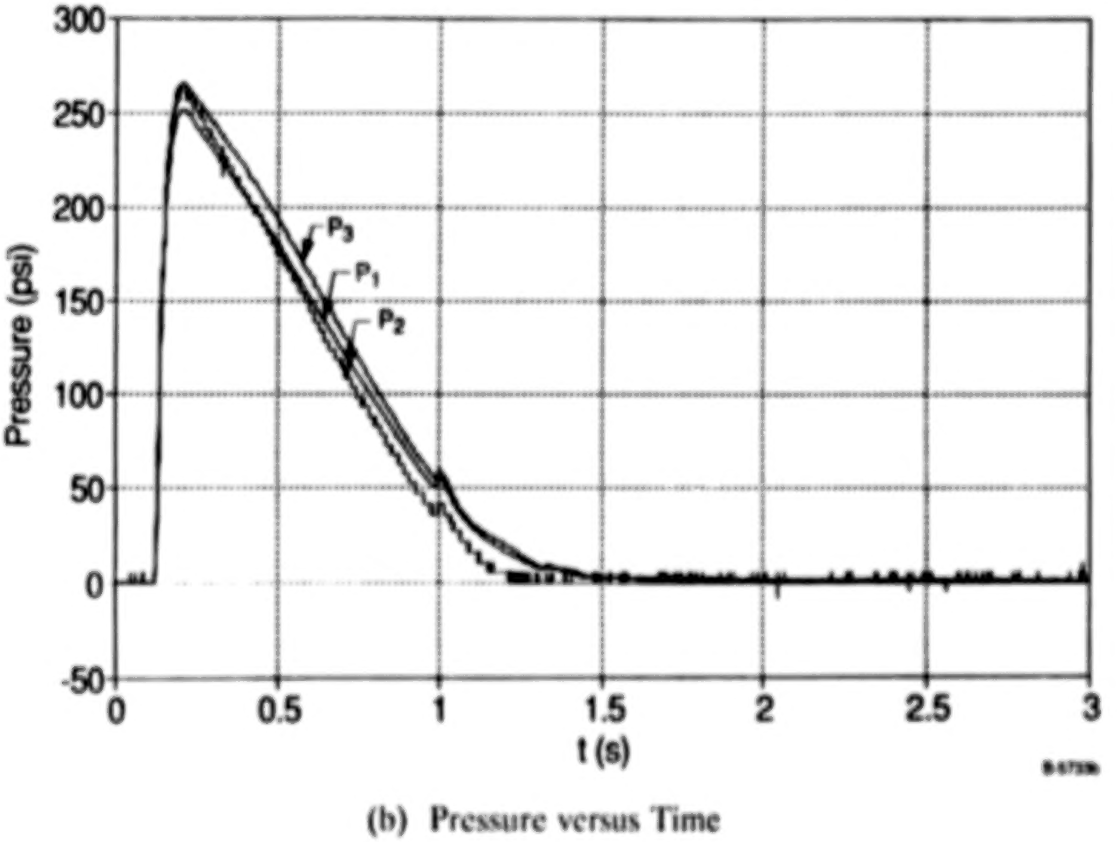

(b) Pressure versus Time

Figure 12. Effect of Copper Plug Structure on Thrust and Pressure Time History (large pin, 0.098-in.diameter nozzle, one set of 1 mm copper spheres, plus bronze wool, horizontal orientation)

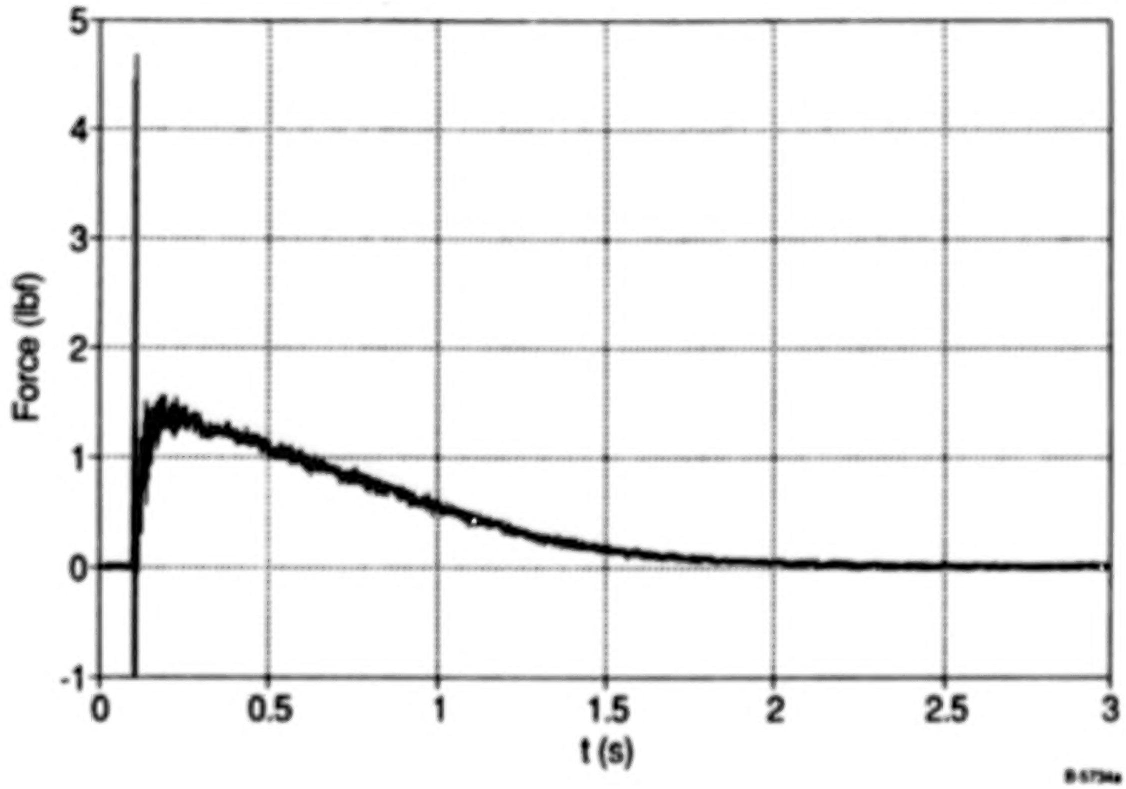

(a) Thrust versus Time

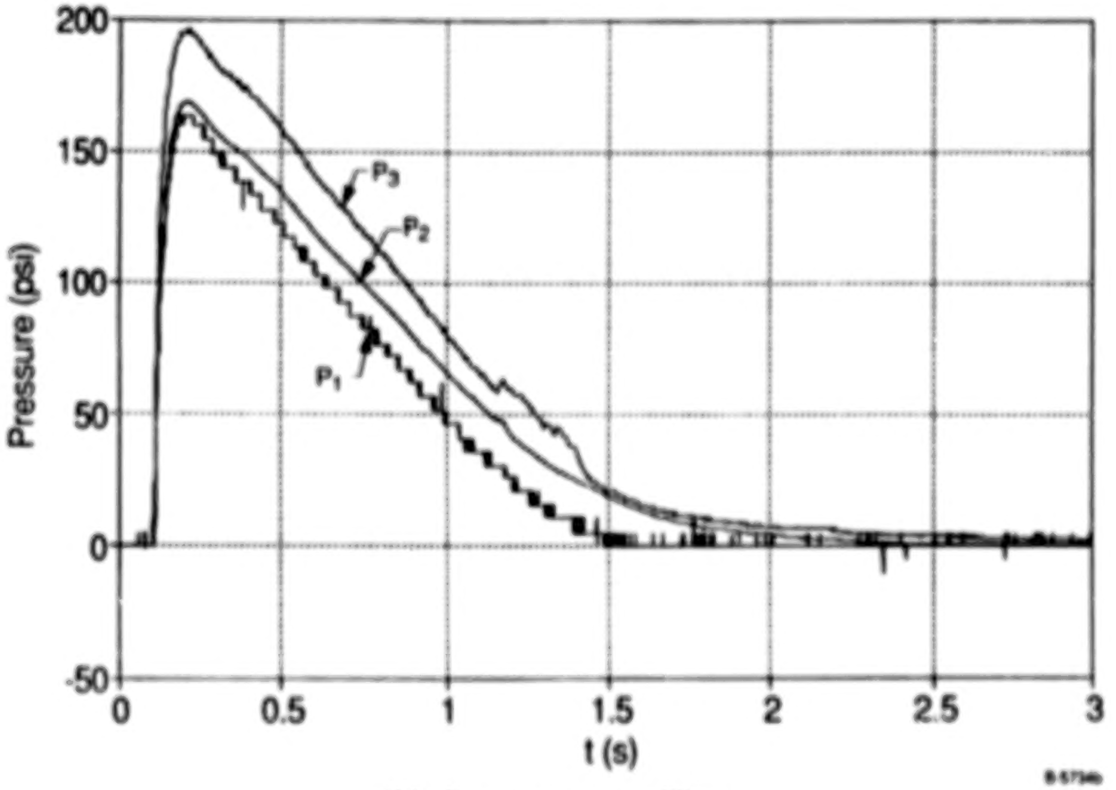

(b) Pressure versus Time

Figure 13. Effect of "Smaller" Pin on Thrust and Pressure Time History
(0.098-in.diameter nozzle, one set of 1 mm copper spheres,
plus bronze wool, horizontal orientation)

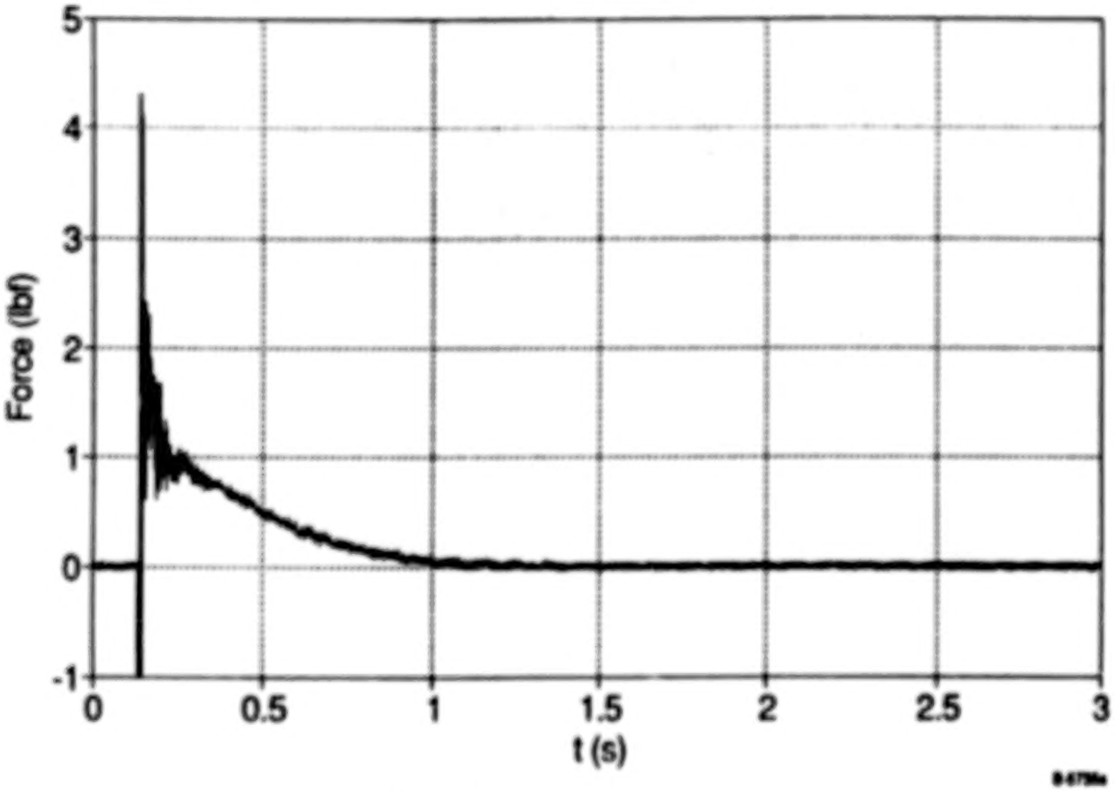

(a) Thrust versus Time

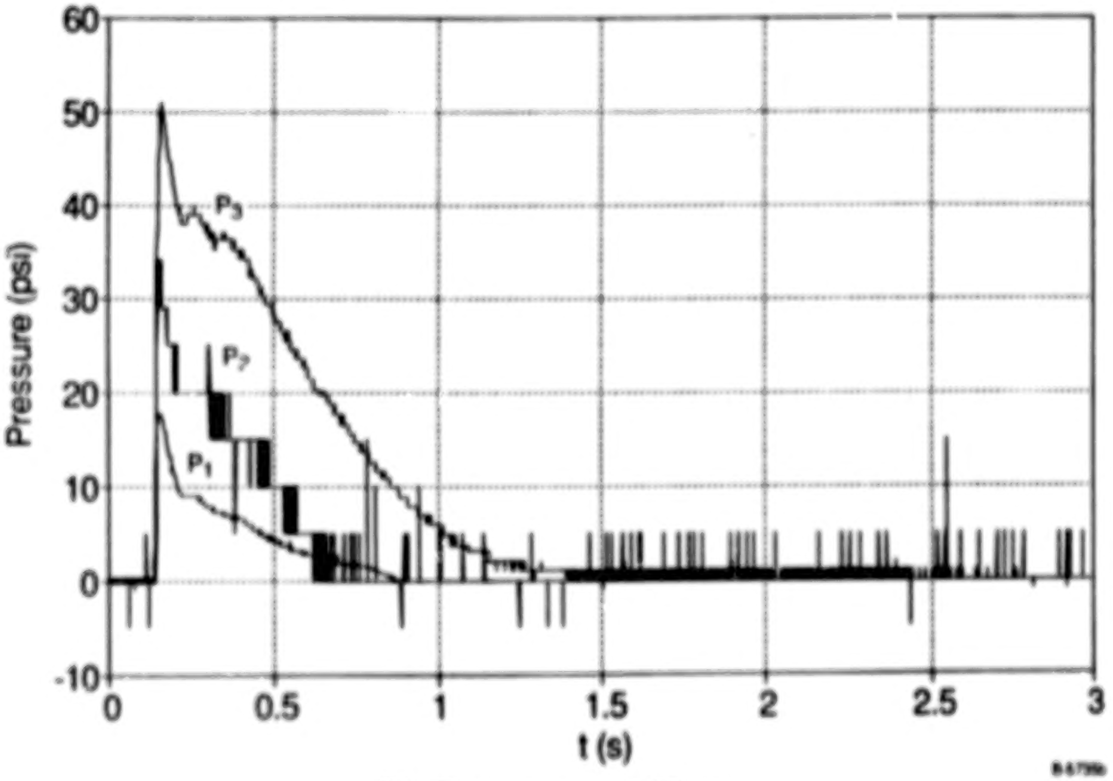

(b) Pressure versus Time

Figure 14. Effect of Exit Nozzle Diameter on Thrust and Pressure Time History (large pin, 0.295-in.diameter nozzle, one set of 1 mm copper spheres, plus bronze wool, horizontal orientation)

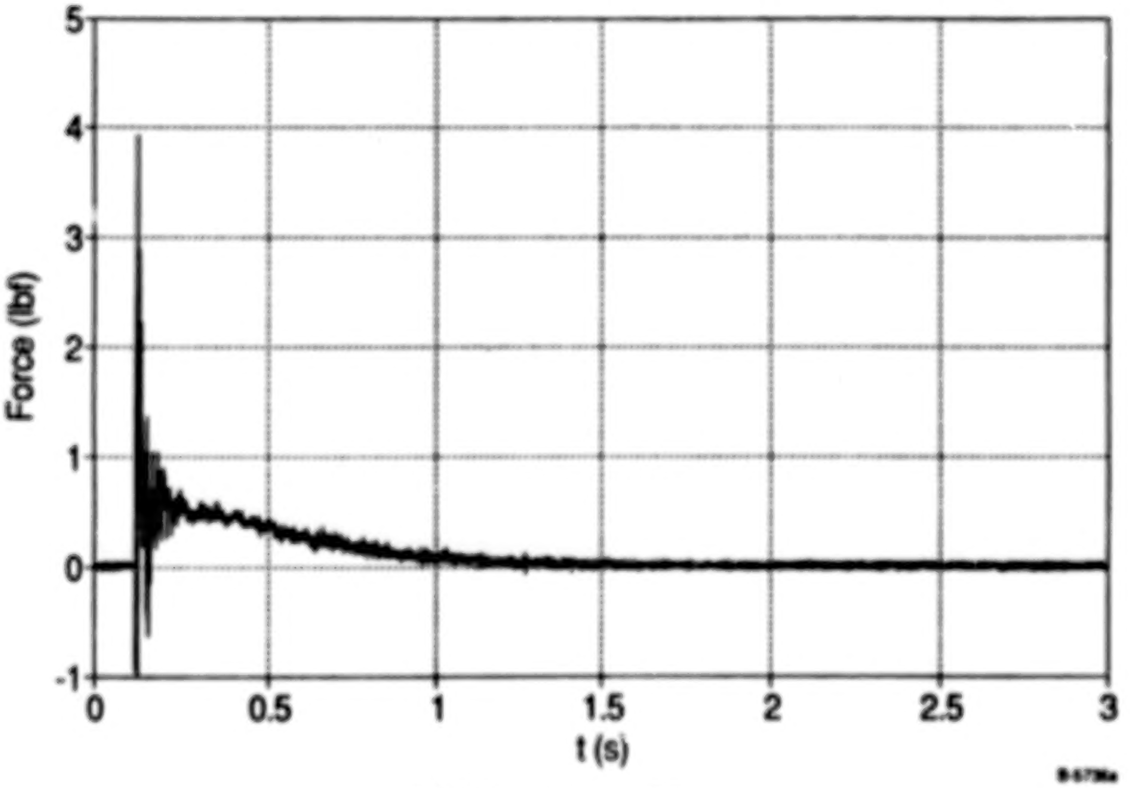

(a) Thrust versus Time

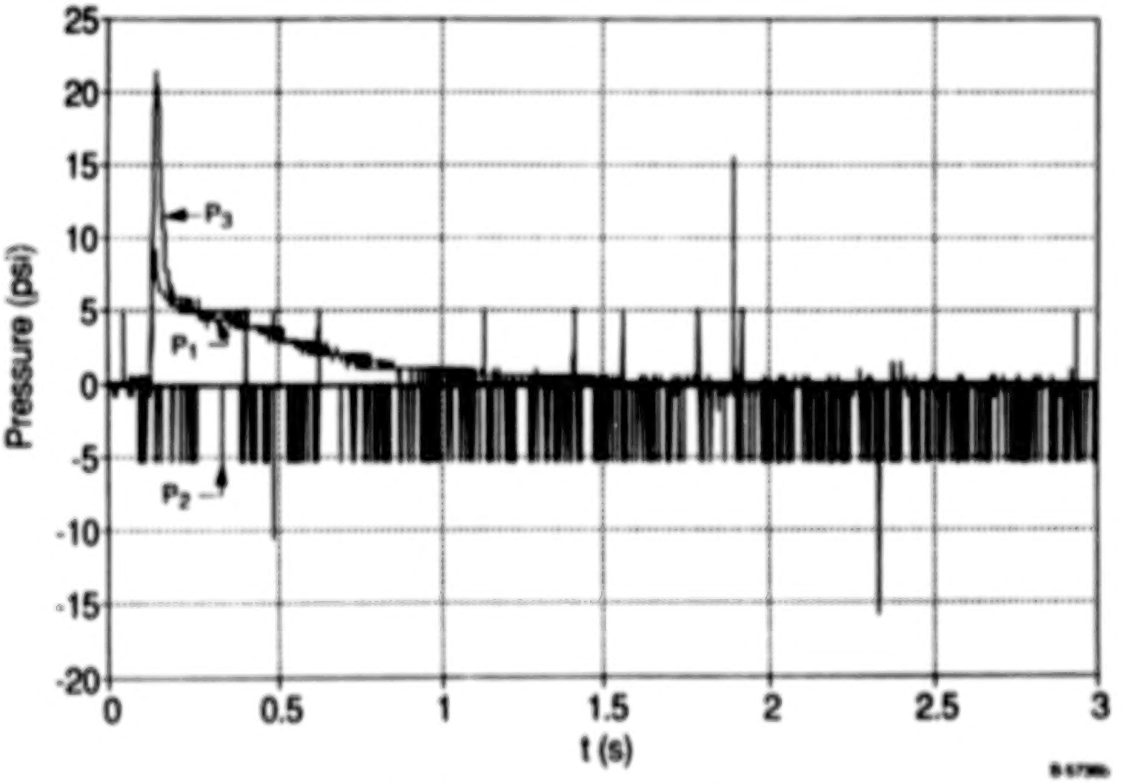

(b) Pressure versus Time

Figure 15. Effect of Removing Copper Plug on Thrust and Pressure Time History of Large Nozzle Diameter Simulator (0.295-in. nozzle diameter, horizontal orientation, large pin)

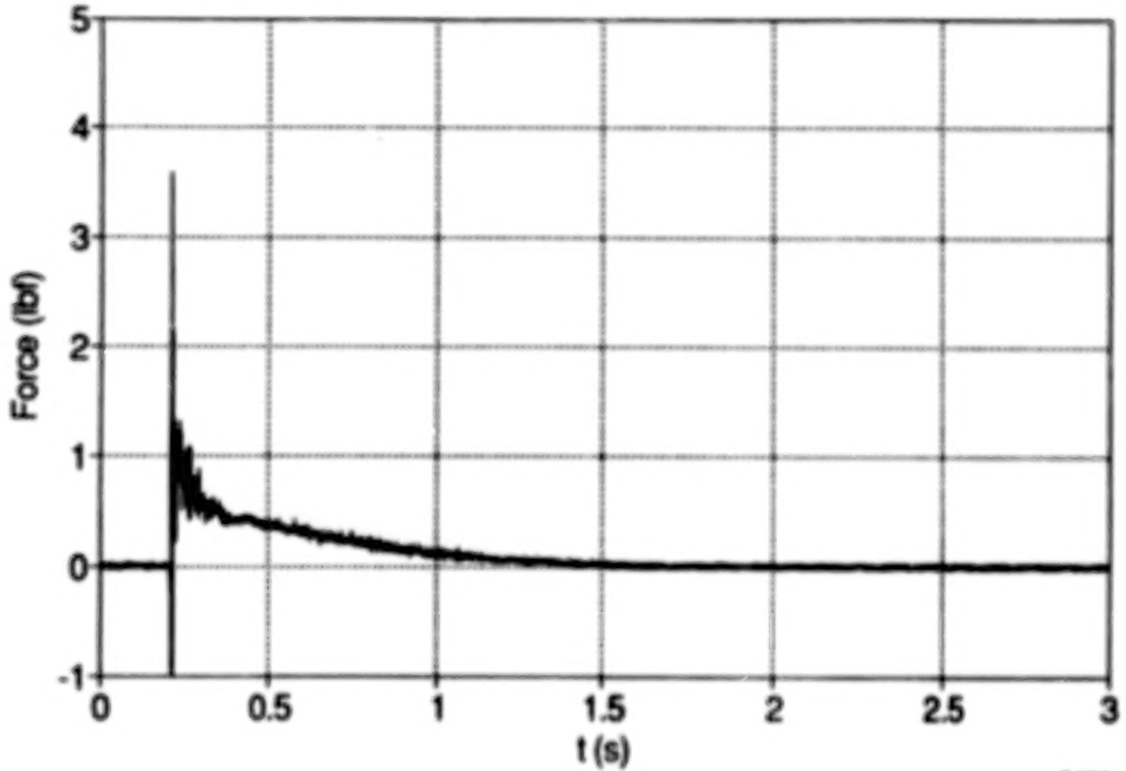

(a) Thrust versus Time

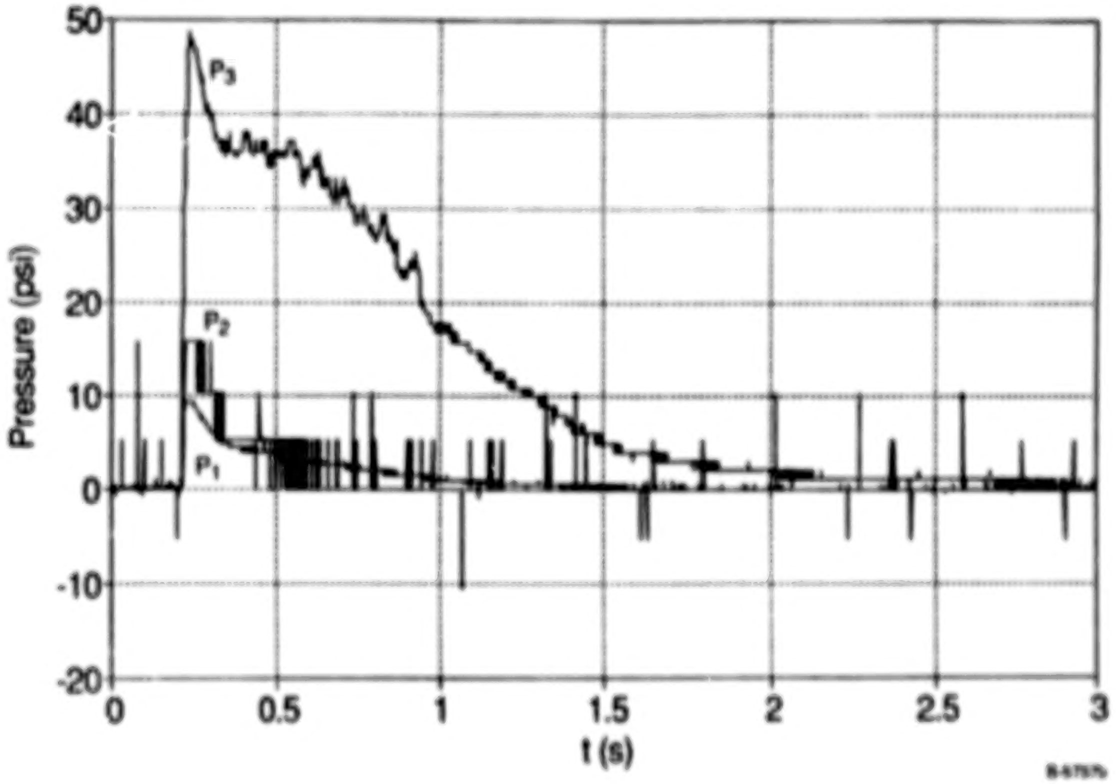

(b) Pressure versus Time

Figure 16. 0.295-in. Nozzle Diameter with "Small" Pin: Thrust and Pressure Time History (one set of 1 mm diameter copper spheres plus bronze wool, horizontal orientation)

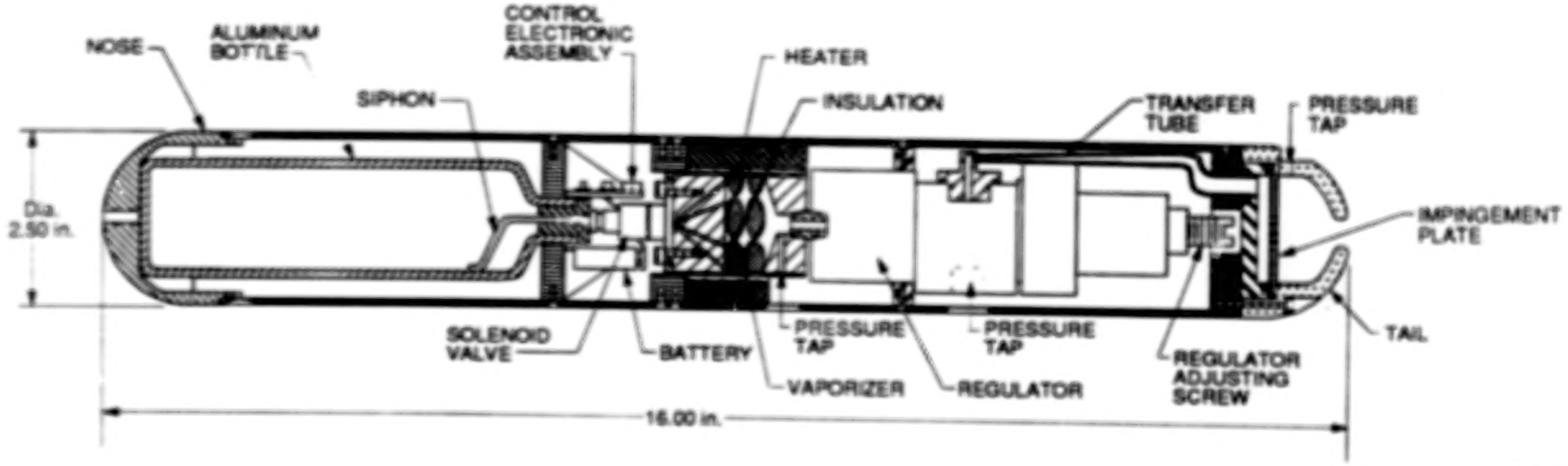
NOSE
ALUMINUM BOTTLE
CONTROL ELECTRONIC ASSEMBLY
HEATER
INSULATION
SIPHON
TRANSFER TUBE
PRESSURE TAP
IMPINGEMENT PLATE
TAIL
Dia. 2.50 in.
SOLENOID VALVE
BATTERY
PRESSURE TAP
VAPORIZER
PRESSURE TAP
REGULATOR
REGULATOR ADJUSTING SCREW
16.00 in.
B-5710

Figure 17. Preliminary Design of Large-Scale Propulsion Simulator

N91-21199

A SOLID-STATE CONTROLLABLE POWER SUPPLY for a MAGNETIC SUSPENSION WIND TUNNEL

Taumi S. Daniels, John S. Tripp
Mail Stop 238
NASA Langley Research Center
Hampton
VA 23665-5225

C-4

Abstract

The NASA Langley 6-Inch Magnetic Suspension and Balance System (6-in. MSBS) requires an independently controlled bidirectional dc power source for each of six positioning electromagnets. These electromagnets provide five-degree-of-freedom control over a suspended aerodynamic test model. Existing power equipment, which employs resistance-coupled thyratron-controlled rectifiers as well as ac to dc motor-generator converters, is obsolete, inefficient, and unreliable. A replacement six-phase bidirectional controlled bridge rectifier is proposed, which employs power MOSFET switches sequenced by hybrid analog/digital circuits. Full-load efficiency is 80 percent compared with 25 percent for the resistance-coupled thyratron system. Current feedback provides high control linearity, adjustable current limiting, and current overload protection. A quenching circuit suppresses inductive voltage impulses.

It is shown that 20-kHz interference from positioning magnet power into MSBS electromagnetic model position sensors results predominantly from capacitively coupled electric fields. Hence, proper shielding and grounding techniques are necessary. Inductively coupled magnetic interference is negligible.

Introduction

The NASA Langley 6-Inch Magnetic Suspension and Balance System (6-in. MSBS) employs six positioning electromagnets to provide five-degree-of-freedom control over a suspended aerodynamic test model. Each positioning electromagnet requires up to +90/−30 A dc, supplied by an independent linearly controllable power source. Three of the original power supplies, as shown in figure 1, are thyratron-controlled rectifier bridges providing a variable voltage up to +250 V (at up to 96 A dc). Each bridge output couples through a resistive T-network to the load and is opposed by a −30 V to −120 V (at up to 1000 A dc) regulated supply. The system is thus capable of providing a variable load voltage between −120 V to +220 V. The resistors, which are water cooled, dissipate excessive wasted energy and have a high failure rate as well. Full-load efficiency of the resistor coupling network is less than 25 percent.

Two of the positioning coils are powered by voltage-controlled ac to dc motor-generator converters (also shown in fig. 1). The remaining coil is powered by a fixed −90 V dc regulated supply. All the existing power equipment is obsolete, bulky, and difficult to maintain because of frequent failures and scarcity of spare parts.

This paper proposes a six-phase 60-Hz bidirectional controlled bridge rectifier employing power MOSFET switches to replace the existing power supply equipment. Elimination of the resistive T-networks increases full-load efficiency to over 80 percent. Bridge switching control pulses are generated by hybrid analog/digital circuitry. A current feedback system provides high control linearity and zero steady state control error (type 1 control).

Symbols

A, B, C	three-phase supply voltages
$-A, -B, -C$	negative supply voltages
$A_C, B_C, C_C,$ $-A_C, -B_C, -C_C$	cyclic control register bits
$A_I(n)$	odd part of *n*th current harmonic
A_p, B_p, C_p $-A_p, -B_p, -C_p$	phase voltages shifted 30°
$A_V(n)$	odd part of *n*th voltage harmonic
$A_{xn}, B_{xn}, C_{xn},$ $-A_{xn}, -B_{xn}, -C_{xn}$	negative comparison pulses
$A_{xp}, B_{xp}, C_{xp},$ $-A_{xp}, -B_{xp}, -C_{xp}$	positive comparison pulses
$B_I(n)$	even part of *n*th current harmonic
$B_V(n)$	even part of *n*th voltage harmonic
BW	bandwidth
$C_I(n)$	*n*th current harmonic
$C_{OA}, C_{OB}, C_{PA}, C_{PB}$	fault detection comparators
C_V	fault protection capacitor
$C_V(n)$	*n*th voltage harmonic
$D_1, \ldots, D_6$	gated firing pulse
E_I	current control command voltage
E_M	absolute peak of phase voltage
EPS	electromagnetic position sensor
$e(t)$	time varying phase voltage
$G_A, G_B, G_C,$ G_{A-}, G_{B-}, G_{C-}	sequential phase firing window pulses
H_0	open loop transfer function
I_{av}	average steady state load current

i	instantaneous load current
i_0	steady state load current at $x = 0$
$i(x)$	steady state load current at angular time x
K	linear gain constant
L	load inductance, H
MOSFET	metal-oxide-semiconductor field effect transistor
MSBS	magnetic suspension and balance system
N	440-V neutral
n	Fourier series coefficient index
PI	proportional plus integral
Q_F	set bit for quenching thyristor
R, R_L	load resistance
R_C	fault-limiting resistance
R_Q	quenching resistance
rms	root mean square
S_x	sign of input command voltage
s	Laplace transform variable
T	time duration of periodic waveform, sec
T_Q	quenching thyristor
t	time
V_{bias}	bias voltage
V_R	average load voltage
$V_{R,\max}$	maximum attainable absolute load voltage
x	angular time, radians
$y(t)$	T-second averaging integrator output
θ	phase angle, radians
τ_D	dominant closed loop time constant
ϕ	MOSFET firing angle, radians
ϕ_R	firing angle required for average load voltage V_R, radians
ω	frequency, radians/sec
ω_0, ω_1	break frequencies, radians/sec

Design Description

Six-Phase Power Source

Three-phase 440-V power is stepped down via either a 440-V wye to a 63.5-V six-phase star (as shown in fig. 2) which can furnish 85.3 average dc volts, or via a 440-V three-phase delta to a 110-V six-phase star (not shown) which can furnish 148 dc volts. The resistance of each positioning magnet coil determines the required power supply voltage range.

Voltage-Controlled Bridge Rectifier

Bidirectional conduction in each leg of the six-phase bridge rectifier is controlled by two power-MOSFET switches connected in parallel with opposing polarities, as illustrated in figures 3 and 4. Note that each MOSFET is protected by a series reverse-blocking diode. This bidirectional design allows load voltage to be controlled entirely by varying the switching times at each leg. Hybrid analog/digital circuitry determines sequential switching times at successive bridge legs necessary to produce dc load voltage proportional to the control voltage. Load inductance provides natural current smoothing. In case of bridge current interruption, a quenching circuit shunts load current to ground to prevent inductive voltage impulses.

All MOSFET gates are optically isolated from control circuits. Isolation is necessary because none of the bridge MOSFET source terminals can be grounded; all source terminals must connect either to the load or to a phase voltage leg. Refer to figure 4 for bridge leg details. Isolation also protects 5-V control logic from ac power circuits. Gate voltage is supplied to the MOSFET through an opto-isolator from a floating dc power supply which adds a fixed dc bias to the bridge leg voltage. To drive the active MOSFET into saturation, each bridge leg requires an independent bias supply. During cutoff a bleeder resistor from gate to source drains off gate charge, which accumulates because of opto-coupler off-state leakage. A blocking diode in series with the floating bias supply is provided to prevent reverse conduction through the opto-coupler.

Timing Control Circuit

Figure 5 illustrates the six-phase voltage waveforms labeled A, $-C$, B, $-A$, C, and $-B$ referred to as phase voltages. Angular time ωt (also denoted by x) is expressed in radians relative to the positive zero crossing of phase A voltage. Note that in figures 5 and 8, a corresponding time axis is used. Switch-off time is coincident with the switch-on time of the succeeding phase. At steady state, each bridge leg conducts for a $\pi/3$-radian duration.

The relation between firing time in radians, hereafter denoted firing angle ϕ, and control voltage E_I required for linear control of dc load voltage is now derived. For algebraic convenience let time t equal zero when phase voltage $e(t)$ turns on. Thus

$$e(t) = E_M \sin(\omega t + \phi) \tag{1}$$

where

$$\pi/3 \le \phi \le 5\pi/6$$

and ωt ranges from 0 to $\pi/3$. Load current i is described by

$$di/dt + Ri/L = (E_M/L) \sin(\omega t + \phi) \tag{2}$$

where L is the load inductance and R is the series load resistance. The solution to equation (2) is

$$i(x) = i_0 e^{-Rx/\omega L} - \left[E_M \Big/ \sqrt{R^2 + (\omega L)^2}\,\right]\left[\sin(\phi - \theta)e^{-Rx/\omega L} - \sin(x + \phi - \theta)\right] \tag{3}$$

where $x = \omega t$

$\theta = \tan^{-1}(\omega L/R)$

$i_0 = i(0)$

$\omega = 120\pi$

During steady state operation, x passes from 0 to $\pi/3$ radians. Because the load is inductive, $i(x)$ will be continuous at switching points. Therefore

$$i_0 = i(\pi/3) \tag{4}$$

Solving equations (3) and (4) for i_0 yields

$$i_0 = \frac{E_M\left[\sin(\pi/3 + \phi - \theta) - e^{-\pi R/3\omega L}\sin(\phi - \theta)\right]}{\left(1 - e^{-\pi R/3\omega L}\right)\sqrt{R^2 + (\omega L)^2}} \tag{5}$$

Combine equations (5) and (3) to obtain steady state load current as a function of angular time x; thus

$$i(x) = \frac{E_M\left[\cos(\phi - \theta + \pi/6)e^{-Rx/\omega L}\Big/(1 - e^{-\pi R/3\omega L}) + \sin(x + \phi - \theta)\right]}{\sqrt{R^2 + (\omega L)^2}} \tag{6}$$

where $0 \le x \le \pi/3$.

Average steady state load current is obtained by integrating equation (6) over the $\pi/3$-radian conduction interval to give

$$I_{av}(\phi) = [3E_M/(\pi R)] \sin(\phi + \pi/6) \tag{7}$$

where $\pi/3 \le \phi \le 5\pi/6$.

Firing angle ϕ_R required to produce average load voltage V_R is determined electronically as shown in figures 6(a) and 6(b). This analog circuit solves equation (7) for ϕ_R, given V_R, as

$$\phi_R = \sin^{-1}(\pi V_R/3E_M) - \pi/6 \qquad (8)$$

and $V_{R\max} = 3E_M/\pi$ is the maximum available average dc load voltage.

Lead circuits shift the six phase voltages $\pi/6$ radian. These shifted voltages, labeled $A_p, \ldots, -B_p$, are compared with V_R, producing comparison pulses $A_{zp}, \ldots, -B_{zp}$ for positive V_R and $A_{zn}, \ldots, -B_{zn}$ for negative V_R. The rising edge of each comparison pulse occurs at the proper firing angle ϕ_R for the corresponding phase voltage.

The comparator and logic circuit shown in figure 7 generates six sequential pulses, labeled $G_A, \ldots, G_{B-}$, beginning at $\pi/3$-radian intervals. Each pulse has a $\pi/2$-radian duration and defines the $\pi/3$- to $5\pi/6$-radian firing window during which the corresponding phase may turn on, as shown in figure 8. Pulses $G_A, \ldots, G_{B-}$ are combined with comparison pulses $A_{zp}, \ldots, -C_{zp}, A_{zn}, \ldots, -C_{zn}$ in the network of figure 9 to produce gated firing pulses $D_1, \ldots, D_6$. This circuit selects the proper comparison pulse, depending on the polarity of V_R, and blocks spurious impulses outside the $\pi/3$ to $5\pi/6$ firing window for each phase. Pulses $D_1, \ldots, D_6$ sequentially set gating bits $A_C, \ldots, -B_C$ in the six-bit cyclic register illustrated in figure 10. Register bits A_C through $-B_C$ drive the corresponding opto-couplers, which in turn drive the corresponding MOSFET gates.

The protective logic network, shown in figure 10, resets the previously active register bit. Table I lists, for each active bit, the allowable bits which may be set by the next gated firing pulse (possible next bit), and also previously active bits reset by the protective gating network (bits which active bit turns off). This design assures that at most only one bit of the six is set (only one bridge leg is active), which prevents phase-to-phase short circuits. Furthermore, all bits are reset if an error condition is detected, which opens all legs of the bridge and closes both quenching switches.

Figures 11 through 16 illustrate simulated transient responses of bridge output voltage and load current (without current feedback) to step and ramp control inputs for an L/R time constant of 0.012 sec. Responses to step inputs of 100 percent, 50 percent, and −20 percent of full load appear in figures 11 through 13. Output voltage centers about the control input within 1/360 sec. Load current response is nearly exponential with an additive 360-Hz ripple. Figures 14 and 15 illustrate current and voltage responses to a ramp input with a slope of 100 percent of and −100 percent of full scale in 20 msec, which is equal to the maximum slope of an 8-Hz sine wave. Note that the sawtooth-shaped load voltage is well-centered about the control input ramp voltage. However, load current lags the control voltage. Although initially zero, current lag increases to the normal constant lag of a first-order ramp response. Response to a ramp control input with a slope of 200 percent of full scale in 20 msec appears in figure 16. Output voltage is no longer symmetric about the control input voltage. Load current, initially zero, attempts to follow the input with first-order lag.

The switching control logic will maintain sequential switching synchronism despite discontinuous or rapidly changing control voltage. Additional simulation studies verify that the switching control circuits function correctly for high-frequency control voltage disturbances.

Table I. State Transition Table for Cyclic Control Register

Active bit	Bits which turn off active bit	Bits which active bit turns off	Possible next bit
A	$-C, C, -A$	$B, -B, -A$	$-C, C$
$-C$	$B, -B, C$	$A, -A, C$	$-B, B$
B	$-A, A, -B$	$C, -C, -B$	$-A, A$
$-A$	$C, -C, A$	$-B, B, A$	$-C, C$
C	$-B, B, -C$	$A, -A, -C$	$-B, B$
$-B$	$A, -A, B$	$-C, C, B$	$-A, A$

Current Feedback Circuit

Current feedback provides four improvements to power source performance:

1. Adjustable dc current limiting
2. dc current overload protection
3. Improved linearity between control input voltage and average dc output
4. Zero steady state control error

Current limiting and feedback circuitry appears in figure 17. The current limiting feature provides an adjustable bound on average load current magnitude, which also prevents current overload. The nonlinear saturation block in the figure employs clamping diodes which restrict input control voltage magnitude $|E_f|$ to an adjustable reference voltage. This, in turn, limits the command voltage at the summing input of the current feedback circuit.

Load current is sensed by a bidirectional Hall-effect current transducer followed by a 30-Hz low-pass filter. The error voltage, conditioned by a proportional plus integral compensator, drives the bridge firing control input.

Table II. Positioning Coil Constants

Coil	Load resistance R, Ω	Load inductance L, H	Coil BW, Hz	Time constant L/R, sec
Axial	2.0	0.36	0.88	0.18
Inner saddle	.5	.008	9.9	.016
Outer saddle	.9	.016	9.0	.018
Drag	2.0	.016	19.9	.008
Side and lift	1.0	.40	.40	.40

Resistance and inductance of the positioning coils limit open-loop bandwidths of the positioning circuits, as listed in table II. The current feedback control loop is modeled in figure 18 as a first-order linear plant, PI compensator, and low-pass filter. With a single-pole filter, the open-loop transfer function is

$$H_0(s) = (K/R)(1 + s/\omega_1)/[s(1 + Ls/R)(1 + s/\omega_0)] \tag{9}$$

Root locus analysis is employed to determine the best loop gain K/R for each of the positioning coils listed in table II. Figure 19 illustrates the root locus plot (ref. 1) of equation (9) for the axial coil circuit, with time constant $L/R = 0.16$ sec and break frequencies $\omega_0 = 60\pi$ radians/sec and $\omega_1 = 20\pi$ radians/sec. It can be seen in figure 19 that the fastest closed-loop time response with acceptable damped oscillation occurs for a loop gain of K/R of 1500, providing a closed-loop time constant of 0.0189 sec and a damping coefficient of 0.375. Although practical loop gain K/R is limited by amplifier and rectifier bridge saturation, as well as noise sensitivity, the circuit is unlikely to saturate for error voltages less than 0.5 V for $K/R = 1500$.

Figure 20 illustrates the root locus plot for the inner saddle coil ($L/R = 0.016$ sec), with break frequencies ω_0 and ω_1 unchanged. For these constants, the dominant closed-loop time constant τ_D can be decreased only to a minimum of 0.0113 sec at a loop gain of 47.5. Note that loop gains greater than 47.5 merely produce unwanted damped oscillation with no improvement in time response.

Similar root locus analyses are required to determine closed-loop gains for the remaining positioning coil control circuits.

Fault Protection Circuits

Although the current feedback system limits average dc load current, instantaneous bridge leg current can exceed safe magnitudes and durations if a load short circuit occurs. In addition, an open-circuit failure in a conducting bridge leg will produce a sharp inductive overvoltage impulse across the other nonconducting bridge legs. Both fault conditions can destroy bridge leg semiconductors. Overvoltage and overcurrent detecting circuits are provided to quickly turn off the bridge and to shunt inductive load current to ground in case of a fault.

The load overvoltage fault protection circuit is shown in figure 21. If supply current is interrupted, capacitor C_V, which is connected in parallel with load L, accumulates load current. As soon as the increasing inductive load voltage exceeds the fault threshold level detected by comparators C_{PA} and C_{PB}, bit Q_F is set. This bit, in turn, fires quenching thyristor T_Q, which shunts load current through resistor R_Q to ground. Figures 22 and 23 illustrate a worst case load voltage inductive impulse and quenching transient following a source current interruption. (Fig. 22 shows the initial 100 μsec of the fault.)

Capacitor C_V is sized to limit increasing inductive load voltage to a safe level before thyristor T_Q fires. This capacitor adds an open-loop time constant of $C_V(R_C + R_L)$, which is too small (1×10^{-5}) to affect the previous root locus analysis. Likewise, resistor R_Q is chosen low enough to safely limit load voltage during inductor current quenching. The decay time constant is $L/(R_L + R_Q)$.

The current overload detection circuit of figure 24 is activated when the load inductor becomes shorted. Instantaneous load current is averaged by a $T/2$-sec delay two-pole Bessel filter, which closely approximates a T-sec averaging integrator of the form

$$y(t) = 1/T \int_{t-T}^{t} i(t)\, dt \tag{10}$$

Averaging eliminates load current transient impulses of short duration. Delay $T/2$ is chosen sufficiently small to protect bridge leg semiconductors from short-circuit current damage. Whenever a current overload is sensed, the bridge is disabled, and quenching thyristor T_Q fires.

A short circuit is more likely to occur in a bridge leg semiconductor than in a positioning coil. Internal bridge short circuit protection circuitry would have to be replicated in each of the six bridge legs. Since the expense of internal short circuit protection circuits would exceed the cost of replacement bridge semiconductors, protection against short circuits internal to the bridge itself is provided by power transformer circuit breakers and fuses only.

Harmonic Analysis of Rectified Load Voltage and Current

The 6-in. MSBS is equipped with an electromagnetic position sensing system (EPS) which employs a set of five sensor coil pairs wound on a cylindrical cage installed in the test section. An amplitude-modulated 20 kHz sinusoidal carrier inductively couples into the EPS sensor coils. Interference from positioning magnet power harmonics near 20 kHz can interfere with EPS operation. Fourier series analysis of positioning magnet voltage and current waveforms at steady state allows computation of their harmonic amplitudes.

As the firing angle varies from $\pi/3$ to $5\pi/6$ radians, load voltage becomes increasingly discontinuous, thus increasing the ratio of each voltage harmonic to the maximum dc voltage level at $\phi = \pi/3$. Since the inductance of the positioning coil forces load current to be continuous, the ratios of current harmonic amplitudes to maximum dc current are significantly less than the corresponding voltage harmonic ratios. The Fourier series coefficient equations for load voltage and current, as functions of firing angle, are derived in the appendix.

Table III lists rms levels of the 55th and 56th voltage and current harmonics (19.80 and 20.16 kHz) in dB, relative to full-load average dc level for firing angles ranging from $\pi/3$ to $5\pi/6$ radians in $\pi/12$ radian increments. Circuit constants are $R/\omega L = 0.1$, $R = 1\Omega$, and $\omega = 120\pi$.

Table III. The rms Load Voltage and Current Harmonic Levels Relative to Full-Load dc

Firing angle, radians	Percent of full load dc	55th harmonic 19.80 kHz		56th harmonic 20.16 kHz	
		Voltage, dB	Current, dB	Voltage, dB	Current, dB
$\pi/3$	100	-98.1	-117.4	-98.4	-117.7
$5\pi/12$	96.6	-59.5	-116.0	-59.6	-116.3
$\pi/2$	86.6	-53.8	-115.3	-53.9	-115.6
$7\pi/12$	70.7	-50.8	-115.2	-50.9	-115.5
$2\pi/3$	50.0	-49.0	-115.7	-49.2	-115.0
$3\pi/4$	25.9	-48.0	-117.0	-48.2	-117.3
$5\pi/6$	0	-47.8	-119.1	-47.9	-119.4

Note that current harmonic amplitudes vary only slightly with firing angle ϕ, whereas voltage harmonic amplitudes increase markedly with ϕ. Moreover, relative voltage harmonic amplitudes are 60 to 70 dB greater than corresponding relative current harmonic amplitudes for ϕ greater than $\pi/3$ radians. Since voltage harmonics predominate and current harmonic amplitudes are more than 115 dB below the maximum dc level, only capacitively coupled interference from positioning magnet voltage into EPS sensor coils is significant at 20 kHz. Thus, appropriate grounding and shielding mesures are necessary to minimize positioning system interference into the EPS system. Although inductively coupled interference is low, the 6-in. MSBS is equipped with a Faraday shield installed around the EPS coil cage to attenuate inductive coupling from positioning circuits.

Concluding Remarks

This paper has proposed a solid state voltage-controlled power source to drive positioning magnets in a magnetic suspension and balance system. The design employs a six-phase bidirectional bridge switched by power MOSFET switches controlled, in turn, by hybrid analog/digital sequential switching circuitry. Load voltage level and polarity are entirely determined by switching times at each bridge leg, such that dc load voltage is proportional to input control voltage. Control circuits are optically isolated from power circuits. An automatic quenching circuit shunts load current to ground if bridge current is interrupted.

Positioning coil time constants limit open-loop transient response. Current feedback with integral plus proportional compensation provides improved linearity between the control input and dc output along with zero steady-state error and current overload protection. Integral plus proportional feedback compensation also improves transient decay time in coil currents.

Fourier series analysis of steady state load voltage and current shows that voltage harmonics relative to full-load dc volts predominate over corresponding relative load current harmonics by 60 to 70 dB. Consequently, positioning system power interference into the electromagnetic position sensing system arises primarily from a capacitively coupled electric field. For this reason, proper shielding and grounding procedures are necessary to minimize EPS interference near 20 kHz.

A low voltage prototype of this design has been developed. Laboratory testing and extensive circuit simulation confirm that design criteria have been met.

Reference

1. Kuo, Benjamin C.: *Automatic Control Systems*. Prentice Hall, Inc., 1987.

Appendix

Obtaining Fourier Series Coefficients

The Fourier series coefficient $C_V(n)$ of the nth voltage harmonic is obtained by integrating equation (1) over the period of conduction. Thus

$$A_V(n) = 6E_M/\pi \int_0^{\pi/3} \sin(x+\phi)\sin 6nx\,dx = \left[36E_M n/\pi(36n^2-1)\right]\sin(\phi-\pi/3) \tag{A1a}$$

$$B_V(n) = 6E_M/\pi \int_0^{\pi/3} \sin(x+\phi)\cos 6nx\,dx = \left[6E_M/\pi(36n^2-1)\right]\sin(\phi-\pi/6) \tag{A1b}$$

$$C_V(n) = \left[A_V^2(n) + B_V^2(n)\right]^{1/2} \tag{A1c}$$

Similarly, the Fourier series coefficient $C_I(n)$ of the nth current harmonic is obtained from equation (6) as

$$\begin{aligned} A_I(n) &= \left[6E_M n/\pi\sqrt{R^2+(wL)^2}\right]\int_0^{\pi/3}\Big\{\cos(\phi-\theta+\pi/6)\left[e^{-Rx/\omega L}\Big/\left(1-e^{-\pi R/\omega L}\right)\right] \\ &\quad + \sin(x+\phi-\theta)\Big\}\sin 6nx\,dx \\ &= 36E_M/\pi\sqrt{R^2+(wL)^2}\left\{\cos(\phi-\theta+\pi/6)\left[(R/\omega L)^2-1\right]\Big/\left[36n^2+(R/\omega L)^2\right](36n^2-1)\right\} \end{aligned} \tag{A2a}$$

$$\begin{aligned} B_I(n) &= \left[6E_M n/\pi\sqrt{R^2+(wL)^2}\right]\int_0^{\pi/3}\Big\{\cos(\phi-\theta+\pi/6)\left[e^{-Rx/\omega L}\Big/\left(1-e^{-\pi R/\omega L}\right)\right] \\ &\quad + \sin(x+\phi-\theta)\Big\}\cos 6nx\,dx \\ &= 6E_M/\pi\sqrt{R^2+(wL)^2}\Big\{\left[\sin(\phi-\theta+5\pi/6)/(36n^2-1)\right] \\ &\quad - \left[\cos(\phi-\theta+\pi/6)/36n^2+(R/\omega L)^2\right]\Big\} \end{aligned} \tag{A2b}$$

$$C_I(n) = \left[A_I^2(n) + B_I^2(n)\right]^{1/2} \tag{A2c}$$

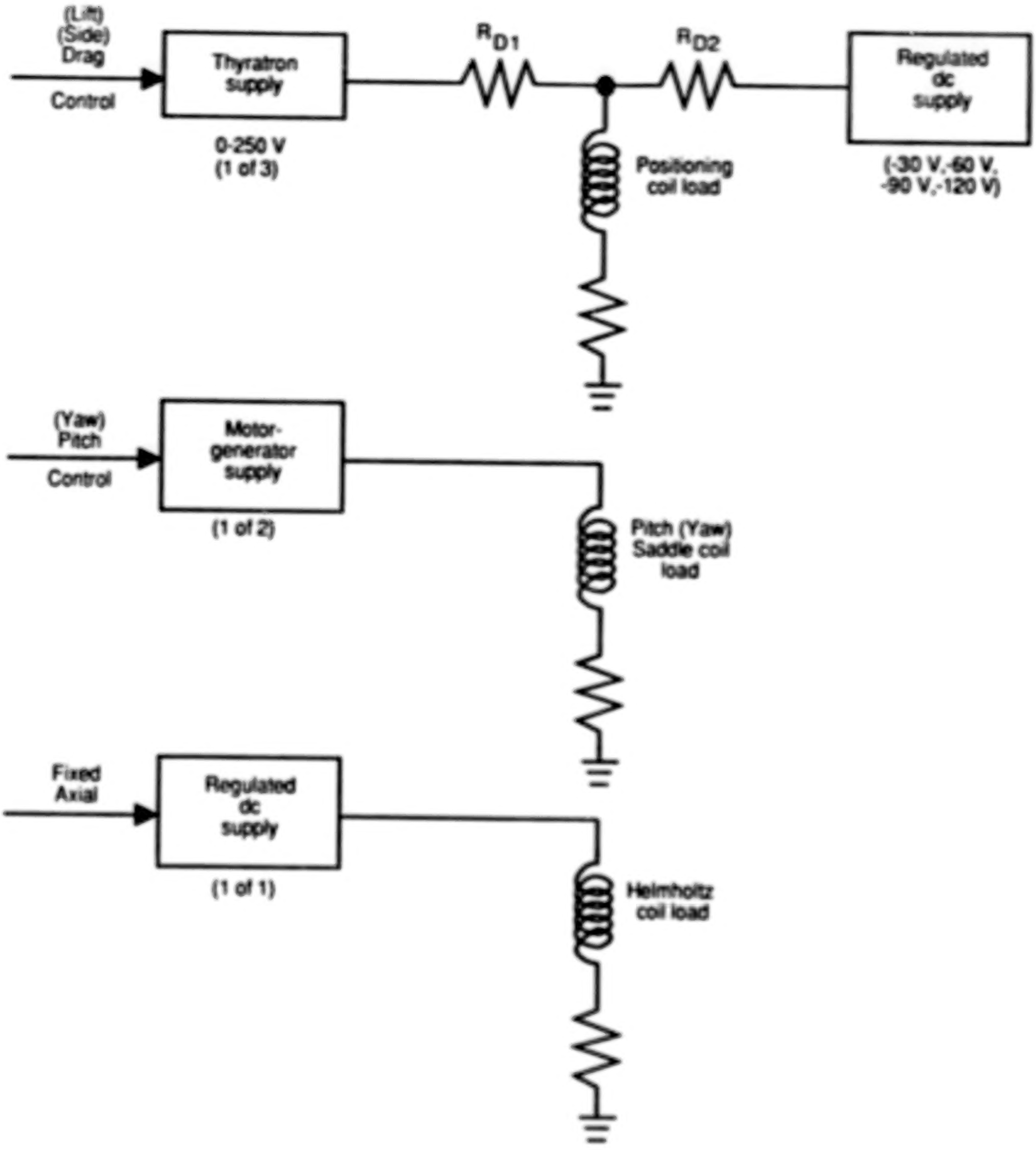
(Lift)
(Side)
Drag
Control
Thyratron supply
0-250 V
(1 of 3)
R_{D1}
R_{D2}
Regulated dc supply
(-30 V,-60 V, -90 V,-120 V)
Positioning coil load
(Yaw)
Pitch
Control
Motor-generator supply
(1 of 2)
Pitch (Yaw) Saddle coil load
Fixed
Axial
Regulated dc supply
(1 of 1)
Helmholtz coil load

Figure 1. Existing controlled power supply configuration.

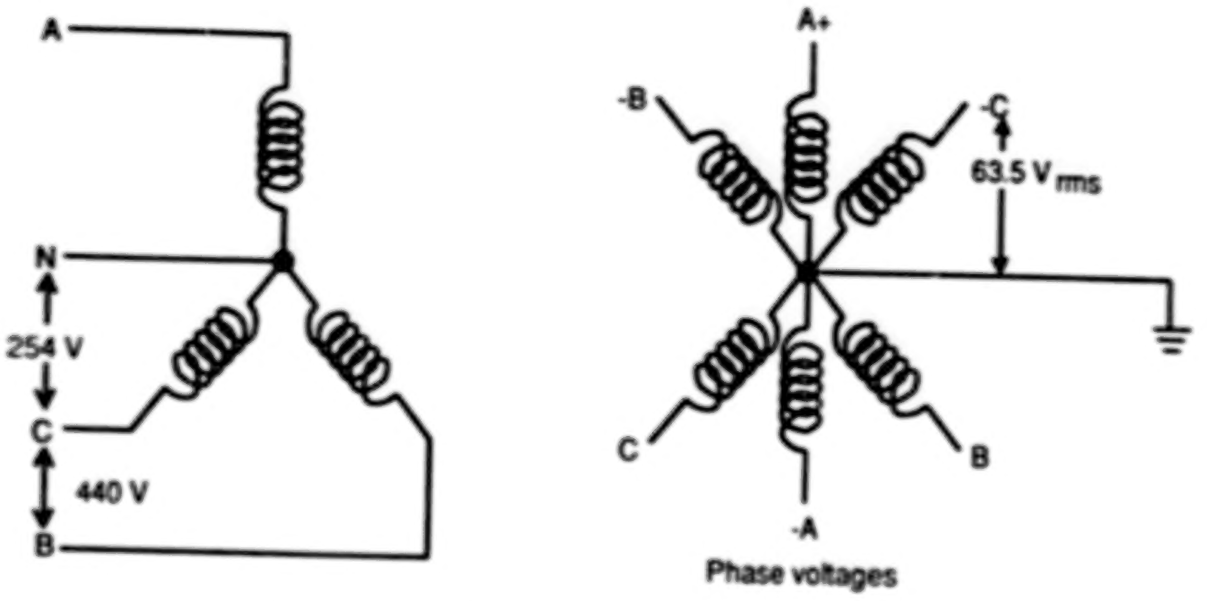
A
N
254 V
C
440 V
B
A+
-B
-C
63.5 V rms
C
B
-A
Phase voltages

Figure 2. Three-phase wye to six-phase star transformer.

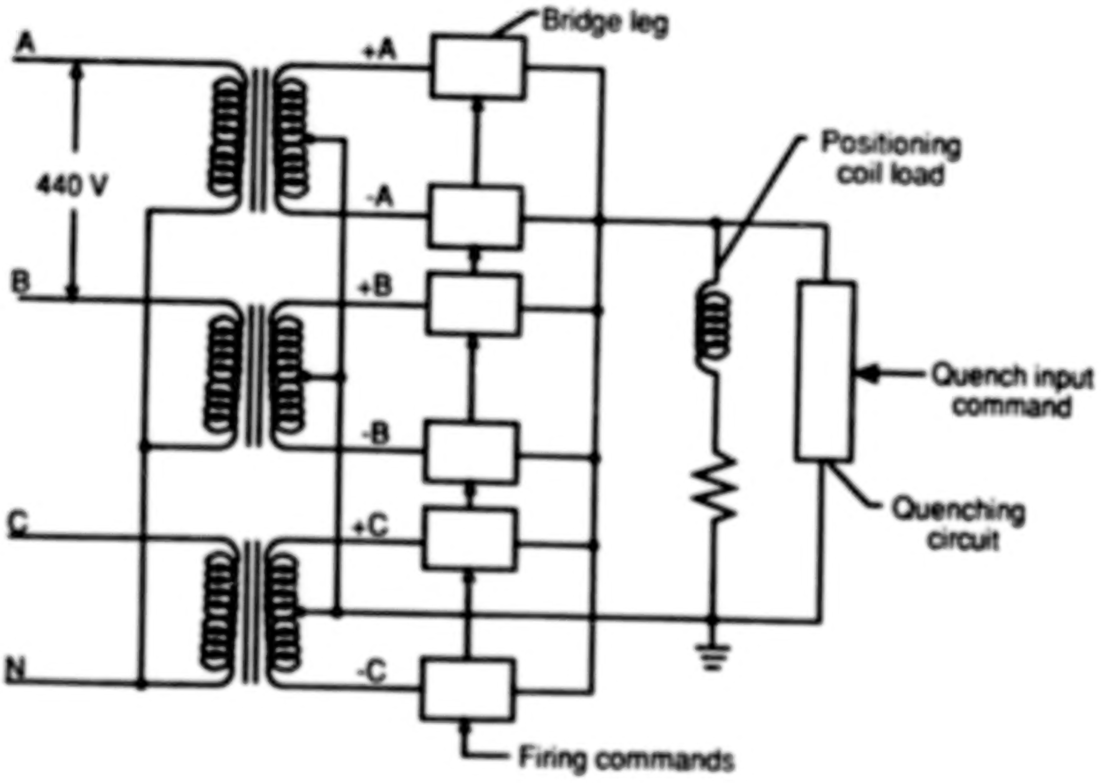
Bridge leg
A
+A
440 V
-A
Positioning coil load
B
+B
-B
Quench input command
Quenching circuit
C
+C
N
-C
Firing commands

Figure 3. Six-phase bidirectional rectifier bridge with quenching circuit.

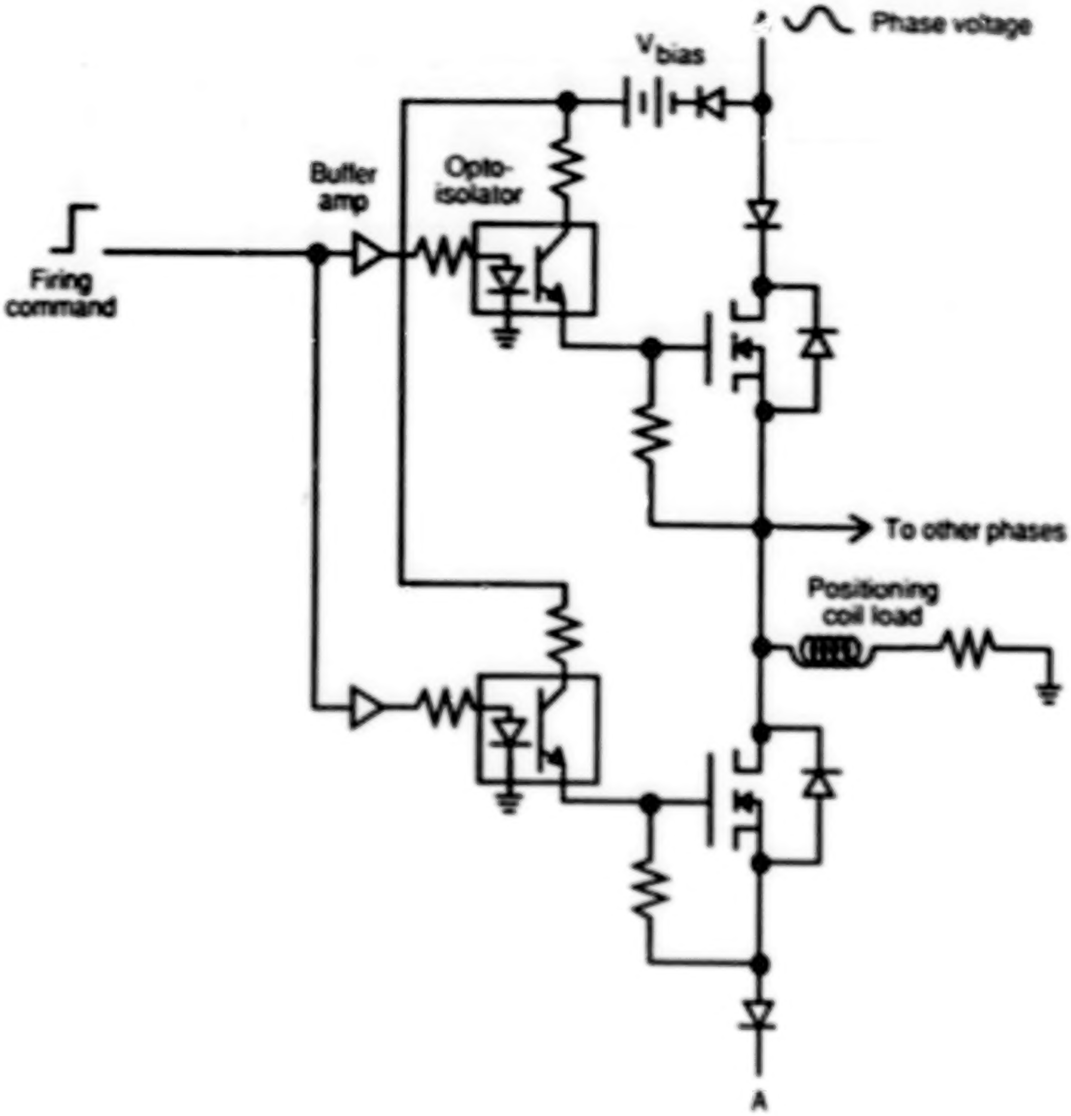
Phase voltage
V bias
Buffer amp
Opto-isolator
Firing command
To other phases
Positioning coil load
A

Figure 4. Optical isolation and biasing circuit for phase-*A* gate circuits.

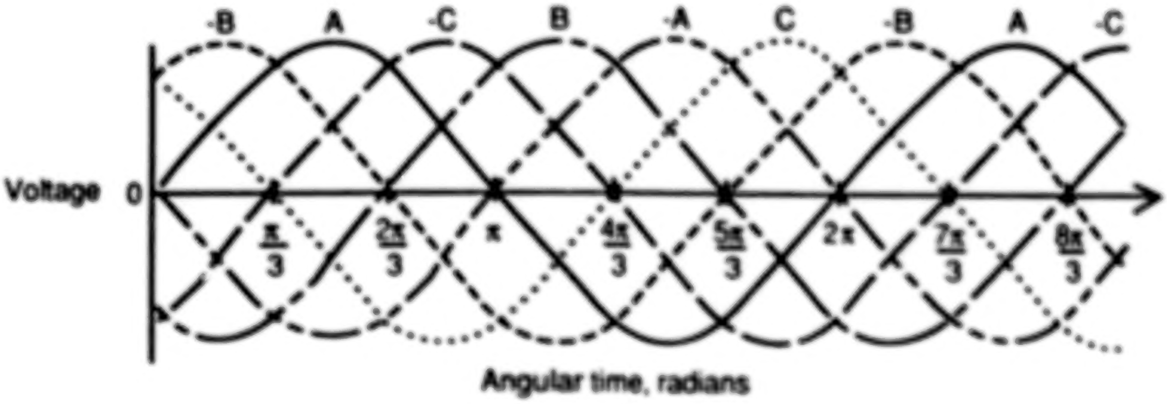

Figure 5. Six-phase sinusoidal voltages.

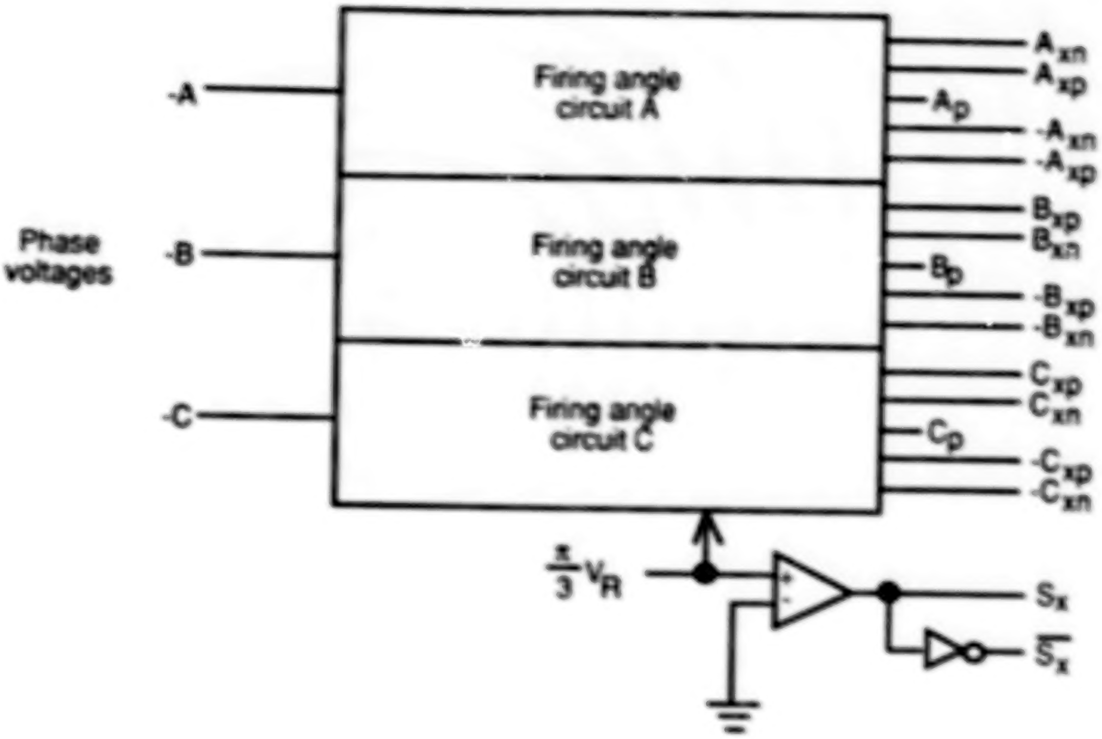
Phase voltages
-A
-B
-C
Firing angle circuit A
Firing angle circuit B
Firing angle circuit C
A_{xn}
A_{xp}
A_p
$-A_{xn}$
$-A_{xp}$
B_{xp}
B_{xn}
B_p
$-B_{xp}$
$-B_{xn}$
C_{xp}
C_{xn}
C_p
$-C_{xp}$
$-C_{xn}$
$\frac{\pi}{3}V_R$
S_x
$\overline{S_x}$

(a) Circuit block diagram.

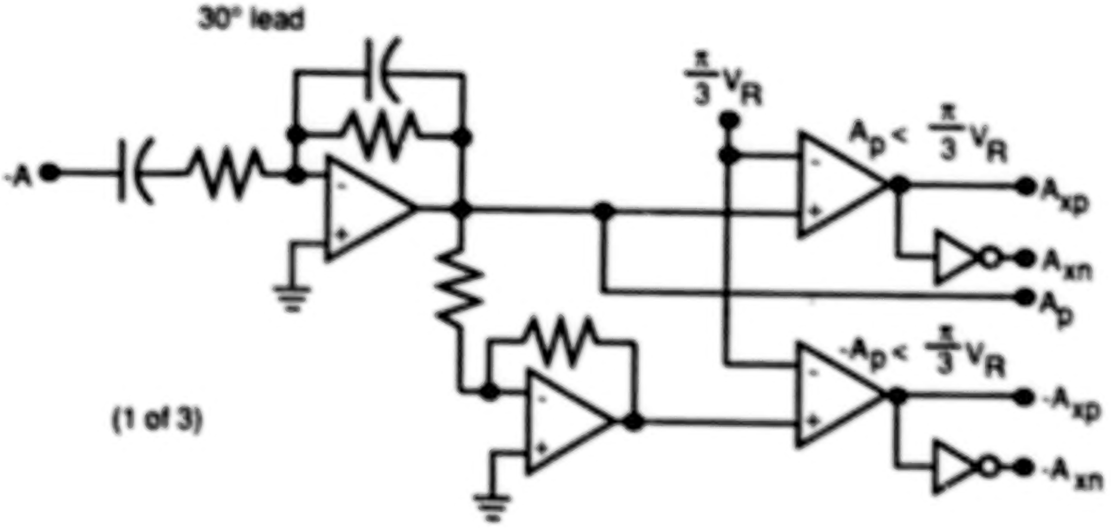
30° lead
-A
$\frac{\pi}{3}V_R$
$A_p < \frac{\pi}{3}V_R$
A_{xp}
A_{xn}
A_p
$-A_p < \frac{\pi}{3}V_R$
$-A_{xp}$
$-A_{xn}$
(1 of 3)

(b) Circuit detail.

Figure 6. Determination of firing angle.

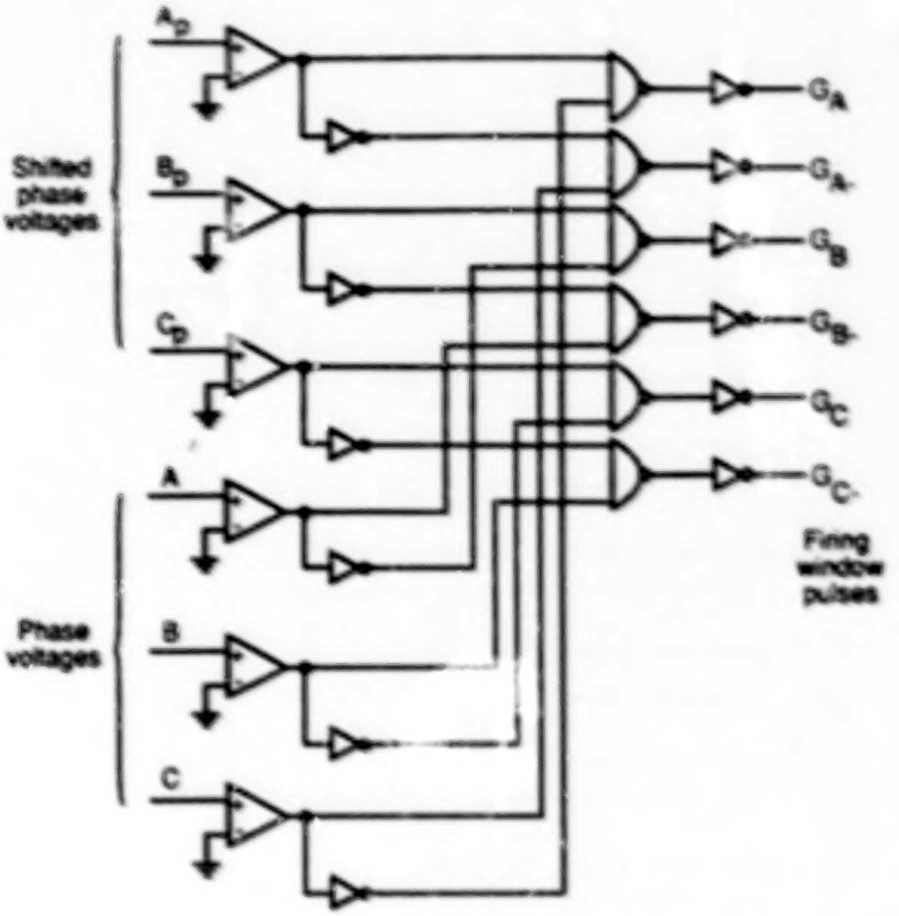
Shifted phase voltages
A_p
B_p
C_p
Phase voltages
A
B
C
G_A
G_{A-}
G_B
G_{B-}
G_C
G_{C-}
Firing window pulses

Figure 7. Phase firing window detection logic circuit.

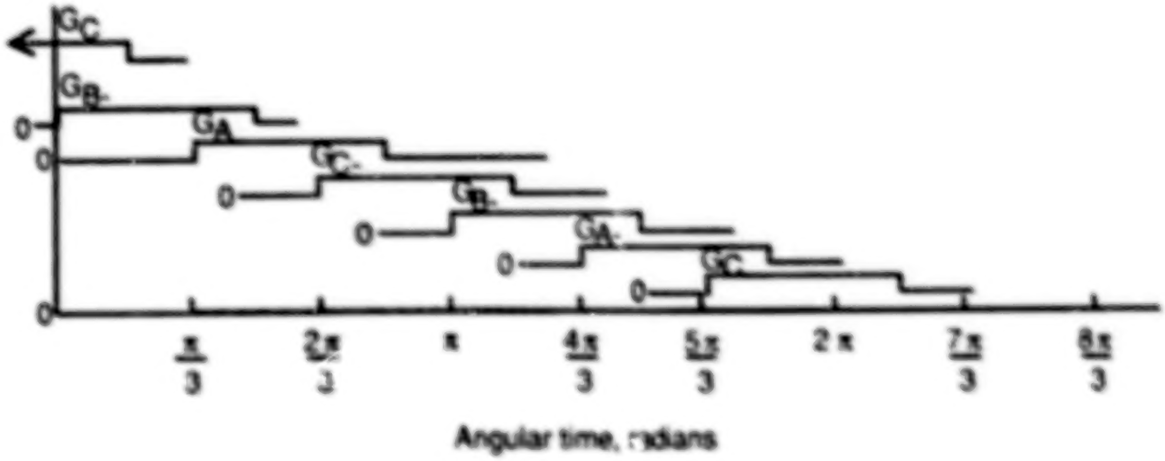

Figure 8. Phase firing windows.

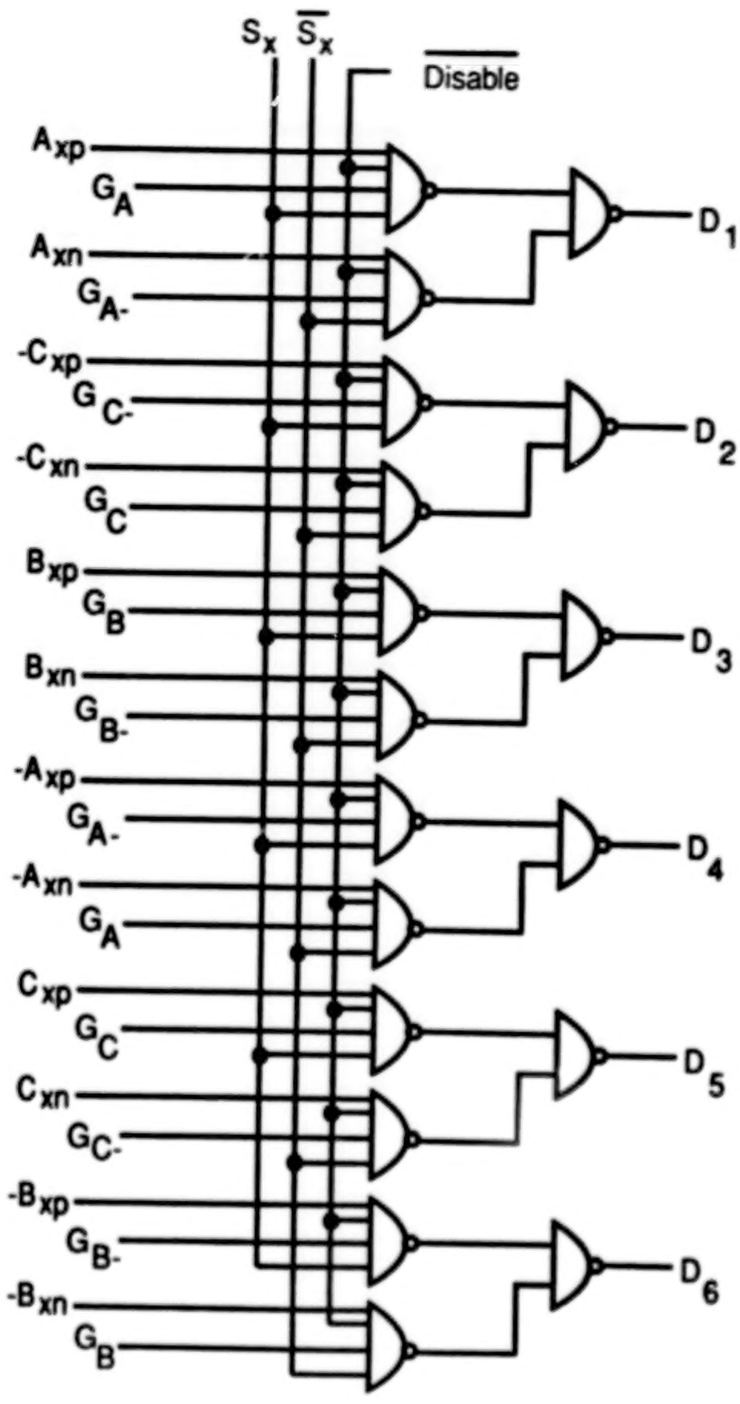

S_x
$\overline{S_x}$
$\overline{\text{Disable}}$
A_{xp}
G_A
A_{xn}
G_{A-}
$-C_{xp}$
G_{C-}
$-C_{xn}$
G_C
B_{xp}
G_B
B_{xn}
G_{B-}
$-A_{xp}$
G_{A-}
$-A_{xn}$
G_A
C_{xp}
G_C
C_{xn}
G_{C-}
$-B_{xp}$
G_{B-}
$-B_{xn}$
G_B
D_1
D_2
D_3
D_4
D_5
D_6

Figure 9. Commutation logic for cyclic control register.

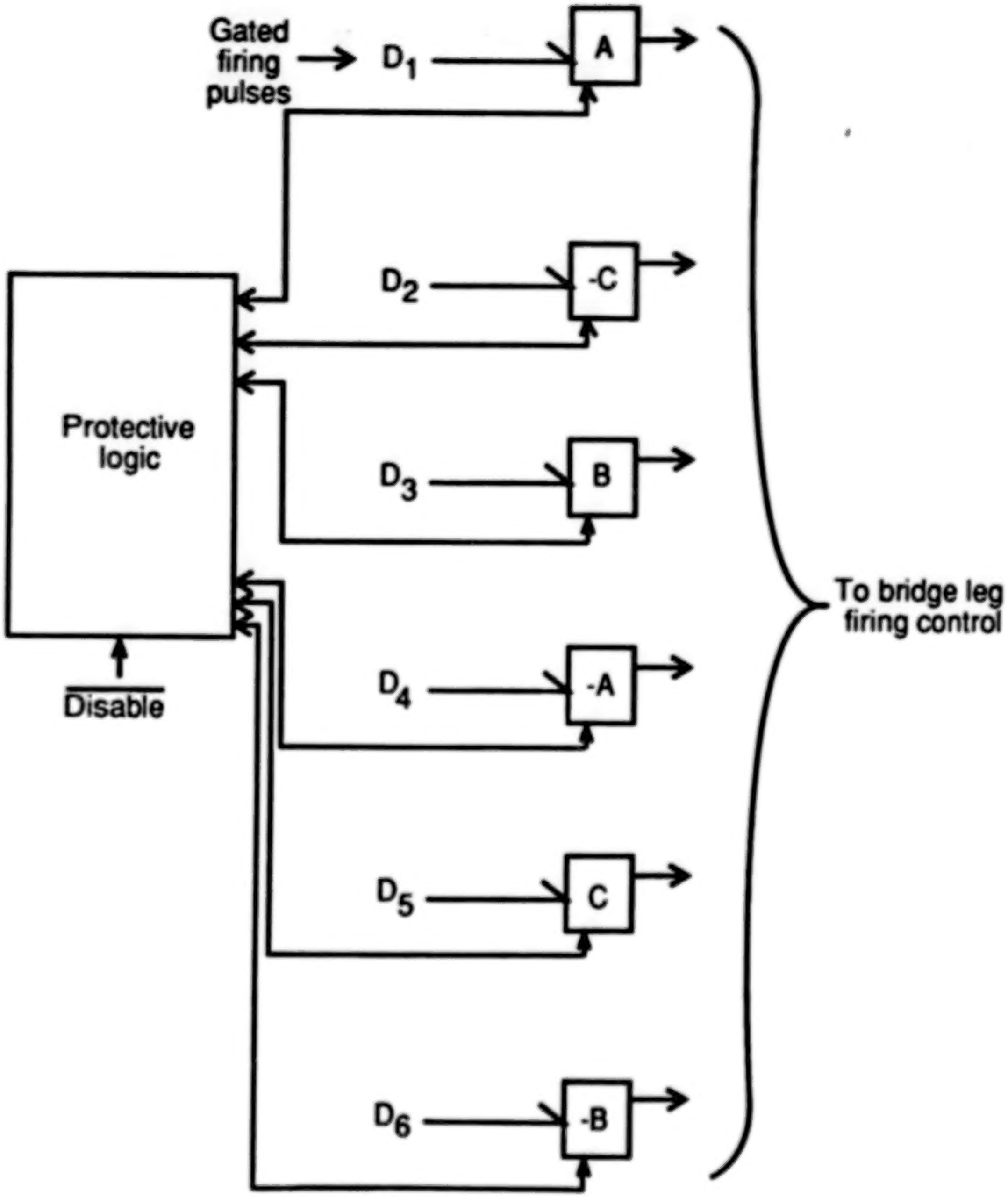
Gated firing pulses
D1
A
D2
-C
Protective logic
D3
B
To bridge leg firing control
D4
-A
Disable
D5
C
D6
-B

Figure 10. Cyclic control register.

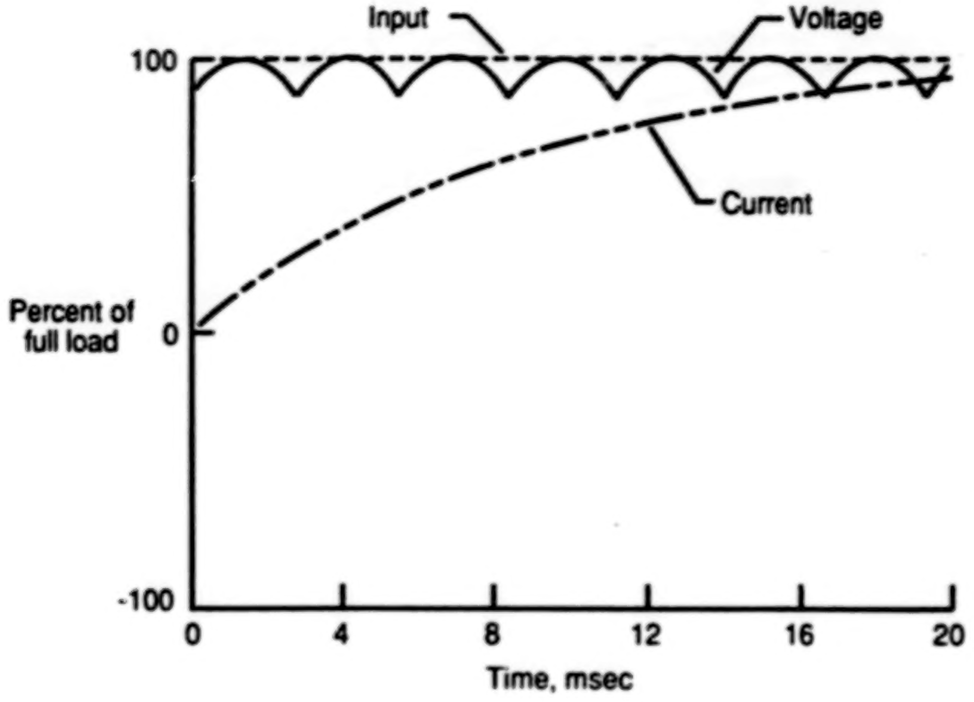

Figure 11. Load voltage and current response to a 100-percent step input.

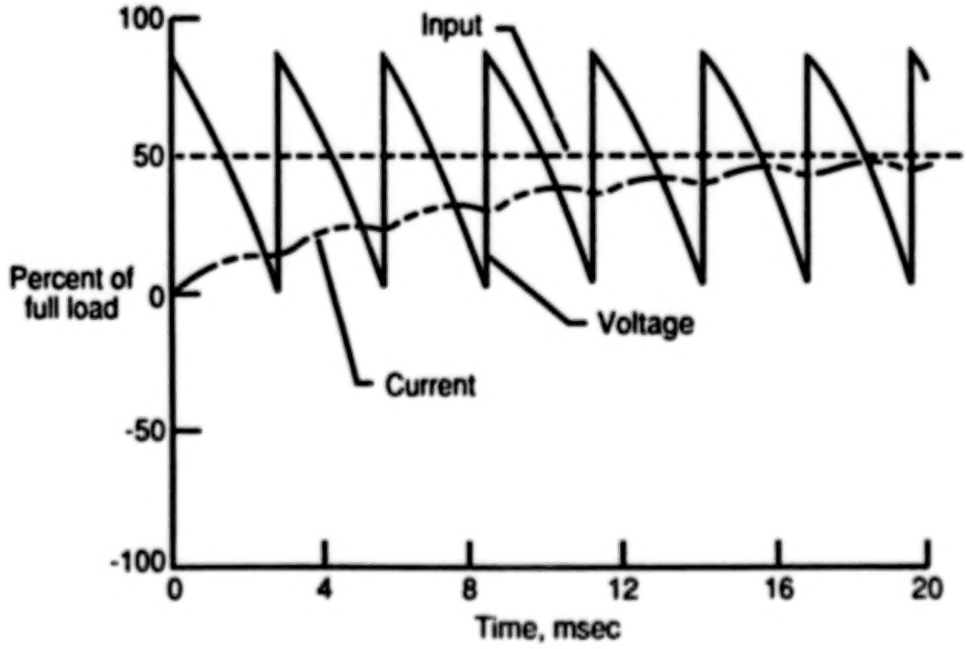

Figure 12. Load voltage and current response to a 50-percent step input.

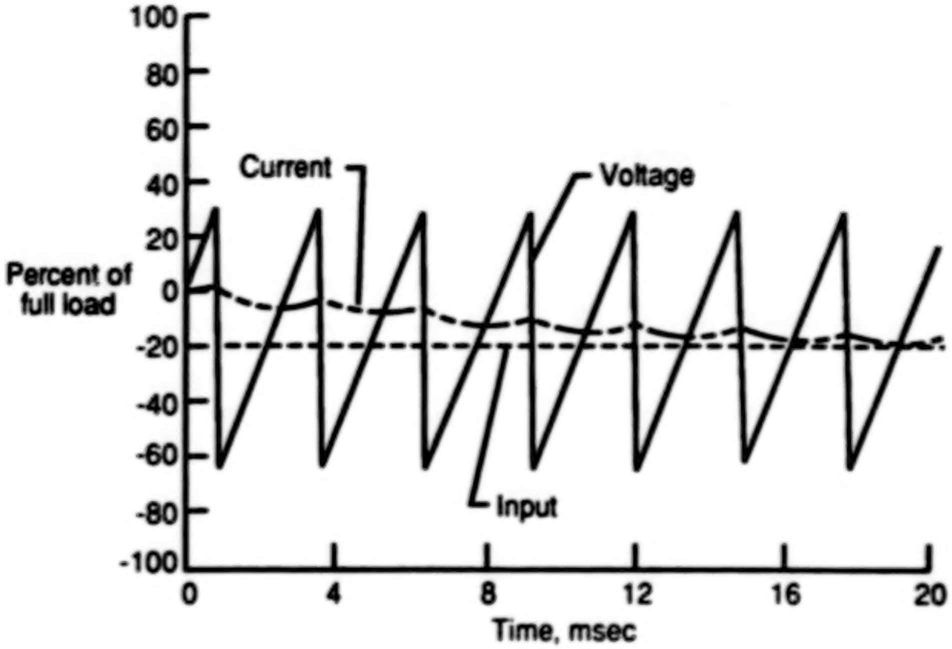

Figure 13. Load voltage and current response to a −20-percent step input.

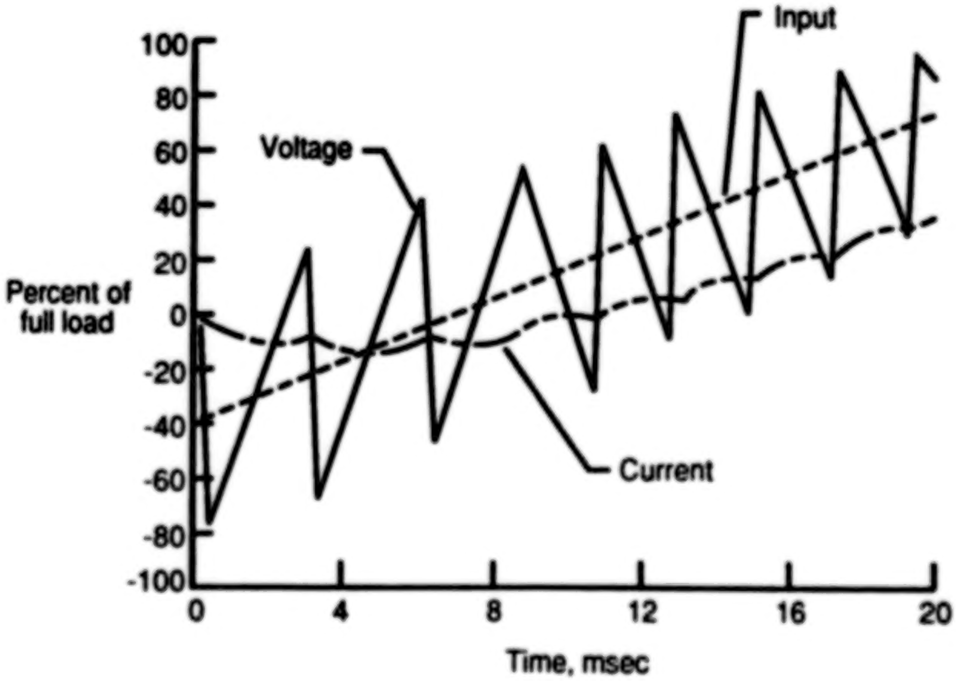

Figure 14. Load voltage and current response to a 100-percent, 20 msec ramp input.

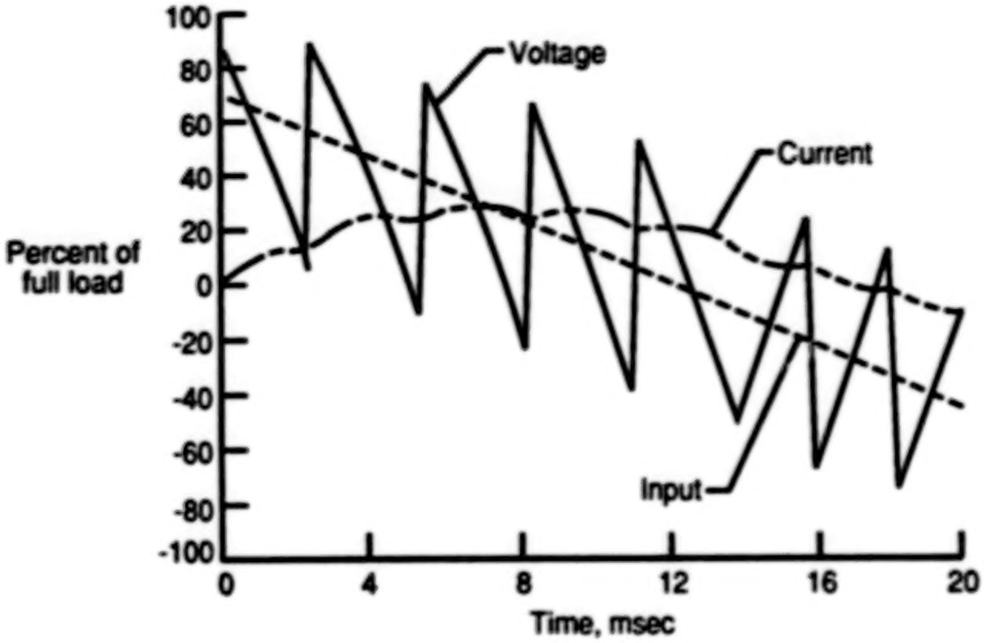

Figure 15. Load voltage and current response to a −100-percent, 20 msec ramp input.

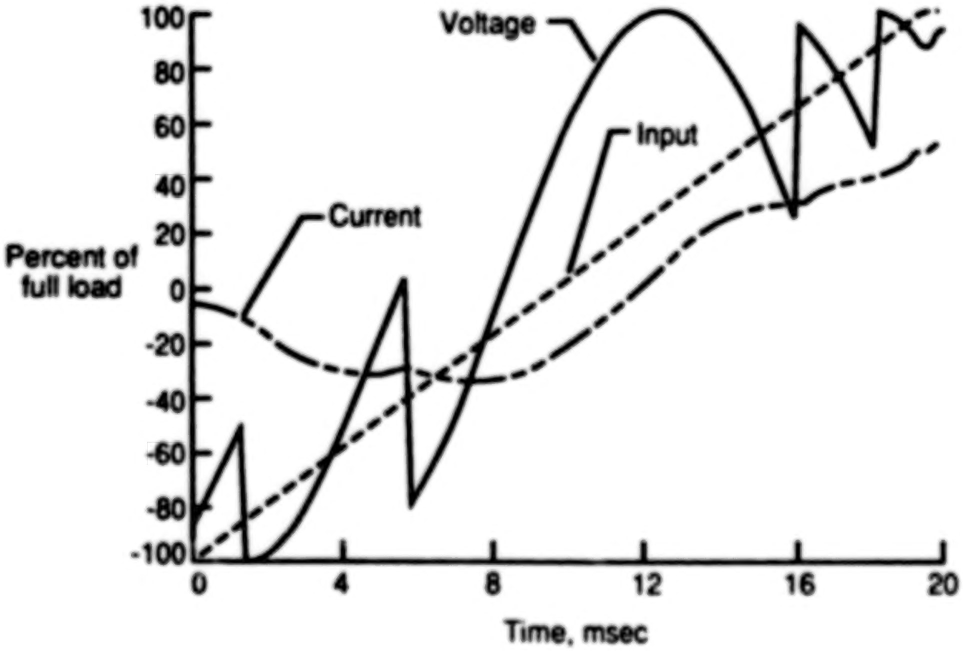

Figure 16. Load voltage and current response to a 200-percent, 20 msec ramp input.

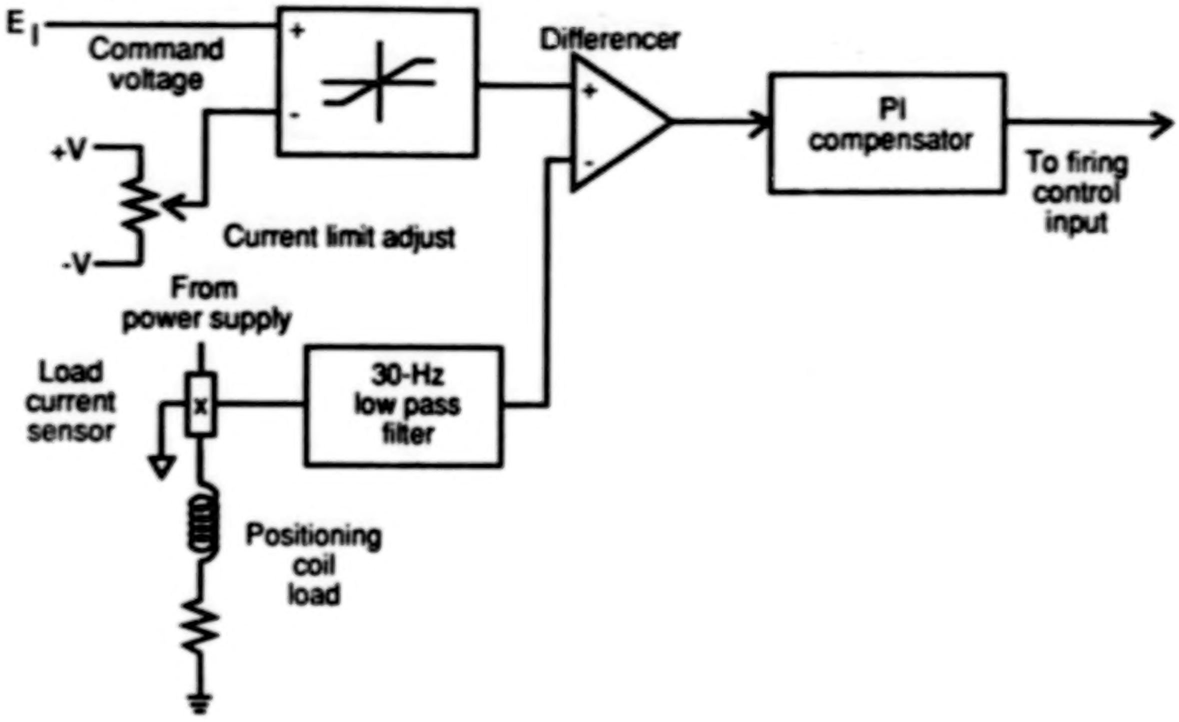
E_I
Command voltage
+
-
Differencer
+
-
PI compensator
To firing control input
+V
-V
Current limit adjust
From power supply
Load current sensor
x
30-Hz low pass filter
Positioning coil load

Figure 17. Current limiting and current feedback circuit.

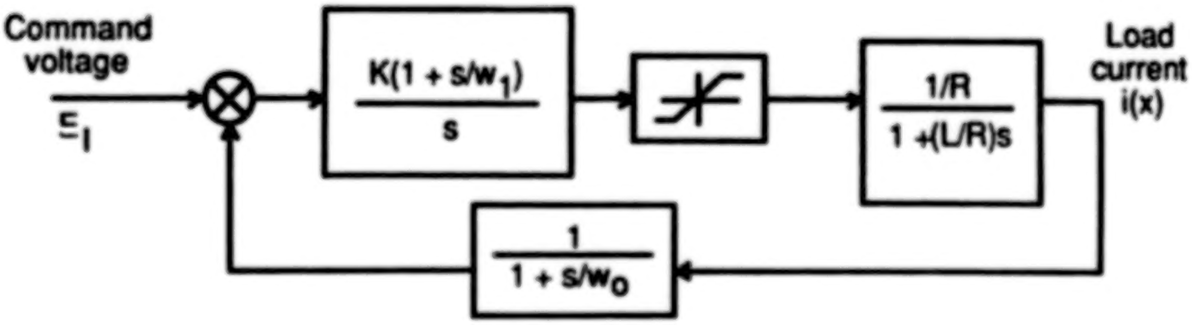
Command voltage
E_I
K(1 + s/w_1) / s
1/R / 1 +(L/R)s
Load current i(x)
1 / 1 + s/w_o

Figure 18. Positioning magnet current feedback control.

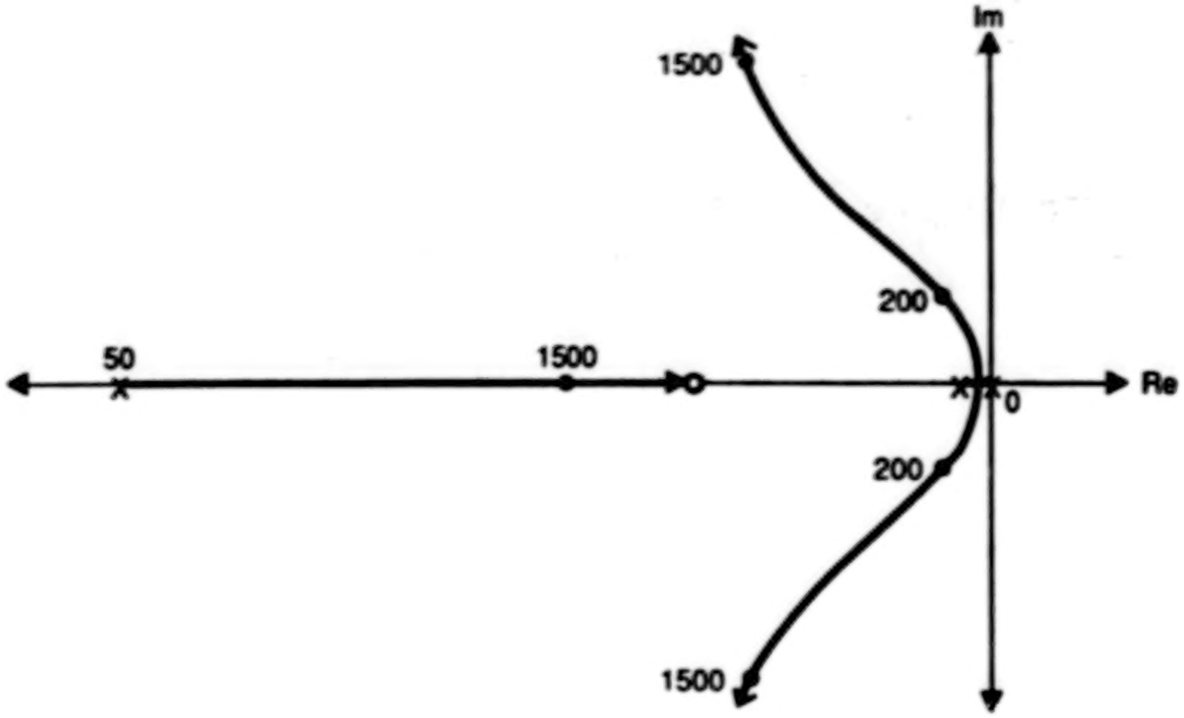
Im
1500
200
50
1500
0
Re
200
1500

Figure 19. Root locus for PI current feedback control. $L/R = 0.16$ sec.

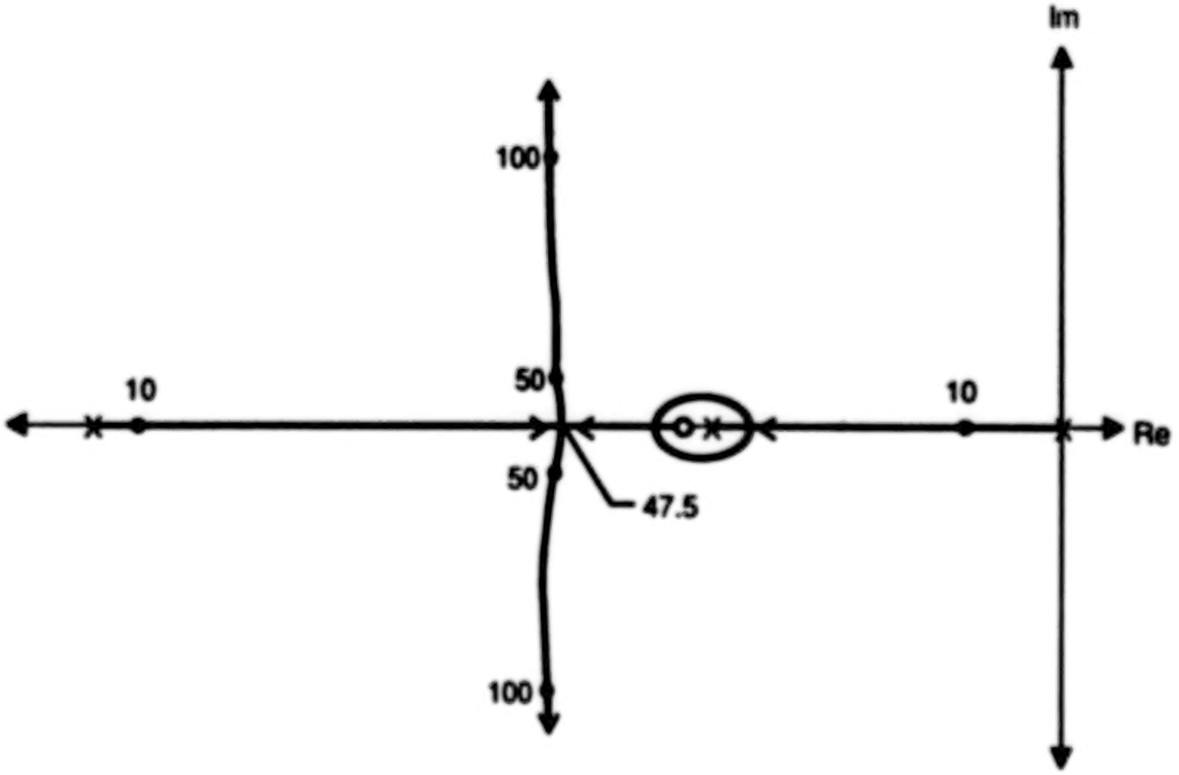
Im
100
10
50
10
Re
50
47.5
100

Figure 20. Root locus for PI current feedback control. $L/R = 0.016$ sec.

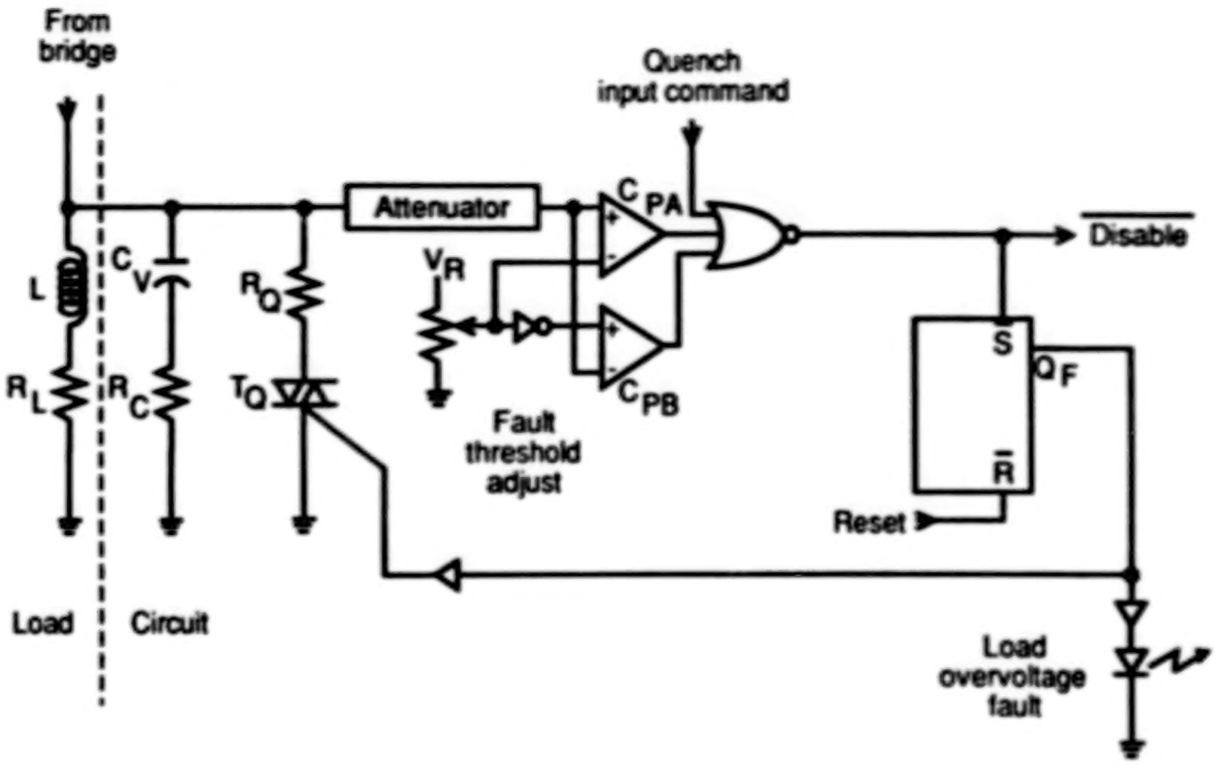
From bridge
Quench input command
Attenuator
C_{PA}
V_R
$\overline{\text{Disable}}$
L
C_V
R_Q
R_L
R_C
T_Q
S
Q_F
$\overline{R}$
C_{PB}
Fault threshold adjust
Reset
Load
Circuit
Load overvoltage fault

Figure 21. Load overvoltage fault detection and quenching circuit.

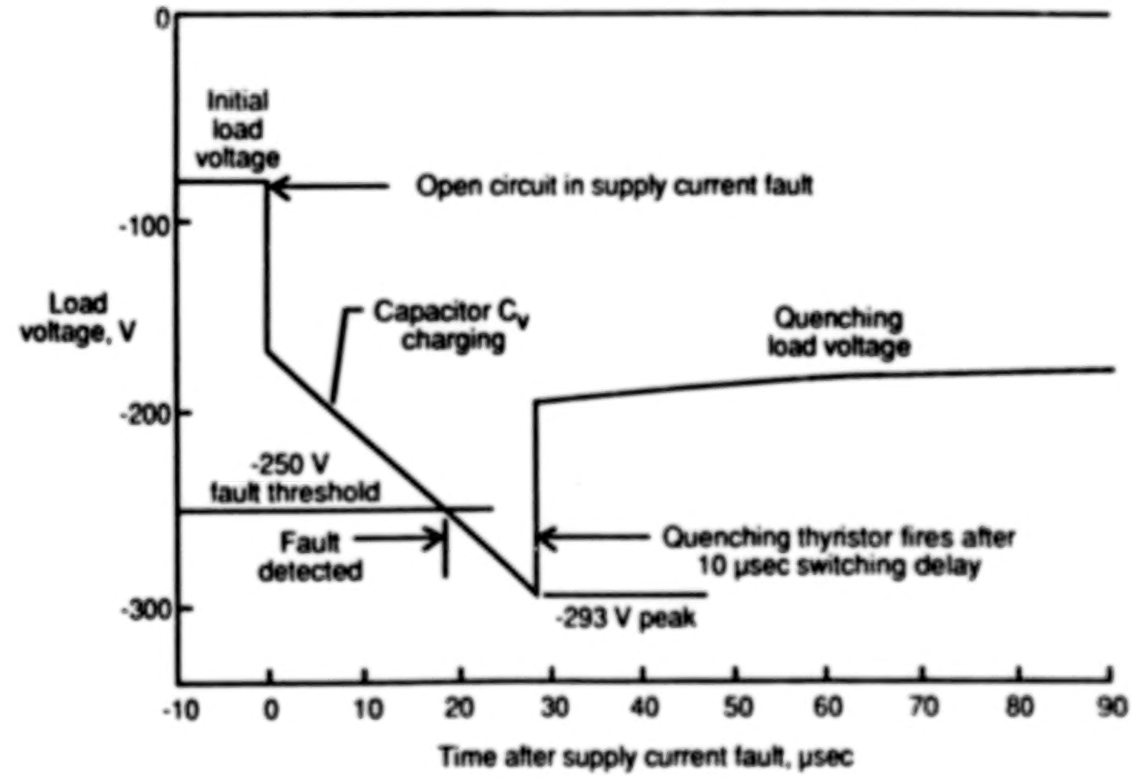

Figure 22. Inductive load voltage impulse after bridge open circuit.

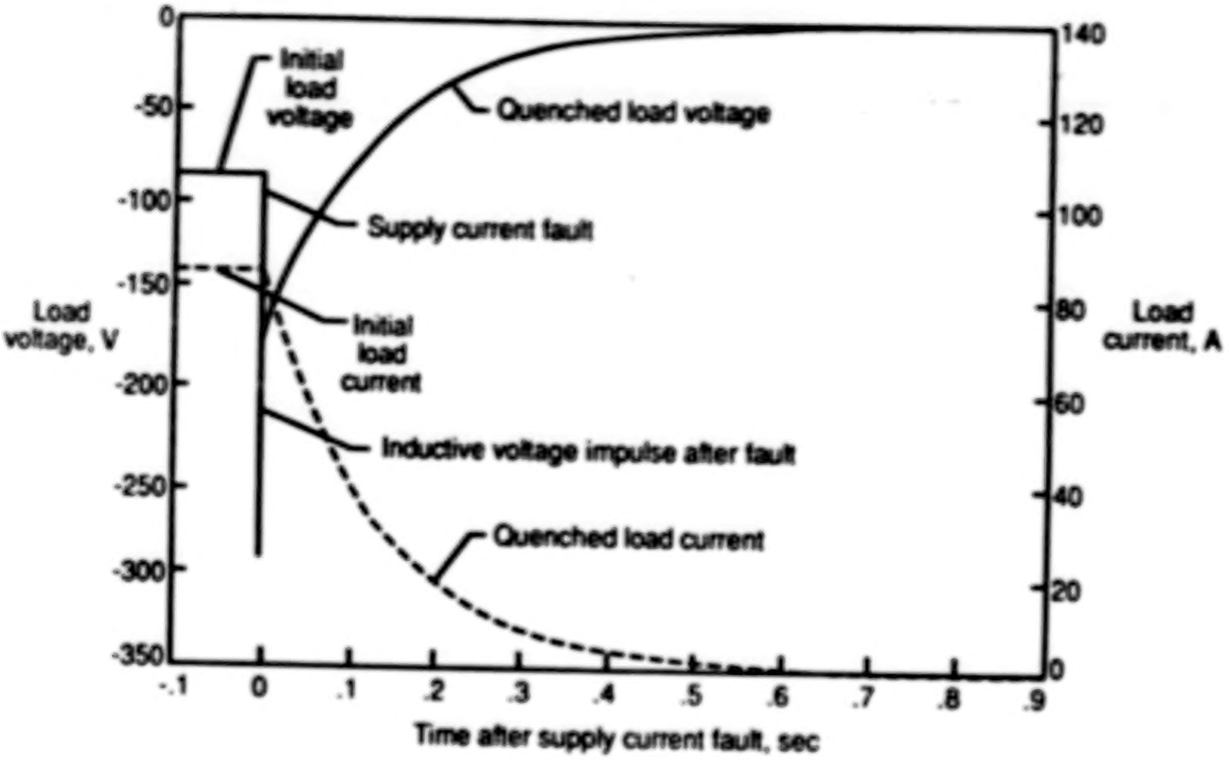

Figure 23. Quenched load voltage and current after bridge open circuit.

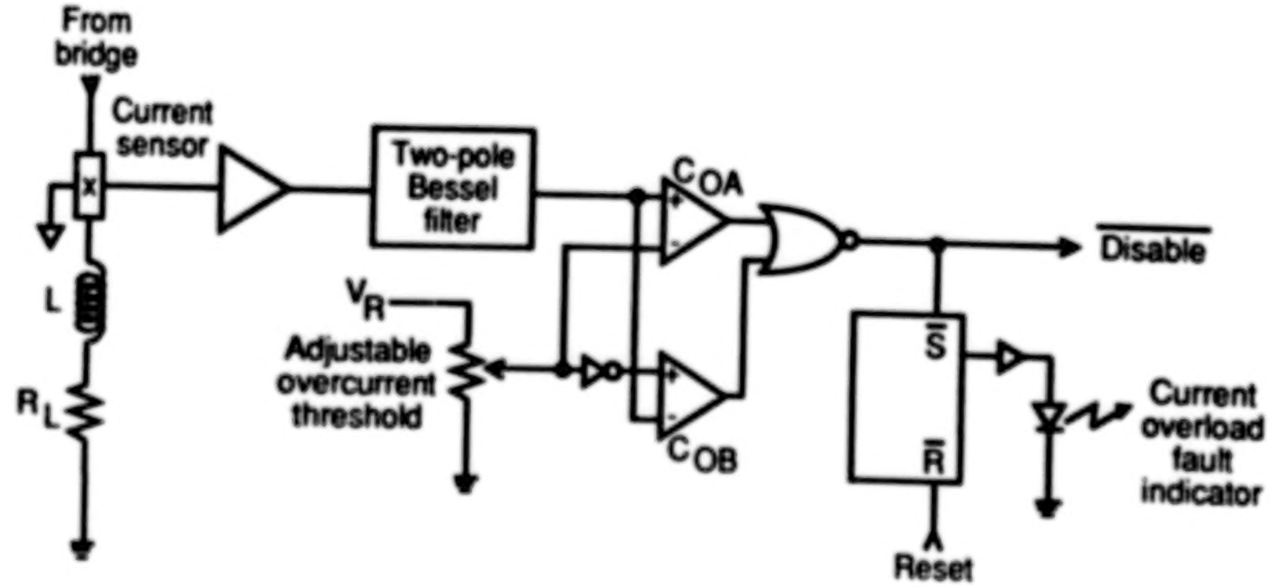
From bridge
Current sensor
X
L
R_L
Two-pole Bessel filter
C_{OA}
C_{OB}
V_R
Adjustable overcurrent threshold
Disable
S̄
R̄
Reset
Current overload fault indicator

Figure 24. Current overload fault detection circuit.

N91-21200

DESCRIPTION of the LARGE-GAP MAGNETIC SUSPENSION SYSTEM (LGMSS) GROUND BASED EXPERIMENT

Nelson J. Groom
Mail Stop 161
NASA Langley Research Center
Hampton
VA 23665-5225

INTRODUCTION

The purpose of this paper is to provide an overview of the Large Gap Magnetic Suspension System (LGMSS) ground-based experiment. An outline of the paper is presented in figure 1. A description of the experiment, as originally defined, and the experiment objectives and potential applications of the technology resulting from the experiment will be presented. Also, the results of two studies which were conducted to investigate the feasibility of implementing the experiment will be presented and discussed. Finally, a description of the configuration which was selected for the experiment will be described and a summary of the paper presented.

PRESENTATION OUTLINE

- Experiment Description
- Objectives
- Applications
- Feasibility Studies
- Selected Concept
- Summary

Figure 1. - Presentation Outline

EXPERIMENT DESCRIPTION

The LGMSS ground-based experiment, as originally defined, is shown schematically in figure 2. It consists of a cylindrical suspended element which has a core composed of permanent magnet material embedded in it. Levitation forces and control forces and torques are produced on the permanent magnet core by air core electromagnets which are required to fit within an eight foot by eight foot square by four foot high volume. The core is suspended a total distance of three feet above the top surface of the electromagnet volume. In addition to the permanent magnet core, the suspended element also contains an array of LEDs and associated electronics and power supply. The LEDs are embedded in the surface of the suspended element and provide active targets for a photogrammetric optical position measurement system which is being developed at Langley Research Center (ref. 1). Each LED target is imaged by a cylindrical lens on a linear Charge Coupled Device (CCD) sensor. Position and orientation of the model is determined from the position of the projected target images. There are two sensors per sensing unit and a total of eight sensing units which are positioned symmetrically about and approximately six feet above the suspended element. The optical position measurement system provides six-degrees-of-freedom position information for the control system.

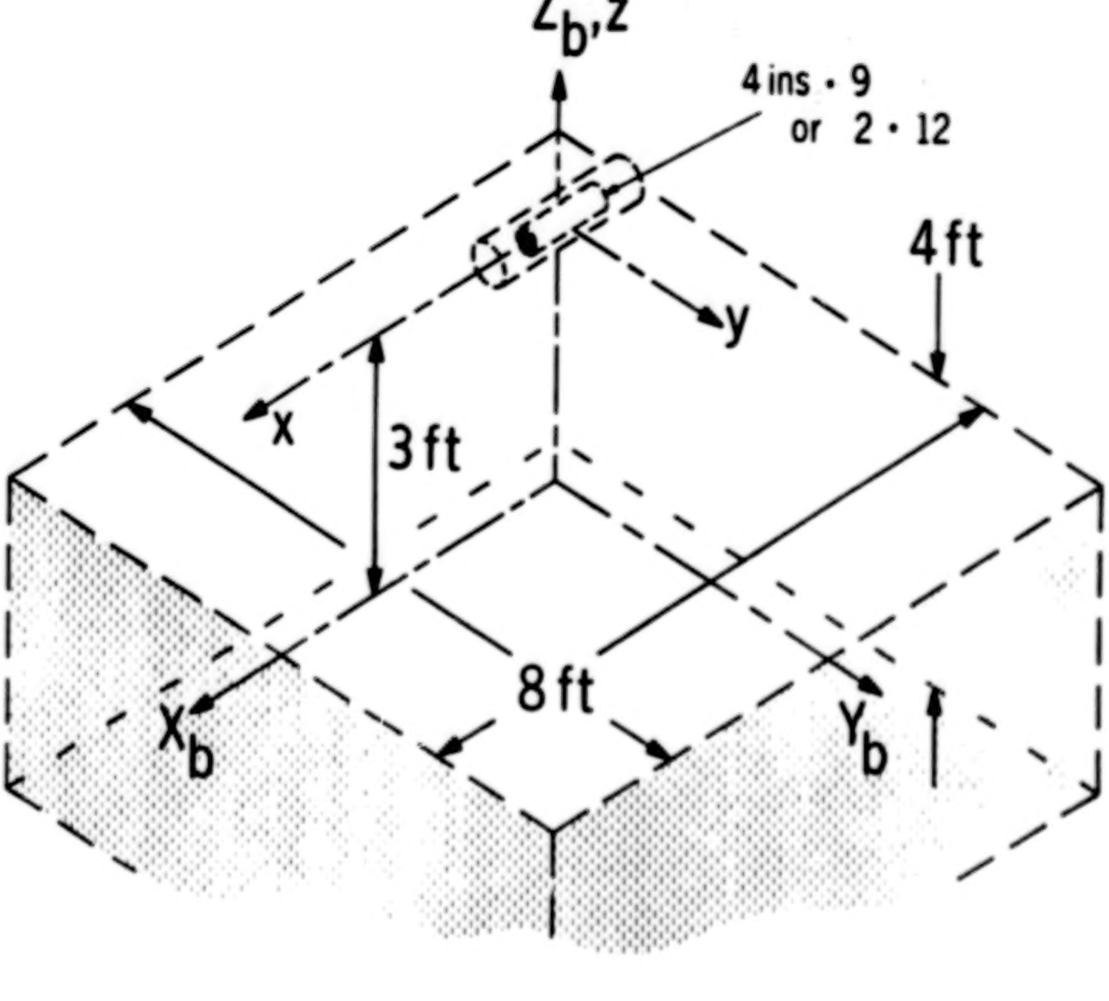
Z_b, z
4 ins · 9
or 2 · 12
4 ft
y
x
3 ft
8 ft
X_b
Y_b

Figure 2. - Experiment Definition

EXPERIMENT OBJECTIVES

The objectives of the LGMSS ground-based experiment are to investigate the technology issues associated with magnetic suspension, accurate suspended element control, and accurate position sensing at large gaps and suspended element control over large angles (fig. 3).

OBJECTIVES

- Investigate Technology Issues Associated with:
  - Magnetic Suspension at Large Gaps
  - Accurate Position Sensing at Large Gaps
  - Accurate Suspended Element Control at Large Gaps
  - Suspended Element Control Over Large Angles

Figure 3. - Experiment Objectives

TECHNOLOGY APPLICATIONS

The technology which should result from the LGMSS experiment has potential applications in a wide range of areas including microgravity and vibration isolation systems, magnetically suspended pointing mounts, large-angle magnetic suspension systems for advanced actuators, wind tunnel magnetic suspension systems, and remote manipulation/control/positioning of objects in space (fig.4).

APPLICATIONS

- Potential Applications of Technology Include:
  - Microgravity and Vibration Isolation Systems
  - Magnetically Suspended Pointing Mounts
  - Large-Angle Magnetic Suspension Systems for Advanced Actuators
  - Wind Tunnel Magnetic Suspension Systems
  - Remote Manipulation/Control/Positioning of Objects in Space

Figure 4. - Technology Applications

FEASIBILITY STUDIES

After defining the LGMSS experiment, two studies were performed to verify the feasibility of building a system to meet the experiment requirements and to investigate approaches to implement it. One study was performed by Madison Magnetics, Inc. and resulted in a proposed configuration of five electromagnets mounted in a planar array (ref. 2). This approach was designated the five-coil approach. The other study was performed by SatCon Technology Corporation and resulted in a proposed configuration of six electromagnets mounted in a planar array. This approach was designated the six-coil approach.

Five-coil system.- A summary of the Madison Magnetics study is presented in figure 5. An important conclusion was that the implementation of the LGMSS experiment was feasible. The proposed implementation is shown schematically in figure 6 and consists of a planar array of five electromagnets mounted in a circular configuration. Since the LGMSS requirement is for five-degrees-of-freedom control, this represents the minimum number of actuators. The electromagnets are conventional liquid-helium cooled superconductors and combine the functions of levitation and control. The magnetization vector is horizontal (parallel to the long axis of the core) and the system is capable of providing 360 degrees yaw (rotation about the vertical axis) control.

FEASIBILITY STUDIES

- Five-Coil System (Summary)
  - Feasible
  - Minimum Configuration
  - 360 Degree Yaw Control
  - Horizontal Magnetization Vector (Parallel to Long Axis of Core)
  - Combined Superconducting Levitation and Control Coils

Figure 5. - Summary of Five-Coil System

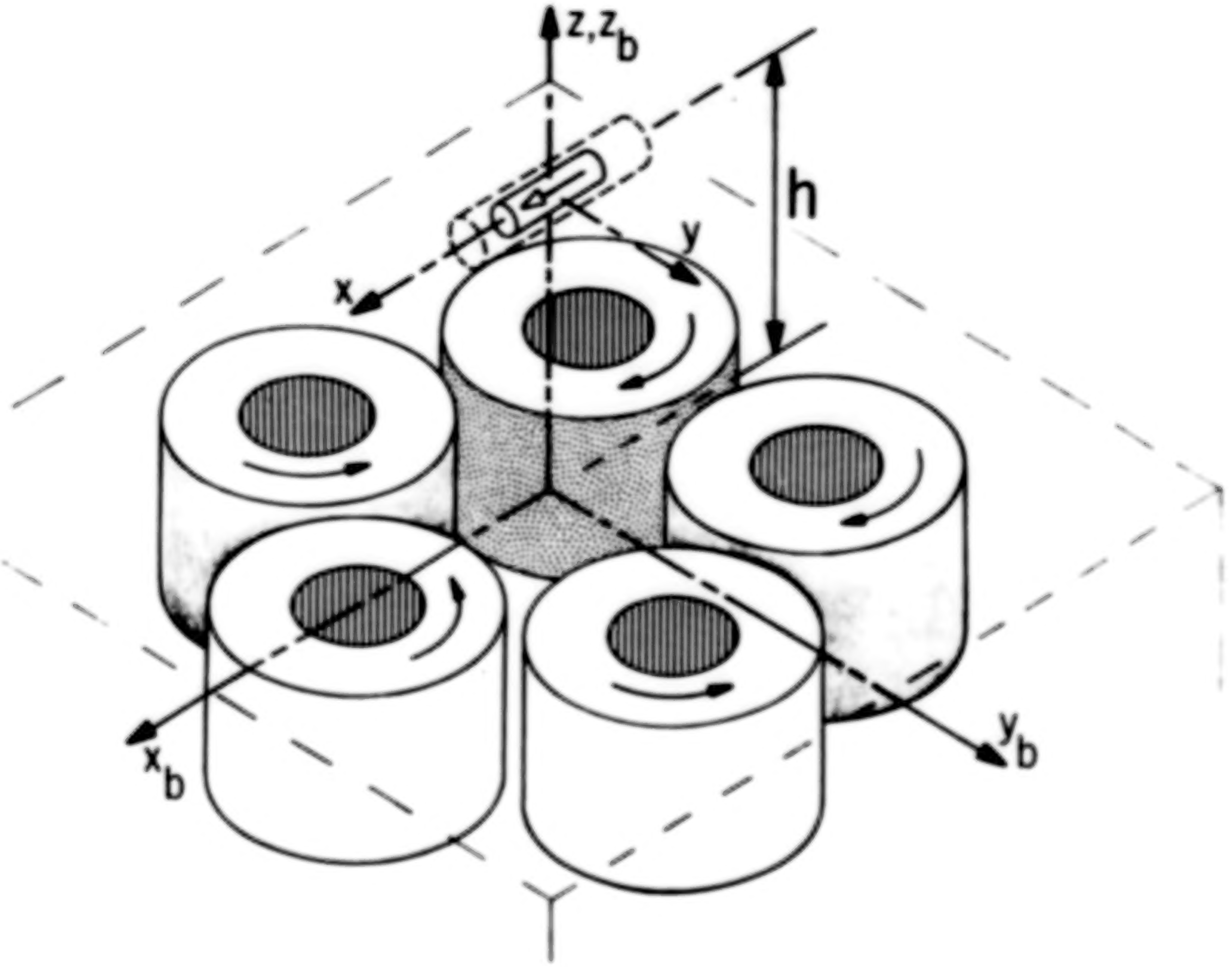
z,z_b
h
x
y
x_b
y_b

Figure 6. - Schematic Representation of Five-Coil System

FEASIBILITY STUDIES (Cont.)

Six-coil system.- A summary of the SatCon study is presented in figure 7. SatCon also concluded that it was feasible to implement the LGMSS experiment. Their proposed approach is shown in figure 8 and consists of a planar array of six electromagnets mounted in a circular configuration. The two approaches are similar with the major differences being in the control approach and the number of coils. The six-coil configuration also uses electromagnets which are conventional liquid-helium cooled superconductors and which combine the functions of levitation and control. The magnetization vector is horizontal (parallel to the long axis of the core) and the system is capable of providing 360 degrees yaw control. The main reasons for adding a sixth coil were control system related. The six coil system results in a symmetrical configuration and also results in an overspecified system from the standpoint of control inputs. The sixth coil could be fitted in the allowable volume without a significant increase in total Ampere-turns.

FEASIBILITY STUDIES (CONTINUED)

- Six-Coil System (Summary)
  - Feasible
  - Symmetric Configuration
  - Overspecified (Control Inputs)
  - 360 Degree Yaw Control
  - Horizontal Magnetization Vector (Parallel to Long Axis of Core)
  - Combined Superconducting Levitation and Control Coils

Figure 7. - Summary of Six-Coil System

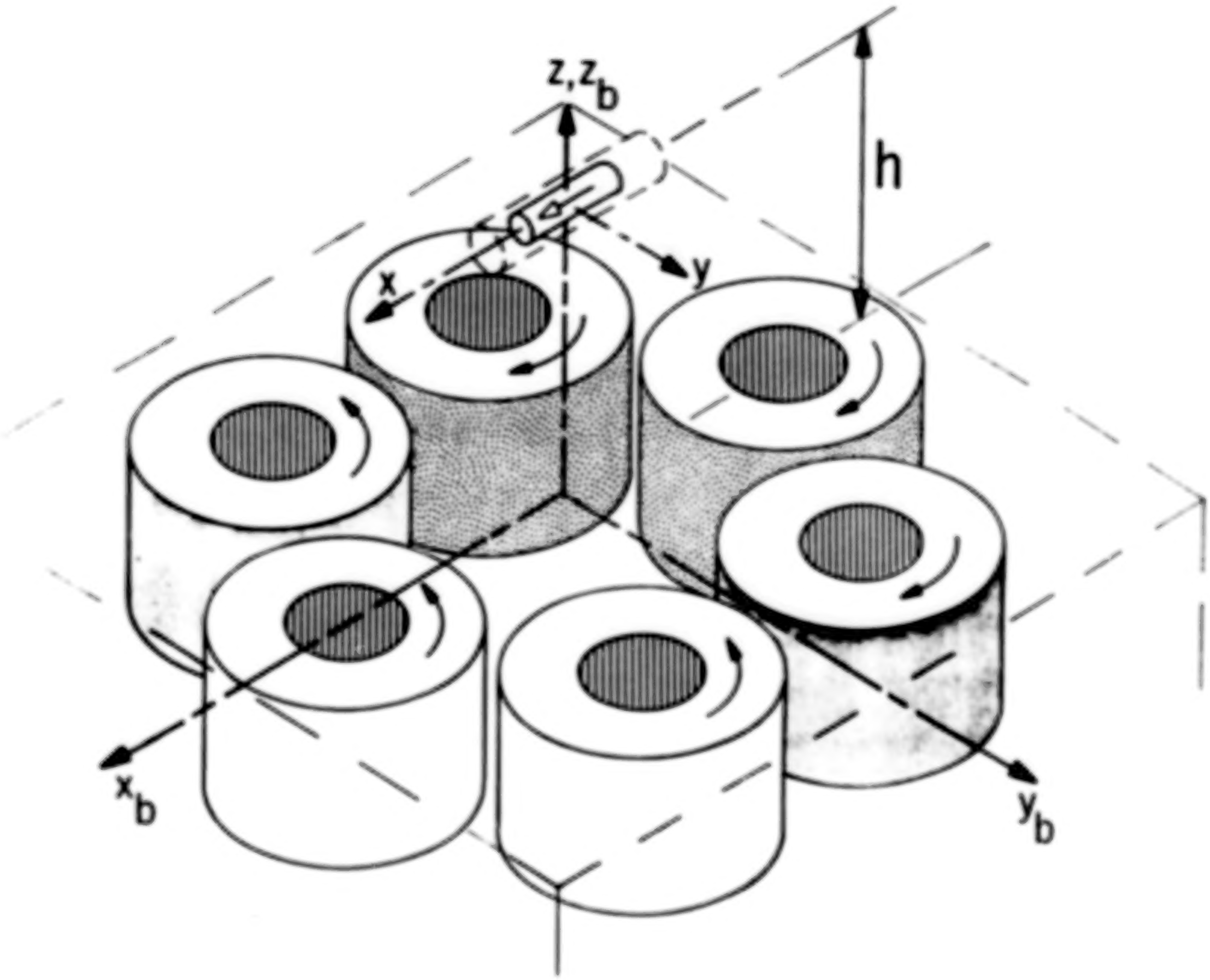
z, z_b
h
x
y
r
x_b
y_b

Figure 8. - Schematic Representation of Six-Coil System

SELECTED CONFIGURATION

As a result of the feasibility studies and further in-house studies, the requirements for the LGMSS experiment were refined and a decision was made to procure the design, fabrication, installation, and test of an LGMSS. A competitive procurement effort resulted in the selection of a configuration proposed by Intermagnetics General Corporation. This configuration is shown schematically in figure 9. As shown in the figure, there are two large concentric levitation coils and a separate set of control coils. The levitation coils are superconducting coils which are operated in the persistent mode. In the persistent mode, a superconducting coil is charged up to a certain current value and the terminals are shorted through a persistent mode switch. Since the superconductor has zero resistance, the current continues to flow, or persist, in the coil. In the configuration shown, the coils have currents flowing in opposite directions. The control coils are shown in a generic configuration since the contract is in the design phase and a final configuration has not been selected. The control coils are conventional room temperature coils.

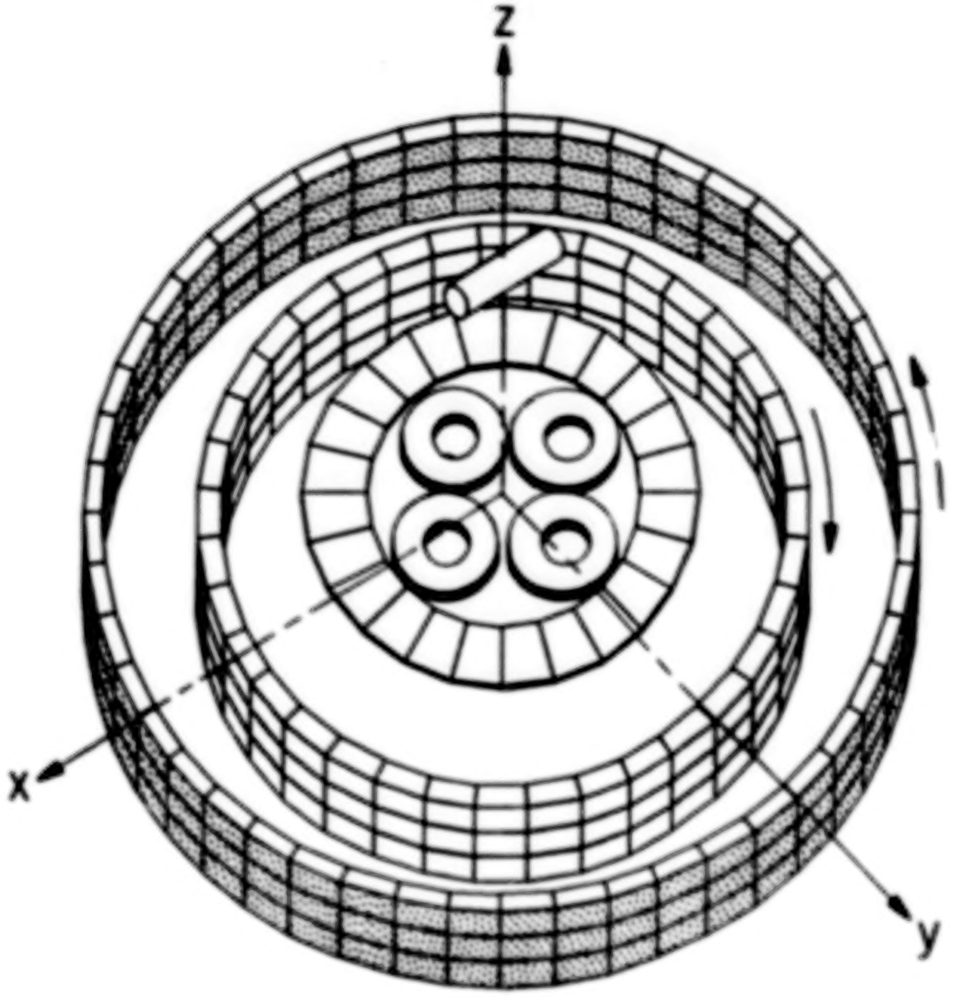

Figure 9. - Schematic Representation of Selected Configuration

SELECTED CONFIGURATION (Cont.)

Figure 10 shows the levitation coils and permanent magnet core in more detail. As shown in the figure, the magnetization vector of the core is vertical (perpendicular to the long axis). By adjusting the persistent-mode currents to the correct values, a vertical field and gradient can be produced at the location of the core which will produce a stable levitation force and also a stable torque about the roll and pitch axes. Required control forces and torques are provided by the separate control coils. Yaw torque in this configuration is provided by producing a second-order gradient (gradient of a gradient) along the long axis of the core in the x-y plane. It should be noted that this configuration has the potential for providing active roll control.

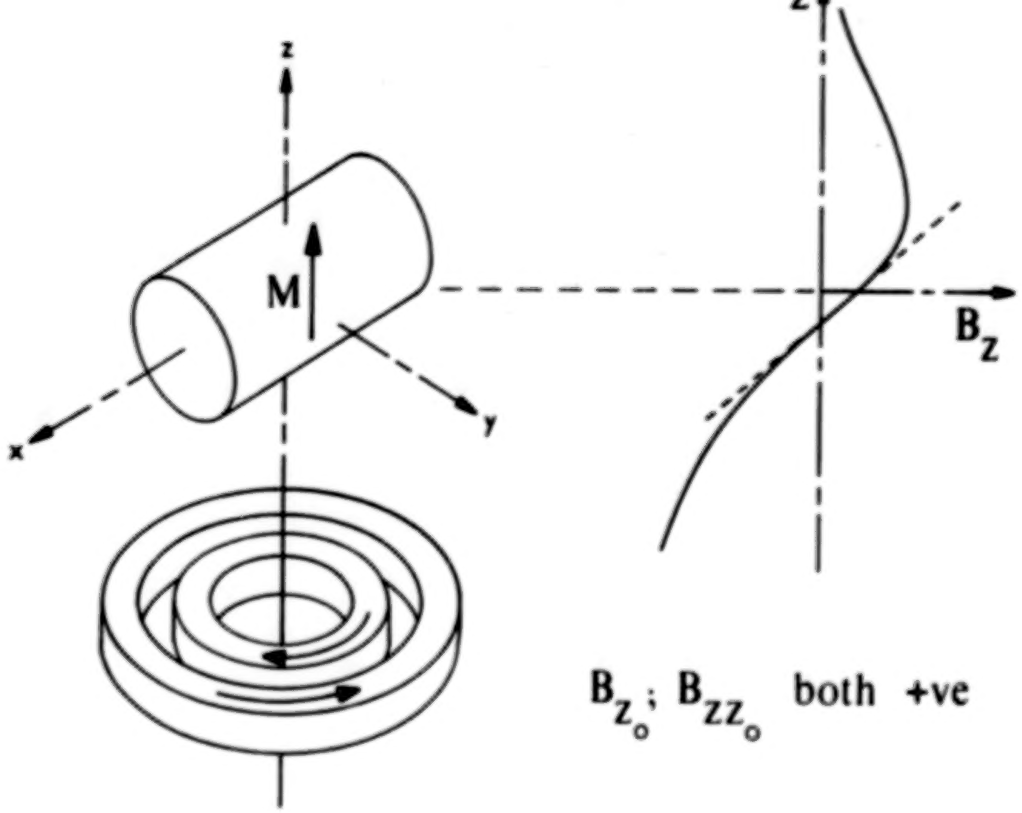

B_{z_o}; B_{zz_o} both +ve

Figure 10. - Levitation Approach For Selected Configuration

SUMMARY

In summary (fig. 11), an LGMSS ground-based experiment has been defined and two studies performed to investigate the feasibility of implementing the experiment. Both studies concluded that implementation was feasible and a decision was made to procure the design, fabrication, installation, and test of an LGMSS. A competitive procurement effort resulted in the selection of a configuration proposed by Intermagnetics General Corporation. The configuration utilizes a permanent magnet core with a vertical magnetization vector (perpendicular to the long axis of the core), superconducting levitation coils and room temperature control coils, and has the potential for six-degrees-of-freedom control.

SUMMARY

- Configuration for LGMSS Ground-Based Experiment Selected
  - Vertical Magnetization Vector (Perpendicular to Long Axis of Core)
  - Superconducting Levitation Coils and Room Temperature Control Coils
  - Potential for Six-Degrees-of-Freedom Control
- Design Phase Complete by End of 1990
- System Delivery and Acceptance by End of 1991

Figure 11. - Summary

REFERENCES

1. Welch, Sharon S; and Clemmons, James I., Jr.: The Optical Position Measurement System for a Large Gap Magnetic Suspension System (LGMSS). Presented at the Aerospace Applications of Magnetic Suspension Technology Workshop, NASA Langley Research Center, Hampton, VA, September 25-27, 1990.

2. Boom, R.W.; Abdelsalam, M.K.; Eyssa, Y.M.; and McIntosh, G.E.: Repulsive Force Support System Feasibility Study. NASA CR-178400, October 1987.

N91-21201

LARGE GAP MAGNETIC SUSPENSION SYSTEM

Moustafa K. Abdelsalam, Y.M. Eyssa
Madison Magnetics Incorporated
216 Walnut Street
Madison
WI 53705

I. SYSTEM CONFIGURATION

I.1. Model Core.

The model core size envelope is 30.48 cm (12") long and 10.16 cm (4") OD. The model core can be either a permanent magnet of 1.2 tesla average remnant magnetism or a superconducting coil with or without a holmium core, in a liquid helium dewar.

I.1.1. Superconducting Option.

Epoxy-impregnated coils with current densities in excess of 20 kA/cm² at fields of 6-9 tesla may be used. Such coils do not contain much copper or cooled surfaces, and their ability to tolerate disturbances is limited to the adiabatic heat capacity of the conductor material. However, the absence of large amounts of copper and helium in the windings allows such coils to operate at current densities up to ten times as large as those for cryostable coils, which is needed for model cores.

Higher values of magnetic moments may be achieved through using holmium core if space permits. Holmium has superior magnetic properties at 4.2 K with a saturation magnetic moment of 3.9 tesla. Table I-1 lists the magnetization of holmium at 4.2K [1,2].

Table I-1.

Holmium Magnetization vs. Applied Field at 4.2 K.

Magnetization force (T)	0	0.1	0.52	1.0	1.5	2.5	3.5	4.5	6.5
Magnetization (T)	0	1.6	2.48	2.9	2.98	3.12	3.25	3.35	3.7

The total magnetic pole strength per unit mass vs. design maximum field, B, and operating current density, J, are listed in Tables I-2 and I-3 with and without holmium core. As shown, the presence of holmium does not add to the values of Q/M significantly, since there is limited space in the core. Table I-4 lists the specifications of the model coil design. A gross current density of 30 kA/cm^2 at 6 T field with no holmium core is selected.

Table I-2.

Model Core Magnetic Pole Strength per Unit Mass Q/M vs. Design Maximum Field, B, and Operating Current Density, J. All cases have OD = 0.09 m, ID ≥ 0.05 m, and mandrel thickness = 1.27 mm. MH is the holmium magnetization, RI is the winding inner radius, QM is the winding pole strength, QH is the holmium pole strength, and Q is the sum of QM + QH. The mass M is the mass of the winding and holmium in addition to 10 kg for the model, dewar, and helium mass.

B(T)	J(A/m**2)	MH(T)	RI(m)	QH	QM	Q(Am)	Q/M(Am/kg)
4.00	0.20E+09	3.23	0.29E-01	0.12E+04	0.14E+05	0.151E+05	0.925E+03
4.00	0.30E+09	3.23	0.34E-01	0.38E+04	0.16E+05	0.197E+05	0.118E+04
4.00	0.40E+09	3.23	0.37E-01	0.53E+04	0.17E+05	0.222E+05	0.132E+04
4.00	0.50E+09	3.23	0.39E-01	0.62E+04	0.18E+05	0.237E+05	0.140E+04
4.00	0.60E+09	3.23	0.40E-01	0.69E+04	0.18E+05	0.248E+05	0.146E+04
5.00	0.20E+09	3.46	0.25E-01	0.00E+00	0.16E+05	0.158E+05	0.974E+03
5.00	0.30E+09	3.46	0.32E-01	0.26E+04	0.19E+05	0.212E+05	0.129E+04
5.00	0.40E+09	3.46	0.35E-01	0.45E+04	0.20E+05	0.246E+05	0.147E+04
5.00	0.50E+09	3.46	0.37E-01	0.57E+04	0.21E+05	0.268E+05	0.159E+04
5.00	0.60E+09	3.46	0.38E-01	0.65E+04	0.22E+05	0.283E+05	0.167E+04
6.00	0.20E+09	3.63	0.21E-01	0.00E+00	0.17E+05	0.171E+05	0.107E+04
6.00	0.30E+09	3.63	0.29E-01	0.13E+04	0.21E+05	0.222E+05	0.136E+04
6.00	0.40E+09	3.63	0.33E-01	0.35E+04	0.23E+05	0.265E+05	0.160E+04
6.00	0.50E+09	3.63	0.35E-01	0.49E+04	0.24E+05	0.293E+05	0.175E+04
6.00	0.60E+09	3.63	0.37E-01	0.59E+04	0.25E+05	0.313E+05	0.186E+04
7.00	0.20E+09	3.75	0.17E-01	0.00E+00	0.18E+05	0.180E+05	0.113E+04
7.00	0.30E+09	3.75	0.26E-01	0.76E+02	0.23E+05	0.229E+05	0.141E+04
7.00	0.40E+09	3.75	0.31E-01	0.25E+04	0.26E+05	0.281E+05	0.171E+04
7.00	0.50E+09	3.75	0.34E-01	0.41E+04	0.27E+05	0.315E+05	0.190E+04
7.00	0.60E+09	3.75	0.36E-01	0.53E+04	0.29E+05	0.339E+05	0.203E+04
8.00	0.20E+09	3.82	0.13E-01	0.00E+00	0.19E+05	0.186E+05	0.117E+04
8.00	0.30E+09	3.82	0.24E-01	0.00E+00	0.24E+05	0.244E+05	0.151E+04
8.00	0.40E+09	3.82	0.29E-01	0.14E+04	0.28E+05	0.293E+05	0.179E+04
8.00	0.50E+09	3.82	0.32E-01	0.32E+04	0.30E+05	0.333E+05	0.202E+04
8.00	0.60E+09	3.82	0.34E-01	0.45E+04	0.32E+05	0.362E+05	0.218E+04
9.00	0.20E+09	3.83	0.92E-02	0.00E+00	0.19E+05	0.189E+05	0.120E+04
9.00	0.30E+09	3.83	0.21E-01	0.00E+00	0.26E+05	0.257E+05	0.160E+04
9.00	0.40E+09	3.83	0.27E-01	0.40E+03	0.30E+05	0.302E+05	0.186E+04
9.00	0.50E+09	3.83	0.31E-01	0.23E+04	0.33E+05	0.349E+05	0.212E+04
9.00	0.60E+09	3.83	0.33E-01	0.37E+04	0.35E+05	0.382E+05	0.231E+04

Table I-3.

Model Core Magnetic Pole Strength, per Unit Mass Q/M vs. Design Maximum Field, B, and Operating Current Density J. All cases have OD = 0.09 m. There is no holmium mandrel in the core. The mass M is the mass of the winding in addition to 10 kg for the model, dewar and helium mass.

B(T)	J(A/m**2)	MH(T)	RI(m)	QH	QM	Q(Am)	Q/M(Am/kg)
4.00	0.20E+09	3.23	0.29E-01	0.00E+00	0.14E+05	0.139E+05	0.899E+03
4.00	0.30E+09	3.23	0.34E-01	0.00E+00	0.16E+05	0.159E+05	0.114E+04
4.00	0.40E+09	3.23	0.37E-01	0.00E+00	0.17E+05	0.169E+05	0.129E+04
4.00	0.50E+09	3.23	0.39E-01	0.00E+00	0.18E+05	0.175E+05	0.140E+04
4.00	0.60E+09	3.23	0.40E-01	0.00E+00	0.18E+05	0.180E+05	0.148E+04
5.00	0.20E+09	3.46	0.25E-01	0.00E+00	0.16E+05	0.158E+05	0.955E+03
5.00	0.30E+09	3.46	0.32E-01	0.00E+00	0.19E+05	0.186E+05	0.126E+04
5.00	0.40E+09	3.46	0.35E-01	0.00E+00	0.20E+05	0.201E+05	0.147E+04
5.00	0.50E+09	3.46	0.37E-01	0.00E+00	0.21E+05	0.211E+05	0.162E+04
5.00	0.60E+09	3.46	0.38E-01	0.00E+00	0.22E+05	0.218E+05	0.173E+04
6.00	0.20E+09	3.63	0.21E-01	0.00E+00	0.17E+05	0.171E+05	0.985E+03
6.00	0.30E+09	3.63	0.29E-01	0.00E+00	0.21E+05	0.209E+05	0.135E+04
6.00	0.40E+09	3.63	0.33E-01	0.00E+00	0.23E+05	0.230E+05	0.160E+04
6.00	0.50E+09	3.63	0.35E-01	0.00E+00	0.24E+05	0.244E+05	0.179E+04
6.00	0.60E+09	3.63	0.37E-01	0.00E+00	0.25E+05	0.253E+05	0.194E+04
7.00	0.20E+09	3.75	0.17E-01	0.00E+00	0.18E+05	0.180E+05	0.997E+03
7.00	0.30E+09	3.75	0.26E-01	0.00E+00	0.23E+05	0.228E+05	0.141E+04
7.00	0.40E+09	3.75	0.31E-01	0.00E+00	0.26E+05	0.256E+05	0.171E+04
7.00	0.50E+09	3.75	0.34E-01	0.00E+00	0.27E+05	0.274E+05	0.194E+04
7.00	0.60E+09	3.75	0.36E-01	0.00E+00	0.29E+05	0.286E+05	0.212E+04
8.00	0.20E+09	3.82	0.13E-01	0.00E+00	0.19E+05	0.186E+05	0.998E+03
8.00	0.30E+09	3.82	0.24E-01	0.00E+00	0.24E+05	0.244E+05	0.145E+04
8.00	0.40E+09	3.82	0.29E-01	0.00E+00	0.28E+05	0.279E+05	0.180E+04
8.00	0.50E+09	3.82	0.32E-01	0.00E+00	0.30E+05	0.301E+05	0.206E+04
8.00	0.60E+09	3.82	0.34E-01	0.00E+00	0.32E+05	0.317E+05	0.228E+04
9.00	0.20E+09	3.83	0.92E-02	0.00E+00	0.19E+05	0.189E+05	0.993E+03
9.00	0.30E+09	3.83	0.21E-01	0.00E+00	0.26E+05	0.257E+05	0.148E+04
9.00	0.40E+09	3.83	0.27E-01	0.00E+00	0.30E+05	0.298E+05	0.186E+04
9.00	0.50E+09	3.83	0.31E-01	0.00E+00	0.33E+05	0.326E+05	0.216E+04
9.00	0.60E+09	3.83	0.33E-01	0.00E+00	0.35E+05	0.345E+05	0.241E+04

Table I-4.

Model Core Coil Specifications (Superconducting Solenoid).

Winding outer radius (cm)	4.5
Winding inner radius (cm)	2.9
Mandrell thickness (cm)	0.127
Winding length (cm)	22.86
Winding current density (kA/cm^2)	30.00
Winding maximum field (T)	6.0

I.1.2. Permanent Magnet Material Option.

A new superior permanent magnet material $Nd_{15}Fe_{77}B_8$ is planned for the model core [3,4]. The magnetic properties are listed in Table I-5.

Table I-5.

Magnetic Properties of $ND_{15}Fe_{77}B_8$ Magnetic Material.

	Br (T)	Hc (kA/m)	(BH)max (kJ/m^3)	Tc (K)
$Nd_{15}Fe_{77}B_8$	1.23	960	290	585
$Nd_{15}(Fe_{0.9}Co_{0.1})_{77}B_8$	1.23	800	290	670
$Nd_{15}(Fe_{0.8}Co_{0.2})_{77}B_8$	1.21	820	260	740

As shown in Fig. I-1, the new permanent magnet material has large values of M_r (residual magnetism) and H_c (demagnetization critical field). M_r stays well above 1.2 tesla for most of the demagnetizing field and well over 1.15 tesla up to H_c = 960 kA/m (1.21 tesla). With M_r = 1.2 tesla, the magnetic properties of the model core are listed in Table I-6.

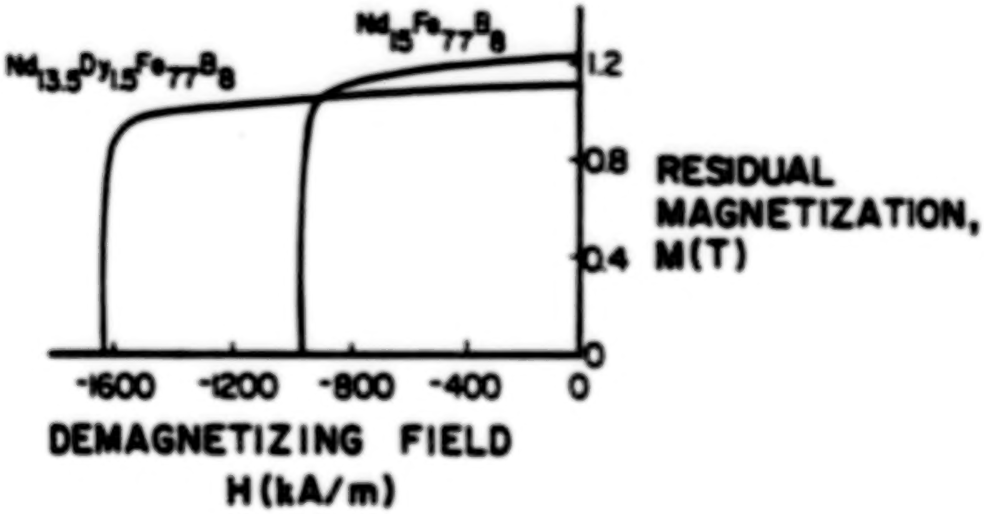

Figure I-1. Demagnetized curve of $Nd_{13.5}Dy_{1.5}Fe_{77}B_8$ sintered magnet

Table I-6.

Model Core Coil Specifications (Permanent Magnet).

Remnant magnetization (T)	1.2
Core length (cm)	30.48
Core diameter (cm)	10.16
Core mass (kg)	16.41
Model mass (kg)	6.7
Total mass, M (kg)	23.11
Pole strength, Q (Am)	7.742×10^3
Q/M (Am/kg)	335.

I.2. Levitation Magnet System.

The system under study is to levitate, position and control a 15 lb. model. The model is to be suspended 36" above the cryostat top plate. The array of magnets will control the position of the model in 5 degrees of freedom, namely the x, y, z displacements and the yaw and pitch rotations. Model rolling is controlled with eccentric weights.

I.2.1. Levitation Magnet System Configuration.

The system consists of "n" vertical solenoids arranged around the system center. The tops of the magnets are located as close as possible to the table surface. Because the model is allowed to assume any position between 0 and 360 degrees in the yaw direction, it is reasonable to assume that the magnet system should be arranged symmetrically around the vertical z-axis. The magnets may be arranged in one or more rings. Furthermore, each ring may perform a separate function. For example, a magnet array in one circle may be responsible for levitation and positioning while another array may be responsible for control and stability.

The first object of this study is to find the currents in the magnet array that satisfy a required F_z (lift), and control F_x, F_y, T_y and T_z at any position for the model. Since the number of forces and torques is 5, there is a need for at least 5 solenoids in the magnet array. A larger number of coils allows other constraints which depend on the nature of the system. For a superconducting magnet system, the minimum ampere-meters is usually desired; while for resistive coils the criteria may be minimum ohmic heat losses in the coils. In the next section the procedure to optimize these two systems is analyzed.

I.2.2. Magnet System Optimization.

For both superconductive and resistive systems the optimization problem may be divided into two parts: first to find the optimum magnet dimensions and secondly to find the optimum current distribution in the magnet array that satisfies the force constraints. First, an approximate formula is used to derive closed form expressions for optimum magnet dimensions. Second, using these expressions for the dimensions, an "exact" approach is used to calculate the optimum current distribution in the magnet array.

I.2.2.1. Superconducting Magnets Optimum Size.

The main function of the magnet array is to produce a lift force on the model. The lift force on the model due to one magnet in the array may be approximated by

$$F_z = KQ_1 \ (\pi/3) \ Jb^3 \ (1-a^3) \ [H^{-3} - (H+L)^{-3}] \qquad (1)$$

where

K = constant for given locations of the magnet and the model
Q_1 = magnetic pole strength of the model
J = current density in the magnet
b = outer radius of the magnet
a = inner to outer diameter ratio of the coil
H = vertical distance between top of coil and center line of model, and
L = length of coil .

From Equation 1, we may define F_o to be:

$$F_o \equiv (F_z H^3/KQ_1) = (\pi/3)\ Jb^3\ (1-\alpha^3)\ \chi\ , \qquad \text{where}$$

$$\chi = 1 - (1+x)^{-3}$$

$$x = L/H\ .$$

The ampere-meters of the coil are

$$A = \pi Jb^2L(1-\alpha^2).$$

At any location the minimum of the ampere-meters A subject to the constraint F_o = constant is achieved when the following conditions are met:

b is as large as possible for this location, and (2)

$\alpha = \sqrt{m+(1/2)} - 1/2$, and (3)

$m = 2/(x^3+4x^2+6x+1)$. (4)

I.2.2.2. Superconducting Magnets Optimum Current Distribution.

The forces and torques acting on the model due to the magnet array system may be presented as

$$\{F_i\} = [S_{ij}]\ \{I_j\} \tag{5}$$

where $\{F_i\}$ is the force vector, i=1,5

$[S_{ij}]$ is a pseudo-stiffness matrix whose elements S_{ij} represent the force on the model in the i^{th} direction due to a unit current in the j^{th} coil .

The ampere-meters of the magnet array is

$$\Sigma A_j = \Sigma|I_j \ell_j| \quad , \quad j=1,n$$

where I_j and ℓ_j are the current and conductor length of the j^{th} coil .

For identical coils $\Sigma A_j = \ell\ \Sigma|I_j|$ (6)

Equation 6 shows that for fixed coil dimensions, minimum ΣA_j occurs at minimum ΣI^2_j .

Thus it is required to minimize ΣI^2_j subject to the constraints of Equation 5.

Using Lagrange's approach, the problem reduces to minimizihg an objective function G defined as

$$G = \Sigma\, I_j^2 + \Sigma\, \lambda_i\, \Sigma\, S_{ij}\, I_j - \Sigma \lambda_i F_i \tag{7}$$

where $i = 1$ to 5

$j = 1$ to n

This function has an optimum value at the set of currents I_j satisfied by the following (n+5) simultaneous equations:

$$(\partial G/\partial I_j) = 2\, I_j + \Sigma\, \lambda_i\, \Sigma\, S_{ij} = o \qquad j=1,n$$

$$(\partial G/\partial \lambda_i) = \Sigma\, S_{ij}\, I_j - F_i = o \qquad i=1,5$$

Arranging these equations in a matrix form we get

$$[B]\ \{x\} = \{c\} \tag{8}$$

where

$$[B] = \left[\begin{array}{c|c} 2[I]_{nxn} & [S]^T_{nx5} \\ \hline [S]_{5xn} & [o]_{5x5} \end{array}\right]$$

where [I] = identity matrix

$$\{x\} = \begin{Bmatrix} I_1 \\ : \\ I_n \\ \lambda_1 \\ : \\ \lambda_5 \end{Bmatrix}$$

$$\{c\} = \begin{Bmatrix} 0 \\ \vdots \\ 0 \\ F_1 \\ \vdots \\ F_5 \end{Bmatrix}$$

Manipulating Equation 8 and solving for the current distribution, we get

$$\{I_j\}_{nx1} = [S]^T_{nx5} \, [SS^T]^{-1}_{5x5} \, \{F_i\}_{5x1} \tag{9}$$

The elegance of equation (9) is that regardless of the number of magnets "n", the matrix to be inverted is always 5x5.

Solving Eq. (9) gives the current distribution in the magnet array that satisfies the force constraints and results in a minimum total ampere-meters in the coils.

I.2.2.3. Resistive Magnets Optimum Size

The power loss P_1 in one magnet in the array is

$$P_1 = I^2R = \rho \pi J^2b^2L \, (1-\alpha^2), \text{ where} \tag{10}$$

J = the gross current density, and

ρ = the effective resistivity.

Minimizing the power dissipation subject to the force condition of Eq. (1) results in the following conditions:

b is as large as possible,

$$\alpha = 0.366 \quad \text{and} \tag{11}$$

$$L = 0.7373 \, H \, . \tag{12}$$

I.2.2.4. Resistive Magnets Optimum Current Distribution

The total power dissipation in the coil array is

$$P = \Sigma I_j^2 R_j \qquad j = 1,n$$

For identical magnets the resistance R_j is the same,

$$P = R \, \Sigma \, I_j^2 \tag{13}$$

where R is the resistance of one coil.

Equation (13) shows that for an array of magnets with the same given dimensions, minimum power dissipation coincides with the minimum of ΣI_j^2. This is the same condition for minimum ampere-meters. Consequently, the current distribution given by equation (9) results in a minimum power dissipation in the magnet array.

II . SYSTEM OPTIONS

The six combinations of superconducting or permanent model magnets with superconducting or copper levitation magnets are listed in Table II-1.

Table II-1.

Model Core/Levitation Magnet Combinations.

Model	Magnets	Comment
S/C	S/C	smallest magnets
P/M	S/C	simple model
S/C	Cu	(LN_2 cooled magnets)
PM	Cu	
S/C	Cu	(H_2O cooled magnets)
PM	Cu	

S/C ≡ superconducting
PM ≡ permanent magnets
Cu ≡ copper magnets

II.1. Superconducting Levitation Coils.

The superconducting magnet array is optimized for minimum total ampere-meters. Five and six arrays are studied at varying location radii for current densities ranging from 50 MA/m^2 to 300 MA/m^2. Table II-2 lists magnet parameters for an S/C model core.

The superconducting model in this table has a magnetic pole strength of 1350 Am/kg of total mass. The other parameters in this table are:

NC = Number of coils in the array

R = Location radius

L, RI, RO = Optimum coil dimensions (I = inner, O = outer)

Table II-2.

Minimum Ampere-Meters S/C Magnet Arrays for Levitation of an S/C Model.

```
MODEL Q/M      = 1.350E+03 Am/KG          FX/W       FY/W       FZ/W       TY/W       TZ/W
MODEL LENGTH   = 3.000E-01 m           .000E+00   .000E+00   1.000E+00   .000E+00   .000E+00
MIN DISTANCE   = 5.000E-02 m
```

NC	R	L	RI	RO	JMAX	BMAX	ISTOT	N*IS
5	.400	.924	.069	.210	1.500E+07	2.54	5.576E+06	8.575E+06
5	.450	.387	.120	.240	1.500E+07	1.76	2.552E+06	3.918E+06
5	.500	.262	.160	.269	1.500E+07	1.34	1.882E+06	2.887E+06
5	.550	.204	.195	.298	1.500E+07	1.10	1.589E+06	2.435E+06
5	.600	.170	.229	.328	1.501E+07	.95	1.430E+06	2.202E+06
5	.650	.148	.260	.357	1.500E+07	.85	1.358E+06	2.079E+06
5	.700	.133	.291	.386	1.501E+07	.79	1.323E+06	2.024E+06
5	.750	.122	.321	.416	1.501E+07	.74	1.317E+06	2.015E+06
5	.800	.114	.350	.445	1.500E+07	.70	1.334E+06	2.040E+06
5	.400	.459	.097	.210	2.000E+07	2.42	3.257E+06	5.006E+06
5	.450	.273	.140	.240	2.000E+07	1.73	2.106E+06	3.233E+06
5	.500	.200	.177	.269	2.001E+07	1.36	1.677E+06	2.572E+06
5	.550	.162	.212	.298	2.001E+07	1.14	1.464E+06	2.242E+06
5	.600	.138	.244	.328	2.001E+07	1.00	1.350E+06	2.067E+06
5	.650	.122	.275	.357	2.001E+07	.91	1.291E+06	1.975E+06
5	.700	.110	.306	.386	1.999E+07	.84	1.266E+06	1.936E+06
5	.750	.102	.335	.416	2.001E+07	.80	1.267E+06	1.938E+06
5	.800	.096	.364	.445	1.998E+07	.76	1.289E+06	1.972E+06
6	.450	.758	.072	.200	1.500E+07	2.27	4.939E+06	7.459E+06
6	.500	.393	.112	.225	1.500E+07	1.70	2.793E+06	4.227E+06
6	.550	.280	.145	.250	1.500E+07	1.36	2.168E+06	3.288E+06
6	.600	.223	.174	.275	1.500E+07	1.16	1.881E+06	2.857E+06
6	.650	.189	.202	.300	1.500E+07	1.02	1.736E+06	2.639E+06
6	.700	.167	.228	.325	1.501E+07	.93	1.667E+06	2.537E+06
6	.750	.152	.253	.350	1.500E+07	.87	1.643E+06	2.503E+06
6	.800	.141	.278	.375	1.500E+07	.83	1.658E+06	2.528E+06
6	.400	1.349	.049	.175	2.000E+07	3.13	9.523E+06	1.436E+07
6	.450	.423	.096	.200	2.000E+07	2.20	3.245E+06	4.906E+06
6	.500	.277	.131	.225	2.000E+07	1.69	2.313E+06	3.503E+06
6	.550	.212	.161	.250	2.000E+07	1.38	1.919E+06	2.912E+06
6	.600	.175	.190	.275	2.001E+07	1.19	1.721E+06	2.615E+06
6	.650	.152	.217	.300	2.000E+07	1.07	1.616E+06	2.459E+06
6	.700	.136	.243	.325	2.000E+07	.99	1.572E+06	2.393E+06
6	.750	.125	.268	.350	2.000E+07	.92	1.563E+06	2.382E+06
6	.800	.117	.293	.375	2.001E+07	.89	1.587E+06	2.420E+06

JMAX = Maximum current density in the magnet array

BMAX = Maximum field in the magnets

ISTOT = Operational ampere-meters at the specified model location

N*IS = Total ampere-meters capacity of the system.

It is seen that increasing the allowable current density in the magnets has a small effect on the total ampere-meters capacity.

The total ampere-meters in five- and six-coil S/C arrays are plotted versus array location radius for an S/C model (Fig. II-1). The optimum ampere-meters is at a location radius of 70 cm. The five-coil array uses less ampere-meters than the six-coil array. Table II-3 lists parameters for the S/C arrays for a permanent magnet model (PM). In Fig. II-2 the ampere-meters of the five-coil and six-coil S/C arrays are plotted versus magnet location radius. The optimum ampere-meters occurs around the 70 cm radius.

II.2. Resistive Levitation Coils.

The minimization of power consumption is the main goal for water-cooled or nitrogen-cooled coil designs. Water-cooled or cryocooled copper magnet arrays are shown to be feasible. Tables II-4 and II-5 list magnet array parameters for S/C and permanent magnet models. The significant parameters are:

Cu Ratio: ratio of copper in the windings

L, RI, RO: optimum magnet dimensions

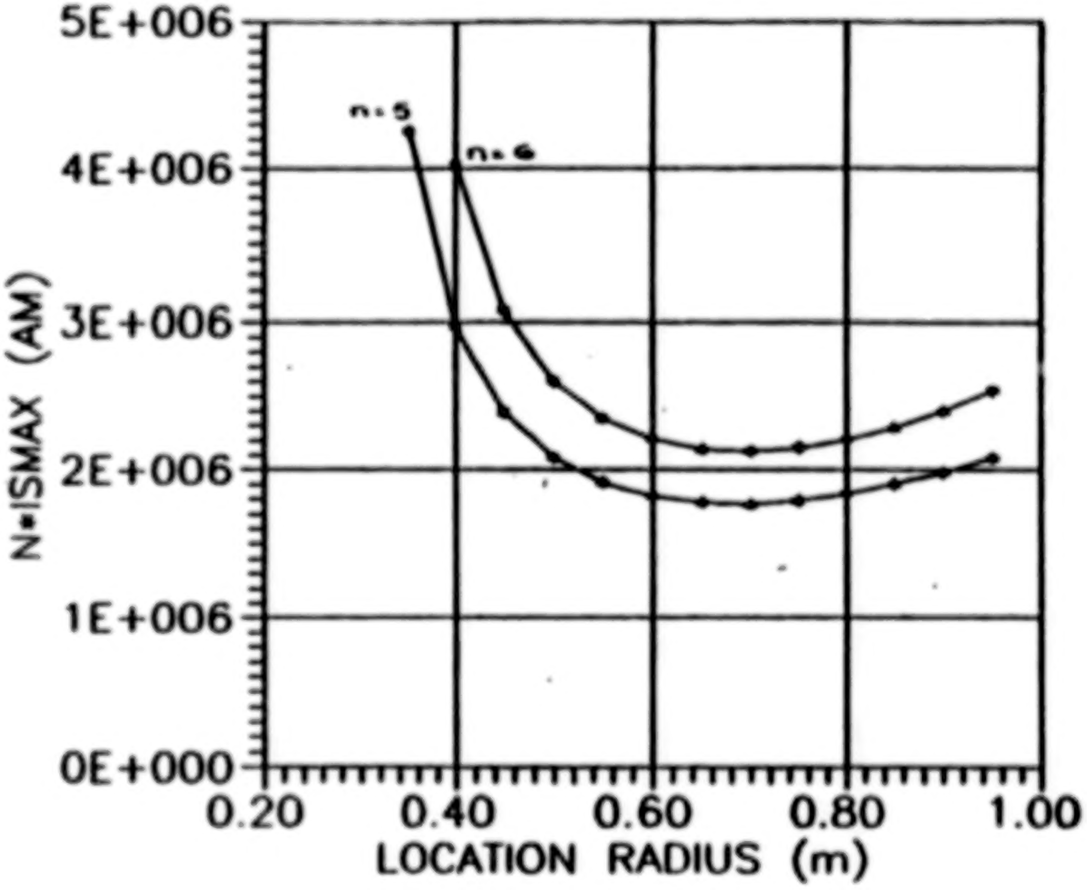

Figure II-1. Total ampere-meters of S/C magnet array at current density of 50 MA/m². Plots are for 5-coil and 6-coil arrays with 5 cm distance between adjacent coils. Optimum location radius is around 70 cm. Model is an S/C magnet.

Table II-3.

Minimum Ampere-Meter S/C Magnet Arrays for Levitation of a PM Model.

MODEL Q/M = 3.350E+02 Am/KG
MODEL LENGTH = 3.000E-01 m
MIN DISTANCE = 5.000E-02 m

FX/W	FY/W	FZ/W	TY/W	TZ/W
.000E+00	.000E+00	1.000E+00	.000E+00	.000E+00

NC	R	L	RI	RO	JMAX	BMAX	ISTOT	N*IS
5	.600	1.397	.090	.328	1.500E+07	4.28	2.129E+07	3.268E+07
5	.650	.670	.136	.357	1.500E+07	3.45	1.135E+07	1.739E+07
5	.700	.493	.173	.386	1.500E+07	2.92	9.072E+06	1.390E+07
5	.750	.403	.205	.416	1.500E+07	2.57	8.117E+06	1.243E+07
5	.800	.348	.234	.445	1.500E+07	2.33	7.679E+06	1.175E+07
5	.550	1.168	.088	.298	2.000E+07	5.00	1.941E+07	2.980E+07
5	.600	.579	.135	.328	2.000E+07	3.91	1.057E+07	1.621E+07
5	.650	.418	.173	.357	2.000E+07	3.24	8.385E+06	1.285E+07
5	.700	.339	.206	.386	2.000E+07	2.81	7.446E+06	1.140E+07
5	.750	.291	.237	.416	2.000E+07	2.52	6.996E+06	1.071E+07
5	.800	.260	.266	.445	2.000E+07	2.33	6.812E+06	1.042E+07
6	.700	.900	.104	.325	1.500E+07	3.82	1.735E+07	2.629E+07
6	.750	.663	.135	.350	1.500E+07	3.35	1.289E+07	1.956E+07
6	.800	.530	.162	.375	1.500E+07	3.02	1.128E+07	1.714E+07
6	.600	2.124	.066	.275	2.000E+07	5.18	3.773E+07	5.707E+07
6	.650	.745	.109	.300	2.000E+07	4.23	1.446E+07	2.191E+07
6	.700	.525	.141	.325	2.000E+07	3.64	1.118E+07	1.697E+07
6	.750	.423	.160	.350	2.000E+07	3.23	9.874E+06	1.500E+07
6	.800	.364	.193	.375	2.000E+07	2.95	9.298E+06	1.414E+07

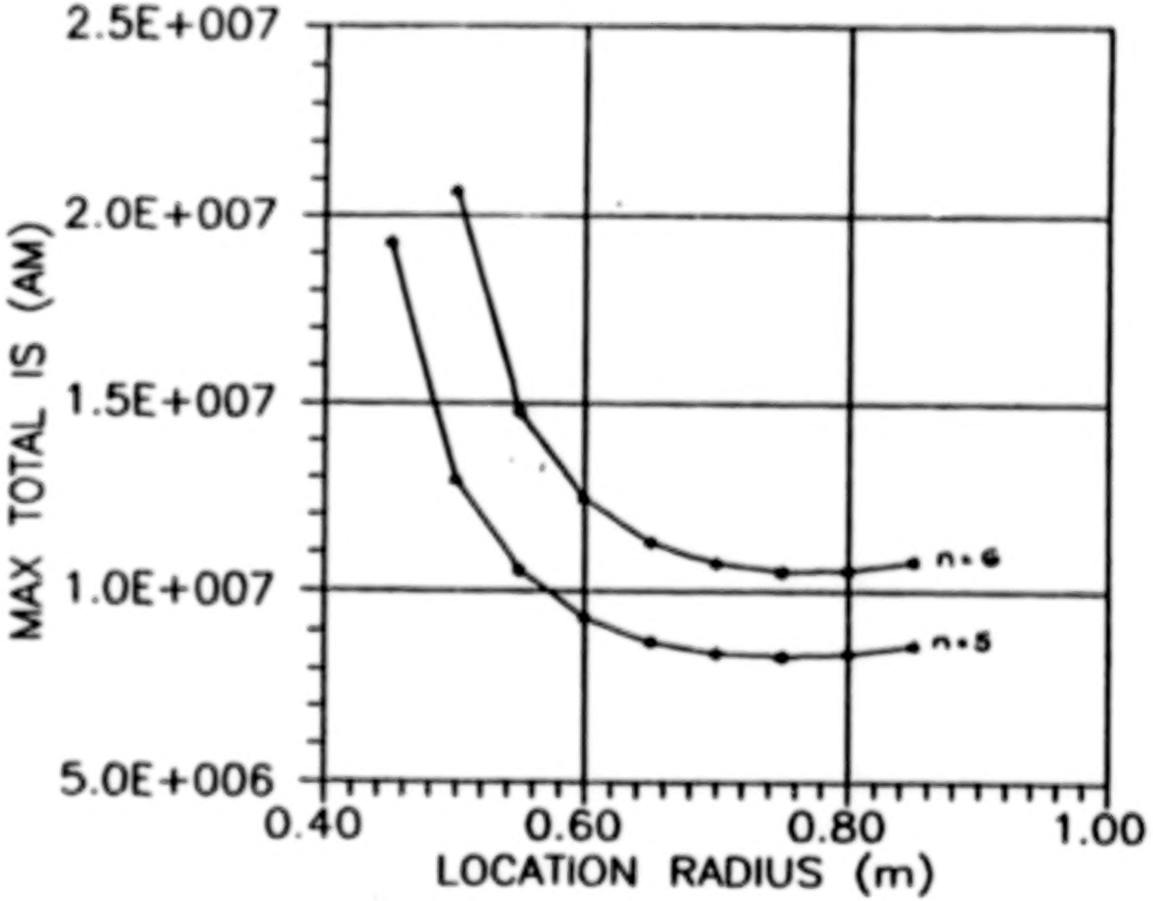

Figure II-2. Total ampere-meters of S/C magnet array at current density of 50 MA/m². Plots are for 5-coil and 6-coil arrays with 5 cm distance between adjacent coils. Optimum location radius is around 70 cm. Model is a PM.

Table II-4.

Minimum Power Copper Magnet Arrays for Levitation of an S/C Model.

MODEL Q/M = 1.350E+03 Am/kg

MODEL LENGTH = 3.000E-01 m

CU RATIO = 7.500E-01

MIN DISTANCE = 5.000E-02 m

FX/W	FY/W	FZ/W	TY/W	TZ/W
.000E+00	.000E+00	1.000E+00	.000E+00	.000E+00

X	Y	Z	YAW	PITCH
.000E+00	.000E+00	1.000E+00	.000E+00	.000E+00

NC	R	L	RI	RO	JMAX	BMAX	CU-WT	N*IS	PTOT*	N*PMAX*
5	.300	.737	.055	.151	4.779E+07	5.54	1.544E+03	1.098E+07	7.029E+06	1.399E+07
5	.350	.737	.066	.181	2.620E+07	3.50	2.201E+03	8.583E+06	3.016E+06	5.997E+06
5	.400	.737	.077	.210	1.604E+07	2.50	2.976E+03	7.104E+06	1.530E+06	3.039E+06
5	.450	.737	.088	.240	1.068E+07	1.87	3.866E+03	6.143E+06	8.817E+05	1.749E+06
5	.500	.737	.098	.269	7.584E+06	1.46	4.873E+03	5.500E+06	5.612E+05	1.112E+06
5	.550	.737	.109	.298	5.675E+06	1.19	5.997E+03	5.064E+06	3.870E+05	7.664E+05
5	.600	.737	.120	.328	4.431E+06	1.00	7.237E+03	4.772E+06	2.849E+05	5.638E+05
5	.650	.737	.131	.357	3.504E+06	.86	8.593E+03	4.583E+06	2.215E+05	4.388E+05
5	.700	.737	.141	.386	2.906E+06	.76	1.007E+04	4.473E+06	1.802E+05	3.562E+05
5	.750	.737	.152	.416	2.552E+06	.69	1.166E+04	4.426E+06	1.524E+05	3.011E+05
5	.800	.737	.163	.445	2.228E+06	.63	1.336E+04	4.429E+06	1.332E+05	2.631E+05
5	.850	.737	.174	.475	1.981E+06	.59	1.518E+04	4.477E+06	1.198E+05	2.365E+05
6	.300	.737	.046	.125	7.036E+07	6.82	1.264E+03	1.323E+07	1.235E+07	2.483E+07
6	.350	.737	.055	.150	3.797E+07	4.37	1.820E+03	1.028E+07	5.171E+06	1.041E+07
6	.400	.737	.064	.175	2.297E+07	3.05	2.477E+03	8.469E+06	2.574E+06	5.188E+06
6	.450	.737	.073	.200	1.515E+07	2.26	3.235E+03	7.295E+06	1.460E+06	2.948E+06
6	.500	.737	.082	.225	1.069E+07	1.77	4.095E+03	6.511E+06	9.182E+05	1.856E+06
6	.550	.737	.091	.250	7.952E+06	1.44	5.055E+03	5.982E+06	6.269E+05	1.268E+06
6	.600	.737	.101	.275	6.182E+06	1.21	6.117E+03	5.627E+06	4.580E+05	9.275E+05
6	.650	.737	.110	.300	4.984E+06	1.05	7.279E+03	5.399E+06	3.539E+05	7.175E+05
6	.700	.737	.119	.325	4.143E+06	.93	8.543E+03	5.267E+06	2.868E+05	5.818E+05
6	.750	.737	.128	.350	3.534E+06	.84	9.908E+03	5.211E+06	2.419E+05	4.911E+05
6	.800	.737	.137	.375	3.083E+06	.77	1.137E+04	5.219E+06	2.112E+05	4.291E+05
6	.850	.737	.146	.400	2.742E+06	.72	1.294E+04	5.281E+06	1.900E+05	3.862E+05
7	.300	.737	.038	.105	1.007E+08	8.27	1.044E+03	1.564E+07	2.089E+07	4.199E+07
7	.350	.737	.046	.127	5.339E+07	5.25	1.519E+03	1.207E+07	8.533E+06	1.718E+07
7	.400	.737	.054	.149	3.190E+07	3.64	2.082E+03	9.885E+06	4.171E+06	8.409E+06
7	.450	.737	.062	.170	2.083E+07	2.69	2.735E+03	8.479E+06	2.333E+06	4.710E+06
7	.500	.737	.070	.192	1.458E+07	2.10	3.476E+03	7.542E+06	1.450E+06	2.932E+06
7	.550	.737	.078	.214	1.078E+07	1.71	4.307E+03	6.910E+06	9.815E+05	1.987E+06
7	.600	.737	.086	.235	8.341E+06	1.44	5.226E+03	6.486E+06	7.120E+05	1.443E+06
7	.650	.737	.094	.257	6.698E+06	1.24	6.234E+03	6.214E+06	5.473E+05	1.110E+06
7	.700	.737	.102	.279	5.552E+06	1.10	7.330E+03	6.056E+06	4.417E+05	8.965E+05
7	.750	.737	.110	.300	4.726E+06	1.00	8.516E+03	5.989E+06	3.718E+05	7.548E+05
7	.800	.737	.118	.322	4.117E+06	.92	9.790E+03	5.998E+06	3.239E+05	6.585E+05
7	.850	.737	.126	.344	3.659E+06	.86	1.115E+04	6.072E+06	2.913E+05	5.924E+05

*PTOT & N*PMAX are for water-cooled copper magnets at 60°C. For liquid nitrogen-cooled magnets, divide by a factor of 10.

JMAX: maximum overall current density in the array

BMAX: maximum field

PTOT: optimum total power consumption at this configuration

N*PMAX: number of coils times the maximum power consumption of any of them (reflects the size of the power supplies and serves as an upper bound on the power requirements).

From Tables II-4 and II-5 it is seen that the six-coil array requires 55% more power than the five-coil array; and in either case, the power consumption is not prohibitive. Figure IV-3 shows the upper bound for the power requirements versus the location radius for the five- and six-coil arrays. It is clear from this sketch that the larger the location radius of the magnets, the less power consumption of the system.

Table II-6 lists comparisons between the six different options discussed earlier. Ampere-meters in the magnets relate to forces on the model which may be a 20,000 Am pole strength S/C model or a 7,740 Am pole strength PM model. The S/C magnets are optimized for minimum ampere-meters and the copper magnets are optimized for minimum power. The power supply is required to charge (for S/C coils) and to maintain I^2R losses (for Cu coils).

Water-cooled copper magnets seem to offer no benefits. LN_2 cooled copper appears interesting with S/C models. The S/C + S/C and S/C + PM models seem attractive, particularly for extrapolation to larger systems.

Table II-5.

Minimum Power Copper Magnet Arrays for Levitation of a PM Model.

MODEL Q/M = 3.350E+02 Am/kg
MODEL LENGTH = 3.000E-01 m
CU RATIO = 7.500E-01
MIN DISTANCE = 5.000E-02 m

FX/W	FY/W	FZ/W	TY/W	TZ/W
.000E+00	.000E+00	1.000E+00	.000E+00	.000E+00

X	Y	Z	YAW	PITCH
.000E+00	.000E+00	1.000E+00	.000E+00	.000E+00

NC	R	L	RI	RO	JMAX	BMAX	CU-WT	N*IS	PTOT*	N*PMAX*
5	.300	.737	.055	.151	1.926E+08	22.34	1.544E+03	4.424E+07	1.141E+08	2.272E+08
5	.350	.737	.066	.181	1.056E+08	14.41	2.201E+03	3.459E+07	4.898E+07	9.739E+07
5	.400	.737	.077	.210	6.465E+07	10.09	2.976E+03	2.863E+07	2.485E+07	4.936E+07
5	.450	.737	.088	.240	4.303E+07	7.52	3.866E+03	2.476E+07	1.432E+07	2.841E+07
5	.500	.737	.098	.269	3.056E+07	5.89	4.873E+03	2.216E+07	9.114E+06	1.806E+07
5	.550	.737	.109	.298	2.287E+07	4.79	5.997E+03	2.041E+07	6.285E+06	1.245E+07
5	.600	.737	.120	.328	1.786E+07	4.03	7.237E+03	1.923E+07	4.627E+06	9.156E+06
5	.650	.737	.131	.357	1.444E+07	3.48	8.593E+03	1.847E+07	3.597E+06	7.114E+06
5	.700	.737	.141	.386	1.203E+07	3.08	1.007E+04	1.803E+07	2.926E+06	5.785E+06
5	.750	.737	.152	.416	1.028E+07	2.77	1.166E+04	1.783E+07	2.475E+06	4.890E+06
5	.800	.737	.163	.445	8.977E+06	2.54	1.336E+04	1.785E+07	2.163E+06	4.273E+06
5	.850	.737	.174	.475	7.985E+06	2.36	1.518E+04	1.804E+07	1.945E+06	3.841E+06
6	.300	.737	.046	.125	2.836E+08	27.49	1.264E+03	5.333E+07	2.006E+08	4.032E+08
6	.350	.737	.055	.150	1.530E+08	17.60	1.820E+03	4.143E+07	8.397E+07	1.690E+08
6	.400	.737	.064	.175	9.258E+07	12.27	2.477E+03	3.413E+07	4.180E+07	8.426E+07
6	.450	.737	.073	.200	6.106E+07	9.13	3.235E+03	2.940E+07	2.372E+07	4.787E+07
6	.500	.737	.082	.225	4.306E+07	7.14	4.095E+03	2.624E+07	1.491E+07	3.013E+07
6	.550	.737	.091	.250	3.204E+07	5.81	5.055E+03	2.411E+07	1.018E+07	2.060E+07
6	.600	.737	.101	.275	2.491E+07	4.89	6.117E+03	2.267E+07	7.437E+06	1.506E+07
6	.650	.737	.110	.300	2.008E+07	4.23	7.279E+03	2.176E+07	5.748E+06	1.165E+07
6	.700	.737	.119	.325	1.669E+07	3.75	8.543E+03	2.122E+07	4.657E+06	9.448E+06
6	.750	.737	.128	.350	1.424E+07	3.38	9.908E+03	2.100E+07	3.928E+06	7.975E+06
6	.800	.737	.137	.375	1.242E+07	3.11	1.137E+04	2.103E+07	3.430E+06	6.968E+06
6	.850	.737	.146	.400	1.105E+07	2.90	1.294E+04	2.128E+07	3.085E+06	6.271E+06
7	.300	.737	.038	.105	4.058E+08	33.34	1.044E+03	6.302E+07	3.392E+08	6.819E+08
7	.350	.737	.046	.127	2.152E+08	21.15	1.519E+03	4.862E+07	1.386E+08	2.790E+08
7	.400	.737	.054	.149	1.285E+08	14.26	2.082E+03	3.984E+07	6.773E+07	1.366E+08
7	.450	.737	.062	.170	8.395E+07	10.85	2.735E+03	3.417E+07	3.789E+07	7.650E+07
7	.500	.737	.070	.192	5.875E+07	8.46	3.476E+03	3.039E+07	2.356E+07	4.762E+07
7	.550	.737	.078	.214	4.345E+07	6.88	4.307E+03	2.784E+07	1.594E+07	3.226E+07
7	.600	.737	.086	.235	3.361E+07	5.79	5.226E+03	2.614E+07	1.156E+07	2.343E+07
7	.650	.737	.094	.257	2.699E+07	5.01	6.234E+03	2.504E+07	8.887E+06	1.802E+07
7	.700	.737	.102	.279	2.237E+07	4.44	7.330E+03	2.440E+07	7.173E+06	1.456E+07
7	.750	.737	.110	.300	1.905E+07	4.02	8.516E+03	2.414E+07	6.034E+06	1.226E+07
7	.800	.737	.118	.322	1.659E+07	3.70	9.790E+03	2.417E+07	5.261E+06	1.069E+07
7	.850	.737	.126	.344	1.474E+07	3.45	1.115E+04	2.447E+07	4.730E+06	9.621E+06

*PTOT & N*PMAX are for water-cooled copper magnets at 60°C. For liquid nitrogen-cooled magnets, divide by a factor of 10.

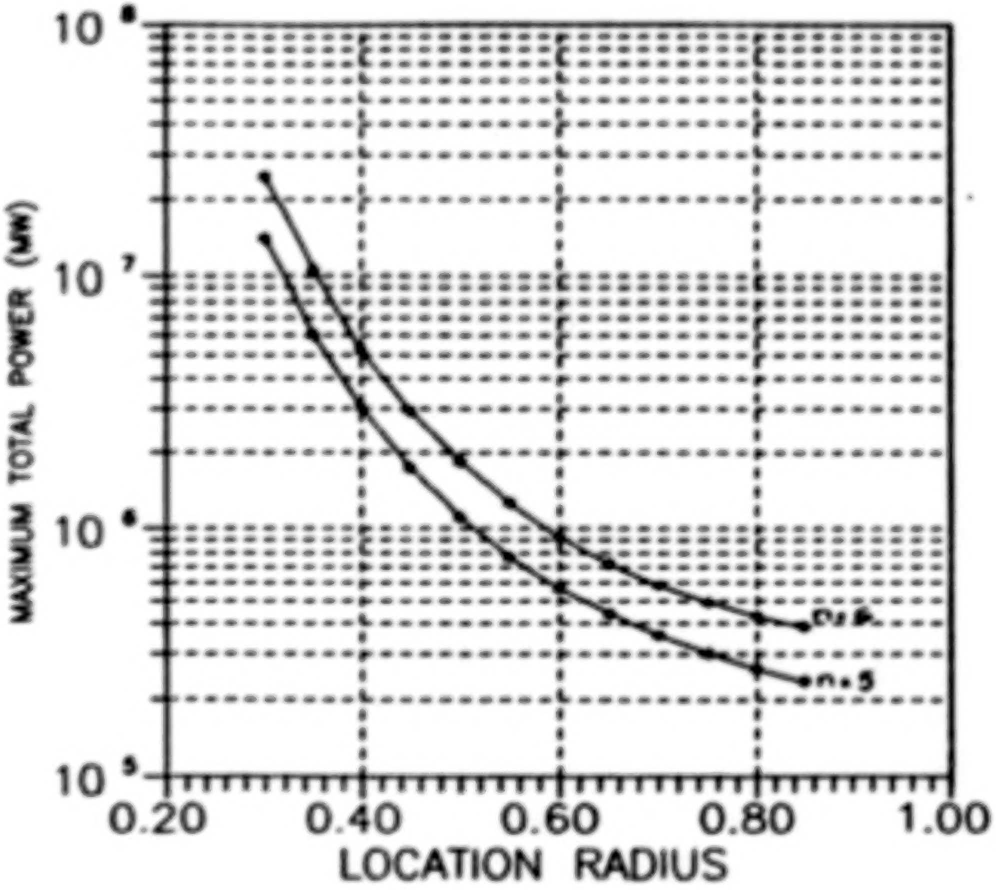

Figure II-3. Maximum power requirements for an array of water-cooled copper magnets. The plots are for 5-coil and 6-coil arrays with 5 cm distance between adjacent coils. The model is a superconducting magnet.

II-3. Levitation Coils Dimensions.

Three representative magnet cross-sections are sketched in Fig. II-4 for the 5 levitation coils. The top sketch is for S/C model and S/C magnets at 2 kA/cm^2. The middle sketch is for a PM model and S/C magnets at 2 kA/cm^2. The bottom sketch is for an S/C model with low current density copper magnets or for a PM model with higher current density copper magnets. Either copper magnet set could be cooled with water or liquid nitrogen.

Table II-6.

System Comparison.

Model Core Levitation Magnets	S/C S/C	PM S/C	S/C CU WATER COOLED	PM CU	S/C CU L. NITROGEN	PM CU
AMPERE-METERS (MAm)	2.1	14.7	4.5	18.0	4.5	18.0
CURRENT DENSITY (kA/cm^2)	1.5	1.5	0.3	1.2	0.3	1.2
DC POWER SUPPLY (kW)	0.0	0.0	360.0	5800.0	36.0	580.0

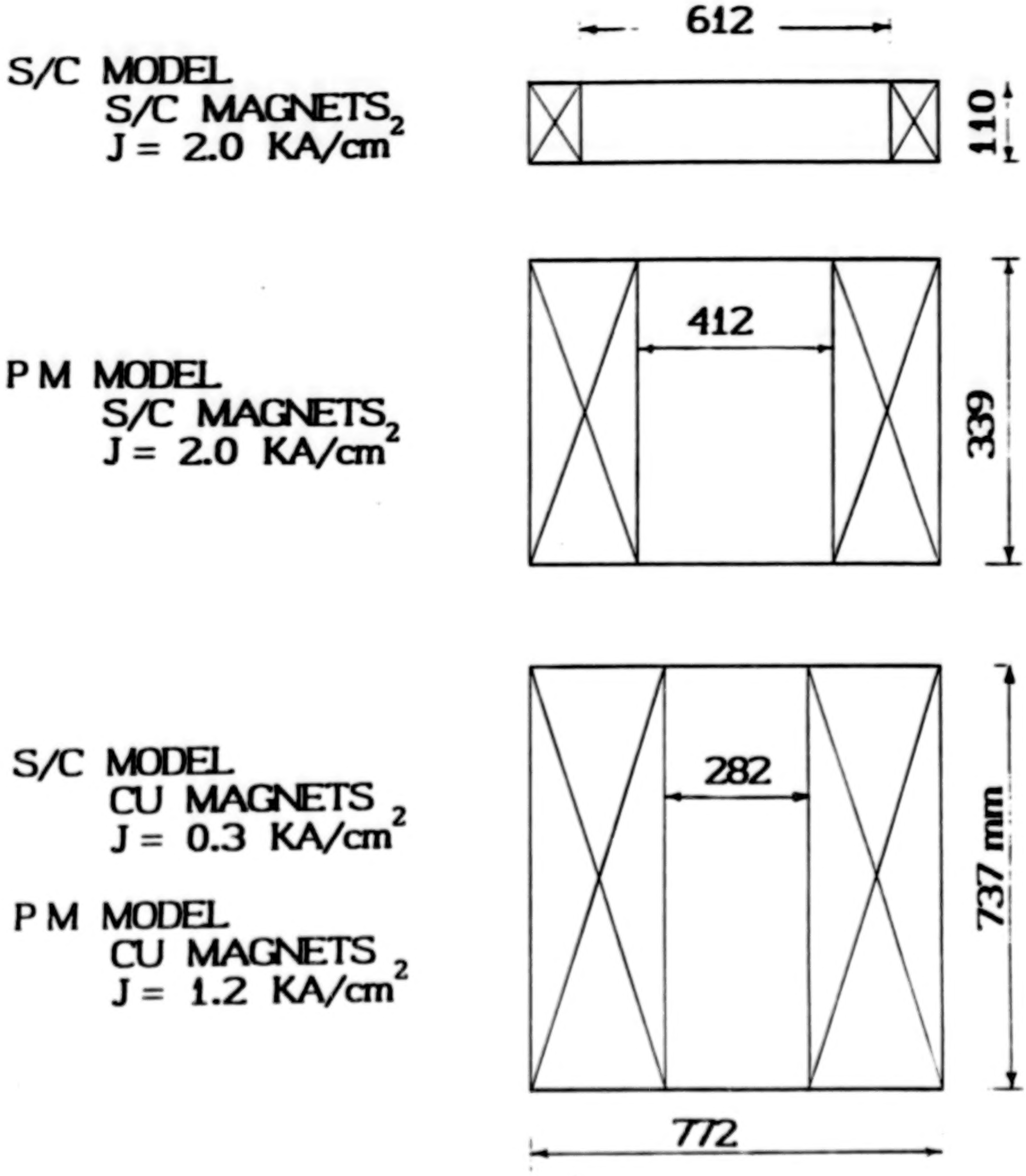
S/C MODEL
S/C MAGNETS
J = 2.0 KA/cm²
612
110
P M MODEL
S/C MAGNETS
J = 2.0 KA/cm²
412
339
S/C MODEL
CU MAGNETS
J = 0.3 KA/cm²
P M MODEL
CU MAGNETS
J = 1.2 KA/cm²
282
737 mm
772

Figure II-4. Support Magnets for S/C and PM Models.

III. LEVITATION MAGNET SYSTEMS

Two options have been chosen for magnet system design. The first is superconducting coils and permanent magnet model. The second is nitrogen cooled coils and permanent magnet model.

III.1. Superconducting Levitation Magnets

TableIII1.

Specifications for the 5 Superconducting Levitation Magnets.

Number of Magnets	5.0
Location radius (m)	0.7
Magnet inner radius (m)	0.206
Outer radius (m)	0.386
Height (m)	0.339
Magnet top to model distance (m)	1.0
Maximum current density (A/m^2)	2.0×10^{7}
Maximum winding field (T)	3.0
Magnet current (A)	500.0

TableIII1 lists the specifications of the 5 superconducting solenoids used to levitate the permanent magnet core. The coils are optimized to have the least ampere-meters. The 500 A conductor chosen for this design is a one triplex of an 11 kA ac conductor used in our previous suspension designs.[1,2] The 500 A triplex has a twist pitch of 2.2 cm. Each part of the triplex is a seven-strand conductor. The seven-strand conductor is six OFHC copper wires twisted around a superconducting center conductor and all soldered with Staybrite. Since the requirements of low ac losses and cryostability conflict with each other, the basic principle chosen for this conductor is to achieve cryostability within the basic cable. Each superconducting strand has a diameter of 0.051 cm and contains 2041 filaments of 6.7 μm dia with a twist pitch of 1.27 cm. The copper-to-superconductor ratio for each superconducting strand is 1.8. The reported losses on this conductor at a cycle that has $\dot{B} = 9$ T/s during charge and discharge are summarized in TableIII2.

TableIII2.

ac Losses of the 500 A Triplex Conductor.

Eddy current losses (J/cycle/m)	0.21
Hysteresis loss (J/cycle/m)	10^{-5}

Exact losses have not been calculated because finding the rms value of the correction currents is beyond the scope of this work. $|\Delta I/I|$ ranges between 10^{-4} to 10^{-2} depending on the yaw position and off-center signals. An estimate of ac losses for 500 A triplex conductor is about 200 W. The inductance matrix for the 5 levitation magnets is listed in Table V-3, as based on single turn coils. The maximum possible force between magnets is 18.5×10^4 N.

A distance of 9 cm from the top of the cryostat to the tip of the magnets is assumed for calculation purposes. It now appears that 13 cm is a more practical choice for final design.

TableIII3.

Inductance Matrix in H for the 5 Superconducting Levitation Magnets Based on Single Turn Coils.

	Coil #1	2	3	4	5
Coil #1	2.99×10^{-7}	--	--	--	--
2	1.09×10^{-8}	2.99×10^{-7}	--	--	--
3	2.49×10^{-9}	1.09×10^{-8}	2.99×10^{-7}	--	--
4	2.49×10^{-9}	2.49×10^{-9}	1.09×10^{-8}	2.99×10^{-7}	--
5	1.09×10^{-9}	2.49×10^{-9}	2.49×10^{-9}	1.09×10^{-8}	2.99×10^{-7}

III. 2. Nitrogen Cooled Magnet System

TableIII4 lists the specifications for 5 nitrogen cooled copper solenoids used to levitate the permanent magnet model core. The coils are optimized for minimum ohmic heating. Each of the 5 levitation coils is a stack of pancakes of rectangular OFHC copper turns. The cooling surface is the surface between pancakes. For the optimized dimensions listed in Table V.1, the maximum heat flux q in W/cm^3 at the cooling surface for N pancakes is

$$q = 14.2/N \quad .$$

For N = 30 the heat flux is less than 0.5 W/cm^2 (which is small). Each pancake is 12 turns of 6kA square conductor 1.95 cm high. The separation between pancakes is 0.524 cm. There is 1 mm of insulation between turns. The maximum turn to turn ohmic voltage is 0.5 volt. The space between pancakes allows outward flow in the radial direction.

TableIII4.

Specification of LN_2-Cooled Levitation Coils with PM Model Core

Number of magnets	5
Location radius (m)	0.7
Inner radius (m)	0.141
Outer radius (m)	0.386
Magnet height (m)	0.737
Magnet top to model distance (m)	1.0
Maximum gross current density (A/m^2)	1.203×10^7
% Copper volume	75
Total copper weight (kg)	1.007×10^4
Total power for 5 magnets (w)	2.926×10^5
Maximum power per magnet (w)	1.157×10^5
Magnet current (kA)	5

Each coil will be cooled as follows:

1. Variable flow along bore (single phase)
2. Constant radial outward flow (two phase)
3. Variable two phase flow along outer circumference.

Using low pressure 2 atm. boiling nitrogen cooling the flow rate for each coil is 124 gallon/m (994 ft^3/hr) at 10% exit quality. The pressure drop along the central bore (1) is negligible compared to the pressure drop between pancakes (2) which is 0.05 psi. The pressure drop in the outer region (3) is 0.0077 psi/ft. This is so low compared to the 0.05 psi drop across pancakes that the flow will be close to uniform.

Preliminary design of the liquid nitrogen cryostat is aimed at determining minimum practical spacing from the top of the magnets to the upper surface of the vacuum jacket plate. Results of these calculations are presented in TableIII5.

TableIII5.

Magnet to Warm Surface Spacing for Liquid Nitrogen-Cooled Solenoids.

Item	Space cm	Accumulated Space cm
Top of magnet	0	0
Flow space	0.3	0.3
Cold structure	2.0	2.3
Pressure deflection	0.3	2.6
Composite cold top plate	2.5	5.1
Insulation space	2.5	7.6
Top plate deflection	0.8	8.4
Composite top plate	2.0	10.4
Minimum total space from top of magnet		10.4

N91-21202

STABILITY CONSIDERATIONS for MAGNETIC SUSPENSION SYSTEMS USING ELECTROMAGNETS MOUNTED in a PLANAR ARRAY

Nelson J. Groom
Mail Stop 161
NASA Langley Research Center
Hampton
VA 23665-5225

Colin P. Britcher
Department of Mechanical Engineering and Mechanics
Old Dominion University
Norfolk
VA 23529-0247

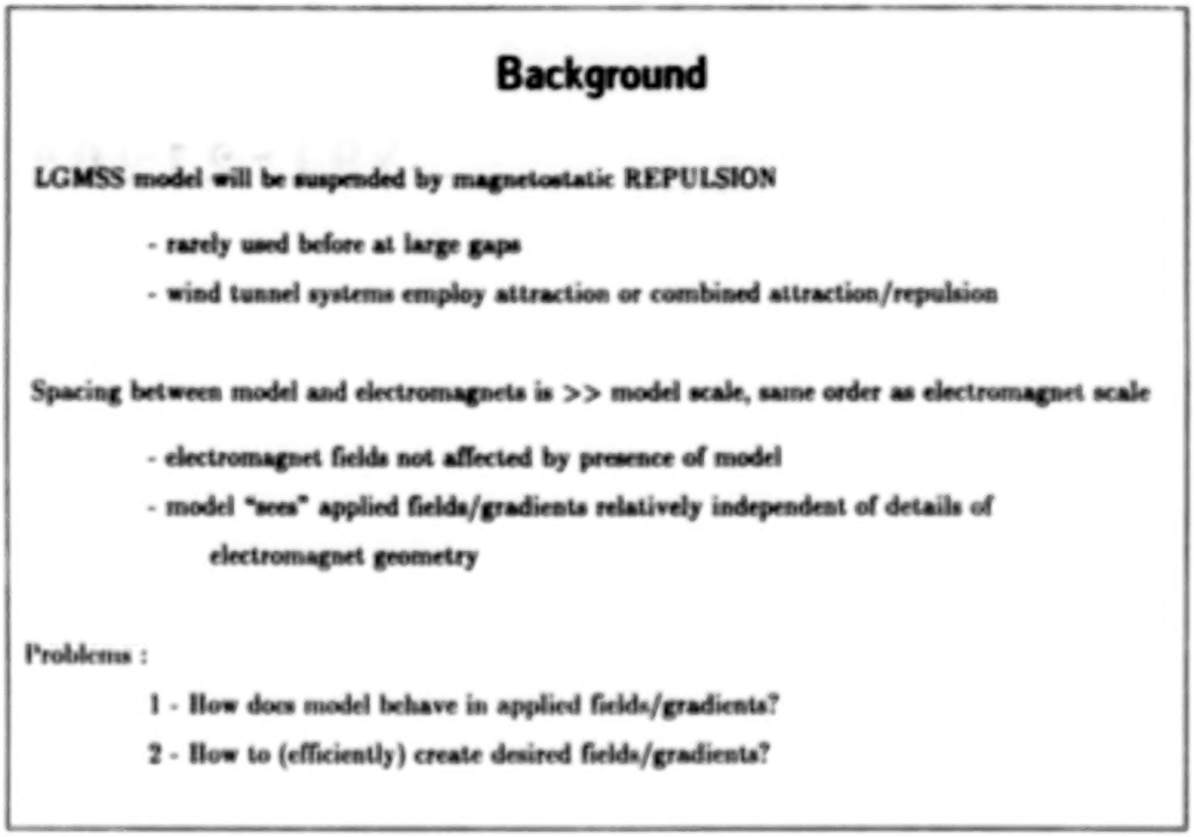

Background

LGMSS model will be suspended by magnetostatic REPULSION

- rarely used before at large gaps
- wind tunnel systems employ attraction or combined attraction/repulsion

Spacing between model and electromagnets is >> model scale, same order as electromagnet scale

- electromagnet fields not affected by presence of model
- model "sees" applied fields/gradients relatively independent of details of electromagnet geometry

Problems :

1 - How does model behave in applied fields/gradients?
2 - How to (efficiently) create desired fields/gradients?

The Large Gap Magnetic Suspension System (LGMSS) has been described in the two previous presentations. The analytic approach adopted is similar to that used for many years with wind tunnel Magnetic Suspension and Balance Systems (MSBS), which are also large-gap systems. The motivation for the present study is the concern that the use of a repulsive suspension approach may present new problems of stability and dynamics.

Model

Model is cylindrical permanent magnet, uniformly magnetized in the $\overline{X}$ direction

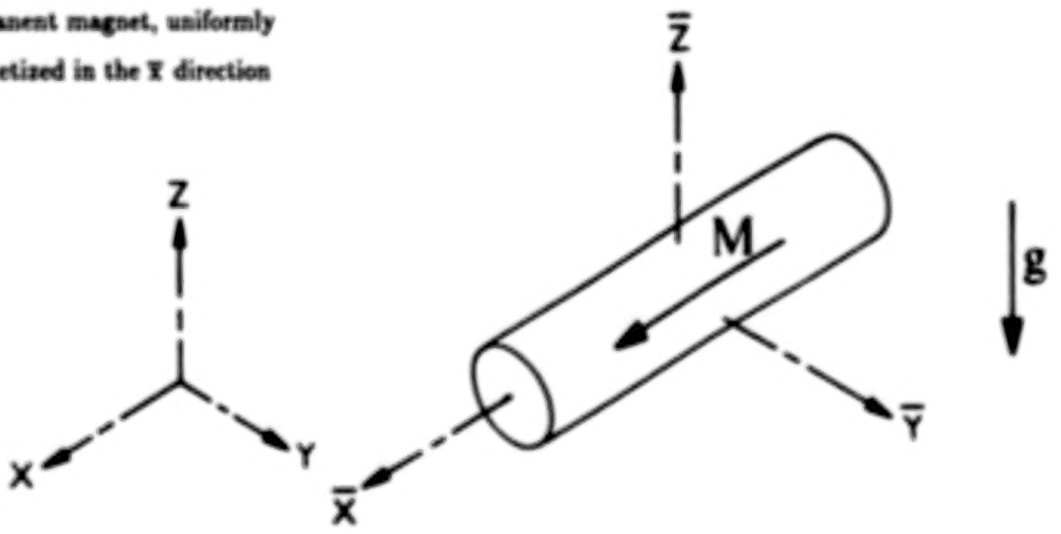

Allow small translations and rotations from datum

Use Euler angles - θ_x (roll), θ_y (pitch), θ_z (yaw) to specifiy orientation

The cylindrical model core (magnetic material contained within the final model envelope) is the originally specified configuration. Axial magnetization is the most natural choice and is the configuration chosen for wind tunnel MSBSs. The key point of interest is the natural behaviour of the model in the quasi-steady applied fields required to suspend the deadweight of the model.

Governing Equations

$$\delta\vec{F} = (\vec{M}\,.\,\nabla)\vec{B}\;\delta V \qquad\qquad \delta\vec{T} = (\vec{M}\times\vec{B})\;\delta V$$

$\vec{B}$ is applied $\vec{B}$ from electromagnets,
Provided $\vec{M}$, $\vec{B}$ are relatively uniform over magnetic core then :

$$\vec{F} \simeq \mathrm{Vol}\,(\vec{M}\,.\,\nabla)\,\vec{B}_{\mathrm{centroid}}$$

$$\vec{T} \simeq \mathrm{Vol}\,(\vec{M}\times\vec{B}_{\mathrm{centroid}})$$

For the configuration chosen, these approximate and simplified equations are adequate and again correspond to traditional practice with wind tunnel MSBSs [Refs 1,2]

Force and Torque Equations

Expanding force and torque expressions and using small rotations :

$$T_{\bar{y}} = \text{Vol}\ M_{\bar{x}}\ (-\theta_y B_x - B_z)$$

$$T_{\bar{z}} = \text{Vol}\ M_{\bar{x}}\ (-\theta_z B_x + B_y)$$

$$F_{\bar{x}} = \text{Vol}\ M_{\bar{x}}\ (B_{xx} + 2\,\theta_z\, B_{xy} - 2\,\theta_y\, B_{xz})$$

$$F_{\bar{y}} = \text{Vol}\ M_{\bar{x}}\ (-\theta_z\, B_{xx} + B_{xy} + \theta_z\, B_{yy} - \theta_y\, B_{yz})$$

$$F_{\bar{z}} = \text{Vol}\ M_{\bar{x}}\ (\theta_y\, B_{xx} + B_{xz} + \theta_z\, B_{yz} - \theta_y\, B_{zz})$$

With small displacements :

$$B_x \simeq \left\{B_x\right\}_o + \left\{B_{xx}\right\}_o x + \left\{B_{xy}\right\}_o y + \left\{B_{xz}\right\}_o z + \text{etc} \cdots$$

$$B_{xx} \simeq \left\{B_{xx}\right\}_o + \left\{(B_{xx})_x\right\}_o x + \left\{(B_{xx})_y\right\}_o y + \text{etc} \cdots$$

Following some manipulation, the force and torque equations reduce to this form. Further details can be found in References 3,4. By way of illustration, the {Vol $M_{\bar{x}}$ B_z} term in the $T_{\bar{y}}$ equation is considered the "primary" term and arises directly from the expansion of the vector cross-product. In the same equation, the {Vol $M_{\bar{x}}$ $\theta_y B_x$} term indicates a tendancy for the magnetization vector to align itself with an applied field - the "compass needle" effect.

The effect of core translations is incorporated in the evaluation of fields at the model centroid. The subscript "o" implies evaluation at the datum, untranslated origin.

Reduction to State-Space Form

Choose model STATE of $\left\{ \Omega_y \;\; \Omega_z \;\; \theta_y \;\; \theta_z \;\; V_x \;\; V_y \;\; V_z \;\; x \;\; y \;\; z \right\}$

- no torque about x axis - roll degree-of-freedom
- model is initially in equilibrium (determined separately)

Write perturbation equations in STATE-SPACE form -

$$\left\{\delta \dot{X}\right\} = \mathcal{A} \left\{\delta X\right\} + \mathcal{B} \left\{\delta I\right\}$$

Specify "weighting" matrix ($\mathcal{W}$), carry model mass and inertia on leading diagonal

With further manipulation, detailed more fully in References 3,4, the equations of motion can be reduced to State-Space form, where the model state is actually a perturbation from equilibrium. The equilibrium conditions, notably the electromagnet currents, are determined seperately.

"A" and "B" matrices

$$\mathcal{A} = \mathrm{Vol}\ M_{\overline{X}}\ \mathcal{W} \begin{bmatrix} 0 & 0 & -B_x & 0 & 0 & 0 & 0 & -B_{xz} & -B_{yz} & -B_{zz} \\ 0 & 0 & 0 & -B_x & 0 & 0 & 0 & B_{xy} & B_{yy} & B_{yz} \\ 1 & 0 & 0 & 0 & 0 & 0 & 0 & 0 & 0 & 0 \\ 0 & 1 & 0 & 0 & 0 & 0 & 0 & 0 & 0 & 0 \\ 0 & 0 & -2\,B_{xz} & 2\,B_{xy} & 0 & 0 & 0 & (B_{xx})_x & (B_{xx})_y & (B_{xx})_z \\ 0 & 0 & B_{yz} & (B_{yy}-B_{xx}) & 0 & 0 & 0 & (B_{xy})_x & (B_{xy})_y & (B_{xy})_z \\ 0 & 0 & (B_{xx}-B_{zz}) & B_{yz} & 0 & 0 & 0 & (B_{xz})_x & (B_{xz})_y & (B_{xz})_z \\ 0 & 0 & 0 & 0 & 1 & 0 & 0 & 0 & 0 & 0 \\ 0 & 0 & 0 & 0 & 0 & 1 & 0 & 0 & 0 & 0 \\ 0 & 0 & 0 & 0 & 0 & 0 & 1 & 0 & 0 & 0 \end{bmatrix}$$

$$\mathcal{B} = \mathrm{Vol}\ M_{\overline{X}}\ \mathcal{W} \begin{bmatrix} -K_{z_1} & \cdots & & \\ \vdots & \ddots & & \\ & & (10 \bullet 5) & \\ & & & \end{bmatrix}$$

The $\mathcal{A}$ matrix determines the system's dynamics. The form shown above is reasonably general. The field and field gradient terms are the equilibrium suspension values. Thus for any desired system configuration and detail design, values can be quickly evaluated and the model dynamics found from the eigenvalues and eigenvectors.

The $\mathcal{B}$ matrix is filled with coefficients specifying the field and field gradient components generated by each electromagnet in turn.

5 - Coil System

$$I_o = I_{max} \left\{ -0.7753,\ -0.2417,\ 0.6293,\ 0.6293,\ -0.2417 \right\}$$

Coil #	B_x (Tesla)	B_y	B_z	B_{xx} (T/m)	B_{xy}	……
1	0.0216	0	-0.0198	0.0092	0	
2	0.0067	0.0206	-0.0198	-0.0269	0.0118	
3	-0.0175	0.0127	-0.0198	-0.0046	-0.0191	
4	-0.0175	-0.0127	-0.0198	-0.0046	0.0191	
5	0.0067	-0.0206	-0.0198	-0.0269	-0.0118	

- calculated using OPERA (from VF/GFUN, TOSCA), using cartesian polynomial fitting of field at grid points

Natural Modes

MODE 1	14.3 rad/s	Unstable divergence	x, θ_y	Axial + pitch
MODE 2	4.6 rad/s	Stable oscilliatory	x, θ_y	Axial + pitch
MODE 3	12.9 rad/s	Unstable divergence	θ_z	Yaw rotation
MODE 4	5.0 rad/s	Stable oscilliatory	z	Vertical motion
MODE 5	2.5 rad/s	Unstable divergence	y	Lateral translation

The electromagnet configuration corresponds to one of the final designs emerging from the Madison Magnetics Incorporated design study (Reference 5). Equilibrium suspension is achieved with the current distribution shown, e.g. 77.53% of maximum design current in Coil number 1, the sign determined by the arbitrary sign convention chosen (see later Figure). The $\mathcal{B}$ matrix can be constructed directly from the field and field gradient terms indicated in the Table. The coefficients of the $\mathcal{A}$ matrix are found by summation of the products of each coefficient with the relevant current fraction. Field calculations are carried out using an analysis and post-processing package, "OPERA", which uses numerically evaluated integral expressions for field around simple conductor geometries. Once the $\mathcal{A}$ matrix is found, eigenvalues and eigenvectors are found using "PC-MATLAB". The frequency, stability and shape of each mode is of interest. Mode 5 is rather benign (low frequency) and represents the model, in a sense, "falling off" the suspension electromagnets. Stability in suspension height is expected in a repulsive mode suspension and is shown in Mode 4. Mode 3 is the "compass needle" effect, with the model attempting to reverse direction so as to align the magnetization vector with the axial (B_x) field. Mode 1 appears to represent similar behaviour in the orthogonal plane, though coupling into translation is exhibited. Mode 2 is an unexpected result. Unstable translation would have been expected by analogy with Mode 5.

5-Coil System

Inner radius	**0.173m**
Outer radius	**0.386m**
Depth	**0.493m**
Location radius	**0.7m**
Max. current density	**1535.87 A/cm^2**

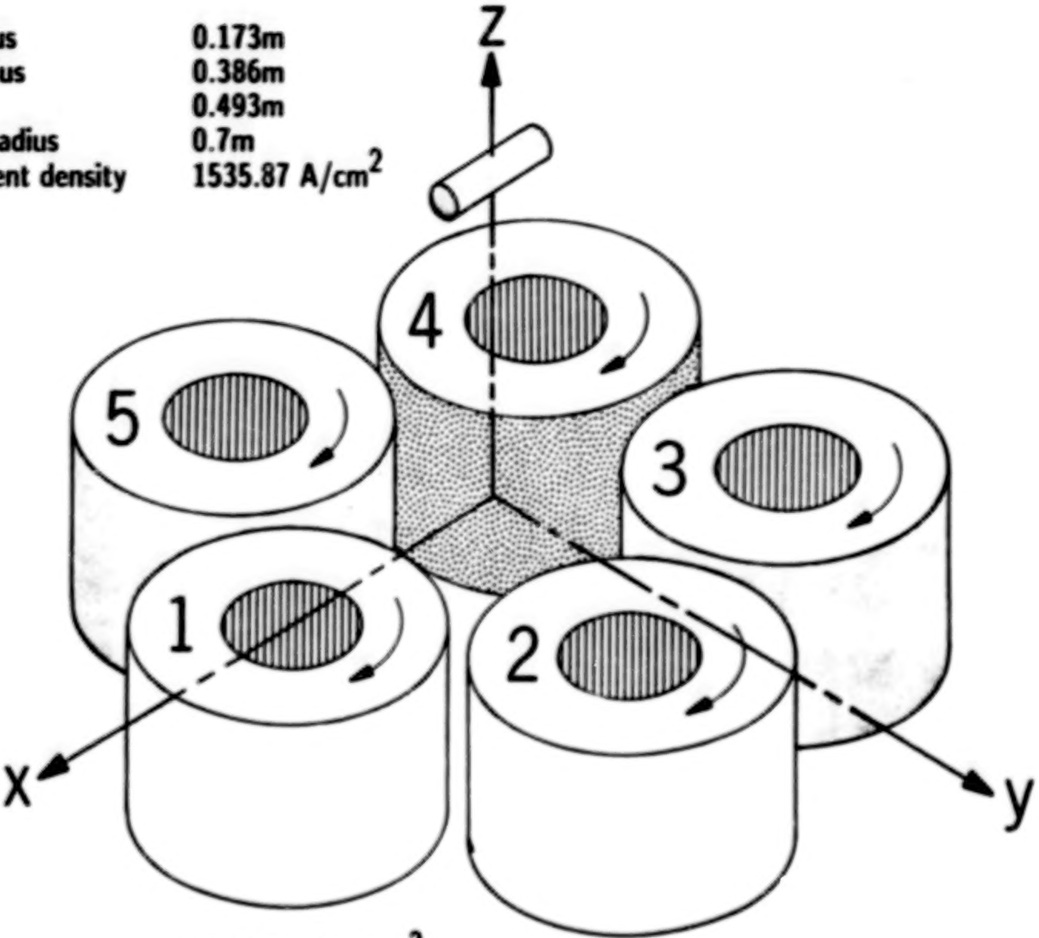

Model	**23.11 kg, 0.6kg m^2**
Permanent magnet	**0.1016m dia. * 0.3048m, 1.2 Tesla**

The important dimensions of the Madison Magnetics design and the sign convention for positive current direction are shown here. The levitation height, measured from the model axis to the top face of the electromagnets, is 0.9144m (36 inches).

Natural Modes

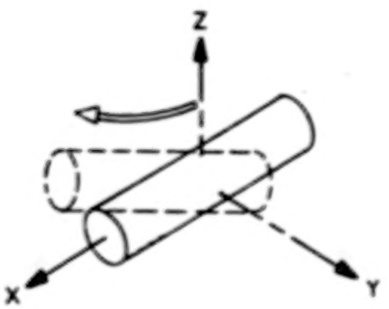

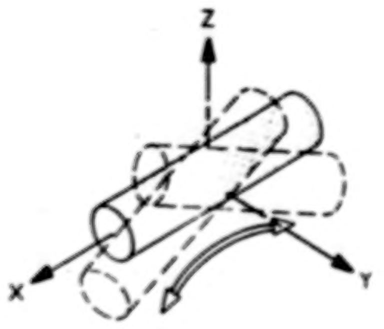

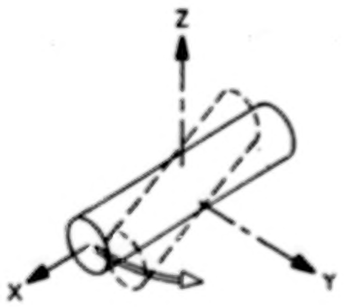

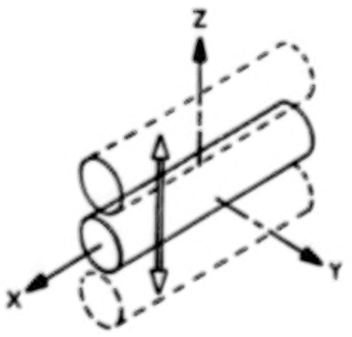

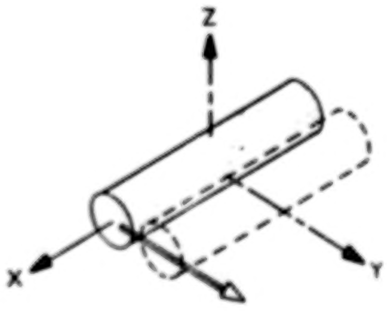

The three unstable modes are :-

Mode 1 - shown top left; Mode 3 - shown center and Mode 5 - lower right

The two stable, oscilliatory modes are :-

Mode 2 - shown top right and Mode 4 - shown lower left

Origins of Modes ?

Suppose only B_{xz} applied (to support weight of model)

MODE A	9.3 rad/s	Unstable divergence	x, θ_y	Axial + pitch
MODE B	9.3 rad/s	Stable oscilliatory	x, θ_y	Axial + pitch

Adding B_x (typical value)

MODE A	14.3 rad/s	Unstable divergence	x, θ_y	Axial + pitch
MODE B	6.9 rad/s	Stable oscilliatory	x, θ_y	Axial + pitch
MODE C	12.9 rad/s	Unstable divergence	θ_z	Yaw rotation

In order to better understand the origin of Modes 1 and 2, the $\mathcal{A}$ matrix was re-solved with unnecessary field and field gradient terms arbitrarily zeroed. With only the gradient required to generate the lifting force on the model (opposing weight), two modes are found, vaguely approximating Modes 1 and 2 as previously shown. If the axial field is re-applied, still holding all "second-order gradients" (terms of the form $(B_{ij})_k$ zero, the stable oscilliatory mode is moved to a lower frequency, the unstable mode to a higher frequency. The "compass-needle" mode (Mode 3) now appears.

Effect of Rotation in Azimuth (Yaw)

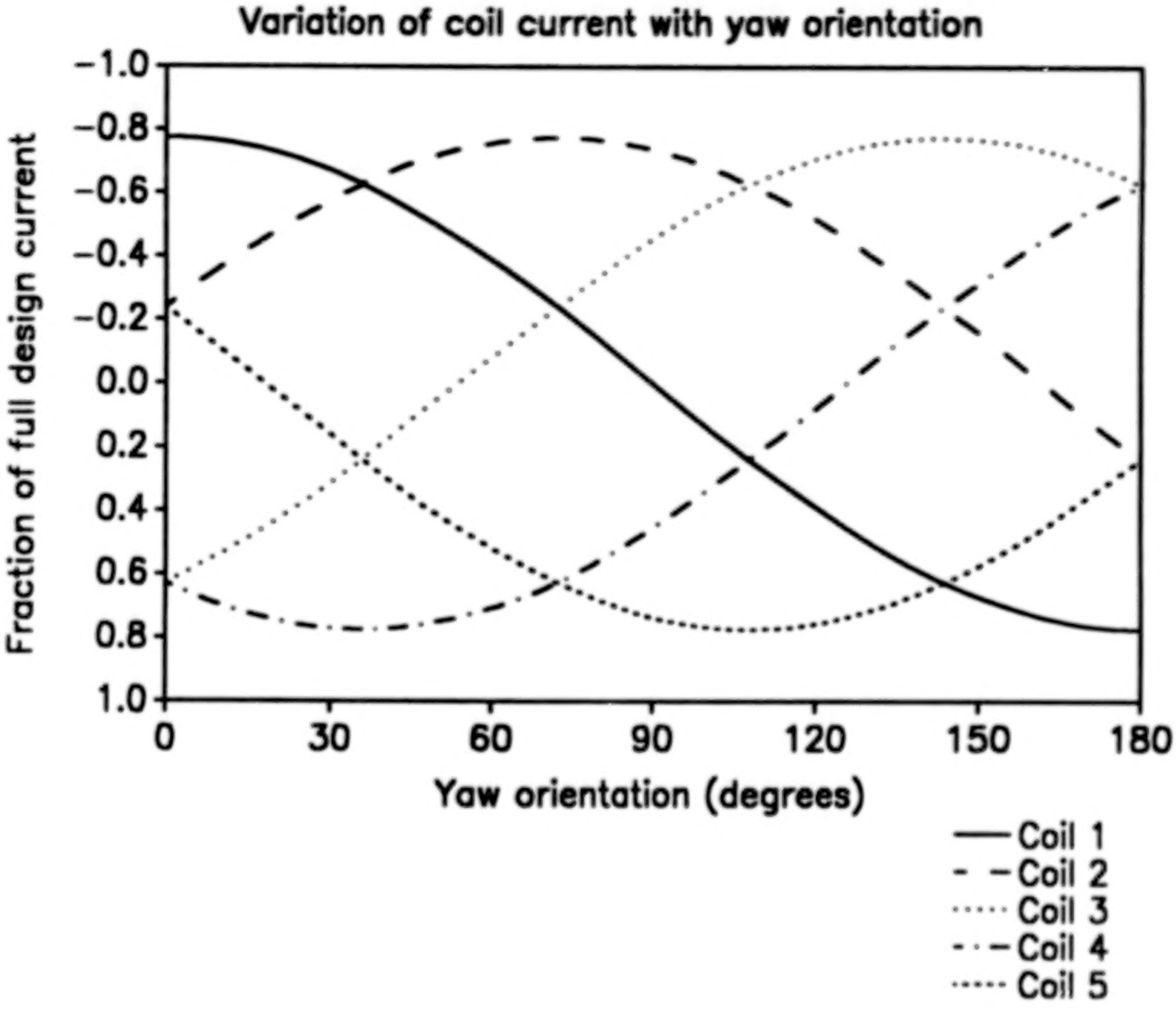

As the model rotates about the vertical axis, electromagnet currents are smoothly redistributed between electromagnets. The current variation in each electromagnet is virtually sinusoidal. It is found that there are no significant changes in the model's modes of motion as the rotation proceeds.

Six Coil System

Try to control B_x ($\Rightarrow 0$).

$$\text{Find } \frac{I_{B_x}}{I_{B_{xz}}} = \begin{bmatrix} 0.933 \\ 1.0 \\ 1.0 \\ 0.933 \\ 1.0 \\ 1.0 \end{bmatrix}$$

Currents are all large and roughly +/-/+/-/+/- for normal suspension with $B_x = 0$

In an attempt to lower the frequency of the highest frequency unstable mode, an attempt is made to control the value of B_x, preferably forcing it to zero. This is only feasible if an additional eletromagnet is added to the configuration. This is done by preserving the same individual electromagnet geometry and spacing between electromagnets, but locating all at a larger radius.

It is quickly found that the resulting configuration is ineffective in controlling B_x. This is due to the fact that the current distribution required to generate the gradient B_{xz} is virtually identical to that required to generate B_x, each field or field gradient component being generated independently of all others in both cases.

6-Coil System

Inner radius	0.173m
Outer radius	0.386m
Depth	0.493m
Location radius	0.822m
Max. current density	1535.87 A/cm^2

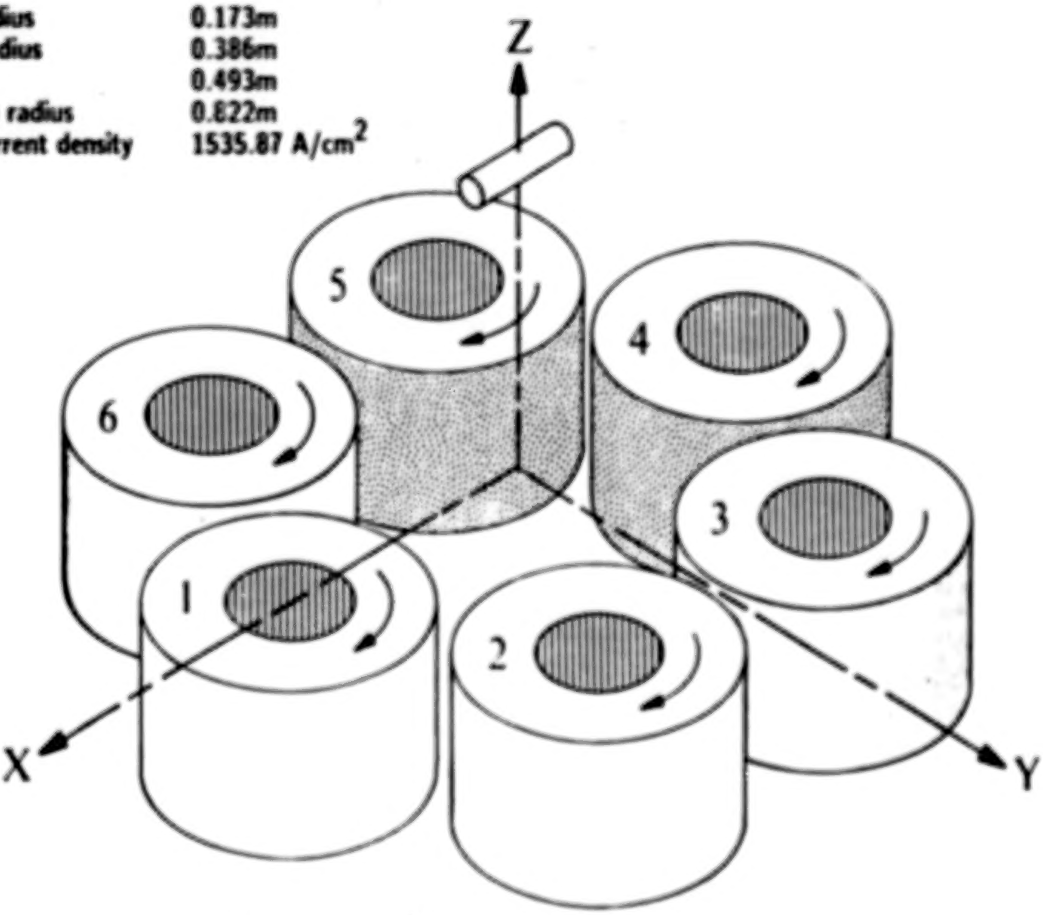

Model	23.11 kg, 0.6kg m^2
Permanent magnet	0.1016m dia. × 0.3048m, 1.2 Tesla

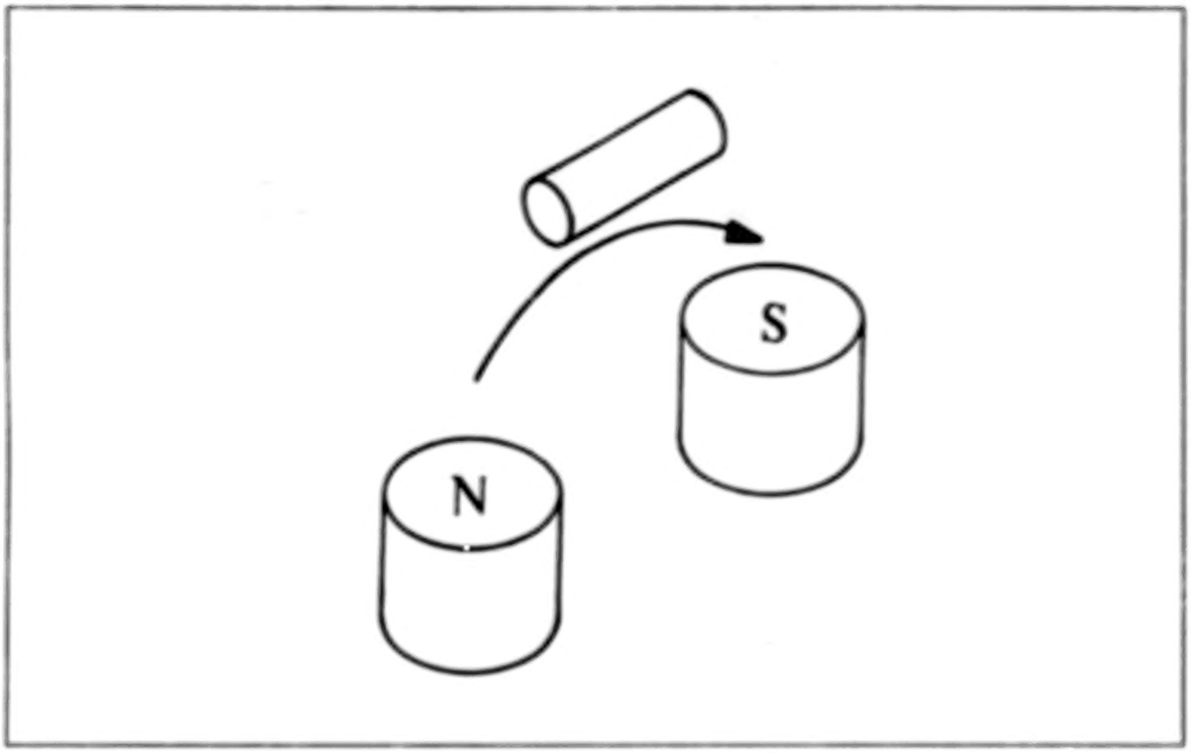

The cause of the problem is easily understood with a North-South pole representation. The model requires a N-S pole pair distributed along the x axis as shown. This inevitably generates an axial field in the direction opposite to the model magnetization.

It can be noted that in wind tunnel MSBSs, this problem either does not arise, if electromagnets are located symmetrically above and below the model, or is exploited, where electromagnets are only positioned above the model, creating a useful natural magnetizing field.

Seven / Eight Coil Systems

Attempt to control B_{xz_y} to produce rolling moment (T_x) with non-axisymmetric core.

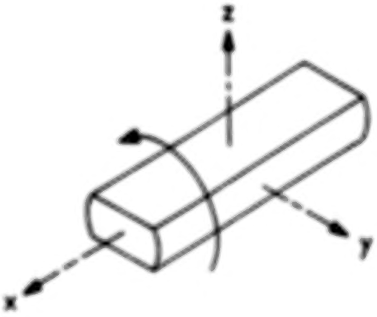

Problem:

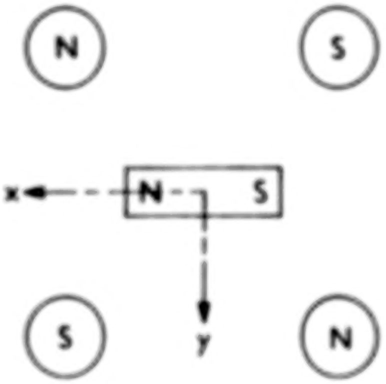

Nevertheless, apparently just possible with 7-coil system

8-coil system has excessive symmetry and will not produce B_{xz_y}

Wind tunnel systems have high level symmetry with coils clustered on all sides of suspended model

Assuming that the axial field cannot be sensibly controlled, attention is turned to the possibility of generating a lateral gradient of the "lift" field gradient, B_{xz_y}, which has been exploited in wind tunnel MSBS work in the past, for generation of rolling moment. If possible, this would provide a means for controlling the 6th degree of freedom, presently presumed to be passively stabilized.

It is found that the system does not work for the 6-electromagnet arrangement, due to the "roll" field being generated by a current distribution identical to that required for the generation of lateral force, F_y. Additional electromagnets are therefore added, in this case requiring a reduction in size of each, along with an increase in the radius of their centers. The total ampere-turns in each electromagnet is held constant. It is found that the problem of inseparability of roll and sideforce again arises with the 8-electromagnet arrangement. With only 7 electromagnets, the symmetry of the arrangement is of a sufficiently low order to permit separation of these two fields, though not very effectively.

7-Coil System

Inner radius	**0.160m**
Outer radius	**0.358m**
Depth	**0.457m**
Location radius	**0.883m**
Max. current density	**1785.5 A/cm^2**

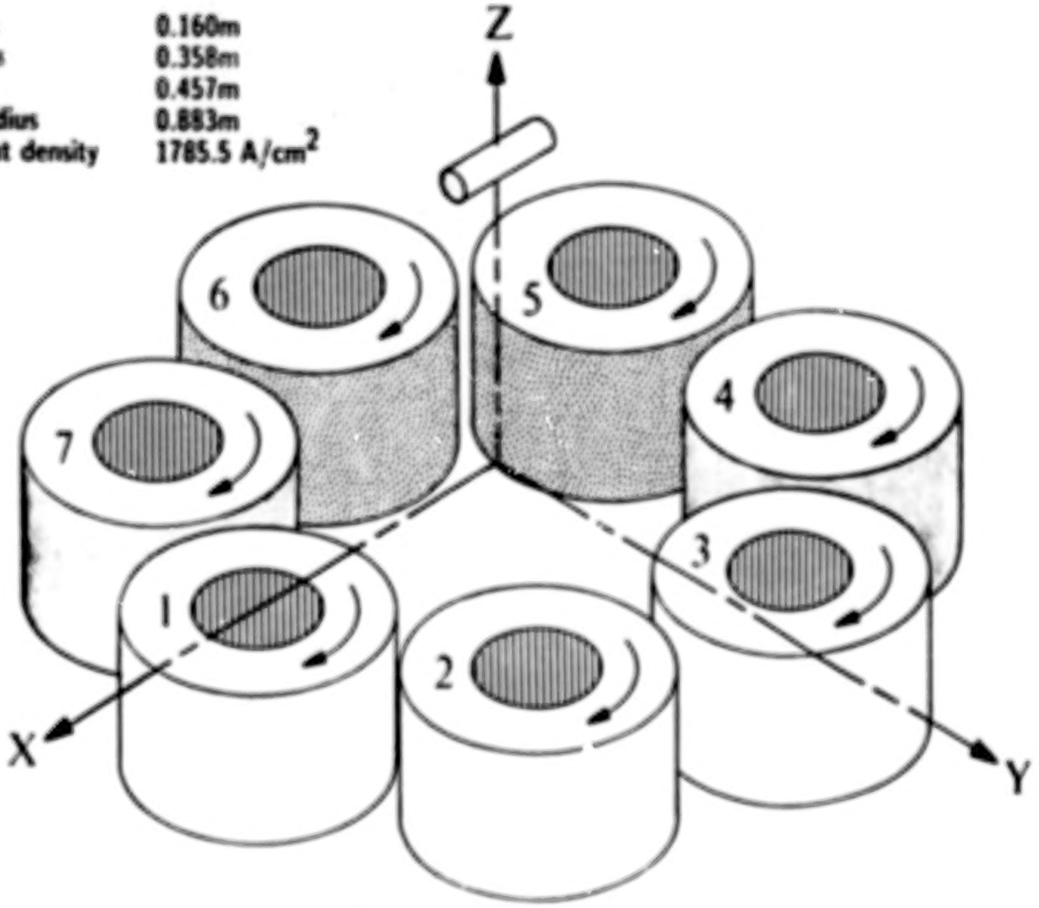

Model	**23.11 kg, 0.6kg m^2**
Permanent magnet	**0.1016m dia. • 0.3048m, 1.2 Tesla**

8-Coil System

Inner radius	**0.152m**
Outer radius	**0.339m**
Depth	**0.433m**
Location radius	**0.952m**
Max. current density	**1991.83 A/cm^2**

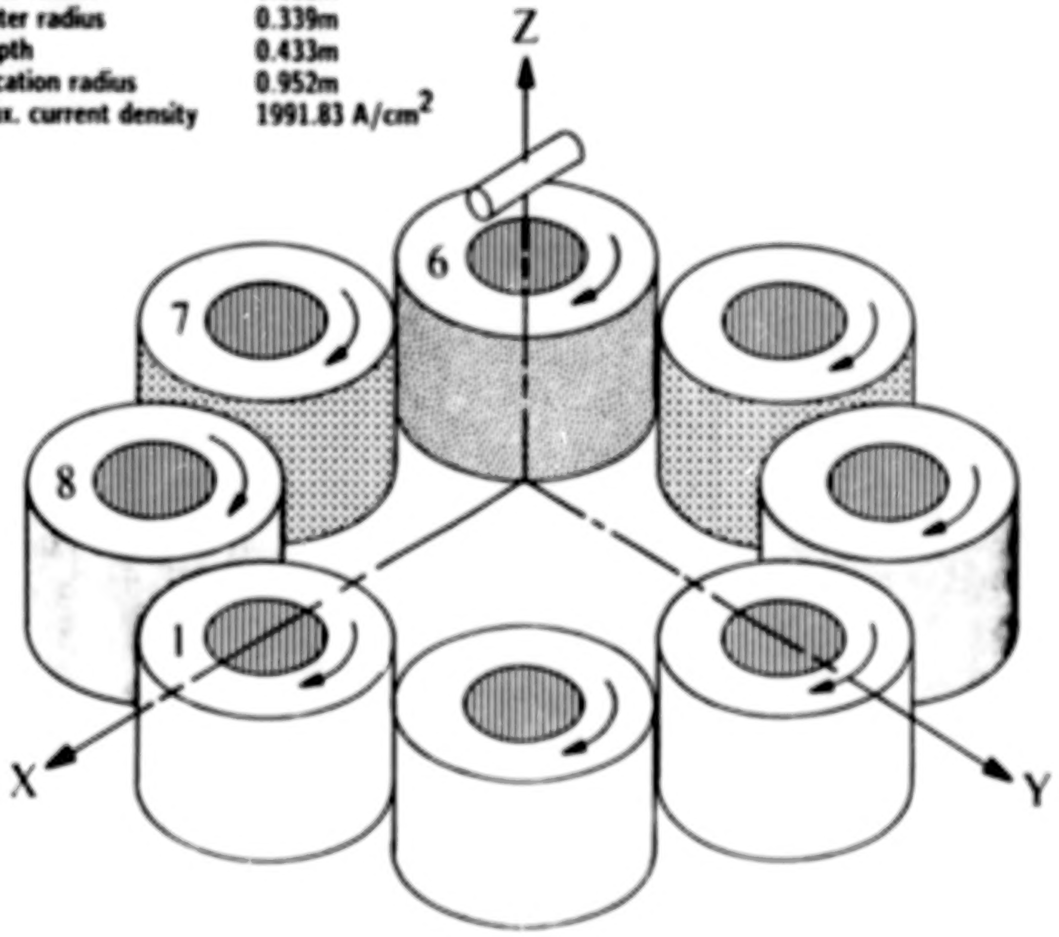

Model	**23.11 kg, 0.6kg m^2**
Permanent magnet	**0.1016m dia. • 0.3048m, 1.2 Tesla**

Future Work

Incorporate modal analysis into control system simulation and design

- may require coupled axial and pitch degrees-of-freedom
- high frequency unstable modes place burden on power supplies and controller in LGMSS application

Study second-order effects

Study influence of eddy currents

Simulation efforts are underway, extending work reported in References 3,4. To achieve optimum performance, the coupling between the axial translation and pitch degrees-of-freedom needs to be addressed. Existing work with wind tunnel MSBSs has dealt with similar effects by insertion of a "decoupling" matrix into the control loops, such that the controller can be configured as 5 (or 6) parallel and quasi-independent loops, each stabilizing one of the natural degrees-of-freedom. Other approaches are possible.

Conclusions - N-coil ring

Will work for 5 degree-of-freedom control

360 degree azimuth (θ_z) range easily achieved

Large motion capability around datum expected

Have to control all currents in (superconducting) electromagnets

6th degree-of-freedom can be passively stabilized if $\vec{g}$ present

Alternative roll control schemes are available

If $\vec{g}$ present, highest frequency modes are a problem

With $\vec{g}$ absent, modes may not be a problem

These conclusions are based on this study and the results of previous design studies for 5- and 6-electromagnet configurations. At present, design work for the LGMSS is focusing on an alternative configuration, where the axis of magnetization is vertical, parallel with the gravity vector.

Speculation

Change the direction of magnetization ??

With vertical magnetization (parallel to $\vec{g}$), B_{zz} would support weight. Can (must) arrange B_z to provide roll/pitch stability.

Modes would be :

Stable oscilliatory	θ_x	Provided B_z is correct sign
Stable oscilliatory	θ_y	Provided B_z is correct sign
Neutral	θ_z	Depends on system axisymmetry
Unstable divergent	x	Highly dependant
Unstable divergent	y	on electromagnet
???????	z	configuration

It appears possible to achieve a lower value of the frequency of the highest frequency unstable modes, by aligning the magnetization vector with the gravity vector. Further analysis is required of this and other possible configurations.

C-5

References

1. Britcher, C.P.: Some Aspects of Wind Tunnel Magnetic Suspension Systems with Special Application at Large Physical Scales. NASA CR-172154, September 1983.

2. Britcher, C.P.: Technical Background for a Demonstration Magnetic Levitation System. NASA CR-178301, May 1987.

3. Groom, N.J.: Analytical Model of a Five Degree of Freedom Magnetic Suspension and Positioning System. NASA TM-100671, March 1989.

4. Groom, N.J.; Schaffner, P.R.: An LQR Controller Design Approach for a Large Gap Magnetic Suspension System (LGMSS). NASA TM-101606, July 1990.

5. Boom, R.W.; Abdelsalam, M.K.; Eyssa, Y.M.; McIntosh, G.E.: Repulsive Force Support System Feasibility Study. NASA CR-178400, October 1987.

Acknowledgements

This work was partly supported by NASA Grant NAG-1-1056, Technical monitor Nelson J. Groom.

National Aeronautics and Space Administration

Report Documentation Page

1. Report No. NASA CP-10066, Part 1	2. Government Accession No.	3. Recipient's Catalog No.

4. Title and Subtitle Aerospace Applications of Magnetic Suspension Technology	5. Report Date March 1991
	6. Performing Organization Code
7. Author(s) Nelson J. Groom and Colin P. Britcher, Editors	8. Performing Organization Report No.
	10. Work Unit No. 590-14-11-02
9. Performing Organization Name and Address NASA Langley Research Center Hampton, VA 23665-5225	11. Contract or Grant No.
	13. Type of Report and Period Covered Conference Publication
12. Sponsoring Agency Name and Address National Aeronautics and Space Administration Washington, DC 20546-0001	14. Sponsoring Agency Code

15. Supplementary Notes

Nelson J. Groom: Langley Research Center, Hampton, Virginia.
Colin P. Britcher: Old Dominion University Research Foundation, Norfolk, Virginia.

16. Abstract

In order to examine the state of technology of all areas of magnetic suspension with potential aerospace applications, and to review related recent developments in sensors and controls approaches, superconducting magnet technology, and design/implementation practices, a three-day Workshop on Aerospace Applications of Magnetic Suspension Technology was held at the Langley Research Center in Hampton, Virginia, on September 25-27, 1990. A total of 28 papers were presented covering the areas of pointing and isolation systems, microgravity and vibration isolation, bearing applications, wind tunnel model suspension systems, large gap magnetic suspension systems, controls, rotating machinery, science and applications of superconductivity, and sensors. In addition to the presentations, there was a panel discussion on applications of superconductivity. A copy of each paper presented at the workshop and an edited transcript of the panel discussion is included. A list of attendees is presented in an Appendix.

17. Key Words (Suggested by Author(s)) Magnetic Bearings, Magnetic Suspension, Large Gap Magnetic Suspension, Small Gap Magnetic Suspension, Sensors, Superconducting Magnetic Suspension Systems, Control Systems	18. Distribution Statement Unclassified - Unlimited Subject Category 18

19. Security Classif. (of this report) Unclassified	20. Security Classif. (of this page) Unclassified	21. No. of pages 385	22. Price A17

NASA FORM 1626 OCT 86 For sale by the National Technical Information Service, Springfield, VA 22161-2171

END

DATE

FILMED

JUN 3 1991